Springer Proceedings in Physics 136

Jongmin Lee
Chang Hee Nam
Karol A. Janulewicz *Editors*

X-Ray Lasers 2010

Proceedings of the 12th International Conference on X-Ray Lasers, 30 May – 4 June 2010, Gwangju, Korea

Springer

Springer Proceedings in Physics 136

Springer Proceedings in Physics

Please view available titles in *Springer Proceedings in Physics* on series homepage http://www.springer.com/series/361/

Editors

Jongmin Lee · Chang Hee Nam
Karol A. Janulewicz

X-Ray Lasers 2010

Proceedings of the 12th International Conference on X-Ray Lasers, 30 May–4 June 2010, Gwangju, Korea

Springer

Jongmin Lee
Advanced Photonics Research Institute
Gwangju Institute of Science and Technology
Gwangju 500-712
Republic of Korea

Chang Hee Nam
Department of Physics and
Coherent X-ray Research Centre
Korea Advanced Institute of Science
and Technology
Daejeon 305-701
Republic of Korea

Karol A. Janulewicz
Advanced Photonics Research Institute
Gwangju Institute of Science and Technology
Gwangju 500-712
Republic of Korea

Published by Springer,
P.O. Box 17, 3300 AA Dordrecht, The Netherlands
In association with
Canopus Academic Publishing Limited,
15 Nelson Parade, Bedminster, Bristol, BS3 4HY, UK

www.springer.com and www.canopusbooks.com

ISSN 0930-8989 e-ISSN 1867-4941
ISBN 978-94-007-1185-3 e-ISBN 978-94-007-1186-0
DOI 10.1007/978-94-007-1186-0
Springer Dordrecht Heidelberg London New York

Library of Congress Control Number: 2011921002

Preface

The 12th International Conference on X-Ray Lasers was held at the Gwangju Institute of Science and Technology between 30 May and 4 June 2010. The talks were presented in the International Collaboration Building belonging to the complex of the Advanced Photonics Research Institute's Ultra-short Quantum Beam Facility hosting the Korean petawatt laser system. The conference was held in Korea for the first time and gave, in a series of oral and poster sessions, a broad review of the activities in the field of coherent short-wavelength sources.

The meeting brought about 80 attendees from 14 countries in the world. It was a great pleasure for the organizers to host the many participant family members who enjoyed their first visit to such an exotic and fascinating country. The participant list confirmed a well-established core of conference visitors, but we found, not without satisfaction, that "newcomers" also enjoyed the conference and were satisfied with its environment. The event also provided an opportunity to publicize X-ray laser research to the Korean based science community and to boost X-ray laser research in Korea.

The conference program was organized to promote closer contacts and better understanding between different subfields of the research into coherent short-wavelength radiation sources. That was the reason for organizing separate sessions dedicated to X-ray Free Electron Lasers (XFELs), sources based on relativistic interaction with matter and incoherent sources in both the keV and XUV spectral ranges. This aspect is not fully covered by this book for different reasons, but it was interesting to observe that the idea "caught on". The conference confirmed the well-established status of X-ray lasers with their well-understood physics, and presented intriguing questions to be answered for further progress and development. This point was clearly supported by the increased number of contributions relating to applications of the short-wavelength sources.

The scientific schedule of the conference was supplemented by a social program, including trip to an amazing ecological system of the Suncheon Bay, a wetland preservation area registered in the Ramsar convention. The conference dinner, held in the Oryong Hall – the GIST convention center – was preceded by a stunning demonstration of traditional Korean music and dance. This event culminated in a joint performance by the artists and conference attendees.

There were many people who contributed to the successful organization of the conference. We are not able to list all of them but we would like to express our special gratitude to Drs Chul Min Kim, Hyung Taek Kim and I Jong Kim as well as to Mrs Ga Young Cha and Mr Ho Jong Kang from APRI staff. In addition, we acknowledge the generous sponsorship from the Gwangju Convention and Visitors Bureau, Korean Physical Society, Optical Society of Korea, the Ultra-Short Quantum Beam Facility Program of the Ministry of Knowledge Economy of Korea, Korea Electro-Optics, DPI, Dada, Laser Spectra, CVI Melles Griot, Coherent, Horiba Korea Ltd., Jinsung Laser, Alcatel Korea, Golden Light Co., Lee Optics, Qbic Laser System Inc. and Thales Laser.

Finally, we owe a pleasant debt of appreciation to the conference attendees and contributors for their willingness to participate in the conference and finally to contribute to this book.

Jongmin Lee
Chang Hee Nam
Karol A. Janulewicz


12th International Conference on X-Ray Lasers
May 30 – June 4, 2010 Ultrashort Quantum Beam Facility
Hosted by APRI GIST
Sponsored by
apri
고등광기술연구소

Contents

Part 1: X-Ray Laser Systems

Recent results and future plans for XRLs using the TARANIS laser facility

C.L.S. Lewis[1], T. Dzelzainis[1], D. Riley[1], D. Doria[1], S. Whyte[1], M. Borghesi[1] G. Nersisyan[1], D. Marlow[1], K. McKeever[1] and G.J. Tallents[2]

[1] Center for Plasma Physics, Queen's University Belfast, Belfast, BT9 5ED
[2] Physics Department, University of York, Y010 5DD, UK.

Abstract. The results of an investigation into X-ray lasing in Ni-like Sm, pumped by a frequency doubled pre-pulse and a fundamental short pulse, are presented. Strong lasing was observed across the $4d_{3/2}$-$4p_{3/2}$ transition at 7.3 nm. A weaker laser line of wavelength 6.9 nm was also present from the $4d_{3/2}$-$4p_{1/2}$ transition. The XRL output was seen to be sensitive to both delay between the pre-pulse and the heating pulse and also to the energy in the heating pulse. The results are compared to those from a similar experiment employing pre-pulses at the fundamental wavelength and the output of the XRL is shown to be enhanced by at least two orders of magnitude for the same target lengths. An application for an XRL pumped by Taranis is discussed.

1 Introduction

Lasing in the region below 10 nm using a ~psec pump pulse been has been the subject of a limited number of experimental investigations [1],[2]. Extending the scheme to elements heavier than Sm poses problems. Firstly, the psec scheme employs a time delay between the pre-pulse and the main pulse to allow the plasma to expand. This reduces density gradients and subsequently refraction of the XRL pulse in the plasma to a point where the pulse can propagate the entire length of the plasma within the gain region. This must be balanced against the cooling of the plasma with expansion, so that a peak delay is found where the density gradients are sufficiently shallow, but the plasma is still at the required ionisation stage. With higher Z-elements, the higher temperature required to achieve a substantial Ni-like population, and the increased electron density required to increase the collisional excitation rate to compensate for the increased radiative decay rate between the laser levels requires the delay to be shorter until the point is reached where the optimum time for the pump pulse is almost directly after the pre-pulse, into steep density gradients. This is usually the case for elements with $Z>62$ (Sm). For higher Z-number elements the additional problem arises of the optimum pumping density being higher than the critical density of Ti:Sapphire and Nd:Glass systems, which are commonly used XRL pump lasers. The problem

J. Lee et al. (eds.), *X-Ray Lasers 2010,* Springer Proceedings in Physics 136,
DOI 10.1007/978-94-007-1186-0_1,

of the high density gradients can be overcome by using a combination of second harmonic pre-pulse and fundamental main pulse. This allows the plasma/solid interface to be pushed back to higher densities than the region pumped by the main pulse, allowing the high temperatures, high densities and shallow density gradients to co-exist. The dynamics of short wavelength x-ray lasers pumped with ~ps pulses was the subject of a recent study by Pert [3],[4] where simulations of XRLs pumped with a laser such as VULCAN, using the second harmonic for the prepulse and the fundamental wavelength for the main heating pulse are discussed. The studies by Pert form the theoretical basis for the following experiment. Two colour pumping has previously been investigated with lower Z-number targets and was found to enhance the output of a Ni-like Ag XRL at 13.9nm and, furthermore, stimulate emission on a previously unobserved line identified as the $4f\,^1P_1 - 4d\,^1P_1$ transition [5].

2 Experimental Configuration

The experiment was carried out at the Central Laser Facility, UK and the chamber layout is shown in Figure 1.

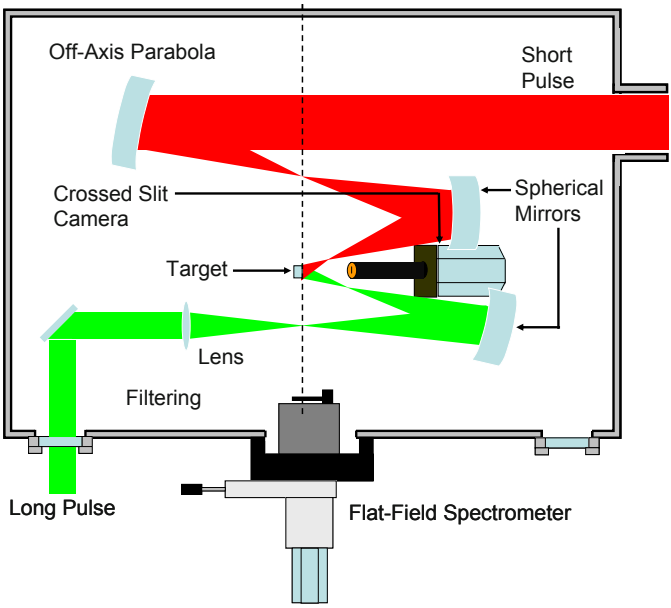

Fig 1. Experimental layout for investigation into short wavelength lasing with two-colour pumping.

The pre-plasma is formed by one or two ~300 ps, frequency-doubled beams, focussed to a line of nominal length 6 mm by identical focusing systems. The focusing system consists of a lens followed by a tilted spherical mirror, giving a near normal incidence line focus. The beams were able to focus at the same

point in the chamber by exploiting the cylindrical symmetry of the optical system about the XRL axis. Energies up to 120 J were available in second harmonic for the pre-pulse, giving a maximum possible average irradiance of 3×10^{14} Wcm^{-2} on target. The short pulse was focussed initially by an off-axis-parabola, and then allowed to expand before being focussed to a line by the tilted spherical mirror. Energies up to 100 J in a pulse of ~750 fs were available at the fundamental wavelength, giving a maximum possible average irradiance of ~10^{17} Wcm^{-2}. Traveling wave pumping was achieved by the tilting of the wave-front by insertion of a grating into the beam path before it entered the target area. This is a technique that has been employed successfully on Vulcan in previous experiments [6][7]. The traveling wave speed was measured with an optical streak camera to be ~0.94c. Samarium coated glass slabs were placed at the overlap position of the three beams. A crossed slit camera was used to observe the uniformity and overlap of the line foci. This observed the plasma column from below the experimental plane. A crystal spectrometer with a KAP crystal, positioned above the experimental plane confirmed the presence of Ni-like ions in the plasma as in Figure 2.

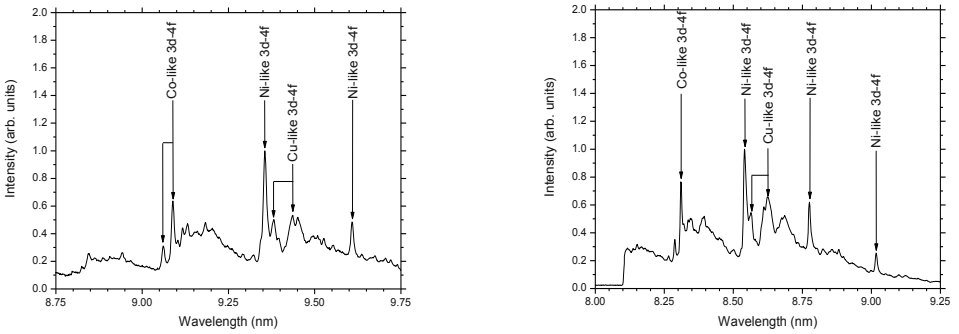

(a) (b)

Fig 2. Spectral line-outs from the crystal spectrometer showing Ni-, Co- and Cu-like emission. Although the line ratios are similar in Sm (a) to those observed in Gd (b) only the Sm targets showed strong laser action.

3 Results

3.1 Samarium

Strong lasing was observed for Samarium targets with 40-50 J in the pre-pulse (average irradiance ~10^{14} Wcm^{-2}) and 60-70 J in the short pulse (average irradiance ~5 × 10^{16} Wcm^{-2}). A spectral line-out of a strong laser shot using these energies is shown in Figure 3. Two lasing lines are seen in first and second order. The strongest emission was observed at 7.3 nm arising from the

$4d_{3/2}$-$4p_{3/2}$; lasing is also seen on the $4d_{3/2}$-$4p_{1/2}$ transition, but considerably weaker. Figure 4 shows the angular distribution of the two laser lines. The stronger line is fitted with a Gaussian centred at 5.32 ± 0.03 mrads and with a FWHM of 5.56 ± 0.09 mrads.

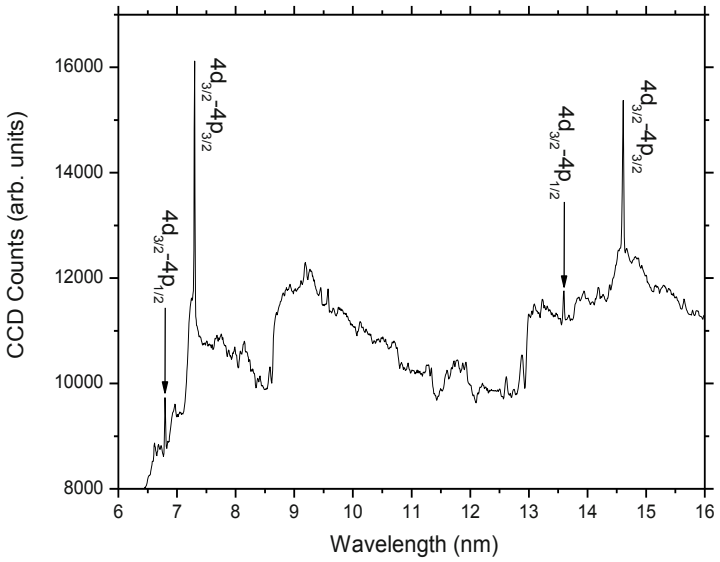

Fig 3. Spectral line-out of the image obtained from the FFS. The two Sm XRL lines are seen in first and second orders. The $4d_{3/2}$-$4p_{3/2}$ is seen to dominate the spectrum.

The output of the XRL was observed to vary with both the energy in the CPA beam and delay between long and short pulses. Figure 5 (LHS) gives a summary of the measured XRL output at varying delay and with differing energy in the CPA and long pulses. The data taken with 30-40 J in the CPA and 40-50 J in the long pulse suggests maximum output at delays between 100 and 150 ps, with low signal seen at 50 ps and no lasing observed at 200 ps. The shots taken with 60-70 J in the CPA pulse and 40-50 J in the long pulse with a 150 ps delay show a much higher energy output than for the 30-40 J data. There is also slightly increased emission at 200 ps when 110-120 J were used in the long pulse and 60-70 J in the CPA. Time constraints prevented a full parameter scan being carried out and so the information about the behaviour of the XRL output with respect to pump energy and delays is very limited. The dependence on short pulse energy of the XRL output suggests that the short pulse energy was near the threshold for generation of laser action.

In order to assess the success of this pumping scheme, we can compare the results to those reported by King et al [2]. Such a comparison requires confidence in the data analysis procedures used in each case (ie different experiments and different detector setup). We have used a rigorous approach

to make reliable estimates of all the relevant factors (eg counts to energy conversion, QE of CCD, filter transmissions, grating efficiency etc) and in all cases where there is uncertainty we have erred on the side of reducing the "measured" XRL energy. In reference [2] the fundamental wavelength was

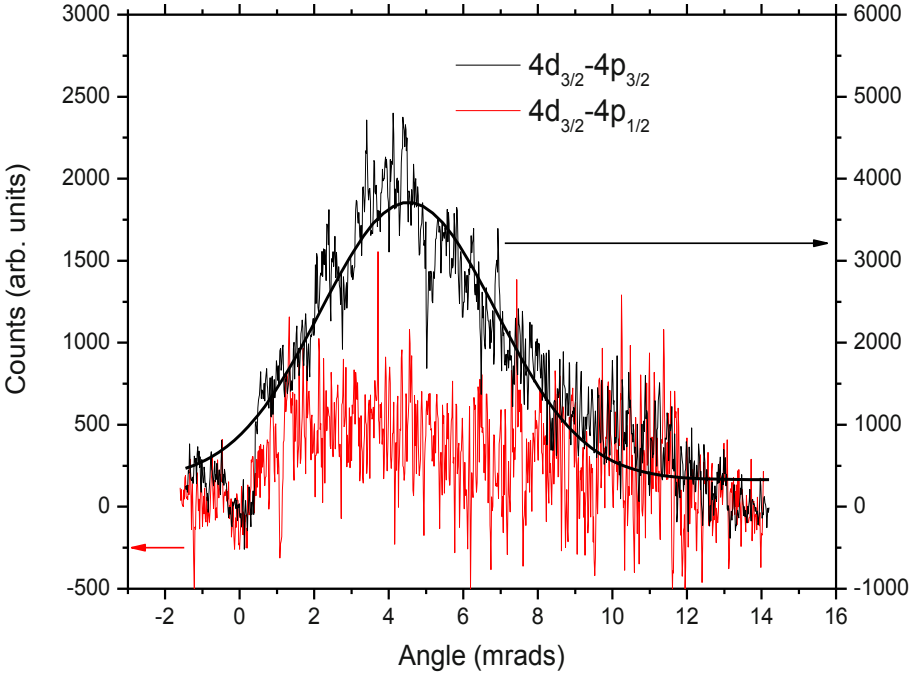

Fig 4. Angular distributions of the two lasing lines. The stronger $4d_{3/2}$-$4p_{3/2}$ line is fitted with a Gaussian curve centred at 5.32 ± 0.03 mrads, with a FWHM of 5.6 ± 0.1 mrads

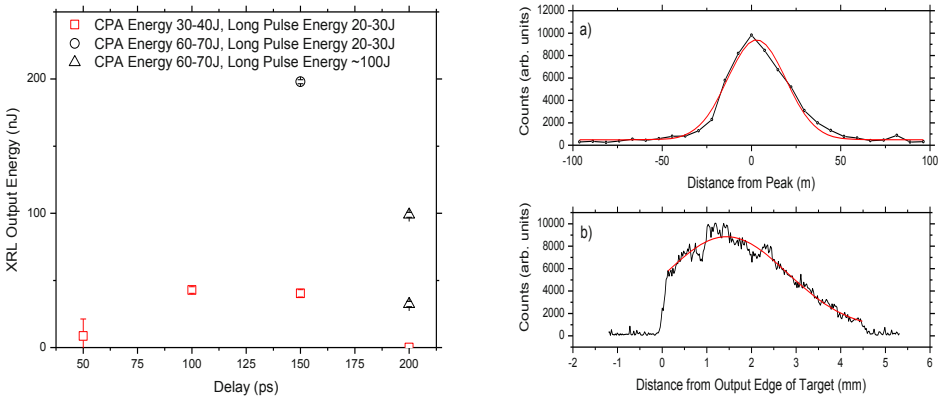

Fig 5. (LHS) Summary of the Sm XRL energy for a range of pumping conditions with 5 mm long targets and (RHS) Line focus profiles in the directions perpendicular a) and parallel b) to the XRL axis.

used for the pre-pulse with an irradiance of ~1 × 10^{13} Wcm^{-2} and pulse duration 280 ps, which is similar to the irradiance and pulse duration used in this experiment to obtain strong lasing in Sm ($2\times10^{13}Wcm^{-2}$). In reference [2], the pump pulse used had an intensity of ~3 × 10^{15} Wcm^{-2} with a duration of 3 ps, and the XRL energy output was ~1nJ for target lengths of 5 mm. As shown in Figure 5 (LHS), the two colour pumping method demonstrated here produced an XRL output of ~50 nJ for 5 mm target lengths using an energy of 30-40J in the pump pulse and ~200nJ of XRL energy using an energy of 60-70J in the pump pulse, corresponding to pump pulse intensities of ~1.5-2.9 × 10^{16} Wcm^{-2}. Some of the observed fluctuation in output can be attributed to line focus alignment issues. Profiles of the linefocus used in this experiment are shown in Figure 5 (RHS). The transverse profile is fitted with a Gaussian with a FWHM of 38 ± 6 μm. The axial lineout is fitted with a Gaussian with a FWHM of 3.2 ± 0.1 mm. The intensity profile shows strong emission at the output end of the XRL target, but due to the short linefocus length slightly underfills the 5 mm target. The linefocus width was seen to vary from shot to shot, reaching up to 100 μm FWHM. The asymmetry in the wider line foci suggest this was due to misalignment between the long and short pulses. It is likely that this added to the lack of reproducibility of the XRL which was also affected by fluctuations in the energy output of the VULCAN laser itself.

Although the data is limited we are nevertheless confident that that the range of outputs observed (circa 100 nJ) with 2ω-ω pumping is about 100 times higher than observed previously (circa 1 nJ) with ω-ω pumping. Also, it has to be appreciated that the pump pulse used in the current experiment was measured to be more than 4 times shorter than that used by King et al, meaning that the energy densities along the 5 mm line focus conditions in the two experiments are, in fact, very similar.

Modeling of the previous experiment was presented in [3] where it was concluded that the highest gain generated was in a region of steep density gradients which prevented efficient amplification in this region but that a region of reduced gain present further from the target in a region of lower density gradients was sufficient to observe significant output. The large increase in output energy observed supports the predictions made by the simulations that the second harmonic pre-pulse is generating a plasma with reduced density gradients at the turning point for the short pulse, and hence allowing effective XRL pulse propagation in the high electron density, and hence high gain, region.

3.2 Gadolinium and Dysprosium

Unsuccessful attempts were made to use this method to produce XRL output from Ni-like Gd and Ni-like Dy. Spectra obtained from the crystal spectrometer show that the plasma reached the Ni-like ionisation stage but

failed to show lasing action. The spectrum from Gd (see Figure 2b) showed line ratios extremely similar to those seen for a Sm target which produced strong lasing. Attempts to observe lasing were made with energies in the long pulse far in excess of those suggested necessary by simulation to achieve the correct ionisation stage in the pre-plasma, implying that the Ni-like population shown to be present by the crystal spectrometer data was generated during the long pulse, and not the result of a pre-plasma with lower than required ionisation being further heated by the main pulse. Unfortunately no spectra were obtained for shots using the long pulse only. We would also not have expected that high energy in the long pulse would have heated the plasma to the point where it is over-ionised, since lasing was observed in Sm for the highest long pulse energies. The problem is likely to lie with the main pulse and a failure to sufficiently raise the electron temperature to the point where effective gain generation occurs. The short pulse was measured during this experiment to be ~700 fs (ie shorter than the ~ 2 psec expected) and probably not optimum for efficient heating of the electrons.

4 XRL data from TARANIS

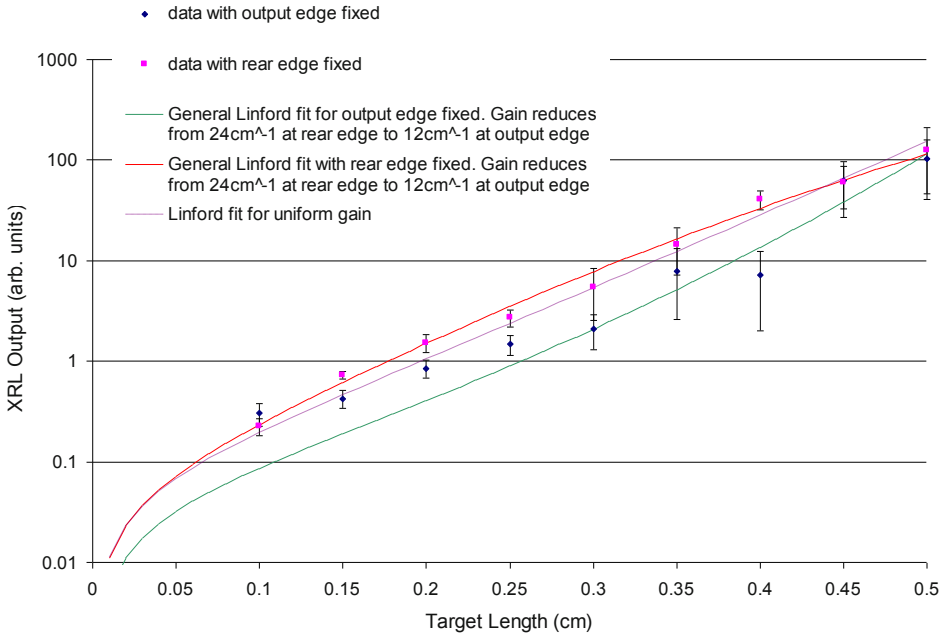

Fig 6. Growth curves for the $4d_{3/2}$-$4p_{3/2}$ line of Ni-like Mo at 18.9 nm showing asymmetry based on choice of where to fix the target edge within the line focus.

We have reported previously on preliminary saturated XRL output from Ni-like Mo and Ag targets pumped in the GRIP mode by the dual beam CPA laser housed in QUB [8],[9],[10]. During these investigations issues were raised as to the interpretation of growth curve shapes. To help elucidate the various factors, Figure 6 depicts an example where we have used right-angled triangular targets of sheet Mo mounted so that the vertical edge can be kept in a fixed location relative to the line focus pump distribution as the target is raised/lowered to access new lengths for shooting. The maximum target length (5 mm) was centred to align with the line focus but in one sequence the fixed edge was closest to the observing FFS (XUV flat field spectrometer) and in the second sequence it was furthest away. Several shots were taken for all lengths shot to monitor reproducibility and Figure 6 shows that a real trend exists. At the shortest and maximum lengths in each case XRL output is similar but the growth curves have clearly different shapes. In this particular case, it is probably mainly due to non-uniformity of pump intensity along the line affecting the local gain coefficient but amplification details can also be affected by axial variation of the travelling wave velocity and the spatial location (in the normal direction to the target surface) of the peak gain zone. Both of these are dependent on the optics focussing the heating pulse in the GRIP scenario and their optimisation will be a topic for future reports.

Analytical and numerical modelling can help design optimum conditions and experimentally these can be tested. Velocity mis-matches can be tested through "tilting" wave fronts and/or varying short pump pulse durations; axial pump uniformity can be controlled with phase plates and/or shaped masks in pump beam; the spatial gain zone envelope within the plasma can be controlled with F-number/optics to minimise XRL refractive "walk off", all of these need to be compatible with the most efficient pump coupling possible.

5 WDM probed by an XRL beam

The acceleration of proton beams from laser-irradiated solid targets has been investigated employing the TARANIS laser system operating in the compressed pulse mode. The laser pulse from one of the main compressors was focused onto a thin metal foil with an f/3, f = 300 mm off-axis parabola (OAP). The pulse after compression was ~ 10 J in energy and ~ 560 fs in duration, and the focal spot diameter (measured in the low power, non amplified mode) was ~ 10 µm, leading to an intensity on target ~ 5×10^{18} Wcm^{-2}. The targets were Aluminium foils of thickness ranging from 0.7 to 100 µm. The proton beam emitted from the rear target surface (i.e. the non-irradiated surface) in the target normal direction was detected employing multi-layer stacks of Gafchromic type HD-810 Radiochromic Films (RCFs). The RCF packs were wrapped in 11 µm aluminium foils in order to cut

unwanted heavy ion and soft x-ray signals and to shield the pack from target debris, therefore giving a minimum detectable proton energy of about 1 MeV. The multi-layer arrangement of the RCF stacks ensured a spectral multi-frame capability of the detection system. Protons with higher energies penetrate deeper in the stack and release their energy mainly in proximity of the Bragg peak. Each film in the stack acts as a filter for the following ones and spectrally selects the protons whose Bragg peak is localized within or in proximity of the active layer. Data from a typical RCF stack shows a spectrum resembling a truncated Boltzmann-like distribution, with a temperature of 2.3 ± 0.1 MeV, with small variations depending on the target thickness and with small shot to shot fluctuations. The total number of particles accelerated in a single shot is $\sim 5 \times 10^{11}$, corresponding to a integrated particle energy of ~ 0.5 J for particles with energy above 3 MeV (~ 1 J considering particles above 1 MeV) and to an efficiency in the conversion from laser energy into energetic protons of 0.5% (~ 1%). The dependence of the maximum proton energy on the target thickness was also investigated and a maximum proton energy of ~ 12 MeV was obtained for a target thickness between 6 and 10 μm. A detectable proton beam was accelerated for targets as thin as 1 μm, which is an indication of the high contrast level of the TARANIS laser system.

Since we have the capability of combining proton beams and XRL beams it is of interest to consider how they can be usefully applied. A possible scenario

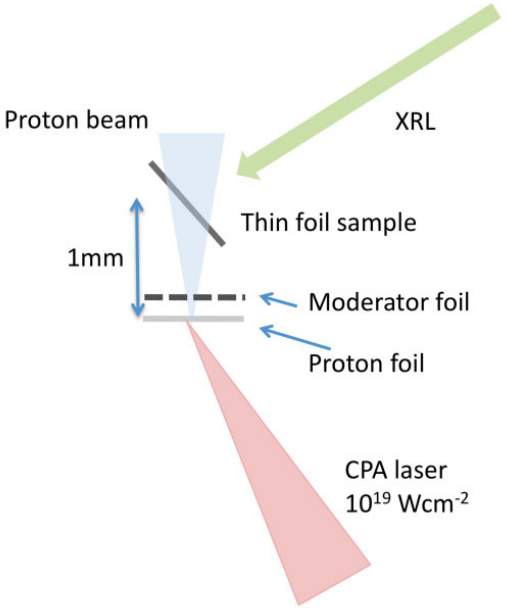

Fig 7. Schematic of a possible opacity experiment on proton heated matter. It is feasible for TARANIS to synchronously generate both the proton and XRL pulses.

is illustrated in Figure 7 whereby protons heat a thin foil to a few eV at near solid density and an XRL is used to makes opacity measurements of the resultant WDM.

Because there is a range in proton energies and a finite distance to the sample foil, the energy is deposited over a finite time as depicted in Figure 8a where we can see the temporal history of the deposition in a thin slice of the foil, buried 10 microns into the foil. This is simulated by assuming all energy is deposited into electrons and inserting this profile as an electron heating term into the Hyades hydrodynamic code for a case where we have a 10 micron thick moderator foil that slows the protons before they enter an 0.8 micron Al foil where they deposit energy uniformly in space but with the temporal history of Figure 8a. The resultant profile of density and temperature at the end of the heating pulse of protons is depicted in Figure 8b, where the density has remained high and the temperature has reached ~1.5eV. This will provide a benchmarking parameter for detailed hydrodynamic simulations comparing the effects of changing the equation of state and/or ionisation model on the hydrodynamic conditions and predicted opacity.

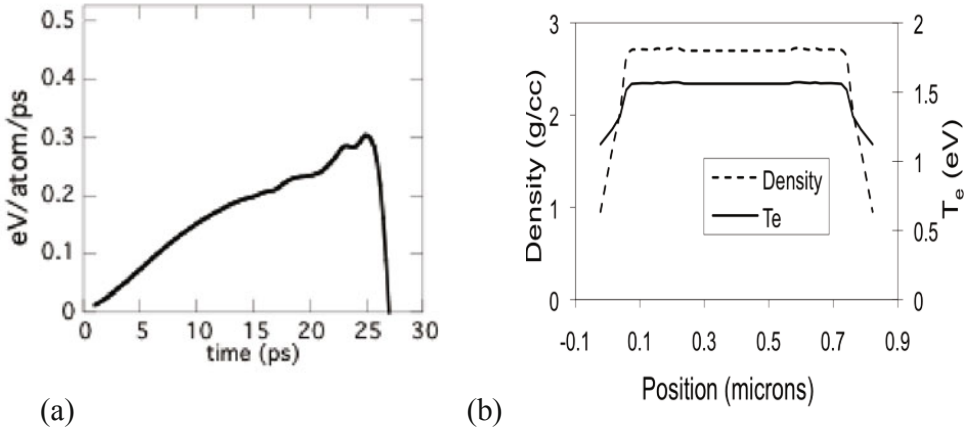

Fig 8..(a) Temporal history of proton heating effect and (b) Resulting WDM conditions to be probed with an XRL beam of psec duration.

Summary

An experiment at the Vulcan laser has demonstrated that two-colour pumping can significantly boost the XRL output for targets with atomic number in the region of Z ~ 60 and this is probably due to an ability to access and heat plasma at a higher density with sufficiently small density gradients to avoid serious refraction problems. The TARANIS laser has been used to generate

very bright beams of 18.9 nm and 13.9 nm XRLs and also proton beams with high fluence at up to ~12 MeV energy. We suggest an experiment to generate warm dense matter (WDM) conditions with protons to be diagnosed, with XRL photons as a means of validating equation of state (EOS) data.

Acknowledgements

The authors are grateful for financial support from the UK Engineering and Sciences Research Council under grants EP/C003586/1, EP/G007462/1 and EP/D06337X/1

References

1. Kawachi, T., et al.: 'Observation of strong soft-x-ray amplification at 8:8nm in the transient collisional-excitation scheme' *Phys. Rev. A.*, 69, 033805, 2004.
2. King, R. E., et al.: 'Saturated x-ray lasers at 196 and 73 a pumped by a picosecond traveling-wave excitation' *Phys. Rev. A.*, 64, 053810, 2001
3. Pert, G. J.: 'Optimizing the performance of nickel-like collisionally pumped x-ray lasers' *Phys. Rev. A.*, 73, 033809, 2006
4. Pert, G. J.: 'Optimizing the performance of nickel-like collisionally pumped x-ray lasers. ii. lasers for the wavelength range 50-100 Angstrom' *Phys. Rev. A.*, 75, 023808, 2007
5. Kuba, J., et al.: 'Two-color transient pumping in Ni-like silver at 13.9 and 16.1 nm' *Phys. Rev. A.*, 62, 043808, 2000
6. Lin, J. Y., et al.: 'Travelling wave chirped pulse amplified transient pumping for collisional excitation lasers' *Opt. Comm.*, 166, 211-218, 1999
7. Collier, J., et al.: 'The travelling wave focus on Vulcan' *Central Laser Facility Annual Report*, 1, 209-210, 1997
8. Nersisyan, G., et al.:'TARANIS: A pump source for X-ray lasers' *X-ray Lasers 2008 - Springer Proc. in Physics.* 130, 65-70, 2009
9. Dzelzainis, T., et al.: 'Ni-like X-ray lasing action pumped by the TARANIS laser system' *Proc. SPIE (Soft X-ray lasers and Applications VIII*, 7451, 745119, 2009
10. Dzelzainis, T., et al.: 'The TARANIS laser: A multi-Terawatt system for laser-plasma investigations' *Laser and Particle Beams*, 28, 451-461, 2010

Source Development and Novel Applications of Laser-Driven Plasma X-ray Lasers in JAEA

T. Kawachi[1], N. Hasegawa[1], M. Nishikino[1], M. Ishino[1], T. Imazono[1], T. Ohba[1], T. Kaihori[1], M. Kishimoto[1], Y. Ochi[1], M. Tanaka[1], M. Koike[1], M. Kado[1], K. Namikawa[2], T. Suemoto[3], K. Terakawa[3], T. Tomita[4], M. Yamamoto[1,4], N. Sarukura[5], H. Nishimura[5], A. Y. Faenov[1], S. Bulanov[1] and H. Daido[6] and Y. Kato[7]

[1]Quantum Beam Science Directorate, Japan Atomic Energy Agency (JAEA)
[2]Department of Physics, Tokyo University of Science
[3]Institute of Solid State Physics (ISSP), University of Tokyo
[4]Faculty of Engineering, University of Tokushima
[5]Institute of Laser Engineering (ILE), Osaka University
[6]Applied Laser Technology Institute, Japan Atomic Energy Agency (JAEA)
[7]Graduate School for the Creation of New Photonics Industries (GPI)

Abstract. This paper gives an overview of recent progress in the study of laser-driven plasma x-ray lasers in Japan Atomic Energy Agency (JAEA). Fully spatial coherent plasma soft x-ray laser (SXRL) at 13.9 nm with 0.1 Hz repetition rate is now routinely used in the wide variety of the applications: The highlights of these applications are the study of fluctuation in the atomic structure of ferroelectric substances under the phase transition using double SXRL probe technique and the first observation of surface dynamics of laser ablation with 10 ps-time and 1 nm-depth resolution using a single-shot SXRL interferometer.

1 Introduction

Advent of transient collisional excitation (TCE) scheme makes it possible for us to realize small size coherent soft x-ray lasers (SXRLs) [1-3]. In Japan Atomic Energy Agency (JAEA), we have firstly demonstrated fully spatial coherent x-ray laser beam at the wavelength of 13.9 nm by the method of double targets, in which the first gain medium works as the soft x-ray oscillator and the second gain medium works as the soft x-ray amplifier [4]. Successive optimization of the pumping condition such as the intensity of the pump, the temporal separation of the pre- and main-pulses and travelling wave realizes high quality and intense x-ray laser beam. The typical

J. Lee et al. (eds.), *X-Ray Lasers 2010,* Springer Proceedings in Physics 136,
DOI 10.1007/978-94-007-1186-0_2,

parameters of SXRL in JAEA are the beam divergence of better than 1 mrad, 1 μJ output energy and more than 10^9 photons in the coherent volume [5].

In a view point of the applications of the SXRLs, one of the most serious limitations so far was the repetition-rate. Typical shot interval of CPA Nd:glass driver was ~ 10 min, and this prohibited many potential users from conducting application experiments. The GRIP (grazing incidence pumping) scheme induced breakthrough in this problem: The 5-10 Hz spatially coherent SXRL with several tens nJ output energy has been obtained by the combination with higher-order harmonics as the x-ray seeder [6].

While this high average power SXRL is powerful tool for the soft x-ray imaging and nano-fabrication using multiple-shot exposure, there is also strong interest and requirement from material scientists for the probe beam to observe *non-periodic* or *non-repeatable* ultra-fast phenomena. For examples, nano-meter scale deformation of domain structure of substances under the phase transition is essentially *unrepeatable* phenomena; therefore single-shot observation is indispensable to observe the temporal or spatial correlation function of the generation and annihilation of the domains. Laser ablation is also *unrepeatable,* and observation of transient behaviour from solid phase to plasma phase is quite interesting in the view points of not only solid state physics and plasma physics but also the industrial applications such as laser processing and welding.

In order to improve the repetition-rate of SXRL, JAEA x-ray laser group has upgraded the pumping laser driver in 2008. The new driver system, TOPAZ, which is based on CPA Nd:glass laser. The highlight of TOPAZ is the zigzag slab-type amplifier chain, which enables us to operate this system with 0.1 Hz repetition-rate [7]. By use of TOPAZ laser, now the spatially coherent SXRL beam at 13.9 nm is routinely used for the application researches with adding minor revisions to improve the performance.

2 Application of SXRLs

The 13.9 nm laser in JAEA has been used for wide variety of application researches, such as material science [8,9], plasma physics, atom and molecular physics [10], soft x-ray imaging and laser processing [11] under the collaborations with universities and other institutes. For the next 5 years, FY2010-2014, one of the main objectives of soft x-ray laser research program in JAEA is development of the method to observe nano-scale dynamics of ultra-fast phenomena in substances, therefore we continue these collaborations to establish the optical pump & SXRL probe using x-ray speckle technique, x-ray interferometer and x-ray diffraction imaging. On the other hand, interaction of short-pulse SXRL with matter is quite interesting in terms of industrial application such as nano-scale laser fabrication and warm

dense matter physics which is the intermediate region of material science and plasma physics. In the following, we show several results of SXRL applications for these topics.

2.1 Observation of temporal correlation of fluctuation dynamics of domain of $BaTiO_3$ under the phase transition condition

A couple of years ago, we have firstly observed pico-second snap-shot of domain-structure of ferro-electric substrates, $BaTiO_3$, by use of the x-ray laser speckle technique [8], and the successive experiment revealed the existence of collective dipole moments (polarization clusters) under the phase transition condition of $BaTiO_3$ [9]. We extended this technique to *double* SXRL probes and tried to reveal the temporal correlation function of the polarization clusters by comparing two speckle signals temporally separated by τ.

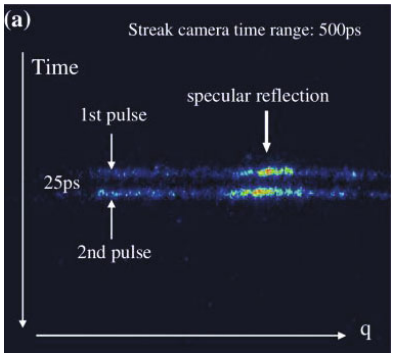

Fig.1. Soft x-ray speckle signal from double x-ray probes. From the comparison of these two speckles for various delay times, the temporal correlation of the domain fluctuation in $BaTiO_3$ is derived [12].

Temporal correlation of the two speckle signals is expressed by fourth order correlation of the scattered electric fields of SXRL pulses. The intensity correlation, $g^{(2)}$, is represented as follows.

$$g^{(2)} = \frac{\langle I(t)I(t+\tau)\rangle}{\langle I(t)\rangle_\tau^2} = 1 + \beta \exp\left(-\frac{2\tau}{\tau_0}\right) \qquad (1).$$

In Eq. (1), t and τ_0 is the time of the speckle measurement and the relaxation time of the polarization clusters. β is the square of the visibility defined by the first order correlation function of the incident electric fields of SXRL, *i.e.*, $E_0(t)$ and $E_0(t+\tau)$, where we assume that the delay is much larger than the relaxation time, *i.e.*, $\tau > \tau_0$.

In the experiment, the 13.9 nm laser was divided into two beams by Michelson-type double pulse generator based upon a free-stand Mo/Si multi-layer beam splitter. With certain delay time, two x-ray laser pulses probed the surface of $BaTiO_3$, and we recorded two speckle signals in the different time by the x-ray streak camera. Figure 1 shows typical speckle signals obtained

by this double SXRL probes. The abscissa is q and the ordinate is the time. In this case, the time delay was set to be 25 ps. Similar double probe measurements were repeated for various time delays, and the temporal correlation function was determined [12].

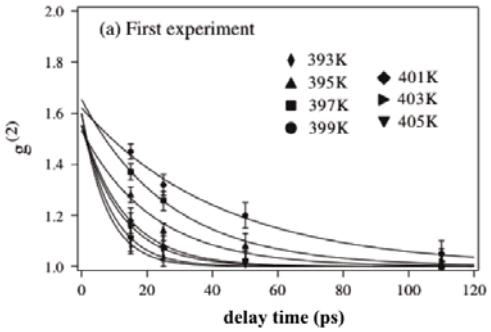

Fig.2. Correlation factor $g^{(2)}$ as the function of delay time. From these decay curves, the relaxation time of collective dipole moments in the domain of $BaTiO_3$ is estimated to be several tens ps [12].

Figure 2 shows the obtained $g^{(2)}$ for the temperatures from 2 K below the T_c of $BaTiO_3$ up to 10 K above T_c by 2K step as the function of the delay time. We obtained $\beta \sim 0.6$ from the intercept at the delay $\tau = 0$ ps, The visibility of SXRL (= 0.8) derived from this β value is almost consistent with typical value of our 13.9 nm laser. The relaxation times obtained by fitting are an order of several tens of picoseconds.

Comparison with theoretical works implies that the present relaxation mode is not due to the flipping of the dipole direction of the polarization clusters, whose time scale is much longer, but due to the hopping the position of Ti ion in the unit cell. Another interesting point is that the minimum relaxation time is not obtained at T_c, but at 399 K, *i.e.*, 4.5 K above T_c. This may be due to the effect of additional electric fields originated from the collective dipole moments. For further information, it is desirable to compare the present result with theoretical works.

2.2 Development of soft x-ray laser interferometer toward single shot imaging of nano-meter scale dynamics

In order to obtain single-shot image of the nano-scale structure and its dynamics, new x-ray laser interferometer has been developed. The SXRL interferometer was designed with groups of Institute of Solid State Physics (ISSP) and university of

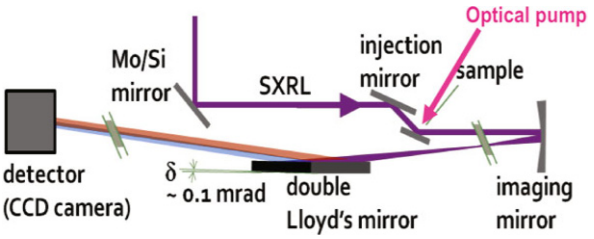

Fig.3. The set-up of SXRL interferometer using double Lloyd's mirrors.

Tokushima together with our experiences obtained by the collaborations with PALS and Université de Paris Sud. Schematic of the x-ray interferometer is shown in Fig. 3. The fully spatial coherent 13.9 nm laser beam with the output energy of 1 μJ and the duration of 7 ps, passing through the 0.1 μm-thick Zr filter was steered by a planar Mo/Si multi-layer mirror to the sample position. The angle of the incidence of the XRL probe to the sample was set to be $\theta = 70°$ with respect to surface normal. The image of the illuminated area on the sample was transferred to the CCD position by a Mo/Si spherical imaging mirror with the focal length of 250 mm. The distance from the sample to the imaging mirror and that from the imaging mirror to the CCD was about 260 mm and 4800 mm, respectively, which led to the magnification factor of 17. Interference pattern was obtained by putting a double Llyod's mirrors between the imaging mirror and the CCD. The angle of the incidence for the double Lloyd's mirrors was 87° with respect to surface normal. The double Lloyd's mirrors consisted of two Pt coated 400 μm-thick Si wafers, which were fixed with a relative incline angle of $\eta = 0.006°$ (= 0.1 mrad). One of the mirrors covered the portion of the x-ray laser beam affected by the surface deformation, and the other was used as the reference. The two components of the SXRL beam are merged at the position of the CCD.

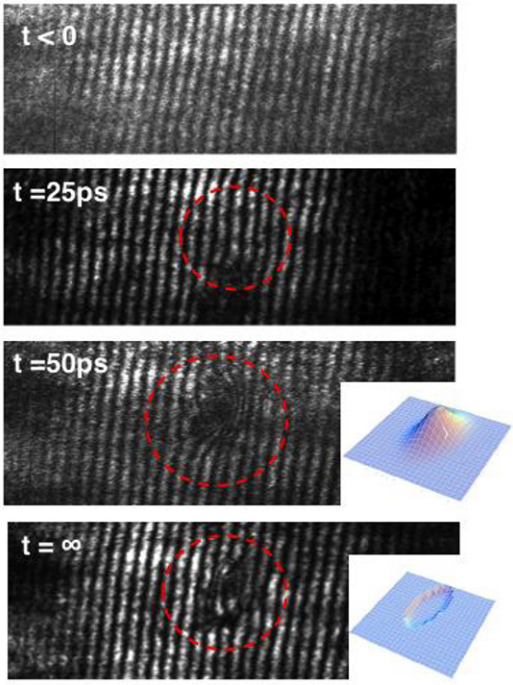

Fig.4. Temporal evolution of the interferogram of the Pt surface pumped by ultra-short laser pumping pulse, where t is the time measured from the timing of the pump laser. $t < 0$ means before the pump, and $t = \infty$ means more than 10 seconds after the pump. At $t = 50$ ps, apparent expansion of the surface can be seen, where the height of the peak is 30 nm.

In order to estimate the depth resolution of this interferometer, at first we took the interferogram of a test sample. The test sample was several pairs of grooves with the depth of 6 nm. The line and space of the pairs of grooves were from 8 μm through 1μm, and the line and space of 1.5μm were clearly

resolved. The fringe shift for the 6 nm-depth grooves was 6-8 pixels in our CCD, therefore the depth-resolution was estimated to be around 1 nm. It should be noted that the present lateral resolution could be improved upto 50 ~ 100 nm by replacing the spherical imaging mirror by Fresnel zone plate.

By use of this interferometer, nano-scale dynamics of the initial stage of laser ablation was firstly observed. The sample was 300 μm-thick Pt bulk, which was irradiated by a Ti:Sapphire ultra-short laser pulse with the duration of 100 fs and fluence of 2 J/cm^2. The timings of the pump laser and the XRL probe pulse were synchronized by use of master clock generator within 10 ps.

Figure 4 shows the temporal evolution of the interferogram of the Pt surface and the retrieved profile, respectively. After the laser irradiation, very small but substantial change starts at around 25 ps. (See the inside of the dotted circle at t = 25 ps.) At around t = 50 ps, apparent expansion of the surface can be seen, and the height of the peak reaches 30 nm. Finally a crater is generated. This is the first observation of the initial stage of laser ablation [13]. Precise comparison of the present result with theoretical calculations can be used as the benchmark test of the hydrodynamics codes, and this will contribute to deep understanding of the fundamental processes in the laser-matter interaction and dynamics of domain in photo-induced phase transition.

2.3 Observation of low-threshold ablation of substances by use of pico-second duration of SXRL laser

Laser ablation has many technological applications in material processing and nano-structure fabrication. The laser-induce damage of the materials has been intensively studied and its dependence upon the pulse width, the photon energy, and the fluence has come to be understood. For the relatively long duration optical laser pulses with > 20 ps, it is shown that the damage of dielectrics is mainly originated from the heating of conduction band electrons and transferring of electron energy to the lattice. Damage occurs if the deposited energy is sufficient to melt the dielectric material. For the short enough pulses, the laser energy is absorbed by the electrons much faster than it is transferred to the lattice, resulting in drastically decrease in the ablation threshold energy.

The same situation can occur in extreme ultraviolet or SXRL. In the recent studies, a well-defined ablation threshold at 0.06 for CaF_2 and 0.11 J /cm^2 for LiF has been found for pulse energy 0.3 mJ of the Ne-like Ar x-ray laser at the wavelength of 46.9 nm with the duration of 1.7 ns, and much lower threshold energy can be expected in the case of transient collisional excitation laser with several picoseconds duration.

Our 13.9 nm SXRL from a single target was focused on a 2 mm-thick LiF crystal with the diameter of 20 mm. The output energy of the SXRL was 1 μJ, and the vertical and horizontal beam divergence was 12 x 5 mrad^2,

respectively. The focusing optics was a normal incidence Mo/Si multi-layer spherical mirror with the curvature of 1050 mm, which was placed at a distance of 2715 mm from the XRL output and used at the incident angle of 2°. A 0.2 μm thick Zr filter was settled or removed in front of the x-ray mirror at 800 mm from the XRL exit in order to reduce the scattered optical radiation and the thermal x-ray emissions from the laser-produced plasma. The LiF crystal was moved after each shot along the XRL propagation direction and also perpendicular to it, in order to record the beam patterns at different focusing distances on the fresh LiF crystal surface. The total energy of the XRL beam on the LiF crystal was 170 nJ in each shot. The luminescence of stable color centers, CCs, formed by the x-ray laser radiation, was used to measure the intensity distribution in the XRL laser focal spot. The CCs in LiF crystal were observed by using a confocal fluorescence laser microscope after irradiation of the LiF crystal with the x-ray laser [11, 14].

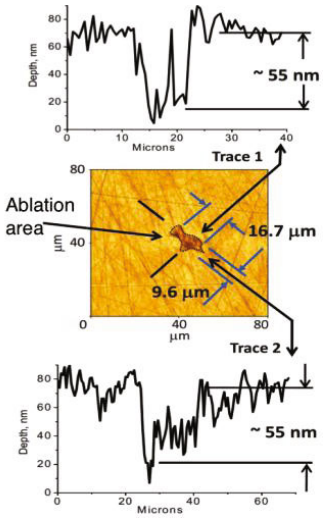

Fig.5. The optical micro-scope image of the crater due to the illumination of SXRL pulse (middle), and the AFM traces of the crater (top and bottom)

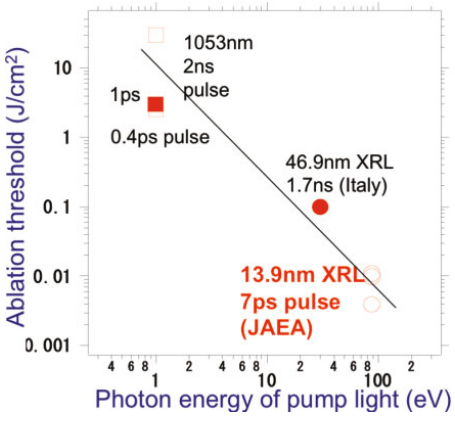

Fig.6. The ablation threshold fluence (J/cm^2) of LiF crystal for various photon energies of the lasers and the durations.

Figure 5 shows the optical microscope image of the LiF crystal irradiated by the 13.9 nm laser (middle) together with the AFM traces of the ablation area (upper and lower). The ablation area is indicated by dotted line. From visible microscope image and AFM trace, we can clearly see the surface alteration of LiF crystal. In the AFM trace 1 and 2 show that the ablation depths vary between 30 and 55 nm, which are almost consistent with the absorption depth of 28 nm for 13.9 nm radiation.

In the present experiment, the beam energy of the x-ray laser to

generate the surface alteration is only 10.2 mJ/cm^2, which is 3400, 300, and 10 times smaller compared with previously measured thresholds for nanosecond and femtosecond Ti:sapphire lasers, and for nanosecond 46.9 nm soft x-ray laser, respectively (See Fig. 6.). To explain such a strong reduction in LiF crystal ablation threshold in the case of using picoseconds x-ray laser, an ablation mechanism for dielectrics is connected with a 100% laser absorption in a thin surface layer and formation of negative pressure zone, followed by thermomechanical fragmentation, under a sufficiently strong tensile stress. As a rule, this mechanism works for metals and semiconductors irradiated by ultrashort visible laser pulses [15].

3 Ultra-short x-ray pulse generation and its biological application

High energy monochromatic x-ray pulse from laser-produced plasmas (LPP) has potential as the radiation source to study biological science, medical treatment, non destructive testing of materials and photo-pumping x-ray lasers [16]. One of the most attractive features of LPP x-ray sources is the spatially coherent focusing due to the small source size with a few tens microns. This characteristic is quite attractive when we consider the high energy density science or radiation damage of organic matter and inorganic substance as the applications of this radiation source. From FY2007, we have started the collaboration with Institute of Laser Engineering (ILE) to study efficient monochromatic x-ray micro-beam generation and its applications.

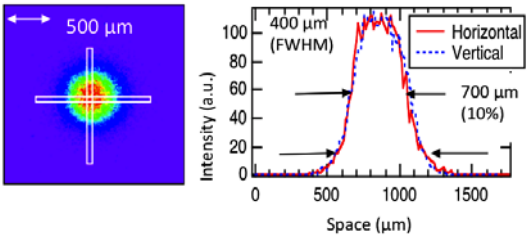

Fig.7. Typical image of the focus spot of the x-ray micro-beam using poly-capillary x-rav lens.

The LPP x-ray source was generated by use of a 10Hz Ti:sapphire laser system at JAEA. This laser provides a 150 mJ-energy laser pulse with the duration of 70 fs at a wavelength of 790 nm. Copper (Cu) slab target was irradiated at an intensity of 3x10^{17} W/cm^2 under the *p*-polarization condition, and characteristic Kα x-ray spectral line with the photon energy of 8.0 KeV is generated. The energy conversion efficiency from pump laser to Kα x-ray was around 1x10^{-5} which corresponded to the Kα photon numbers of 2 x 10^{11} photons/4πsr/pulse. In the present experiment, we put a poly-capillary x-ray tube to collect the diverging x-rays from the source position to obtain the x-ray point focus. Figure 7 shows the typical image of the x-ray spot recorded by back-illuminated CCD. The diameter is around 400 μm (Full width at half

maximum), and 700 μm at full width at 10% maximum. The gain in the intensity is derived from the comparison of x-ray photon number with and without the poly-capillary and is around 50.

By use of this x-ray micro beam, we have demonstrated the generation of DNA double-strand breaks (DSBs) in the nucleus of culture cells. Biological specimens are irradiated are irradiated through the 1 μm-thick Si_3N_4 membrane window fabricated on the bottom of culture dishes so that the specimen does not need to be extracted from the dish during the x-ray exposure. The sample was A549 cell line (human lung adenocarcinoma cell line), and the dose rate was estimated to be 0.1 mGy/pulse.

The DNA DSBs were investigated using phosphorylated histone H2AX (γ-H2AX) and phosphorylated ataxia telangiectasia murated (ATM) immunostaining. By use of this method we can detect the DSBs of the DNA as the foci of γ-H2AX and ATM. Figure 8 shows the image of A549 cells after 2Gy x-ray exposure [17]. The field of irradiation is indicated by the dotted circle, in which the fosi of γ-H2AX are clearly shown. This implies that the present x-ray micro beam system has potential to study radiation effects on culture cells as the same with conventional x-ray sources such as 4MV medical linac. It is also noted that the present result shows apparent boundary of irradiated area and non-irradiated area, therefore present x-ray micro-beam system can be used to study the bystander effect in culture cells in near future. Practical application of this x-ray micro-beam system together with improvement of x-ray source such as the energy conversion efficiency is currently underway.

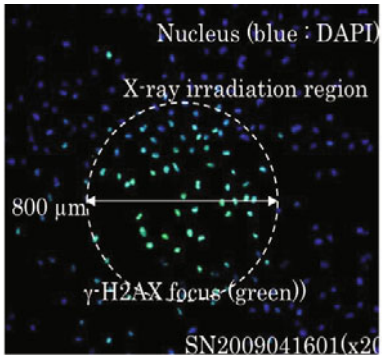

Fig.8. The image of A549 culture cells by use of fluorescence micro-scope. The total dose is 2 Gy. The dotted circle represent the irradiation field of LPP x-rays [17].

Acknowledgement

This work is partly supported by auspices of MEXT (Japanese Ministry of Education, Culture, Sports, Science and Technology) project on "Mono-energetic quantum Beam Science with PWlaser" and Japan Grant-in-Aid for Scientific Fundation, Kiban (B), No. 21360364.

References

1. Luther B. M., *et al.*, "Saturated high-repetition rate 18.9-nm tabletop laser in nickellike molybdenum" *Opt. Lett.* **30**, 165-167, 2005.
2. Kawachi T., *et al.*, "Gain saturation of nickel-like silver and tin x-ray lasers by use of a tabletop pumping laser system", *Phys. Rev. A* **66**, 033815, 2002.
3. Dunn J, *et al.*, "Gain saturation regime for laser-driven tabletop, transient Ni-like ion x-ray laser", *Phys. Rev. Lett*. **84**, 4834-4837, 2000.
4. Tanaka M., et al., "X-ray laser beam with diffraction-limited divergence generated with two gain media", *Opt. Lett.* **28**, 1680-1682, 2003.
5. Nishikino M., *et al.*, "Characterization of a high-brilliance soft x-ray laser at 13.9 nm by use of an oscillator-amplifier configuration", *Appl. Opt.* **47**, 1129-1134, 2008.
6. Wang Y, *et al.*, "High-brightness injection-seeded soft x-ray-laser amplifier using a solid target.", *Phys. Rev. Lett.* **97**, 123901, 2006.
7. Ochi Y., *et al.*, "Development of a chirped pulse amplification laser with zigzag slab Nd:glass amplifiers dedicated to x-ray laser research", *Appl. Opt.* **46**, 1500-1506, 2007.
8. Tai R. Z., *et al.*, "Picosecond snapshot of the speckle from ferroelectric $BaTiO_3$ by means of x-ray lasers", *Phys. Rev. Lett*. **89**, 257602, 2003.
9. Tai R. Z., *et al.*, "Picosecond view of microscopic-scale polarization clusters in paraelectric $BaTiO_3$," *Phys. Rev. Lett.* **93**, 087601, 2004.
10. Namba S., *et al.*, "Enhancement of double Auger decay probability in Xe clusters irradiated with a SXRL pulse.", *Phys. Rev. Lett.* **99**, 043004, 2007.
11. Faenov A. Ya., *et al.*, "Low-threshold ablation of dielectrics irradiated by picosecond soft x-ray laser pulses", *Appl. Phys. Lett*. **94**, 231107, 2009.
12. Namikawa K, *et al.*, "Direct Observation of the Critical Relaxation of Polarization Clusters in $BaTiO_3$ Using a Pulsed X-Ray Laser Technique", *Phys. Rev. Lett*. **103**, 197401, 2009
13. Suemoto T. *et al.*, "Single-shot picosecond interferometry with one-nanometer resolution for dynamical surface morphlogy using a soft x-ray laser", *Opt. Exp*. **18**, 14114, 2010.
14. Faenov A. Ya., *et al.*, "Submicrometer-resolution in situ imaging of the focus pattern of a soft x-ray laser by color center formation in LiF crystal", *Opt. Lett.* **34**, 941-943, 2009.
15. Inogamov N. A., *et al.*, "Spallative ablation of dielectrics by X-ray laser ", *Appl. Phys. A,* **101**, 87-96, 2009.
16. Kawachi T and Kato Y, "X-ray absorption by highly charged ions in plasmas: toward photo-pumping x-ray laser", *J. Phys.: Conf. Ser*. **163**, 012100, 2009.
17. Nishikino M et al., "Application of laser produced plasma Kα x-ray probe in radiation biology", *Rev. Sci. Instr.* **81**, 026107, 2010.

Theoretical Study of Ni-like Ta XRL Driven by One 2ω Pulse with Duration of 100ps on Upgraded Shenguang Ⅱ Facility

Guoping, Zhang, Xiumei Qiao, Wudi Zheng[1]

[1]Institute of Applied Physics and Computational Mathematics, Beijing, 100094, China

Abstract. As ~ 250J laser energy could be available for the 100ps pulse at 1.053μm wavelength on the upgraded Shenguang II laser facility in the near future, Ni–like Ta X-Ray laser driven by a single 100ps laser pulse at 0.53μm wavelength on the upgraded Shenguang II laser facility was theoretically studied. Simulations show that by properly designing, several sequential or serial targets could overcome plasma aging and refraction. One laser beam normally irradiates the Ta target, producing a 10mm long 120μm width focus line. Two sequential targets driven by one laser beam and four serial targets driven by two laser beams from opposite direction were proposed, with each target of 4mm long. If quasi-traveling pumping method was adopted, for the latter scheme, the gain-length product of ~26 could be achieved. Research in this paper would help achieve high gain or saturated Ni-like Ta X-Ray laser on upgraded Shenguang II laser facility.

1 Introduction

As X-ray laser at water-window wavelength could be widely used both in scientic and technical fields, such as holographical photography of living cells, and its saturation output is always one of aims in X-ray laser research. And the maximum Gain-Length product is 8, which is obtained by LLNL in 1990s on the Nova laser facility by driving the exploding target [1].

The 1.5 dimensional hydrodynamic code JB19, atomic kinetics code ALPHA and 2 dimensional ray-tracing code XPBA constitute the serial codes of simulating the process of x-ray laser[2-5]. We proposed a scheme in which the two laser beams at respectively 1ω and 2ω wavelength were combined to

J. Lee et al. (eds.), *X-Ray Lasers 2010,* Springer Proceedings in Physics 136,
DOI 10.1007/978-94-007-1186-0_3,

drive Ni-like Ta X-ray laser with 21 degree incident angle with the target normal direction[6], and in 2002, the corresponding experiment was done on Shenguang II laser facility[7] with the help of Institute of Laser Plasma in Shanghai, it was found that the unsymmetrical driving produced a very wide gain region in the width direction of the focus line, and large electron density gradient appeared in this direction, the X-ray laser was deflected out of the gain region and deviated from the axis, and Gain-length product is only ~ 5.2. In the following years, three experiments were done on Shenguang II laser facility, and no better result was obtained. In 2006, we simulated the experiments with the newly developed 2 dimensional hydrodynamic code XRL2D[8], and found that for prepulse and main pulse driving case, and if the laser pulse is 100ps Gaussian pulse, only ~ 60% to 70% laser energy was deposited in the focus line , and with this assumption in JB19, and choosing the electron heat flux limiter of 0.6 for prepulse and 0.2 for main pulse, better agreement with experiment could be obtained.

In this paper, according to the capability of the upgraded Shenguang II laser facility, the Ni-like Ta X-Ray laser normally driven by one 2ω laser beam with ～100ps duration was theoretically designed, and two sequential targets driven by one laser beam and four sequential targets driven by two laser beams from opposite direction were designed.

Result

On the upgraded Shenguang II laser facility, ～ 250J energy could be obtained for the 100ps laser beam at 1 ω wavelength, and if the energy efficiency of transferring laser beam from 1ω to 2ω is ~60%, the output energy for the 2ω laser at 100ps duration is ~173J, and the driving laser intensity was～$1.37\times10^{14}W\bullet cm^{-2}$ with in 10mm long and 120μm width focus line. it was assumed that ～80% of laser energy was deposited in the focus line, reducing the intensity to ~$1.10\times10^{14}W\bullet cm^{-2}$.

Simulation shows that the maximum electron temperature T_e and ionization Z in the plasma are 1.73KeV and 45.5, respectively. For one 4mm long slab Ta target, the maximum intensity of output X-ray laser is $1.02mJ\bullet sr^{-1}$ with deflection angle θ and divergence angle ϕ of 6.93mrad and 3.88mrad, respectively. The

small signal gain g is ～16.86cm^{-1}， the FWHM(Full Width at Half Maximum) time is～21.4ps. It was found that the rays of XRL which contributes most to the peak intensity, starts at t～6.3ps from the beginning end of the target , and it arrives at the middle at t～13ps, while at t～19.7ps it leaves the target. And plasma status at t～8ps, t～13ps and t～19ps were presented in Fig.1(a-c), respectively. The temporal evolution of gain was presented in Fig.1 (d).

At t=8ps, the maximum gain G_{max} of 28.12cm^{-1} is obtained at 503th grid, and it is located～ 2.86μm away from the initial target surface, with electron density N_e of 3.07×10^{21}cm^{-3},T_e of ~1.65keV, ion temperature T_i~0.262KeV and abundance of Ni-like ion η_{Ni} of ~36.1%. It shows that the gain region extends to the inner side of the critical surface, but detailed analysis shows that gains in this region contributes less to the amplification of the output X-ray laser because of severe refraction. A gentle decrease of N_e occurs at a point outside the critical surface and not far away from the critical surface, if this point was defined as the inner side of gain region, the gain region is ~5.94μm wide, within which N_e ranges from 3.46×10^{21}cm^{-3} to1.00×10^{21}cm^{-3}, and the average electron density gradient is ~ -4.15×10^{24}cm^{-4}. X-ray laser is deflected by 7.46μm with θ of ~ 7.46mrad after propagating half target length in such plasma, which is a bit larger than the width of the gain region.

At t=13ps, G_{max} of ~ 25.33cm^{-1} is located at 476th grid which is ～ 2.83μm away from the initial target surface, with N_e of 3.66×10^{21}cm^{-3},T_e of ~1.42keV, T_i~0.299Kev and η_{Ni} of ~36.3%. The gain region extends from 2.83μm to 10.66μm from the initial target surface (7.83μm wide), and N_e in the gain region varies from 3.66×10^{21} cm^{-3} to 0.81×10^{21} cm^{-3}, with electron density gradient of ~-3.63×10^{24}cm^{-4},the deflection distance is ~ 6.53μm after travelling a half target length in such plasma, which is smaller than the width of the gain region.

At t=18ps, G_{max} of ~ 21.70cm^{-1} is located at 483th grid which is ～ 4.41μm away from the initial target surface, with N_e of 2.62×10^{21}cm^{-3},T_e of ~1.36KeV, T_i~0.313Kev and η_{Ni} of ~38.9%. Similar analysis was also done, and it shows that the deflection distance of ~4.86μm after passing half target is smaller than the width of the gain region.

Fig.1 indicates that with further ionization of plasma, the grid of G_{max} first moves inwards and then outwards. The corresponding N_e undergoes a rise and fall, while other variables monotonically vary, such as decreasing T_e, and increasing η_{Ni}. As time goes on, the whole gain region moves outwards, in 10ps, the position

of G_{max} and the inner and outer side of the gain region (where gain equal to 60% of G_{max}) goes by ~1.95μm, 0.92μm and 4.57μm, respectively, making the whole gain region shifts by ~ 2.62μm resulting a moving angle of 0.87mrad. From t=6.33ps to t=19.67ps, the average electron density gradient is ~-3.50×$10^{24}$$cm^{-4}$, for a half target length, X-ray laser is refracted by ~6.30μm with deflecting angle of 6.30mrad, adding moving angle of the whole gain region, the total deflected angle is ~7.17mrad, which agrees well with the ray trace output of 6.93mrad.

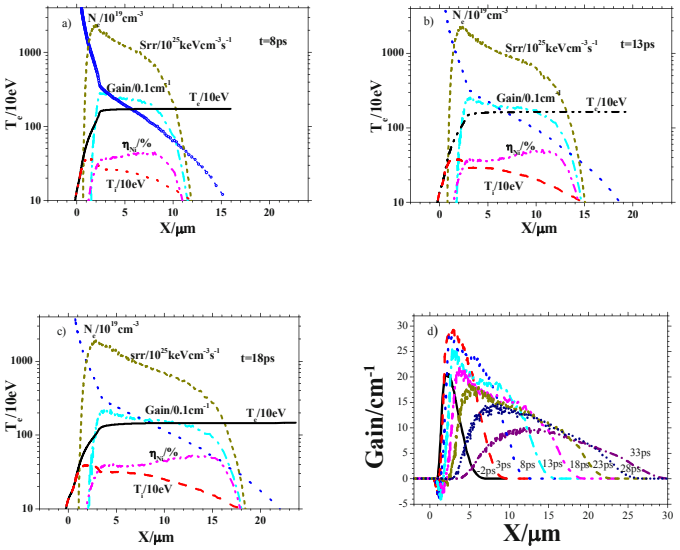

Fig. 1 plasma status at 8ps(a),13ps(b),18ps(c) and temporal evolution of gain(d)

The evolution of plasma status for the 503th, 476th and 483th grid is shown in Fig.2(a-c), it can be found that for the three grids, with increase of time , N_e monotonically decreases , while a single peak appears both for T_e and G and two peaks appear for η_{Ni} .The duration in which T_e is larger than 60% of its maximum is ~30ps, and gain larger than 60% of its maximum lasts ~16ps, but its duration increases to ~25ps, when considering its spatial movement from Fig.1 (d).

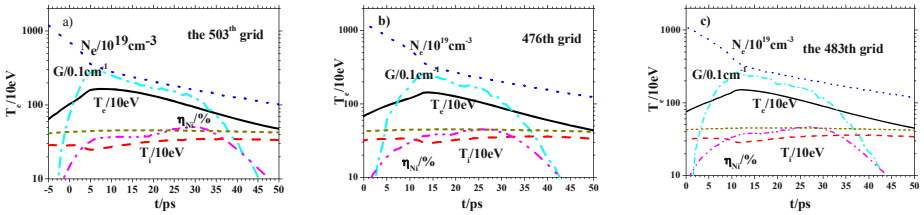

Fig. 2 Temporal evolution of plasma status for grid 503th (a), 476th (b)and 483th (c)

Based on the above simulations, two 4mm long slab sequential targets driven by one laser beam was calculated, the following target is located at 1mm away from the end of the first target in axial direction, and in vertical direction, it moves by ~ 10μm toward incoming direction of the pumping pulse, and it is deflected by ~ 12mrad with respect of the axial direction of the first target, in ray trace calculation quasi-travelling pumping is adopted by using a step mirror to produce ~16.7ps time delay. The maximum output intensity is ~ 0.3180Jsr^{-1}, comparing to the results for one single target, it is amplified by ~311 times, deflection angle and divergence angle are respectively 7.01mrad and 2.84mrad, the output X-ray laser lasts ~8.4ps,with small signal gain of 15.55cm^{-1} producing gain-length product of ~12.44, saturation is not obtained.

By driving four sequential targets formed by two groups of the above two sequential targets by two laser beams from opposite direction, the output intensity could be further enhanced. For each group, parameters for the two targets are similar. The first two targets are normally irradiated by one laser beam, and after ~30ps, a second laser beam drive the latter two targets from the opposite direction. The third target is 2mm away from the end of the second target in the axial direction of the second target, and it is deflected by ~ 1.5mrad with respect of the axial direction of the second target. In vertical direction, the third target moves by ~ 35μm toward incoming direction of the first laser beam. Quasi-travelling pumping is also adopted in ray trace calculation. The maximum intensity of the output X-ray laser is 1.68×10^5 J•sr^{-1}, the output X-ray laser lasts ~4.7ps, with small signal gain of 16.29cm^{-1} producing gain- length product of ~26.06, saturation is obtained.

Discussion

According to the ability of the upgraded Shenguang II laser facility, Ni–like Ta X-Ray laser driven by a single 100ps duration laser pulse at 0.53μm wavelength was theoretically studied, simulation shows that for target longer than 4mm, refraction plays important effect on output X-ray laser. For the 4mm long target, two sequential targets driven by one laser beam and four sequential targets driven by two laser beams were theoretically proposed, for the latter scheme, if quasi traveling is adopted, saturation would be available.

Acknowledgements

This work was supported by Chinese national 863 high technology plan (grant No. AA847010). We would also like to thank Prof. Shichang Li, Quanyu Fang, Guoxin Han and Yu Zou for providing atomic data. We would also like to thank Prof. Maoshen Li for providing EOS data.

Reference

1. MacGowan B J, Da Silva L B, Fields D J, et al. , “Short Wavelength x-ray laser research at the Lawrence Livermore National Laboratory”, *Phys. Fluids B*, 4(7), 2326, 1992
2. G P Zhang, T X Zhang, J Z Wu, *High Power Laser and Particle Beams*,10**,**352 (in Chinese) , 1998
3. G P Zhang, J T Sheng, M L Yang, et al., *High Power Laser and Particle Beams*, 4,521(in Chinese), 1992
4. G P Zhang, T X Zhang, W D Zheng, *High Power Laser and Particle beams*,16,35 (in Chinese) ,2004
5 .Zhang G P,Zhang T X, W D Zheng, *Chinese Physics*,16,2433,2007
6. Zhang G P,Zhang T X, W D Zheng,*Chinese Laser*,29,Supplement ,26,2002
7 .C Wang, W Wang, J Wu,er.al., *Chinese Physics*,53,3752,2004
8. W D Zheng, G P Zhang, *Chinese Physics*,16,2439, 2007

X-ray laser developments at PHELIX

B. Zielbauer[1,2]*, T. Kuehl[1,3], B. Aurand[1,3,4], V. Bagnoud[1], B. Ecker[1,2,3], U. Eisenbarth[1], D. C. Hochhaus[1,4,5], P. Neumayer[1,4,5], D. Zimmer[1,3,6], K. Cassou[6], S. Daboussi[6], O. Guilbaud[6], J. Habib[6], S. Kazamias[6], D. Ros[6], J. Seres[7], C. Spielmann[2,7]

[1] GSI Darmstadt, Germany
[2] Helmholtz Institute Jena, Germany
[3] Johannes Gutenberg University Mainz, Germany
[4] EMMI, GSI Darmstadt, Germany
[5] Johann-Wolfgang-Goethe University Frankfurt, Germany
[6] Université Paris Sud 11, France
[7] Friedrich Schiller University Jena, Germany

Abstract. Development of x-ray lasers using the PHELIX laser at the GSI Helmholtz center for heavy-ion research [1] is targeting a number of applications of novel x-ray sources in combination with energetic heavy-ion beams. This includes Thomson scattering diagnostics of heavy-ion driven plasmas, x-ray opacity measurements, and x-ray laser spectroscopy of highly-charged ions. Developments centered on the application of a novel double-pulse GRIP-like pumping scheme, DGRIP, where non-normal incidence geometry is used for both the pre- and the main pulse for transient pumped Ni-like x-ray lasers [2,3]. This scheme was used at lower energy levels to pump soft x-ray lasers in the 50 – 100 eV regime as well as for pulse energies above 100 J for the pumping of shorter wavelength soft x-ray lasers [4].

PHELIX is a member of Laserlab Europe, offering access as a European infrastructure.

1 Status of the PHELIX system

The PHELIX (**P**etawatt **H**igh Energy **L**aser for **H**eavy **I**on **E**xperiments) at GSI Helmholtz Center for Heavy Ion Research, Darmstadt, Germany has been in routing user operation now for more than 2 years. About 150 days per year of laser beamtime has been provided to internal and external user experiments, either in standalone operation or in combination with the heavy ion beam provided by the UNILAC (**U**niversal **L**inear **A**ccelerator). Application

J. Lee et al. (eds.), *X-Ray Lasers 2010,* Springer Proceedings in Physics 136,
DOI 10.1007/978-94-007-1186-0_4,

experiments range from particle acceleration [5] and target surface electron transport investigations [6] to stopping power measurements of swift heavy-ions in plasmas [7] and x-ray source development [8].

A schematic overview of the PHELIX facility and its connection to the adjacent accelerator experiment site is presented in figure 1. The seed pulse for the high-energy amplifier stages can be provided from either a Ti:Sapphire based frontend or a fiber based nanosecond frontend. In the first case, selected pulses from a commercial femtosecond oscillator with a duration of 100 fs at 1053 nm are passed through a pulse stretcher, amplified in two consecutive regenerative amplifier stages and cleaned temporally by ultra-fast Pockels cells. Alternatively, the seed pulse can be created by a fiber-based nanosecond frontend which allows for arbitrarily shaped temporal pulse forms in the range of 700 ps to 20 ns and which is brought to the required energy level by a flash-lamp pumped ring amplifier. Currently, the system is modified to enable the combination of both frontend beams in sub-apertures of the full PHELIX beam with variable delay which will enable two-beam experiments with spatially separated beams.

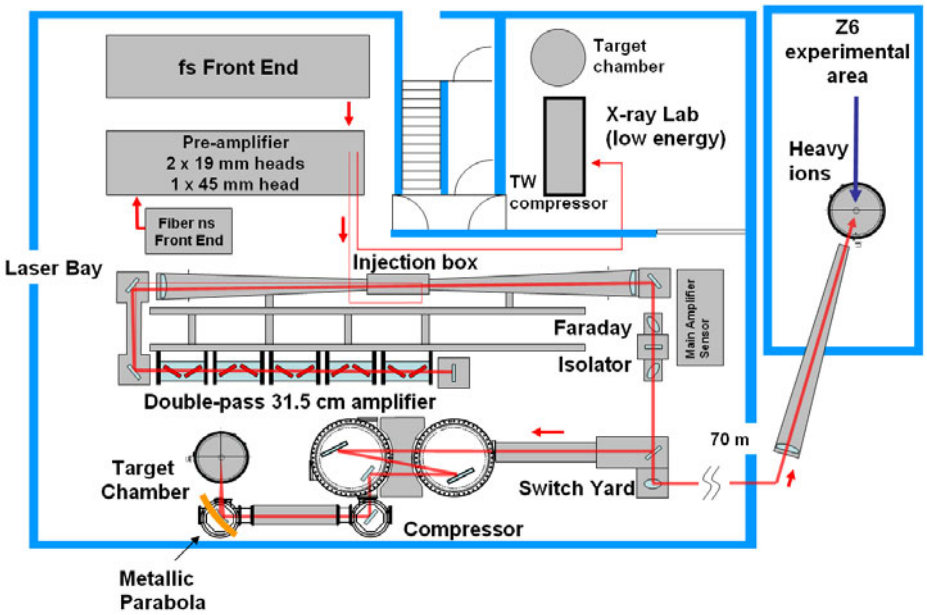

Fig. 1. Schematics of the PHELIX installation

The preamplifier section consists of three flash-lamp pumped Nd:glass rod amplifiers with 19 mm and 45 mm diameter. Before entering this section, the beam is spatially shaped and cleaned by using serrated apertures and spatial

filters to provide a top-hat beam profile. A closed-loop wavefront correction system with a Shack-Hartmann sensor and a deformable mirror enables the correction of thermal aberrations from the heat buildup in the main amplifier, which helps to increase the shot repetition rate of the full system.

After the preamplifier, the laser pulses of 5 to 10 J pulse energy can either be used directly for experiments in a separate low-energy lab or be injected into the main amplifier section which consists of 10 Nd:glass slab amplifiers which are also pumped by flash-lamps and set up in a double-pass configuration, yielding up to 1 kJ at its output in the ns energy regime. Those pulses are either sent via a transport telescope to the accelerator area where they are frequency doubled for long-pulse experiments or into a grating-based vacuum compressor where chirped pulses can be re-compressed down to below 500 fs at energies of up to 200 J. Table 1 gives an overview of the actually available beam parameters. Further details can be found in [1].

	Long pulse	**Short pulse**
Pulse duration	**0.7 – 20 ns**	**0.4 – 20 ps**
Energy	**0.3 – 1 kJ**	**200 J**
Max intensity	**10^{16} W/cm^2**	**10^{20} W/cm^2**
Repetition rate at maximum power	**1 shot every 60 min**	
Intensity contrast	**50 dB**	**60 dB**

Tab. 1. Present beam parameters of the PHELIX system

2 Short-wavelength X-Ray Laser development

Due to the long-standing experience in the creation of temporally tailored double-pulses in the cooperation between the PHELIX group and the LASERIX group of Université Paris Sud 11, Orsay, France, the PHELIX system is predestinated for soft x-ray laser (SXRL) experiments with large-aperture, high-energy pump laser beams. Compared to earlier experiments, the setup is greatly simplified by the fact that the two pulses necessary for the plasma creation and its heating up to the Ni-like ionization state are created in

the laser frontend and follow the same beam path up to the target. This brings the advantage of an intrinsically perfect overlap between the two pulses which enables reproducible results even at low repetition rate. The double-pulse generation is achieved by a Mach-Zehnder type interferometer setup which creates two collinear pulses with adjustable delay of 0 to 3 ns, energy ratio and, due to the introduction of an additional double-pass grating compressor in one arm, separately selectable pulse duration, as well [3, 4].

We report on an experimental campaign at PHELIX in spring 2010 which was aiming at the reproduction of the Sm SXRL results reported in [11] and the extension of the data set. In contrast to the focusing system in the earlier experiment which was imaging the focus with a tilted spherical mirror, the horizontal tilt of the main laser beam 90° off-axis copper parabola with a focal length of 1500 mm by about 4° was used to produce a line focus. It was possible to obtain a focus length of 10 mm and a width of only 20 µm, measured by directly placing a CCD camera chip at the SXRL target position. The target plane was tilted by 17° off the normal incidence. From the line focus shape, irradiances of ~ 5 x 10^{13} W/cm^2 for the pre-pulse and ~ 1.5 x 10^{15} W/cm^2 for the main pulse can be deduced for a total pump laser energy of 40 J.

Since the traveling wave speed of the laser pulse front hitting the target was not corresponding intrinsically to the pulse propagation along the SXRL plasma column, a small adjustment of the PHELIX PW single-pass compressor by turning the second grating was necessary. In order to measure the traveling-wave speed online during the compressor adjustment, a simple diagnostic has been developed which allowed circumventing the difficult streak camera measurement. It relies on the fact that in the laser frontend, two short pulses with a known delay can be produced. These pulses hit a test plate situated in the target plane with small holes near the line focus edges. The two beam samples passing through these holes are focused into a frequency doubling crystal are used to create an autocorrelation signal which depends only on the geometry of the setup and the delay between the two pulses as shown in figure 2. Thus, the traveling-wave speed of the line focus could be adjusted to 1 +/- 0.1 c.

The SXRL emission which followed the target surface except for a small refraction angle due to the refraction caused by the plasma density gradient was separated from the strong high-energy plasma emission background by a flat, uncoated mirror substrate with an RMS surface roughness of 1.5 nm in grazing incidence. This allowed the pointing of the SXRL beam onto an XUV flat-field grating spectrometer with 1200 lines/mm through two 0.8 µm carbon filters as the primary diagnostics. In addition, the outer edges of the SXRL beam which would not reach the grating surface due to the small acceptance angle at such short wavelengths were guided via a slotted grazing incidence mirror and an XUV multilayer mirror onto the chip of a back-illuminated

CCD. This way, the speckle structure, which is a typical feature of an SXRL near-field, as well as the spectrum could be registered for the same shot.

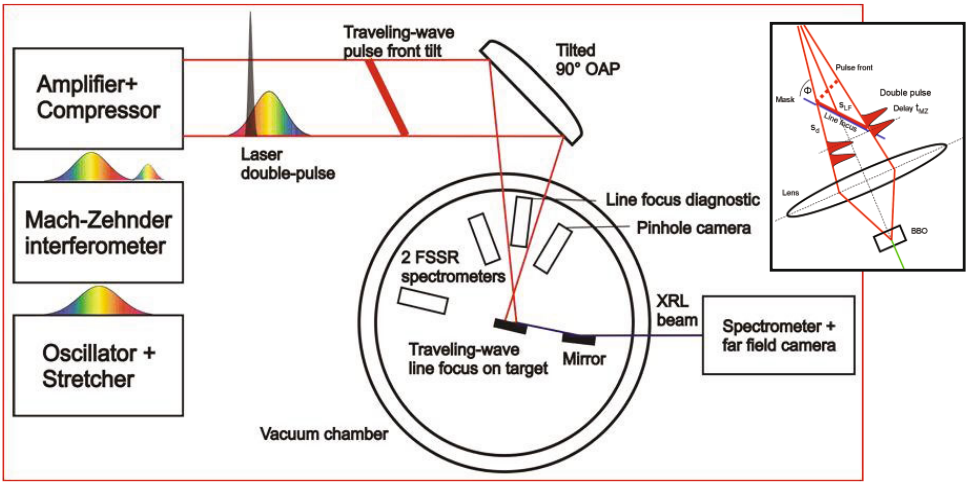

Fig. 2. Principle of DGRIP SXRL setup for high energies and the traveling-wave speed measurement [9, 10]

The experiment series was performed with massive Sm targets of 10 x 10 mm^2 surface size and 1 mm thickness which were polished and stored under high purity inert gas to avoid corrosion in air as long as possible before mounting them onto the target holder shortly before evacuation. For each shot, the target was moved to a fresh surface position.

A detailed scan of the delay between the two pulses from 20 ps to 375 ps was performed in order to determine the delay for the highest SXRL output (see figure 3). Likewise, the double-pulse energy ratio was varied between 10 % and 70 % and the total pump energy was lowered successively from 85 J down to 36 J which was the lowest value for which lasing could still be detected. The pulse durations were set to 200 ps and 7 ps for the pre-pulse and the main pulse, respectively. A pulse contrast level of 10^{-6} except for an extra pre-pulse of 10^{-3} about 900 ps before the double-pulse was measured.

In the obtained SXRL spectra, the lasing $4d_{(3/2)} - 4p_{(3/2)}$ transition at 168.5 eV (7.36 nm) was clearly visible. The spectral recording was corrected for the transmission characteristics of the spectrometer system. From the spatial axis of the spectrometer image, a vertical divergence of the SXRL beam of ~6 mrad FWHM could be inferred, clearly showing the directionality of the SXRL beam.

The SXRL pulse energy was calculated by the integration of the background corrected counts of the lasing line in the spectrum on the XUV CCD camera chip With this procedure and taking into account the acceptance angle of the spectrometer and the reflectivity and transmission of the employed optics and filters, the highest obtained SXRL pulse energy of ~ 1.6 +/- 0.5 µJ deduced. This value was found at 90 ps delay with a total pump energy of 80 J with a 50 % ratio between the pre-pulse and the main pulse.

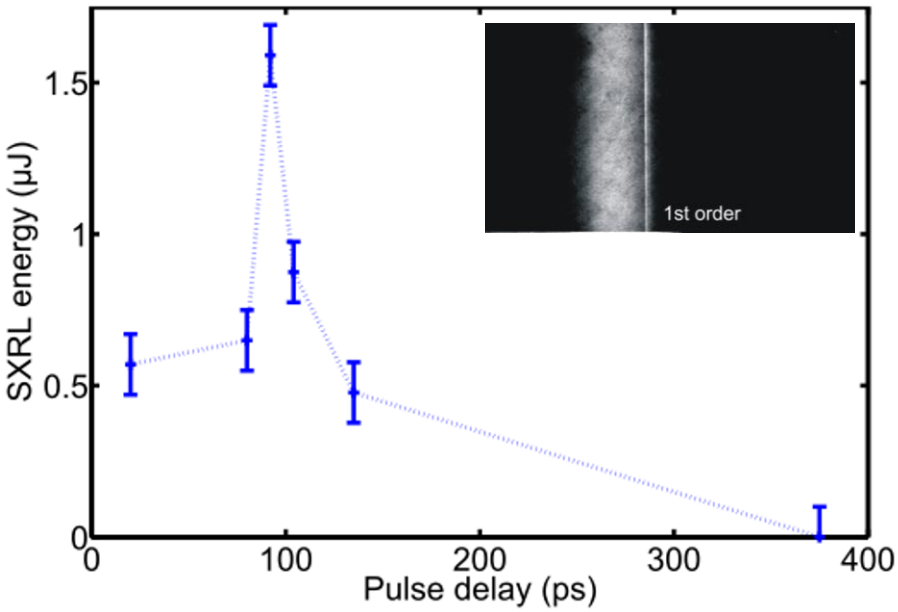

Fig. 3. Spectrum of the 7.3 nm SXRL (inset) and the SXRL energy dependence on the double-pulse delay [9, 10]

3 Wide-range HHG wavelength tuning for SXRL seeding

The seeding of plasma-based SXRLs with sources like those produced by higher harmonics generation (HHG) has been demonstrated by several groups [12-15]. The foremost goal is the transfer of the high beam quality provided by HHG sources to the higher pulse energy levels available with plasma SXRLs which would greatly widen their field of application. Using such a scheme at a hybrid Ti:Sa / Nd:glass CPA system like PHELIX is tempting because of the high IR pulse energy available for producing homogeneous, large-volume plasma amplification media. However, such an undertaking is complicated by the low repetition rate of flash-lamp pumped glass systems and the inability to match the seed wavelength to the SXRL wavelength by

tuning the IR fundamental wavelength due to the narrow gain bandwidth of Nd:glass.

The first topic has been addressed by the development of a highly stable compressor setup with two separate grating systems and the introduction of the double-pulse pumping scheme mentioned above, allowing for a good reproducibility of the optical alignments for the two sources. For matching the HHG wavelength to the SXRL lasing line, the adiabatic and the non-adiabatic frequency shift by quantum path control has been employed successfully at PHELIX. In this way, many popular SXRL lasing wavelengths in the range of 18.9 nm (Mo) to 26.9 nm (Mn) can be reached [16-18].

4 Conclusions and Outlook

With the routine operation in the double-pulse, single-beam non-normal incidence pumping and the simplified focusing system with just the off-axis parabola of the pump laser system, the results for a Sm SXRL could be reproduced and a scan of the pump laser parameters was performed. The low pumping threshold of less than 40 J are suitable for experiments at higher repetition-rate laser systems like LASERIX. Together with the advances in the implementation of a seeding scheme adopted to the needs of a hybrid glass system, the application of the SXRL as diagnostics source for laser or heavy-ion generated plasmas and as spectroscopy source at the current GSI accelerator facility as well as the Facility for Antiproton and Ion Research FAIR come into reach.

The experiments were supported through the Laserlab Europe Integrated Infrastructure Initiative. The XUV multilayer mirrors were manufactured at LCFIO by the CEMOX facility under the supervision of F. Delmotte.

References

1. V. Bagnoud et al., *Appl. Phys. B*, DOI 10.1007/s00340-009-3855-7
2. D. Zimmer et al., *Optics Express* 16, 10398 (2008),
3. D. Zimmer et al., *Opt. Lett*. 35, 450 (2010)
4. D. Zimmer, D. Ros et al., *Phys. Rev. A* 82, 013803, (2010)
5. I. Albers et al., *Phys. Plasmas* 17, 023107 (2010)
6. P. Neumayer, Ch. Labaune et al., *Phys. Plasmas* 17, 103103 (2010)
7. A. Frank et al., *Phys. Rev. E* 81, 026401 (2010)
8. J. Seres et al. *Nature Physics* 6, 455 (2010)
9. D. Zimmer et al., *Proc. SPIE*, Vol. 7721, 77211O (2010)

10. D. Zimmer, Thesis 2010, http://ubm.opus.hbz-nrw.de/volltexte/2010/2329/
11. D. Zimmer et al., *Springer Proceedings in Physics, Vol. 130, X-Ray Lasers 2008*, 92 (2009)
12. Ph. Zeitoun et al., *Nature* 431, 426 (2004)
13. Y. Wang et al., *Nature Photonics* 2, 94 (2008)
14. T. Ditmire et al., *Phys. Rev. A* 51, R4337 (1995)
15. N. Hasegawa et al., *Jap. J. Appl. Phys*. 48, 012503 (2009)
16. D. C. Hochhaus et al., *Appl. Phys. B* 100,711 (2010)
17. B. Ecker et al., *this conference*
18. D. Reitze et al., *Opt. Lett* 29,86 (2004)

LASERIX : an open facility for developments of EUV and soft X-ray lasers and applications.

D. Ros[1,2]*, K. Cassou[1,2], B. Cros[1,2], S. Daboussi[1,2], J. Demailly[2], O. Guilbaud[1,2], G. Jamelot[1], J. Habib[1], S. Kazamias[1,2], J.-C. Lagron[1,2], G. Maynard[2], O. Neveu[1,2], M. Pittman[1], B. Zielbauer, [1,2,3] D. Zimmer[1,2,3], T. Kuehl[3], V. Bagnoud[3], F. Delmotte[4], D. Joyeux[4], S. De Rossi[4], A. Klisnick[5], S. Lacombe[5], C. Le Sech[5], E. Porcel[5], M.-A. du Penhoat[6], A. Touati[6], P. Zeitoun[7], J.-P. Chambaret[8], F. Mathieu[8] and G. Mourou[8].

[1] CLUPS-LUMAT, Université Paris Sud 11 - CNRS, France
[2] LPGP, CNRS- Université Paris Sud 11, France
[3] GSI Darmstadt, Germany
[4] LCFIO, IOGS, France
[5] ISMO, CNRS- Université Paris Sud 11, France
[6] IMCP, Paris VI, France
[7] LOA, ENSTA-Ecole Polytechnique-CNRS, France
[8] ILE, France

Abstract. LASERIX is a high-power laser facility delivering *High-repetition-rate XUV laser beams pumped by Titanium:Sapphire laser.* The aim of this laser facility is to offer to the users community Soft XRLs in the 30-7 nm range and auxiliary IR beam for a broad range of applications. In this contribution, the main results concerning both the development of XUV sources and their use for applications (irradiation of DNA samples) are presented, as well the present status and some perspectives for LASERIX.

1 Introduction : an overview of LASERIX facility

For more than 25 years, many inversion mechanisms have been considered to produce a lasing effect in the XUV range: recombination [1] and collisional schemes [2]. Taking into account the previous work performed by the French group in the 30 last years [3], we have designed and built a laser facility to mainly develop TCE and GRIP X-ray lasers in the 30-7 nm range, called LASERIX [4-7].

J. Lee et al. (eds.), *X-Ray Lasers 2010,* Springer Proceedings in Physics 136,
DOI 10.1007/978-94-007-1186-0_5,

The main technology of the LASERIX driver is based on Ti:Sa crystals [5, 6]. The general architecture of the Ti:Sa laser is schematically presented in figure 1.

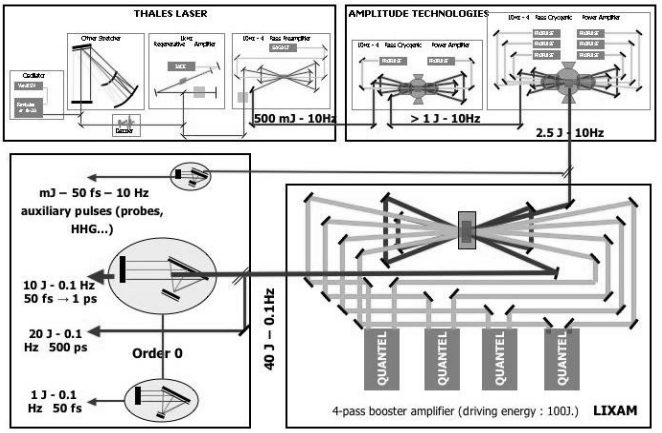

Figure 1 : Schematic view of the LASERIX driver architecture

The front-end is designed as a customized laser system based on standard modules, developed by several French laser companies (THALES LASER and AMPLITUDE TECHNOLOGIES). It is composed by two main parts: one for the shaping and pre-amplification of the oscillator pulse, the other for two cryogenic amplifiers. The output energy at the front-end is more than 2J at 10Hz repetition rate. This energy, as shown in figure 1, can be divided in two parts: one long pulse of 1 Joule (≅ 500 ps) to create the plasma and one short pulse (compressed from 50 fs to 10ps) to achieve the inversion of population. Besides, a small part of the beam, 100 mJ, can be used to create a source to seed X-ray lasers or to implement pump/probe experiments.

The front-end beam is then injected in the main amplifier, which relies on a large Ti:Sa crystal (diameter 100 mm). The crystal is pumped by a 4-module Nd:glass laser delivering 100 Joules of 2ω green light, developed by the French laser company QUANTEL. The energy deposition on each side of the crystal is homogenized using lens arrays. The crystal is supported in a mount in which a special liquid is circulating all around the crystal to limit transverse lasing. After 4 successive passes through the crystal, the expected output before compression is ≅ 40 Joules at the repetition rate of 0.1 Hz. Basically, the 40 joules are divided in two beams, respectively 20 Joules of 500 ps and 10 Joules of 50fs-1ps (after compression). Besides, a small part of the energy at the exit of the front-end, ≅100 mJ in 50 fs pulse duration at the repetition rate of 10Hz, can be delivered. The development of the LASERIX facility was achieved following different phases. The first achievement consisted in the validation of the use of the Ti:Sa technology to reach the 40 infra-red Joules [5,6,8], from 2004 to 2006. The investigations performed a good 4 Pass-

Amplifier with 8 beams delivering 100 J at 0.1 Hz, assuming homogenized pump laser profiles, direct liquid cooling of the Crystal and transverse lasing management.

Then, LASERIX was implemented in a temporary room of the LOA-ENSTA in Palaiseau, France. From mid-2006 to mid-2009, we used this temporary implementation to develop the XUV sources at 10 Hz repetition rate. We mainly focused our investigations on the Mo Ni-lie XRL @ 18.9 nm. Then we investigated the seeding of HHG in XRL plasma and we improved the stability of the XUV laser source with the main objective to use it for applications, like DNA irradiation that will be presented in section 2.

Mid 2009, LASERIX was implemented in a new ENSTA building. This building is both dedicated to the implementation of LASERIX facility and ILE project. The ILE project will be developed in the ground floor including its frond-end and pumping laser system, called respectively LUIRE and APOLLON. On the same floor we installed the QUANTEL pumping laser system of the last amplifier stage of LASERIX facility. The underground floor is dedicated to LASERIX facility; this implementation facilitates the synergy between the QUANTEL lasers of LASERIX and the ILE project. The present status of the LASERIX project will be developed in section 3.

2 Researches on XUV sources and applications from 2007 to 2009.

During this period we focused our attention on the development and the use of the front-end at 10 Hz repetition rate. The final goal was to clearly make the demonstration of the interest of X-Ray lasers at 10 Hz for external users.

« First » users run : jan – jul 2008
• **Biological samples irradiation (LCAM – IMPC)** Resp. S. Lacombe
• Soft X-ray laser longitudinal coherence (LIXAM) Resp. A. Klisnick
• Seeding of soft x-ray laser (TUIXS - LIXAM) Resp. P. Zeitoun
XUV sources development
• X-ray laser optimisation.
• X-ray laser focussing.
• XUV dosimetry.
• IR single shot autocorrelator for PW lasers (coll. ILE)
• **Effect of prepulses on XRL properties** (Resp J. Habib)
• Automated irradiation system (Resp. B. Zielbauer)
« Second » users run : sept 2008– march 2009
• **Single-beam GRIP x-ray laser (GSI) - DGRIP** Resp. T. Kuehl/D. Zimmer
• **Biological samples irradiation (LCAM – IMPC)** Resp. S. Lacombe

Table 1: Summary of the investigations on LASERIX from 2008 to 2009, by type of investigation (XUV sources development or external users).

As indicated in table 1, we offered access to the LASERIX facility (starting from the beginning of 2008) and in parallel continued to "optimize" the stability of the XUV laser sources for applications, especially in the perspectives of DNA irradiations.

2.1 XUV sources development for applications.

The LASERIX configuration that was used for the development of the XUV sources is the low energy/high repetition rate part of the full system, as described in the first section of this paper. Typically, we used 2 Joules of uncompressed infrared energy per pulse coming out from the last Ti:Sa amplifier stage of the front-end. The final amplified beam is equally split into two new beams. The first one remains uncompressed (700 ps) and the second one enters an in-vacuum compressor providing durations varying from 40 fs to several 10 ps.

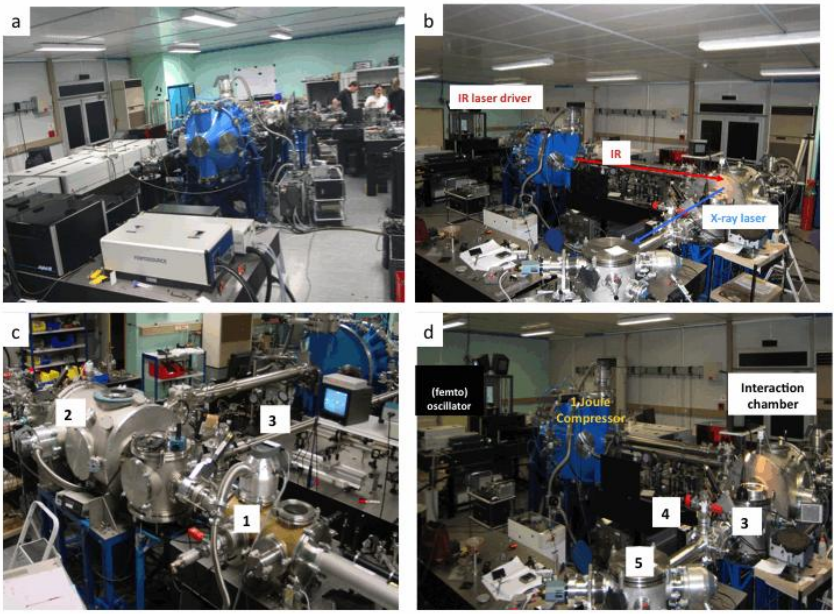

Figure 2: Experimental set-up for the XRL generation in the 10 Hz repetition-rate configuration. The figure a gives a general view of the arrangement of the experimental area, including the pumping laser up to the front-end part, the compressor chamber (at the centre of the image) and the XUV sources investigations zone (at the back of the image). Different views of the experimental area are presented in figures 2b, 2c and 2d.

The equipments indicated by the numbers 1 and 2 in figure 2c are respectively the chamber for the production of HHG sources and the target chamber for X-ray lasers. Several diagnostics were used to monitor the energy, as indicated in figure 2d, the source size and the beam uniformity of the x-ray laser, or the HHG source: the near-field imaging system (identified by the number 3), far-field system (identified by the number 4), grating spectrometer (identified by the number 5). Near field images were obtained using an XUV aspherical mirror (f=500mm) forming the image of the exit aperture of the source on an XUV CCD camera with a magnification of 13 (following the tube, identified by the number 3 in figure 2c).

In order to offer the most suitable and reproducible XUV laser sources for external users, we performed several specific investigations. We focused our attention on the optimization of the Mo Ni-like X-ray laser emitting at 18.9 nm, following our recent investigations at the Lund Laser Center, in collaboration with Pr. C.-G. Wahlström in a Grazing incidence pumping (GRIP) [9-11]. Thus as mentioned in more details in [12], we first investigated the possibility of performing several shots at the same target area including the influence of a pre-pulse. This last parameter seems to be very critical in the effect of increasing both the output energy of the X-Ray laser source and the number of shots at the same target place. Thus, as illustrated in Figure 3, the use of a pre-pulse, with an energy greater than 20 mJ, increases the output energy of the X-ray laser by a factor 2 in the best configuration (prepulse of ≈ 50 mJ energy) and provides a constant output (with 10% fluctuation) during 100 shots at the same target area.

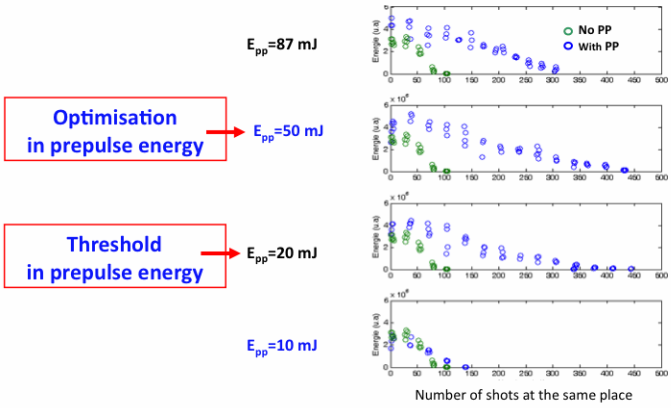

Figure 3: Output Energy of the X-Ray laser versus the number of the number of shots at the same target area for different values of prepulse energy. Green dots represent the results in case of absence of prepulse.

Then, finally to increase the stability of the XUV laser source, we implemented a setup, developed in GSI and called Double-pulse single-beam in grazing incidence (DGRIP) [13-15], bringing the advantage of an

intrinsically perfect overlap between the two pulses which enables reproducible results, particularly useful for applications. The double-pulse generation is achieved by a Mach-Zehnder type interferometer set-up which creates two collinear pulses with adjustable delay of 0 to 3 ns, adjustable energy ratio and, due to the introduction of an additional double-pass grating compressor in one arm, separately selectable pulse durations.

2.2 First investigations of applications at 10 Hz repetition-rate.

All the previous investigations lead to obtain a stable and reliable operation of a soft X-ray laser for application [16]. To illustrate the high interest of this optimization work, we used our "optimized" source @ 18.9 nm to irradiate DNA samples.

Several DNA samples were placed in the irradiation chamber on a multi-target holder wheel and aligned under vacuum in the XRL beam using a combination of visible and XUV cameras. The soft X-ray laser beam was filtered by a 200 nm Al filter and focused by an f = 300 mm spherical multilayer mirror aligned slightly off-axis to match the sample surface. Up to 21 000 pulses are delivered during a time of 90 minutes operation at a repetition rate of 10 Hz and average pulse energy of 200 nJ with the Mo target area changed every 10s. We checked that from one 100 shots dose accumulation to another one, the integrated dose fluctuations do not exceed 5%. The latter consideration appears to be the most relevant for the present application. We thus decided to irradiate DNA samples by shooting 100 times on the same Molybdenum target groove. An on-line measurement of the photon number delivered on target during the irradiation is used to monitor the irradiation process, measuring the photocurrent on the surface of the last multilayer mirror.

The three samples (DNA, DNA+PtTC, DNA+NP) were irradiated with the same procedure. The results presented in figure 4 show that the irradiation by soft X-ray laser photons induces significant amounts of SSB and DSB. The values of SSB in figure 4 were corrected for the presence of SSBs in the control. The DNA sample shows a significant number of SSBs which increases by a factor of two in presence of platinum (DNA+PtTC, DNA+NP). The number of DSB increases by 76% in presence of PtTC and double in presence of nano-particles.

This unique experiment demonstrates that low energy X-Rays irradiation induces DNA damage, as previously seen with low energy ions and electrons.

This confirms the effect of direct processes in DNA breaks.

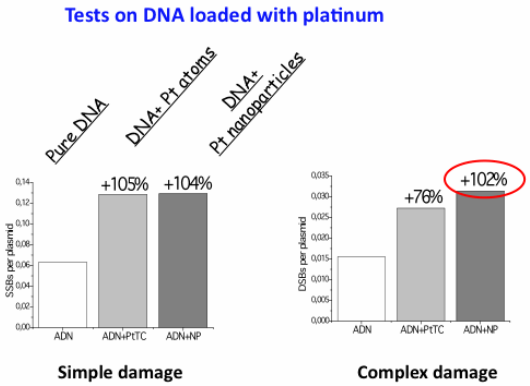

Figure 4: Single (SSB) and double (DSB) strand breaks induced in DNA samples in the case of pure DNA, DNA-PtTC complexes and DNA-NP complexes

These experiments should be obviously repeated in order to confirm this observation. The experimental stabilization and characterization of soft x-ray irradiation is now sufficient to provide a reliable source for systematic and quantitative studies of such effects.

3 Present status of LASERIX in 2010.

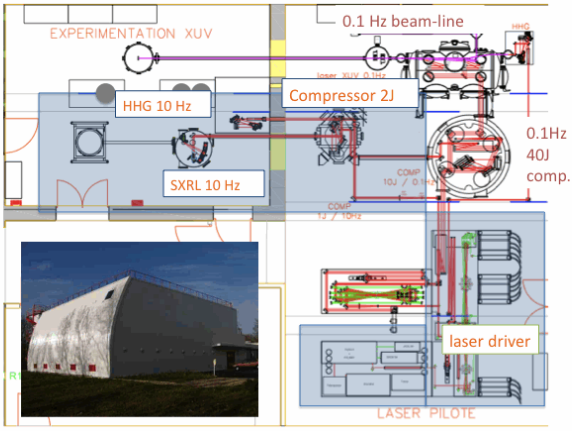

Figure 5: Schematic view of the implementation of LASERIX in the new building (on the left bottom) and the arrangement of the 10 Hz and 0.1 Hz beam lines.

The main part of LASERIX is now implemented in the underground floor of the new building, as indicated in figure 5. Two rooms compose the area. In

the first one (14.5×7.2 m^2) are implemented the pumping laser system (except the QUANTEL pumping lasers), the full energy compressor and the main interaction chamber for the production of X-Ray lasers in the 0.1 Hz configuration. A supplementary compressor is added to compress the 1Joule beam at 10 Hz repetition-rate. The second room (5.6×7.2 m^2) is dedicated to the production of XUV laser sources in the 10 Hz rep-rate and to the use of the X-Ray Lasers in 10 Hz and 0.1 Hz rep-rates for applications. Two holes in the wall separating the two rooms enable transport of the X-Ray laser beams running at 0.1Hz rep-rate and the compressed and uncompressed pumping energy for the production of the X-Ray laser running at 10Hz rep-rate.

4 Conclusions and Outlook

LASERIX will be useful to develop transient collisional XRLs of various wavelengths comprised between 7 and 30 nm. Wavelengths shorter than 10 nm will become progressively available, and a shot-to-shot control of the source will be installed, useful for application experiments. Pump-probe experiments with a temporal resolution of 40 femtoseconds and without jitter will be also possible.

Access will start in the beginning of 201& for external users. The first semester of 2011 will be also dedicated to the development of the 0.1 Hz rep-rate facility and access could be available for this set-up in the beginning of 2012.

References

1. L.I. Gudzenko et al., Sov. Phys. Doklady 10, 147, 1965
2. R.C. Elton, Appl. Optics 14, 97, 1975
3. D. Ros et al, Laser ans Particle Beams Journal, 20, 23 (2002)
4. G. Jamelot et al., in X-Ray Lasers 2002, AIP Proc. N° 641, 563 (2002).
5. G. Jamelot et al., in X-Ray Lasers 2004, IOP Conf Series N° 186, 677 (2005).
6. D. Ros et al., in X-Ray lasers 2006, Springer Proc. in physics115,192 (2007).
7. D. Ros et al., in X-Ray lasers 2008, Springer Proc. in physics 130,14 (2009).
8. F. Plé et al., Opt. Lett 32, 238 (2007).
9. K. Cassou et al., Opt. Lett. 32, 139 (2007).
10. P. Lindau et al., Opt. Express 15, 9486 (2007).
11. S. Kazamias et al., Phys. Rev. A 77 (2008).
12. O. Guilbaud et al. In soft X-Ray lasers and Applications VIII 7451, OT (2009).
13. D. Zimmer et al., Opt. Lett. 35, 450 (2010).
14. D. Zimmer, et al., Phys. Rev. A 82, 013803, (2010).
15. B. Zielbauer et al, in this proceedings book
16. B. Zielbauer et al., Appl. Phys. B - lasers and Optics – **100,** 731 (2010).

Using the X-FEL as a source to investigate photo-pumped X-ray lasers

Joseph Nilsen and Howard A. Scott

Lawrence Livermore National Laboratory, Livermore, CA 94551

Abstract. H-like and He-like resonantly photo-pumped laser schemes were proposed for producing X-ray lasers nearly four decades ago. However, demonstrating these schemes in the laboratory has proven to be elusive. One major challenge has been the difficulty of finding an adequate resonance between a strong pump line and a line in the laser plasma that drives the laser transition. After finding a good resonance, a second challenge has been to simultaneously create the pump and laser plasma in close proximity so as to allow the pump line to transfer its energy to the laser material. With the construction of the X-ray free electron laser (X-FEL) at the SLAC Linac Coherent Light Source (LCLS) researchers now have a tunable X-ray laser source that can be used to replace the pump line in previously proposed laser schemes and allow them to study the physics and feasibility of photo-pumped laser schemes. In this paper we model the Na-pumped Ne X-ray laser scheme that was proposed and studied many years ago by replacing the Na He-α pump line at 1127 eV with the X-FEL at LCLS. We predict large gains greater than 400 cm^{-1} on the 4f – 3d transition at 231 Å.

1 Introduction

Resonantly photo-pumped laser schemes using H-like and He-like ions were proposed for producing X-ray lasers from the earliest days of lasers [1]. Demonstrating these schemes in the laboratory has proven to be very elusive. A major challenge has been the difficulty of finding an adequate resonance between a strong pump line and a line in the laser plasma that drives the laser transition. After finding a good resonance, a second challenge has been to create both the pump and laser plasma in close proximity so as to allow the pump line to transfer its energy to the laser material. With the availability of the X-FEL at LCLS [2] we now have a tunable X-ray laser source that can be used to replace the pump line in previously proposed laser schemes and allow researchers to study the physics and feasibility of photo-pumped laser schemes. In this paper we model the Na-pumped Ne X-ray laser scheme that was proposed and studied many years ago by replacing the Na He-α pump line at 1127 eV with the X-FEL at LCLS. We predict gain on the 4f – 3d transition at 231 Å that is orders of magnitude larger than the gains predicted [3] two decades ago using the Saturn pulsed power machine at Sandia

J. Lee et al. (eds.), *X-Ray Lasers 2010,* Springer Proceedings in Physics 136,
DOI 10.1007/978-94-007-1186-0_6,

Table 1. Resonantly photo-pumped laser schemes with 4f – 3d lasing in H and He-like ions

Pump Line		λ_P (Å)	Absorbing Line		λ_A (Å)	$\Delta\lambda_P/\lambda_P$ (%)	λ_L (Å)
Na	He-α_S	11.003	Ne	He-γ_S	11.000	0.022	231
K	Ly-α_2	3.3521	Cl	Ly-γ_2	3.3511	0.029	64.8
Cr	He-α_T	2.1925	Sc	Ly-γ_2	2.1917	0.036	42.5
Mn	Ly-α_1	1.9247	V	He-γ_S	1.9255	0.040	38.7
Cu	Ly-α_1	1.4253	Fe	Ly-γ_2	1.4253	0.006	27.7
Sr	Ly-α_2	0.82708	Se	Ly-γ_1	0.82765	0.069	16.2
Nb	He-α_S	0.72175	Rb	He-γ_T	0.72143	0.044	14.4

National Laboratory to create the Na pump line. Table 1 shows all the resonantly photo-pumped H and He-like schemes that could lase on the 4f – 3d line that were identified many years ago but which have not yet been demonstrated. The X-FEL can now replace any of these pump lines and enable us to study these lasing schemes.

2 The characteristics of the X-FEL beam at LCLS

With the advent of the X-FEL at the LCLS facility we looked at the characteristics [4] of this laser to see if it would be relevant for exploring photo-pumping X-ray laser schemes. The basic feature of the X-FEL is that it can produce a tunable X-ray source that extends from 800 to 8500 eV. It operates at a 120 Hz repetition rate with approximate output of 10^{12} photons per pulse. The beam has a spectral bandwidth of 0.1% of the fundamental, a pulse duration of 100 - 200 fs, and an unfocused spot size of 400 μm square.
The beam can be focused down to a 1 μm square using X-ray optics. The beam can be rapidly tuned over 3% of the fundamental energy by adjusting the electron beam energy. In earlier calculations [5] we predicted that the photo-ionization rate of Ne gas is about 10 per μsec for the unfocused beam, which is much too slow for using the X-FEL is photo-ionize Ne gas down to the He-like iso-electronic sequence. In this paper we look at the case of a focused X-FEL beam with a 1 μm spot size and 100 fs pulse duration. Using these numbers gives a spectral intensity $I_\varepsilon = 1.6 \times 10^{17}$ W / (eV cm^2). The line strength of the X-FEL beam in photons per mode $n_\varepsilon = 1.579 \times 10^{-5}\ I_\varepsilon / \varepsilon^3$ where ε is the photon energy in eV. Looking at some typical photon energies $n_\varepsilon = 1765$ at 1127 eV and drops to 9.45 at 6442 eV for the focused beam. For a photo-pumped laser scheme the beam strength in photons per mode is the ratio of the stimulated rate to the spontaneous rate. This is approximately the

same as the maximum fractional population divided by the statistical weight of the level being pumped when the beam strength is much less than one. When the beam strength exceeds one it mean the stimulated rate is much larger than the spontaneous rate and the two levels will be locked into equilibrium with similar populations per statistical weight.

3 Description of the He-like Ne X-ray laser scheme

One of the resonantly photo-pumped schemes that were tried experimentally many years ago was the Na-pumped Ne scheme that used the He-α line of Na to photo-pump the He-γ line of Ne and create gain on several n = 4 to n = 3 transitions in He-like Ne. Figure 1 shows the three principal laser lines that were predicted to have gain, the 4f – 3d line at 231.1 Å, the 4d – 3p line at 231.6 Å, and the 4p – 3s line at 222.7 Å. The 4p – 3s line lases directly from the 4p level that is being photo-pumped. However, it is important to understand that the other two laser lines depend on collisional excitation to transfer population from the 4p to 4d to 4f states. Since these states are very close in energy they tend to equilibrate very quickly if the density of the plasma is high enough.

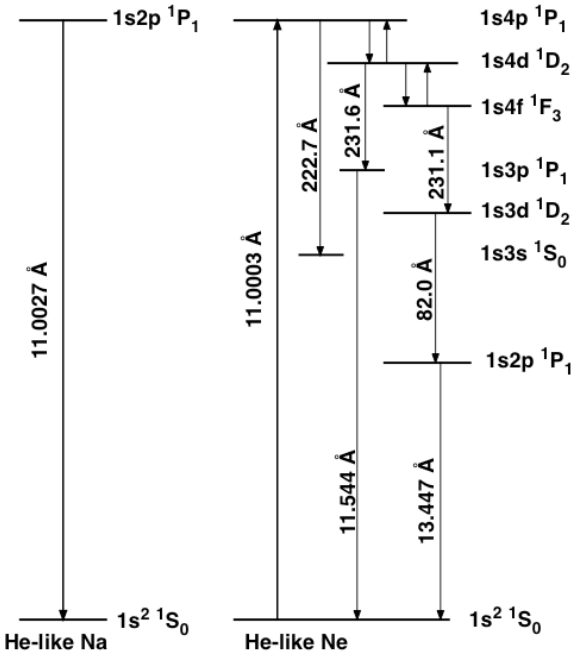

Fig. 1. Energy level diagram for the Na-pumped Ne X-ray laser.

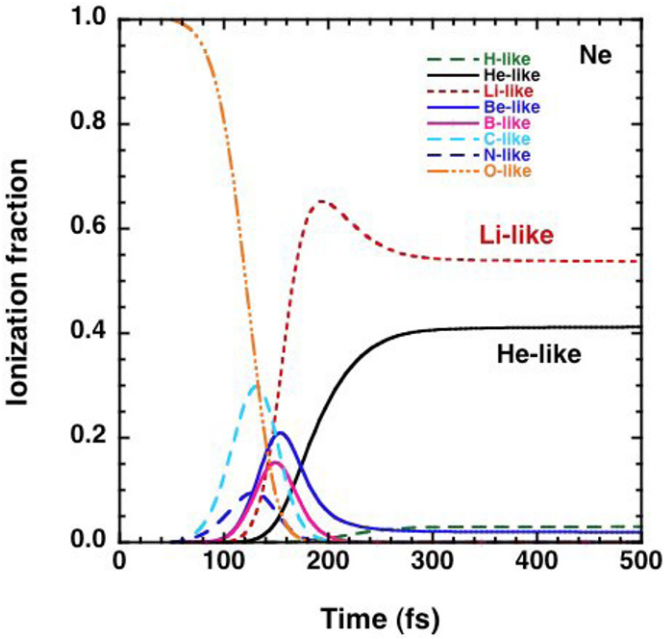

Fig. 2. Fractional population of Ne iso-electronic sequences versus time.

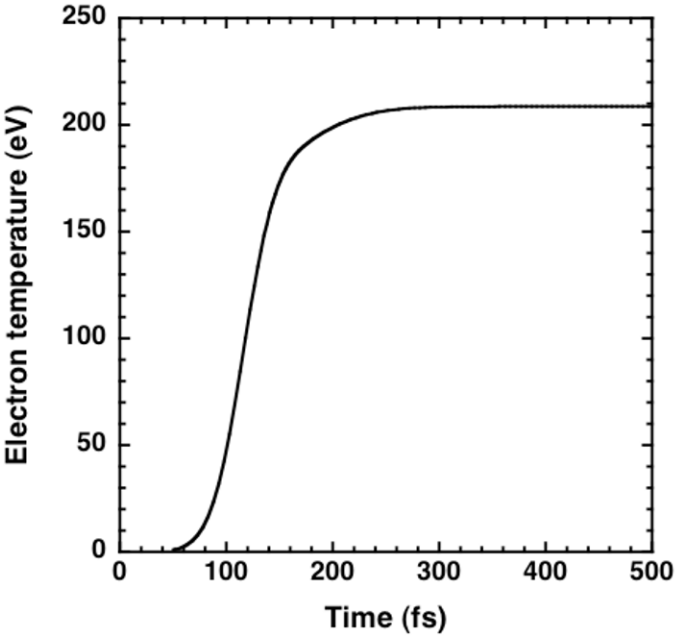

Fig. 3. Electron temperature of Ne plasma versus time.

To model this system we used an ion density of 1018 cm-3 for the Ne gas, which is the same as used in the Saturn pulsed power experiments that were done many years ago [3]. Because of the complexity of the atomic model for near neutral sequences we started the calculation in O-like Ne with an electron temperature of 1 eV and an ion temperature of 0.025 eV. In He-like Ne the atomic model had 252 levels including doubly excited states up to 2p5f while O-like Ne has 1537 levels. The CRETIN code [6] was used to model the kinetics in one dimension (1D). We created an input file that represented the monochromatic X-FEL beam at 1127 eV with a full width of 1.1 eV and a 100 ps full-width half maximum (FWHM) duration Gaussian pulse. The pulse peaks at 200 ps in the various figures. Under these conditions the peak photo-ionization rate for the Ne plasma in the Li-like sequence is 5 psec-1. Figure 2 shows the ionization fraction of the various iso-electronic sequences versus time. One observes that the plasma quickly reaches 40% He-like and 55% Li-like shortly after the peak of the pulse. Figure 3 shows the electron temperature of the Ne plasmas versus time. The plasma quickly reaches an electron temperature of 208 eV while the ion temperature stays near room temperature and only slowly doubles to 0.05 eV by 1100 ps. For these short pulse driven low-density plasmas the ions stay very cold and are decoupled from the electrons.

Another important issue to understand is the fractional populations divided by the statistical weight of the upper laser states and the ground state in He-like Ne. The lower laser states have very small populations initially. Figure 4 shows the fractional populations versus time for the He-like ground state and three of the upper laser levels. One can observe how the 1s and 4p levels are locked together by the strong X-FEL and then diverge as the X-FEL turns off. As the population of the 4p level decays one observes the populations of the 4d and 4f levels rise as collision processes try to equilibrate the populations of these levels. The calculation is done so that the X-FEL pulse peaks at 200 fsec on the time axis. Figure 5 shows the predicted gain for the three strongest laser lines in He-like Ne. The dominant line is the 4f – 3d transition that has a peak gain of 438 cm^{-1} at 1067 fs. This line has a FWHM gain duration of 1840 fs. In contrast the 4d – 3p line has a peak gain of 270 cm^{-1} at 496 fs and the 4p – 3s line has a peak gain of 333 cm^{-1} at 301 fs. The 4f – 3d gain peaks almost 900 fs after the peak of the X-FEL drive pulse because of the time needed for electron collisions to transfer population from the 4p level via the 4d level. With these high gains a plasma length of 0.1 cm should be more than sufficient to obtain saturated output for the laser lines. If we look at the absorption coefficient for the 1s – 4p He-like line that is being pumped it has a value of 0.24 cm^{-1} at 200 fs, the peak of the X-FEL pump pulse and remains less than 1 cm^{-1} until 300 fs, which is when the X-FEL pump is mostly over.

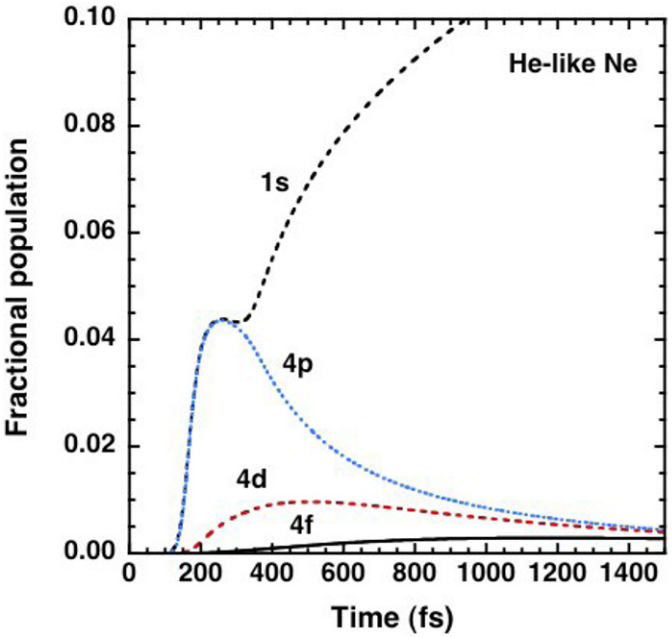

Fig. 4. Fractional population of He-like Ne ground state and upper laser state levels versus time.

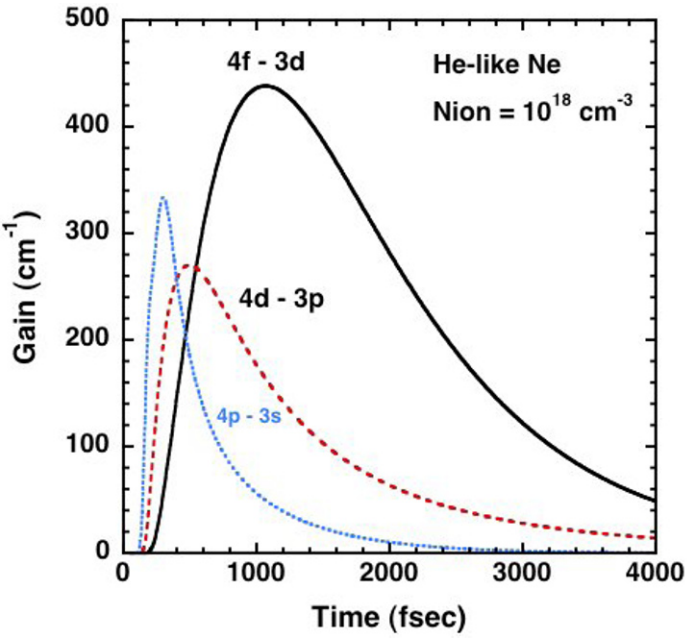

Fig. 5. Gain of three n=4 – n=3 laser transitions of He-like Ne versus time.

4 Conclusions

Since the early days of laser research H-like and He-like resonantly photo-pumped laser schemes have been proposed for producing X-ray lasers. However, demonstrating these schemes in the laboratory has proved to be elusive. One challenge has been the difficulty of finding an adequate resonance between a strong pump line and a line in the laser plasma that drives the laser transition. Given a good resonance, a second challenge has been to create both the pump and laser plasma in close proximity so as to allow the pump line to transfer its energy to the laser material. With the advent of the X-FEL at LCLS we now have a tunable X-ray laser source that can be used to replace the pump line in previously proposed laser schemes and allow researchers to study the physics and feasibility of photo-pumped laser schemes. In this paper we model the Na-pumped Ne X-ray laser scheme that was proposed and studied many years ago by replacing the Na He-α pump line at 1127 eV with the X-FEL at LCLS. We predict gain on the 4f – 3d transition at 231 Å. Given the tunable nature of the X-FEL we are no longer restricted to studying photo-pumping in just the materials that have accidental resonances with strong pump lines but we can now study any ion of interest that falls within the spectral range of the X-FEL. In addition to looking for gain and lasing the X-FEL can also be used to study the kinetics of these laser systems by observing the dynamic evolution of the fluorescent lines.

Acknowledgements. This work was performed under the auspices of the U.S. Department of Energy by Lawrence Livermore National Laboratory under Contract DE-AC52-07NA27344.

References

1. Joseph Nilsen, James H. Scofield, and Elaine A. Chandler, "*Reinvestigating the Early Resonantly Photo-Pumped X-ray Laser Schemes*," Appl. Opt. **31**, 4950 – 4956 (1992).
2. See SLAC National Accelerator Laboratory web site http://lcls.slac.stanford.edu/
3. Joseph Nilsen and Elaine Chandler, "*Analysis of the resonantly photo-pumped Na-Ne X-ray laser scheme*," Phys. Rev. A **44**, 4591 – 4598 (1991).
4. Richard (Dick) W. Lee from LLNL – private communications.
5. Joseph Nilsen, "Using short pulse lasers to drive X-ray lasers." *SPIE Proceedings 7451 - Soft X-ray Lasers and Applications VIII,* edited by Gregory J. Tallents and James Dunn (SPIE Press, Bellingham, 2009), pp. 74510N-1-8
6. Howard A. Scott, *"Cretin - a radiative transfer capability for laboratory plasmas,"* JQSRT **71**, 689 - 701 (2001).

Part 2: Repetitive X-Ray Lasers

Demonstration of an all-diode pumped soft x-ray laser and other advances in table-top soft x-ray lasers

Jorge J. Rocca[1,2], B. Reagan[1], F. Furch[1,2], Y. Wang[1], D. Alessi[1], D. H. Martz[1], M. Berrill[1], V.N. Shlyaptsev[1], B. M. Luther[1], A. H. Curtis[1]
rocca@engr.colostate.edu

[1]NSF ERC for Extreme Ultraviolet Science and Technology and Department of Electrical and Computer Engineering, Colorado State University, Fort Collins, Colorado 80523, USA
[2] Department of Physics, Colorado State University, Fort Collins, Colorado 80523, USA

Abstract. We report the first demonstration of an all-diode-pumped soft x-ray laser system. Lasing was achieved in the λ = 18.9 nm line of Ni-like Mo ions pumping with a diode-pumped cryo-cooled Yb:YAG chirped-pulse-amplification laser system that generates 1 J pulses of 8.5 ps duration. Driver lasers pump by diodes opens the possibility to develop a new generation more compact soft x-ray lasers operating at significantly increased repetition rates for applications.

In a separate development we have demonstrated a gain-saturated table-top λ=10.9 nm laser operating at 1 Hz repetition rate with an average power of 1 μW in the $4d^1S_0 \rightarrow 4p^1P_1$ transition of nickel-like Te and observed lasing at 8.8 nm in nickel-like La in plasmas exited by a Ti:sapphire laser. Utilizing the same pump laser we obtained laser pulse energies of up to 10 μJ and an average power of 20 μW in the 13.9 nm line of Ni-like Ag.

In a third set of experiments we characterized the beam properties of an injection-seeded soft x-ray laser based on the amplification of high harmonic pulses in a solid-target plasma soft x-ray laser amplifier. Injection-seeding is shown to dramatically improve the far-field laser beam profile and reduce the beam divergence. Measurements and 2-dimensional simulations for a 13.9 nm nickel-like Ag amplifier show that the amplified beam divergence depends strongly on the seed divergence, and can therefore be tailored by selecting it.

1. Demonstration of a Diode-pumped soft x-ray laser

The development of high average power soft x-ray lasers (SXRL) is interesting for a number of applications. As summarized below in Section 2, gain-saturated table-top soft x-ray lasers pumped by infrared chirped pulse amplification (CPA) laser systems have been demonstrated at wavelengths down to 10.9 nm [1], and with average powers up to 20 μW at 13.9 nm [2]. However the repetition rate and therefore the average power of these flashlamp-pumped lasers is typically limited to less than 10 Hz. The small quantum defect of Yb doped materials and the high pumping efficiency that

J. Lee et al. (eds.), *X-Ray Lasers 2010,* Springer Proceedings in Physics 136,
DOI 10.1007/978-94-007-1186-0_7,

results from pumping with a narrow bandwidth source of the optimum wavelength allow for the development of solid state laser systems that are significantly more compact. Additionally, when cooled to cryogenic temperature the thermal conductivity increases nearly an order of magnitude and the saturation fluence decreases by a factor of 7 allowing efficient operation at very high average powers.

Herein we discuss the demonstration of a table-top SXRL pumped by very compact all diode pumped CPA laser system based on cryogenically-cooled Yb:YAG amplifiers [3]. The pump laser produces 1 J, picosecond pulses at 10 Hz repetition rate. To the best of our knowledge this is the highest energy demonstrated to date for a diode-pumped system producing sub-10 ps pulses. A block diagram of the CPA system is illustrated in Fig.1. The system consists of a modelocked oscillator, pulse stretchers, two stages of amplification and a grating pulse compressor. The SXRL system is completed with a focusing optics chamber and the target chamber. The entire laser system with the exception of the pulse compressor fits onto a single standard 12'x5' optical table. The pump laser system consists of a SESAM modelocked Yb:KYW oscillator pumped by a 30 W, 980 nm, laser diode, two grating stretchers (only one shown in schematic of Fig.1) , a regenerative amplifier, a cryo-cooled Yb:YAG amplifier and a dielectric grating compressor. The laser oscillator produces a 1.2 W train of 300 fs pulses at a repetition rate of 57 MHz. The beam exiting the oscillator is split into three

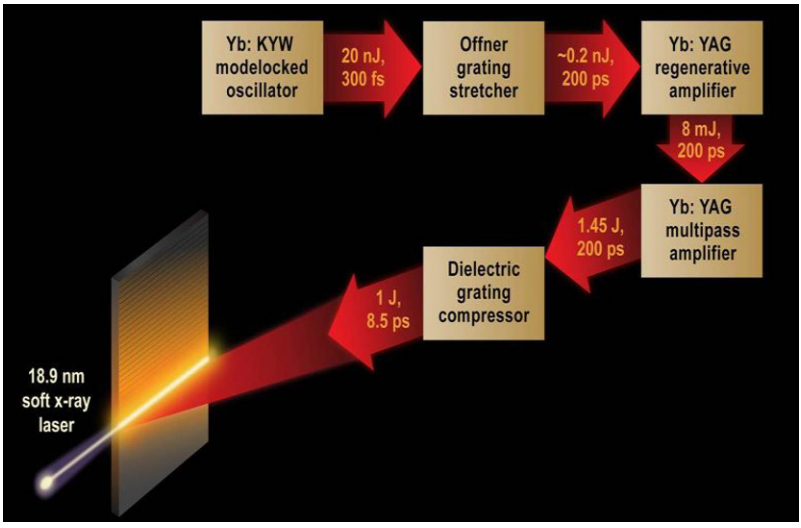

Fig. 1: Schematic Block diagram of the diode pumped soft x-ray laser system.

pulses and sent through two different grating stretchers before being recombined into a single beam to create a train of two 160 ps pulses with negative group velocity dispersion (GVD) and a 200 ps pulse with positive

GVD. These stretched pulses are subsequently amplified in two cryo-cooled Yb:YAG amplifiers. The first amplifier is a regenerative amplifier pumped by a 90 W fiber-coupled laser diode emitting at 940 nm. The cavity of the regenerative amplifier ensures that the three stretched pulses are collinear throughout the system. The regenerative amplifier boosts the pulse energy to ~ 7 mJ. The regenerative amplifier was demonstrated to maintain the pulse energy and beam quality at repetition rates up to 100 Hz (Fig.2).

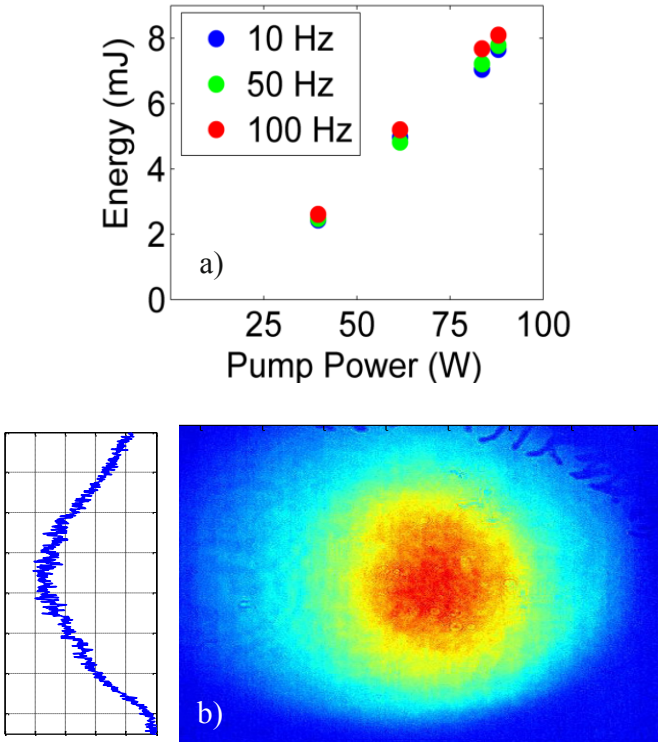

Fig. 2. a) Output pulse energy of the cryo-cooled Yb:YAG regenerative amplifier as a function of diode pump power for three repetition rates. b) Output beam profile.

The second amplification stage, shown in Fig. 3, consists of a 12-pass multipass amplifier which utilizes to two cryo-cooled, Yb:YAG disks in the active mirror configuration. Each crystal is pumped by a 3.5 kW diode stacks producing 2 ms pulses . This stage amplifies the pulses to energies of 1.45 J at 10 Hz repetition rate (Fig 3b). Following amplification, the pulses are compressed by a 70 % efficient dielectric grating pair to produce 8.5 ps duration 1 J pulses.

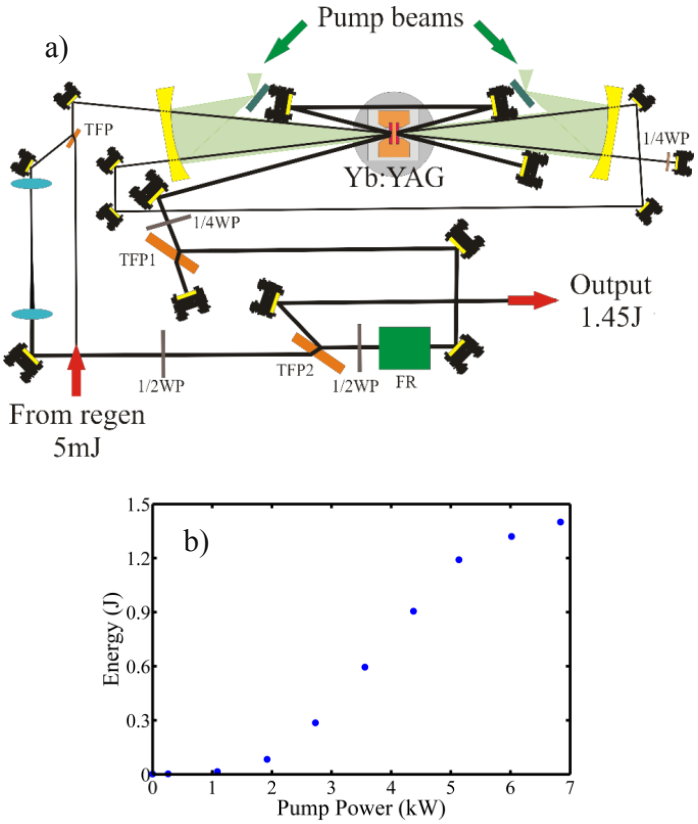

Fig. 3: a) Schematic layout of the 12-pass Yb:YAG cryocooled amplifier. WP = waveplate; TFP = Thin Film Polarizer; FR = Faraday Rotator . b) Output pulse energy of the Yb:YAG amplifiers as a function of diode pump power. The data was obtained at 10 Hz repetition rate.

The all-diode-pumped CPA laser described above was used to pump a λ=18.9 nm soft x-ray laser. The train of pulses generated by the pump laser was focused at grazing incidence onto a Mo target [4,5] to form a 4mm long by 35 μm wide line. Two pre-pulses with 350 ps FWHM duration create and ionize the plasma that is subsequently rapidly heated by a 8.5 ps FWHM pulse to produce a transient population inversion in the 18.9 nm transition of Ni-like Mo ions. Figure 4 (a) shows a single shot on-axis spectrum corresponding to a plasma create by focusing 700 mJ of total pump energy incident on target. The intensity of the 18.9 nm Ni-like Mo laser line is similar to that of other plasma lines. Increasing the pump energy to 940 mJ results in dramatic growth of the laser line intensity, accompanied by a significant angular narrowing of the line, a clear evidence of strong laser amplification (Fig. 4 (b)). This new type of compact diode-pumped SXRLs will be capable to operate at greatly increase repetition rates, producing high average power for applications.

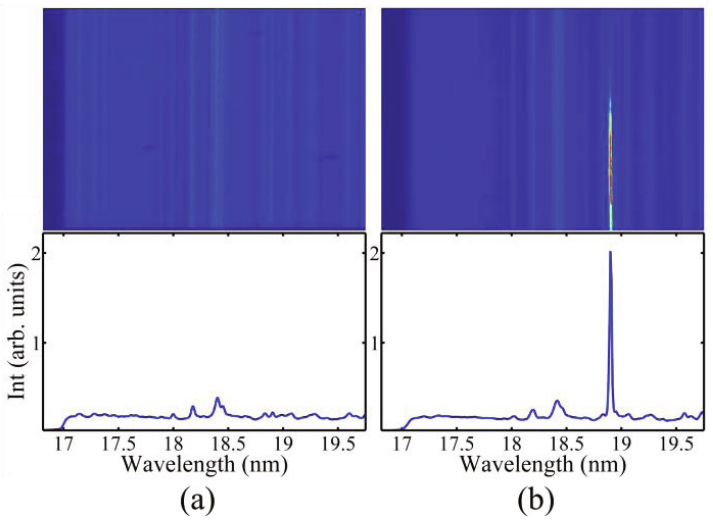

Fig. 4. Soft x-ray spectra of a molybdenum plasma heated by the diode pumped Yb:YAG CPA laser system (a) On-axis soft x-ray spectrum taken with a total pump energy on target of 0.7 J. (b) The same spectrum taken with 0.94 J of pump energy, showing laser amplification in the 18.9 nm laser line of Ni-like Mo.

2. Gain-saturated 10.9 nm SXRL at 1 Hz repetition rate and lasing at 8.8 nm.

There is also interest in extending table-top SXRLs to shorter wavelengths. However, the steep wavelength scaling of the energy necessary to pump such lasers imposes a challenge to the demonstration of gain-saturated high repetition rate lasers at shorter wavelengths. As a result, the use of table-top SXRLs in applications has been limited to wavelengths above 13.2 nm [6,7]. We have recently demonstrated a gain-saturated table-top 10.9 nm laser in the $4d^1S_0 \rightarrow 4p^1P_1$ transition of nickel-like Te that operates at 1 Hz repetition rate. Lasing in nickel-like Te was first demonstrated using 520 J of optical laser pump energy to heat a collisionally pumped plasma [8]. More recently gain in this transition was obtained in a table-top set up using ~ 1 J pulses of 8 ps duration impinging at a grazing angle of 23 degrees to heat a pre-created plasma [9]. However, the output laser intensity was far from saturation, producing an insufficient photon flux for applications.

Gain-saturated lasing was generated by rapidly heating a 5 mm wide solid Te slab target using a CPA Ti:sapphire laser system that produces λ = 800nm pulses with energies up to 5.5 J before compression. After the third amplification stage the stretched pulses have a duration of 210 ps. A beam

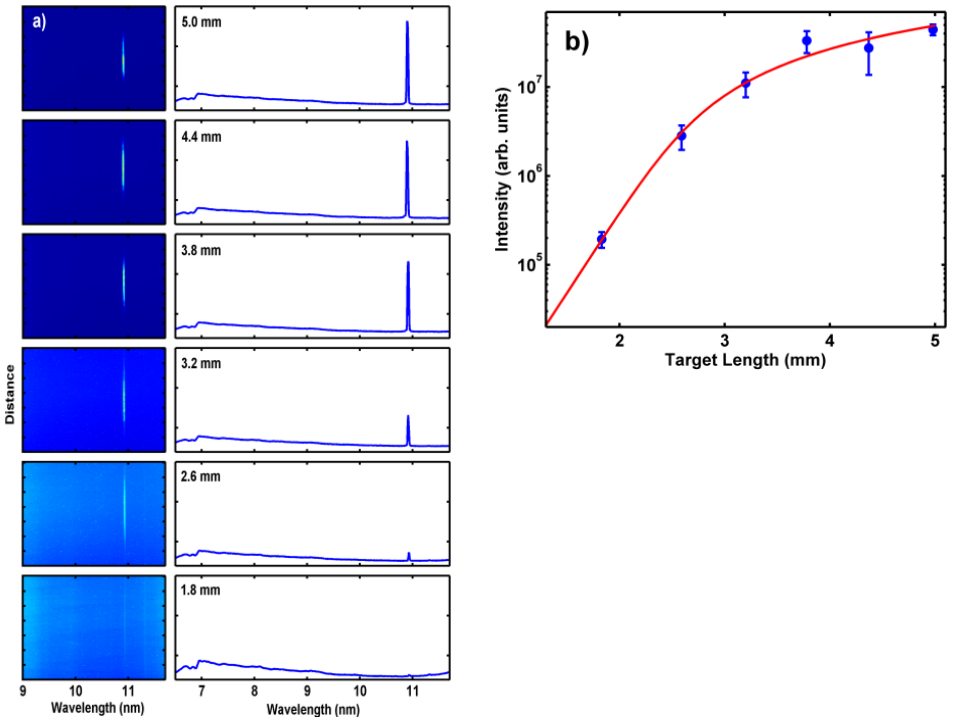

Fig. 5. a) On axis single-shot spectra from the Te plasma for increasing plasma column up to 5 mm. Strong lasing is observed at 10.9 nm. b) Measured laser line intensity as a function of plasma column length. Each data point is an average of eight laser shots.

splitter placed after the final amplification stage was used to re-direct 40% of the energy into a pre-pulse arm used to create a plasma with relatively smooth density gradients. Two pre-pulses pulses were focused into a 30 μm x 5 mm FWHM line onto the target. The remaining 60% of the energy was compressed into a 5 ps FWHM pulse and was focused at 30 degrees grazing incidence into an overlapping line of the same dimension.

Figure 5a shows a series of on-axis single-shot spectra and their corresponding vertical integrations for plasmas of different lengths between L = 1.8 and 5 mm. The total pump energy on target was fixed at 3.4 J. The SXRL intensity rapidly grows with target length to dominate the entire spectra, eventually reaching saturation. From these spectra it was determined that for the 5 mm target the SXRL beam divergence in the direction parallel to the target is 8.5 ± 1 mrad. The measured SXRL intensity as a function of target length is shown in Fig. 5b. The fit shows a small signal gain of g_0= 45.3 cm^{-1} and an integrated gain length product of 14.1 at 5 mm. At about 3 mm, the intensity starts to show signs of saturation. Strong soft x-ray lasing was observed to take place over a relatively narrow range of excitation delays centered at 200 ps. Lasing is observed to cease when the delay is increased to

400 ps. However, further increase of the delay results in weak lasing around 550 ps. This late laser pulse, predicted by the simulations, occurs when Co-like ions recombine into Ni-like ions, indicating the plasma is slightly over-ionized at the time of peak laser gain. A SXRL average power of ~ 1 μW was obtained pumping a 6 mm wide Te target with 4.2 J of total laser pump energy on target at a repetition rate of 1 Hz. The most intense laser pulses reach an energy of ~ 2 μJ. Assuming a laser pulse duration of 4 – 5 ps and a near-field laser spot ~ 15 μm in diameter from 3-D post processor ray trace simulation to a 1.5 D hydrodynamic/atomic physics simulation, the laser beam intensity is estimated to reach an intensity of ~ 2.5×10^{11} Wcm^{-2}. This intensity exceeds the 0.6-1.4×10^{10} Wcm^{-2} computed saturation intensity of this line for the plasma conditions of the experiment. This is the shortest wavelength gain-saturated table-top laser reported to date.

Using a sequence of Ti:sapphire laser pulses with a total energy of 5.2 J to heat a lanthanum target lasing was observed in the $4d^1S_0 \rightarrow 4p^1P_1$ transition of nickel-like La. Fig.6 is a single shot on-axis spectra of the lanthanum plasma showing amplification at 8.8 nm in this transition.

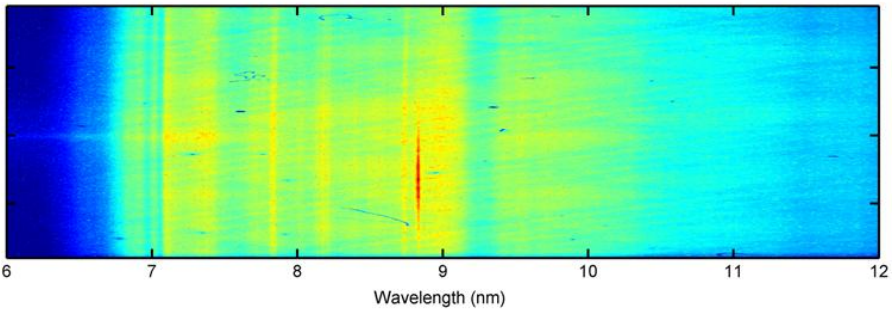

Fig.6. On axis spectra of a lanthanum plasma column showing lasing in the 8.8 nm line of nickel-like La.

3. Demonstration of high pulse energy 13.9 nm laser at 2.5 Hz repetition rate

Table-top SXRLs with wavelengths in the 13 nm spectral region have produced picosecond laser pulses with energy of ~1 μJ and average powers up to 2 μW when operating at 5-10 Hz repetition rate [9,10]. Significantly larger SXRL pulse energies, of ~10-25 μJ at a rate of one laser shot every several minutes have been produced using more energetic pump lasers [11,12]. We have recently obtained a significant increase in laser pulse energy of muti-Hz table top SXRL in the 13 nm spectral region by demonstrating a table-top

laser that is capable of producing laser pulses with average energy of 7 μJ at 2.5 Hz repetition rate at 13.9 nm [2]. With an average power of ~20 μW this laser will make possible new applications of coherent soft x-ray light on a table-top.

The SXRL pulses are generated in a narrow line focus Ag plasma heated by a sequence of pulses generated by a CPA Ti:Sapphire laser consisting of a Kerr mode-locked laser oscillator and three stages of amplification. The third amplification stage is pumped by a high energy frequency-doubled Nd-glass slab laser developed in house, designed operate at a repetition rates of a few Hz (Fig. 7). The front end of this pump laser consists of a Q-switched Nd:YLF oscillator that is subsequently amplified in two double-pass Nd:YLF rods. The output of the pre-amplifier is split into two beam and each of them is amplified by 8 passes thought a flash-lamp pumped Nd:glass slab amplifier (Fig 1.b). The output of each arm is frequency doubled in a KDP crystal to produce up to 10 J of 532 nm light, which is relay imaged into the third stage Ti:sapphire amplifier rod to produce λ=800 nm laser pulses with up to 7.5 J energy at 2.5 Hz repetition rate.

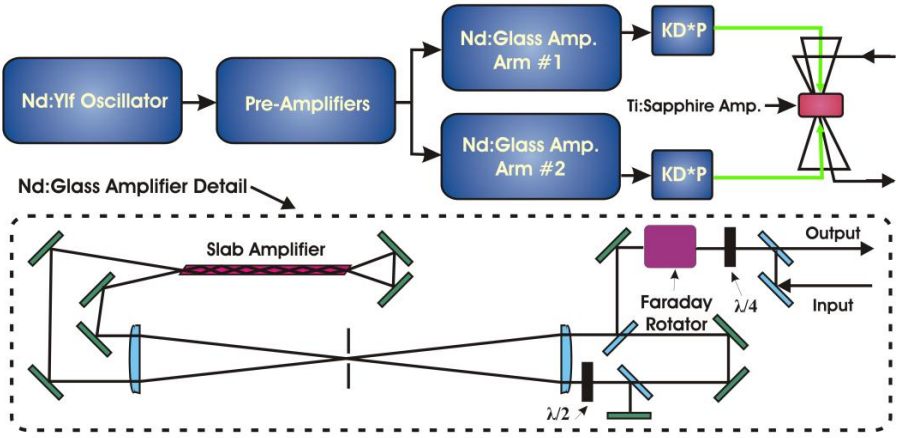

Fig.7. Block diagram of the third amplification stage of the Ti:sapphire laser used to pump the SXRL.

SXRL experiments at 13.9 nm were conducted by focusing up to 4.9 J of Ti:Sapphire laser energy into a line focus ~30 μm wide and 6.3 mm in length on the surface of a Ag slab target. Part of the output energy from the third amplification stage is directed to a pre-pulse arm using a 40% beam splitter. The rest of the energy was compressed to 6 ps in a vacuum compressor using dielectric gratings. Pre-pulses of 210 ps duration with a total energy of ~2.2 J were directed at normal incidence onto the target to create a Ag plasma that subsequently is rapidly heated by a 6 ps pulse impinging at 23 degree grazing incidence. A highly saturated SXRL beam results. The rapid heating of the

plasma to electron temperatures of up to ~ 550 eV generates a transient population inversion and amplification in the λ = 13.9 nm $4d^1S_0 \rightarrow 4p^1P_1$ transition of nickel-like Ag. The laser emits a single highly monochromatic line at 13.9 nm. Figure 8 shows the shot-to-shot variation of the laser output pulse energy when the laser is operated at 2.5 Hz repetition rate. The most energetic pulses exceed 8 μJ and the average power

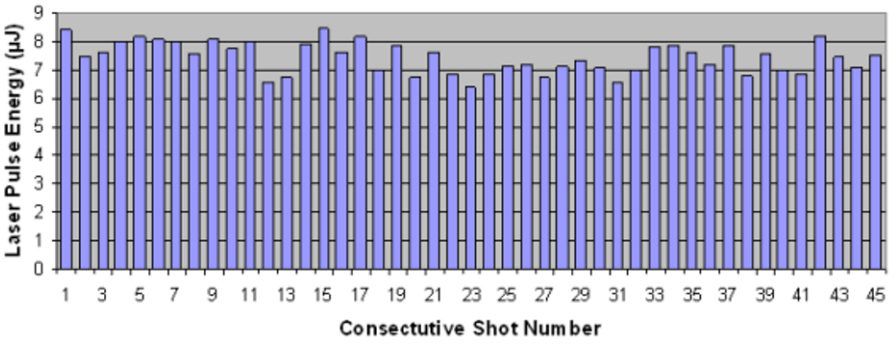

Fig. 8. Laser pulse energy output of the 13.9 nm laser when operated at 2.5 Hz repetition rate. The average power is ~ 20 μW and the shot-to-shot laser pulse energy variation is σ = 7 %.

approaches 20μW. The average pulse energy is 7.4 μJ and the shot-to-shot energy variation is characterized by a standard deviation of 7%. This relatively high shot-to-shot laser energy stability for a plasma amplifier is the result of the highly saturated regime of operation of this soft x-ray laser amplifier.

4. Beam Characteristics of an Injection-Seeded Solid-Target Soft X-Ray laser

Injection-seeding of these ASE SXRL amplifiers with high harmonic pulses can produce intense SXRLs with full spatial and temporal coherence, shorter pulse duration, reduced divergence, near-gaussian spatial beam profiles, and defined polarization [13-18]. We summarize results of the recent characterization of the near-field and far-field spatial distribution and laser line profile of a seeded and self-seeded (ASE) solid target SXRL amplifier.

The experiments were conducted by seeding a nickel-like Ag SXRL amplifier (λ = 13.9 nm) with 59th harmonic pulses of a Ti:sapphire laser. A Ti:sapphire laser centered at 815nm was used to create and heat the plasma with a sequence of two pre-pulses followed by an ~0.9 J heating pulse of 6.7 ps duration impinging at a grazing incidence angle of 23°. The pump pulses were focused onto a 3 mm wide Ag target to form a 30 μm×4.1mm FWHM long line. A small portion of the pump laser energy was focused in a Ne gas jet to generate the high harmonic seed. The output of the gas jet was relay imaged onto a ~100 μm diameter spot at the input of the plasma amplifier

using a gold-coated toroidal mirror designed to operate at a grazing incidence angle of 10°. Figure 9 shows the measured far-field beam profile of the unseeded and seeded SXRL amplifier using a back illuminated CCD placed 0.86 m from the source. Injection seeding dramatically reduces the beam divergence and results in a nearly Gaussian far field profile (Fig. 9b).

Laser experiments were conducted using two different seed pulse divergences to study the dependence of the amplified beam on the seed. When a harmonic seed pulse with a FWHM divergence of 0.5±0.03 x 0.7±0.04 mrad in the directions perpendicular and parallel to the target respectively was used to seed the plasma, an amplified pulse with a divergence of 1.4±0.14 x 0.7±0.07 mrad was measured to result. Simulations agree in showing that the divergence of the amplified beam in the direction parallel to the target surface

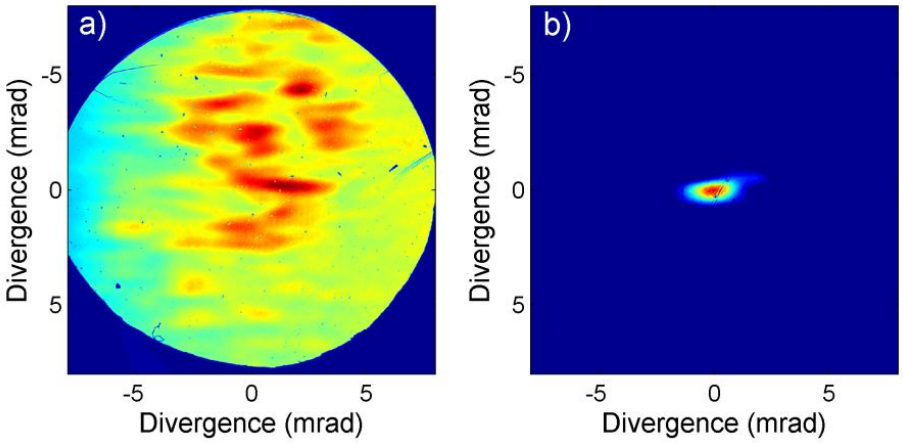

Fig. 9. Measured far-field distribution of an (a) self-seeded (ASE) and (b) seeded 13.9nm Ag solid-target SXR laser. The circular aperture in (a) is caused by the aperture of a thin-film filter.

closely resembles that of the seed beam, while the divergence perpendicular to the target surface is larger due to refraction [18]**.** When the divergence of the harmonic seed was increased to 1.6±0.3 x 1.4±0.4 mrad pulse, an amplified pulse with a divergence of 1.5±0.08 x 1.2±0.15 mrad was measured. The results show that when the divergence of the input harmonic seed is larger than ~1 mrad the far field of the amplified seed is almost completely dominated by the seed characteristics, while for smaller divergences it is controlled by both the input seed and refraction. These beam divergences are nearly an order of magnitude smaller than those corresponding to the unseeded amplifier. The near-field beam profiles of the self-seeded (Fig. 9a) and seeded (Fig. 9b) amplifier beams were measured using a 15.2x magnification imaging system. The measured near-field and far-field profiles were compared to simulations (Fig. 10). The location of the center of the near-field beam spot respect to the target surface, which is dominantly determined

by the position of the peak of the gain, was measured to be at a distance of 33±4 μm, in good agreement with the simulated near field profile. The near-field beam size of both the seeded and unseeded lasers is shown to be determined by the size of the gain region and the divergence of the amplified beams. The larger near-field spot size of the ASE laser in the direction parallel to the target surface is due to the larger divergence of the ASE laser, which allows rays with different trajectories to amplify across the entire gain region.

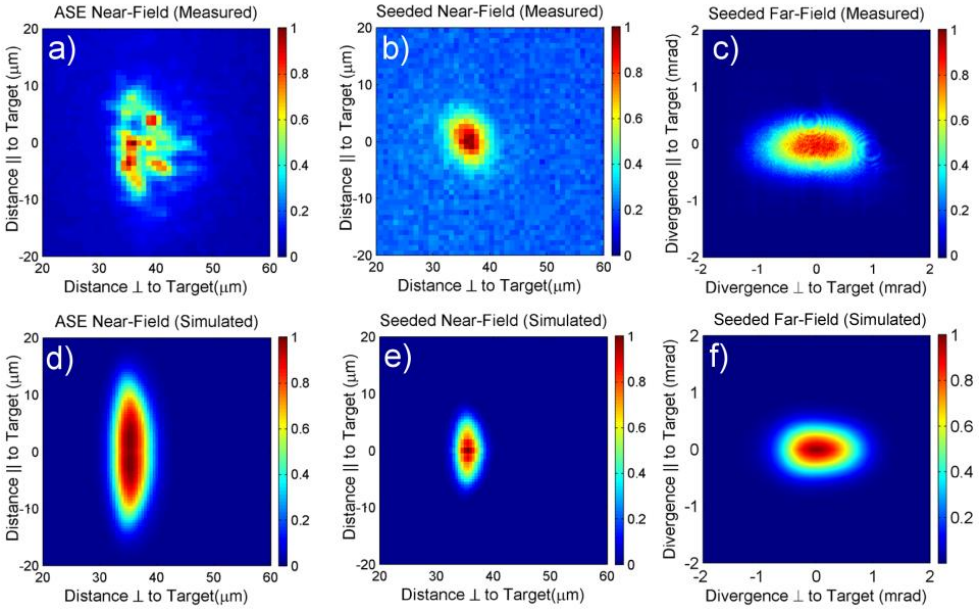

Fig. 10. Measured and simulated near field profiles of a self-seeded and seeded ASE amplifiers, and comparison of measured and simulated far-field profiles for the seeded laser.

Another paper in these proceedings discusses the results of the study of the temporal coherence of this type of injection-seeded solid-target amplifier utilizing a variable pass difference bi-mirror interferometer [19].

5. Acknowledgments

This work was sponsored by the NSF Engineering Research Center for Extreme Ultraviolet Science and Technology, award EEC-0310717, and the and by the Chemical Sciences, Geosciences and Biosciences Division, Office of Basic Energy Sciences, Office of Science, U.S. Department of Energy (DOE). M. B. acknowledges support from the Department of Energy (DOE) CSGF grant DEFG02-97ER25308.

6. References

1. D. Alessi, D.H. Martz, Y. Wang, M. Berrill, B.M. Luther, and J.J. Rocca, Opt. Lett. **35**, 414 (2010).
2. D. Martz, D. Alessi, B.M. Luther, Y. Wang, D. Kemp, M. Berrill, and J.J. Rocca, Opt. Lett. **35**, 1632 (2010).
3. F. Furch, B. Reagan, B. Luther, A. Curtis, S. Meehan and J.J. Rocca, Opt. Lett. **34**, 3352 (2009).
4. R. Keenan, J. Dunn, P. K. Patel, D. F. Price, R. F. Smith, and V. N. Shlyaptsev, Phys. Rev. Lett. **94**, 103901 (2005)
5. B. M. Luther, Y. Wang, M. A. Larotonda, D. Alessi, M. Berrill, M. C. Marconi, J. J. Rocca, and V. N. Shlyaptsev, Opt. Lett. **30**, 165-167 (2005)
6. G. Vaschenko et al., Opt. Lett. **31**, 1214 (2006).
7. F. Brizuela, S. Carbajo, A. Sakdinawat, D. Alessi, D.H. Martz, Y. Wang, B. Luther, K.A. Goldberg, I. Mochi, D. T. Attwood, B. La Fontaine, J.J. Rocca, and C.S. Menoni, Opt. Express, **18**, 14467 (2010).
8. H. Daido, S. Ninomiya, T. Imani, R. Kodama, M. Takagi, Y. Kato, K. Murai, J. Zhang, Y. You, and Y. Gu, Opt. Lett. **21**, 958-960 (1996).
9. Y. Wang, M.A. Larotonda, B.M. Luther, D. Alessi, M. Berrill, V.N. Shlyaptsev, Phys. Rev. A **72**, 053807 (2005).
10. H. T. Kim, I. W. Choi, N. Hafz, J. H. Sung, T. J. Yu, K. H. Hong, T. M. Jeong, Y. C. Noh, D. K. Ko, K. A. Janulewicz, J. Tümmler, P. V. Nickles, W. Sandner, and J. Lee, Phys. Rev. A 77, 023807 (2008).
11. J. Dunn, Y. Li, A. L. Osterheld, J. Nilsen, J. R. Hunter, and V. N. Shlyaptsev, Phys. Rev. Lett. **84**, 4834 (2000).
12. T. Kawachi, M. Kado, M. Tanaka, A. Sasaki, N. Hasegawa, A. V. Kilpio, S. Namba, K. Nagashima, P. Lu, K. Takahashi, H. Tang, R. Tai, M. Kishimoto, M. Koike, H. Daido, and Y. Kato, Phys. Rev. A **66**, 033815 (2002).
13. Ph. Zeitoun, et al., Nature **431**, 426 (2004).
14. Y. Wang, E. Granados, M.A. Larotonda, M. Berrill, B.M. Luther, D. Patel, C.S. Menoni, and J.J. Rocca, Physical Review Letters **97**, 123901 (2006).
15. Y. Wang, E. Granados, F. Pedaci, D. Alessi, B. Luther, M. Berrill, and J.J. Rocca, Nature Photonics **2**, 94 (2008).
16 Y. Wang, M. Berrill, F. Pedaci, M. M. Shakya, S. Gilbertson, Zenghu Chang, E. Granados, B. M. Luther, M. A. Larotonda, and J. J. Rocca, Phys. Rev. A **79**, 023810 (2009).
17 Kawachi, T. et al., Proc. SPIE **5919**, 155 (2005).
18 M. Berrill, D. Alessi, Y. Wang, S.R. Domingue, D.H. Martz, B. Luther, Y. Liu, and J. J. Rocca, Optics Lett. **35**, 2317 (2010).
19. A. Klisnick et al. in these Proceedings.

Saturated XUV lasing down to 8.85 nm using the grazing-incidence scheme

J.E. Balmer, C. Imesch, and F. Staub

Institute of Applied Physics, University of Bern, Switzerland

Abstract. We report on recent progress achieved in x-ray laser research at the Institute of Applied Physics of the University of Bern. Using the existing 10-TW Nd:glass CPA (chirped-pulse amplification) laser system in the grazing-incidence pumping (GRIP) scheme, saturated x-ray lasing has been obtained on the 4d $\rightarrow$ 4p, J = 0-1 lines of Ba and La at wavelengths of 9.2 and 8.85 nm, respectively, using main pumping pulse energies of 9 J (Ba) and 12 J (La). For handling convenience, compound targets (BaF_2, LaF_3) were used, either in the form of windows or coated onto glass slides. Crucial to these results was the introduction of a second, relatively intense (>10%) prepulse less than ~100 ps before the main pulse.

1 Introduction

Important progress towards higher efficiency, reduced size, and higher repetition rate of XUV/X-ray lasers was achieved in recent years by combining the transient-collisional-excitation (TCE) scheme [1] with the the grazing-incidence pumping (GRIP) scheme [2]. In this configuration, a nanosecond-duration laser pulse at 10^{11}-10^{12} W/cm^2 generates the plasma and the required closed-shell (Ne-like or Ni-like) ionization conditions. The plasma is allowed to expand for a given time to allow the electron density gradients to relax. A second, much shorter (ps-duration) laser pulse at 10^{14}-10^{15} W/cm^2 then irradiates the plasma column at an oblique (grazing) angle θ. The angle of incidence is chosen such that density at the apex point of the pump radiation - given by refraction as $n_e = n_{ec}\theta^2$, where n_{ec} is the critical density for the pump wavelength - coincides with the density for which maximum gain is predicted for a given x-ray laser wavelength. Absorption of the pump energy thus occurs directly and very efficiently into the gain region. In addition, the fast temperature rise allows efficient pumping without perturbing the ionization. Very high x-ray laser gain coefficients (>100 cm^{-1}) have been predicted with the possibility of saturated gain for target lengths of a few millimeters. Experimentally, saturated x-ray lasers in Ni-like antimony (Sb, Z = 51) and tellurium (Te, Z = 52) at wavelengths of 11.4 and 10.9 nm, respectively, and for pumping energies of 2.8 and 4.3 J, have been demonstrated [3,4] to date.

J. Lee et al. (eds.), *X-Ray Lasers 2010,* Springer Proceedings in Physics 136,
DOI 10.1007/978-94-007-1186-0_8,

Simulations predict that sub-10-nm lasing should be feasible with 5-10 J of pump energy, and ~100 J would be required to generate an x-ray laser close to the water window (2.5-4.4 nm). A particular feature of the GRIP scheme is an intrinsic travelling wave, causing the excitation to propagate along the line focus at a velocity $v_{ex} = c/\cos\theta$. This substantially reduces the effect of the short gain lifetime inherent to the TCE scheme. In the first experimental demonstration of the GRIP scheme reported for the 18.9-nm line of Ni-like molybdenum (Mo, Z = 42) [2], the optimum angle was 18° and the travelling-wave velocity $v_{ex} = 1.05c$. Intense lasing was observed with 150-mJ/1.5-ps pulses from a Ti:sapphire laser at 10-Hz repetition rate.

In this work, we report on saturated x-ray lasing on the 4d → 4p, J = 0–1 lines of Ba and La at wavelengths of 9.2 and 8.85 nm, respectively, using the grazing-incidence pumping (GRIP) scheme. This was achieved with pump pulse energies of 9 J (Ba) and 12 J (La). For handling convenience, compound targets (BaF_2, LaF_3) were used, either in the form of windows or coated onto glass slides. Crucial to these results was the introduction of a second, relatively intense (>10%) prepulse less than ~100 ps before the main pulse.

2 Optimum density for Ni-like x-ray lasers

Lasing in Ni-like ions occurs predominantly on the 4d → 4p, J = 0 – 1 transition, where J denotes the total angular momentum of a particular ionic level. When moving towards shorter wavelengths, the optimum density for gain increases, and so does the optimum grazing angle in the GRIP geometry. In the case of Ne-like ions, the scaling of the optimum density with atomic number, Z, can be approximated by $n_{opt} = 4 \cdot 10^{15} (Z - 9)^{3.75}$ cm^{-3} [5]. For the Ni-like ions, on the other hand, no simple scaling law is known to date, due mainly to the more complicated level structure. However, simulations [6] have shown that the optimum plasma conditions of some Ni-like x-ray lasers (Ag, Cd, In, Sn, etc.) are very similar to those of corresponding Ne-like lasers (Fe, Co, Ni, Cu, etc.). It is therefore tempting to adopt the above formula for the optimum Ne-like density to the corresponding Ni-like lasers. The result is shown as the solid line in Fig. 1 (units of 10^{19} cm^{-3}). Also shown in this plot is the corresponding optimum GRIP angle in degrees (triangles), the resulting x-ray laser wavelength in Ångstroms (diamonds), and the critical density n_{ec} for the 1054-nm pump laser. It is seen that the optimum density rapidly approaches n_{ec} for ions with atomic numbers greater than ~55 (Cs), and thus for lasing wavelengths below ~10 nm. At the same time, the optimum GRIP angle approaches 90°, i.e., normal incidence, so that all the advantages of the GRIP scheme are lost. One way out of this problem would be to use shorter pump laser wavelengths, e.g. the second or third harmonic of the Nd laser.

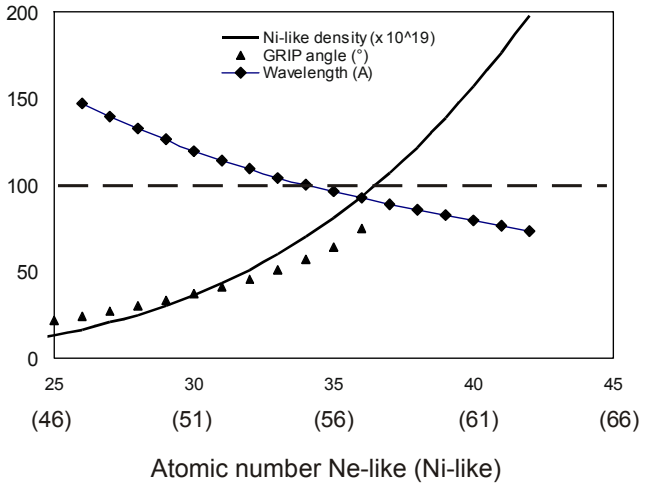

Fig. 1. Optimum electron density for Ni-like x-ray lasers (solid line) according to Refs. [5,6]. The dashed line marks the critical density for the 1054-nm pump laser.

3 Experimental setup

The experiments were conducted using the existing 1054-nm Nd:glass CPA laser system, re-configured to provide a maximum output energy of ~20 J in a very short pulse (~1.5 ps). As the maximum energy of the system is limited by the damage threshold of the 190 × 350 mm^2 size, 1740-lines/mm compressor gratings, given as 250 mJ/cm^2 by the manufacturer, a beam-expanding telescope including a vacuum spatial filter was installed to increase the beam diameter to 130 mm (the maximum that can be handled by standard 150-mm optics and 200-mm beam steering mirrors) at the input of the compressor gratings. Taking into account the 4-pass geometry of the compressor, the diffraction efficiency of the gratings (~90%), and the 2:1 peak-to-average ratio of the beam fluence distribution, a maximum of ~20 J is thus available for x-ray laser experiments.

As a consequence of the increased beam diameter, the length of the line focus increased to 19.6 mm (FWHM), with a concomitant reduction in pump irradiance. In order to keep the on-target irradiance as high as possible, the beam diameter was reduced back to 80 mm by an additional telescope after compression, as shown schematically in Fig. 2. For the 45° angle of incidence on the target, this restored the line focus length to the 12.5 mm (FWHM) used in previous experiments.

With this length of the line focus and a travelling-wave velocity of $v = 1.41c$, this results in a temporal mismatch of $\Delta t \approx 12$ ps between the pump pulse and the x-ray laser pulse at the output end of the target.

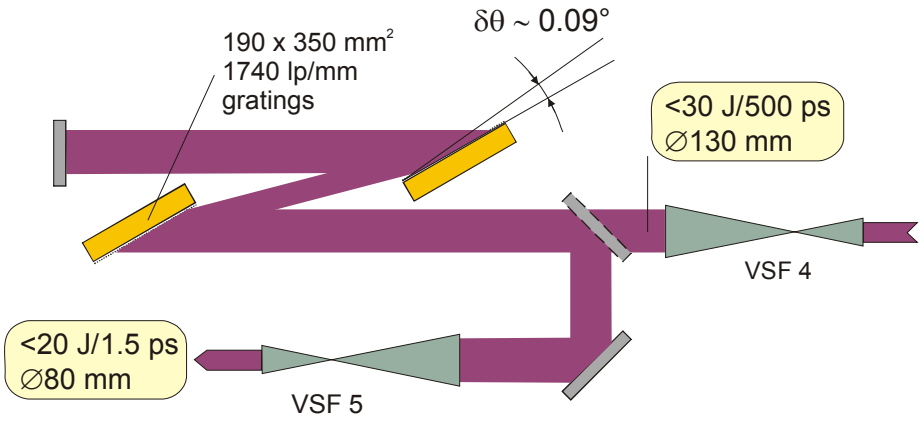

Fig. 2. Configuration of the beam expansion/reduction scheme for maximum laser output energy.

Among the techniques to modify the pulse front tilt and thus the travelling-wave (or pulse front) velocity along the line focus, we chose the one that introduces a slight tilt on one of the compressor gratings [7]. Calculations showed that, in order to reduce the travelling-wave velocity to $v = c$, the second compressor grating had to be tilted by 0.09° and shifted by −11 mm along the incident beam direction. The resulting pulse front velocity along the line focus was measured at the target position using an optical streak camera (Imacon 600) and yielded a value of $v = 1.02c$, in excellent agreement with the calculations.

The main diagnostics of the plasma emission was an on-axis, time-integrating XUV spectrometer that consists of a 1200-lines/mm, aberration-corrected Hitachi grating (radius of curvature: 5649 mm), working at a grazing-incidence angle of 3°. The grating disperses the incident radiation onto a 40-mm diameter P20 phosphor screen, which is imaged to a cooled CCD camera having a pixel size of 23×23 μm^2. The wavelength coverage of the spectrometer is between ~5 and 25 nm with a spectral resolution of ~0.2 nm. The relatively poor resolution is a consequence of the slitless operation of the spectrometer, which results in source broadening making the dominant contribution to the measured linewidth.

4 Experimental results

The effect of the matched pulse front velocity on the x-ray laser performance was tested with the well-established 11.9-nm Sn laser and it was found that the addition of a second prepulse ~100 ps before the main pulse lead to a dramatic increase of the x-ray laser output. A preliminary series of prepulse optimisation was conducted with the results shown in Fig. 3. Best results were

obtained with a weak (0.5%) first prepulse at 2.8 ns and a second, 16% prepulse ~50 ps before the main pulse. This is in marked discrepancy with previous measurements where best results were obtained with a single 2.8% prepulse, 4.4 ns before the main pulse. The reason for this behaviour is not understood to date, but is most likely due to the different history of low-intensity precursors to the main pulse, the so-called "pedestal". Work is currently under way to clarify the role and importance of these pedestal pulses, which may have their origin in the incomplete pulse compression as a consequence of the grating tilt described above.

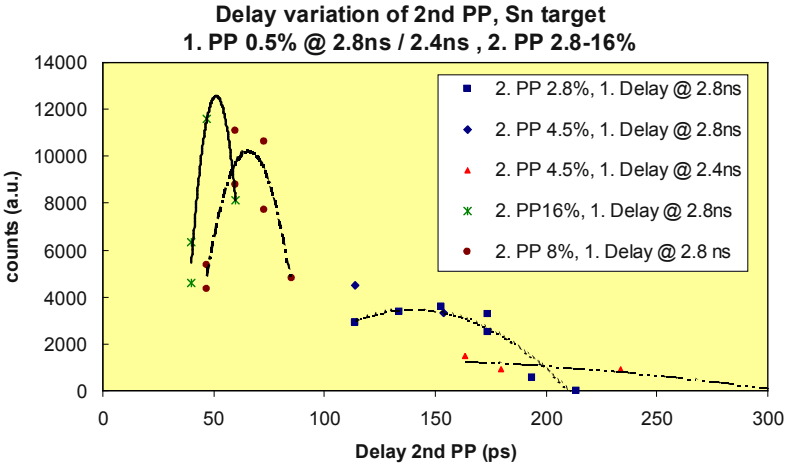

Fig. 3. 11.9-nm line intensity of Ni-like Sn versus delay with respect to the second prepulse for a range of prepulse amplitudes.

Motivated by the remarkable performance of the Sn laser, a new attempt was made to achieve lasing on the 9.2-nm line of Ni-like barium (Ba, Z = 56). Since pure Ba oxidizes very rapidly in ambient air (as found in previous, unsuccessful attempts), targets in the form of BaF_2 plates were used. Lasing was indeed observed with the prepulse configuration described above and using a main pulse energy of 14 J. Fig. 4 shows the on-axis spectrum with the lasing line seen to clearly dominate the spectrum in first and second order. According to the previous energy calibration of our diagnostic system, a signal level of 15'000 cts corresponds to an x-ray pulse energy of 6 μJ.

Further optimisation was undertaken in a series of shots at varying prepulse amplitudes and delays. It was found that even stronger signals (~2×) were obtained when the first prepulse was increased to 2.8%, while the second prepulse was set at 43 ps before the main pulse, the shortest achievable with our prepulse setup. The threshold for lasing was observed at a main pulse energy of ~7 J, while multi-microjoule output was obtained with ~9 J. The comparison with our previous gain measurements on the Sn and Sb lasers

[8,9], taking into account the dependence of the saturation irradiance on electron density and atomic number [10], implies that saturation has been reached at these output levels.

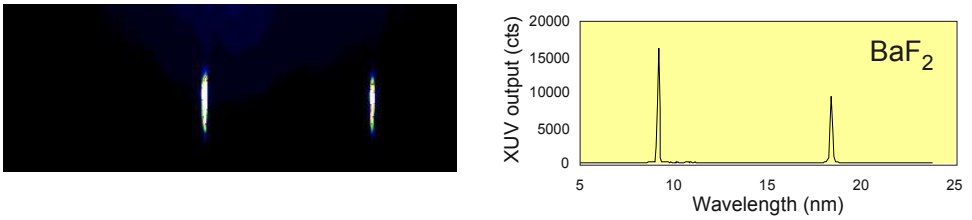

Fig. 4. 9.2-nm lasing line of Ni-like Ba in first and second order for a pump energy of 14 J in a 1.5-ps pulse.

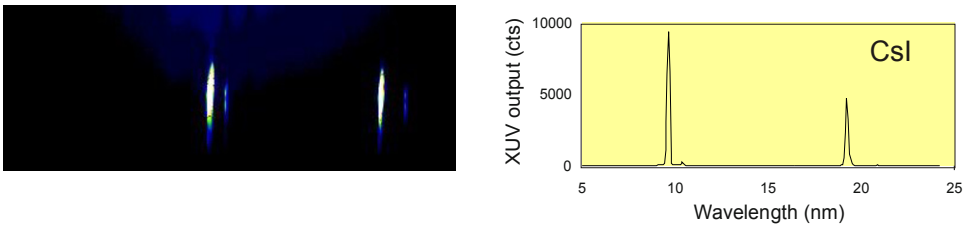

Fig. 5. 9.6-nm lasing line of Ni-like Cs in first and second order for a pump energy of 9.8 J in a 1.5-ps pulse. Also seen, although very weakly, is the 10.4-nm lasing line of Ni-like I.

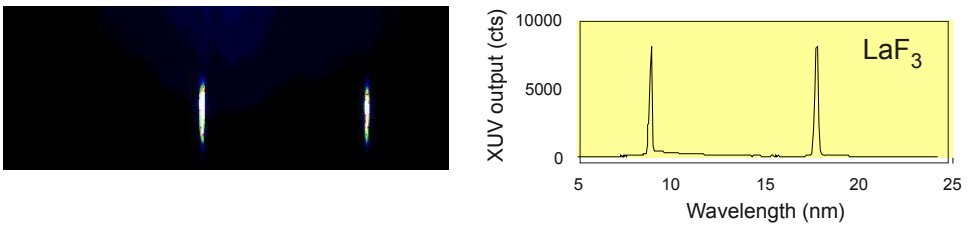

Fig. 6. 8.8-nm lasing line of Ni-like La in first and second order for a pump energy of 16 J in a 1.5-ps pulse.

Using the optimum prepulse parameters found in the Ba experiments, intense lasing was also obtained in Ni-like cesium (Cs, Z = 55) and lanthanum (La, Z = 57), when targets of LaF_3 and CsI were irradiated. Figs. 5 and 6 show the corresponding lasing lines at 9.6 nm (Cs) and 8.8 nm (La). Weak lasing is also observed on the 10.4-nm line of Ni-like iodine (I, Z = 53) in the case of the CsI target (Fig. 5).

The measured output levels of ~10'000 cts correspond to an energy of ~4 μJ, implying that saturation has been reached or very closely approached.

Again, this is based on the comparison with the gain measurements on the Sn and Sb lasers [8,9]. A comparison with published results from RADEX simulations [11] further shows that the pumping energies required in our experiments agree very well with those predicted.

5 Discussion

An interesting outcome of the current work is that compound targets (CsI, BaF_2, LaF_3) perform unexpectedly well, although the concentration of the lasing ions is strongly diluted by the presence of the particular compound ions. In order to quantify the dilution effect, we make a rough estimate of the density of the lasant ions in the compound plasma, n_{BaF} in the case of BaF_2, as compared to the density in the pure element plasma, n_{Ba}. Since the ionisation energies of Cs^{26+}, Ba^{27+}, and La^{28+} are all of order 1 keV, which corresponds closely to the ionisation energy of F^{8+}, we may assume that, in the lasing plasma, the fluorine ions are fully ionised ($z_F = 9$). In the case of BaF_2, we can then write the charge neutrality condition in the plasma as

$$n_e = z_{Ba} n_{BaF} + 2 z_F n_{BaF}$$

and, for simplicity, we assume that all the lasant ions are in the Ni-like ionisation state Ba^{28+}. For a pure Ba plasma, the charge neutrality condition reads

$$n_e = z_{Ba} n_{Ba}$$

Since the electron densities in the lasing region are identical in the two cases (given by the GRIP angle), we obtain

$$\frac{n_{BaF}}{n_{Ba}} = \frac{z_{Ba}}{z_{Ba} + 2 z_F} \approx 0.61$$

In the same way, we obtain a value of 0.52 for the case of LaF_3 and 0.5 for CsI. This shows that, as expected, the presence of compound ions leads to a substantial reduction in the density of the lasant ions with a concomitant reduction of the gain coefficient.

Acknowledgements

The authors would like to acknowledge the technical assistance of B. Locher and W. Lüscher for target preparation. This work was supported in part by the Swiss National Science Foundation.

References

1. Yu.V. Afanas'ev and V.N. Shlyaptsev, *"Formation of a population inversion of transitions in Ne-like ions in steady-state and transient plasmas"*, Sov. J. of Quant. Electron. 19, 1606 (1989)
2. V.N. Shlyaptsev et al., "*Numerical study of transient and capillary x-ray lasers and their applications*", Proc. SPIE, Vol. 5197, pp. 221-228, 2003; R. Keenan et al., "*Efficient pumping scheme for high-average brightness collisional x-ray lasers*", ibid., pp. 213-220
3. C. Imesch, F. Staub, and J.E. Balmer, *"Gain-saturated Ni-like antimony laser at 11.4 nm in grazing-incidence pumping geometry"*, Opt. Commun. 282, 267 (2009)
4. J.J. Rocca et al., "*Progress in the development of compact high-repetition-rate soft-x-ray lasers: gain saturation at 10.9 nm and first demonstration of an all-diode-pumped soft x-ray laser*", Proc. SPIE, Vol. 7451, pp. 06-1 (2009)
5. R.C. Elton, "*X-ray Lasers*" (Academic Press, San Diego,1990) p. 99ff
6. F. Yan et al., *"Similarity of plasma conditions of some Ne-like X-ray lasers and their partner Ni-like X-ray lasers"*, Appl. Phys. B 79, 229 (2004)
7. J.-C. Chanteloup et al., *"Pulse-front control of 15-TW pulses with a tilted compressor, and application to the subpicosecond traveling-wave pumping of a soft-x-ray laser"*, J. Opt. Soc. Am. B 17, 151 (2000)
8. M Grünig et al., *"Saturated X-ray lasing in Ni-like Sn at 11.9 nm using the GRIP scheme"*, Opt. Commun. 282, 267 (2009)
9. C. Imesch et al., *"Gain-saturated Ni-like antimony laser at 11.4 nm in grazing-incidence pumping geometry"*, Opt. Commun. 283, 66 (2010)
10. A. Sasaki et al., *"The gain distribution of the transient collisional excited X-ray lasers"*, J. Quant. Spec. Rad. Transf. 71, 665 (2001)
11. V.N. Shlyaptsev et al., *"Pumping efficiency of transverse, longitudinal and grazing incidence schemes"*, "X-ray Lasers 2004", ed. J. Zhang, IOP Conf. Series No.186, 103 (2005)

Double-pulse single-beam grazing-incidence pumping

D. Zimmer [1,2,3] , B. Zielbauer [2], M. Pittman [1], O. Guilbaud [1], J. Habib [1], S. Kazamias [1], D. Ros [1], V. Bagnoud [2], and T. Kuehl [2,3]

[1] LASERIX-CLUPS, LPGP UMR 8578, Université Paris-Sud 11, F-91405 Orsay, France
[2] GSI Helmholtzzentrum für Schwerionenforschung GmbH, D-64291 Darmstadt, Germany
[3] Institut für Physik, Johannes Gutenberg-Universität Mainz, D-55099 Mainz, Germany

Abstract. The paper reports on the optimization of a table-top nickel-like molybdenum transient collisionally excited soft x-ray laser (SXRL) at 18.9 nm, performed by double-pulse single beam grazing incidence pumping (DGRIP) [1]. This scheme allows for the first time the full control of the pump laser parameters including the pre-pulse duration, optimally generating the SXRL amplifier under grazing incidence. The single beam geometry of collinear double-pulse propagation guarantees the ideal overlap of the pre- and main pulse from shot to shot, resulting in a more efficient, highly stable SXRL output. SXRL energies up to 2.2 μJ are obtained with a total pump energy less than 1 J for several hours at 10 Hz repetition rate without re-alignment under once optimized double pumping pulse parameters including energy ratio, time delay, pre- and main pulse duration and line focus width [1].

1 Introduction

The introduction of the DGRIP scheme improves the efficiency and stability of table-top high-repetition soft x-ray lasers and shows the attractiveness of this pumping scheme for high average power operation. On one hand the low costs and the easy and rapid alignment procedure fulfill the requirements for a sophisticated installation, and on the other hand the highly stable output, compared to the jittering output of previous systems, satisfies the need for a reliable strong SXRL source. As an outlook, this system proves to be a milestone for the introduction of multiple pulse capability in Ti:sapphire CPA laser systems for future experiments [1].

J. Lee et al. (eds.), *X-Ray Lasers 2010,* Springer Proceedings in Physics 136,
DOI 10.1007/978-94-007-1186-0_9,

2 Set-up

The DGRIP set-up is shown in **Fig. 1**. After the double-pulse generation, the pump laser beam is guided in the focusing system consisting of a spherical mirror with a focal length of 600 mm aligned 10 degrees of the normal incidence, generating the line focus of ~ 3 mm FWHM length and ~ 60 µm FWHM width. The line focus width monitoring was realized in the IR using a high resolution imaging device.

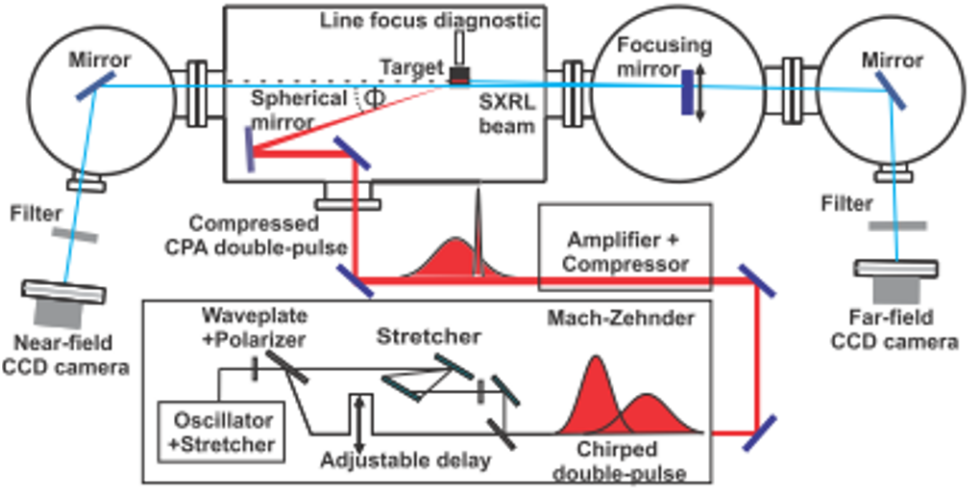

Fig.1. Set-up of long/short pulse DGRIP.

The optimal grazing incidence angle of 20 degrees was chosen in accordance to earlier results. This corresponded for 805 nm irradiation to a turning point electron density of $n_e \approx 2.0 \times 10^{20}$ cm^{-3}. The target was a 5 cm high and 4 mm wide slab of polished molybdenum. Since Mo was weakly ablated by the pump laser compared to other lasing materials, it was suitable for an operation at 10 Hz repetition rate, allowing for up to 200 shots at the same target position, with still high SXRL output. The generated SXRL beam propagated either to near- or far-field diagnostics. A monochromatic near-field imaging system showed the SXRL source size and position relative to the target surface and a far-field imaging system provided the divergence and profile of the SXRL beam after 1 m propagation [1].

3 Comparison between short/short pulse DGRIP and long/short pulse DGRIP

The two variants of DGRIP apply the common principle of double pump pulses in a single beam under grazing incidence, allowing for the same set-up,

but by changing the pre-pulse duration from ~10 ps for the short/short pulse configuration to ~200 ps for the long/short pulse configuration, significant differences occur. Completely other optimal pump parameters were obtained during the SXRL output optimization resulting in SXRL beams with different near- and far-field characteristics. The results of SXRL energy for different pump parameters are presented in **Fig. 2** [2].

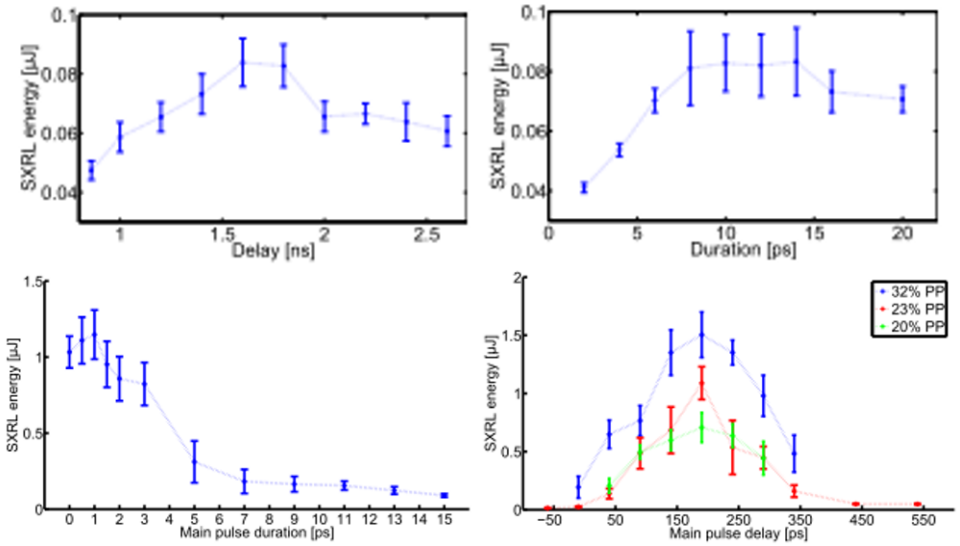

Fig.2. SXRL energy for different pump parameters in short/short and long/short pulse configuration.

In Tab. 1 a summary of the optimal pump parameters is given together with the output characteristics for both DGRIP variants [2]. The strongest differences in the pump parameters are observed in the delay and duration of the double-pulses. The main pulse duration of 10 ps in the short/short pulse configuration differs strongly from the long/short configuration, in which a main pulse duration of only 1 ps is applied. Moreover in the case of short/short pulse pumping the very long delay of ~ 1500 ps clearly stands in contrast to the rather short delay of 200 ps for the long/short pulse configuration.

4 Comparison between GRIP and DGRIP

In conclusion, a comparison between DGRIP and GRIP in terms of efficiency and stability during the experiment has been considered. Since the DGRIP scheme applied two collinear pulses, which passed through the grating

Tab. 1. Summary of characteristics of both DGRIP configurations.

DGRIP	short/short pulse	long/short pulse
PP duration	$\sim 10\,\mathrm{ps}$	$\sim 200\,\mathrm{ps}$
MP duration	$\sim 10\,\mathrm{ps}$	$\sim 1\,\mathrm{ps}$
PP energy	$\sim 250\,\mathrm{mJ}$	$\sim 250\,\mathrm{mJ}$
MP energy	$\sim 750\,\mathrm{mJ}$	$\sim 750\,\mathrm{mJ}$
Delay	$\sim 1600\,\mathrm{ps}$	$\sim 200\,\mathrm{ps}$
Focus width	$\sim 60\,\mu\mathrm{m}$	$\sim 60\,\mu\mathrm{m}$
PP intensity	$\sim 3 \times 10^{12}\,W/cm^2$	$\sim 6 \times 10^{11}\,W/cm^2$
MP intensity	$\sim 5 \times 10^{13}\,W/cm^2$	$\sim 4 \times 10^{14}\,W/cm^2$
Number of pulse trains N	~ 5	~ 2.5
Max. output fluence	$\sim 0.07\,mJ/cm^2$	$\sim 0.5\,mJ/cm^2$
Max. output energy	$\sim 0.3\,\mu J$	$\sim 2\,\mu J$

compressor at LASERIX with a transmission of ~50%, the total pump energy was reduced by ~ 25 % from ~1.2 J on target for the GRIP operation to ~ 0.9 J on target for the DGRIP operation. Despite the lack of pump energy in the DGRIP case, both methods yielded about the same maximal output energy of ~2μJ, resulting in a higher efficiency of the DGRIP scheme. This corroborated the high gain value of ~ 65 cm^{-1} in DGRIP. Moreover, the more compact source size of ~ 350 μm^2 in DGRIP compared to ~700 μm^2 in GRIP lead to a doubled SXRL fluence of ~ 0.5 J/cm^2. Instead, the vertical divergence in the DGRIP output was increased to ~ 10 mrad, contrary to the horizontal divergence of ~ 4 mrad, which is a typical value for both dimensions in the GRIP scheme. The resulting peak brilliance of ~ 2×10^{25} photons/(s mm^2 $mrad^2$) in 0.01% bandwidth for the DRIP scheme equaled again the values of GRIP SXRLs, and amounted to a factor of ten less than the brightest seeded GRIP SXRL.

Since in this study only a gain length of ~2.5 mm was investigated, possible limiting refraction effects due to the higher density operation, could not be observed. In terms of stability, the DGRIP scheme came with an intrinsically perfect overlap of the line foci for both pulses, resulting in a more stable SXRL operation, compared to the jittering output of GRIP. On top of that, the easy and rapid alignment procedure simplified the utilization of the DGRIP scheme for applications [2].

References

1. Zimmer, D.; Zielbauer, B.; Pittman, M.; Guilbaud, O.; Habib, J.; Kazamias, S.; Ros, D.; Bagnoud, V.; Kuehl, T., "Optimization of a table-top high repetition rate soft x-ray laser pumped in double-pulse single beam grazing incidence," *Opt. Lett*. 35, 450 (2010)

2. Zimmer, D., *A new double laser pulse pumping scheme for transient collisionally excited plasma soft X-ray lasers,* Thesis (2010), **http://ubm.opus.hbz-nrw.de/volltexte/2010/2329/**

Development and application of plasma-waveguide based soft x-ray lasers

Jiunn-Yuan. Lin*[1], Ming-Chang Chou[2], Ping-Hsun Lin[2], Ru-Ping Huang[1,2], Szu-Yuan Chen[2,3], Hsu-Hsin Chu[3] and Jyhpyng Wang[2,3,]

[1] Department of Physics, National Chung Cheng University, Chia-Yi 621, Taiwan
[2]Institute of Atomic and Molecular Sciences, Academia Sinica, Taipei 106, Taiwan
[3]Department of Physics, National Central University, Jhongli 320, Taiwan

Abstract. We experimentally demonstrate the amplification of optical-field-ionization soft x-ray lasers in an optically preformed plasma waveguide for pure xenon, krypton, and argon gases, respectively. The lasing photon number of Ni-like Kr laser at 32.8 nm generated in waveguide is dramatically enhanced by about three orders of magnitude in comparison to that without plasma waveguide, resulting in a photon number of $\sim 5\times10^{11}$ and an energy conversion efficiency of $\sim 5\times10^{-6}$ with a pump pulse of ~500 mJ. By seeding optical-field-ionization plasma with high harmonic signals, 32.8-nm Kr laser produces brighter x-ray laser beams with much smaller divergence, enhanced spatial coherence, and controlled polarization. Single-shot x-ray digital holographic microscopy with an adjustable field of view and magnification is demonstrated successfully with the illumination of high-brightness 32.8-nm x-ray laser. The ultrashort x-ray pulse duration combined with single-shot capability offers great advantage for flash imaging of delicate samples.

1 Introduction

Significant progress has been made in the past two decades to push the x-ray lasers toward higher intensity, shorter pulse duration, higher coherence, and particular compact size with high repetition rate. Since the first collisionally excited optical-field-ionization (OFI) x-ray laser was demonstrated by Lemoff [1], OFI collisional-excitation x-ray lasers pumped by femtosecond high-repetition-rate lasers have been shown to be a promising scheme that meets the requirements of practical applications. Saturated lasings on Pd-like Xe and Ni-like Kr were achieved by Sebban et al. to produce lasing output of $> 5\times10^{9}$ photons/pulse using few hundred mJ pump pulses[2,3]. With the versatility of gas jets, our group demonstrated x-ray lasing in Xe and Kr clustered gas jets with outputs of 2×10^{10} x-ray photons/pulse and 1×10^{9} photons/ pulse, respectively [4,5].

J. Lee et al. (eds.), *X-Ray Lasers 2010,* Springer Proceedings in Physics 136,
DOI 10.1007/978-94-007-1186-0_10,

A serious problem for longitudinally pumped OFI x-ray lasers is the limited gain length caused by ionization-induced refraction. Here we report the demonstration dramatic enhancement of the OFI krypton 32.8-nm laser in a gas jet by an optically preformed plasma waveguide. With pump energy of 500 mJ, an output level of $>5\times10^{11}$ photon/shot is reached at an energy conversion efficiency of 5×10^{-6}. The large gain-length product also resulted in lasing at an additional line around 33.5 nm. Optically preformed plasma waveguide in a gas jet [6–8] allows guiding of the pump pulse and damage-free long-term high-repetition-rate operation for practical applications. With the assistance of plasma waveguide, the high-threshold low-gain transition in Ne-like Ar ions at 46.9 nm is also achieved in OFI plasma channel at the first time, demonstrating the capability of guiding the pump beam at high intensity in the waveguide. Taking advantage of the high atom density and large gain length provided by the plasma waveguide, simultaneous lasing at 32.8 and 46.9 nm in two ion species is generated in a 10-mm gas jet with Kr and Ar mixtures.

However, the soft-x-ray lasers discussed above are all based on amplified spontaneous emission (ASE) which offers only a limited quality in the waveform of the output pulse. It is known that seeding from high harmonic generation (HHG) can reduce the beam divergence, shorten the pulse duration, and enhance the spatial coherence. Amplification of HHG seed was first demonstrated by Ditmire et al. in a gallium target, but the amplification factor was low due to the strong refraction caused by dense plasma [9]. Recently HHG-seeding with high gain was achieved in OFI x-ray-lasers in gas cells [10] and collisonal-ionization x-ray lasers in solid targets [11]. In view of high efficiency of OFI soft-x-ray lasers based on optically preformed plasma waveguide in gas jets, it is highly desirable to see how HHG seeding will enhance the performance of such lasers. We report the integration of waveguide-based OFI soft-x-ray laser amplifiers and high harmonic generation to achieve strongly saturated soft-x-ray lasing for Ni-like krypton at 32.8 nm. The amplified seed pulses have a divergence of only 1.1 mrad, a photon number of 1×10^{11}, enhanced spatial coherence, and an amplification factor of $\sim 10^4$.

Since the invention of holography by Gabor in 1948[12], great efforts have been made for realizing this technique with short-wavelength light sources in order to resolve the structure of matter in the nanometer scale. Here we also report the demonstration of flash digital Fourier holographic microscopy with single exposure pulse from a tabletop optical-field-ionization Ni-like Kr x-ray laser at 32.8 nm. An imaging x-ray concave mirror is added between CCD and sample to overcome the limit of the pixel size of CCD and increase the effective numerical aperture of the imaging system simultaneously. The amplitude and phase contrast images of sample are obtained by numerically solving Fresnel integral for a certain propagation distance via 2D fast Fourier

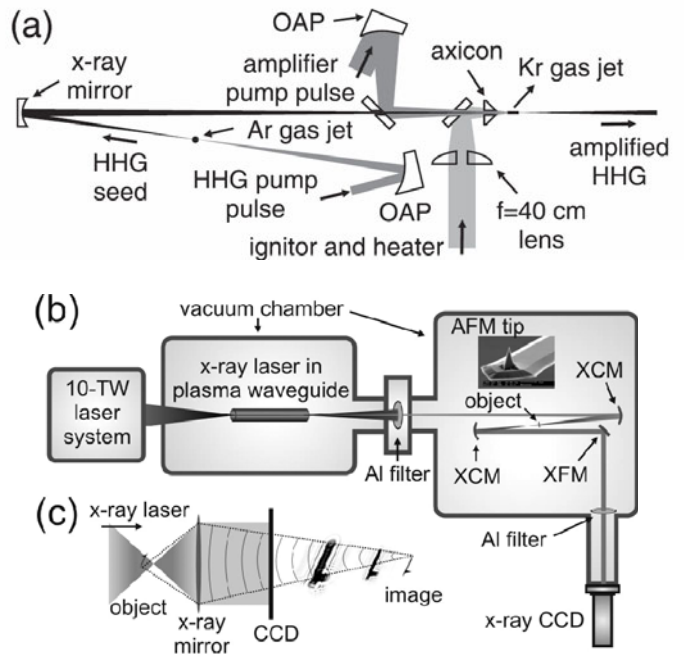

Fig. 1. (a) Experimental setup for x-ray lasers generated in a preformed plasma waveguide with or without a seeded pulse, (b) Schematic diagrams of the experimental setup and (c) the working principle of soft x-ray digital holographic microscopy. OAP: off-axis parabolic mirror; XCM: x-ray concave mirror, XFM: x-ray flat mirror.

transforms. For a 1024 × 1024 hologram, the reconstruction process takes only 1 second in a fast PC. In addition to the capability of high-speed imaging and post-processing, this technique also provides the way, like optical microscope, to study large objects and their details with adjustable field of view. By translating the object away from or toward the x-ray concave mirror, one can observe the sample in large scale and then zoom in to a small region of interest.

2 Experimental arrangement

The experimental setup is shown in figure 1(a). A 20-TW, 40-fs, 810-nm, and 10-Hz Ti:sapphire laser system [13] based on the chirped-pulse amplification technique was used in this experiment. The soft x-ray laser amplifier was driven by three pulses. A 235-mJ, 40-fs, circularly polarized pulse was used for preparation of the lasing ionization stages and ATI heating of electrons.

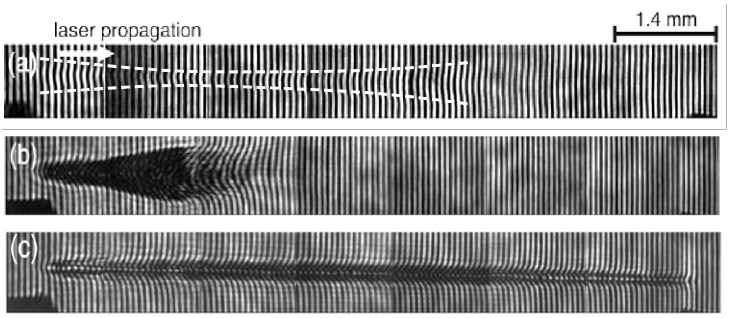

Fig. 2. Interferograms of the plasma taken at 10 ps after the pump pulse passed through the gas jet. (a) Using only the pump pulse with a focal position at 2.75 mm behind the entrance of the gas jet. Krypton atom density = 8×10^{17} cm^{-3}. (b) Using only the pump pulse with a focal position at 500 μm behind the entrance of the gas jet. Krypton atom density = 1.6×10^{19} cm^{-3}. (c) Using a 45-mJ ignitor pulse, a 225 mJ heater pulse and a 235-mJ pump pulse. Krypton atom density = 1.6×10^{19} cm^{-3}.

The other two pulses, referred to as the ignitor and the heater, were used for fabricating a plasma waveguide based on the axicon-ignitor-heater scheme.[8] In this experiment, the ignitor was 45 mJ in energy, 40 fs in duration, and s-polarized, and the heater was 270 mJ in energy, 160 ps in duration, and p-polarized. The ignitor-heater separation and heater-pump separation are 200 ps and 2.5 ns, respectively. After combined by a thin-film polarizer, these two pulses propagate collinearly and were then focused by a center-drilled lens and an axicon on a 10-mm slit gas jet. The gas jet profile had a flat-top region of 8-mm length and a boundary of 500-μm length at both edges along the long axis. For x-ray laser seeded with HHG, an 11-mm-diameter 3.8-mJ pulse was focused with an off-axis parabolic mirror (OAP) of 30-cm focal length onto an Ar clustered gas jet. The Ar gas jet was produced by a 1-mm-diameter conical nozzle and a pulsed valve. The atom density was set at 7.1×10^{18} cm^{-3}. The focal spot size of the pulse was 30 μm in FWHM with 87% energy enclosed in a Gaussian-fit profile. The focus was placed at 1.3 mm after the entrance of Ar gas jet. The beam diameter, laser energy, atom density, and focal position are chosen for maximizing the 25th harmonic. Matching of the central wavelength of the HHG seed to that of the Ni-like Kr 32.8-nm x-ray laser amplifier was achieved by setting the pump pulse of HHG to a duration of 360 fs and a positive chirp. The produced HHG pulse was imaged onto the entrance of the soft-x-ray amplifier by a soft-x-ray multilayer concave mirror of 30-cm focal length and propagates collinearly with the amplifier pump pulse. A reflecting mirror with a hole at its center was used to combine the HHG pulse and the amplifier pump pulse. The orientation of the linearly polarized HHG soft-x-ray pulse was controlled by rotating the polarization of its pump pulse with a half-wave plate.

A flat-field grazing-incidence x-ray spectrometer, consisting of a 1200-line/mm aperiodically ruled grating and a back-illuminated 16-bit x-ray CCD camera is used to measure the spectrum and angular distribution of x-ray lasing in the direction of pump-laser propagation. Two 0.25 μm-thick Al filter is used to block the pump beam and to attenuate x-ray emission. Mach-Zehnder interferometry with a probe pulse passing transversely through the cluster jet was used to measure plasma density distribution and to monitor the propagation of the pump pulse in the cluster jet. By calibrating the grating reflectivity, the filter transmittance, and the CCD response, the absolute emission yield was obtained.

The experimental setup of x-ray digital holographic microscopy is shown in Fig. 1(b). A 0.25-μm-thick aluminum filter was used to eliminate the copropagating driving laser light. The x-ray holographic microscopy consisted of three Mo/B4C/Si multilayer mirrors with a reflectivity of 19% at 32.8 nm and a 16-bit back-illuminated x-ray CCD camera. The first x-ray concave mirror of 30-cm focal length was used to collect and focus the 32.8-nm beam and the second x-ray concave mirror of 20-cm focal length was used as an imaging lens. The 45° flat mirror was used to redirect the x-ray beam to the x-ray CCD camera. The holograms were recorded by the x-ray CCD camera with a 1024 × 1024 array of 13-μm pixels. The sample was placed between the two x-ray concave mirrors and the inherent magnification of this imaging system was 7.6. An AFM cantilever and a carbon-foil mesh were served as the test objects. The AFM cantilever has physical characteristics : cantilever length 125 μm, width 30 μm, thickness 4 μm, tip height 10－15 μm. The carbon foil is a square mesh made of a two-dimensional array of 7 μm × 7 μm holes and 2-μm bars with ~20-nm thickness. The objects were mounted on a motorized translation stage moving parallel to x-ray beam propagation.

3 Result and discussion

3.1 Enhancement of Optical-Field-Ionization Soft X-Ray Lasers by an Optically Preformed Plasma Waveguide

In order to increase the lasing signal by increasing the atom density and extend the length of the gain region simultaneously, a plasma waveguide was implemented to overcome the adverse effect of ionization-induced refraction. Figure2(a) shows the interfeorgram taken at 10 ps after the pump pulse has passed through the 10-mm Kr gas jet without preformed plasma waveguide. The maximum x-ray lasing of Ni-like krypton at 32.8 nm was observed at an atom density of 8×10^{17} cm^{-3} and a pump focal position of 2.75 mm behind the entrance of the gas jet as the optimal balance between pump beam convergence and ionization-induced refraction was achieved to produces the

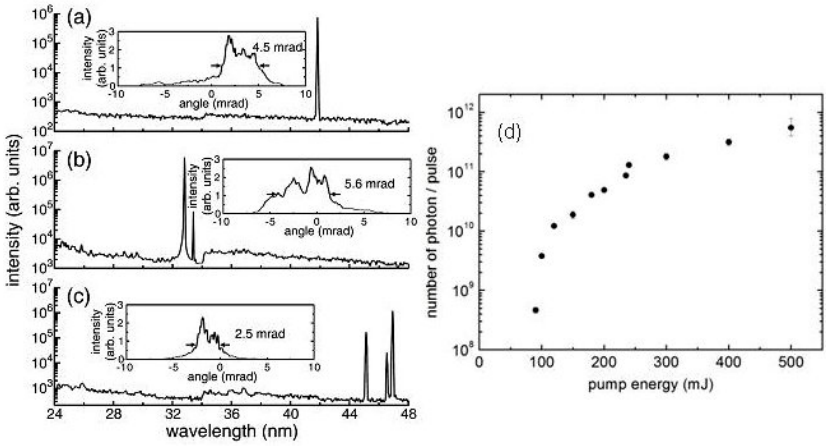

Fig. 3. X-ray spectra for an atom density of (a) $N_{Xe} = 4\times10^{19}$ cm^{-3}, (b) $N_{Kr} = 1.6\times10^{19}$ cm^{-3}, and(c) $N_{Ar} = 2.7\times10^{19}$ cm^{-3}. The heater energies were 180, 225, and 325 mJ, and the heater-pump delays were 5.5, 2.5, and 1.5 ns, respectively. The ignitor energy was 45 mJ and the ignitor-heater separation was 200 ps. Insets show the angular distributions of the 41.8 nm Xe^{8+}, 32.8 nm Kr^{8+}, and 46.9 nm Ar^{8+} lasing lines, respectively. (d) The lasing output for Kr laser at 32.8 nm as a function of pump energy at an atom density of 1.6×10^{19} cm^{-3}.

longest gain region and the shortest x-ray re-absorption region. The number of photons at the 32.8-nm lasing line was 2×10^{8} which is 5 times lower that that produced from a 5-mm gas jet due to a longer absorption length. Figure 2(b) shows the interferogram of the plasma taken at the same condition as in Fig. 2(a) except that the krypton atom density is raised to 1.6×10^{19} cm^{-3} and the pump focal position was moved to 500 μm behind the entrance of the gas jet. Severe ionization-induced refraction drastically reduces the length of the gain region, and thus no x-ray lasing is observed at this condition. The interferogram of the plasma waveguide taken at 10 ps after the pump pulse has passed through the gas jet is shown in Fig. 2(c). The 235-mJ pump pulse was circularly polarized with a focal position of 500 μm behind the entrance of the gas jet and a delay of 2.5 ns after the heater. An uniform plasma waveguide extended to ~9 mm at a ~40-μm diameter was observed. The guided beam size was measured to be <15 μm (FWHM) with more than 50% of the energy in the vacuum focal spot transmitting through the preformed waveguide. With the plasma waveguide the x-ray lasing photon number is dramatically enhanced by a factor of 400 compared to that with only the pump pulse at the optimal condition. The output reached $\sim1\times10^{11}$ photon/pulse with 10% fluctuation and the x-ray beam divergence was decreased to 5.6 mrad in FWHM with 20% fluctuation. The beam divergence was close to the aspect ratio of the waveguide. The spectrum and angular distribution of Ni-like Kr

laser generated in the plasma waveguide are shown in Fig. 3(b). It is interesting to note that another lasing line at around 33.5 nm was also observed in the case of pure krypton plasma waveguide with an output of 4.4×10^{8} photon/pulse. It was found that the output of the 33.5-nm lasing line is always about two orders of magnitude smaller than that of the 32.8 nm lasing line for various atom densities, pump polarizations, pump energies, and heater energies. This seems to indicate that the 33.5-nm lasing line comes from a transition from the same upper level to another satellite lower level close to that of the primary lower level. It may be attributed to the $3d^9\,4d\ ^1S_0 - 3d^9\,4p\ ^3D_1$ transition. The first time observation of this satellite lasing line verifies a high gain length of such an x-ray laser scheme.

Under the same configuration of the pump and waveguide-forming pulses, high-threshold OFI collisional excitation Ne-like Ar laser at 46.9 nm was also achieved for the first time as shown in Fig. 3(c). The output photon of Ar laser was 3.4×10^{9}, and the beam divergence was 2.5 mrad at an atom density of 2.7×10^{19} cm^{-3}. This result suggests the presence of plasma waveguide is beneficial to x-ray laser generations required high pumping intensity. In addition to the lasing transition at 46.9 nm in Ne-like Ar ions, two other lasing lines at 45.1 and 46.5 nm were also observed and designated as $3d\ ^1P_1 - 3p\ ^1P_1$ and $3d\ ^1P_1 - 3p\ ^3P_1$ line respectively. These two lasing lines are predicted to have lasing gains when self-photo-pumping mechanism is considered. Similarly strong lasing for Xe^{8+} ions at 41.8 nm was also achieved as shown in Fig. 3(a). The output photon of Pd-like Xe laser was 2.7×10^{9}, and the beam divergence was 4.5 mrad at an atom density of 5.1×10^{18} cm^{-3}. With a mixed-gas (Kr:Ar = 1:1) plasma waveguide x-ray lasing in Ni-like Kr at 32.8 nm and Ne-like Ar at 46.9 nm were obtained simultaneously under adequate conditions. The output photon number for Kr and Ar x-ray lasers was about 8×10^{8} each. Simultaneous x-ray lasing in multiple ion species may become a power tool in plasma nonlinear optics.

With the deployment of the plasma waveguide, we increase the pump energy to enhance the pumping rate and thus increase the lasing gain coefficient. The lasing output for Ni-like krypton at 32.8 nm as a function of pump energy is shown in Fig. 3(d) with the plasma waveguide. The other parameters are the same as that for Fig. 3.(b). With only 500-mJ pump energy, more 5×10^{11} x-ray photons is generated from the OFI plasma column and results in an energy conversion efficiency of $\sim5\times10^{-6}$.

3.2 Seeding of a waveguide-based Kr laser by High harmonic generation

Figure 4 shows the angular profiles of the HHG seed, the ASE soft-x-ray laser, and the seeded soft-x-ray laser. With seeding the divergence of the soft-x-ray laser is greatly reduced from 4.5 mrad to 1.1 mrad in FWHM, which is about the same as that of the HHG seed. The pointing and angular profile of

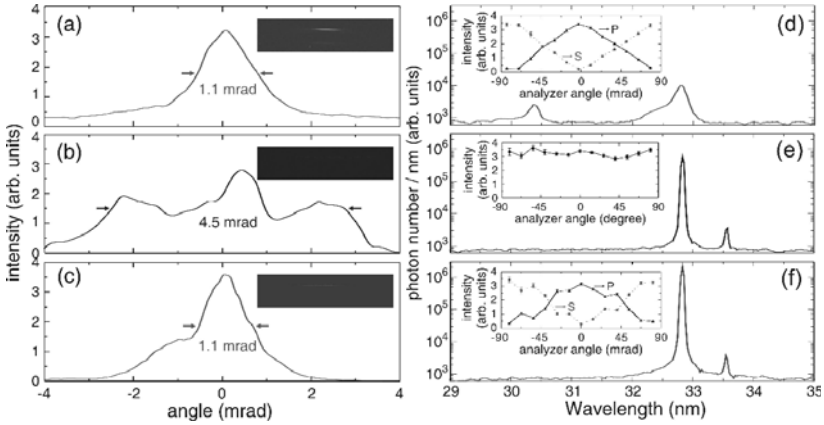

Fig. 4. X-ray spectra for an atom density of (a) $N_{Xe} = 4\times10^{19}$ cm^{-3}, (b) $N_{Kr} = 1.6\times10^{19}$ cm^{-3}, and (c) $N_{Ar} = 2.7\times10^{19}$ cm^{-3}. The heater energies were 180, 225, and 325 mJ, and the heater-pump delays were 5.5, 2.5, and 1.5 ns, respectively. The ignitor energy was 45 mJ and the ignitor-heater separation was 200 ps. Insets show the angular distributions of the 41.8 nm Xe^{8+}, 32.8 nm Kr^{8+}, and 46.9 nm Ar^{8+} lasing lines, respectively.

the seeded soft-x-ray laser follow that of the HHG seed and the fluctuation is negligible (~ 0.13 mrad). In contrast, the angular profile of the ASE soft-x-ray laser has a much larger fluctuation. The residual ASE contribution is estimated to be less than 10%. Figure 3 shows the spectra for the HHG seed, the ASE soft-x-ray laser, and the seeded soft-x-ray laser. The photon numbers for the HHG seed, ASE, and seeded soft-x-ray lasers are 1×10^{7}, $\sim1\times10^{11}$, and $\sim1\times10^{11}$, respectively. Since the residual ASE contribution is less than 10%, the amplification factor can be obtained approximately as 10^{4}. The absolute photon number of the seeded soft-x-ray laser is about the same as that of the ASE soft-x-ray laser. The energy fluctuation of the seeded soft-x-ray laser is about 10%, which is dominated by that of the soft-x-ray amplifier. The increase in the output of the 32.8-nm lasing line upon seeding observed in Fig. 4(f) is simply a result of the reduction of beam divergence which changes the collection efficiency of the spectrometer grating in the dispersion plane. In contrast, the photon number and beam divergence for the additional lasing line at 33.5 nm do not change with seeding, because the wavelength does not match with the HHG. This indicates that the waveguide-based ASE soft-x-ray laser already reaches the strongly saturated regime, in which the energy stored in the population inversion for most part of the length of the amplifier are efficiently extracted to the laser output even with only the spontaneous emission, so that the photon number cannot be significantly increased upon seeding. It is also found the polarization state of seed x-ray laser follow that of HHG closely as expected.

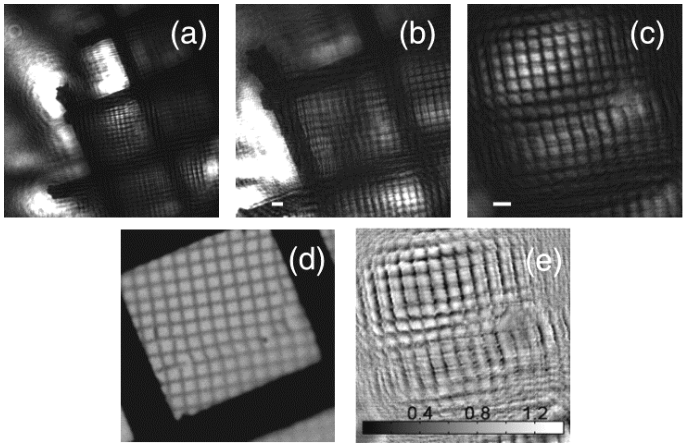

Fig. 5. Reconstructed intensity images of the carbon foil with magnifications of 17.9(a), 28.7(b), and 54.(c), respectively. The scale bar in each figure is 20 μm. The optical microscope image of the carbon foil is shown in (d). (e) shows the reconstructed phase image of the carbon foil with a magnification of 54.6.

3.3 X-ray digital holographic microscopy

As shown in Fig. 1(b), the imaging x-ray mirror produces a magnified image of the testing object, and the inherent magnification of the imaging system was 7.6 on CCD. By translating the specimen further toward the imaging mirror, the image plane will locate behind CCD to form a larger magnified object and a smaller field of view. The image recorded on CCD can be regarded as the hologram produced by the magnified object and the transmitted x-ray beam. In order to record sub-micron holographic images with a single picosecond x-ray exposure, the specimen was illuminated with a focused x-ray laser beam for producing stronger scattering signal and thus high-contrast holograms. Since two concave x-ray mirrors were arranged in a confocal geometry, the untouched beam was collected and collimated by the imaging mirror to form the reference beam on CCD. With such arrangement, the digital reference beam can be assumed as a plane wave without the need to know the exact parabolic phase function of the divergent reference beam. Image reconstruction was based on Fresnel-Kirchhoff diffraction integral of the recorded hologram with a propagation distance to the magnified image plane (focusing plane). A simple double fast Fourier transform algorithm treating the diffraction integral as the convolution function was used to reconstruct the amplitude and phase contrast images in 1 second. Fig. 5 shows the reconstructed intensity images of a 20-nm carbon-foil mesh with various system magnifications. As can be seen, x-ray DHM demonstrates the flexibility for observing specimen in a large field of view and studying the

details of the sample at high resolutions without complicate alignments and movements. The broken and bending mesh bars on the carbon foil caused by the sample cutting process are clearly seen in the reconstructed images and show good agreements with the observation using optical microscope shown in Fig. 5(d). The phase contrast image of the carbon foil at a magnification of 54.6 is shown in Fig. 5(e). The non-uniformity of the phase pattern mainly comes from the distortion (bending) of the sample as some parts of the image are not in focus. The spatial resolution of the reconstruction image derived from the edge responses of carbon mesh and AFM tip is ~ 480 nm due to the limit of the numerical aperture of imaging optics (~0.05).

References

1. Lemoff, B. E *et al.*: 'Demonstration of a 10-Hz femtosecond-laser-driven XUV laser at 41.8 nm in Xe IX', *Phys. Rev. Lett.* 74, 1574–1577, 1995.
2. Sebban S. *et al.*: 'Saturated amplification of a collisionally pumped optical-field-ionization soft X-ray laser at 41.8 nm', *Phys. Rev. Lett.* 86, 3004–3007, 2001.
3. Sebban S. *et al.*: 'Demonstration of a Ni-like Kr optical-field-ionization collisional soft X-ray Laser', *Phys. Rev. Lett.* 89, 253901, 2002.
4. Chu H.-H. *et al.*: 'Collisional excitation soft x-ray laser pumped by optical field ionization in a cluster jet', *Phys. Rev. A* 71, 061804(R), 2005.
5. Chou M.-C. *et al.*: 'Experimental investigation of the parameter space for optical-field-ionization cluster-jet x-ray lasers', *Phys. Rev. A* 74, 023804, 2006.
6. Durfee III C. G., Lynch J., and Milchberg H. M.: 'Development of a plasma waveguide for high-intensity laser pulses', P*hys. Rev. E* 51, 2368–2396, 1995.
7. Volfbeyn P., Esarey E., and Leemans W. P.: 'Guiding of laser pulses in plasma channels created by the ignitor-heater technique', *Phys. Plasmas* 6, 2269–2277, 1999.
8. Xiao Y.-F. *et al.*: 'Efficient generation of extended plasma waveguides with the axicon ignitor-heater scheme', *Phys. Plasmas* 11, L21–L24, 2004.
9. Ditmire, T. *et al.*: 'Amplification of xuv harmonic radiation in a gallium amplifier', Phys. Rev. A 51, R4337, 1995.
10. Zeitoun Ph. *et al.*: 'A high-intensity highly coherent soft X-ray femtosecond laser seeded by a high harmonic beam', *Nature* 431, 426, 2004.
11. Wang, Y. *et al.*: 'Phase-coherent, injection-seeded, table-top soft-X-ray lasers at 18.9 nm and 13.9 nm', *Nat. Photonics* 2, 94, 2008.
12. Gabor D. : 'A new microscopic principle', *Nature* 161, 777, 1948.
13. Chu H.-H. *et al.*: 'A versatile 10-TW laser system with robust passive controls to achieve high stability and spatiotemporal quality', *Appl. Phys. B* 79, 193, 2004.

Development of Silver Tape Target System for High Repetition X-ray Laser

Masaharu Nishikino, Yoshihiro Ochi, Noboru Hasegawa, Tetsuya Kawachi, Toshiyuki Ohba, Takeshi Kaihori, and Keisuke Nagashima

Quanum Beam Science Directorate, Japan Atomic Energy Agency,
8-1-7 Umemidai, Kizugawa, Kyoto 619-0215, Japan.

Abstract. The development of continuous pumping to the target system is an important issue for realizing an x-ray laser (XRL) with the high repetition rate. We have developed a 13.9 nm XRL using a silver tape target and demonstrated a highly coherent XRL with an oscillator-amplifier configuration using two tape target systems and the TOPAZ laser system with a 10-J and a 0.1-Hz repetition rate. The output energy is comparable to the x-ray laser generated with a silver-deposited slab target, and the pointing stability using the new tape target system is better than conventional slab target.

1 Introduction

The improvement of XRL generation so as to have a high repetition rate will open up the possibility of still more new applications. In last decade, progress in reducing the required pump energy for the x-ray lasing and raising the repetition rate has been achieved by adopting new technologies; The transient collisional excitation (TCE) scheme[1, 2] using chirped pulse amplification (CPA)[3] enables us to obtain XRLs with a pumping energy of about 10 J under the normal incident pumping geometry, and recently it was reported that 0.1 Hz operation was realized by the development of a CPA laser using Nd:glass zigzag slab amplifiers.[4] Moreover, grazing incidence pumping (GRIP)[5] has made possible 5-10 Hz operation of a gain-saturated XRL using a tabletop CPA Ti:Sapphire laser system with the pumping energy of 1 J.[6] In the GRIP configuration, the pumping energy is significantly reduced by the adjustment of energy deposition region. Recently, experimental studies to achieve fully spatial and temporal coherence have been reported using an injection-seeded GRIP-XRL with high-order harmonics of an optical laser.[7] Under such circumstances, the continuously supply targets is an important issue for realizing an XRL with the high repetition rate. With optical field ionization[8] and discharged capillary plasma XRLs[9] which use a gaseous target, highly coherent XRL operation with a repetition rate of up to 10 Hz has been achieved. In the cases of TCE XRLs using a solid target, a fresh part of the

J. Lee et al. (eds.), *X-Ray Lasers 2010,* Springer Proceedings in Physics 136,
DOI 10.1007/978-94-007-1186-0_11,

target material is required for every laser shot. Thus, the number of the XRL shots is limited typically to 15-20 shots by the size of the solid target. In order to a realize larger number of continuous shots, a variety of target configurations has been developed, such as a disk target,[10] drum target,[11] and tape target.[12, 13] In the case of the disk and the drum target, the number of shots is still limited by the target size. In contrast to these targets, a single long tape makes it possible the large number of continuous shots without replacing the target. While the tape target has been used to continuously supply targets for the generation of incoherent x rays or high energy ions, no significant results have been reported in tape target XRL development up to now. An XRL employing the quasi-steady state (QSS) collisional excitation scheme requires a gain medium length of about 25 mm to attain gain saturation intensity.[14] It is difficult to maintain the flatness of the surface of such a wide tape target. Employing the TCE scheme, a higher gain coefficient of 30-80 per centimeter has been achieved, and a gain medium length of only 4-6 mm is sufficient for the generation of the XRL with saturated intensity.[15] As a result, a TCE XRL can be generated with a shorter flat length of the tape target than a QSS XRL. Here, we describe the generation of a 13.9 nm XRL using a silver (Ag) tape target and the demonstration of a highly coherent XRL produced with an oscillator-amplifier configuration[16, 17] using two tape target systems and TOPAZ laser system[4].

2 Tape target driver system

For the generation of a Ni-like Ag XRL, the Ag target must have a flat surface like a commercial Ag foil or an Ag film deposit on the polished surface of a glass slide. The thickness of the Ag layer need only be the laser ablation depth of a few μm, but a thin Ag foil has the risk of breaking after ablation by the laser shot and during the rotation of tape. Therefore, we used 30-μm and 50-μm thick Ag tape targets for the XRL generation. Even when the thickness of the Ag tape target is 30-50 μm, since the tape at the irradiation position of the laser shot is broken by the ablation shock wave, the width of the tape needed to be larger than the length of the line focus of the pumping laser. In the case of line focus length of 7 mm, it was necessary for the stable XRL generation that a 15-mm wide tape target with the thickness of 30 μm be used. A photograph of the tape target driver is shown in Fig. 1(a). The direction of the XRL was parallel to the surface of the tape target. The main components of the tape target driver were two DC motors coupled with planetary gear mechanisms and a tape head. These motors and gear mechanisms are specialized for vacuum use. One DC motor with a 1:1526 speed-reducing gear was mounted on the upper-mounted spool and rolled up the Ag tape between the laser irradiation periods. The other DC motor with a 1:134 speed-reducing

gear was mounted on the lower-mounted spool and pulled the tape in the direction opposite that in which it moves during the operation. Since the torque of the upper-mounted motor was greater than that of the lower-mounted motor, the Ag tape target was tightly stretched, and sufficient flatness of the surface of the tape target was realized at the laser irradiation position. When the imprint of laser irradiation is made on the tape target every 10 mm, it is possible for the tape target driver to maintain the flatness of the tape target. Figure 1(b) shows laser irradiated target with the imprint of laser ablation.

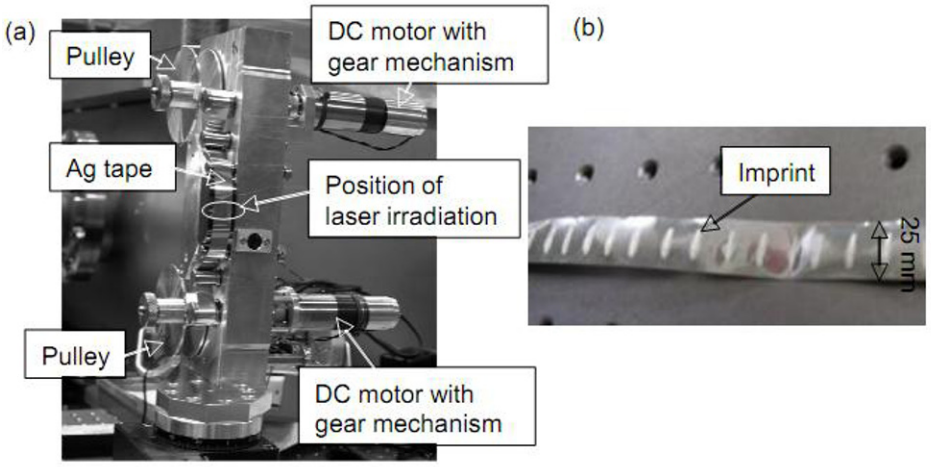

Fig. 1. (a) Photograph of tape target driver and (b) laser irradiated target.

3 Experimental setup

The Ag tape target was irradiated with a pumping laser beam from the pumping laser system "TOPAZ (Twin Optical Amplifiers using Zigzag slab)" using a Ti:sapphire regenerated amplifier" operating at 1.053 μm.[4] We have already constructed and demonstrated a nickel-like Ag laser at wavelength of 13.9 nm using an Ag deposited slab target and the TOPAZ laser system.[4] The pumping laser was normally incident to the target, and focused to a line shape of 20 μm width and 7 mm length on the target by quasi-traveling-wave pumping using a 4-step mirror.[15] The irradiation consisted of two laser pulses, the duration of each pulse being 4 ps with a pulse-to-pulse separation of 1.2 ns. The total pumping energy of the first and second target was set to 5 and 7 J, respectively. The energy ratio of a prepulse to the main pulse was 1:8 on the target. The contrast ratio of the ASE level to the peak intensity was about 5×10^{-4}, and the pedestal level of the main pulse was about 1×10^{11} W/cm^2. The XRL beam was reflected on a molybdenum-silicon multilayered mirror with an incident angle of 45° and filtered with a

zirconium foil. The far-field pattern (FFP) and time-integrated energy of XRL were obtained with an x-ray charged-couple device camera.

4 Experiment

4.1 X-ray laser generation using tape target

We carried out an experiment comparing the XRLs generated by the slab and by the tape target using one beam of the TOPAZ lasers. Figure 2(a) shows an FFP of the XRL from the Ag deposited slab target. The beam divergences along vertical and horizontal axes were 7 and 5 mrad FWHM, respectively. The output energy was about 2 μJ. Figure 2(b) shows an FFP of the XRL from an Ag tape target with 30-μm thickness. The beam divergences along vertical and horizontal axes were 5 and 7 mrad FWHM, respectively. The output energy was about 1.5 μJ and the FFP was a rounder pattern than the XRL from the slab target. The target surface is on the right-hand side in the figure, and the refraction angle was 6 mrad from the target surface in both cases. These XRL beams were considered in the gain-saturated region by comparison with the output energy of previous experimental results[4]. Figure 2(c) shows an FFP of the XRL from an Ag tape target with 50-μm thickness. The FFP image when the thickness of the tape target was 50-μm was similar to when the thickness was 30-μm, but the output energy of XRL decreased to about 1/3 that of the 30-μm thickness target. The 50-μm thickness tape target was hard, and therefore the tape target drive system could not pull the target with sufficient tension. When the tape was pulled only by the upper mounted motor, there was no tension on the tape, and the XRL was not generated. Therefore, the flatness of the tape target needed for the XRL generation was found to be achieved with the tension induced by the lower mounted motor.

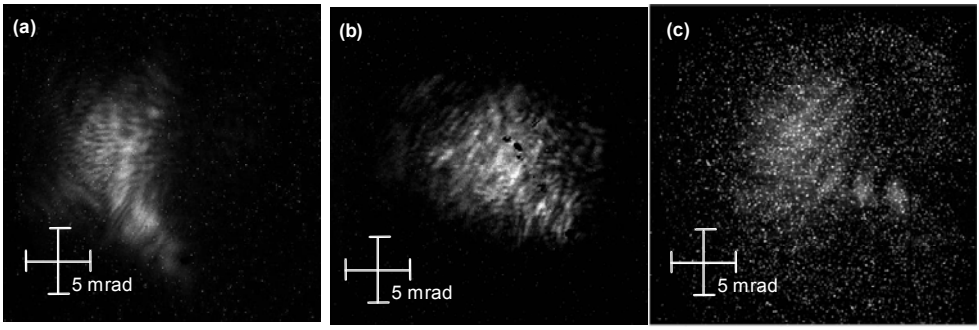

Fig. 2. FFPs of (a) the XRL using Ag deposited slab target, (b) the XRL using Ag tape target with 30-μm thickness, and (c) the XRL using Ag tape target with 50-μm thickness.

4.2 Generation of highly coherent X-ray laser

We attempted the generation of the highly coherent XRL using the oscillator-amplifier configuration[16, 17] with two tape target systems. Figure 3 shows FFPs of the highly coherent XRL (a) from the Ag deposited slab target and (b) from the Ag tape target with 30-μm thickness. The output energy of each beam was about 0.4 μJ. The divergences of the beams along the vertical and horizontal axes were roughly similar, 0.5 and 0.4 mrad FWHM, respectively. The beam pointing varied about ±1.0 and ±0.5 mrad in the vertical and horizontal directions, respectively. Figure 3(c) shows the comparison of pointing stability between the slab and the tape target. The pointing stability of the target systems in the vertical direction was roughly similar, largely influenced by the pointing stability of the pumping laser. The beam pointing of the tape target in the horizontal direction was improved so that pointing stability was about half that of the slab target.

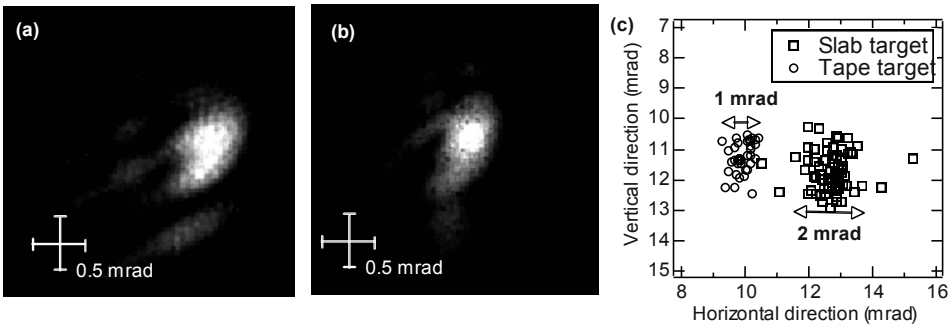

Fig. 3. FFPs of (a) the highly coherent XRL using Ag deposited slab target and (b) the highly coherent XRL using Ag tape target. (c) The comparison of the pointing stability of highly coherent XRL

5. Summary

We have constructed and demonstrated a XRL using an Ag tape target for continuous XRL generation. The output energy and divergence are comparable to the XRL from a slab target. The installation of new tape target systems for the oscillator-amplifier configuration was successful, and a highly coherent XRL was generated with a 0.1 Hz repetition rate using the TOPAZ laser system. The pointing stability of this highly coherent XRL is improved by the elimination of target exchange during operation, which requires opening of the vacuum target chamber.

Acknowledgement

The authors are grateful to Dr. T. Kimura and Professor Y. Kato of the Japan Atomic Energy Agency and the staff of the x-ray laser research group for their technical support.

References

1. P.V. Nickles, V.N. Shlyaptsev, M. Kalachnikov, M. Schnuer, I. will, and W. Sandner, Phys. Rev. Lett. **78**, 2748(1997).
2. J. Dunn, A.L. Osterheld, R. Shepherd, W.E. White, V.N. Shlyaptsev, and R.E. Stewart, Phys. Rev. Lett. **80**, 2825(1998).
3. D. Strickland and G. Mourou, Opt.Commun. **56**, 219 (1985).
4. Y. Ochi, N. Hasegawa, T. Kawachi, and K. Nagashima, Appl. Opt. **46**, 1500 (2007).
5. R. Keenan, J. Dunn, P.K. Patel, D.F. Price, R.F. Smith and V.N. Shlyaptsev, Phys. Rev. Lett. **94**, 103901(2005).
6. J. J. Rocca, Y. Wang, M. A. Latrotonda, B. M. Luther, M. Berrill, and D. Alessi, Opt. Lett. **30**, 2581 (2005).
7. Y. Wang, E. Granados, F. Pedaci, D. Alessi, B. Luther, M. Berrill and J. J. Rocca, Nature Photonics. **2**, 94 (2008).
8. S. Sebban, R. Haroutunian, Ph. Balcou, G. Grillon, Arousse, S. Kazamias, T. Marin, J.P. Rousseau, L. Notebaert, M. Pittman, J.P. Chambaret, A. Atonetti, D. Hulin, D. Ros, A. Klisnick, A. Carillon, P. Jaeglé, G. Jamelot, and J.F. Wyart, Phys. Rev. Lett. **86**, 3004 (2001).
9. Y. Liu, M. Seminario, F.G. Tomasel, C. Chang, J.J. Rocca, and D.T. Atwood, Phys. Rev. A **63**, 033802 (2001).
10. Y. Hironaka, Y. Fujimoto, K.G. Nakamura, and K. Kondo, Appl. Phys. Lett. **74**, 1645 (1999).
11. T. Mochizuki, Proc. SPIE **3886**, 306 (2000).
12. Y. Hisada, P. Abraha, K. Takamoto, N. Yamaguchi, and T. Hara, Jpn. J. Appl. Phys. **37**, 5071 (1998).
13. E. Fill, J. Bayerl, and R. Tommasini, Rev. Sci. Instrum. **73**, 2190 (2002).
14. H.Daido, S. Ninomiya, T. Itami, R. Kodama, M. Takagi, Y. Kato, K. Murai, J. Zhang. Y. You, and Y. Gu, Opt. Lett. **21**, 958 (1996).
15. T. Kawachi, A. Sasaki, M. Tanaka, M. Kishimoto, N. Hasegawa, K. Nagashima, M. Koike, H. Daido, and Y. Kato, Phys. Rev. A **66**, 033815 (2002).
16. M. Tanaka, M. Nishikino, T. Kawachi, N. Hasegawa, M. Kado, M. Kishimoto, K. Nagashima, and Y. Kato, Opt. Lett. **28**, 1680 (2003).
17. M. Nishikino, M. Tanaka, K. Nagashima, M. Kishimoto, M. Kado, T. Kawachi, K. Sukegawa, Y. Ochi, N. Hasegawa, and Y. Kato, Phys. Rev. A **68**, 061802(R) (2003).

Part 3: X-Ray Laser Amplifiers – Seeding

Temporal coherence and spectral width of seeded and ASE XUV lasers

A. Klisnick[1*], O. Guilbaud[2,6], J.P. Goddet[3], F. Tissandier[3], L.M. Meng[1], , L. Urbanski[4], J. Gautier[3], S. de Rossi[5], D. Alessi[4] ,Y. Wang[4], B. Luther[4], D. Martz [4], S. Domingue[4], G. Maynard[6], D. Benredjem[7], A. Calisti[8], S. Sebban[3], M. Marconi[4] , D. Joyeux[5] , J.J.Rocca [4]

[1] ISMO, Bât. 350, CNRS, Université Paris-Sud 11, Orsay, France
[2] LASERIX, Université Paris-Sud 11, Orsay, France
[3] LOA, ENSTA-Ecole Polytechnique, Palaiseau, France
[4] NSF Center for EUV Science and Technology Colorado State University, Fort Collins, United States
[5] Lab Charles Fabry, Institut d'Optique Graduate School, Palaiseau, France
[6] LPGP, CNRS, Université Paris-Sud 11, Orsay, France
[7] LAC, CNRS, Université Paris-Sud, Orsay, France
[8] PIIM, CNRS, Université de Provence, Marseille, France

Abstract. We review recent experimental work devoted to the characterization of the spectral profile and linewidth of two types of XUV lasers seeded by high-order harmonic radiation. The spectral properties were deduced from the measurement of the temporal coherence of the XUV laser pulse, using a variable pathlength interferometer. In this paper an optical-field ionization XUV laser developed at LOA laboratory (France), emitting at 32 nm, and a grazing incidence, and a transient XUV laser developed at Colorado State University (US), emitting at 18.9-nm, both operated in the injection-seeded mode, were investigated. We show that in both cases the measured temporal coherence length is slightly larger than when the lasers are operated in the amplified spontaneous emission (ASE) mode. The corresponding bandwidth is observed to be larger for the transient pumping system, which should more easily scale to sub-picosecond pulse durations.

1 Introduction

Recently new promising prospects to the utilization of high-brightness, plasma-based XUV lasers have been opened by the demonstration of injection-seeding high-order harmonic radiation at the entrance plane of a plasma amplifier, pumped either in optical-field-ionization [1] or grazing incidence transient [2] scheme. In particular it was shown that the spatial

J. Lee et al. (eds.), *X-Ray Lasers 2010,* Springer Proceedings in Physics 136,
DOI 10.1007/978-94-007-1186-0_12,

coherence of the output beam was dramatically improved [3, 4] over the amplified spontaneous emission (ASE) operation. On the other hand plasma-based XUV lasers are characterized by an extremely high monochromaticity, associated with a longitudinal (or temporal) coherence that is close to the output pulse duration, of the order of one or several picoseconds. This narrow spectral width actually limits the ultimate shortest duration that can be achieved with currently operational XUV lasers to typically 1 picosecond [5]. For several challenging applications, like coherent imaging or interaction with matter at high XUV intensities, it will be necessary to extend the duration of the XUV laser sources towards the sub-picosecond, or even femtosecond range. This will require significant enlargement of their linewidth, through plasma broadening at other density and temperature. In order to progress towards this goal we need to progress in the characterization and understanding of the spectral properties of XUV lasers, by clarifying the respective contribution of homogeneous versus inhomogeneous broadening and by identifying the potential strategies that could be used to control the spectral with of the XUV laser amplifier. Finally our experimental study can provide useful benchmarking to existing models and numerical codes which are used to calculate the spatial and temporal features of XUV lasers.

Due to their extremely narrow bandwidth (typically $\Delta\lambda/\lambda \sim 10^{-5}$) the measurement of the spectral width of the XUV laser lines is challenging, as it lies at the limit or beyond the resolution capacity of existing spectrometers in this spectral range. This is why we have used a wavefront-division interferometer, which was specifically designed to measure the temporal coherence of the source, from which the spectral linewidth is inferred. Previous experiments involving this interferometer were already reported earlier [6-8]. In this paper we discuss the results obtained in the two latest experimental campaigns performed at the LOA laboratory (France) on the one hand, and at the NSF Center for EUV Science and Technology (Colorado State University, USA) on the other hand. Apart from a preliminary demonstration recently reported in Japan [9], these two laboratories are until now the only places in the world where injection-seeded XUV lasers are generated. As will be shown, the possibility to compare the temporal coherence exhibited by the XUV laser pulse in each laboratory is highly interesting because they rely on distinct techniques to generate the plasma XUV amplifier. At LOA the plasma is produced from optical-field ionization of krypton gas with a 30 fs pump laser [10], with laser emission at 32 nm. At CSU the plasma is produced by irradiation of a molybdenum slab with a sequence of two (210 ps and 3.3 ps) pulses, with laser emission at 18.9 nm. These differences in the pumping conditions lead to significantly different plasma parameters in the amplifying zone, which then affect the spectral profile of the XUV laser lines.

In section 2 we recall the experimental method that was used to measure the temporal coherence of the XUV laser pulse and to infer their spectral width. The results obtained of the OFI laser and the grazing incidence transient laser are presented and discussed in section 3 and 4 respectively. A summary of our observations and the prospects for future work are outlined in section 5.

2 Experimental method

As explained in the introduction the characterization of the spectral linewidth was inferred from the measurement of the longitudinal (or temporal) coherence using a wavefront-division interferometer that was specifically designed for that study. This device, represented in figure 1, is composed of two dihedrons, tilted towards each other with a small angle. The incoming beam is separated in two beamlets that slightly converge towards each other after reflection on the dihedrons. In their overlaping region, interférence fringes can be recorded using a XUV CCD camera. One of the dihedrons can be accurately translated vertically in order to introduce a path difference between the interfering beams. Using dihedrons instead of flat mirrors ensures a constant lateral overlapping geometry, thus constant spatial coherence conditions, when changing the delay.

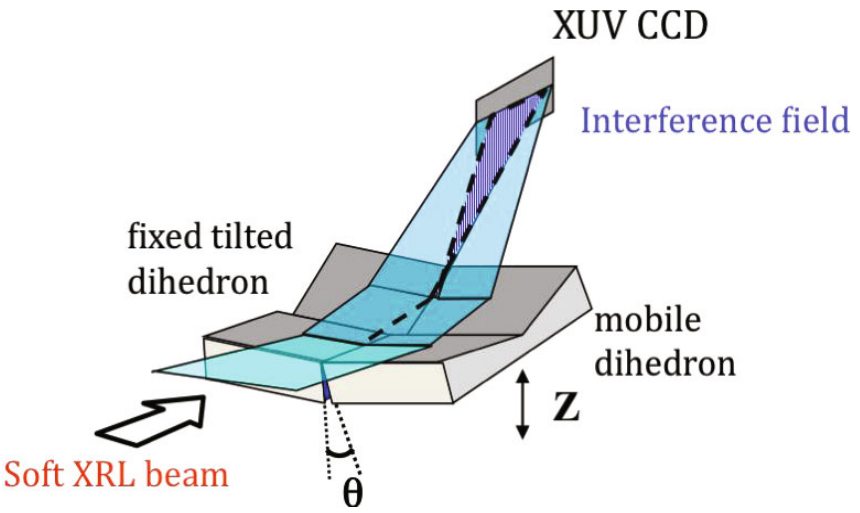

Fig. 1. Schematic view of the wavefront-division interferometer

By following the evolution of the fringe visibility as a function of the delay with successive shots performed in identical conditions, it is possible to reconstruct the spectral profile of the incoming radiation through a Fourier

transform. In the experiments described below the interferometer was implemented and aligned along the XUV laser beamline at a distance of ~3 m from the source. For each pathlength the measurement of the fringe visibility was based on 5 to 10 individual interferograms, in order to account for shot-to-shot variations. Each interferogram was numerically processed with a method described in a companion paper [11].

3 Seeded OFI XUV laser at 32 nm

The wavefront interferometer was used to investigate the seeded OFI XUV laser emitted at 32 nm in Ni-like Kr, and developed at LOA [1]. The plasma amplifier in which harmonic radiation is injected is produced by irradiating a krypton gas cell with a 35 fs, 600 mJ infrared laser pulse. In a first experiment performed with this laser [8] it was found that the measured coherence time of ~5 ps was very close to the pulse duration that was inferred indirectly from the variation of the amplification factor with the seeding delay. In the new experimental campaign described in this paper, the quality of the alignment and of the interferograms was improved, allowing for a more detailed investigation [12].

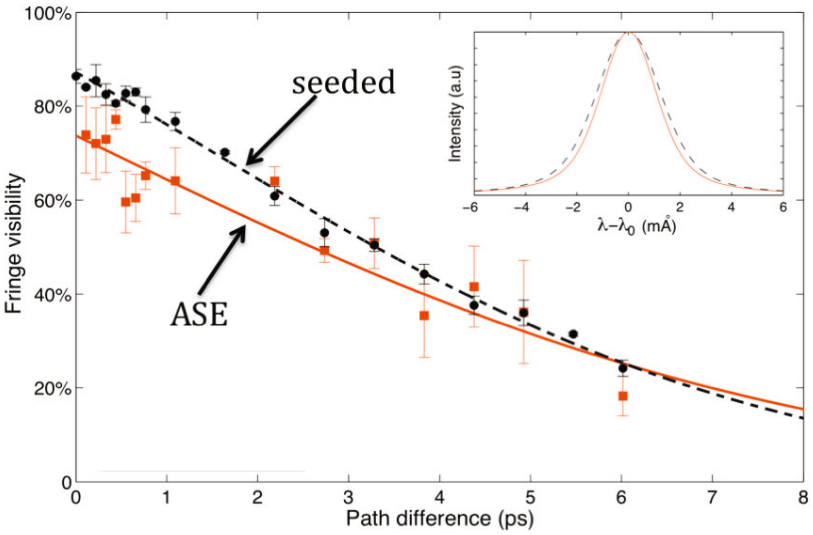

Fig. 2. Measured fringe visibility as a function of the time delay between the interfering beams, for seeded and ASE operation at 32 nm. Each data set was fitted to a functional form defined as the product of a Gaussian and a decreasing exponential. This fit is used to recover the spectral profiles, shown in the insert (dotted curve: seeded; solid line: ASE), through a Fourier transform.

In particular we were able to compare the temporal coherence of the 32 nm laser operated either in the seeded mode, or in the unseeded, ASE mode. In both cases the plasma amplifier length was 6 mm. The results are shown in figure 2. The measured fringe visibility is plotted as a function of the path difference, here expressed in picoseconds, for the two operating modes. Each data point is the average over 5 to 10 shots, the error bar represents the standard deviation. The experimental data were then fitted with a functional form defined as the product of a Gaussian and a decreasing exponential.

The coherence time is defined as the path difference at which the visibility is decreased by a factor 1/e. One can see from Fig. 2 that the coherence time is slightly larger for the ASE case ($\tau_c = 5.5 \pm 0.3$ ps) than for the seeded case ($\tau_c = 5.1 \pm 0.2$ ps), although the difference is close to our error bar. According to the Wiener- Khintchin theorem, the evolution of the fringe visibility with the time difference is the Fourier transform of the spectral power density of the source. The spectral profiles have been calculated from the fitted visibility evolutions, and correspond to a spectral Voigt profile with a full width half-maximum (FWHM) of $\Delta\nu = 8.9 \pm 0.6\ 10^{10}$ Hz, or $\Delta\lambda = 3.2 \pm 0.2$ mÅ for the seeded SXRL and $\Delta\nu = 7.5 \pm 0.8\ 10^{10}$ Hz, or $\Delta\lambda = 2.7 \pm 0.3$ mÅ for the ASE pulse. Seeding with harmonic radiation produces a pulse with an initial bandwidth that much larger the ASE one and more of that bandwidth is preserved.along amplification.

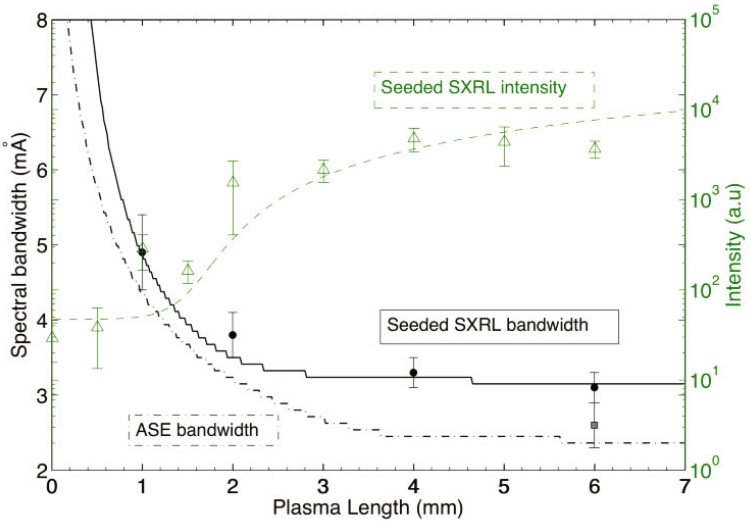

Fig. 3. Effect of varying the amplifier length. Left axis: Spectral linewidth of the 32 nm laser for the seeded and ASE cases. Right axis: Time and spectrally integrated intensity of the seeded XUV laser pulse. The experimental data are compared to the predictions of numerical simulations (solid and dotted lines).

The same measurement was carried out for the seeded XUV laser with shorter plasma amplifiers, namely 1, 2 and 4 mm. The results are summarized in Figure 3, along with the intensity versus length measured in the same experiment. One can see that the spectral with undergoes a significant narrowing while the length is increased from 1 to 3 mm, while the narrowing is weaker for the longest 6 mm length. The measured data were compared to numerical simulations based on a radiative transfer model in which homogeneous and inhomogeneous broadening of the gain were included, as well as the effect of saturation [8]. The agreement of the calculations with the observed behaviour is satisfactory for both the seeded and the ASE case. It can be seen that no rebroadening of the line is observed in the saturation regime, which is reached at ~3 mm.

4 Seeded grazing-incidence transient laser at 18.9 nm

More recently the wavefront-division interferometer was implemented at the NSF Center for EUV Science and Technology (Colorado State University, USA) to investigate the other type of seeded XUV laser developed in this laboratory [2]. Here the plasma amplifier is produced in the transient regime, by irradiating a preformed Mo plasma by ~1 J, 3.3 ps infrared laser pulse, using the grazing incidence pumping (GRIP) geometry. Compared to the OFI XUV laser described above, population inversions and gain are produced by the same mechanism (collisional excitation), but at a higher electron density since the plasma is produced from a solid target.

Figure 4 shows the variation of the fringe visibility with the path difference, here expressed in μm, which was measured for the seeded 18.9 nm Mo laser. The length of the plasma amplifier is 4 mm. For this measurement the visibility curve was extended towards negative values of the path difference, in order to improve the accuracy around the zero path difference in the determination of the shape. As above, each data point results from an average over 5 to 10 shots and the error bar shows the standard deviation of the shot-to-shot fluctuation. Using the same definitions as above, we find that the coherence time is $\tau_c = 1.4 \pm 0.2$ ps, i.e. significantly shorter than what was obtained with the OFI seeded XUV laser. The experimental data in Fig.4 was fitted to several functional forms among which the double-sided decreasing exponential yielded the best fitting coefficients. This fit was then used to recover the spectral profile of the line, which leads to a Lorentzian shape, with a FWHM linewidth of $\Delta\lambda = 2{,}7 \pm 0.4$ mÅ.

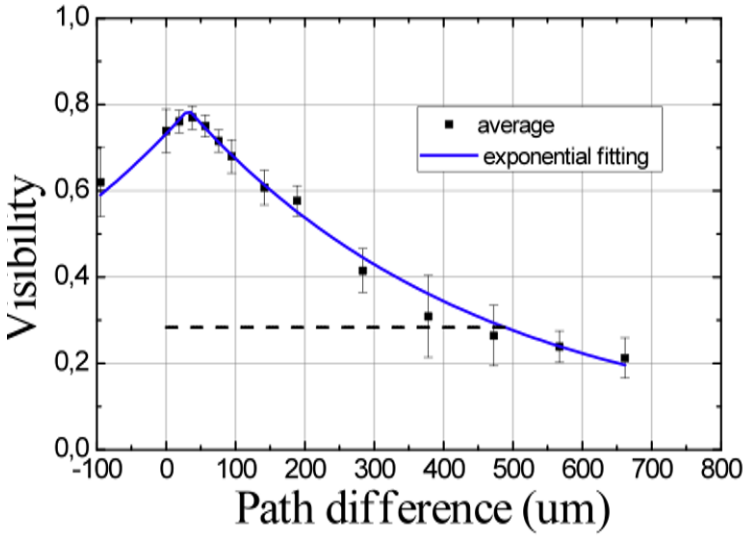

Fig. 4. Measured fringe visibility as a function of the path difference between the interfering beams, for the seeded Mo laser emitted at 18.9 nm. The experimental data are fitted with a double-sided decreasing exponential function.

We repeated the measurements of the seeded pulse for shorter Mo plasma amplifiers, namely 2 and 3 mm. The experimental data are shown in [11]. We found that the visibility curves obtained for the different plasma lengths exhibit slightly different shapes, which were fitted by different functions to maximize the fitting coefficients. This eventually leads to some inconsistency between the measured coherence time and the inferred FWHM linewidth, since these two quantities are inversely proportional, with a constant numerical factor that depends on the shape of the visibility curve, i.e. the choice of the fitting function. In order to overcome this difficulty it is more appropriate to use another definition for the coherence time and the spectral linewidth, based on the quadratic means of these quantities, as discussed in [13]:

$$\tau_c^{\,2} = \frac{\int_0^\infty t^2 \cdot \left|V^2(t)\right| \cdot dt}{\int_0^\infty \left|V^2(t)\right| \cdot dt} \qquad \Delta\nu^2 = 2\frac{\int_0^\infty \upsilon^2 \cdot \left|G^2(\nu+\overline{\nu})\right| \cdot d\nu}{\int_0^\infty \left|G^2(\nu+\overline{\nu})\right| \cdot d\nu} \qquad (1)$$

where V(t) is the visibility as a function of the path difference (given by the analytical fit), G(ν) is the spectral power density and $\overline{\nu}$ is the average central frequency of the line. G(ν) is given by the Fourier-transform of V(t). Note that the above definition of Δν assumes that the spectral profile is symmetrical with respect to the central frequency $\overline{\nu}$.

This quadratic definition is much less sensitive to the particular shape of the spectral profile, which is difficult to assess with a high accuracy in our experiment, mainly due to shot-to-shot fluctuations of the measurements.

Using the definitions (1) for the seeded, 4 mm XUV pulse we find a coherence time τ_c = 1 ± 0.2 ps corresponding to a spectral linewidth $\Delta\lambda$ = 2.7 ± 0.4 mÅ. For the shorter plasma lengths (2 mm and 3 mm) the measured linewidth values are of 3.4 ± 0.4 mÅ and 3 ± 0.6 mÅ respectively, i.e. slightly larger than the 4 mm case but within the error bar. This result is consistent with the predictions of numerical simulations which show that most of the line narrowing due to amplification occurs in the first 2 mm of the plasma column. However when the plasma length is reduced to less than 2 mm the amplified signal dramatically drops down, hence preventing reliable interferometric measurements to be performed. In the ASE mode we find a linewidth $\Delta\lambda$ = 2.3 ± 0.2 mÅ that is slightly narrower (although again within the error bar) than in the seeded mode, for the 4 mm plasma length. Such a trend was also observed in the measurements performed with the OFI laser presented above. This is also in agreement with the calculations performed with the radiative transfer code.

5 Conclusions and prospects

We have presented the results of two recent experimental campaigns aimed at characterizing the temporal coherence and spectral linewidth of two types of injection-seeded XUV lasers, emitted at 32 nm and 18.9 nm respectively. Both systems exhibit similar trends that the temporal coherence is slightly larger in the unseeded, ASE mode than in the seeded mode. In both cases we did not observe any rebroadening of the line at saturation, in agreement with the predictions of numerical simulations.

We propose to use an alternative definition for the coherence time and spectral linewidth, which is less sensitive to the choice of the functional form used to fit the experimental data.

Finally the comparison of the coherence times for the OFI and GRIP transient XUV laser suggest that the latter will be more favourable for the development of XUV lasers with shorter, sub-picosecond duration.

Further work is needed to better characterize the respective role of homogeneous versus inhomogeneous broadening in the spectral properties of XUV lasers. In order to progress towards this goal we have recently carried out at CSU new measurements with another type of XUV laser, based on capillary discharge pumping and emitting at 46.9nm [14]. Here the population inversions and gain are again induced by collisional excitation from the free electrons, but the plasma has significant lower density. Since the ion temperature is also relatively large, this leads to a larger contribution of the Doppler inhomogeneous broadening component. Preliminary analysis of the experimental data show that the temporal coherence of this laser, operated in

the ASE mode, is of the order of 2 ps, which is much shorter than the pulse duration.

Acknowledgements:

The technical assistance of J-C Lagron is gratefully acknowledged. The experiment performed at LOA was partially funded through the EC 7th Framework Programme (LASERLAB Europe, contract No. 228334). The experiment performed at Colorado State University was funded by the NSF Center for Extreme Ultraviolet Science and Technology under NSF Award Number EEC-0310717, and by the Chemical Sciences, Geosciences and Biosciences Division, Office of Basic Energy Sciences, Office of Science, U.S. Department of Energy

References

1. Ph. Zeitoun et al., *Nature* 431, 426, 2004
2. Y. Wang et al., *Phys. Rev. Lett.* 97, 123901, 2006; Y. Wang et al., *Nat. Phot.*,2, 94, 2008
3. J-Ph. Goddet et al., *Opt. Lett.* 34, 2438, 2009
4. M. Berrill et al., *Opt. Lett.* 35, 2317, 2010
5. Y. Wang et al., *Phys. Rev. A* 79, 023810, 2009
6. A. Klisnick et al., *J. Quant. Spectr. Rad. Trans.* 99, 370, 2006
7. J. Habib et al., *X-ray lasers 2008 Proceedings*, Springer Proceedings in Physics, Vol.130, 115, 2009
8. O. Guilbaud et al., *Opt. Lett.* 35, 1326, 2010
9. N. Hasegawa et al., *Jap. J. Appl. Phys*., 48, 012503, 2009
10. S. Sebban et al., *Phys. Rev. Lett.* 89, 253901, 2002
11. L. Meng et al., *This Conference*
12. F. Tissandier et al., *Phys. Rev. A* 81, 063833, 2010
13. M. Born and E. Wolf, *"Principles of Optics"* 6th edition, Pergamon Press, p. 540, 1980
14. B. Benware et al., *Phys. Rev. Lett.* 81, 5804, 1998

Wave perspective on high harmonics amplification in a high-gain medium with level degeneracy

Chul Min Kim, Karol A. Janulewicz, Jongmin Lee

Advanced Photonics Research Institute, Gwangju Institute of Science and Technology, Gwangju 500-712, South Korea

Abstract. Amplification of a high-harmonic-signal in an amplifying medium of an X-ray laser is analysed by applying Maxwell-Bloch equations. The model includes time-dependent high swept-gain, randomized spontaneous emission component and laser level degeneracy. The output characteristics including energy extraction, pulse shape and polarization of the output radiation are obtained within the formulated model and discussed in detail.

1 Introduction

Enormous progress in material and life sciences strengthened the interest in short-wavelength sources enabling penetration of matter features with exceptional spatial and temporal resolution. Newly developed X-ray free electron lasers of unprecedented parameters [1] comes along with well established plasma based X-ray lasers as the strongest sources of coherent radiation in extreme ultra-violet (XUV) and soft X-ray spectral range. However, all the progress in the development of these devices working typically in the regime of amplified spontaneous emission could not eliminate some critical drawbacks of these lasers. While plasma based X-ray lasers are only partially coherent (1-5%), of undefined polarization and with a pulse length of few picoseconds, the XFELs show very poor temporal coherence originated in the generation mechanism.

It is commonly expected that injection of an external signal (in many aspects of superb quality) into the amplifying medium of X-ray lasers (XRLs) would help to overcome the listed above deficits [2]. These hopes are based on the assumption of conserving the seed quality in the amplification process. High harmonic seemed to be an excellent candidate for the seed not only due to the signal features but also for easily implementable generation technique. Amplification of ultra-short pulses belongs to the basic processes of modern optical science and technology. In the optical or IR regions of spectrum, it is accomplished by exploiting a relatively broad-band gain medium (few tens of nm) and chirped-pulse-amplification (CPA) technique. In this technique a weak femtosecond (fs) pulse is stretched by a factor of about 10^6 and

J. Lee et al. (eds.), *X-Ray Lasers 2010,* Springer Proceedings in Physics 136,
DOI 10.1007/978-94-007-1186-0_13,

subsequently incoherently amplified in the gain medium (factor larger than 10^3). After being recompressed the amplified pulse achieves almost the initial length. In the spectral region of extreme ultraviolet (XUV) or soft x-rays, this successful and reasonably efficient technique cannot be employed due to the lack of efficient optical components and sufficiently broadband (in absolute values) gain medium (X-ray laser shows at 10 nm $\Delta\lambda \leq 10^{-3}$ nm).

2 The Model

The typical situation in the current practice is as follows: the weak ultra-short pulse in the form of high harmonic signal has a pulse width of few fs ($\Delta\lambda$=20 nm) and is amplified in a spectrally much narrower gain medium (plasma) [2,3]. The relaxation time of the medium macroscopic polarization determined by the medium bandwidth is longer than the width of the input pulse and one faces the situation that amplification occurs in the coherent regime. That means the levels populations can oscillate due to consecutive up-and-down transitions. This is a very unique experimental situation. The gain of the medium is very high, reaching 70 cm^{-1}, and the random character of strong spontaneous emission can significantly affect the amplification process. As a consequence, the proper description of the medium kinetics and the interaction process should reflect all these elements which usually are not observed in the optical and near-infrared regions.

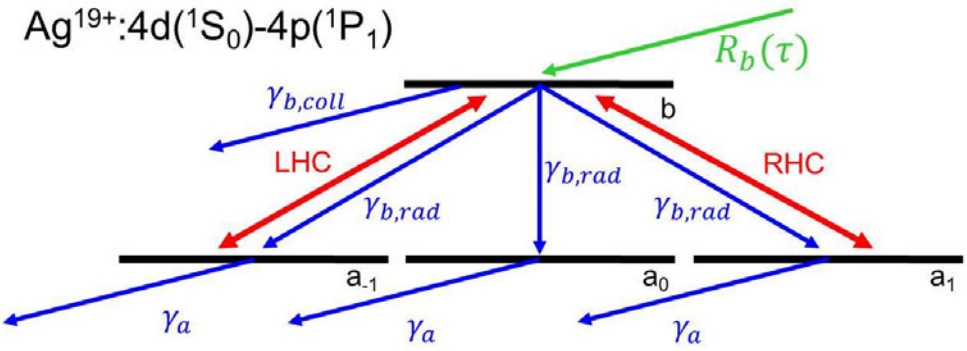

Fig.1. Atomic level; structure for the J=0 – 1 transition in a nickel-like Ag^{+19} ion. The effective rates of the basic kinetic processes are given together with the lasing transitions marked as left- or right-handed polarised ones (forced by the selection rules in this atomic levels scheme).

A model based on Maxwell-Bloch equations without adiabaticity assumption was used to treat all these elements in the most comprehensive

way. The model incorporates the random character of spontaneous emission [4], time-dependent gain by using the pump function obtained from laser-plasma simulation, and level degeneracy by treating separately the states of the degenerate energetic level (see Fig.1). The values for given specific kinetic parameters are quoted in [5]. With this model, the complete information on the radiation field, i.e. both amplitude and phase can be obtained. The crucial and novel point of the analysis is polarisation of the emitted radiation. In the randomisation process it was assumed that the complex amplitudes of two components of the circular polarisation are uncorrelated, i.e. independent of each other. This difference gave us the spontaneous noise of undefined polarisation, in accordance with the physical process occurring in the medium. Polarisation changes of the amplified radiation were observed during the amplification process by tracking the degree of polarisation $P \in (0,1)$(e.g. defined in [6])

$$P = \sqrt{1 - \frac{4\det(J)}{Tr(J)^2}} \tag{1}$$

where

$$J = \begin{vmatrix} \langle E_x E_x^* \rangle & \langle E_x E_y^* \rangle \\ \langle E_y E_x^* \rangle & \langle E_y E_y^* \rangle \end{vmatrix} \tag{2}$$

and < > means averaging over the time. For a pulse the degree of polarisation appears as a single value. The angle between the two perpendicular components of the electric field E_x, E_y is defined as

$$\varphi(\tau) = \tan^{-1} \left| \frac{E_y(\tau)}{E_x(\tau)} \right| \tag{3}$$

and at each moment of time it is equal to:

$$\begin{cases} 0 & \text{x – pol.} \\ \pi/4 & |E_x| = |E_y| \\ \pi/2 & \text{y – pol.} \end{cases} \tag{4}$$

It has to be stressed that this is a 1-D analysis (uniform approximation) that does not take into account inherent inhomogeneity of the X-ray laser medium. Thus, the model describes correctly behaviour of the medium and amplified radiation within an infinitesimally narrow (in the radial direction) layer of the medium with a quasi-constant density and irradiated uniformly. Randomisation method causes that the polarisation direction of the amplified radiation obtained from each code run changes accidently but the relation between its perpendicular components is reproduced from run to run.

The model enables also detailed analysis of the saturation effect and its consequences for the energy extraction and behaviour of the basic features of the amplified radiation.

3 Results and Discussion

This analysis provides a new perspective on the amplified spontaneous emission and coherent amplification of ultra-short pulses in a high-gain medium where competition between the strong random emission and the deterministic seed coherently interacting with the medium play crucial role. This strong competition of both processes causes that the output signal as a whole shows at some propagation length (corresponding roughly to the saturation onset) loss in its superb features due to coupling between the branches of Λ-type transition in the strong-field regime. Polarisation and beam coherence are the main deteriorated parameters. The polarisation loss is limited but noticeable. The typical pulse shape and polarization of the amplified injected pulse without including level degeneration are shown in **Fig.2**;

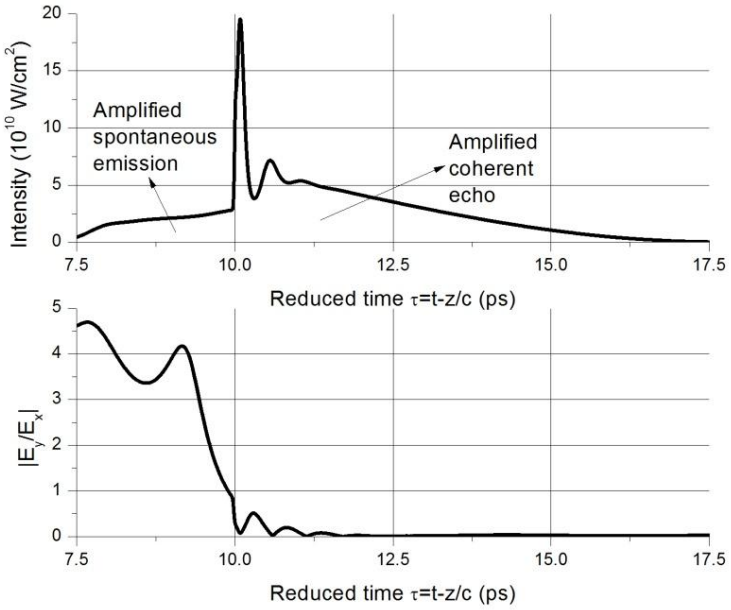

Fig2. Pulse shape and polarization of the pulse after propagating in a 5-mm-long gain medium. τ=10 ps is the moment of the seeding pulse arrival counted from the gain beginning. The seed is initially polarized along the x-axis.

the amplified pulse consists of the coherent part, induced by the fully coherent seed of precisely defined linear polarization and the amplified spontaneous emission (ASE) of inherently random nature [5,7].

Compared to the conventional XRLs, a significant enhancement of the peak intensity and pulse shortening were obtained due to the coherent interaction. However, the amplified spontaneous emission, when allowed to grow too strongly, combined with the level degeneracy limited inheritance of the superb polarization and coherence of the seed. The effect is presented in **Fig.3** where the atomic coherence represented by $max|\rho_{1,-1}|$ – the amplitude of the oscillating density matrix, is shown as a function of the medium length. As maximizing the coherent component is crucial, practicable solutions in the form of precise control of the amplifier parameters or multi-seed are proposed. This is very important in designing the multi-stage amplifiers considered as the next step in evolution of the plasma-based XRLs.

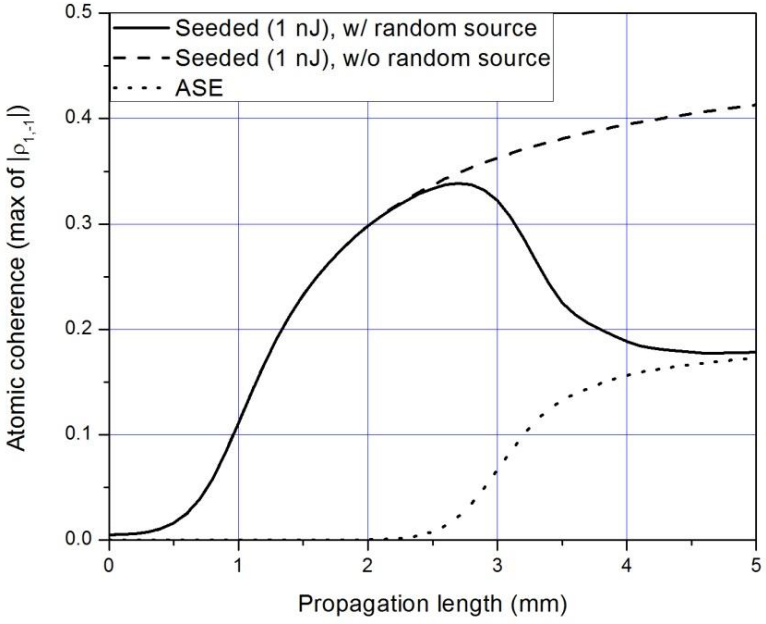

Fig.3. The maximum of the non-diagonal density matrix element vs. the propagation length in the active medium. Three possible variants of the amplification are compared.

The formulated model enabled to derive the output pulse shape in the case of photon-flux build-up from noise as well as the energetic (extraction) characteristics in both seeding and ASE cases. The results of simulations on

the photon-flux build up from noise are valid for the non-seeded XRLs. Starting with the temporal gain profile obtained from hydrodynamics simulations with the EHYBRID code [8] and assuming randomised two circular components (RHC and LHC) of the noise we have got the output pulse profile shown in **Fig.4**. The plot includes an inset showing the temporal gain

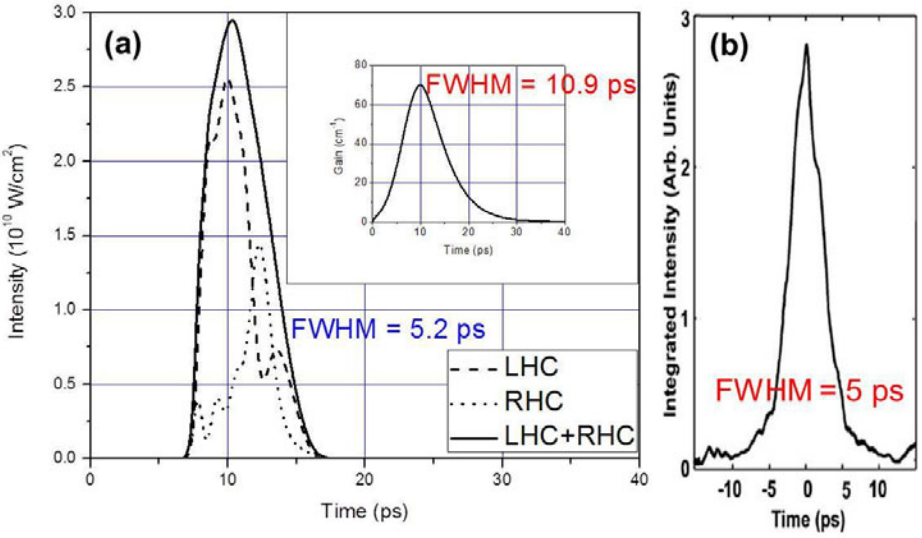

Fig.4. Modelled output XRL pulse and its components of the different polarisation state. The inset includes the temporal profile of the gain coefficient. The plot b) shows the experimental reference for the modelled waveform obtained by Colorado State University group [9].

profile of the gain coefficient as well as temporal shapes of both differently polarised components. Comparing the modelling result with the experimental reference shown in Fig.4 proves the validity of our model. The output pulse is in excellent accordance with the measured profiles.

The energy extraction is shown in **Fig.5** where the intensity for different options of the composition seed+ASE is drawn as a function of the medium length. One can see that the amplification rate of the ASE is bigger than that of the seeded signal. However, the seeded signal is much stronger than the spontaneous noise and starting from a higher level the seed amplification gives higher output energy. The ASE signal tends asymptotically to the same level with the increase in the medium length. Additionally, it appears that the presence of the random signal during seeding is hardly changing the

amplification characteristics observed in a deep saturation. However, one should remember that this deep saturation level is not useful due to deterioration of both polarisation and coherence in the way described earlier.

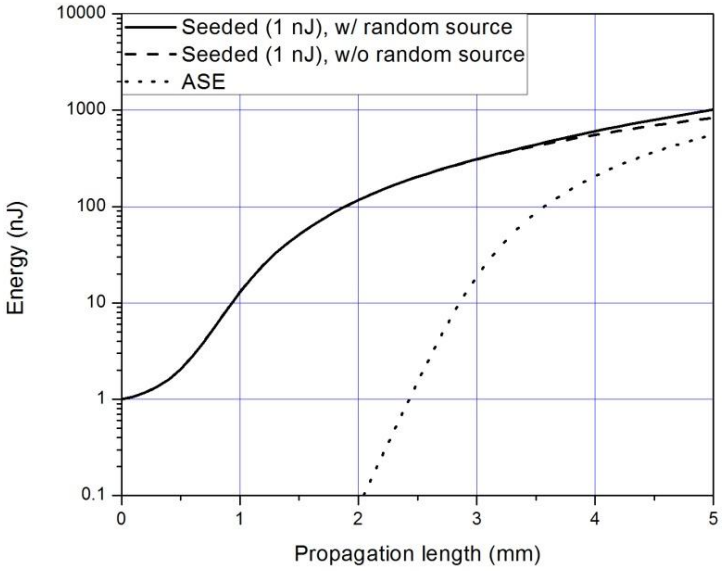

Fig.5. Energy of the amplified radiation as a function of the amplifying medium length. The plots for different combinations of ASE and the seeded signal are shown.

4 Relation to the Experimental Conditions

A real plasma being the amplifying medium is even under idealised conditions inhomogeneous. First the existing density gradients cause the corresponding gradients of the refraction index and the radiation will move within different quasi-homogeneous layers of the medium with a different phase velocities υ_{ph}. This effect can be markedly limited by well relaxed density gradients in optimised target irradiation conditions. More influential can be a very high level of the gain coefficient. Its regular spatial profile is generally also distorted by the density inhomogeneity. However, for the qualitative analysis we can assume a perfect Gaussian profile with a peak small-signal gain coefficient g_0 of 80 cm^{-1}. It is known from [10] that the group velocity can be expressed by the formula $v_{gr} = c/(1+\beta)$, where $\beta = cg_0\sqrt{ln2}/\left(\pi^{3/2}\Delta\nu_D\right)$. Using the peak value of $g_0 = 80\ cm^{-1}$ we get for the group velocity a value of *0.735c* while for a gain coefficient of *50 cm^{-1}*

this value is equal to *0.816c*. For a typical medium length of *4 mm* the arising time difference between two pulse parts propagating through the areas of the quoted gain coefficients will be about *1.8 ps*. Moreover, a typical seeding beam is also rather of Gaussian than rectangular intensity distribution. As a consequence, different intensities in different parts of the seeding beam will have different dynamics (Rabi oscillations will be switched-on at different moments) leading to an effective smearing of the ideal profile with the oscillations shown in **Fig.2**. This can be deduced from the analytical solutions of the two-level atom problem where the oscillating part of the intensity resulting from coherent interaction between the medium and a laser beam of rectangular-shape is given by [11]

$$I(t) \sim J_0[\wp E(t - t_0)/\hbar] \qquad (5)$$

while for the Gaussian profile it is given by

$$S(t) \sim \frac{\wp E}{\hbar(t - t_0)} J_1\left[\frac{\wp E}{\hbar}(t - t_0)\right] \qquad (6)$$

where $S = 2\pi \int_0^\infty I(R)\, RdR$ is the signal after integration and averaging over the entire beam profile. As both Bessel functions are very similar and only the shift in phase by $\pi/2$ occurs while the oscillation frequencies stay within 2%. From this it is clear that the spike of optical nutation will be softened by elongation in addition to the weakening by the factor equal to $t\text{-}t_0$. In the quoted formulae $\wp$ is the transition dipole moment E is the electric field amplitude and t_0 is the beginning of the time counting (switch-on moment).

5 Summary

The model of the amplification process including temporal gain dependence, and level degeneracy has been formulated in terms of the Maxwell-Bloch equations to analyse dynamics of seeded X-ray lasers. The model confirmed its validity by reproducing many features of the X-ray lasers working in the regime of the amplified spontaneous emission. This model has been used to analyse coherent amplification process in the case of seeding a very high-gain amplifying medium with an ultra-short high harmonic signal. It was found that the coupling between the σ - transitions in the saturation regime diminishes the superb quality of the seeding signal. It can be a serious

problem for the staging technique. The energy extraction is determined more by a high level of the seeding signal than by the amplified spontaneous noise.

The model confirmed its validity by a reasonable reproduction of the output pulse shape and length in the case of pure ASE process. As far as the amplification of seed is concerned the problem is more complex as the medium inhomogeneity has serious influence on the temporal characteristic of the output pulse causing smearing of the profile obtained in simulations under uniform approximation. Moreover, the important differences between the coherent and incoherent (described by the rate equations) amplification processes occur on a relatively low level and it might be difficult to reveal it in an experiment with a streak camera having as a rule very limited dynamic range.

6 Acknowledgments

This work was supported by the Ministry of Knowledge and Economy of Korea through the Ultrashort Quantum Beam Facility Program and also partially by the Basic Science Research Program through the National Research Foundation of Korea (NRF) funded by the Ministry of Education, Science and Technology (No. R15-2008-006-03001-0).

References

1. Ackermann W. *et al*., *Nature. Photon.* 1, 336 (2007)
2. Costello J., "From tiny seeds to coherent beams", *Nature. Photon*. 2, 67 (2008)
3. Wang Y. *et al.*,"Phase-coherent, injection-seeded, table-top soft-X-ray lasaers at 18.9 nm and 13.9 nm", *Nature Photon.,* 2,94 (2008)
4. Larroche O., Ros D., Klisnick A., Sureau A., Möller C., and Guennou H., "Maxwell-Bloch modeling of x-ray-laser-signal buildup in single- and double-pass configurations", *Phys. Rev. A* 62, 043815 (2000).
5. Kim C. M., Janulewicz K. A., Kim H. T., and Lee J., "Amplification of a high-order harmonic pulse in an active medium of a plasma-based x-ray laser", *Phys. Rev. A* 80, 053811 (2009).
6. Born M. and Wolf E., *Principles of Optics*, Cambridge University Press, Cambridge, 2005, 7th ed.
7. Kim C. M., Lee J., and Janulewicz K. A., "Coherent Amplification of an Ultrashort Pulse in a High- and Swept-Gain Medium with Level Degeneracy", *Phys. Rev. Lett*. 104, 053901 (2010)
8. G.J. Pert, "Optimizing the performance of nickel-like collisionally pumped x-ray lasers ", *Phys. Rev. A* 73, 033809 (2006)

9. Larotonda M.A. *et al.*, "Pulse duration measurements of grazing-incidence-pumped hifgh repetition rate Ni-like Ag and Cd transient soft x-ray lasers", *Opt. Lett.* 31, 3043 (2006)
10. Casperson L. W., Yariv A., „Pulse Propagation in a High-Gain Medium", *Phys. Rev. Lett.* 26, 293 (1971)
11. Shoemaker R. L.: *Coherent Transient Infrared Spectroscopy*, p.251 in: *Laser and Coherence Spectroscopy*, Steinfeld J.I. ed., Plenum Press, New York, 1978

Laser driven parametric amplification in the xuv and soft-x-ray spectral range

J. Seres[1], E. Seres[1], D. Hochhaus[2,3,4], B. Ecker[2,5,6], D. Zimmer[2,6,7], V. Bagnoud[2], T. Kuehl[2,6], C. Spielmann[1]

[1] Friedrich-Schiller-University Jena, Max-Wien-Platz 1, 07743 Jena, Germany
[2] GSI Helmholtz Centre for Heavy Ion Research, Planckstr. 1, 64291 Darmstadt, Germany
[3] ExtreMe Matter Institute, Planckstr. 1, 64291 Darmstadt, Germany
[4] Johann-Wolfgang von Goethe University, 60325 Frankfurt, Germany
[5] Helmholtz Institut Jena, Helmholtzweg 4, 07743 Jena, Germany
[6] Johannes Gutenberg University Mainz, Saarstr. 21, 55099 Mainz, Germany
[7] Université Paris-Sud 11, 91405 Orsay, France

Abstract. We present the first experimental realization of a new x-ray laser scheme based on strong-field parametric amplification of high-order harmonic radiation. With a simple semi-classical model, we can identify the most important experimental parameters, the spectral range and the small signal gain in gases. Using a single amplifier stage a small signal gain of 8000 has been obtained in Argon for the spectral range of 40-50 eV, using 350 fs, 7 mJ pulses at 1.05 μm. In Helium, we observed a small signal gain of 280 around 300 eV using 6 fs, 1.5 mJ pulses at 800 nm.

1 Introduction

The development of pulsed laser opened a new area in time-resolved laser spectroscopy. Ultra-short pulses can generated with lasers and the wavelength range can be extended with nonlinear frequency conversion techniques. For studying nuclear, inner atomic, or structural dynamic the extension of the wavelength range into the x-ray regime is necessary while preserving the ultra-short pulse duration[1] or narrow line-width[2].

Several schemes for plasma based x-ray lasers (XRL) have been realized in the last few years. The necessary pump energy has been reduced and currently Ni-like x-ray lasers can be operated with sub-J pumping[3] at higher repetition rates[4]. The other route is the nonlinear frequency conversion of laser pulses into the XUV range by high harmonic generation (HHG), which can produce sub-femtosecond XUV or x-ray pulses in a laser like beam[5] with compact and high repetition rate laser systems. The major drawback of HHG is its rather low conversion efficiency.

J. Lee et al. (eds.), *X-Ray Lasers 2010,* Springer Proceedings in Physics 136,
DOI 10.1007/978-94-007-1186-0_14,

Adding a HHG based seed source to a plasma XRL[6,7] is a promising way towards spatially and temporally coherent x-ray source with higher pulse energy. Unfortunately the spectral range is limited to a few possible atomic transitions. This restriction can be circumvented, if the upper or the upper and lower laser levels are virtual states, namely with parametric or Raman amplifiers. Raman amplifiers in the x-ray regime has been proposed[8], but never realized. Here we present the first experimental realization of the parametric amplification of HHG radiation. The amplification process has been explained by semi-classical model and we have demonstrated parametric amplification in Ar and He in the range of 50 eV and 300 eV, respectively.

2 Theory for strong-field parametric amplification of x-rays

To describe x-ray parametric amplification (XPA), we use a simple semi-classical description[9] similar as for HHG[10]. An intense laser field tunneling ionizes atom. The freed electrons are accelerated in the field and return to the parent ion, where they can recombine or scatter inelastically (Fig. 1a). The excess energy of the electron is emitted in a photon and the emission process can be spontaneous (HHG) or stimulated (XPA).

For weak x-ray fields the process can be described by a pair of coupled differential equations: the evolution of the x-ray field is described by a wave equation and the motion of the electron is represented by an equation for a forced parametric oscillator:

$$\partial_x^2 E(t,x) - \frac{1}{c^2}\partial_t^2 E(t,x) = \mu_0 \partial_t J_{y,coh}(t,x) \tag{1}$$

$$\partial_t^2 y + \Gamma \partial_t y + \omega_0^2 (1 + h(t)) y = -\frac{e}{m} E_q \tag{2}$$

Coupling is provided by the coherent electron current originating from the ionized electrons during every half optical cycle[11] and is proportional to the electron density n_e in the coherent current. The small displacement x_0 as shown in Fig 1a is caused by the magnetic field accelerating the electron into the direction of the laser propagation. At the instant of collision, the resonance frequency depends on x_0 and the time dependent detuning h(t) can be expressed as a Taylor series of the Coulomb potential. The damping term (Γ) considers the radiation loss and its magnitude can be estimated from our experimental data. The source term E_q is the incident x-ray field generated by conventional HHG. If the frequency of the x-ray field (q-th harmonics of the laser frequency ω_1) is tuned to near resonance $\omega_0=\omega_q=q\omega_1$, we can expect parametric amplification.

From the imaginary part of the complex propagation constant we can derive a formula for the small signal gain

$$g_{q,max} \approx \frac{-e^2 n_0}{2\varepsilon_0 mc\omega_q \Gamma}\left(Z\gamma_{q0} + 2\partial_t Z\right) \tag{3}$$

where $n_e(t)=n_0 Z(t)$, n_0 is the atomic density of the amplifying medium and Z is the ionization rate during one half optical cycle, which can be calculated by known theories[12].

For a comparison with our experiments, we express the gain as the product of atomic density and the emission cross section (σ_e). Fig. 1b shows the calculated σ_e for Ar in the parameter range accessible with our laser systems. The maximum gain can be expected in a spectral range of 40-50 eV for a laser intensity of 1.0-1.5x10^{14} W/cm². In this range also XUV radiation can be efficiently generated via HHG in Ar with at the same laser intensity to seed for the parametric amplification.

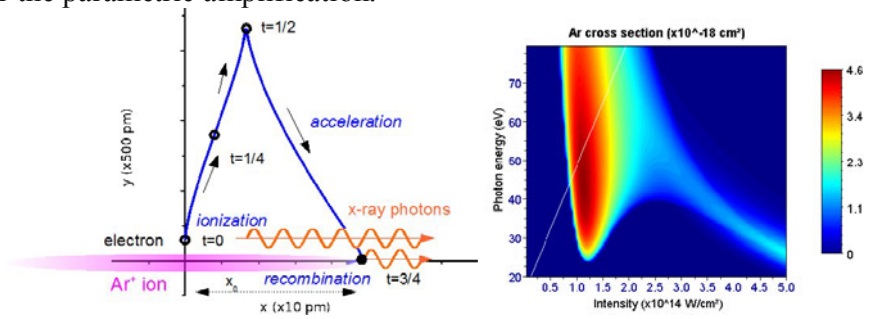

Fig. 1. (a) Schematic of strong-field parametric x-ray amplification. There are ionization and electron acceleration by the strong laser field and the stimulated emission happens at the instant of recombination. The electron moves mainly along the y-direction of the polarization of the laser field. However due to the magnetic field the electron is also slightly accelerated into the forward direction. Note the different scaling on the two axes. (b) Calculated stimulated emission cross-section for Argon in the parameter range accessible with our laser system.

3 Parametric amplification in the XUV

XPA in the XUV range has been demonstrated with the femtosecond front-end of the PHELIX laser system[13] delivering 350-fs-long, 7 mJ pulses at 1054 nm and a repetition rate of 10 Hz, resulting in a peak intensity of 2x10^{14} W/cm². The 2-mm-long gas cell was placed at about 7 mm before the focus and the generated x-ray radiation was measured with a home-made spectrograph. The laser light and the lower order harmonics were efficiently suppressed by two 200-nm-thick Al foils.

We varied the backing gas pressure of the gas cell in a range from 0.05 to 1.6 bar allowing easy control of the gain. We can clearly distinguish between two different regimes (Fig. 2a and 2b): For photon energies above 52 eV, the x-ray yield scales with a sine squared function, which can be well explained

by HHG with a finite coherence length. In the range of 45-52 eV, the measured radiation increases exponentially with the pressure (Fig. 2c). Above 0.8 bar saturation sets in. An exponential increase is a clear indication of the predicted stimulated emission and parametric amplification. The measured small signal gain was in the order of 1100 at this intensity and up to 8000 was reached at 1.2×10^{14} W/cm². Both the range and the magnitude of the observed amplification are in reasonable agreement with the predictions of our model. A further proof of the amplification is a narrowing of the harmonic lines. In Fig. 2d and 2e we show the spectral evolution of the width of 41st harmonic as a function of the pressure. The observed line narrowing is in good agreement with the predictions, and cannot explained by phase matched HHG.

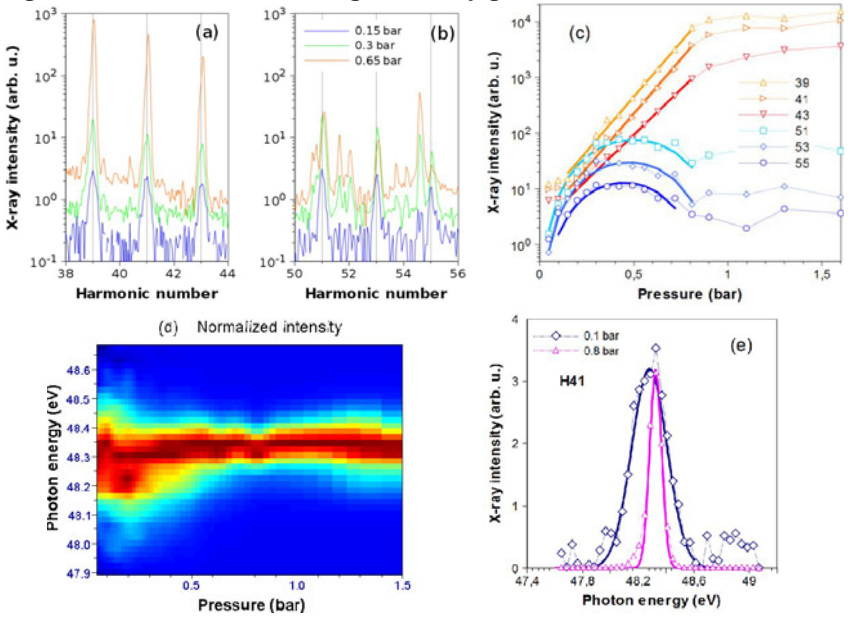

Fig. 2. Evolution of the XUV signal as a function of the pressure around the (a) 41st and (b) 51st they follow the expectation. (c) The measured exponential and sin² increase are clear indications for XPA and HHG, respectively. (d) The spectral narrowing of the emitted radiation of the 41st harmonic is a further indication of the finite gain bandwidth. (e) The spectrum for low and optimal pressure together with the Gaussian fits.

4 Parametric amplification in the soft-x-ray regime

The theory also predicts suitable gain for shorter wavelengths where the HHG conversion efficiency is much lower. In this spectral range, the XPA requires a very high ionization rate within one half optical cycle, which can be only realized by using few cycle driver laser pulses with high intensity. For parametric amplification at around 300 eV, we must reach a peak intensity of about 1 to 3×10^{16} W/cm² in He. For the experiment we used a two-stage

Ti:sapphire based amplifier running at 1 kHz[14]. The output pulses were compressed in a filament to 6-fs with a final energy of 1.5 mJ. With a spherical mirror we obtained an intensity of $2x10^{16}$ W/cm² in a 1-mm-long gas jet. The measured spectra as a function of the backing pressure are shown in Fig. 3a without correcting for the effect of the additional thin metal foils (200 nm Ti + 100 nm Al). Again we can identify two different regimes: Outside the range of approx. 250 to 350 eV the x-ray yield follows the scaling of HHG with a finite coherence length. In the range from 270-330 eV, the x-ray intensity increases exponentially with the pressure up to a maximum pressure of 45 mbar before saturation sets in. The only explanation for the observed scaling is parametric x-ray amplification. In this range we can estimate the maximum small signal gain to about 280 at 45 mbar and 320 eV.

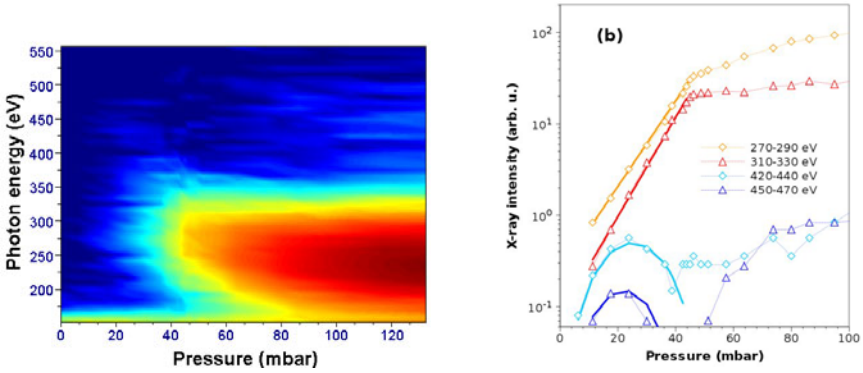

Fig. 3. (a) Soft-x-ray spectra were measured as a function of the pressure using 6 fs, 1.5 mJ laser pulses. (b) An exponential increase at around 300 eV implies stimulated emission by parametric amplification. At around 450 eV, the signal evolution is well explained by HHG with a finite phase-matching length.

5 Summary and perspectives

We demonstrated parametric amplification of high order harmonics in noble gases. The measured small signal gain and the spectral ranges are in good agreement with our model calculations. We reached a maximum gain of about 8000 at 50 eV and 280 at 300 eV, respectively. With the current setup it is possible to amplify the HHG pulses in Argon from a few pJ to few nJ. A further amplification is restricted by the velocity mismatch between the pump laser and the x-ray pulses. This can be solved by using two or more amplifier stages, with a separation chosen to fulfill the conditions for group velocity matching between the electron and x-ray pulse.

With the demonstrated parametric x-ray amplification it will be possible to realize a new class of bright x-ray sources for spectroscopy combining the advantages of conventional x-ray lasers and HHG. The excellent beam quality and ultra-short pulse duration of HHG pulses will be then available at much

higher pulse energy. So it will be feasible to realize for the first time brilliant sources in the few hundred eV range with a repetition rate of 1 kHz.

6 Acknowledgments

This study has been sponsored by the Austrian Science Fund grant F016 P03, DFG grant TR18 P10 and SE 1911/1-1, TKM grants B154-09030 and B 715-08008. The authors acknowledge access to the laser system provided by the Institute of Photonics, Vienna University of Technology and the PHELIX laser team at GSI Darmstadt.

References

1. Seres, E. & Spielmann, C. Time-resolved optical pump X-ray absorption probe spectroscopy in the range up to 1 keV with 20 fs resolution. J. Mod. Opt. 55, 2643-2651 (2008)
2. Gumberidze, A. et al. X-ray spectroscopy of highly-charged heavy ions at FAIR. NIM B 267, 248–250 (2009)
3. Zimmer, D. et al. An improved double-pulse non-normal incidence pumping geometry for transient collisionally excited soft X-ray lasers, Opt. Exp. 16, 10398-10403 (2008)
4. Heinbuch, S., Grisham, M., Martz, D. & Rocca, J.J. Demonstration of a desk-top size high repetition rate soft x-ray laser, Opt. Exp. 13, 4050-4055 (2005)
5. Winterfeldt, C., Spielmann, C. & Gerber, G. Control of High Harmonic generation. Rev. Mod. Phys. 80, 117 (2008)
6. Zeitoun, Ph. et al. A high-intensity highly coherent soft X-ray femtosecond laser seeded by a high harmonic beam. Nature 431, 426-429 (2004)
7. Wang, Y. et al. Phase-coherent, injection-seeded, table-top soft-X-ray lasers at 18.9 nm and 13.9 nm. Nature Phot. 2, 94-98 (2008)
8. Hudis, E., Shkolnikov, P. L., & Kaplan, A. E. X-ray stimulated Raman scattering in Li and He. Appl. Phys. Lett. 64, 818-820 (1994)
9. Seres J. et al. Laser driven amplification of soft-x-rays by parametric stimulated emission in neutral gases, Nature Phys. (2010) online, DOI: 10.1038/nphys1638
10. Lewenstein, M. et al. Theory of high-harmonic generation by low-frequency laser field. Phys. Rev. A 49, 2117-2132 (1994)
11. Hopf, F. A., Meystre, P., Scully, M. O. & Louisell W. H. Classical theory of a free-electron laser, Opt. Comm. 18, 413-416 (1976)
12. Bauer, D. & Mulser, P. Exact field ionization rates in the barrier-suppression regime from numerical time-dependent Schrodinger-equation calculations. Phys. Rev. A 59, 569-577 (1999)
13. Kuehl, T. et al. Optimization of the non-normal incidence, transient pumped plasma X-ray laser for laser spectroscopy and plasma diagnostics at the facility for antiproton and ion research (FAIR). Laser and Part. Beams 25, 93-97 (2007)
14. Seres, J. et al. Sub-10-fs, terawatt-scale Ti:sapphire laser system. Opt. Lett. 28, 1832-1834 (2003)

Characterization of a seeded optical-field ionized collisional soft x-ray laser

S. Sebban[1], F. Tissandier[1], J.P. Goddet[1], O. Guilbaud[2], J. Gautier[1], Ph. Zeitoun[1], C. Valentin[1], G. Lambert[1], G Maynard[2], B.Robillard[2], A. Klisnick[4], T. Mocek[3] and J. Nejdl[3]

[1] Laboratoire d'Optique Appliquée, chemin de la hunière, 91128 Palaiseau
[2] LPGP, Université Paris-Sud, 91405 Orsay, France
[3] Institute of Physics, Department of X-Ray Lasers, Prague, Czech Republic
[4] ISMO, Bât. 350, CNRS, Université Paris-Sud 11, Orsay, France

Abstract. We report spatial and spectral characterization an optical-field-ionized high-order harmonic-seeded soft-x-ray laser showing. We show that it can be controlled between a regular Gaussian shape and a Bessel profile exhibiting several rings via the IR laser pump intensity. The temporal coherence and spectral linewidths of both the seeded and unseeded soft-x-ray lasers were experimentally measured using a varying path difference interferometer. It showed that the high-order harmonic is subject to a strong spectral narrowing during its propagation in the plasma amplifier without rebroadening at saturation.

1 Introduction

Soft-x-ray lasers (SXRL) have been proven to be tools of great interest for practical applications. Due to the short soft-x-ray gain lifetime and the absence of high reflectivity optics in the soft-x-ray region, most of the SXRLs operating at saturation result from the single pass amplification of spontaneous emission (ASE). An ASE soft-x-ray radiation is characterized by an inhomogeneous beam profile, a low spatial coherence and strong wavefront distortions that seriously limit the use of SXRLs for applications requiring intense and coherent soft-x-ray photon flux in sub-micrometric spot-sizes. The seeding of a soft-x-ray plasma amplifier with a high order harmonic (HOH) [1] is an essential technique allowing dramatics enhancements of the spatial properties of the soft-x-ray beam. Recent studies have shown that the amplifier acts as a spatial filter for the harmonic and that the output beam exhibits a Gaussian spatial profile [2] [3] [4] with a very low divergence, a full spatial coherence and a diffraction-limited wavefront [5].

J. Lee et al. (eds.), *X-Ray Lasers 2010,* Springer Proceedings in Physics 136,
DOI 10.1007/978-94-007-1186-0_15,

2 Experimental set up

The experiment was performed using a setup very similar to that described in [1]. We used a 10 Hz repetition rate, multi-terawatt Ti: Sapphire infrared (IR) laser system providing two independent 35fs-pulses at a central wavelength of 815 nm. The main pulse is used to generate the plasma amplifier. It is focused by a 1 m focal length spherical mirror at an intensity up to 10^{18} W/cm^2 into a low-density 6 mm-long Krypton-filled cell at a pressure of 30 mbar. Its polarization is made circular by a quarter wave plate to allow proper heating of the free electrons of the plasma that will pump the population inversion on the $3d^9 4d \rightarrow 3d^9 4p$ transition at 32.8nm of the Kr^{8+} ions [6]. A second pulse, containing about up to 20 mJ, is focused by a 1.5 m focal length lens into a gas cell filled with 30 mbar of Argon to generate the HOH beam. The HOH source is imaged by a grazing incidence toroidal mirror into the SXRL plasma amplifier with a magnification of 1.5. The far-field profile of the SXRL beam was recorded using a CCD camera located 4 m after the plasma amplifier.

We have investigated the spectral bandwidth of the SXRL. Due to its extremely narrow linewidth, the spectral profile cannot be resolved by the transmission grating spectrometer. We used instead an interferometric method based on the measurement of the temporal coherence of the SXRL pulse. The SXRL beam is directed toward a variable path difference interferometer based on the Fresnel mirrors system. The beam is splitted by reflecting on two slightly tilted grazing-incidence mirrors (open book configuration). The path difference between the two resulting beamlets is created by vertically translating one of the two mirrors with respect to the other one. To ensure that varying the path difference will not result in a loss of spatial coherence, the mirrors mentioned hereinbefore are actually dihedrons.

3 Far-field characterization

Using a system composed by a half-wave plate and a polarization beam splitter (Glan-Taylor prism) before the compression of the main IR pulse, we have been able to generate the plasma amplifier with different pump intensity ranging from 2.5×10^{17} W/cm^2 to 10^{18} W/cm^2. For intensities lower than 2.5×10^{17} W/cm^2, no soft-x-ray amplification was observed. Within this range of waveplate angles (30 degrees), no spectral modulations or any other effect on the pulse shape has been observed [7].

The results of these measurements are presented in Figure 1. In a) is given the far-field profile of the SXRL beam in standard operation conditions, i.e. at a pump IR intensity of 10^{18} W/cm2, along with the integrated radial profile. It is composed by a very collimated central spot and several rings. The central spot has a very low divergence of 0.45mrad (first zero) and the first ring is located at a divergence of 0.65mrad with a maximum intensity counting for 10% of the beam peak intensity, which clearly excludes the possibility of an Airy beam profile. As the pump intensity decreases (b), c) and d)), the rings tend to fade and the divergence of the central spot increases to more than 1 mrad at a pump intensity of 2.5×10^{17} W/cm^2. It has already be shown that the effects of the plasma on the harmonic can be easily understood by modeling the plasma by a circular aperture. The spatial profile of the amplified harmonic then results of spatial filtering by a pinhole in the plasma plane. This simple model does not properly describe the presence of several intense rings around the central spot, but can extended by considering spatial filtering by an annular aperture in the plasma plane. For a pump intensity of 10^{18} W/cm^2, this annular aperture would have an outer diameter of 50 μm and an inner diameter of 25 μm. This aperture would change into a circular hole of 35μm diameter for a pump intensity of 2.5×10^{17} W/cm^2. A far-field intensity profile such as that obtained with a pump intensity of 10^{18} W/cm^2 cannot be perfectly fitted by the square a first-kind 0th-order Bessel function (where the first ring peak intensity is 16% of the maximum intensity), but still makes a good approximation of a true Bessel beam.

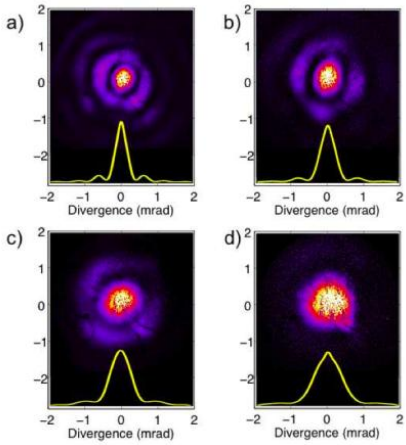

FIG. 1: Measured far-field profiles of the seeded soft-xray laser pumped by an intensity of a) 10^{18} W/cm^2 b) 6×10^{17} W/cm^2 c) 4×10^{17} W/cm^2 d) 2.5×10^{17} W/cm^2 , and the corresponding integrated radial profiles

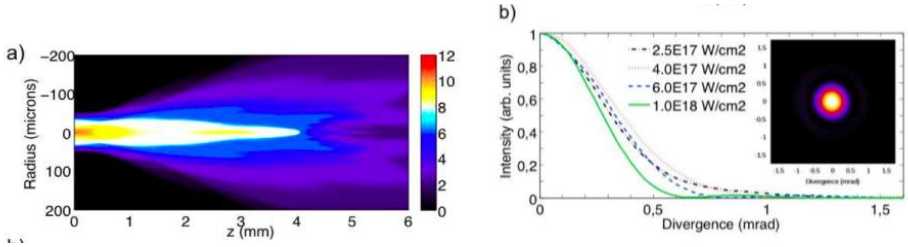

FIG. 2: a) Calculated ionization map of the plasma at a Krypton pressure of 30 mbar and a pump intensity of 10^{18} W/cm^2. The laser pulse propagates from left to right and the lasing Kr^{8+} ions are in the white-colored region. b) Integrated farfield radial profiles of the harmonic amplified by a plasma generated using different pump intensities. Insert: Calculated far-field intensity profile of the output beam resulting from amplification by a plasma generated with 10^{18} W/cm2.

On Figure 2 is given in a) the 2D map of the simulated average ionization state of a Krypton plasma after the passage of a pump pulse focused at an intensity of 10^{18} W/cm^2 in 6 mm-long cell. The white-colored region indicates the lasing Kr^{8+} ions. The pump pulse was assumed to have a Gaussian shape in the focal plane with a 38µm-diameter ($1/e^2$), which is what me measured in our experiment. The laser pulse propagates from left to right, and the focal plane position was set to 1.5 mm into the long cell. As it can be seen, the strong pump intensity allows ionization of Krypton to stages greater than 8 near the axis, thus causing a loss of gain in that region, and giving elements of justification of filtering by an annular aperture. What is also noticeable is the shape of the Kr^{8+} region. Its diameter varies along the axis, indicating a gain region that may have very smooth edges. In b) are plotted the integrated

intensity profiles of the soft-x-ray output of the plasma generated by different pump intensities, and the calculated image of the far-field profile of the seeded SXRL pumped by 10^{18} W/cm^2. This profile does not exhibit rings like the experimentally measured profile, and the reasons are probably to be found in the smoothness of the gain zone edges. The near-field profile of the beam was also studied as part of the simulation, and showed an overall annular shape of smooth outer radius around 20μm (and 10μm inner radius) directly linked to the shape of the amplifying plasma and explaining the attenuation of the secondary rings. Though a far-field Bessel profile does not arise from the simulations, there is nonetheless a good agreement between the calculated and measured divergence of the soft-xray beam. Its variations with the pump intensity are also supported by the simulations: it goes from 0.6 mrad (larger than experimentally measured) for a pump intensity of 10^{18} W/cm^2 to 1 mrad for 2.5×10^{17} W/cm^2.

To further investigate the role of the pump pulse and the resulting plasma profile, we made the same calculations at a lower plasma density. This was mainly motivated by the fact that the Krypton pressure we measured was the backing pressure of our regulator system, and we had no accurate way to measure it in the gas cell. Some losses may occur within gas transportation from the regulator to the actual cell. The result of the 2D propagation code are presented in Figure 3.

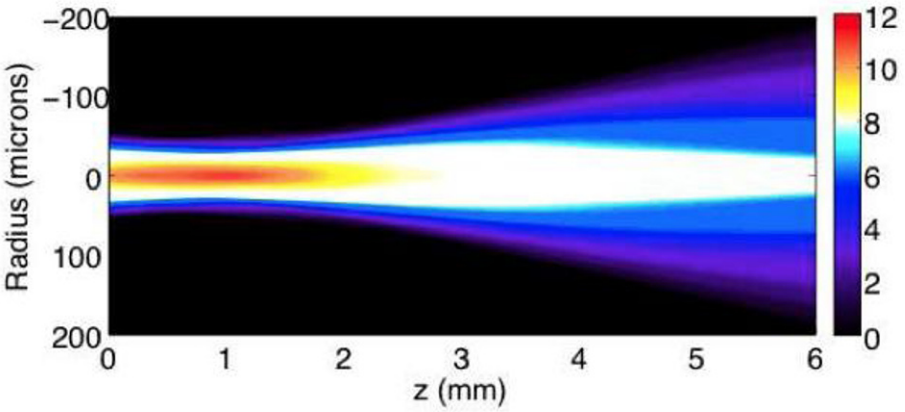

FIG. 3: Calculated ionization map of the plasma at a Krypton pressure of 5mbar and a pump intensity of a) 10^{18} W/cm^2.

Figure 3 represents the 2D ionization map of the 5mbar-Krypton pressure plasma created with a pump intensity of 10^{18} W/cm^2, to be compared with Figure 2- a). As expected the pump laser is much less refracted, allowing a longer Kr^{8+} plasma to be created. The transverse dimension of this plasma

are comparable with that obtained with 30 mbar of Krypton, but, contrary to that case, does not vary much along the axis. This can be seen as a plasma with sharper edges. Another important difference is that in the case of a low 5mbar pressure, overionization is stronger and the area where it occurs is longer due to less refraction. Its transverse dimension also accounts for a greater part of the Kr^{8+} zone.

In Figure 4 are given, as in Figure 1, the calculated far field profiles of the soft-x-ray output of the plasma generated by different pump intensities. These look much like experimentally measured profiles, with a tighter central spot and an intense ring. While not strongly different from the profile obtained with 30 mbar of Krypton, the near-field profile in this case had slightly more energy in the intense ring-shaped area and this area had a sharper outer edge, as expected from the plasma shape. This may be the cause of the differences observed on the far-field profiles. The expected variations with the pump intensities are also confirmed, the intensity of the secondary rings decreasing with the pump intensities. Note that the profile obtained with a low 2.5×10^{17} W/cm^2 does not seem to follow the general tendency, which is due to the fact that there is much less gain at such a low density, causing a very weak amplification and filtering of the harmonic seed.

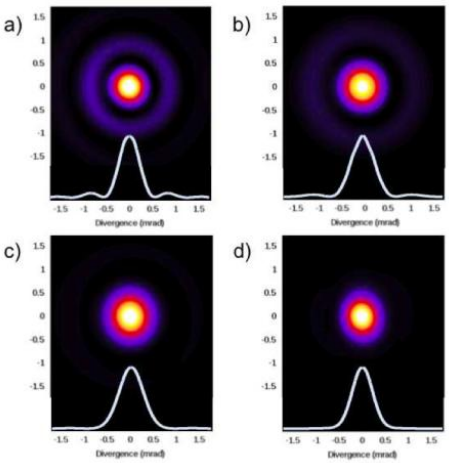

FIG. 4: Calculated far-field profiles of the harmonic-seeded 5mbar-Krypton pressure amplifier pumped by an intensity of a) 10^{18} W/cm^2 b) 6×10^{17} W/cm^2 c) 4×10^{17} W/cm^2 d) 2.5×10^{17} W/cm^2, and the corresponding integrated radial profiles

4 Spectral characterization

The experimental measurement of fringe visibility variations with the path difference is presented for both the ASE and the seeded SXRL in Figure 5.

Each point results from an average over several shots and the error bar stands for the standard deviation. This experimental data was accurately fitted by the product of a Gaussian function and a decreasing exponential function (dotted lines). The coherence time τc of the pulses, defined by the time at which the visibility is decreased by a factor 1 , is not the same for the the two radiations. It was inferred as 5.1±0.2 ps for the seeded SXRL pulse and a slightly larger 5.5±0.3 ps for the ASE SXRL pulse. According to the Wiener-Khinchin theorem, the fringe visibility is the Fourier transform of the spectral density of the source.

The spectral profiles have been calculated from the fitted visibility evolutions, and correspond to spectral Voigt profiles with a full width half-maximum (FWHM) of $\Delta\nu = 89 \pm 6$ GHz, or $\Delta\lambda = 3.2 \pm 0.2$ mÅ, for the seeded SXRL and $\Delta\nu = 75\pm8$GHz, or $\Delta\lambda = 2.7\pm0.3$ Å for the ASE. The spectral linewidth is determined by homogeneous (natural) broadening and inhomogeneous broadening. The processes responsible for homogeneous broadening include radiative decay and electron collision-induced transitions. They lead to a Lorentzian line profile with a FWHM of $\Delta\lambda H = 5$mÅ in the case of the 32.8nm Ni-like laser. This value has been calculated with a collisional-radiative model taking into account the non-Maxwellian electron energy distribution [9]. Stark effect has been introduced as a source of inhomogeneous spectral broadening, but numerical simulations have shown that it can be neglected [10]. The process responsible for inhomogeneous broadening is actually the Doppler effect due to the hot ions. Ions are indeed rapidly heated after ionization by the laser field. Theoretical works [11] have shown that strong correlations exist in OFI plasmas, which rapidly relax into an uncorrelated form with a characteristic time equal to the plasma period (a few hundreds of fs). The ion equilibrium temperature in the case of our low-density OFI plasma is Ti = 6 eV, thus leading to a Gaussian line profile with a FWHM of $\Delta\lambda D = 7$ mÅ for the 32.8 nm Ni-like laser. This very low homogeneous and inhomogeneous broadening values explain the strong monochromaticity of this type of SXRL ($\Delta\lambda/\lambda \sim 10^{-5}$). Using a variable-length gas cell, we have been able to measure the temporal coherence of the seeded SXRL for different plasma lengths of 1mm, 2mm, 4mm and 6mm. The signal level of the ASE at such short plasma lengths was too weak to allow proper measurements. The calculated spectral density from the fitted visibility evolutions are plotted in Figure 6 for each plasma length. The spectrum right before amplification, i.e. the unamplified harmonic spectrum, is not represented here. We were nevertheless able to measure it using the soft x-ray spectrometer. Its FWHM was evaluated to be $\Delta\lambda HHG = 100 \pm 20$ Å, which is much larger than after even only 1 mm of amplification ($\Delta\lambda = 4.8 \pm 0.5$ m). The harmonic is subject to a spectral narrowing which is strong, due to the very low bandwidth of the laser transition, and fast, i.e. after a very short

distance of propagation in the amplifier, due to the very high gain values (60 cm^{-1}). Indeed we can guess that much of that spectral narrowing occurs during the first hundreds of microns, or even less, of propagation since from 1mm of propagation to 6mm the spectral linewidth stay in the same order of magnitude. We did not observe any saturation re-broadening, which suggests that homogeneous broadening contribution is predominant at saturation. The Voigt line profile also seems to tend more to a Lorentzian profile at longer propagation lengths in the plasma.

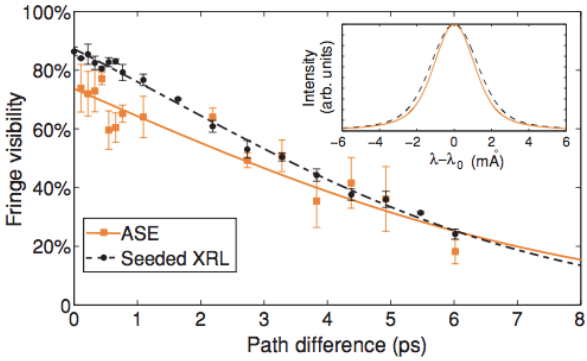

FIG. 5. (Color online) Visibility of the interference fringes as a function of the time difference for the ASE and seeded SXRL. The lines represent the result of fitting by a relevant function (defined in text). Inset: Reconstructed spectra from Fourier transforms of the fit functions.

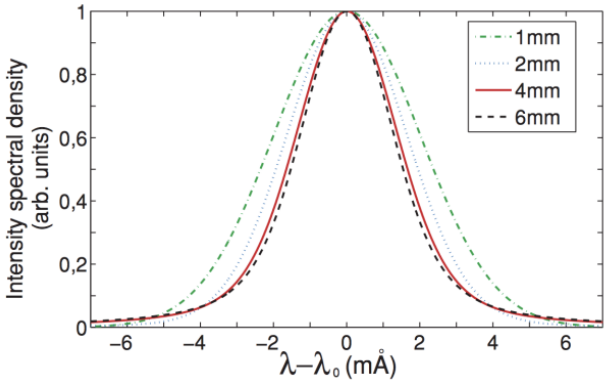

FIG. 6. (Color online) Spectral density of the SXRL laser line at different propagation lengths in the plasma.

By seeding of a laser created plasma amplifier we have demonstrated that it is possible to generate an intense soft x-ray beam having all the fundamental properties of common visible/IR/UV lasers. In a near future we anticipate a significant improvement of this concept, e.g. by using waveguiding technique to increase the length of the amplifier and thus boost up the SXRL output energy by at least one order of magnitude.

References

[1] P. Zeitoun, G. Faivre, S. Sebban, T. Mocek, A. Hallou, M. Fajardo, D. Aubert, P. Balcou, F. Burgy, D. Douillet, S. Kazamias, G. de Lach`eze-Murel, T. Lefrou, S. le Pape, P. Merc`ere, H. Merdji, A.-S. Morlens, J.-P. Rousseau, and C. Valentin, Nature 431 (2004).
[2] Y. Wang, E. Granados, M. A. Larotonda, M. Berrill, B. M. Luther, D. Patel, C. S. Menoni, and J. J. Rocca, Phys. Rev. Lett. 97, 123901 (2006).
[3] J.-P. Goddet, S. Sebban, A.-S. Morlens, J. Gautier, J. P. Rousseau, F. Burgy, P. Zeitoun, C. Valentin, C. Hauri, G. Maynard, A. Boudaa, J. P. Caumes, H. Merdji, T. Mocek, M. Kozlova, and K. Jakubczak, Opt. Lett. 32, 1498 (2007).
[4] Y. Wang, E. Granados, F. Pedaci, D. Alessi, D. Luther, B. Berrill, and J. J. Rocca, Nat. Photon. 2, 94 (2008).
[5] J.-P. Goddet, S. Sebban, J. Gautier, P. Zeitoun, C. Valentin, F. Tissandier, T. Marchenko, G. Lambert, M. Ribiere, D. Douillet, T. Lefrou, G. Iaquaniello, F. Burgy, G. Maynard, B. Cros, B. Robillard, T. Mocek, J. Nejdl, M. Kozlova, and K. Jakubczak, Opt. Lett. 34, 2438 (2009).
[6] S. Sebban, T. Mocek, D. Ros, L. Upcraft, P. Balcou, R. Haroutunian, G. Grillon, B. Rus, A. Klisnick, A. Carillon, G. Jamelot, C. Valentin, A. Rousse, J. P. Rousseau, L. Notebaert, M. Pittman, and D. Hulin, Phys. Rev. Lett. 89, 253901 (2002).
[7] Y. Zhao, Y. Jia, J. Yang, and X. Zhu, Opt. Eng. 46, 044301 (2007).
[8] B. Cros, T. Mocek, I. Bettaibi, G. Vieux, M. Farinet, J. Dubau, S. Sebban, and G. Maynard, Phys. Rev. A 73, 033801 (2006).
[9] B. Talin, A. Calisti, L. Godbert, R. Stamm, R. W. Lee, and L. Klein, Phys. Rev. A 51, 1918 (1995).
[10] G. Maynard, F. Lambert, N. Andreev, B. Robillar, A. Boudaa, J. Clerouin, B. Cros, A. Lenglet, T. Mocek, and S. Sebban, Contrib. Plasma Phys. 47, 352 (2007).
[11] J. A. Koch, B. J. MacGowan, L. B. Da Silva, D. L. Matthews, J. H. Underwood, P. J. Batson, R. W. Lee, R. A. London, and S. Mrowka, Phys. Rev. A 50, 1877 (1994).

Optimization of soft x-ray amplifiers by tailoring plasma hydrodynamic

E. Oliva[1,2]*, Ph. Zeitoun[2], P. Velarde[1], M. Fajardo[3], K. Cassou[4], D. Ros[4], D. Portillo[1] and S. Sebban[2]

[1] Instituto de Fusión Nuclear, Universidad Politécnica de Madrid, Madrid, Spain.
[2] Laboratoire d´Optique Apliquée, ENSTA ParisTech, École Polytechnique, CNRS, Palaiseau, France.
[3] Instituto de Plasmas e Fusão Nuclear, Instituto Superior Técnico, Lisbon, Portugal.
[4] Laboratoire de Physique des Gaz et des Plasmas, CNRS, Université Paris Sud XI, Orsay, France
*Email address: eduardo@din.upm.es

Abstract. Plasma-based soft x-ray lasers have the potentiality to generate high-energy, highly coherent, short pulse beam. Thanks to their high density, plasmas created by interaction of intense laser with solid target should store the highest amount of energy among every plasma amplifiers. However, to date output energy from solid amplifiers remains as low as 60 nJ [1]. For 30 μm micrometer focal line width, we demonstrated with the 2D hydrodynamic code with radiation transport in AMR ARWEN [2] that deleterious hydrodynamic effects, as the lateral expansion and thermal conduction, reduce the amplification surface and the gain coefficient. Thus, carefully tailoring the plasma shape is crucial for extracting energy stored in the plasma. With 1 mm wide plasma, energy as high as 20 μJ in sub-ps pulse is achievable [3]. With such tailored plasma, pumping efficiency has been increased by nearly a factor of 10 as compared to former plasma amplifiers.

1 Introduction

Seeded Soft X-Ray Lasers are a promising source of coherent soft X-ray radiation. Seeding has already been demonstrated in gaseous amplifiers [4] and solid amplifiers [1]. Nevertheless, the extracted energy and pulse duration need to be improved so as to match the experimental needs [5].

Computational modelling is a powerful tool to comprehend the physics of plasma amplifiers and to optimize these sources of soft X-ray radiation. In this paper we present the simulations done with the 2D hydrodynamic code with radiation transport in Adaptive Mesh Refinement ARWEN [2]. This code was

J. Lee et al. (eds.), *X-Ray Lasers 2010,* Springer Proceedings in Physics 136,
DOI 10.1007/978-94-007-1186-0_16,

originally developed for Inertial Confinement Fusion studies but in the last years it has been upgraded to be used in other fields of plasma physics as laboratory astrophysics and plasma-based soft X-ray lasers. With this code we have studied the impact on the gain of several bidimensional hydrodynamic effects, as lateral expansion of the plasma or inhomogeneities induced by target´s roughness or defects in the laser beam.

The layout of the paper is as follows: in section 2 we will briefly explain the impact of the inhomogeneities on the plasma. In section 3 we will study the evolution of the plasma and its lateral expansion, explaining some experimental results. Finally, conclusions will be given in section 4.

2 Impact of the inhomogeneities

In this section we will briefly explain the impact of target's roughness and defects in the laser beam. As we will concentrate on *Transient Collisional Excitation* (TCE) scheme, we will study separately the effects of the long laser pulse and the short laser pulse.

2.1 Impact of target defects

Target's defects have been simulated as a sinusoidal modulation of the target surface. This perturbation is immediately transferred to the plasma, creating in the early instants of the evolution a complicated pattern of velocities and electron density. These induced gradients of density modify the laser absorption profile. The short pulse, charged of heating the electron fluid to create the population inversion, deposes its energy in a very irregular way and thus, the gain profile presents strong variations (Fig 1. left), which will be imprinted in the amplified beam.

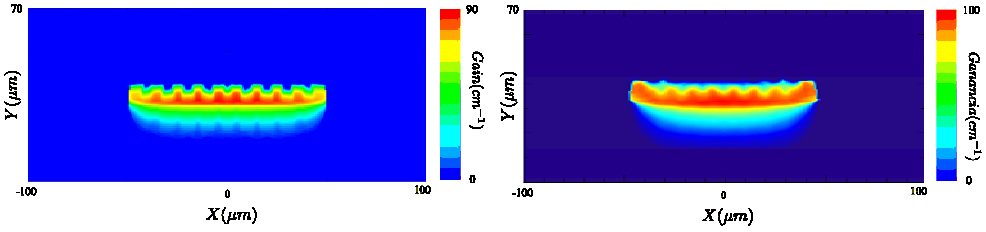

Fig. 1 Gain profile of a plasma created from an inhomogeneous target. The laser comes from the bottom to the top and the plasma expands inversely. Simulations have been done without (left) and using (right) a ray-tracing subroutine.

As the inhomogeneous profile of electron density could induce refraction effects on the laser, a ray-tracing subroutine was introduced in the ARWEN

code to take into account refraction effects in the energy deposition. In Fig. 1 right, the gain profile is shown. It can be seen that the profile is still inhomogeneous, imprinting the amplified beam, but, if we compare both figures, we see several differences in the gain extension (being the gain region greater in the ray-tracing case) and in the homogeneity (the ray-tracing case has a more homogeneous gain). The energy deposition profile without using the ray-tracing subroutine is strongly peaked near the critical density region, where electron density is highly perturbed. Refraction tends to homogenise the energy deposited in regions far from the critical density, arriving less energy to the most perturbed zone and thus having a larger and more homogeneous gain zone.

2.2 Impact of laser beam defects

TCE amplifiers are created using a long laser pulse (several hundredths of picoseconds), which ionises the plasma, and a short pulse (less than several picoseconds) charged of heating the electrons and create the population inversion. Due to the completely different duration of the pulses (the driving force of the perturbation) the impact on the plasma varies whether the perturbed pulse is the short or the long one. These defects on the laser have been modelled as a sinusoidal perturbation of variable amplitude.

The short pulse, acting during several picoseconds or less than a picosecond, only affects the electron temperature, perturbing it. The effect of this perturbation in the plasma evolution and the gain region appears to be negligible, as the perturbation has no time to develop and diffusive process destroy it rapidly, homogenising the plasma.

If the perturbed pulse is the long one, the plasma behaves differently than the previous case. Now, the pulse lasts several hundredths of picoseconds and the perturbation has enough time to develop, affecting not only the temperature, but also the density profile. Nevertheless, the perturbation induced in the plasma is much smaller than the one induced by target roughness. In addition to this, reducing the amplitude of the perturbation is only worth for big perturbations which imprints strongly the plasma. Smaller ones, inducts perturbations in density and temperature which are dumped by diffusive and hydrodynamic effects so it is not necessary to have a perfect beam.

3. Impact of the transverse focal linewidth.

In previous works [6], the laser focal linewidth profile has been optimized, demonstrating that using a supergaussian profile augments the gain region and the values of small signal gain. In this section we will study the impact of

using different widths of this profile (i.e. different widths of the plasma in x direction, as shown in fig. 2) in the small signal gain.

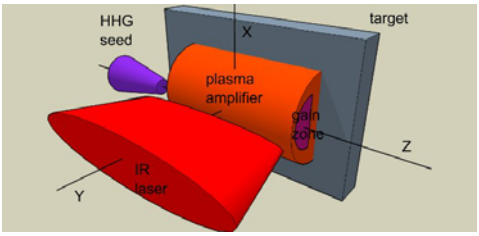

Fig 2. Scheme of the simulations done. The simulation window lies on the x-y plane.

Simulations consists on three laser pulses (a prepulse which creates the pre-plasma, a main pulse of 100 ps which heats it and a short pulse of 0.5 ps to create the population inversion) of widths (i.e. *Full Width at Half Maximum* FWHM of the supergaussian profile) ranging between 20 μm and 1 mm. For the sake of comparison, intensities have constant values of $1.25\times 10^{11} W/cm^2$, $1.25\times 10^{12} W/cm^2$ and $1.16\times 10^{15} W/cm^2$ in all simulations. Three relevant cases (30 μm, 150 μm and 1 mm) will be highlighted to explain the evolution of the amplifiers.

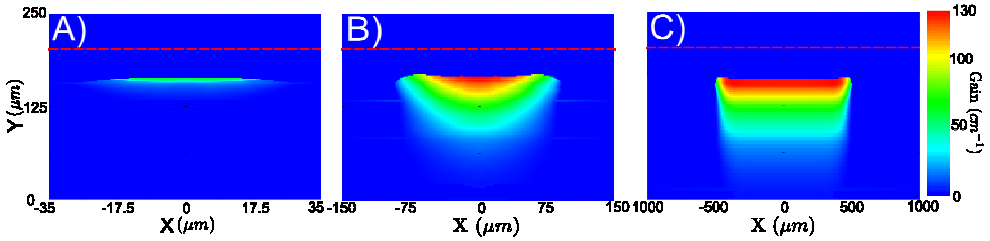

Fig 3. Gain regions for the 30 μm (A), 150 μm (B) and 1 mm (C) cases.

In fig 3. the gain regions of the three highlighted cases are shown. Several differences are observed. The maximum small signal gain in the 30 μm case has a value of only 60 cm^{-1}, half of the maximum value of 126 cm^{-1} of the 150 μm and 1 mm cases. In addition to this, a much more striking correlation is shown in fig 3: increasing the width of the laser in x direction augments the extension of the gain region in y direction. The third difference observed in the figure will be the key to explain this effect. In the 30 μm case, the horizontal extension of the gain region is significantly wider than the laser focal width (the width is one and a third greater, approximately 40 μm). This effect is observed also, but softer, in the 150 μm case and some curvature in the gain zone appears. Finally, in the 1 mm case the gain region has the same

x extension as the linewidth and no curvature appears, having a rectangular shaped gain region. The conclusion is that not only the expansion of the plasma in the y direction plays a role in its evolution, but also the expansion in the x direction, widening the gain region in the narrowest plasmas where these 2D effects are strong, whereas in the widest plasmas, this expansion is negligible compared to the width of the plasma and its behaviour is 1D.

The lateral expansion (a hydrodynamical process) is linked with the gain creation (an atomic process) by electron density. In fig. 4 vertical cuts of electron density at the centre of the plasma are shown.

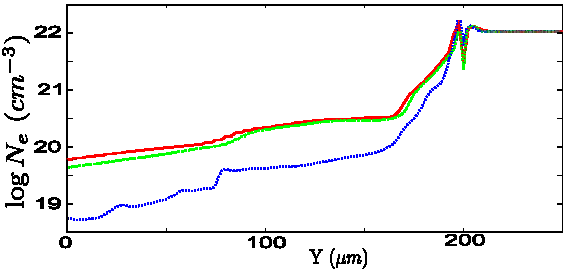

Fig 4. Electron density in Y direction at the centre of the plasma (x = 0 μm) for the 30 μm case (blue), 150 μm case (green) and 1 mm case (red). The plasma expands from left to right.

In this figure it is shown that the 30 μm case has a reduced gain region with small values of small signal gain due to the low value of electron density. On the other hand, the 150 μm and 1 mm cases present similar values of gain at the central region of the plasma as electron density has similar profiles.

The explanation is as follows: in the 30 μm case, the lateral expansion of the plasma arrives at its centre in the early stages of the evolution, diminishing the density of the central region. When the pumping pulse arrives, it can be only efficiently absorbed in a small region near the critical density. In addition to this, the low values of electron density cannot trigger a population inversion via collisional excitation with the exception of the region above mentioned. The gain region is thus small and presents lower values of small signal gain coefficient. In the 150 μm case, the lateral expansion has not arrived yet to the centre of the plasma when gain is produced, having a 1D behaviour. Nevertheless, the expanded region is not negligible and the gain region presents some curvature, typical of 2D effects. Finally, in the 1 mm case, the region affected by the lateral expansion when gain is produced is completely negligible, presenting a huge, rectangular 1D gain zone.

A conservative computation of the extracted energy can be estimated as ten times the saturation energy, given by our code [3]. The extracted energy for the 30 μm case is about 60 nJ, in very good accord with experiments [1]. This

energy rises up to 3.1 μJ for the 150 μm case and up to 22 μJ for the 1 mm case.

Conclusions

Simulations of soft x-ray plasma based amplifiers done with the 2D hydrocode ARWEN have been presented in this paper. The impact of different defects on target´s surface and laser profile have been studied, concluding that the defects on the target are the only ones that have a strong impact on the gain region. In addition to this, and continuing previous works [6], plasmas created with different focal widths have been simulated. It has been found that 2D hydrodynamic effects have a strong impact in the evolution of the plasma, destroying gain in the narrowest plasmas. On the other hand, these effects are negligible in wider plasmas (1 mm width), presenting a homogeneous and bigger gain zone, much more better for amplification purposes.

Acknowledgments

The authors would like to thank the financial support provided by the ELI-PP212105 project and the Spanish Ministerio de Educación y Ciencia within the program ENE2009-09837/FTN.

References

1. Wang, Y. *et al* : 'Phase coherent, injection-seeded, table-top soft-X-ray lasers at 18.9 nm and 13.9 nm'*, Nature Photonics*, 2, 2008
2. Ogando, F. and Velarde, P. : 'Development of a radiation transport fluid dynamic code under AMR scheme', *J. Quant. Spectrosc. Radiat. Transf*, 71, 2001
3. Oliva, E. *et al*: 'Optimization of soft x-ray amplifier by tailoring plasma hydrodynamics' *Opt. Lett.,* 34 (17), 2640-2642, 2009
4. Zeitoun, Ph. *et al:* 'A high intensity highly coherent soft x-ray femtosecond laser seeded by a high harmonic beam', *Nature,* 431, 2004
5. Neutze, R. *et al:* 'Potential for biomolecular imaging with femtosecond x-ray pulses', *Nature,* 406, 2000
6. Cassou, K. *et al:* 'Transverse spatial improvement of a transiently pumped soft x-ray amplifier', *Phys. Rev. A*, 74, 2006

Measurement of the Temporal Coherence of a Seeded GRIP Transient Mo Soft X-ray Laser

L.M. Meng[1]*, D. Alessi[2], O. Guilbaud[3], Y. Wang[2], S. Domingue[2], B. Luther[2], J.J. Rocca[2] and A. Klisnick[1]

[1] ISMO, Bât. 350, CNRS, Université Paris-Sud 11, Orsay, France
[2] NSF Center for EUV Science and Technology Colorado State University, Fort Collins, United States
[3] LPGP, Bât. 210, CNRS, Université Paris-Sud 11, Orsay, France
*Email address:limin.meng@u-psud.fr

Abstract. We present the results of an experiment performed at the NSF Center for EUV Science and Technology (Colorado State University) in which a wavefront division interferometer was used to investigate the temporal coherence of seeded and unseeded GRIP transient Mo X-ray laser emitting at 18.9 nm. We find that the coherence time of the X-ray laser pulse is of the order of 1.7 ps in the ASE mode and slightly smaller when the amplifier is seeded with a high-order harmonic pulse. The spectral linewidth is subject to a gain narrowing when increasing the length of the plasma amplifier. Such behaviour is consistent with another experiment performed with the OFI seeded Ni-like krypton X-ray laser, using the same interferometer.

1 Introduction

High-intensity, high-resolution x-ray lasers are needed in special area, such as lithography, high resolution imaging, phase coherent probing of atomic and molecular system, and structural biology [1-3]. Meanwhile, the spatial and temporal coherence of these sources are important for these applications. Recent works report some exciting results for high quality x-ray laser [4-7]. The most interesting progress is the injection-seeded x-ray laser [8-10]. More attention is paid for the temporal coherence and the spectral width of these kinds of laser.

In this report, we will discuss the spectral properties of a nickel-like molybdenum x-ray laser [11]. We will first briefly recall the conditions of the experiment, and we will discuss the analysis of the experimental data, in particular with respect to the existence of fluctuations of the fringe visibility. The variation of fringe visibility as a function of the path difference between the interfering X-ray laser beams was used to infer the temporal coherence length [12]. We will show how the spectral profile of the laser line was deduced from the experimental measurement of the temporal coherence [13].

J. Lee et al. (eds.), *X-Ray Lasers 2010,* Springer Proceedings in Physics 136,
DOI 10.1007/978-94-007-1186-0_17,

2 Experimental method

Our experiment was carried out at the NSF Center for EUV Science and Technology, Colorado state University at Colorada, USA during July 2009. We have studied the beam of a Ni-like Mo X-ray laser operating at 18.9 nm, seeded with a high-order harmonic pulse, as described in [11].

The X-ray laser beam was first monitored with a far-field imaging system. The uniformity, divergence, and deflection angle of the beam were characterized. Figure 1 shows examples of the images obtained in either the seeded mode (Figure 2-a), or the ASE mode (Figure 2-b). In the seeded mode the bright spot at the center of the image is the harmonics beam amplified in the X-ray laser plasma amplifier, which appears over the ASE background. In the ASE mode the beam exhibits speckle patterns, due to the limited spatial coherence and high temporal coherence [13].

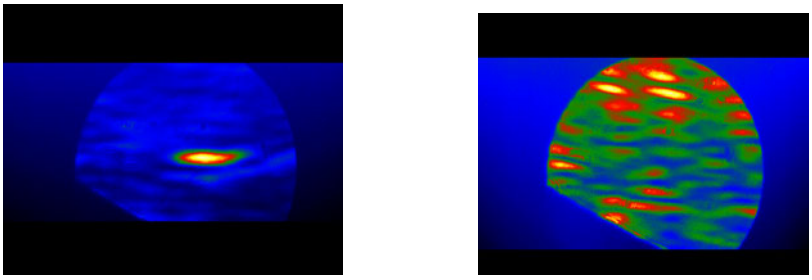

(a) (b)

Fig. 1. Far field images of the X-ray laser beam. (a) seeded mode; (b) ASE mode

The X-ray laser beam was finally directed toward a wavefront division interferometer specifically designed for measuring the temporal coherence. This diagnostic was placed at a distance of 3.3 m from the source, in order to ensure a significant transverse coherence length of the beam at the entrance of the interferometer. A complete description of this interferometer can be found in [12]. The incident beam, with a 6° grazing incidence angle, is reflected on a pair of dihedrons into two separated half-beams that slightly converge towards each other and overlap. The fringes that are formed in the overlapping region are detected onto an XUV CCD (1024x1024pixels, 16 bits, Andor Technology) which is placed at 150 cm from the dihedrons, and tilted at angle of 35° from the incident beam in order to increase the apparent fringe spacing. The path difference between the two interfering half-beams was varied from shot to shot by accurately translating one of the two dihedrons vertically.

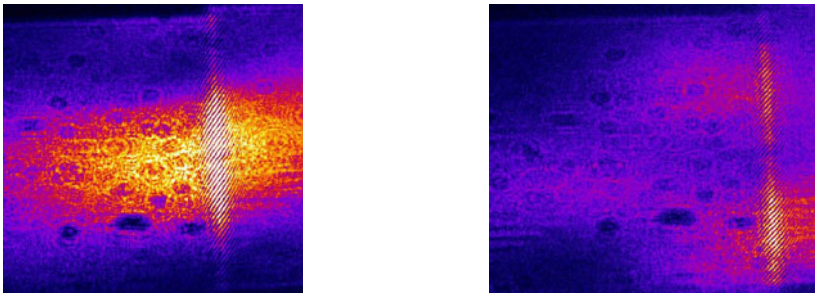

(a) **(b)**

Fig. 2. Interferograms of the X-ray laser beam. (a)seeded mode; (b) ASE mode. Plasma length is 4 mm

Figure 2 presents typical interferograms, obtained with the path difference set to zero, and a plasma length of 4 mm, in either the seeded mode (Fig. 2-a) or the ASE mode (Fig. 2-b). The interferograms obtained for increasing values of the path difference were processed numerically in the zone containing the interference fringes by applying a background subtraction, followed by a numerical Fourier transform processing performed with a small sliding window. This yields the map of local fringe visibility V (x,y) over the interference field.

The fringe visibility was found to vary spatially across the interference field. This spatial variation was attributed mainly to the non-uniformities in the X-ray laser beam. This eventually leads to unbalanced time-averaged intensities I_1 and I_2 in the two interfering half-beams and to a local reduction of the fringe visibility. In the analysis of our interfometric data we have thus made the two following important assumptions: (i) the spatial and longitudinal coherence of the X-ray laser beam is constant within the small part (1.56 mrad × 0.20mrad) sampled by the dihedron pair; (ii) the relevant value of fringe visibility in each interferogram is the maximum one, which is the best estimation of the visibility that would be produced by equal intensity interfering beams ($I_1 = I_2$).

3 Results

Figure 3 shows the graphs of the measured fringe visibility V (l) as a function of the path difference l, for 3 different lengths of the plasma amplifier in which the harmonic pulse is injected: 2 mm (Fig. 3a), 3 mm (Fig. 3b), 4 mm (Fig. 3c). Figure 3d shows the same measurement performed with a 4 mm plasma length in Amplification of Spontaneous Emission (ASE) mode.

Several shots were performed for each value of the path difference, at fixed irradiation conditions. The black squares plotted in Figure 3 are the shot-averaged value of the measured visibilities for each path difference l. The

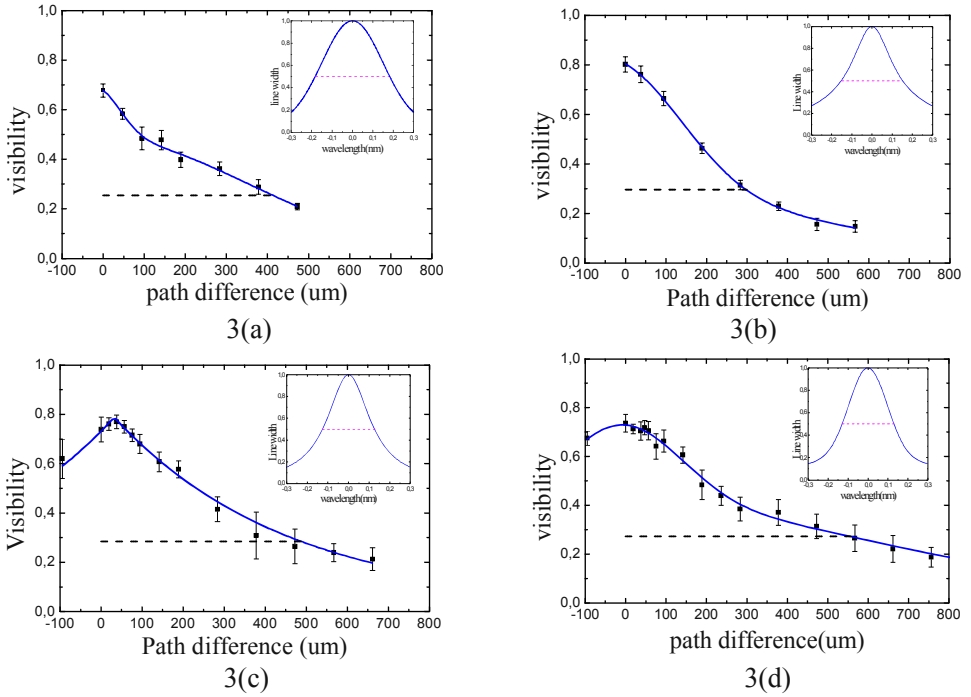

Fig. 3. fringe visibility V (*l*) as a function of the path difference *l*. (a) plasma length 2mm, seeded mode; (b) plasma length 3mm, seeded mode; (c) plasma length 4mm, seeded mode; (d) plasma length 4mm, ASE mode;

vertical error bars give the visibility standard deviation. One can see that the fringe visibility for $l = 0$ μm is smaller than 1. That is because the seeded and ASE laser source are partially spatially coherent. On the other hand the visibility is strongly reduced while increasing the path difference from 0 mm to 0.5 mm (or 104λ). The experimental data were then fitted with a linear superposition of Gaussian and exponentially decreasing functions. The corresponding curves, which gave the best fitting coefficients, are shown by the solid lines in Figures 3.

The values of the longitudinal coherence length L_C, which is defined as the path difference that decreases the maximal visibility by a factor 1/e, are summarized in Table 1 for the 4 cases shown in Figures 3.

Using the Wiener-Khintchine theorem [14], which states that the spectral line profile ρ(ν) is proportional to Fourier transform of the longitudinal degree of coherence γ(τ), the spectral width and the profile of the laser line can be deduced from visibility curves. The resulting spectral profiles are shown in the insert of the Figures 3 separately. The values of the FWHM linewidth Δν and Δλ are summarized in Table 1.

Table 1. Summary of the measured coherence length and spectral width

Mode	Plasma length L(mm)	Coherent length L_c(μm)	Coherence time τ_c(ps)	Line width Δλ(mÅ)	Spectral width Δν(10^{11}Hz)
seeded	2	440±50	1.46±0.16	3.7±0.3	3.11±0.25
seeded	3	298±28	0.99±0.09	3.1±0.5	2.60±0.42
seeded	4	424±65	1.41±0.22	2.7±0.4	2.27±0.34
ASE	4	495±70	1.65±0.24	2.6±0.4	2.18±0.34

One can see that the measured linewidth is of the order of 3 mÅ. For the 4mm plasma, it is slightly smaller in the ASE mode than in the seeded mode. On the other hand the spectral linewidth is observed to decrease slightly, when increasing the length of the plasma amplifier from 2 mm to 4 mm. Such behaviour is consistent with gain narrowing and was already observed in another experiment performed with the OFI seeded X-ray laser [7,15].

By comparing in Table 1 the values of the spectral width to the corresponding values of the coherence length it can be noted that these two quantities do not exhibit the same behaviour. In particular, since we have mentioned that the linewidth is inversely proportional to the coherence length, we should observe that the coherence length increases when the length of the plasma gets larger. This apparent contradiction is due to the fact that different shapes of the visibility curves (hence spectral profiles) were used in each case (see Figures 3), yielding different numerical factors relating Lc to Δν(FWHM). In order to overcome this problem we have used another definition for these two quantities, based on quadratic means, which are less sensitive to the choice of the fitting function used to describe the experimental data. This analysis of the data is described in another paper in these Proceedings [16].

4 Conclusion

We have measured the linewidth of the 18.9 nm Mo X-ray laser, in both the seeded mode and the ASE mode, and for several lengths of the plasma amplifier. We have observed gain narrowing of the line width when increasing the amplifier length in seeded mode. For seeded and ASE mode in same plasma length, the line width in seeded mode is a little larger than in the ASE mode, and the maximum visibility is a little larger. These conclusions are consistent with a previous experiment performed in LOA with an OFI-pumped X-ray [7, 15].

Acknowledgements:

The experiment performed at LOA was partially funded through the EC 7th Framework Programme (LASERLAB Europe, contract No. 228334). The experiment performed at CSU was funded by the NSF Center for EUV Science and Technology under NSF Award Number EEC-0310717, and by the Chemical Sciences, Geosciences and Biosciences Division, Office of Basic Energy Sciences, Office of Science, U.S. Department of Energy.

References

1. Trebes, J.E et al.: 'Demonstration of X-ray Holography with an X-ray Laser', *Science*, 238, 517-519, 1987
2. London, R.A et al.: 'Wavelength choice for soft x-ray laser holography of biological samples', *Applied Optics,* 28, 3397-3404, 1989
3. Suckewer, S.: 'Soft X-Ray Lasers and Their Applications', *Science,* 247, 1553-1557, 1990
4. Wang, Y et al. : 'Demonstration of high-repetition-rate tabletop soft-X-ray lasers with saturated output at wavelengths down to 13.9 nm and gain down to 10.9 nm', *Phys. Rev. A*, 72, 053807(1-7), 2005
5. Rocca, J. J et al.: 'Saturated 13.2 nm high-repetition-rate laser in nickel-like cadmium', *Opt. Lett.,* 30, 2581–2583, 2005
6. Ackermann, W et al.: 'Operation of a free-electron laser from the extreme ultraviolet to the water window', *Nature Photon*., 1, 336–342, 2007
7. Tissandier, F et al.: 'Observation of spectral gain narrowing in a high-order harmonic seeded soft-x-ray amplifier', *Phys. Rev. A.,* 81, 063833, 2010
8. Zhang, X et al.: 'Highly coherent light at 13 nm generated by use of quasi-phase-matched highharmonic generation', *Opt. Lett.,* 29, 1357–1359, 2004
9. Zeitoun, P et al.: 'A high-intensity highly coherent soft X-ray femtosecond laser seeded by a high harmonic beam', *Nature,* 431, 426–429, 2004
10. Wang, Y et al.: 'High-brightness injection-seeded soft-X-ray-laser amplifier using a solid target', *Phys.Rev. Lett.,* 97, 123901, 2006
11. Wang, Y et al.: 'Phase-coherent, injection-seeded, table-top soft-X-ray lasers at 18.9 nm and 13.9 nm', *Nature Photonics,* 2, 94(1-5), 2008
12. Klisnick, A et al.: 'Experimental study of the temporal coherence and spectral profile of the 13.9nm transient X-ray laser', *J.Q.S.R.T.,* 99, 370-380, 2006
13. Guilbaud, O et al.: 'Longitudinal coherence and spectral profile of a nickel-like silver transient soft X-ray laser', *Eur. Phys. J. D.,* 40, 125-132, 2006
14. Born, M et al.: *Principles of optics.* Cambridge University Press; 2002
15. Guilbaud, O et al.: 'Fourier-limited seeded soft x-ray laser pulse', *Opt. Lett.,* 35, 1326, 2010
16. Klisnick, A et al.: 'Temporal coherence and spectral width of seeded and ASE XUV lasers', *this Conference*

Part 4: Sources Based on Relativistic Interaction

Extreme Field Limits in the Ultra-Relativistic Interaction of Electromagnetic Waves with Plasmas

S. V. Bulanov[1], T. Zh. Esirkepov[1], M. Kando[1], J. K. Koga[1], A. S. Pirozhkov[1], Y. Kato[2], S. S. Bulanov[3], G. Korn[4] and A. G. Zhidkov[5]

[1]Advanced Photon Research Center, JAEA, Kizugawa, Kyoto, Japan
[2]The Graduate School for the Creation of New Photonics Industries, Hamamatsu, Japan
[3]University of California, Berkeley, CA 94720, USA
[4]Max Plank Institute of Quantum Optics, Garching, Germany
[5]Central Research Institute of Electric Power Industry, Yokosuka, Kanagawa, Japan

Abstract. The progress in the development of laser systems generating the femtosecond optical pulses of intensity (10^{20} – 10^{25}) W/cm^2 opens up wide possibilities to get the unique sources of x-ray pulse emission with fs pulse duration and energy in the range from a few keV up to a few MeV. Its applications include the experiments on the fundamental physics. We discuss the possibility of abundant electron-positron pair creation via the multi-photon Breit-Wheeler process, and possibility of reaching the critical field of Quantum Electrodynamics (the Schwinger field) which would lead to the vacuum polarization and breakdown.

1 Introduction

Implementation of powerful sources emitting ultrashort pulses of x-ray radiation, is of great importance for various applications including the bio-medical applications [1]. They will allow performing single shot high contrast imaging of bio-objects. In atomic physics and spectroscopy powerful sources will make possible the multi-photon ionization and producing high Z hollow atoms. In material science these sources will reveal novel properties of matter exposed to the high power x-rays. The development and utilization of the synchrotron sources have for many years led to the progress in science and technology. Future applications require much shorter (sub fs) x-ray pulses of mJ energy. The schemes of x-ray generation also include laser and discharge pumped x-ray lasers, gas high order harmonics, relativistic harmonics in plasmas, and free electron lasers. Another method for coherent x-ray generation based on the Flying Mirror concept has been proposed in Ref. [2]. It uses the laser pulse compression, frequency up-shift, and focusing by

J. Lee et al. (eds.), *X-Ray Lasers 2010,* Springer Proceedings in Physics 136,
DOI 10.1007/978-94-007-1186-0_18,

counter-propagating breaking plasma waves – relativistic parabolic mirrors. In the proof of principle experiments for this concept [3-5], narrow band XUV generation was demonstrated.

Further developments of the Flying Mirror concept are aimed at employing it for developing a compact, tunable high-power coherent x-ray source, which will expand considerably the range of applications.

Utilization of the plasma nonlinear properties for the electromagnetic (EM) wave intensification can result in much higher intensity and power. We note the fruitfulness of the relativistic mirror concept for solving a wide range of problems in modern theoretical physics. Relativistic mirrors are important elements in the theory of the dynamical Casimir effect [6], with regard to the Unruh radiation [7] and other nonlinear vacuum phenomena [8].

The studying of physical mechanisms of high power coherent x-ray generation also paves the way towards the intensities at which the nonlinear quantum electrodynamics processes can be probed [8].

2 Extreme Field Limits

Physical systems obey scaling laws, which can also be presented as similarity rules. In the theory of similarity and modeling the key role is played by dimensionless parameters that characterize the phenomena under consideration [9]. The dimensionless parameters that characterize the high intensity EM wave interaction with matter can be found in Ref. [10]. The key in the extreme field limit parameters are as follows.

1. Normalized dimensionless EM wave amplitude, $a_0 = eE_0 / m_e\omega_0 c = eE_0 \lambda\!\!\!^{-}_0 / m_e c^2$, where $\lambda\!\!\!^{-}_0 = c/\omega_0$. At $a_0 = 1$ corresponding to the intensity $1.37\times10^{18}(1\,\mu\mathrm{m}/\lambda_0)^2$ W/cm^2, the laser electric field E_0 acting on the electric charge e produces a work equal to $m_e c^2$ over the distance $\lambda\!\!\!^{-}_0$. The quiver electron energy becomes relativistic.

2. The parameter characterizing the EM emission by an electron, ε_{rad}, is 2/3 of the ratio between the classical electron radius and the EM wavelength, $\varepsilon_{rad} = 2r_e / 3\lambda\!\!\!^{-}_0$. The radiation effects are dominant at $a_0 > \varepsilon_{rad}^{-1/3}$, i.e. in the limit $I > 10^{23}(1\,\mu\mathrm{m}/\lambda_0)^2$ W/cm^2 [11, 12].

3. Quantum electrodynamics (QED) effects become important, when the energy of the photon generated by Compton scattering is of the order of the electron energy, i.e. $\hbar\omega_m = \gamma_e m_e c^2$. An electron with energy $\gamma_e m_e c^2$ rotating with frequency ω_0 in a circularly polarized wave emits photons with energy

$\hbar\omega_m = \hbar\omega_0\gamma_e^3$. The quantum effects come into play when $\gamma_e > \gamma_Q = (m_e c^2/\hbar\omega_0)^{1/2} \approx 600(\lambda_0/1\,\mu\text{m})^{1/2}$, i.e. when the laser normalized amplitude equals $a_Q = 2e^2 m_e c/3\hbar^2\omega_0 = (2r_e/3\lambda\!\!\!^{-}_C)(m_e c^2/\hbar\omega_0)$ where $\lambda\!\!\!^{-}_C = \hbar/m_e c = 3.86\times10^{-11}$ cm is the Compton wavelength [12].

4. The limit of the critical QED field, also called the Schwinger field, $E_S = m_e^2 c^3/e\hbar = m_e c^2/e\lambda\!\!\!^{-}_C = 1.32\times10^{16}$ V/cm corresponding to the intensity of 10^{29} W/cm^2, is characterized by the normalized laser amplitude $a_S = m_e c^2/\hbar\omega_0 \approx 5.1\times10^5(\lambda_0/1\mu\text{m})$. The electric field E_S acting on the electric charge e produces a work equal to $m_e c^2$ over the distance equal to the Compton wavelength $\lambda\!\!\!^{-}_C$ [13 - 15].

5. In QED the charged particle interaction with EM fields is determined by the relativistically and gauge invariant parameter $\chi_e = \sqrt{(F_{\mu\nu}^2 p_\nu)^2}/m_e c E_S$, where $F_{\mu\nu}$ is the EM field tensor. The parameter χ_e characterizes the probability of the gamma-photon emission by the electron with Lorentz factor γ_e in the field of the EM eave[16]. It is of the order of the ratio E/E_S in the electron rest frame of reference. Another parameter, $\chi_\gamma = \sqrt{(F_{\mu\nu}^2 \hbar k_\nu)^2}/m_e c E_S$, is similar to χ_e with the photon 4-momentum, $\hbar k_\nu$, instead of the electron 4-momentum, p_ν. It characterizes the probability of the electron-positron pair creation due to the collision between the high energy photon and EM field [17 - 20].

The above mentioned regimes require the laser intensity of the order of or above $I > 10^{23}$ W/cm^2. This will bring us to experimentally unexplored domain. At such intensities the laser interaction with matter becomes strongly dissipative, due to efficient EM energy transformation into high energy gamma rays [12, 21]. These gamma-photons in the laser field may produce electron-positron pairs via the Breit-Wheeler process [22]. Then the pairs accelerated by the laser generate high energy gamma quanta and so on [18-20], and thus the conditions for the avalanche type discharge are produced at the intensity $\approx 10^{23}$ W/cm^2. The occurrence of such "showers" was foreseen by Heisenberg and Euler [14].

Relativistic mirrors may lead to an EM wave intensification resulting in an increase of pulse power up to the level when the electric field of the wave reaches the Schwinger limit when electron-positron pairs are created from the vacuum and the vacuum refractive index becomes nonlinearly dependent on the EM field strength. In quantum field theory particle creation from the

vacuum under the action of a strong field attracts a great attention, because it provides a typical example of non perturbative processes. In future, nonlinear QED vacuum properties can be probed with such strong and powerful EM pulses.

3 Flying Mirror Concept: Towards Extreme EM Field Limits

The concept of flying mirror is based on the fact that an EM wave reflected off a moving mirror undergoes frequency multiplication with the multiplication factor $(1+\beta_M)/(1-\beta_M)$ in the limit $\beta_M \to 1$ proportional to the square of the Lorentz factor of the mirror, $\gamma_M = \left(1-\beta_M^2\right)^{1/2}$. It makes this effect an attractive basis for a source of powerful high-frequency radiation. Here $\beta_M = v_M / c$ is calculated for the mirror velocity, v_M. There are several other schemes for developing compact, intense, brilliant, tunable X-ray sources by using the relativistic mirrors formed in nonlinear interactions in laser plasmas, whose realization will open new ways in nonlinear electrodynamics of continuous media in the relativistic regime (see articles, Refs. [2, 23-28]).

The interaction of regular nonlinear structures (such as EM solitons, electron vortices, and wake Langmuir waves) with a strong wake wave in a collisionless plasma has been proposed as a method for producing ultrashort EM pulses [24]. The EM field of the nonlinear structure is partially reflected by the electron density modulations of the incident wake wave and a single-cycle high-intensity EM pulse is formed. Due to the Doppler effect the length of this pulse is much shorter than that of the nonlinear structure.

Dense laser-driven electron sheets accelerated by the laser pulse interacting with a thin plasma slab are considered as relativistic mirrors for coherent production of brilliant X-ray and gamma-ray beams [25-28].

3.1 Flying Mirror with the nonlinear wake waves

Here we consider the *flying mirror* [2] based on utilization of the wake plasma waves. It uses the fact that the dense shells formed in the electron density in a nonlinear plasma wake, generated by a laser pulse, reflect a portion of a counter-propagating EM pulse. In the wake wave, electron density modulations take the form of a paraballoid moving with the phase velocity close to the speed of light in vacuum [29, 30]. At the wave breaking the electron density in the nonlinear wake wave tends towards infinity. The formation of peaked electron density maxima breaks the geometric optics approximation and provides conditions for the reflection of a substantially

high number of photons of the counter propagating EM pulse. As a result of the EM wave reflection from such a "relativistic flying mirror", the reflected pulse is compressed in the longitudinal direction. The paraboloidal form of the mirrors leads to a reflected wave focusing into a spot with the size determined by the shortened wavelength of the reflected radiation (**Fig. 1**).

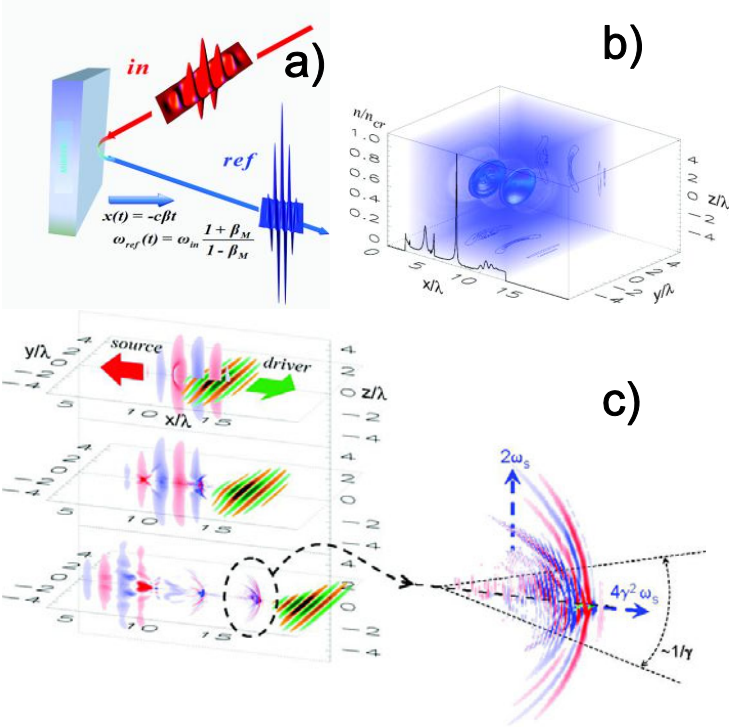

Fig. 1. a) Flying Mirror Concept. b) Paraboloidal modulations of the electron density in the plasma wake wave. c) The electric field pattern of the laser pulse driver and of the reflected EM wave. Inset: The reflected EM pulse intensity is increased, it is focused and its frequency is upshifted [2].

The key parameter in the problem of the Relativistic Flying Mirror (RFM) is the wake wave gamma factor, $\gamma_{ph,W}$, which plays a role of the reflecting mirror gamma factor, γ_M. The number of photons back reflected at the density singularity of the form $n(x) \sim x^{-2/3}$ is proportional to $\gamma_{ph,W}^{-4}$ (for details see Ref. [31]), which results in the reflected light intensification

$$I / I_0 = \gamma_{ph,W}^2 \left(S / \lambda_0 \right)^2 . \qquad (1)$$

Here S is the transverse size of the laser pulse efficiently reflected at the RFM. The reflected pulse power is the same as in the incident pulse $\mathcal{P} = \mathcal{P}_0$. If the singularity can be approximated by the Dirac delta-function,

$n(x) \sim \delta(x)$, the reflection coefficient is proportional to $\gamma_{ph,W}^{-3}$ with reflected light intensification [2]

$$I / I_0 = 8\gamma_{ph,W}^3 \left(S / \lambda_0\right)^2 . \quad (2)$$

The reflected pulse power increases as $\mathcal{P} = \mathcal{P}_0 \gamma_{ph,W}$.

This mechanism allows generating extremely short, femto-, attosecond duration pulses of coherent EM radiation with extremely high intensity.

3.2 Experimental demonstration of frequency multiplication in nonlinear interaction of two counter-propagating laser pulses

A demonstration of the Flying Mirror concept has been accomplished in the experiments of Refs. [3,4]. Two beams of terawatt laser radiation interacted with an underdense plasma slab. The first laser pulse excited the nonlinear wake wave in a plasma with parameters required for the wave breaking. The achievement of this regime was verified by observing the quasi-mono-energetic electron generation and the stimulated Raman scattering. The second counter-crossing laser pulse has been partially reflected from the relativistic mirrors formed by the wake plasma wave. EM pulses with a duration of femtoseconds and wavelengths from 7 nm to 15 nm were detected (see **Fig. 2**).

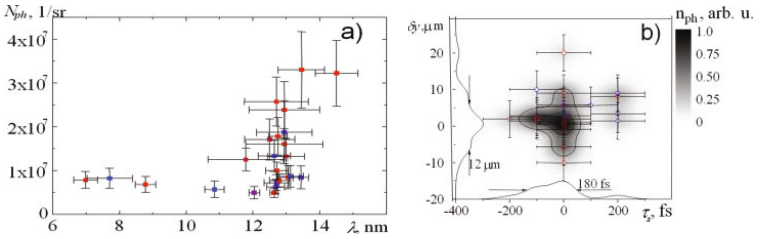

Fig. 2. a) Reflected photon numbers in 24 shots. b) Dependence of the reflected photon number on the source delay and the vertical misalignment δy. The gray scale denotes the normalized reflected photon density, n_{ph}, (sr μm ps)$^{-1}$; the contour lines are separated by 0.33 [3,4].

The experiments with the 0.5 J, 15 TW laser in the counter-propagating configuration [5] demonstrated dramatic enhancement of the reflected photon number in the extreme ultraviolet wavelength range, **Fig. 3**. The photon number (and reflected pulse energy), is close to the theoretical estimate for the parameters of the experiment.

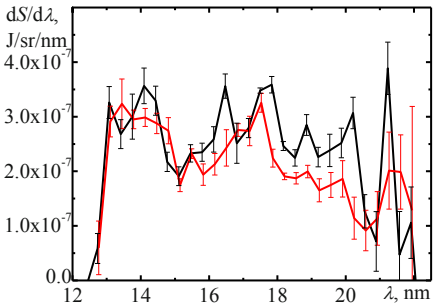

Fig. 3. Spectra in the diffraction order of m=1 (black) and m=-1 (red) [5].

These results demonstrate the feasibility of constructing sources of coherent X-ray radiation with the parameters that are tunable in a broad range of frequencies [5].

3.3 Double-Sided Relativistic Mirror: EM Pulse Compression and Boosted High Order Harmonic Generation

A property of the foil accelerated to relativistic energies by a laser pulse to act as a relativistic flying mirror can also be used in a co-propagating configuration for highly efficient ion acceleration [35-37]. The EM radiation reflected back by the co-propagating relativistic mirror has almost negligible energy compared to the energy in the incident laser pulse, i.e. the laser energy is almost completely transformed into the energy of fast ions with the ion energy per nucleon turning out to be proportional in the ultrarelativistic limit to the EM pulse energy. A high-density thin plasma slab, accelerating in the radiation pressure dominant regime by an ultraintense EM wave, reflects a counter propagating relativistically strong EM wave, producing extremely time-compressed and intensified radiation [38, 39]. The reflected light contains relativistic high order harmonics (HOH) generated at the plasma slab, all upshifted with the same factor as the fundamental mode of the incident light.

The accelerating double-sided mirror (DSM) (**Fig.** 4) efficiently reflects the counterpropagating relativistically strong EM wave [38]. The role of the mirror is played by a high-density plasma slab accelerated by an ultraintense laser pulse (the driver) in the radiation pressure dominated regime [35-37], when a thin plasma slab with the Lorentz factor $\gamma_M \gg 1$ reflects the co-propagating driver, taking a substantial fraction of its energy, $\approx 1-\gamma_M^{-2}$. The plasma slab acts as a mirror also for counterpropagating relativistically strong EM radiation, transferring the energy to the reflected light. Exhibiting the properties of the sliding and oscillating mirrors [40, 41], the plasma slab produces relativistic HOH. In the spectrum of the reflected radiation, the

fundamental frequency of the incident radiation and the relativistic HOH generated at the plasma slab are multiplied by the same factor, $\approx 4\gamma_M^2$.

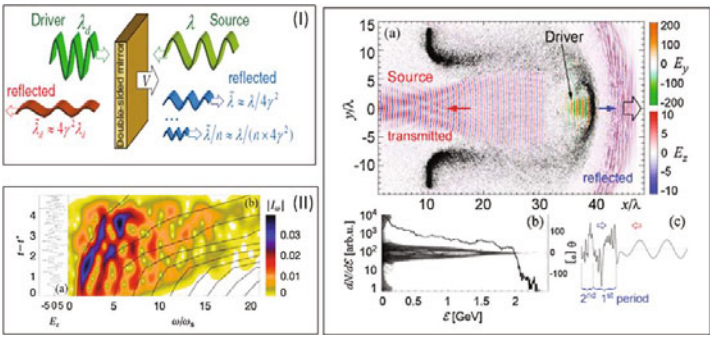

Fig. 4. The accelerated double-sided mirror. Frame I: The reflected EM pulse contains relativistic harmonics, all upshifted with the same factor as the fundamental mode of the incident light. a) The electric field y and z components of driver and source pulses, respectively, and the ion density (black). b) The ion energy spectrum (curve) and angular distribution (gray scale). c) The electric field z component: the first two reflected cycles overlapped with the source pulse. Frame II: a) The electric field component E_z along the *x* axis representing the reflected radiation (emitted in the x axis direction). b) The corresponding spectrum. Dashed curves: the odd harmonics frequency multiplied by the factor $(1+\beta_M)/(1-\beta_M)$ [38].

The particle in cell simulations [38] show that in the interaction of the driver laser pulse with thin foil target (**Fig. 4 a**) the ions are accelerated, as seen from the ion energy spectrum in **Fig. 4 b**. The accelerating plasma reflects the source pulse, which becomes chirped and compressed (**Fig. 4 c** and Frame II).

As the mirror velocity, $c\beta_M$, increases, the reflected light frequency grows as $\omega_0(1+\beta_M)/(1-\beta_M)$; thus, the electric field profile along the *x* axis becomes more and more jagged (**Fig. 4**, frame II). At the beginning, the magnitude of the reflected radiation is higher than that of the incident source, due to an enhancement of the reflectivity of the plasma slab compressed under the radiation pressure exerted by the driver and source pulses. In an instantaneous proper frame of the accelerating mirror, the frequency of the source pulse increases with time; thus, the mirror becomes more transparent. Correspondingly, the source starts to be transmitted through the plasma more efficiently, as seen in **Fig. 4 a**. The reflected radiation has a complex structure of the spectrum. It contains not only the frequency-multiplied fundamental mode of the source pulse but also HOH. Frame II in Figure 4 shows the modulus of the spectrum, $|I_\omega(t)|$, of the E_z component of the EM radiation emitted in the direction of the *x* axis, taken for each moment of time.

In the DSM concept, the reflected EM radiation consists of the fundamental mode and high harmonics, all multiplied by the factor $\approx 4\gamma_M^2$, where the Lorentz factor of the plasma slab, γ_M, increases with time. The reflected radiation is chirped due to the mirror acceleration.

For the mirror velocity above some threshold, in the mirror rest frame of reference, the average distance between electrons becomes greater than the incident wavelength. The reflection is no longer coherent, i.e., the reflected power becomes linearly proportional to the number of particles. Even with this scaling the interaction can provide efficient generation of x-ray pulses via backward (nonlinear) Thomson scattering due to the large number of electrons in a solid-density plasma. We estimate the reflected radiation brightness in two limiting cases. For $2\gamma_M < (n\lambda_0^3)^{1/6}$, the reflection is coherent and the brightness is

$$B_M \approx \mathcal{E}_0(\hbar\omega_r)^3\lambda_0 / 4\pi^5\hbar^4c^3, \tag{3}$$

where $\hbar\omega_r$ is the reflected photon energy and $\mathcal{E}_0$ is the source pulse energy. For larger γ_M, the interaction becomes incoherent. Assuming that the EM radiation is generated via Thomson scattering, we obtain

$$B_T \approx a_d\mathcal{E}_0(\hbar\omega_r)^2 r_e / 8\pi^4\hbar^3c^2\lambda_0. \tag{4}$$

For example, if $\mathcal{E}_0 = 10\text{J}$, $\lambda_0 = 0.8\,\mu\text{m}$, $\hbar\omega_r = 1$ keV, then the brightness of the coherently reflected pulse, $B_M \approx 0.8\times10^{40}$ photons/mm^2 mrad^2 s, is orders of magnitude greater than any existing or proposed laboratory source [42]. For the same parameters of the source pulse and, $\hbar\omega_r = 10\,\text{keV}$ and intensity of the driver pulse equal to $I \approx 10^{23}$ W/cm^2, we have for the brightness of incoherently scattered pulse $B_T \approx 3\times10^{32}$ photons/mm^2 mrad^2 s.

3.4 Comparison with presently available X-ray sources

Table 1 presents a comparison of the parameters of various X-ray sources including the sources based on the Flying Mirror concept.

In Fig. 5 we present a plot with the peak brightness of various light sources including the x- and gamma-ray sources based on the Relativistic Flying Mirror mechanism and on the Double Sided Mirror. The x- and gamma-ray brightness on axis is remarkable: it is comparable or exceeds almost all other sources (for 10 J, 0.8μm source pulse).

Table 1. Comparison of Flying Mirror parameters with typical parameters of presently available coherent X-ray sources.

X-ray source	Wavelength	Pulse duration	Pulse energy	Mono-chromaticity ($\Delta\lambda/\lambda$)	Coherence
XFEL	< 0.1 nm	50 fs	100 μJ	10^{-3}	spatial good
Plasma XRL	13.8 nm	7 ps	10 μJ	10^{-4}	spatial good
HHG	5 nm – 40 nm	100 attosec	1 μJ	10^{-2} - 10^{-3}	spatial and temporal good
Flying Mirror	0.1 nm – 40 nm	<1 fs	1 mJ	10^{-3} - 10^{-4}	spatial and temporal good

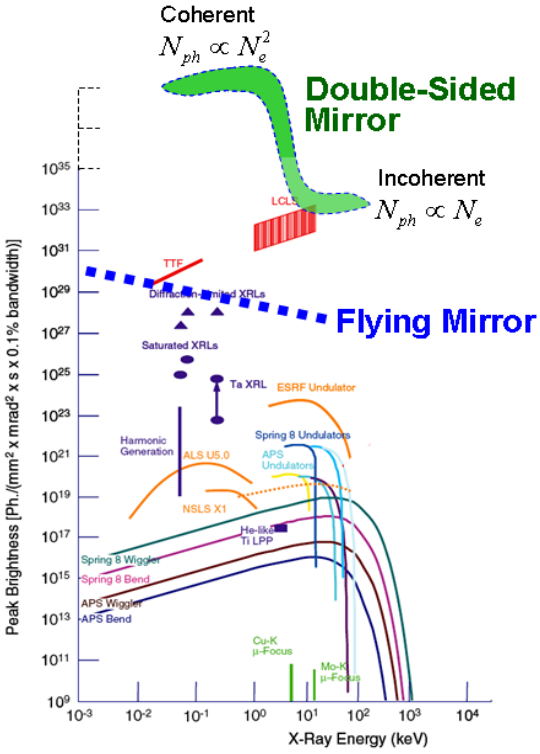

Fig. 5. Peak brightness of various light sources, including the x-ray source based on the interaction between the laser pulse with the Relativistic Flying mirror and Double Sided Mirror in coherent and incoherent regimes.

4 Probing Nonlinear Vacuum

4.1 Electron-positron pair creation from vacuum

Understanding the mechanisms of vacuum breakdown and polarization is challenging for nonlinear quantum field theories and for astrophysics [34]. Reaching the Schwinger field limit at Earth conditions has been considered as one of the most intriguing scientific problems. Demonstration of the processes associated with the effects of nonlinear QED will be one of the main challenges for extreme high power laser physics [8].

Vacuum nonlinearity is determined by the Poincare invariants

$$\mathfrak{F} = \frac{F_{\mu\nu}F^{\mu\nu}}{4} = \frac{\boldsymbol{E}^2 - \boldsymbol{B}^2}{2} \text{ and } \mathfrak{G} = \frac{F_{\mu\nu}\varepsilon^{\mu\nu\rho\sigma}F_{\rho\sigma}}{4} = \frac{\boldsymbol{E}\cdot\boldsymbol{B}}{2}. \tag{5}$$

Here $F_{\mu\nu} = \partial_\mu A_\nu - \partial_\nu A_\mu$ is the electromagnetic field tensor, A_μ is the electromagnetic field 4- vector potential, and $\varepsilon^{\mu\nu\rho\sigma}$ is the fully antisymmetric unit tensor where μ,ν,ρ,σ are integers from 0 to 4. Electron-positron pair creation from vacuum by the EM field [15] is a tunnelling process (see **Fig. 6**) with the probability per unit volume in unit time given by

$$W_{e^+e^-} = \frac{e^2E_S^2}{4\pi^2\hbar^2 c}\mathfrak{e}\mathfrak{b}\coth\left(\frac{\pi\mathfrak{b}}{\mathfrak{e}}\right)\exp\left(-\frac{\pi}{\mathfrak{e}}\right). \tag{6}$$

Here $\mathfrak{e}$ and $\mathfrak{b}$ are the normalized invariant electric and magnetic fields in the frame of reference, where they are parallel: $\mathfrak{e} = \sqrt{\sqrt{\mathfrak{F}^2 + \mathfrak{G}^2} + \mathfrak{F}}\,/E_S$ and $\mathfrak{b} = \sqrt{\sqrt{\mathfrak{F}^2 + \mathfrak{G}^2} - \mathfrak{F}}\,/E_S$. When $\mathfrak{e} \to 0$, the probability $W_{e^+e^-}$ tends to zero. For $\mathfrak{b} \to 0$ we have

$$W_{e^+e^-} = \frac{e^2E_S^2}{4\pi^2\hbar^2 c}\mathfrak{e}^2\exp\left(-\frac{\pi}{\mathfrak{e}}\right). \tag{7}$$

If the EM field varies sufficiently slowly in space in time, i.e. the characteristic scale of this variation is much larger than the characteristic scale of pair production process (it is given by the Compton length), then the field can be considered as constant in each point of 4-volume and the number of pairs is equal to

$$N_{e^+e^-} = \int W_{e^+e^-}d^4x, \tag{8}$$

where the integration is performed over the 4-volume.

Since the pairs are produced near the maximum of the electric field, we express EM field dependence on time and space coordinates locally as

$$\mathfrak{e} \approx \mathfrak{e}_m(1 - x^2/2l_x^2 - y^2/2l_y^2 - z^2/2l_z^2 - t^2/2\tau^2), \qquad (9)$$

and substitute it into Eq. (7) for the probability $W_{e^+e^-}$. Integrating it over the 4-volume according to Eq. (8) we obtain for the number of pairs [43]

$$N_{e^+e^-} = \frac{c\tau l_x l_y l_z}{64\pi^4 \lambda\!\!\!^{-4}_C} \mathfrak{e}_m^4 \exp\left(-\frac{\pi}{\mathfrak{e}_m}\right). \qquad (10)$$

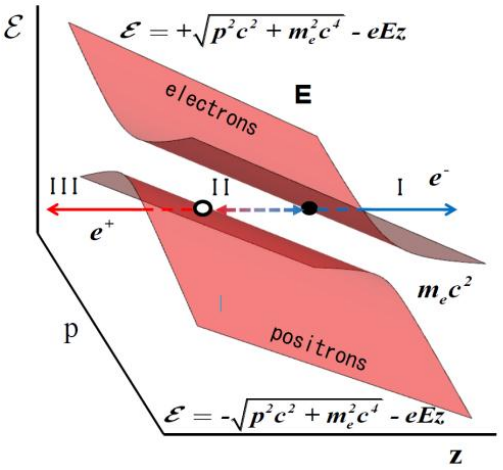

Fig. 6. The energy is plotted against the momentum and coordinate (the electric field E is parallel z-axis). The solution to the Dirac equation [13] shows that the ψ-function is large only in the regions I and III. In the region II, it decreases exponentially. Therefore the transmission coefficient through region II calculated in [13], which gives the pair creation probability, has the order of magnitude $\exp(-\pi m_e^2 c^3/e\hbar E)$, see Ref. [14].

Pair creation requires the first invariant $\mathfrak{F}$ be positive. This condition can be fulfilled in the vicinity of the antinodes of colliding EM waves, or/and in the configuration formed by several focused EM pulses, [44]. Near the focus region this configuration can be modeled by the axially symmetric 3D electromagnetic field comprising time-dependent electric and magnetic fields. As is known, in the 3D case the analog of a linearly polarized EM wave is the TM mode, with poloidal electric and toroidal magnetic fields. The analog of a circularly polarized EM wave is the TE mode, with toroidal electric and poloidal magnetic fields. The EM configurations approximating the EM fields found in Ref. [44] near the field maximum are described by the solution to

Maxwell's equations in vacuum and expressed in terms of Bessel functions and associated Legendre polynomials. The EM fields for the TM and TE modes and the first Poincare invariant are shown in **Fig. 7**. The second invariant, $\mathfrak{G} = \left(\boldsymbol{E} \cdot \boldsymbol{B}\right)$, is equal to zero, i.e. $\mathfrak{b} = 0$ for this EM configuration.

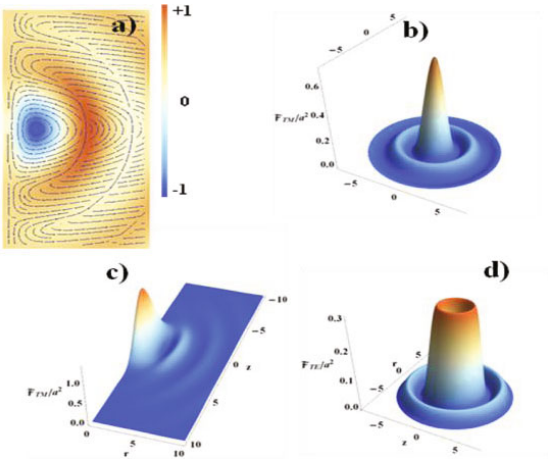

Fig. 7. a) The vector field shows r- and z-components of the poloidal electric field in the r,z plane for the TM mode and r- and z-components of the poloidal magnetic field in the r,z plane for the TE mode. The color density shows the toroidal magnetic field distribution, $B_\phi(r,z)$, in the case of the TM mode and the toroidal electric field distribution, $E_\phi(r,z)$, in the case of the TE mode. b) The first Poincare invariant $\mathfrak{F}$ normalized by the dimensionless laser amplitude a_0^2. for the TM mode: $\mathfrak{F}_{TM}(r,z=0,t=0)$. c) $\mathfrak{F}_{TM}(r,z,t=0)$. d) $\mathfrak{F}_{TE}(r,z=0,t=0)$ for the TE mode. The coordinates are normalized by $k_0 = \omega_0 / c$.

For the TM mode, in cylindrical coordinates r,ϕ,z the z-component of the electric field oscillates in the vertical direction, the ϕ-component of the magnetic field vanishes on the axis being linearly proportional to the radius, and the radial component of the electric field is relatively small.

Using expression for the probability of electron-positron pair creation, Eq. (6), and expanding $\mathfrak{F}_{TM}(r,z,t)$ in the vicinity of its maximum, we find that the pairs are created in a small 4-volume near the electric field maximum with the characteristic size along the r-, z-, and t-direction of about:

$$\delta r \approx \lambda\!\!\!^{-}_0 \left(\frac{5a_0}{\pi a_S}\right)^{1/2}, \quad \delta z \approx \lambda\!\!\!^{-}_0 \left(\frac{10a_0}{\pi a_S}\right)^{1/2}, \quad \delta t \approx \omega_0^{-1} \left(\frac{5a_0}{\pi a_S}\right)^{1/2}. \qquad (11)$$

The normalized Schwinger field, a_S, can also be written as $a_S = m_e c^2/\hbar\omega_0 \approx 5.1\times10^5$ for a wavelength of 800nm. As shown in [44] the first pairs can be observed for an one-micron wavelength laser intensity of the order of $I \approx 2.5\times10^{26}$ W/cm^2, which corresponds to $a_0/a_S = 4\times10^{-2}$, i.e. for a characteristic size approximately equal to $\delta r \approx 0.04\,\lambda_0$.

4.2 Electron-positron gamma-ray plasma generation via the multi-photon Breit-Wheeler process

An electron oscillating along an electric field emits high frequency EM radiation with the power and maximum radiation frequency proportional to the square of electron energy: $\approx \varepsilon_{rad}\omega_0 m_e c^2 \gamma_e^2/2$. Although an electron moving along the oscillating electric field loses energy, radiation friction effects may become important only at $a_{0S} = 2\,\varepsilon_{rad}^{-1}$, i.e. at the electric field $E_0 = 3m_e^2c^4/e^3$, which is of the order of the critical electric field of classical electrodynamics, and more than 400 times larger than the Schwinger field, i.e. the radiation losses in the linearly polarized EM mode can be neglected.

In a linearly polarized oscillating electric field the maximum frequency of emitted photons, ω_m, is proportional to γ_e, and, therefore, quantum effects should be incorporated into the theoretical description at the electron energy corresponding to the gamma-factor $\gamma_e > m_e c^2/\hbar\omega_0$ which is above the Schwinger limit. We see that in the case of electron motion in a linearly polarized oscillating electric field neither radiation friction nor quantum recoil effects are important.

Reaching the threshold of an avalanche type discharge with electron-positron gamma-ray plasma (EPGP) generation via the multi-photon Breit-Wheeler [22] process discussed in Refs. [18-20] requires high enough values of the parameters χ_e and χ_γ defined above. The probability of electron-positron pair creation in the multiphoton Breit-Wheeler process when the incident photon polarization is parallel to parallel to the EM wave polarization is given by [17]

$$W_{\parallel}(\chi_\gamma) = \frac{e m_e^2 c^3}{2\pi^4\hbar^3\omega_\gamma}\int_0^\pi d\psi \int_1^\infty du \int_{-\infty}^{+\infty} d\tau \frac{(2u/\chi_\gamma \sin\psi)^{1/3}}{u\sqrt{u(u-1)}} \left\{\left(1+\tau^2\right)\mathrm{Ai}^2(y) + \left(\chi_\gamma \sin\psi/2u\right)^{2/3}(u-1)\left[y\mathrm{Ai}^2(y) + \mathrm{Ai}'^2(y)\right]\right\}, \tag{12}$$

expressed in unite of inversed time, s^{-1}, with $y = (2u/\chi_\gamma)^{2/3}(1+\tau^2)$ and

the Airy functions, $\mathrm{Ai}(x)=\pi^{-1}3^{-1/2}\mathrm{K}_{1/3}(2x^{3/2}/3)$. In the limit of small parameter $\chi_\gamma \ll 1$ the rate of the pair creation is exponentially small,

$$W_{\parallel}(\chi_\gamma)=\frac{3}{32}\frac{e^2m_e^2c^3}{\hbar^3\omega_\gamma}\left(\frac{\chi_\gamma}{2\pi}\right)^{3/2}\exp\left(-\frac{8}{3\chi_\gamma}\right). \qquad (13)$$

In the limit $\chi_\gamma \gg 1$ the pair creation rate is given by

$$W_{\parallel}(\chi_\gamma)=\frac{27\Gamma^7(2/3)}{56\pi^5}\frac{e^2m_e^2c^3}{\hbar^3\omega_\gamma}\left(\frac{3\chi_\gamma}{2}\right)^{2/3}. \qquad (14)$$

Here $\hbar\omega_\gamma$ is the energy of the photon which creates an electron-positron pair.

Since for the large γ_e, the photon is emitted by the electron (positron) in a narrow angle almost parallel to the electron momentum with the energy of the order of the electron energy, the parameters χ_e and χ_γ are approximately equal to each other, although this is not necessarily so in the limit when the electron emits photons according to classical electrodynamics, i.e. when $\gamma_e<(m_ec^2/\hbar\omega_0)^{1/2}=a_S^{1/2}$. The parameter χ_e can be expressed via the electric and magnetic fields and electron momentum as

$$\chi_e^2=\left(\gamma_e\frac{\boldsymbol{E}}{E_S}+\frac{\boldsymbol{p}\times\boldsymbol{B}}{m_ecE_S}\right)^2-\left(\frac{\boldsymbol{p}\cdot\boldsymbol{E}}{m_ecE_S}\right)^2. \qquad (15)$$

In order to find the threshold for the avalanche development we need to estimate the QED parameter χ_e. The condition for avalanche development corresponding to this parameter should become of the order of unity within one tenth of the EM field period (e.g. see Ref. [18-20]). Due to the trajectory bending by the magnetic field the electron transverse momentum changes as $p_r\approx(a_0/8)k_0\delta r(\omega_0t)^2$, where δr is given by Eq. (11). Assuming ω_0t to be equal to 0.1π, we obtain from Eq. (12) that χ_e becomes of the order of unity, i.e. the avalanche can start, at $a_0/a_S\approx 0.08$, which corresponds to the laser intensity $I\approx 2.5\times10^{27}$ W/cm^2. At that limit the Schwinger mechanism provides approximately 10^7 pairs per one-period of the laser pulse focused to a λ_0^3 region. The first electron-positron pairs can be seen at one order of magnitude lower intensity, $I\approx 2.5\times10^{26}$ W/cm^2 (see Ref. [43,44]).

In the case of two colliding circularly polarized EM waves, the resulting

electric field rotates with frequency ω_0 being constant in magnitude. The radiation friction effects incorporated in the relativistically covariant form of equation of motion of a radiating electron [44] result in

$$m_e c^2 \frac{du^\mu}{ds} = eF^{\mu\nu}u_\nu + \frac{2e^2}{3c} g^\mu . \qquad (16)$$

Here the radiation friction force in the Lorentz-Abraham-Dirac form is determined by $g^\mu = d^2u^\mu / ds^2 - u^\mu (du^\nu / ds\, du_\nu / ds)$, $u_\mu = (\gamma, \boldsymbol{p}/m_e c)$ is the four-velocity, and s is the proper time, $ds = dt/\gamma$.

The power emitted by the electron is proportional to the fourth power of the electron energy $\approx \varepsilon_{rad} \omega_0 m_e c^2 \gamma_e^4$. This is a factor of γ_e^2 larger than in the case of linear polarization. The frequency spectrum has a maximum frequency of $0.29 \times \omega_0 \gamma_e^3$ proportional to the cube of the electron energy. This is a factor of γ_e larger than in the case of linear polarization. For the electron rotating in the circularly polarized colliding EM waves the emitted power becomes equal to the maximal energy gain at the field amplitude $a_0 > \varepsilon_{rad}^{-1/3}$, corresponding to the laser intensity $I \approx 4.5 \times 10^{23}$ W/cm^2. In this limit the radiation friction effects should be taken into account.

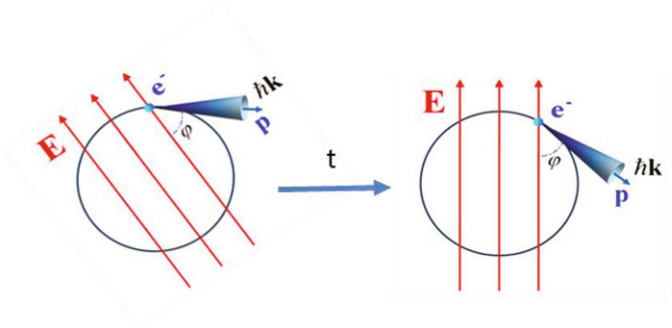

Fig. 8. Electron moving in the rotating electric field of colliding circularly polarized EM waves emits EM radiation. The angle φ between the electron momentum and electric field is determined by Eq. (17).

In order to do this, we represent the electric field and the electron momentum in the complex form: $E = E_y + iE_z = E_0 \exp(-i\omega_0 t)$ and $p = p_y + ip_z = p_\perp \exp(-i\omega_0 t - i\varphi)$, where φ is the phase equal to the angle between the electric field vector and the electron momentum (see **Fig. 8**). In the stationary regime the radiation friction force is balanced by the force acting on the electron from the electric field. The electron rotates with constant energy. The equations for the electron energy have the form

$$a_0^2 = (\gamma_e^2 - 1)(1 + \varepsilon_{rad}^2 \gamma_e^6) \quad \text{and} \quad \tan\varphi = \frac{1}{\varepsilon_{rad}\gamma_e^3} \qquad (17)$$

with $\gamma_e = \sqrt{1 + (p_\perp / m_e c)^2}$. In the limit of weak radiation damping, $a_0 \ll \varepsilon_{rad}^{-1/3}$, the absolute value of the electron momentum is proportional to the electric field magnitude, $p_\perp = m_e c a_0$, while in the regime of dominant radiation damping effects, i.e. at $a_0 \gg \varepsilon_{rad}^{-1/3}$, it is given by $p_\perp = m_e c (a_0 / \varepsilon_{rad})^{1/4}$. For the momentum dependence given by this expression the power radiated by the electron is $m_e c^2 \omega_0 a_0$, i.e. the energy obtained from the driving electromagnetic wave is completely re-radiated in the form of high energy gamma rays. At $a_0 \approx \varepsilon_{rad}^{-1/3}$ we have for the gamma photon energy $\hbar\omega_\gamma \approx 0.45 \hbar\omega_0 (m_e c^3 / e^2)$. For example, if $a_0 \approx \varepsilon_{rad}^{-1/3}$ and $a_0 \approx 400$ the circularly polarized laser pulse of intensity $I \approx 4.5 \times 10^{23}$ W/cm^2 generates a burst of gamma photons of energy about 20 MeV with the duration determined either by the laser pulse duration or by the decay time of the laser pulse in a plasma.

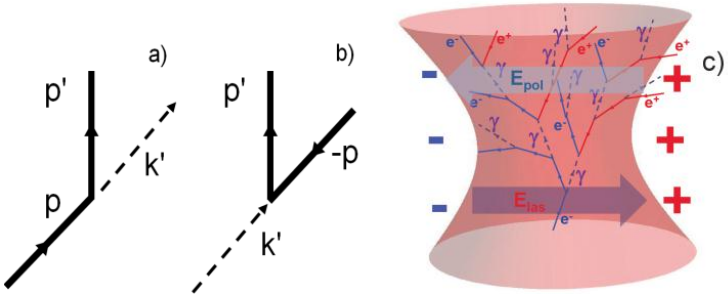

Fig. 9. Feynman diagrams of photon emission by a) an electron, and b) of the electron-positron pair production by a photon in an electromagnetic wave. c) Avalanche type EPGP discharge in an EM wave E_{las} , resulting in the inducing of the polarization electric field E_{pol} .

In the regime when the radiation friction effects are important, i.e. when $a_0 \gg \varepsilon_{rad}^{-1/3}$, the angle φ between the electron momentum and the electric field is small being equal to $-(\varepsilon_{rad} a_0^3)^{-1/4}$, i. e. the electron moves almost opposite the electric field direction. The electron momentum is given by $p_\perp = m_e c (a_0 / \varepsilon_{rad})^{1/4}$. This yields an estimation $\chi_e \approx (a_0 / a_S^2 \varepsilon_{rad})^{1/2}$. This

becomes greater than unity for $a_0 > a_S^2 \varepsilon_{rad} \approx 5.5 \times 10^3$, which corresponds to the laser intensity equal to 6×10^{25} W/cm^2. This is the condition of the electron-positron avalanche onset. We see that the radiation friction effects do not prevent the EPGP cascade to occur in the case of circularly polarized colliding waves, **Fig. 9**.

5 Possibility of Nonlinear Vacuum Probing with Present - Day Laser Systems

5.1 Approaching the Schwinger field limit

Using the expression for the reflected pulse intensity (1) and (2), we obtain that the interaction of two laser pulses with energies 10 kJ and 30 J, respectively, counterpropagating in a plasma with a density $\approx 10^{18}$ cm^{-3} can result in a light intensification of up to $\approx 10^{28}$ W/cm^2. This corresponds to the generation of an electric field with a value close to the nonlinear QED limit, E_S, when electron-positron pairs can be created in vacuum.

Experiments utilizing the EM pulse intensified with the Flying Relativistic Mirror technique may allow studying regimes of higher-than-Schwinger fields, when $E > E_S$. This may be possible because the light reflected by the parabaloidal FRM is focused into a focus spot moving with a relativistic velocity and is well collimated within an angle $1/\gamma_{ph,W}$, [2]. The wave localization within the narrow angle corresponds to the fact that the wave properties are close to the plane wave properties to the extent of the smallness of the parameter $1/\gamma_{ph,W}$. In this case the first Poincare invariant of the EM field, $\mathcal{F}$, has a value of the order of $E^2/2\gamma_{ph,W}^2$. The second Poincare invariant, $\mathcal{G}$, vanishes. Therefore the electric field amplitude in the reflected EM wave can exceed the Schwinger limit by factor $\gamma_{ph,W}$.

We note that a tightly focused EM wave cannot reach an amplitude above E_S, due to the electron-positron pair creation [20] leads to the scattering of the EM wave. While creating and then accelerating the electron-positron pairs the laser pulse generates an electric current and EM field (see **Fig. 9 c**). The electric field induced inside the EPGP cloud with a size of the order of the laser wavelength, λ_0 can be estimated to be $E_{pol} = 2\pi e(n_+ + n_-)\lambda_0$. Here $n_+ \approx n_-$ are the electron and positron density, respectively. Coherent scattering of the laser pulse away from the focus region occurs when the

polarization electric field becomes equal to the laser electric field, $E_{pol} = E_{las}$. This yields for the electron and positron density $n_+ \approx n_- = E_{las}/4\pi e\lambda_0$. The particle number per λ_0^3 volume is about $a_0\lambda_0/r_e$. This is a factor a_0 smaller than required for the laser energy depletion, which has been considered in [18,19,46] as a reason preventing from reaching the Schwinger field.

The nonlinear dependence of the vacuum susceptibilities on the electromagnetic-field amplitude results in the finite value of the Kerr constant of vacuum. It can be found to be $K_{QED} = (7\alpha/90\pi)\left(\lambda\!\!\!^{-3}_C / m_e c\lambda_0\right)$, where $\alpha = e/\hbar c$ is the fine structure constant [2, 47]. The Kerr constant of the vacuum for $\lambda_0 = 1\,\mu$m is of the order of $10^{-27}\,\mathrm{cm^2/erg}$.

In the QED nonlinear vacuum two couter-propagating electromagnetic waves mutually focus each other [48]. The critical power $\mathcal{P}_c = cE^2S_0^2/4\pi$, where S_0 is the laser beam waist, for the mutual focusing is equal to $\mathcal{P}_c = (90/28)cE_S^2\lambda_0^2/\alpha$. For $\lambda_0 = 1\,\mu$m it yields $\mathcal{P}_c \approx 2.5\times10^{24}\,\mathrm{W}$, which is beyond the reach of existing and planned lasers**.** Fortunately, if we take into account that the radiation reflected by the FRM has a shortened wavelength, $\lambda_r = \lambda_0/4\gamma_{ph,W}^2$ and that its power is increased by a factor $\gamma_{ph,W}$, we may find that for $\gamma_{ph,W} \approx 30$, i.e. for a plasma density $3\times10^{17}\,\mathrm{cm^{-3}}$, nonlinear vacuum properties can be seen for laser light the incident on the FRM with a power of about 50 PW.

This makes the Flying Relativistic Mirror concept attractive for the purpose of studying nonlinear quantum electrodynamics effects.

5.2 Multi-photon creation of electron-positron gamma-ray plasma in ultrarelativistic electron beam collision with the EM pulse

Here we discuss requirements for experimental realization of abundant electron-positron pair creation in the PW class laser interaction with relativistic electron beam of moderate energy.[1]

In the experiments [49] on the 527 nm terawatt laser interaction with 46.6 GeV electron from SLAC accelerator beam positrons were observed. The positrons were generated in a two-step process in which laser photons were scattered by the electrons and then arising high-energy photons collided with

[1] Theoretical material of this part is mainly based on review article [50] and qualitative picture drawn in Ref. [51].

several laser photons to produce an electron-positron pair. This corresponds to the multiphoton Breit-Wheeler process,

$$N\omega_0 + \omega_\gamma \to e^+e^-, \tag{18}$$

where N is the number of laser photons colliding with the gamma-photon to produce the pair.

The parameter χ_γ, which determines the probability of the electron-positron pair creation by photon (see Eq. (12-14)), is equal to

$$\chi_\gamma = \frac{\sqrt{(F^2_{\mu\nu}\hbar p_\nu)^2}}{m_e c E_S} \approx \frac{E}{E_s}\frac{\hbar\omega_\gamma}{m_e c^2} = a\frac{\hbar^2\omega_0\omega_\gamma}{m_e^2c^4} = a\frac{\hbar^2\bar{\omega}_0\bar{\omega}_\gamma}{m_e^2c^4}. \tag{19}$$

The r.h.s. term of this expression explicitly shows relativistic invariance of χ_γ. It becomes of the order of unity for the energy of the photon which creates an electron-positron pair equal to

$$\hbar\omega_\gamma = m_e c^2 \frac{m_e c^2}{2\hbar\omega_0 a}. \tag{20}$$

Using this expression we can find the number of laser photons N_l required to create the electron-positron pair. In the reference frame where the electron-positron pair is at the rest we have a relationship $N_l\tilde{\omega}_0 = \tilde{\omega}_\gamma$, which gives $N_l = \tilde{\omega}_\gamma / \tilde{\omega}_0 \approx \omega_\gamma / 4\omega_0\tilde{\gamma}^2$. Here tilde used for quantities in the pair rest frame and $\tilde{\gamma}$ corresponds to the Lorentz transformation to this frame. For the photon energy we have $N_l\hbar\tilde{\omega}_0 = m_e c^2$. Since $\hbar\tilde{\omega}_\gamma = m_e c^2$ and $\tilde{\omega}_0\tilde{\omega}_\gamma = \omega_0\omega_\gamma = m_e^2c^4\chi_\gamma/\hbar^2 a$ we find $\tilde{\gamma} = \chi_\gamma m_e c^2 / 2\hbar\omega_0 a$, which yields

$$N_l = \frac{a}{\chi_\gamma}. \tag{21}$$

Probability of the pair creation by photon is given by Eqs. (13, 14). In the region of $\chi_\gamma \approx 1$, it is of the order of $W \approx 0.1e^2m_e^2c^3/\hbar^3\omega_\gamma$ $= 0.1\alpha\left(m_e c^2/\hbar\right)\left(\hbar\omega_0/m_e c^2\right)a$. The mean free path of the photon of the energy $\hbar\omega_\gamma$ before pair creation is equal to $l_{m.f.p} = c/W$,

$$l_{m.f.p} = \frac{\lambda_0}{0.2\pi\alpha\, a} \approx 220\frac{\lambda_0}{a}. \tag{22}$$

It is about $2\mu m$ for $a = 10^2$.

Now we estimate the parameter χ_e value, which characterizes the nonlinear Compton scattering (see Eqs. (15)). We consider the electron interacting with the plane EM wave. As a result of the interaction with the laser pulse the electron, being inside the pulse, acquires longitudinal and transverse momentum components. Using solution presented in Ref. [45], we find that the component of the electron momentum along direction of the laser pulse propagation can be found from the equation

$$(m_e^2c^2 + m_e^2c^2a^2 + p_x^2)^{1/2} - p_x = (m_e^2c^2 + p_0^2)^{1/2} + |p_0|. \qquad (23)$$

We use the conservation of generalised momentum which yields for the component of the electron momentum parallel to the laser electric field: $p_y = a\, m_e c$. The x-component of the electron momentum before collision with the laser pulse is negative and equal to $-|p_0|$. For a plane EM wave propagating along the x-axis with $\boldsymbol{E} = E(x-ct)\boldsymbol{e}_y$ and $\boldsymbol{B} = E(x-ct)\boldsymbol{e}_z$, where $E = c^{-1}A'(x-ct)$ and $A(x-ct)$ is the y-component of the 4-vector potential and prime denotes differentiation with respect to the variable $x-ct$, the invariant χ_e given by Eq. (15) takes the form

$$\chi_e = \frac{E}{E_S}\left(\gamma_e - \frac{p_x}{m_e c}\right). \qquad (24)$$

Substituting expression (23) to Eq. (24) we obtain

$$\chi_e = \frac{E}{E_S}\left[\frac{(m_e^2c^2 + p_0^2)^{1/2} + |p_0|}{m_e c}\right] = a\frac{\hbar\omega_0}{m_e c^2}\left[\frac{(m_e^2c^2 + p_0^2)^{1/2} + |p_0|}{m_e c}\right]. \qquad (25)$$

For $1\,\mu$m petawatt laser pulse focused to a few micron focus spot the ratio $a = 10^2$ the parameter χ_e becomes equal to unity for $\gamma_0 = 2.5\times10^3$, i.e. for the electron energy of about of 1.3 GeV.

The gamma-ray photons depending on the parameters of the laser-electron interaction can be generated either via nonlinear Thomson scattering in classical electrodynamics regime or via multiphoton inverse Compton scattering, when the quantum mechanical description should be used.

5.2.1 Gamma-ray photon generation via the nonlinear Thomson scattering

At first we analyze nonlinear Thomson scattering. We consider a head-on collision of an ultrarelativistic electron with a laser pulse. The laser

ponderomotive pressure pushes the electron aside the pulse and it is changing the longitudinal component of the electron momentum too. In the electron rest frame the laser pulse duration is $\bar{\tau}_{las} \approx \tau_{las}\sqrt{1+a^2}/2\gamma_e$. The electron is not scattered aside by the laser ponderomotive force provided its energy is large enough,

$$\gamma_e > c\tau_{las}a/2w_\perp , \tag{26}$$

where $w_\perp$ is the focus width. As we see, for one-micron, 1 PW, i.e $a = 10^2$, 30 fs duration laser pulse focused to one-wavelength spot this condition requires $\gamma_e > 500$, i.e. the electron energy above 250 MeV. Further we assume that this condition is respected.

When a counter-propagating electron collides with the laser pulse its longitudinal momentum decreases. According to Eq. (23) it is equal to

$$p_x = -|p_0| + m_e c \frac{a^2 m_e c}{2[(m_e^2c^2 + p_0^2)^{1/2} + |p_0|]} . \tag{27}$$

In the boosted frame of reference where the electron is at the rest the laser frequency is related to the laser frequency in the laboratory frame, ω_0, as [52] (see also Ref. [53] where nonlinear Thomson scattering is discussed)

$$\bar{\omega}_0 = \frac{\omega_0}{\sqrt{1+a^2}}\sqrt{\frac{1-\beta_0}{1+\beta_0}} , \tag{28}$$

where $\beta_0 = p_0/\sqrt{m_e^2c^2 + p_0^2}$. Characteristic frequency of the radiation emitted by the electron in this frame of reference is equal to $\bar{\omega}_m = 0.3\bar{\omega}_0 a^3$, [54]. The photon energy, $\hbar\bar{\omega}_m = 0.3\hbar\bar{\omega}_0 a^3$, satisfies condition (20) for $a = \sqrt{m_e c^2/0.3\hbar\bar{\omega}_0}$, which corresponds to the parameters when the QED description should be used. For lower laser amplitudes the photon generation can be described by the nonlinear Thomson scattering process. The power emitted by the electron in the field of a linearly polarized EM wave is equal to

$$P = \frac{e^2}{c}\bar{\omega}_0^2 a^2\left(1 + \frac{3}{8}a^2\right). \tag{29}$$

Dividing it by the typical energy of the emitted photon, $\hbar\bar{\omega}_m = 0.3\hbar\bar{\omega}_0 a^3$, and multiplying on $2\pi/\bar{\omega}_0$ we find the number of photons emitted by the electron during one wave period,

$$N_\gamma \approx \frac{3\pi}{4}\alpha a\,. \tag{30}$$

The photon energy in the laboratory frame of reference is

$$\hbar\omega_m = 0.3\hbar\omega_0 \frac{a^3}{1+a^2}\frac{1-\beta_0}{1+\beta_0} \approx 1.2\hbar\omega_0 a\gamma_0^2\,. \tag{31}$$

We note that in the interaction of a GeV electron with a PW laser pulse the radiation friction effects must be incorporated. Since for the parameters under consideration the radiation friction force is weaker than the Lorentz force we shall consider it as a perturbation. This approximation corresponds to the Landau-Lifshitz form of the radiation friction force [45],

$$g^\mu = \frac{2e^2}{3m_e c^3}\left[\frac{\partial F^{\mu\nu}}{\partial x^\lambda}u_\nu u_\lambda - \frac{e^2}{m_e c^2}\left(F^{\mu\lambda}F_{\nu\lambda}u^\nu + \left(F_{\nu\lambda}u^\lambda\right)\left(F^{\nu\kappa}u_\kappa\right)u^\mu\right)\right]. \tag{32}$$

Retaining the main order terms in Eqs. (16) and (32), we obtain equation for the x-component of the electron momentum

$$\frac{dp_x}{dt} = -\varepsilon_{rad}\omega_0 a^2(2t)\frac{p_x^2}{m_e c}\,. \tag{33}$$

Its solution is given by

$$p_x(t) = \frac{p_x(0)m_e c}{m_e c + \varepsilon_{rad}\omega_0 p_x(0)\int_0^t a^2(2t')dt'}\,. \tag{34}$$

If we assume a dependence of $a(t)$ of the form $a(t) = a_0\exp(-t^2/2\tau^2)$, Eq. (34) can be rewritten as

$$p_x(t) = \frac{p_x(0)m_e c}{m_e c + \varepsilon_{rad}\omega_0 p_x(0)\tau a_0^2\sqrt{\pi/32}\left[\operatorname{erf}\left(\sqrt{2}t/\tau\right)-1\right]}\,. \tag{35}$$

Here $\operatorname{erf}(x)$ is the error function equal to $\operatorname{erf}(x) = \left(\sqrt{\pi}/2\right)\int_0^x \exp(-t^2)dt$. Eq. (23) shows that for large enough $p_x(0)\tau a_0^2$ the electron momentum tends to the limit of $p_x(t) \underset{t\to\infty}{\to} \sqrt{\pi/8}\left(m_e c/\varepsilon_{rad}\omega_0\tau a_0^2\right)$ in accordance with the theory formulated in Refs. [45, 55] and numerical solution of the equations of the electron motion in the laser field with the radiation friction effects taken

into account [52]. For $a_0 = 10^2$ and $\omega_0 \tau = 6$ the electron momentum is about $p_x(\infty)/m_e c = 500$.

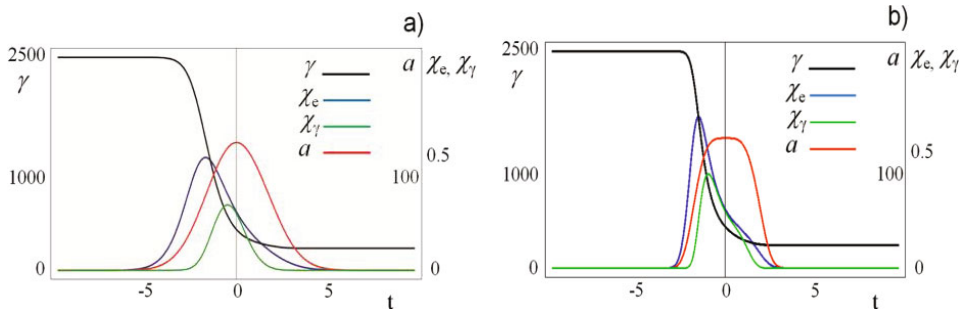

Fig. 10. Time dependence of the electron and photon parameters for a GeV electron beam interaction with a PW laser pulse: the electron energy - black; parameter χ_e - blue; laser pulse profile, parameter χ_γ - green, $a_0 = 100$ - red. The frame a) corresponds to the Gaussian pulse and the frame b) corresponds to the super-Gaussian pulse with the index=4.

In **Fig. 10** we present the time dependence of the electron and photon parameters for a GeV electron beam interaction with the Gaussian PW ($a_0 = 150$, $\tau = 9$ fs) laser pulse, when the ponderomotive force and radiation friction effects are incorporated into the electron equation of motion (16, 32). The electron energy before and after the interaction with the laser pulse equals 1.25 GeV and 0.25 GeV, respectively. The parameter $\chi_e(t) \approx 2(a(t)/a_S)(p_x(t)/m_e c)$ reaches the maximum value of 0.5 inside the laser pulse. The parameter $\chi_\gamma(t) \approx (a(t)/a_S)(\hbar\omega_\gamma(t)/m_e c^2)$ with $\omega_\gamma(t) = 0.29\,\omega_0 \gamma_0 a_0^3(t)$ reaches the maximum value of about 0.3. In the electron interaction with the super-Gaussian pulse, $a(t) = a_0 \exp(-t^4/2\tau^4)$, the parameters acquire higher values, 0.6 for χ_e and 0.4 for χ_γ.

5.2.2 Gamma-ray generation via the multi-photon Compton scattering

For multi petawatt lasers with larger laser amplitudes of the focused light, $a > 3m_e c^2/2\hbar\omega_0\gamma_0 \approx 300$, the gamma rays are generated in the multiphoton Compton scattering of ultrarelativistic electrons,

$$N\omega_0 + e \rightarrow \omega_\gamma + e'. \qquad (36)$$

The kinematic consideration of the multiphoton reaction leads to the relationship between the laser frequency, ω_0, and the frequency of scattered photons, ω_γ. In the frame of reference, where the electron is at rest, we have (e.g. see [51])

$$\bar{\omega}_\gamma = \frac{N\bar{\omega}_0}{1+\left(\frac{N\hbar\bar{\omega}_0}{m_e c^2}+\frac{a^2}{4}\right)(1-\cos\theta)}, \tag{37}$$

where θ is the angle between the laser pulse and the photon propagation directions, and a is the normalized laser field. At $\theta \to \pi$ the scattered frequency tends to its maximal value $\approx m_e c^2/\hbar$. In the laboratory frame of reference, the scattering cross section is maximal in the narrow angle in the backward direction with respect to the laser propagation.
In the rest frame of the electron the intensity of radiation is given by

$$\frac{dI}{du} = -\frac{e^2 m_e^2 c^3}{4\pi^2\hbar^2}\frac{u}{(1+u)^3}\left\{\int_z^\infty \mathrm{Ai}(y)dy + \frac{2}{z}\left[1+\frac{u^2}{2(1+u)}\right]\mathrm{Ai}'(z)\right\}. \tag{38}$$

Here $u = \chi_\gamma/\chi_e$ and $z = \left(u/\chi_e\right)^{2/3}$. At small u the intensity is proportional to $u^{1/3}$, i.e. $I \sim \bar{\omega}_\gamma^{1/3}$, and at large u it decreases exponentially. The maximum of the intensity distribution is at $\chi_\gamma \approx \chi_e^2$ for $\chi_e \ll 1$ and at $\chi_\gamma \approx \chi_e$ if $\chi_e \gg 1$, i.e. at $\bar{\omega}_\gamma \approx m_e c^2 a/\hbar$.

Using expression (28) for $\bar{\omega}_0$ we obtain that the parameter $\chi_\gamma = a\hbar^2\bar{\omega}_0\bar{\omega}_\gamma/m_e^2c^4$ equals $\chi_\gamma = 2\gamma_0 a\hbar\omega_0/m_e c^2$. At $a = 10^2$ it becomes of the order of unity for $\gamma_0 \approx 2.5\times10^3$. We see that the QED consideration gives the same value ≈ 1.25 GeV for the required relativistic electron energy as in the case of the classical approximation corresponding to nonlinear Thomson scattering.

5.2.3 Electron-positron generation in two laser beams interacting with plasmas

In order to construct a compact source of the electron-positron-gamma-ray plasma it is desirable to produce gamma rays in collisions of the laser accelerated electrons with the EM field of the laser pulse (see **Fig. 11**, where three versions of the experimental setup are presented). As is known, the required GeV range electron energy has been achieved in experiments involving a 40 TW ultrashort laser pulse interaction with underdense plasma

[56, 57]. The quasi-mono-energetic electron bunches have been generated in the laser wake field acceleration process [58,59].

In the case of usage of the laser wake-field accelerated electrons, the bunch is optimally synchronised with the laser pulse. In addition, the electron density is substantially higher than in the beam of electrons produced by conventional accelerators. For example, a typical microtron accelerator generates 150 MeV electron beam with the charge of 100 pC and duration of about 20 ps. Being focused into the 50 μm focus spot it provides the electron density $n_b \approx 10^{12}\,\mathrm{cm}^{-3}$. As a result approximately 300 electrons can interact with the laser pulse. According to Eqs. (22) and (30) the maximal number of electron-positron pairs which can be produced is equal to 300 per shot. However, since for a PW range laser pulse the parameters χ_e and χ_γ are small compared to unity, the rate of electron-positron pair generation is exponentially low. If we use the LWFA generated electron bunch with a transverse size of several microns, with ten fs duration and with an electric charge of 1 nC, approximately 10^9 electrons interact with the laser pulse. For the parameters χ_e and χ_γ equal to unity we may expect in the optimal case the generation of approximately 10^9 pairs per shot.

Utilization of the EM wave intensified by the relativistic flying mirror to collide with the LWFA accelerated electrons, as is shown in **Fig. 11 c**, can increase further the efficiency of the electron-positron pair generation. In this case the parameters χ_e and χ_γ increase by a factor equal to $\gamma_{ph,W}$ and can exceed unity, thus providing conditions for the avalanche type prolific generation of the electron-positron pairs.

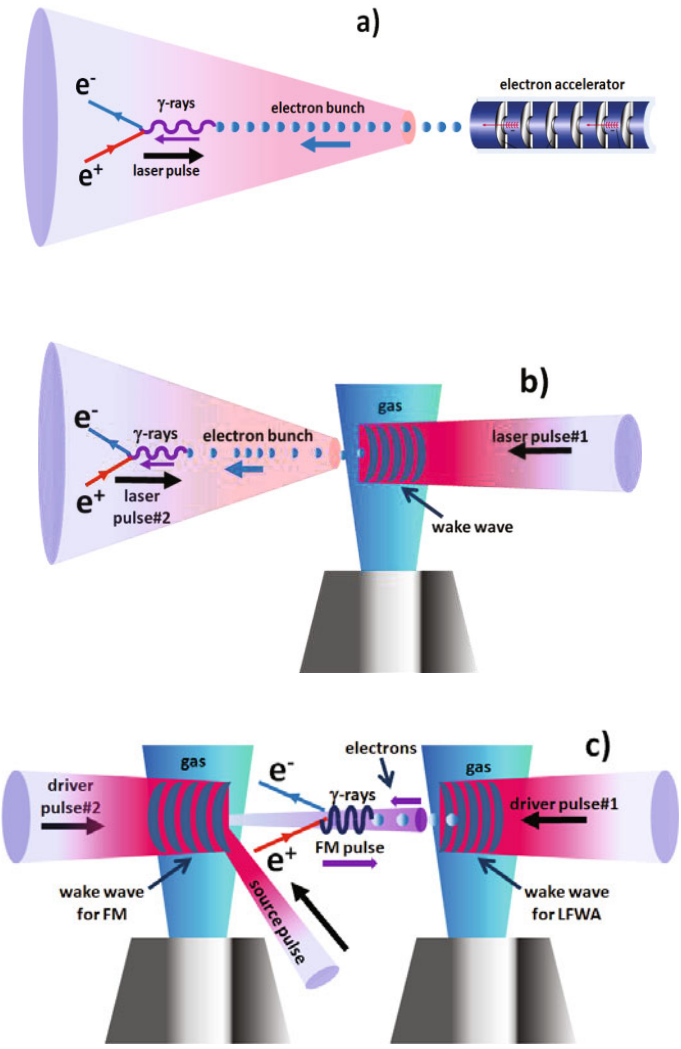

Fig. 11. Schematic setup of the proposed experiment on the electron-positron pair generation via the Breit-Wheeler process. a) Relativistic electron bunch collides with the tightly focused laser pulse, b) Laser pulse collides with the LWFA accelerated electron bunch. c) LWFA accelerated electron bunch collides with the ultra-high intensity EM wave generated with the flying mirror.

Table 2 presents maximum values of the parameters χ_e and χ_γ for different regimes of the electron bunch interaction with laser light.

Table 2. Peak values of the invariants χ_e and χ_γ for PW laser.

$\mathcal{E}_e$	Microtron e^- 150 MeV	LWFA e^- 1.25 GeV	LWFA e^- 1.25 GeV + FM EM pulse ($\gamma_{ph,W} = 5$)
E/E_S	3×10^{-4}	3×10^{-4}	1.5×10^{-3}
χ_e	0.05	0.5	2.5
χ_γ	0.01	0.3	2.5

Conclusion

With the concept of the Relativistic Flying Mirror, relatively compact and tunable extremely bright high power sources of ultrashort pulses of x- and gamma-rays become realizable, which will allow for exploring novel physics, for studying the processes of high importance for accelerator physics [60], and for laboratory modeling of processes of key importance for relativistic astrophysics [2,34]. The experiments in this field will allow modelling under the conditions of a terrestrial laboratory the state of matter in cosmic Gamma Ray Bursts and in the Leptonic Era of the Universe.

We thank N. B. Narozhny, K. Kondo, and S. Iso for discussions, and appreciate the support from the MEXT of Japan, Grant-in-Aid for Scientific Research (A), 29244065, 2008.

References

1. Neutze, R., Wouts, R., D. van der Spoel, Weckert, E., and Hajdu, J.: 'Potential for biomolecular imaging with femtosecond X-ray pulses' *Nature,* 406, 752 – 757, 2000
2. Bulanov, S. V., Esirkepov, T. Zh., and Tajima, T.: 'Light Intensification towards the Schwinger Limit', *Phys. Rev. Lett*. 91, 085001, 2003
3. Kando, M., Fukuda, Y., Pirozhkov, A. S., *et al.*: 'Demonstration of Laser-Frequency Upshift by Electron-Density Modulations in a PlasmaWakefield', *Phys. Rev. Lett*. 99, 135001, 2007
4. Pirozhkov, A. S., Ma, J., Kando, M., *et al.*: 'Frequency multiplication of light back-reflected from a relativistic wake wave', *Phys. Plasmas* 14, 123106, 2007

5. Kando, M., Pirozhkov, A. S., Kawase, K., *et al.*: 'Enhancement of Photon Number Reflected by the Relativistic Flying Mirror', *Phys. Rev. Lett*. 103, 235003, 2009
6. Bordag, M., Mohideen, U., and Mostepanenko, V.M.: 'New developments in the Casimir effect', *Phys. Rep*. 353, 1 – 203, 2001
7. Crispino, L., Higuchi, A., and Matsas, G. E. A.: 'The Unruh effect and its applications', *Rev. Mod. Phys*. 80, 787 – 838, 2008
8. Mourou, G., Tajima, T., and Bulanov, S. V.: 'Optics in the relativistic regime', *Rev. Mod. Phys*. 78, 309 – 371, 2006
9. Sedov, L. I.: *Similarity and dimensional methods in mechanics*, Academic Press, 1959
10. Bulanov, S. V., Esirkepov, T. Zh., Habs, D., Pegoraro, F., and Tajima, T.: 'Relativistic laser-matter interaction and relativistic laboratory astrophysics', *Eur. Phys. J*. D 55, 483 – 507, 2009
11. Zel'dovich, Ya. B.: 'Interaction of free electrons with electromagnetic radiation', *Sov. Phys. Uspekhi* 18**,** 79 – 98, 1975
12. Bulanov, S. V., Esirkepov, T. Zh., Koga, J., and Tajima, T.: 'Interaction of Electromagnetic Waves with Plasma in the Radiation-Dominated Regime', *Plasma Physics Reports,* 30, 196 – 213, 2004
13. Sauter, F.:'Uber das Verhalten eines Electrons im homogenen electrischen Feld nach der relativischen Theorie Diracs', *Z. Phys.* 69, 742-764, 1931
14. Heisenberg, W., and Euler, H.: 'Folgerungen aus der Diracschen Theorie des Positrons', *Z. Phys.* 98, 714 – 732, 1936
15. Schwinger, J.: 'On Gauge Invariance and Vacuum Polarization', *Phys.Rev.* 82, 664 – 679, 1951
16. Beresteskii, V. B., Lifshitz, E.M., and Pitaevskii, L.P.: *Quantum Electrodynamics,* Pergamon, 1982
17. Nikishov, A. I., and Ritus, V. I.: 'Interaction of Electrons and Photons with a Very Strong Electromagnetic Field', *Sov. Phys. Usp.* 13, 303 – 305, 1970
18. Bell, A.R., and Kirk, J.G.: 'Possibility of Prolific Pair Production with High-Power Lasers', *Phys. Rev. Lett.* 101, 200403, 2008
19. Fedotov, A. M., Narozhny, N. B., Mourou, G. and Korn, G.: 'Limitations on the Attainable Intensity of High Power Lasers', *Phys. Rev. Lett.* 105, 080402, 2010
20. Bulanov, S. S., Esirkepov, T. Zh., Thomas, A., Koga, J. K., and Bulanov, S. V.:"On the Schwinger limit attainability with extreme power lasers", arXiv:1007.4306v2, 25 July 2010
21. Zhidkov, A. G., Koga, J., Sasaki, A., and Uesaka, M.: 'Radiation Damping Effects on the Interaction of Ultraintense Laser Pulses with an Overdense Plasma', Phys *Phys. Rev. Lett*., 88, 185002, 2002
22. Breit, G., and Wheeler, J. A.: 'Collision of Two Light Quanta', *Phys. Rev*. 46, 1087 – 1091, 1934
23. Naumova, N. M., Nees, J. A., Sokolov, I. V., Hou, B., and Mourou, G. A.: 'Relativistic Generation of Isolated Attosecond Pulses in a λ3 Focal Volume', *Phys. Rev. Lett*. 92, 063902, 2004
24. Bulanov, S. S., Esirkepov, T. Z., Kamenets, F. F., and Pegoraro, F.: 'Single-cycle high-intensity electromagnetic pulse generation in the interaction of a plasma wakefield with regular nonlinear structures', *Phys. Rev. E* 73, 036408, 2006
25. Kulagin, V. V., Cherepenin, V. A., Hur, M. S., and Suk, H.: 'Flying mirror model

for interaction of a super-intense nonadiabatic laser pulse with a thin plasma layer: Dynamics of electrons in a linearly polarized external field', *Phys. Plasmas* 14, 113101, 2007
26. Habs, D., Hegelich, M., Schreiber, J., Gross, M., Henig, A., Kiefer, D., and Jung, D.: 'Dense laser-driven electron sheets as relativistic mirrors for coherent production of brilliant X-ray and gamma-ray beams', Appl. Phys. B, 93, 349 – 354, 2008
27. Wu, H. -C., Meyer-ter-Vehn, J., Fernandez, J., Hegelich, B. M.: 'Uniform Laser-Driven Relativistic Electron Layer for Coherent Thomson Scattering', *Phys. Rev. Lett*. 104, 234801, 2010
28. Bulanov, S. S., Maksimchuk, A., Krushelnick, K., Popov, K. I., Bychenkov, V. Yu., and Rozmus, W.: 'Ensemble of ultra-high intensity attosecond pulses from laser-plasma interaction', *Phys. Lett*. A, 374, 476 – 480, 2010
29. Bulanov, S. V., and Sakharov, A. S.: 'Induced focusing of the electromagnetic radiation in the wakefield plasma wave', *JETP Lett.* 54, 203-207, 1991
30. Matlis, N. H., Reed, S., Bulanov, S. S., et al.: 'Snapshots of laser wakefields', *Nature Phys.* 2, 749 – 753, 2006
31. Panchenko, A. V., Esirkepov, T. Zh., Pirozhkov, A. S., Kando, M., Kamenets, F. F., and Bulanov, S. V.: 'Interaction of electromagnetic waves with caustics in plasma flows', *Phys. Rev. E* 78, 056402, 2008
32. Narozhnyi, N. B., Bulanov, S. S., Mur, V. D., Popov, V. S.: 'On e(+)e(-) pair production by colliding electromagnetic pulses', *JETP Lett.* 80, 382-385, 2004
33. Bulanov, S. S., Fedotov, A. M., Pegoraro, F.: 'Damping of electromagnetic waves due to electron-positron pair production', *Phys. Rev. E,* 71, 016404, 2005
34. Ruffini, R., Vereshchagin, and G., Xue, S. S.: 'Electron-positron pairs in physics and astrophysics: From heavy nuclei to black holes', *Phys. Rep.* 487, 1-140*,* 2010
35. Esirkepov, T. Zh., Borghesi, M., Bulanov, S. V., Mourou, G., and Tajima, T.: 'Highly Efficient Relativistic-Ion Generation in the Laser-Piston Regime', *Phys. Rev. Lett*. 92, 175003, 2004
36. Pegoraro, F., and Bulanov, S. V.: 'Photon Bubbles and Ion Acceleration in a Plasma Dominated by the Radiation Pressure of an Electromagnetic Pulse', *Phys. Rev. Lett*. 99, 065002, 2007
37. Bulanov, S. V., Echkina, E. Yu., Esirkepov, T. Zh., Inovenkov, I. N., Kando, M., Pegoraro, F., and Korn, G.: 'Unlimited Ion Acceleration by Radiation Pressure', *Phys. Rev. Lett*. 104, 135003, 2010
38. Esirkepov, T. Zh., Bulanov, S. V., Kando, M., Pirozhkov, A. S., and Zhidkov, A. G.: 'Boosted High-Harmonics Pulse from a Double-Sided Relativistic Mirror', *Phys. Rev. Lett*. 103, 025002, 2009
39. Ji, L. L., Shen, B. F., Li, D. X., et al.: 'Relativistic Single-Cycled Short-Wavelength Laser Pulse Compressed from a Chirped Pulse Induced by Laser-Foil Interaction', *Phys. Rev. Lett*. 105, 025001, 2010
40. Bulanov, S. V., Naumova, N. M., and Pegoraro, F.: 'Interaction of ultra short relativistically strong laser pulse with overdense plasmas', *Physics of Plasmas* 1, 745 – 757, 1994
41. Teubner, U., and Gibbon, P.: 'High-order harmonics from laser-irradiated plasma surfaces', *Rev. Mod. Phys.* 81, 445-479, 2009

42. Hartemann, F. V., Siders, C. W., and Barty, C. P. J.: 'Compton Scattering in Ignited Thermonuclear Plasmas', *Phys. Rev. Lett*., 100, 125001, 2008
43. Bulanov, S. S., Narozhny, N. B., Mur, V. D., and Popov, V. S.: 'Electron–Positron Pair Production by Electromagnetic Pulses', *JETP* 102, 9-23, 2006
44. Bulanov, S. S., Mur, V. D., Narozhny, N. B., Nees, J., and Popov, V. S.: 'Multiple Colliding Electromagnetic Pulses: A Way to Lower the Threshold of Electron-Positron Pair Production from Vacuum', *Phys. Rev. Lett*., 104, 220404, 2010
45. Landau, L. D., and Lifshitz, E. M., *The Classical Theory of Fields, Pergamon*, 1975
46. Klein, J. J., and Nigam, B. P.: 'Dichroism of the Vacuum', *Phys. Rev.,* 136, B1540 – B1542, 1964
47. Klein, J. J., and Nigam, B. P.: 'Birefringence of the Vacuum', *Phys. Rev.,* 135, B1279 – B1280, 1964
48. Rozanov, N. N.: 'Self-action of intense electromagnetic radiation in an electron–positron vacuum', *JETP,* 86, 284 – 288, 1998
49. Burke, D. L., Field, R. C., Horton-Smith, G., et al.: 'Positron Production in Multiphoton Light-by-Light Scattering', *Phys. Rev. Lett*., 79, 1626 – 1629, 1997
50. Ritus, V. I.: 'Quantum Effects of the Interaction of Elementary Particles with an Intense Electromagnetic Field', *Tr. Fiz. Inst. Akad. Nauk SSSR* 111, 5 – 151, 1979
51. McDonald, K. T.: 'Fundamental Physics During Violent Accelerations', *AIP Conference Proceedings,* 130, 23 – 54, 1985
52. Koga, J., Esirkepov, T. Zh., and Bulanov, S. V.: 'Nonlinear Thomson scattering in the strong radiation damping regime', *Phys. Plasmas* 12, 093106, 2005
53. Hartemann, F. V., Albert, F., Siders, C. W., and Barty, C. P. J.: 'Low-Intensity Nonlinear Spectral Effects in Compton Scattering', *Phys. Rev. Lett*., 105, 130801, 2010
54. Sarachik, E., and Schappert, G.: 'Classical Theory of the Scattering of Intense Laser Radiation by Free Electrons', Phys. Rev. D 1, 2738– 2753, 1970
55. Pomeranchuk, I.: 'Maximum Energy that Primary Cosmic-ray Electrons Can Acquire on the Surface of the Earth as a Result of Radiation in the Earth's Magnetic Field', J. Phys. USSR, 2, 65 – 69, 1940
56. Leemans, W. P., Nagler, B., Gonsalves, A. J., et al.: 'GeV electron beams from a centimetre-scale accelerator', *Nature Phys.*, 2, 696 – 699, 2006
57. Hafz, N. A. M., Jeong, T. M., Choi, I. W., et al.: 'Stable generation of GeV-class electron beams from self-guided laser-plasma channels', *Nature Photonics*, 2, 571 – 577, 2008
58.Tajima, T., and Dawson, J. M.: 'Laser electron accelerator', *Phys. Rev. Lett*., 43, 267 – 271, 1979
59. Esarey, E., Schroeder, C. B., and Leemans, W. P.: 'Physics of laser-driven plasma-based electron accelerators', *Rev. Mod. Phys*., 81, 1229 – 1285, 2009
60. Chen, P., and Telnov, V. I.: 'Coherent Pair Creation in Linear Colliders', *Phys. Rev. Lett*., 63, 1796 – 1799, 1989

Generation of Coherent X-Ray Radiation with Relativistic Nonlinear Processes

Y. Kato[1,2], M. Kando[2], A. S. Pirozhkov[2], T. Zh. Esirkepov[2], K. Kawase[2], H. Daido[3], H. Kiriyama[2] and S. V. Bulanov[2]

[1] The Graduate School for the Creation of New Photonics Industries, Hamamatsu, Shizuoka, Japan

[2] Advanced Photon Research Center, JAEA, Kizugawa, Kyoto, Japan

[3] Applied Laser Technology Institute, JAEA, Tsuruga, Fukui, Japan

Abstract. Generation of coherent x-ray radiation with plasmas at relativistic intensities is a promising approach which can be scaled to shorter wavelengths without being limited by ionization as in atomic harmonics and plasma x-ray lasers. Here we report experimental results of the two approaches: frequency up-shifting with a relativistic flying mirror and high order harmonic generation in underdense relativistic plasma. Although investigations are in initial stages, both approaches are promising for generating bright x-ray radiation in the xuv to x-ray regions.

1 Introduction

There have been significant advances to generate coherent radiation in the EUV to x-ray regions in these 25 years. The plasma x-ray laser [1-3], which was initially a large-laboratory size facility, has become very compact making them suitable as user-friendly x-ray sources [4-6]. High order harmonic generation with atomic gases now provides coherent radiation in the water window region [7]. With free electron lasers, lasing in the EUV and x-ray regions has been successfully demonstrated [8-10].

In addition to extending these studies, it is important to explore other approaches to develop compact, coherent and bright x-ray sources [11] to

J. Lee et al. (eds.), *X-Ray Lasers 2010,* Springer Proceedings in Physics 136,
DOI 10.1007/978-94-007-1186-0_19,

meet the needs in various applications in science, biology and industry. One of the promising approaches is to investigate the possibility to generate coherent x-ray radiation based on relativistic nonlinear processes in plasmas. The major advantage of this approach is that the wavelength of the coherent radiation could be extended to shorter regions since the generation process is not restricted by ionization of the atoms and the radiation energy scales strongly with the laser intensity.

There have been various proposals and experiments to generate x-ray radiation at relativistic intensities: relativistic nonlinear Thomson scattering [12, 13], synchrotron radiation by laser-accelerated electrons in an ion channel [14], high order harmonics in relativistic interaction at solid surfaces [15], x-ray emission from electrons at radiation dominant regime [16], and frequency up-shifting due to reflection from a relativistic flying mirror [17].

In this paper we will present two approaches to generate coherent radiation from plasmas at relativistic intensities. The first is the frequency up-shifting with a relativistic flying mirror which has been demonstrated at JAEA [18-20]. The second is the generation of high order harmonics in under-dense plasma which has been observed recently.

2 Frequency Up-shifting with a Relativistic Flying Mirror

The new concept of light intensification towards the Schwinger limit has been proposed by Bulanov et al [17]. In this concept, light intensification is achieved when a laser pulse ("source pulse") is reflected by a plasma wake which is formed by an intense counter-propagating laser pulse ("driver pulse"). Since the wake phase velocity v_{ph} is equal to the group velocity of the driver pulse which is close to c (the speed of light in vacuum), the frequency of the source pulse ω_0 is up-shifted to $\omega_x \sim 4\gamma_{ph}{}^2\omega_0$ and the pulse duration τ_0 is compressed to $\tau_x \sim \tau_0/4\gamma_{ph}{}^2$. Here γ_{ph} is the relativistic factor $\gamma_{ph}=[1-(v_{ph}/c)^2]^{-1/2}$ for $v_{ph}/c \sim 1$. Therefore the peak power will be increased by $P_x/P_s=16\gamma_{ph}{}^4R$,

where R is the reflectivity of the plasma mirror. Furthermore the reflected source pulse can be focused to a very small spot close to the diffraction limit of the short wavelength radiation with frequency ω_x, since the surface of the plasma wake becomes close to parabolic [17].

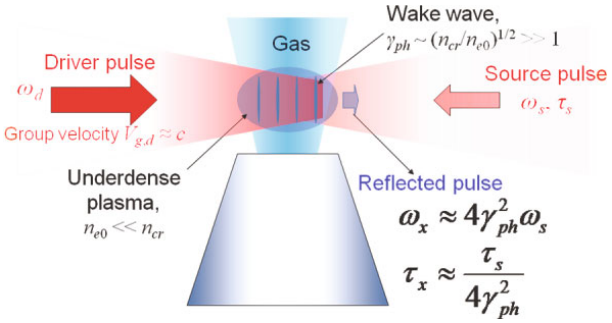

Fig. 1. Frequency up-shift and pulse compression of a source pulse in reflection from a wake wave generated with a driver pulse which moves close to the light velocity.

In order to test this concept, we have made two series of experiments with (a) counter-crossing collision of 2 pulses [18, 19] and (b) head-on collision of 2 pulses [20]. The experimental arrangement of the first experiment is shown in Fig. 2. A driver pulse of 180 mJ energy and 76 fs pulse width (1.8 TW peak power) was focused to a 30 μm-diameter spot (intensity of 5 x 10^{17} W/cm^2) in a He gas jet with an electron density of $N_{e,\,max}$=3-6 x 10^{19} cm^{-3}. This driver pulse was collided in the plasma with a source pulse (11 mJ energy focused to 17 μm diameter) which was incident to the gas jet from the counter crossing direction at 45 degrees to the driver pulse. The spectrum of the source pulse reflected from the plasma was recorded over the 5-15 nm spectral range with a grazing incidence xuv spectrograph located on the axis of the driver pulse. This is the direction expected for the reflected source pulse, considering the relativistic effect. The spectrograph was protected from the driver pulse with

two Mo/C multilayer filters and also from high energy electrons which were deflected with a permanent magnet and monitored to measure their energies.

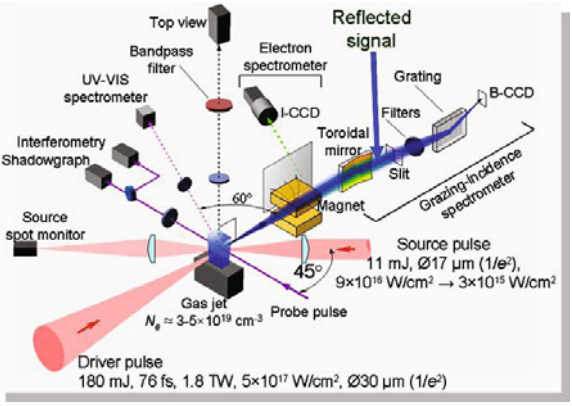

Fig. 2. Experimental setup for observing reflection of a source pulse from a wake wave generated with a driver pulse. The reflected pulse was observed with a spectrograph on the axis of the driver pulse and the helium gas jet interaction region was monitored with a probe laser pulse.

The most crucial part in this experiment was exact spatial and temporal overlap of the driver pulse and the source pulse in the plasma. This was achieved by taking shadowgraph with a probe laser pulse incident from the side direction and also taking the plasma image from the vertical direction.

The xuv spectrograph has recorded the 14.3 nm signal which appears only when the source and driver pulses overlap in the plasma to within 50-fs temporal and 5-μm spatial accuracies. The 14.3 nm wavelength λ_x is 56 times shorter than the wavelength of the source pulse λ_s. By considering the 45-degree collision angle, the relation $\lambda_s/\lambda_x=3.4\gamma_{ph}^2$ provides a Lorentz factor of $\gamma_{ph}=4.1$. This γ value is consistent with the Lorentz factor estimated from the observed electron energy of 19 MeV and also with the PIC simulation for the present experimental condition.

More detailed aspects of the source pulse reflection from the moving plasma mirror was studied in the second experiment, where the driver and the

source pulses were collided head-on and the spectrum was monitored at 13 degrees from the driver pulse axis [20]. The driver pulse energy was increased to 400 mJ providing the intensity at the focus of 3 x 10^{18} W/cm^2. Due to these improved conditions, the photon number of the reflected signal has increased significantly (4-5 orders higher than the first experiment) to 10^9-10^{10} photons within the detection angle of 5.7 msr, corresponding to the energy reflectivity of the relativistic flying mirror of R=1.3~6 x 10^{-4}. This high reflectivity is in close agreement with the theoretically estimated value and supports the experimental observation that the plasma mirror is not fragmented but acts as one smooth mirror.

Although further detailed investigation is necessary to study various factors such as angular dependence, coherence and temporal profile of the reflected radiation, these initial results are very encouraging to consider the relativistic flying mirror as a new approach to generate coherent radiation at short wavelengths. It is expected that this approach can be scaled to generate a coherent atto-second pulse of mJ energy in the water window region, when we use a source pulse of 1 J energy and γ_{ph}=10.

3 High-Order Harmonic Generation in Underdense Relativistic Plasma

High order harmonics have been generated with atomic gases and solid targets. Here we report our new observation of high order harmonics generated in underdense plasmas at relativistic laser intensities. At the irradiation intensity of 6.5 x 10^{18} W/cm^2 in vacuum, resolved harmonics with the wavelength down to 7 nm (harmonic order of > 100) and unresolved spectra down to 4 nm (harmonic order of > 200) have been observed. A new mechanism of harmonic generation is inferred based on the unique features of the observed spectra.

Linearly polarized laser pulses of 9 TW, 27 fs and 820 nm were focused with an off-axis parabola to 25 μm diameter in a He gas jet. The backing pressure of He was varied to produce the plasma with the maximum electron density in the range of $n_{e,max}$=2~7 x 10^{19} cm^{-3}. The xuv emission from the plasma was observed with a grazing incidence spectrograph in the forward direction. At this experimental condition, high energy electrons up to ~100 MeV were measured with an electron spectrometer placed in the forward direction. The spectrum of the transmitted laser pulse, which we have measured independently, was downshifted to 860~940 nm region.

A typical harmonic spectrum taken at $n_{e,max}$ =2.5 x 10^{19} cm^{-3} is shown in Fig. 3(a), where the abrupt changes of the intensities of the signal at 12.5 nm and 13.5 nm are due to the change of the transmittance of the filters used in this experiment. The parts of the spectrum in the expanded scales are shown for ω/ω_0=60~67 in Fig. 3(b) and ω/ω_0=80~100 in Fig. 3(c), respectively. The spectrum in absolute unit $dE/d\hbar\omega/d\Omega$ (nJ/eV/sr), calculated from the observed spectral intensities and the spectrometer throughput, is shown in Fig. 3(d). The spectral intensity is estimated to reach ~200 nJ/eV/sr at $\hbar\omega$=100 eV and ~10 nJ/eV/sr at $\hbar\omega$=190 eV, respectively, which can be compared well with other x-ray sources.

The spectrum shown in Fig. 3 consists of periodic structures with the frequency separation of $\delta\omega = 0.885\omega_0$, where ω_0 is the laser frequency. The unique features in this spectrum are that $\delta\omega$ is smaller than ω_0 and both odd and even harmonics are observed with almost equal intensities. These periodic structures are observed up to $n=\omega/\omega_0\approx100$ as seen in Fig. 5 (c). Above this range, the spectrum extends to approximately 5 nm as an almost continuous spectrum. The harmonic separation δω is not the same in different shots; it changes mostly in the range of $\delta\omega$=0.8~1.0ω_0. Sometimes it is more downshifted to as small as $\delta\omega$=0.5ω_0 or, in a few shots, $\delta\omega$ is larger than ω_0 up to $\delta\omega$=1.4ω_0.

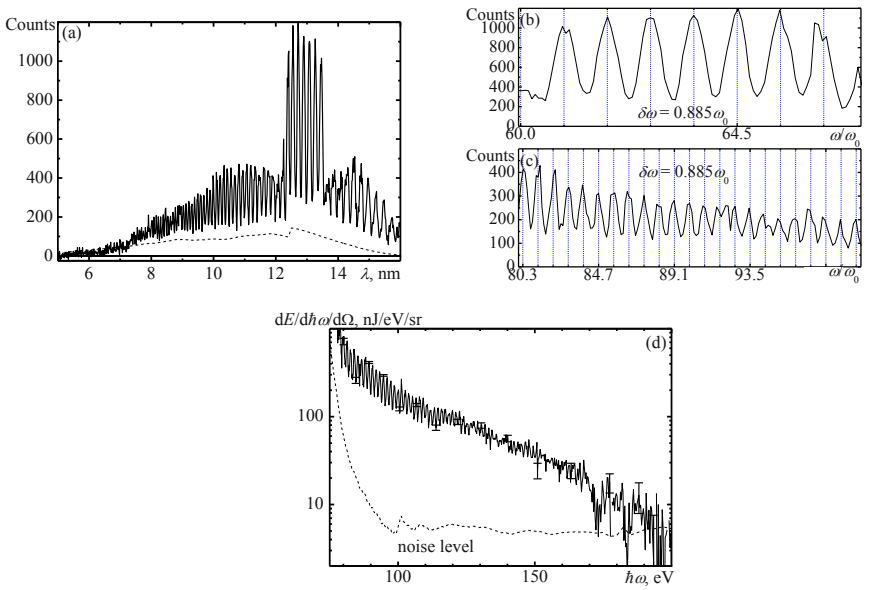

Fig. 3. An example of the observed spectrum. The whole spectrum is shown in (a), whereas parts of the spectrum at different wavelength regions are shown in expanded scales in (b) and (c). The spectrum in the absolute unit is shown in (d).

Additional feature of the spectrum, which have been observed in several shots, is the larger scale and deep modulation with the frequency separation of $\Delta\omega \approx 4\sim17\omega_0$ in addition to the smaller scale modulation of $\delta\omega$, as shown in Fig. 4 for the case of $\Delta\omega \approx 17\omega_0$ and $\delta\omega = 0.872\omega_0$. This spectrum indicates that the harmonic emission arises from a periodic process with the period $T = 2\pi/\delta\omega = 3.1$fs, oscillating over several cycles of T. The large period modulation may arise from an interference between two sources of almost equal intensities which are shifted in time by $\delta t = 2\pi/\Delta\omega = 0.16$ fs.

The clearly resolved small period modulation of $\delta\omega$ implies that the laser frequency should be stable to within $\Delta\omega_0/\omega_0 \approx 0.004$ during the generation process. Otherwise the spectrum will appear as almost continuous due to overlapping of frequency-shifted high-order harmonics. Here we note that the laser frequency decreases during propagation due to nonlinear depletion of the laser pulse [21], as observed in this experiment. From the laser frequency

stability of better than $\Delta\omega_0/\omega_0 \approx 0.004$ estimated above and the theoretical evaluation of the frequency down-shift during propagation, it is inferred that the emission should have taken within the propagation distance of only 4 μm.

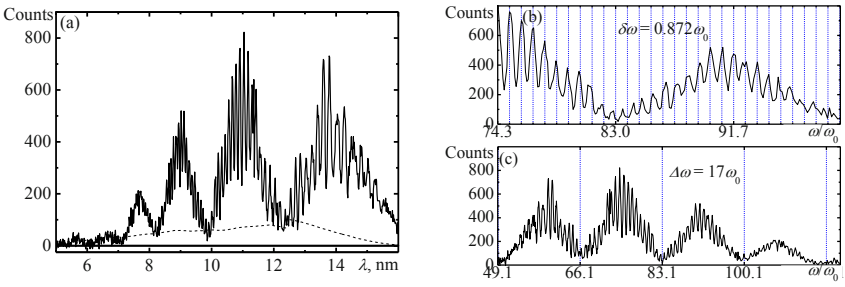

Fig. 4. A typical spectrum with large period modulation of $\Delta\omega \approx 17\omega_0$.and short scale modulation of $\delta\omega = 0.872\omega_0$.

Let us consider the origin of the modulated xuv emissions observed in this experiment. Although the periodic structure $\delta\omega$ is similar to that of atomic harmonics, we can exclude the atomic harmonics since the frequency separation $\delta\omega$ is not equal to ω_0 and both odd and even harmonics are observed in almost equal intensities. Also the laser intensity is so high that the atoms are completely ionized, as evidenced by observation of intense, high energy electrons.

The observed large scale frequency modulation $\Delta\omega$ is close to the feature expected for the nonlinear Thomson scattering [22], where euv radiation is emitted in the forward direction due to the relativistic motion of the electrons. The expected brightness of the radiation due to the nonlinear Thomson scattering is $dE/d\hbar\omega/d\Omega = 2 \times 10^{-19}$ J/eV/sr at $\hbar\omega$=100 eV for a single electron, for a linearly polarized pulse of 4×10^{19} W/cm^2. Comparing this brightness with the value observed in the present experiment ($dE/d\hbar\omega/d\Omega = 100$ nJ/eV/sr), approximately 10^{12} electrons are necessary to generate the observed radiation. This implies that the nonlinear Thomson scattering should occur over the propagation length of ~1 mm, considering the

~2.7 x 10^{19} cm^{-3} electron density and 6 μm beam diameter (the diameter of the self-focusing laser channel at a_0=6). Since this distance is far longer than the emission length of 4 μm as estimated above, it is difficult to ascribe the present emission to the nonlinear Thomson scattering. These evaluations suggest that the observed high order harmonics arise from collective oscillation of the electrons in a localized region of less than 4 μm, such as the high density electron cusp formed at the front of the bow wave [23]. (Detailed account of the generation mechanism will be reported elsewhere.)

Since the brightness of the observed harmonics is quite high and harmonic critical order will scale similar to the nonlinear Thomson scattering as $n_c \sim a_0^3$ [12], where $a_0 = eE_0/mc\omega_0$ is the dimensionless amplitude, this scheme may be promising as the intense coherent source in the x-ray region.

4 Conclusion

We have shown experimental results on the two approaches for generation of coherent x-ray radiation with relativistic nonlinear processes. The first is the frequency upcoversion due to reflection of a laser pulse from a wake wave which acts as a plasma mirror moving at a relativistic velocity. The second is the high-order harmonic radiation generated in the interaction of an intense laser radiation with underdense plasma. Both approaches will be scalable to shorter wavelengths without being restricted by atomic ionization.

References

1. Matthews, D.L., Hagelstein, P.L., Rosen, M.D., *et al*.: 'Demonstration of a soft x-ray amplifier', *Phys. Rev. Lett.* **54**, 110-113, 1985.
2. Suckewer. S., Skinner, C.H., Milchberg, H., Keane, C., and Voorhees, D.: 'Amplification of stimulated soft-x-ray emission in a confined plasma column', *Phys. Rev. Lett*. **55**, 1753-1756, 1985.

3. MacGowan, B.J., Maxon, S., Da Silva, L.B., *et al*.: 'Demonstration of x-ray amplifier near the carbon K edge', *Phys. Rev. Lett*. **65**, 420-423, 1990.

4. Nickles, P.V., Shlyaptsev, V.N., Kalacknikov, M., Schnurer, M., Will, I., and Sandner, W.: 'Short pulse x-ray laser at 32.6 nm based on transient gain in neon-like titanium', *Phys. Rev. Lett*. **78**, 2748-2751, 1997.

5. Keenan, R. Dunn, J., Patel, P.K., Price, D.F., Smith, R.F., and Shlyaptsev, V.N.: 'High repetition-rate grazing-incidence pumped x-ray laser operating at 18.9 nm', *Phys. Rev. Lett.* **94**, 103901, 2005.

6. Benware, B.R., Macchietto, C.D., Moreno, C.H., and Rocca, J.J.: 'Demonstration of a high average power tabletop soft x-ray laser', *Phys. Rev. Lett*. **81**, 5804-5807, 1998.

7. Takahashi, E.J., Kanai, T., Ishikawa, K.L., Nabekawa, Y., and Midorikawa, K.: 'Coherent water window x ray by phase-matched high-order harmonic generation in neutral media', *Phys. Rev. Lett*. **101**, 253901, 2008.

8. Ayvazyan, V., Baboi, N., Bahr, J. *et al.*,: 'First operation of a free-electron laser generating GW power radiation at 32 nm wavelength', *Eur. Phys. J. D* **37**, 297-303, 2006.

9. Shintake, T., Tanaka, H., Hara, T., *et al*.: A compact free-electron laser for generating coherent radiation in the extreme ultraviolet region', *Nature Photonics* **2**, 555-559, 2008.

10. Emma, P., Akre, R., Arthur, J. *et al*.: 'First lasing and operation of an angstrom-wavelength free-electron laser', *Nature Photonics* **4**, 641-647, 2010.

11. Kato, Y. and Kawachi, T.: 'Prospect of Laser-Driven X-Ray Lasers for Extention to Shorter Wavelengths', *Progress in Ultrafast Intense Laser Science **IV*** 215-232, Springer 2008.

12. Esarey, E., Ride, S.K, and Sprangle, P.: 'Nonlinear Thomson scattering of intense laser pulses from beams and plasmas', *Phys. Rev*. *E* **48**, 3003-3021, 1993.

13. Ta Phuoc, K., Rousse, A., Pittman, M., *et al*.,: 'X-ray radiation from non linear Thomson scattering of an intense femtosecond laser on relativistic electrons in a helium plasma, *Phys. Rev. Lett*. **91**, 195001, 2003.

14. Rousse, A., Ta Phuoc, K., Shah, R., *et al*.,: "Production of a keV x-ray beam from synchrotron radiation in relativistic laser-plasma interaction,' *Phys. Rev. Lett.* **93**, 135005, 2004.

15. Teubner, U. and Gibbon, P.: 'High-order harmonics from laser-irradiated plasma surfaces', *Rev. Mod. Phys.* **81**, 445-479, 2009.

16. Zhidkov, A. G., Koga, J., Sasaki, A., and Uesaka, M.: 'Radiation damping effects on the interaction of ultraintense laser pulses with an overdense plasma', *Phys. Rev. Lett*. **88**, 185002, 2002.

17. Bulanov, S. V., Esirkepov, T. Zh., and Tajima, T.: 'Light Intensification towards the Schwinger Limit', *Phys. Rev. Lett*. **91**, 085001, 2003.

18. Kando, M., Fukuda, Y., Pirozhkov, A. S., *et al.*: 'Demonstration of laser-frequency upshift by electron-density modulations in a plasma wakefield', *Phys. Rev. Lett*. **99**, 135001, 2007.

19. Pirozhkov, A. S., Ma, J., Kando, M., *et al.*: 'Frequency multiplication of light back-reflected from a relativistic wake wave', *Phys. Plasmas* **14**, 123106, 2007.

20. Kando, M., Pirozhkov, A. S., Kawase, K., *et al.*: 'Enhancement of photon number reflected by the relativistic flying mirror', *Phys. Rev. Lett*. **103**, 235003, 2009.

21. Bulanov, S. V., Inovenkov, I. N., Kirsanov, V. I., Naumova, N. M., and Sakharov, A. S.: 'Nonlinear depletion of ultrashort and relativistically strong laser-pulses in an underdense plasma', *Phys. Fluids B* **4**, 1935-1942, 1992.

22. Lee, K., Cha, Y. H., Shin, M. S., Kim, B. H., and Kim, D.: 'Relativistic nonlinear Thomson scattering as attosecond x-ray source', *Phys. Rev. E*, **67**, 026502, 2003.

23. Esirkepov, T. Zh., Kato, Y. & Bulanov, S. V.: 'Bow wave from ultraintense electromagnetic pulses in plasmas', *Phys. Rev. Lett.* **101**, 265001, 2008.

Part 5: High-harmonics

Generation of Ultrashort Attosecond High-Harmonic Pulses from Chirp-compensated Ne Harmonics

Dong Hyuk Ko[1], Kyung Taec Kim[1,2], Juyun Park[1], Jae-hwan Lee[1] and Chang Hee Nam[1]

[1]Department of Physics and Coherent X-ray Research Center, KAIST, Daejeon 305-701, Korea
[2] Advanced Photonics Research Institute and Center for Femto-Atto Science and Technology, GIST, Gwangju 500-712, Korea

Abstract. Near transform-limited 63-as high-harmonic pulses were successfully generated by compensating positive attosecond chirp of harmonics using negative group delay dispersion of Ar in broad spectral region. Without proper chirp compensation, the harmonic pulses were split into multiple peaks due to the large phase variation, in addition to the broadening of pulse duration. The chirp-compensated broadband harmonic pulses, approaching the transform-limited duration, will be very valuable for exploring ultrafast dynamics in atoms and molecules with high temporal resolution.

1 Introduction

High harmonics emitted from atoms driven by intense femtosecond laser pulses are a new kind of light source to explore ultrafast dynamics occurring in atoms and molecules [1]. Since high harmonics contain a very broad spectrum with odd harmonics, they can form attosecond pulses. The high harmonic pulses, however, contain inherent chirp coming from harmonic generation processes [2], broadening the pulse duration. The intrinsic chirp is also called as attosecond chirp (or atto-chirp). In order to produce transform-limited attosecond pulses, the chirp contained in the harmonic pulses should be compensated. As the chirp of high harmonics contributed from short trajectory components is positive, its compensation in a material with negative group-delay dispersion (GDD) was proposed [2] and realized using metallic [3,4] and gaseous media [5]. As the negative GDD in a material can be found only in certain limited wavelength regions, the application of this concept to broadband harmonics, necessary for very short attosecond pulse generation, is an important task to achieve.

J. Lee et al. (eds.), *X-Ray Lasers 2010,* Springer Proceedings in Physics 136,
DOI 10.1007/978-94-007-1186-0_20,

2 Intrinsic chirp of high harmonic pulses

High harmonics contain intrinsic chirp originating from recombination process of ionized electrons. The harmonic chirp structure is well explained by the three-step model [6,7]. The inherent chirp of harmonic pulses is related to the fact that the time of recombining electrons increases with higher electron energy, or equivalently harmonics with higher orders, in the case of short-path components [3]. Within one optical cycle of a driving laser pulse, the harmonic frequency increases from the minimum value at the time of 0.25 optical cycle and reach the maximum value at 0.7 optical cycle [2]. The increasing harmonic frequency with time induces the positive chirp of harmonic pulses. After passing the maximum value, the harmonic frequency, then, decreases down to the minimum level until the end of one optical cycle, generating the harmonics of long-path components; long-path harmonics form negatively chirped harmonic pulses. This characteristic temporal frequency-spreading of harmonic pulses exists in a harmonic pulse train that contains an attosecond pulse in every half-optical cycle.

Positively chirped attosecond pulses can be obtained from the short trajectory components of high harmonics. Even though high harmonics are divided by two kinds of frequency components, short path harmonics are dominantly remained after propagating the harmonic generation medium due to the better phase matching conditions compared to those of long-path harmonics. Since the long-trajectory electrons are driven for a longer time than the short-trajectory ones, they are strongly affected by the driving laser field that experiences the geometrically defocusing and temporally spreading effects, weakening long trajectory harmonics [8,9]. Consequently, positively chirped attosecond pulses can be effectively generated from the short-trajectory harmonics.

3 Chirp compensation of attosecond harmonic pulses

The positive chirp of high harmonics can be compensated by employing a material with negative GDD. Common chirp compensation methods for visible/infrared lights cannot be adopted for the compression of harmonic pulses due to the strong absorption in the soft X-ray region. On the other hand, materials, frequently used as X-ray filters for blocking laser pulses co-propagating with harmonics, have large negative GDDs suitable for compensating positive harmonic chirp. Gas media as well as solid metallic foils are also available for the chirp-compensation purpose. Since Ar has good transmittance and large negative GDD in broad spectral region, self-compression of harmonic pulses in Ar was successfully demonstrated,

obtaining transform-limited 206-as attosecond pulses [5]. In this work, we used a Be filter for blocking the co-propagating intense driving laser pulses, and an Ar cell, after the harmonic generation medium, for compensating the positive harmonic chirp to achieve near transform-limited attosecond pulses. The use of a gas medium, in stead of metallic foils, has advantages because a fine chirp tuning by adjusting gas pressure is possible during experiments and the transmission through the medium is much higher.

In order to produce chirp-compensated attosecond pulses, a two-gas-cell geometry was employed for the generation of broadband harmonics in Ne and the chirp compensation in Ar. The first gas cell was filled with Ne to increase the harmonic bandwidth. The Ar cell, placed away from the Ne cell, is used for the atto-chirp compensation. To characterize chirp-compensated attosecond pulses by applying the reconstruction of attosecond beating by interference of two-photon transition (RABITT) method [10], another time-delayed infrared laser pulses were overlapped with harmonic pulses, and focused together to an effusive Ne beam for photoelectron generation. For the measurement of photoelectrons generated by harmonic pulses superposed with infrared laser pulses, photoelectron spectra were acquired using a magnetic-bottle type time-of-flight spectrometer. The measured photoelectron spectra contained side-band peaks between photoelectron peaks generated by odd-order harmonics. The intensity modulation of the sideband peaks was clearly observed with time delay, which is the key element for the temporal reconstruction of attosecond harmonic pulses by the RABITT method.

4 Attosecond pulse compression using material dispersion in Ar

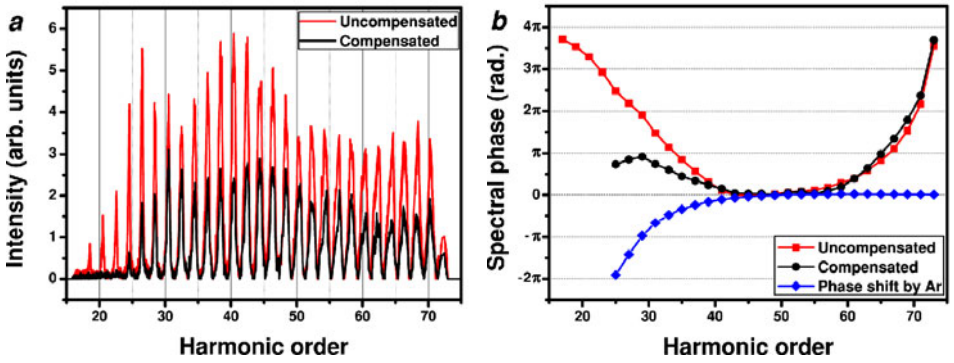

Fig. 1. Harmonic spectra and spectral phases of uncompensated and compensated harmonic pulses. (a) Photoelectron spectra obtained with and without chirp compensation are shown for the harmonics from the 17th to the 73rd order. (b) Spectral phases retrieved from the RABITT measurement for the uncompensated (red square) and compensated (black circle) cases are presented. The spectral phase shift gained while propagating through the 9-mm cell filled with 25 Torr Ar is also shown (blue diamond).

Attosecond harmonic pulses without Ar were analyzed prior to the chirp compensation. The photoelectron spectrum without streaking laser pulse is presented in Fig. 1(a), showing broadband harmonics from the 17th to the 73rd order. The measured spectral phase of Ne harmonics by RABITT method was shown in Fig. 1(b) as red squares, representing a large quadratic curve due to the positive chirp of harmonic pulses. Even though the overall spectral bandwidth was sufficient for achieving transform-limited attosecond pulses with duration of 45 as, the reconstructed temporal profile of the harmonic pulse without chirp compensation contains a multi-peaked structure with a 160-as main pulse, as shown in Fig. 2 as a red dotted line, owing to the large attosecond chirp. The spectral phase analysis probed that the first peak was composed of low-frequency harmonics from the 19th to the 45th order and the second main peak contained high-frequency components from the 47th to the 61st order. Consequently, the compensation of attosecond chirp should be performed to produce attosecond harmonic pulses, close to the transform-limited duration. If not, the intrinsic chirp of high harmonics causes a multi-peaked profile, in addition to a temporal broadening of attosecond pulses.

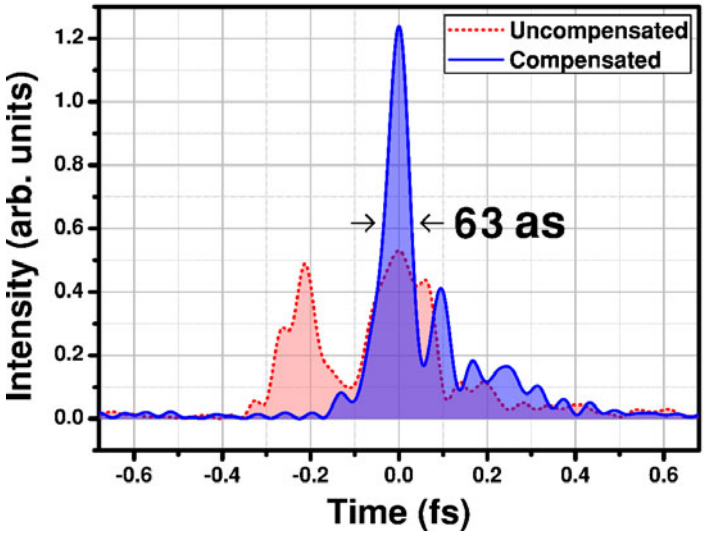

Fig. 2. Reconstructed temporal profiles of harmonic pulses with and without chirp compensation. The uncompensated harmonic pulse (red dotted line) shows multi-peak profile with broadened pulse duration. The compensated harmonic pulse (blue solid line) shows a 63 as pulse, while the transform-limited value is 47 as.

In order to shorten the duration of attosecond pulses, harmonic chirp was compensated by utilizing the material dispersion property in Ar. The temporal characterization was performed with different Ar pressures to figure out the optimal conditions for chirp compensation. The shortest attosecond pulse was

produced with an Ar pressure of 25 Torr. The harmonic spectrum and retrieved spectral phase of the compensated harmonic pulses are presented in Figs. 1(a) and (b), respectively. The harmonics, lower than the 25th order, were strongly absorbed by Ar, increasing the transform-limited duration to 47 as. Figure 1(b) shows that the spectral phase variation below the 41st order decreased dramatically because of the negative GDD of Ar, indicating that the chirp compensation of harmonic pulses was quite effective in the low-frequency region. The spectral phase shift gained while propagating through the 9 mm cell filled with 25 Torr Ar is also shown in Fig. 1(b), which matches well the spectral phase difference between the chirp-compensated and uncompensated attosecond pulses. The spectral phase in Fig. 1(b) shows that the chirp compensation is effective up to the 40th order; however, it shows that the spectral phase variation of the harmonic pulse is less than π up to around the 65th order. This means that a much larger number of harmonics can participate in the short pulse formation through the coherent addition of harmonics than that expected from the range of chirp compensation by Ar. The RABITT analysis clearly showed that the broader participating harmonics resulted in the generation of 63 as pulses, as shown in Fig. 2, corresponding to 1.2 optical cycles. The small satellite peaks in Fig. 2 appeared mainly from the harmonics near 70^{th} orders that were strongly affected by the high-frequency edge of the Be transmission window with large positive GDD. It is noted that the peak intensity of the compensated case became stronger than that of the uncompensated case in Fig. 2, even though the harmonic intensity was reduced to about half of the uncompensated case due to better synchronization of harmonics. Consequently, near transform-limited attosecond high-harmonic pulses, much stronger than the uncompensated case, were generated by achieving effective atto-chirp compensation.

5 Conclusion

Near transform-limited attosecond pulses with duration of 63 as were successfully generated from broadband Ne high harmonics with atto-chirp compensation. The intrinsic positive chirp of high harmonics was effectively compensated by employing a gas medium with negative GDD. As there are a range of gas media, such as Ar, Kr and Xe, that have different spectral regions with large negative GDD, a suitable gas species should be selected to cover an appropriate spectral range for the generation of chirp-compensated harmonic pulses. Since the method of chirp compensation in a gaseous medium is not limited to the generation of transform-limited attosecond pulse trains, it is equally well applicable for the chirp compensation of isolated attosecond pulses generated by using intense few-cycle pulses [11]. The generation of near transform-limited attosecond pulses will be an essential method to improve the temporal resolution in attosecond science for observing electron

dynamics in atoms and molecules.

References

1. Krausz, F. and Ivanov, M.: 'Attosecond physics', *Rev. Mod. Phys.*, 81, 163-234, 2009
2. Mairesse, Y. *et al*.: 'Attosecond Synchronization of High-harmonic Soft X-rays', *Science*, 302, 1540-1543, 2003
3. Kim, K. T., Kim, C. M., Baik, M., Umesh, G., Nam, C. H.: 'Single sub-50-attosecond pulse generation from chirp-compensated harmonic radiation using material dispersion', *Phys. Rev. A*, 69, 051805(R), 2004
4. Lopez-Martens, R. *et al*.: 'Amplitude and Phase Control of Attosecond Light Pulses', *Phys. Rev. Lett.*, 94, 033001, 2005
5. Kim, K. T., Kang, K. S., Park, M. N., Imran, T., Umesh, G., Nam, C. H.: 'Self-Compression of Attosecond High-Order Harmonic Pulses', *Phys. Rev. Lett.*, 99, 223904, 2007
6. Corkum, P. B.: 'Plasma perspective on strong field multiphoton ionization', *Phys. Rev. Lett.*, 71, 1994-1997, 1993
7. Lewenstein, M., Balcou, P., Ivanov, M. Y., L'Huillier, A., Corkum, P. B.: 'Theory of high-harmonic generation by low-frequency laser fields', *Phys. Rev. A*, 49, 2117-2132, 1994
8. Kim, H. T., Kim, I. J., Lee, D. G., Hong, K., Lee, Y. S., Tosa, V., Nam, C. H.: 'Optimization of high-order harmonic brightness in the space and time domains', *Phys. Rev. A*, 69, 031805, 2004
9. Salières, P. *et al*.: 'Feynman's Path-Integral Approach for Intense-Laser-Atom Interactions', *Science*, 292, 902-905, 2001
10. Paul, P. M., Toma, E. S., Breger, P., Mullot, G., Augé, F., Balcou, P., Muller, H. G., Agostini, P.: 'Observation of a Train of Attosecond Pulses from High Harmonic Generation', *Science*, 292, 1689-1692, 2001
11. Goulielmakis, E. *et al*.: 'Single-Cycle Nonlinear Optics', *Science*, 320, 1614-1617, 2008

An intense kHz and aberration-free two-colour high harmonic source for seeding FEL and XRL

G. Lambert[1*], J. Gautier[1], C.P. Hauri[2], F. Tissandier[1], C. Valentin[1], A. Barszczak Sardinha[1, 3], M. Fajardo[3], T. Marchenko[1], J.Ph. Goddet[1], M. Ribiere[1], G. Rey[1], S. Sebban[1] and Ph. Zeitoun[1]

[1] Laboratoire d'Optique Appliquée, ENSTA Paristech-CNRS-École Polytechnique Paristech, Chemin de la Hunière, 91761 Palaiseau, France
[2] Paul Scherrer Institute, 5232 Villigen, Switzerland
[3] Centro de Física dos Plasmas / Instituto Superior Técnico, Av. Rovisco Pais, 1049-001 Lisboa, Portugal
*E-mail address: guillaume.lambert@ensta.fr

Abstract. Free-electron lasers (FEL) and soft X-ray lasers (SXRL) have been recently evolving very fast in the extreme-ultraviolet to soft X-ray region. Once seeded with high harmonics (HH), these light sources deliver amplified emissions with properties which are, for most of them, directly linked to the injected HH beam, e.g. the ultrashort pulse duration for FEL and the high temporal and spatial degree of coherence for both. Here we present a detailed experimental study of a kHz two-colour (fundamental + second harmonic) HH generation and investigate its potential as a suitable evolution of the actual seeding sources. It turns out that this source (both odd and even harmonics) is highly tuneable, and delivers intense radiations with only one order of magnitude difference in the photon yield from 65 nm to 13 nm. We also observed an astonishing "aberration-free" character of these harmonics (aberration below λ/17 rms, λ=44 nm). Then, the implementation of this technique on seeded FEL and XRL would allow amplification to be achieved at wavelengths shorter than previously accessible.

1 Introduction

Seeding FEL [1] and SXRL [2] with High Harmonics generated in gas from the EUV to the soft X-ray region is a quite recent but emerging topic. Indeed, it has already opened significant perspectives for developing the future ultimate relatively compact coherent jitter-free and aberration-free source in order to observe the ultrafast dynamics of matter at nanometre scale. Seeding relies on benefits from the high-quality properties of the HH source, particularly the ultrashort pulse duration or the high degree of spatial and temporal coherence.

J. Lee et al. (eds.), *X-Ray Lasers 2010,* Springer Proceedings in Physics 136,
DOI 10.1007/978-94-007-1186-0_21,

As most of the applications are aiming in the wavelength range from soft to hard X-ray, valuable HH seed intensity is required in this spectral range, where unluckily the efficiency of the classical harmonic generation, from 800 nm Ti: Sa laser system, has a sharp decrease. In addition, for seeding a FEL, the injected peak power must overcome the electron beam shot noise, which is inversely proportional to the wavelength of emission. Finally, HH seeding should not have any constrain on the machine performances. This is why there is an urgent need of developing new HH sources, more intense at shorter wavelengths, with higher repetition rates, larger tuneability, lower distortions, and various polarizations.

We present here a detailed experimental study of a HH technique, which could allow to fulfil all the requirements, in which the harmonics are generated with an orthogonally polarized two-colour laser field [3]-[4], consisting of mixing the fundamental frequency (ω) and its second harmonic (2ω) generated in a Beta Barium Borate (BBO) crystal.

2 High harmonics generated in a two-colour field

While in classical harmonic generation electrons are extracted, accelerated and can be recombined in a radiative process every half optical cycle of the IR driving laser field, in a two-colour field all the events occur only once every optical cycle. As a consequence, spectra do no more present only odd harmonics but also even harmonics, corresponding to the odd harmonics naturally generated by 2ω ($2\times(2n+1)$), and to the harmonics coming from the mixing itself ($2\times(2n)$). "n" is an integer.

Second, there is a "redshift" of the whole spectrum, i.e. a shifting to lower harmonic orders of the cut-off, the region where the number of photons starts to decrease rapidly due to the presence of the 2ω element.

Third, the efficiency of generation can be highly increased, as the specific moment when the electrons are released from the atom corresponds to a 10 times higher ionisation rate than with the single-colour field [5].

3 Experimental set-up

The two-colour harmonic generation experiment has been performed at the Laboratoire d'Optique Appliquée (France) by means of a kHz Ti: Sa laser system at 800 nm (ω) delivering maximum of 7 mJ energy in 35 fs pulses. Fig. 1 presents a scheme of the set-up. In order to generate the 400 nm radiation (2ω), a BBO (type 1, 100 μm thickness) doubling crystal, is directly inserted in the IR beam path between a 1.5 m focusing lens and a gas cell. In this

geometry, the second harmonic component propagates along the same axis as the IR beam, and consequently the spatial overlap between the ω and 2ω parts is automatically achieved in the active medium. Our frequency doubling geometric configuration is then completely straightforward and as a result, it can be easily implemented in HH seeding schemes. Moreover, the polarisation of the second harmonic is in this case perpendicular to the polarisation of the fundamental frequency, which corresponds to the situation of most efficient harmonics generation, according to latest results [3]. Finally, due to the group velocity mismatch between ω and 2ω in the non-linear crystal, the IR beam is delayed (by 18.7 fs for 100 μm thick BBO) compared to the blue beam.

The system for detecting the harmonic intensity content is based on a spectrometer and a solar blind XUV photodiode calibrated in absolute energy. The wave front distortions have been measured in the axis of the harmonic emission with a soft X-ray homemade Hartmann wave front sensor [6] composed of equidistant tiny holes, from which diffracted beamlets are projected and recorded onto a CCD camera. Then, the position of each spot centroïd is compared with the respective reference position determined by a non-aberrant beam. Since the sensor is achromatic, one usually measures the wave front of the polychromatic HH beam. Two thin aluminium filters, are finally added to prevent the IR beam from propagating to the different CCD cameras, but they also drastically suppress the HH signal below 17 nm.

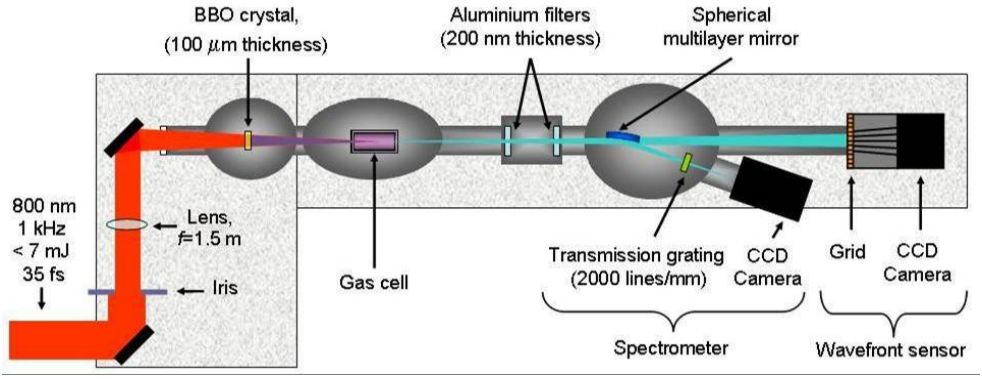

Fig. 1. Top view. Layout of the spectrum and wave front measurement experiment of the kHz two-colour high harmonic generation source.

4 Typical evolutions of spectra

For any type of neutral gas classically used for HH generation, the two-colour effects are visible. To be more precise, Fig. 2 (right) perfectly illustrates the three major evolutions: double harmonic content, redshift and increase of efficiency of generation.

High factor of increase is here observed, even when keeping the same optimisation parameters as for ω. Spectra present a relatively flat distribution (an intensity ratio from odd to even harmonics close to one), and the intensification arises over the whole spectrum. Also this enhancement is clearly dependent on the considered gas, typically He (×~100), Ne (×~25), Ar (×~0.5), Kr (×~0.5) and Xe (×~0.5). For gases typically rather efficient like argon, krypton and xenon, there could even be actually a decrease of the maximum harmonic signal by a factor of 2.

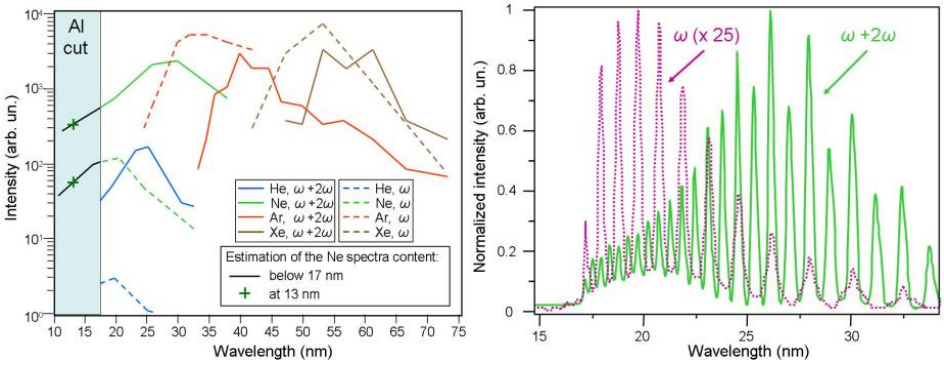

Fig. 2. Left: Schematic representation of the achieved HH experimental intensity for different gases, with either ω or ω+2ω technique and with same optimisation parameters as for ω. Right: zoom on the neon gas.

5 Flux and wave front optimisation

Figure 3 presents spectra and corresponded wave front patterns of the HH source generated from argon gas target in various configurations to optimize both HH intensity and wave front.

First and foremost, just at ω, the harmonic yield has been maximised by clipping the IR beam [7] with an iris of 20 mm aperture; a compromise is performed between considerations of focal geometry and ionisation (for small apertures) and harmonic dipole amplitude and phase (for large apertures). Compared to the fully open IR beam case (40 mm diameter at $1/e^2$), aberrations are decreased by a factor of 6, as the highest components of deformation located in the outer part of the driving laser beam are removed, to λ/6 rms ((2) with λ=37.5 nm, the first main component of the spectrum from red curve of (1)).

In contrast, the two-colour high harmonic generation for a full aperture beam delivers radiations with low aberration properties, λ/5 rms ((3) with λ=44.5 nm, the first major component of the spectrum from the blue curve of (1)), i.e. equivalent to three times the diffraction limit. Moreover high increase of the harmonic yield is observed, reaching tens of nJ per pulse for the

2x(2n+1) orders. Actually the parameters of harmonic yield optimisation for the mixing case are quite different from those employed before: 30 mbar to 16 mbar of pressure inside the gas cell and 8 mm to 4 mm of gas cell length.

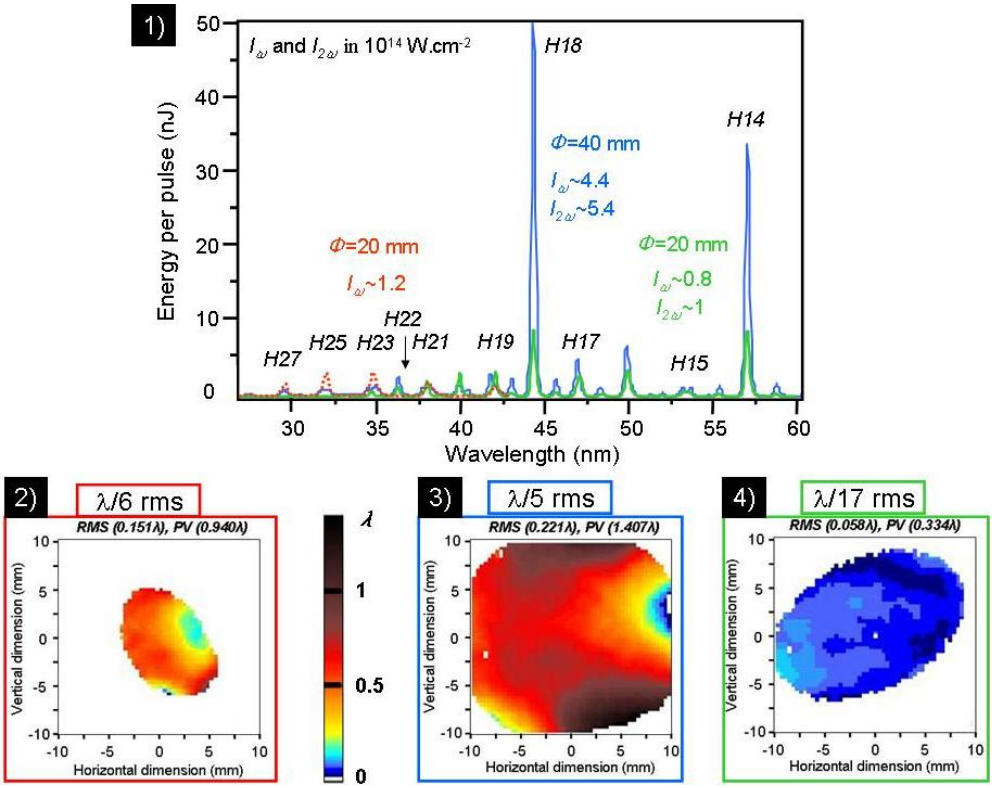

Fig. 3. 1) Normalised HH spectra obtained in argon gas for different conditions of generation, either with ω or ω+2ω and for different driving laser beam diameter apertures (Φ) and intensity at ω and 2ω. Down: wave front distortion amplitudes recorded on the wave front sensor (λ(ω)=37.5 nm and λ(ω+2ω)=44.5 nm). (2) ω technique, Φ=20 mm. (3) ω+2ω technique, Φ=40 mm. (4) ω+2ω technique, Φ=20 mm.

Then, when clipping the IR beam with the same iris aperture as used for ω (20 mm), the generated harmonic beam is now totally free from aberration, with residual deformations at λ/17 rms ((4) with λ=44.5 nm), but the efficiency of generation partly decreased as the iris limits here the available blue energy. Such a very low aberration value has been explained with a spatial filtering of the driving laser wave front by the blue waist which is 1.4 times smaller compared to the IR one in our geometry [8]. This has been proved by evaluating the HH waist values in both cases, accessible here by retro propagating the electric field from the wave front sensor, delivering the HH phase and intensity distribution.

6 Conclusions

In summary, combining this technique with seeding schemes in FEL or SXRL instead of classical harmonic generation is very promising as higher flux and tuneability are provided. Also, as the HH wave front will largely determine the optical quality of the amplified beam, and as the key parameter for these configurations is the energy contained in the diffraction-limited portion of the beam (as well as for phase-imaging experiments) the aberration-free character of the source constitutes a very advantageous solution.

To conclude, in order to attain hard X-ray radiations, the use of higher fundamental wavelength lasers, such parametric amplifiers (1.2-1.5 μm [9]), coupled to the two-colour strong increase effect observed in Ne or He gases, is expected. The so-called water-window (~2-4 nm), vital for the study of biological samples, and perhaps even the Angström region (0.1 nm) could be then reached.

References

1. Lambert, G. et al.: 'Injection of harmonics generated in gas in a free-electron laser providing intense and coherent extreme-ultraviolet light', *Nature Physics*, 4, 296, 2008
2. Zeitoun, P. et al.: 'A high-intensity highly coherent soft X-ray femtosecond laser seeded by a high harmonic beam', *Nature*, 431, 426-429, 2004
3. Kim, IJ. et al.: 'Generation of submicrojoule high harmonics using a long gas jet in a two-color laser field', *Appl. Phys. Lett*., 92, 021125, 2008
4. Lambert, G. et al.: 'A kHz two-colour high harmonic source for seeding free-electron lasers and plasma-based soft X-ray lasers', *New journal of physics*, 11, 083033, 2009
5. Kim, CM. et al.: 'Generation of a strong attosecond pulse train with an orthogonally polarized two-colour laser field', *Phys. Rev. A*, 72, 033817, 2005
6. Mercere, P. et al.: ' Hartmann wave-front measurement at 13.4 nm with $\lambda_{EUV}/120$ accuracy', *Opt. Lett.* 28, 1534, 2003
7. Kazamias, S. et al.: 'High order harmonic generation optimization with an apertured laser beam', *Eur. Phys. J. D*, 21, 353, 2002
8. Lambert, G. et al.: 'Aberration-free high harmonic source generated with a two-colour field', *Eur. Phys. Letter*, 89, 24001, 2010
9. Shan, B. et al.: 'Tunable high harmonic generation with an optical parametric amplifier', *Appl. Phys. B*, 74, 23–26, 2002

Tuning of High-Order Harmonics for Soft X-Ray Laser Seeding

B. Ecker[1,2,3], B. Aurand[1,3,4], D.C. Hochhaus[1,4,6], T. Kuehl[1,3], B. Zielbauer[1,2], D. Zimmer[1,3,5], J. Seres[7], C. Spielmann[7]

[1] GSI Darmstadt, Germany
[2] Helmholtz Institute Jena, Germany
[3] Johannes Gutenberg University Mainz, Germany
[4] EMMI, GSI Darmstadt, Germany
[5] Université Paris Sud 11, France
[6] Johann-Wolfgang-Goethe University Frankfurt, Germany
[7] Friedrich Schiller University Jena, Germany

Abstract. Within this work we present results of an experimental campaign studying the influence of the adiabatic and non-adiabatic blue shift on high-order harmonic (HH) radiation spectra. The results demonstrate that we are able to spectrally tune the HH radiation to cover more than 50% of the spectrum between 17 nm and 35 nm, paving the way to performing injection-seeded soft X-ray laser (SXRL) experiments with Mo, Zr and Y.

1 Motivation

During the last years the SXRL research at GSI has been centered on developing new pumping schemes and more compact and stable experimental designs [1-5]. The goal of these efforts is to supply a versatile tool to perform spectroscopy on heavy, highly charged ions accumulated in the experimental storage ring (ESR) at GSI [6], as it has already been performed by the use of optical lasers on singly charged ions [7,8]. Additionally, a SXRL as a diagnostic tool is of interest for the new storage ring NESR, which is part of the upcoming FAIR facility. However, due to the fact that SXRL are based on amplification of spontaneous emission (ASE), the beam quality in terms of spatial profile, spatial coherence, beam divergence and pointing stability is not comparable to conventional lasers based on resonators. This disadvantage can be circumvented by seeding the SXRL medium with high-order harmonic radiation [9-12]. The beam quality of a HH source is basically depending on the beam quality of the driving laser and therefore much higher compared to SXRL. Seeded SXRL thus benefit from the superior beam quality of HH radiation and the high gain of the SXRL medium and therefore present a variegated tool not only for spectroscopy. One of the key requirements for seeding soft X-ray lasers by use of HH radiation is the spectral overlap

J. Lee et al. (eds.), *X-Ray Lasers 2010,* Springer Proceedings in Physics 136,
DOI 10.1007/978-94-007-1186-0_22,

between one of the harmonic lines and the given SXRL transitions. This can be achieved in various ways, the most straight-forward solution being the choice of a suitable fundamental wavelength to create the HH. This solution can easily be implemented on Ti:Sa laser systems due to the large gain bandwidth of the amplification medium. However, when dealing with a Nd:glass laser system like PHELIX at GSI, this topic becomes a major challenge since, compared to a Ti:Sa system, the fundamental wavelength is rather fixed. The tuning of the HH lines must be performed by controlling the details of the HH generation itself.

2 Spectral Tuning of the HH radiation

The generation process of HH radiation can be depicted in the semi-classical frame of the three-step model. First, the atom is tunnel-ionized by an intense laser field. The freed electron is accelerated, leaving the vicinity of its parent ion. At a certain point in time after the change of sign of the laser field, the electron will change the direction of propagation and return to the ion. Finally, the electron recombines with the ion, emitting a photon with an energy corresponding to the kinetic energy gathered by the acceleration process and the contribution of the ionization potential of the ion. A more detailed analysis shows that there are two possible paths the accelerated electrons might follow, which are referred to as the long and the short trajectory. Depending on the path p an electron follows, it gathers a different amount of additional dipole phase $\phi_{k,p}$, which itself depends on the harmonic order k. The additional phase term leads to a spectral shift referred to as non-adiabatic shift [13], $\delta\omega_{k,p} = \partial\phi_{\mathrm{k,p}}/\partial t \propto \alpha_{k,p}\,\partial I/\partial t$, and depends on the temporal deviation of the driving laser pulse intensity. This quantity can be accessed in experiments by changing either the pulse energy, pulse duration or the position of the gas tube with respect to the focal spot. A second process that causes a spectral blue shift is the adiabatic shift [14]. Due to the strong ionization already during the leading edge of the laser pulse the gas medium forms a plasma. The remaining part of the laser pulse propagates in this medium with a time-varying index of refraction, causing a HH blue shift that can be written in the form $\delta\omega_k^{ad} = \frac{1}{2}\frac{\omega_p^2 L}{c}\frac{dZ}{dt}\cdot\left(\frac{k}{\omega_1}+\frac{1}{k\omega_1}\right)$, with the plasma frequency $\omega_p = \sqrt{e^2 n_e/(\varepsilon_0 m_e)}$ and the fundamental frequency of the laser ω_1. L and dZ/dt denote the length of the plasma and its ionization rate, respectively. The adiabatic shift is therefore proportional to the free electron density n_e,

which can easily be controlled in an experiment by the applied gas pressure. It affects both the short and the long trajectory in same way. The experiment described in the following aimed at analyzing these two effects and ascertain possible SXRL target materials for injection-seeding experiments.

3 Experimental Setup

The HH radiation source is driven by the front-end of the PHELIX laser system, which delivers 7 mJ of pulse energy at 1054 nm center wavelength at a repetition rate of 10 Hz. The pulses are compressed by two subsequent grating compressors to 350 fs. Being focused by either a 60 cm or 40 cm lens, maximum intensities of 3e14 W/cm² and 7e14 W/cm² is reached in the focal spot, respectively. The gas target for creating the HH radiation consists of a Ni tube of 2mm inner diameter, connected to a pulsed valve which is synchronized with the laser pulses. The backing pressure is controlled by another electronic valve that allows for precise adjustment between 50 mbar and 1200 mbar. The position of the gas tube with respect to the focal spot is controlled by a linear translation stage equipped with a stepper motor, resulting in micrometer precision. The spectrometer used is built in-house and is based on a grazing-incidence flat-field grating (Hitachi, 1200 l/mm) and a back-illuminated CCD camera (Andor DX420, 1024 × 256 pixels). The achieved spectral resolution is approximately 0.02 nm/pixel, and the spectral range recorded runs from 36.5 nm to 17.1 nm, limited on the short-wavelength side by the aluminum edge which arises due to two 200 nm thick aluminum filters that are used to block the fundamental laser light.

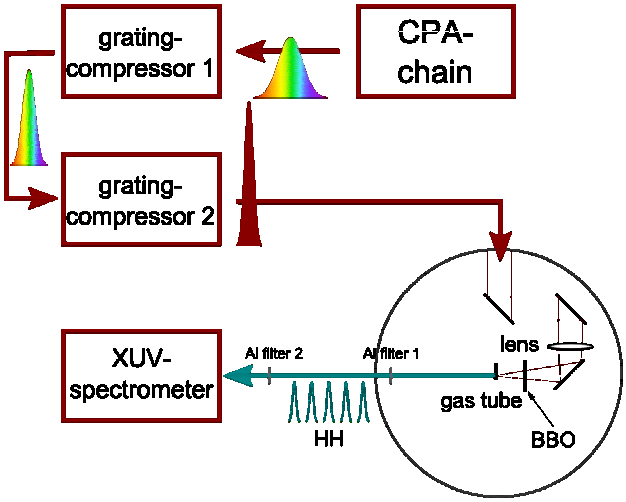

Fig. 1. Experimental setup. The laser pulses generated by the PHELIX front-end are compressed and focused into a Ni tube which is connected to a gas valve. The generated high-order harmonic radiation is detected in an in-house built spectrometer [15].

4 Experimental Results

As described above, it is possible to influence the contribution of the short and the long-trajectory electrons to the HH signal by varying the position of the gas tube with respect to the focal spot. An experimental verification of this behavior is illustrated in figure 2, which shows the result of a tube position scan along the beam axis. The zero position indicates the location of the focal spot, positive numbers correspond to a displacement along the propagation direction of the laser. At negative values the contribution of the long path is put in favor. The lower-order harmonic lines are broadened and blue shifted compared to the HH emission measured at positive values, where the contribution of the short trajectory is dominating. Here the harmonic spectra are slightly more intense and reach a higher cut-off energy.

Tuning of the higher-order harmonics can be reached by varying the applied pressure. Figure 3 shows the results of a pressure scan performed at -2.7 mm, before the focal spot. The harmonic lines are significantly broadened and shifted as the pressure increases, reaching and partly exceeding the neighboring even harmonic.

The combination of these two effects allow for covering over 50% of the spectral range between 17 nm and 35 nm, enabling us to match harmonic lines with several SXRL transitions in this spectral regime. A more detailed analysis of the experimental results, including a study on the correlation between the spectral shape and the pump laser intensity, as well as a more

quantitative theoretical description of the observed line broadening and shift can be found in D.C. Hochhaus, APB 100, 2010 [15].

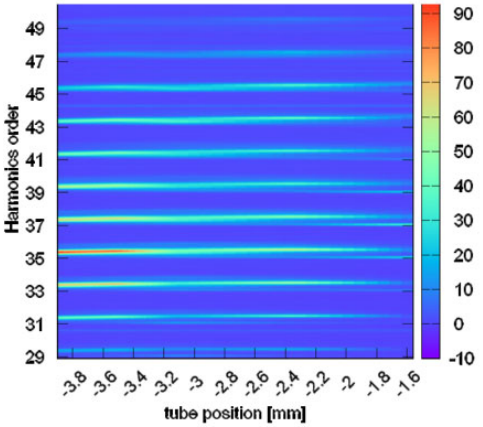

Fig. 2. The strong adiabatic shift tunes the HH radiation even beyond the neighboring even harmonic line. Measurement performed at 600 mbar at full laser intensity.

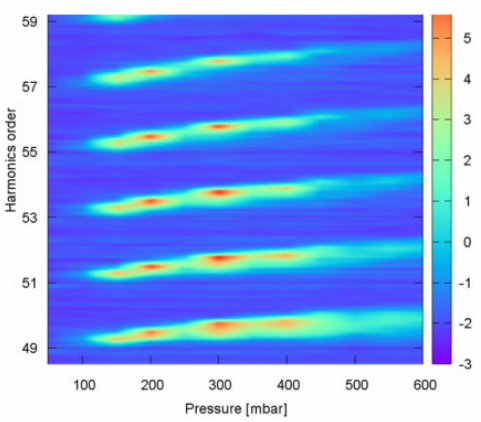

Fig. 3. The non-adiabatic shift influences mainly the HH emission of the long trajectory. Measurement performed at -2.7 mm at full laser intensity.

5 Conclusions and Outlook

The dominant mechanism responsible for the observed spectral blue-shift at lower and intermediate orders was identified as the non-adiabatic shift that affects the HH radiation emitted by electrons following the long trajectory. Higher-order emission from both the short and the long trajectory was controlled by the adiabatic frequency shift. Making use of both mechanisms we were able to cover more than 50% of the spectral range between 17 nm and 35 nm.

In this way, the generated HH radiation can be matched to several Ni-like SXRL transitions, amongst others Mo (18.9 nm), Zr (22.0 nm) and Y (24.0 nm), three of the routine SXRL elements available at GSI. This paves the way for injection-seeding experiments.

References

1. D. Zimmer et al., *Optics Express* 16, 10398 (2008)
2. D. Zimmer et al., *Opt. Lett.* 35, 450 (2010)
3. D. Zimmer, D. Ros et al., *o* 82, 013803, (2010)
4. D. Zimmer, PhD Thesis 2010, http://ubm.opus.hbz-nrw.de/volltexte/2010/2329/
5. B. Ecker, Diploma Thesis 2008
6. A. Gumberidze et al., *Nucl. Instrum. Meth. Phys. Res., Sect. B, Beam Interact. Mater. Atoms* 267, 248 (2009)
7. G. Ewald et al., *Phys. Rev. Lett.* 93, 113002 (2004)
8. R. Sánchez et al., *Phys. Rev. Lett.* 96, 033002 (2006)
9. Ph. Zeitoun et al., *Nature* 431, 426 (2004)
10. Y. Wang et al., *Nature Photonics* 2, 94 (2008)
11. T. Ditmire et al., *Phys. Rev. A* 51, R4337 (1995)
12. N. Hasegawa et al., *Jap. J. Appl. Phys*. 48, 012503 (2009)
13. H. Shin, D. Lee, Y. Cha, J.-H. Kim, K. Hong, C. Nam, *Phys. Rev. A* 63, 053407 (2001)
14. S.C. Rae, K. Burnett, J. Cooper, *Phys. Rev. A* 50, 3438 (1994)
15. D. C. Hochhaus et al., *Appl. Phys. B* 100,711 (2010)

Generation of Small Band Width Coherent Extreme Ultraviolet Radiation and Its Application

L.V. Dao, S. Teichmann, K.B. Dinh, and P. Hannaford

Centre for Atom Optics and Ultrafast Spectroscopy, Australian Research Council Centre of Excellence for Coherent X-Ray Science, Swinburne University of Technology, Melbourne, Australia 3122;

Abstract. We are able to generate by high-harmonic generation (HHG) just a few harmonic orders in the spectral range 10 - 35 nm with a photon flux of ~ 2.10^{12} photons/(harmonic cm^2 s) for argon and ~ 10^{10} photons/(harmonic cm^2 s) for helium. The few-harmonic-order radiation is used for coherent diffractive imaging directly or with a small band-width mirror. A spatial resolution down to 50 nm can be achieved.

1 Introduction

Coherent extreme ultraviolet (XUV) radiation can now be produced by high-order harmonic generation (HHG) of highly energetic femtosecond laser pulses in noble gases [1-3]. Such table top sources will complement large installations such as X-ray free-electron lasers (XFELS) currently under development. The unique properties of HHG emission present opportunities for new applications in atomic and molecular spectroscopy, condensed matter physics, imaging on the nano- and subnano-scale, and plasma physics [4-6]. The brightness (which is related to the conversion efficiency from the near-infrared laser light to XUV light), the spatial and temporal coherence properties and the photon energy are important properties of the source from the point of view of potential applications. The main challenge for the field at this time is to improve and control the properties of the source and to enhance the photon flux and degree of coherence.

Significant enhancement of the efficiency of HHG has been achieved by several groups through quasi phase-matching and the "absorption limit" for which re-absorption limits the effective length of the medium has now been reached. However, the conversion efficiency depends on the HHG configuration even within the absorption limit and the ultimate optimization conditions are still far from being fully characterized.

For many applications, such as coherent diffractive imaging (CDI) [7,8], a monochromatic beam or a beam with a narrow and well characterized bandwidth is an important requirement of the source. In conventional CDI it is normally assumed in the image reconstruction that the source is

J. Lee et al. (eds.), *X-Ray Lasers 2010,* Springer Proceedings in Physics 136,
DOI 10.1007/978-94-007-1186-0_23,

monochromatic with $\lambda/\Delta\lambda > 1000$ [7]. Since the HHG source consists of many harmonic orders, the above assumption represents a fundamental limitation of the applicability of CDI to imaging. A spectrometer is typically used to select the monochromatic radiation; however the transmission of spectrometers in the XUV region is low. The generation of just a few harmonics, and especially a single harmonic, that can be used directly without any spectral selection would be very advantageous for such applications.

In this paper we show that a semi-infinitive gas cell can be used to generate a high flux of narrow-bandwidth coherent XUV HHG radiation. We also demonstrate that the small bandwidth multi-wavelength HHG sources can be applied to produce very high quality coherent diffractive images.

2. Experiments

A 1 kHz multi-stage multi-pass chirped-pulse amplifier laser system, which produces 5 mJ pulses with a duration of 30 fs centred at 805 nm, with beam diameter 15 mm and beam quality $M^2 \sim 1.6$, is used for the HHG experiment. The detailed experimental arrangement for generation and detection of the XUV radiation has been published elsewhere [3]. The laser pulses are focussed by a 300 mm focal length lens into a 200 mm-long gas cell with 150 μm pinholes at the exit which are also used to isolate the vacuum chamber from the gas-filled cell. The pressure in the vacuum chamber outside the 10 mm-long gas cell is kept at $< 1 \times 10^{-3}$ Torr. The beam radius at the focus is about 50 μm and the Rayleigh length is 10 mm. The effective peak intensity at the focus is approximately $5 \times 10^{14} - 10^{15}$ W/cm^2. An aperture with variable diameter, which is placed in the path of the laser beam before the focussing lens, has a strong influence on the intensity and beam profile of the HHG signal [3]. The influence of the size of the aperture is attributed to the effective f-number, the spatial quality of the laser beam and the peak intensity in the focus area. The variation of the aperture introduces phase variations in the laser wave-front that can be used to minimize the mismatch between the laser phase and the intrinsic phase of the harmonics. The high harmonics created on-axis or close to the optical axis pass through a 200 nm-thick aluminium (Al) or zirconium (Zr) filter, which removes the fundamental beam. A very broad range of XUV wavelengths (2 – 80 nm) can be analyzed with high spectral resolution by a grazing incidence XUV spectrometer equipped with a set of four different gratings (150, 300, 600 and 1200 grooves/mm).

For coherent diffractive imaging the sample is mounted on a holder inside an experimental vacuum chamber. The diffraction pattern is detected with a CCD camera (Princeton Instruments) having a 1340 x 1300 array of 20 μm

pixels or a 1024 x 1024 array of 13 μm pixels. The distance between the CCD and the sample is < 6.5 cm. To further reduce scattered light a 5 mm diameter aperture is placed directly downstream from the sample. As a test target we have used a regular pinhole sample. The sample is micro-machined in a thin (~100 nm) gold layer on a Si_3N_4 substrate and exhibits an array of 2 μm-diameter pinholes spaced by 3 μm and arranged in the form of a 20 μm-diameter circle.

i) Generation of few harmonic orders

The intensity of the qth harmonic order in a non-absorbing gas scales as $I_q \propto N_a^2 sinc^2(\Delta k l_{eff})$ [1], where $sinc(x) = \sin(x)/x$, N_a is the atom density, l_{eff} is the effective interaction length between the fundamental laser field and the nonlinear medium, and Δk is the phase mismatch between the fundamental and harmonic field. If the atomic response is constant or varies only slightly over a propagation length that corresponds to the coherence length and the phases between the fundamental and harmonic field are matched, then the harmonic intensity scales as $I_q \propto N_a^2$ or $I_q \propto p^2$, where p is the pressure of the generating gaseous medium. Also, the harmonic intensity will scale as $I_q \propto \Delta z^2$ with increasing interaction length Δz.

The dependence of the intensity for all harmonics for argon and helium gas at the focus point of the laser relative to the exit pinhole of the cell is shown in the Fig. 1 and Fig. 2, where positive distance indicates that the focus position is in the gas cell. Typical XUV HHG spectra are shown in the inset of Fig. 1 and Fig. 2. For these measurements all parameters except the focus position are kept constant. The number of harmonics, the relative intensity and the beam profile are optimized by varying the focus position of the lens, the gas pressure and the size of the aperture. The variation of these parameters influences the atom density and the ionization, and thus macroscopic phase matching can be achieved for a certain interaction length for a few harmonic orders near the cut-off region.

The inset of figure 1 shows the intensity dependence on the pressure in the argon gas cell. The optimized value for the pressure is $p_{Ar} = 58\,\text{Torr}$. For $20\,\text{Torr} < p_{Ar} < 55\,\text{Torr}$ the harmonic emission is phase-matched and $I_q \propto N_{a,Ar}{}^2 \propto p_{Ar}^2$ (fitted solid red line). For $p_{Ar} >> 58\,\text{Torr}$ re-absorption by the gas dominates, and an exponential decay curve can be fitted (dashed green line, marked by large circles). The x-axis is calibrated such that the global intensity maximum is at $z = 0\,\text{mm}$. The laser focus is close to the exit plane and deeper inside the gas cell for larger values of z. The harmonic

intensity scales quadratically with increasing values of z over a propagation length of about 7 mm (fitted solid red line) and thus indicates phase-matched harmonic emission. Thus, when the laser focus is properly positioned inside the gas cell the HHG is phase-matched over the whole Rayleigh range of the laser focus. When the laser focus is placed deeper inside the gas cell, re-absorption by the generating medium dominates and an exponential decay curve can be fitted (dashed green line, marked by large circles).

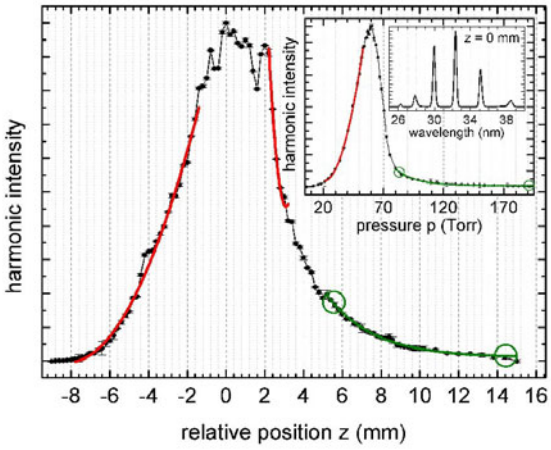

Fig. 1 Argon gas cell: harmonic intensity versus laser focus position. Inset: harmonic intensity versus pressure, and spectral power distribution for position of maximum flux. Red solid line: quadratic fit for phase-matched harmonic emission. Green dashed line (marked by large circles): fit of exponential decay curve.

Comparison of the intensity dependence on the position of the laser focus in the argon gas cell with the helium gas cell can be made by means of figure 2, which was obtained with the same experimental procedure. The x-axis calibration is consistent with figure 1, but comparing the settings of the translation stage for the focusing lens reveals that the laser focus is $\Delta \approx 2.6\,\text{mm}$ deeper inside the gas cell. When varying the position of the laser focus, a coherence length-induced oscillating intensity can be observed with the global and local maximum separated by $\Delta z_{He} \approx 900\,\mu\text{m}$. This value is consistent with the propagation length over which phase matching can be observed and the intensity scales quadratically with z (fitted solid red line). The Gouy phase-related coherence length is given by $l_{c,Gouy}(z) = \pi(z_0 + z^2 / z_0)/q$. At the focus $l_{c,Gouy}(0) = \pi\, z_{0,He}/q$ ranges from $\sim 141 - 178\,\mu\text{m}$ for H97 to H77. For H77 to H97 the plasma-related coherence length $l_{c,plasma}$ ranges from $\sim 538 - 66\,\mu\text{m}$ and is significantly

shorter than Δz_{He}. Thus, when the laser focus is properly positioned inside the gas cell we can exploit the Gouy phase shift to phase-match the harmonics H77 to H97 over a propagation length of $l_{eff,He} \approx 1\,\mathrm{mm}$. When the laser focus is placed deeper inside the gas cell, harmonic emission is dominated by re-absorption by the generating gas and an exponential decay curve can be fitted (dashed green line, marked by large circles). The exponential decay exhibits modulations of order $\leq 538\,\mu\mathrm{m}$ which we attribute to intrinsic plasma formation. For $z = 0\,\mathrm{mm}$ we calculate a total of $\sim 5\times10^{9}$ generated harmonic photons per second, or an energy conversion efficiency of $\varepsilon_{He} \approx 10^{-7}$, which compares with $\varepsilon_{Ar} \approx 5\times10^{-7}$ for the argon gas cell.

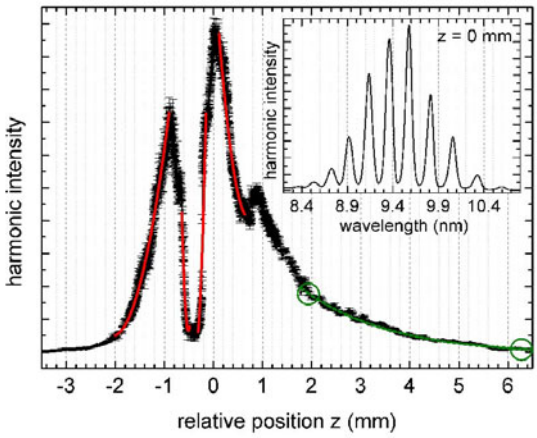

Fig. 2 Helium gas cell: harmonic intensity versus laser focus position. Inset: spectrum for position of maximum flux. Red solid line: quadratic fit for phase-matched harmonic emission. Green dashed line (marked by large circles): fit of exponential decay curve.

ii) Coherent diffractive imaging

HHG radiation from an argon gas source (wavelength ~ 30 nm) with about 5 harmonic orders is used for coherent diffractive imaging. The diffraction imaging from a test sample is shown in Fig. 3a. The diffraction pattern has a strong qualitative resemblance to the pattern that would be produced by an extended periodic sample. Close inspection reveals that the pattern contains some important differences, key among them being that there is significant intensity in between, and structure to, the diffraction "spots" as shown in Fig. 3b. A key feature is that the individual diffraction peaks themselves contain a series of peaks produced by each of the harmonics from the HHG source; so that the diffraction pattern is an incoherent superposition of the diffraction by

each harmonic incident on the sample. Using 13.5 nm source (from helium gas) a spatial resolution of ~ 50 nm can be obtained.

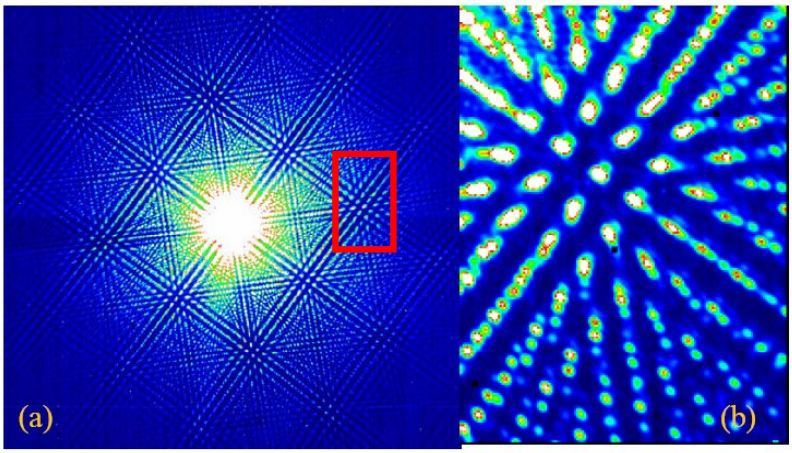

Fig. 3 Diffraction pattern from the 2D pinhole test sample (a) and a zoom of the marked area (b).

References

1. S. Kazamias, D. Douillet, F. Weihe, C. Valentin, A. Rousse, S. Sebban, G. Grillon, F. Augé, D. Hulin, Ph. Balcou, Phys. Rev. Lett. 90, 193901 (2003); C. G. Durfee, III, A. R. Rundquist, S. Backus, C. Herne, M. M. Murnane, and H. C. Kapteyn, Phys. Rev. Lett. 83, 2187 (1999).
2. Y. Tamaki , J. Itatani, Y. Nagata, M. Obara, K. Midorikawa, Phys. Rev. Lett. 82, 1422 - 1425 (1999).
3. L.V. Dao, S. Teichmann, J. Davis, and P. Hannaford, J. Appl. Phys. 104, 023105 (2008); L. V. Dao, S. Teichmann, and P. Hannaford, Phys. Lett. A 372, 5254 (2008); S. Teichmann, P. Hannaford, L.V. Dao, App. Phys. Lett. 94, 171111 (2009).
4. G. Mourou, Z. Chang, A. Maksimchuk, J. Nees, S.V. Bulanov, V.Yu. Bychenkov, T. Zh. Esirkepov, H. Ruhl, Plasma Physics Reports 28, 12 - 27 (2002).
5. R.A. Bartels, A. Paul, H. Green, H.C. Kapteyn, M.M. Murnane, S. Backus, I.P. Christov, Y. Liu, D. Attwood, C. Jacobsen, Science 297, 376 - 378 (2002).
6. M. Hentschel, R. Kienberger, Ch. Spielmann, G.A. Reider, N. Milosevic, T. Brabec, P. Corkum, U. Heinzmann, M. Drescher, F. Krausz, Nature 414, 509 - 513 (2001).
7. R.L. Sandberg et. al., Proc. Natl. Acad. Sci. U.S.A 105, 24-27 (2007).
8. B. Chen, R.D. Dilanian, S. Teichmann, B. Abbey, A.G. Peele, G.J. Williams, P. Hannaford, L.V. Dao, H.M. Quiney, K.A. Nugent, Phys. Rev. A 79, 023809 (2009).

Highly Directive High Harmonic Generation from Solid Target Plasma for Biomedical and Medicine Applications

H. Kuroda[1, 2], M. Baba[2, 1], R. A. Ganeev[2, 3], M. Suzuki[2,4], and S. Yoneya[1]

[1] Ophthalmology and Advanced Laser Medical Centre, Faculty of Medicine, Saitama Medical University
[2] The Institute for Solid State Physics, The University of Tokyo
[3] Scientific Association Akadempribor, Academy of Sciences of Uzbekistan
[4] Present address: Photo-Medical Research Centre, Japan Atomic Energy Agency

Abstract. Current activities on our research of high harmonic generation (HHG) using intense femtosecond laser pulse with solid target plasma are presented. HHG from solid target plasmas shows some interesting phenomena, which were not observed using gas medium. Enhancement of a particular harmonic, due to multi-photon resonance with a strong radiative transition has been obtained. In particular the conversion efficiencies of the 13th harmonic for indium and the 17th harmonic for tin were estimated to be 10^{-4} and the output energy was exceed to 1 μJ. Another interesting characteristic of this scheme is the extension of cutoff energy using doubly charged ions. We have first demonstrated 71st harmonic at the wavelength of 11.2 nm from doubly charged ion using vanadium laser plasma. To date shortest obtained wavelength was further extended up to 7.9 nm using doubly charged ion in manganese laser plasma. Furthermore various patterns of harmonic spectra obtained during HHG in plasma plumes using different bandwidths of pump laser pulses and broadening of the harmonics generating in laser plasma using the laser pulses propagating through the filaments in air have been demonstrated.

1 Introduction

High-order harmonic generation (HHG) is an attractive radiation source for various applications in the extreme ultraviolet (XUV) and soft x-ray region. For these applications, increasing the conversion efficiency and extending the cutoff energy of HHG are major objectives. As a novel approach, we have demonstrated an intensity enhancement of singleHH and extension of cutoff energy by using lowly ionised ions in laser ablated solid target plasma [1-3]. Our current results reported in this proceeding.

J. Lee et al. (eds.), *X-Ray Lasers 2010,* Springer Proceedings in Physics 136,
DOI 10.1007/978-94-007-1186-0_24,

2 Experiments

Figure 1 shows the experimental setup for the HHG. The pump laser used in this research was consisted of chirped-pulse amplification Ti:sapphire laser (Spectra-Physics, Tsunami + TSA10F) operated at a 10-Hz pulse repetition rate, whose output was further amplified using a three-pass amplifier. A portion of uncompressed radiation (pulse energy E=15 mJ, pulse duration t=210 ps, central wavelength λ=796 nm) was split from the main beam by a beam splitter and used as a prepulse. This prepulse was focused by a spherical lens on a solid target located in the vacuum chamber and produced a plume predominantly consisting on neutrals and lowly charged ions. The composition of plasma was analyzed using the time-integrated spectral measurements of plume in XUV, UV, and visible ranges. The focal spot diameter of prepulse beam on the target surface was adjusted to be approximately 600 μm. The intensity of picosecond prepulse, I_{pp}, on the target surface was varied from 7×10^{9} W cm^{-2} to 8×10^{10} W cm^{-2}. After some delay, the femtosecond main pulse (E=15 mJ, t=150 fs, λ=796 nm) was focused on the target plasma from the orthogonal direction using 200-mm focal length lense. Our experiments were carried out up to the maximum intensity of the femtosecond main pulse of $I_{fp}=1\times10^{15}$ W cm^{-2}. The HHs were analyzed by a flat-field grazing-incidence XUV spectrometer with a Hitachi 1200-groove/mm grating. An additional gold-coated grazing-incidence cylindrical mirror was used for the image translation from the plasma area to the detector. The XUV spectrum was detected by a microchannel plate with phosphor screen and recorded by a CCD camera.

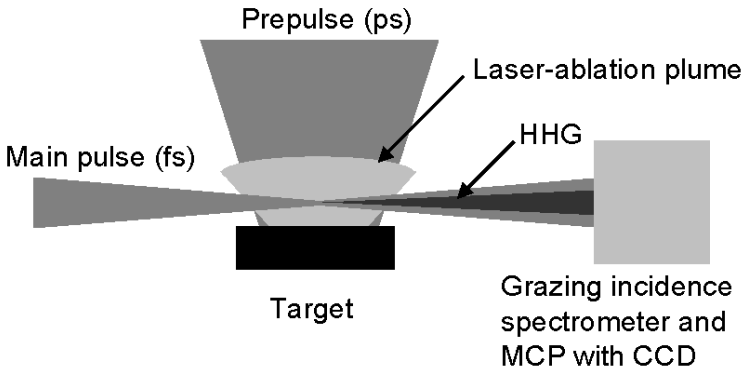

Fig. 1. Experimental setup. The prepulse was focused on the double-target surface and, after 8-88 ns, the femtosecond laser pulse was focused on the laser-ablated plume from the orthogonal direction. The generated HHs were measured using the grazing incidence spectrometer with MCP and CCD camera.

We analyzed the low-order harmonics using the monochromator (Acton VM-502) with sodium salicyilate and photomultiplier tube [4]. At first, by using this system, we calibrated the 3rd harmonic signal measured the known energy of the 3rd harmonic of 796 nm radiation generated in nonlinear crystals. By comparing the known 3rd harmonic intensity from the crystal with unknown 3rd harmonic intensity from Ag plasma, we could estimate the conversion efficiency of the 3rd harmonic from Ag plasma. This calibration gave the absolute conversion efficiency for the 3rd harmonic generated from Ag plasma to be 5×10^{-4}. In second step this system measured the 9th harmonic intensity at the wavelength of 88.4 nm. By comparing the 3rd harmonic intensity with the 9th harmonic intensity, we could estimate the conversion efficiency of the 9th harmonic from Ag plasma. As results, the conversion efficiency was estimated to be 3×10^{-6}. In final step we measured the 9th harmonic from Ag plasma using grazing incidence spectrometer with MCP on phosphor and CCD camera. In this case, the conversion efficiency of the 9th harmonic has already estimated. By comparing the 9th harmonic with the 57th harmonic, we calibrated the spectrometer at the wavelengths of 88.4-13.96 nm.

3 Single harmonic enhancement

Figure 2 shows the typical spectra of HHG from the laser ablation indium plume. In this experiment, the nonlinear medium was indium ablation plume, produced by a low-energy laser pulse, instead of the conventional gas medium. The strong 13th harmonic at a wavelength of 61.26 nm have obtained as can be seen in Fig. 2. Using 10 mJ energy, Ti: Sapphire laser pulse at a wavelength of 796.5 nm, the conversion efficiency of the 13th harmonic at a wavelength of 61 nm was about 8×10^{-5}, which was two orders of magnitude higher than its neighbouring harmonics [5]. The output energy of the 13th harmonic was measured to be 0.8 μJ. The cutoff is 31st harmonic at the wavelength of 25.69 nm has observed in this experiment. For indium, the $4d^{10}5s^2\ {}_1S^0 \rightarrow 4d^9 5s^2 5p\ ({}^2D)\ {}^1P_1$ transition of In II, which has absorption oscillator strength (*gf*–value) of 1.11, can be driven into resonance with the 13th harmonic by AC-Shark shift [6]. The intensity of the 13th harmonic for indium is attributed to such resonance of the harmonic wavelength with that of a strong radiative transition. Figure 3 shows the HHG spectra at the wavelengths of 796 and 782 nm. By changing the laser wavelength from 796 nm to 782 nm, the 15th harmonic at the wavelength of 52.13 nm increased, and the intensity of the 13th harmonic decreased at the same time. The reason of the 15th harmonic enhancement is due to resonance with the $4d^{10}5s5p\ {}^3P_2 \rightarrow 4d^9 5s5p^2\ ({}^2P)\ {}^3F_3$ transition of In II, which has a *gf*-value of 0.30. The enhancement of the 15th order harmonic intensity is lower than that of the

13th harmonic because the *gf*-value of $4d^{10}5s5p\ ^3P_2 \rightarrow 4d^9 5s5p^2\ (^2P)\ ^3F_3$ transition is lower than that of the $4d^{10}5s^2\ ^1S_0 \rightarrow 4d^9 5s^2 5p\ (^2D)\ ^1P_1$ transition. Furthermore the central wavelength of the 13th harmonic was driven away from resonance with the $4d^{10}5s^2\ ^1S_0 \rightarrow 4d^9 5s^2 5p\ (^2D)\ ^1P_1$ transition when using 782 nm wavelength laser, thereby decreasing the 13th order harmonics [7].

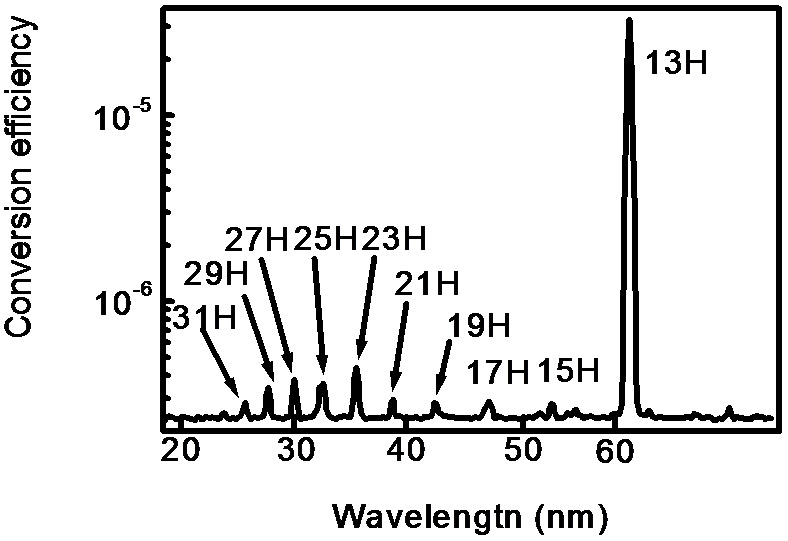

Fig. 2. Spectrum of the HHG from the laser ablation indium plume. The conversion efficiency is 8×10^{-5}.

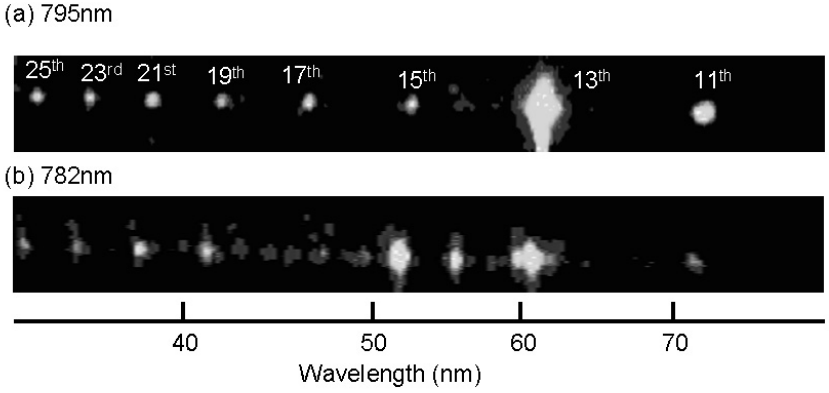

Fig. 3. HHG spectra from indium laser ablation for pump laser with central wavelength of (a) 795 nm, (b) 782 nm. The intensity of the 13th harmonic is two orders of magnitude higher than its neighbouring harmonics.

Figure 4 shows the HHG spectra from laser-ablated (a) tin, (b) antimony, (c) chromium, and (d) tellurium plasma plumes [8-11]. The intensity enhancement of the 17th harmonic at 46.76 nm, the 21st harmonic at 37.67 nm, the 29th harmonic at 27.84 nm and the 27th harmonic at 29.44 nm have been obtained by using tin, antimony, chromium, and tellurium, respectively. These intensities of emission decreased after 10-degree rotation of the quarter-wave plate, which completely disappeared after 50-degree rotation of the quarter-wave plate. This tendency is consistent with that of HHG, which leads us to conclude that the strong emissions should be generated by HHG.

As can be seen Fig 4 (a), the intensity of 17th harmonic at 46.76 nm was 20 times higher that of those neighbouring harmonics. The conversion efficiency of the 17th harmonic was measured to be about 1.1×10^{-4}, and this output energy of 1.1 μJ was obtained from the pump laser energy of 10 mJ. The strong Sn II ion has been shown to possess a strong transition of the $4d^{10}5s\ ^2\!5p^2P_{3/2}\rightarrow 4d^9\!5s^2\!5p^2\ (^1D)\ ^2D_{5/2}$ at the wavelength of 47.256 nm [12]. The *gf*-value of this transition has been calculated to be 1.52 and this value is 5 times larger than other transition from ground state of Sn II. Therefore, the enhancement of the 17th harmonic with 795 nm wavelength laser pulse can be explained be due to resonance with this transition driven by AC-Stark shift. By changing the pumping laser wavelength from 795 nm to 778 nm, the wavelength of the 17th harmonic is changed from 46.76 nm to 45.76 nm.

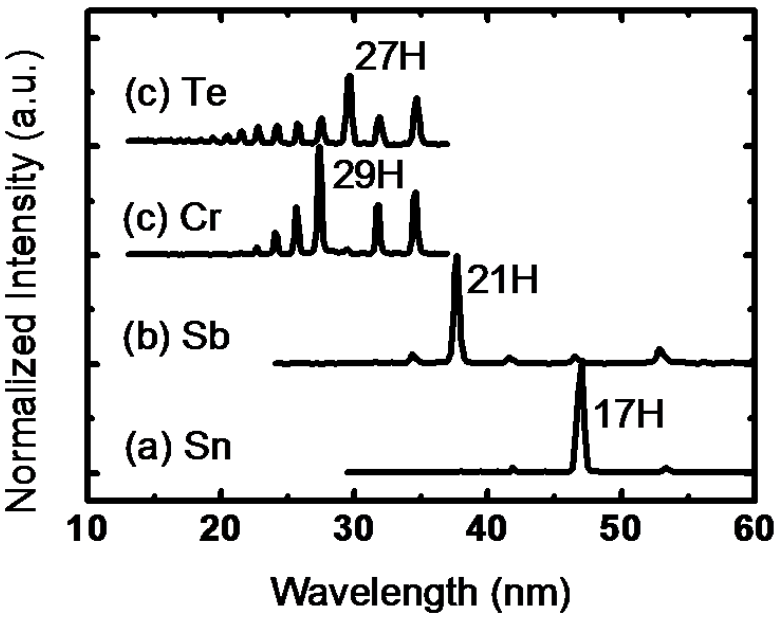

Fig. 4. The HHG spectra from the laser-ablation (a) tin, (b) antimony, (c) chromium, and (d) tellurium plumes. The ordinate of spectra was normalized in the each enhanced peak intensity.

The intensity of the 21st harmonic was 10 times higher than those of the 23rd and 19th harmonics. In Fig. 4 (b) the conversion efficiency of the 21st harmonic was measured to be 2.5×10^{-5} and thus the pulse energy of the 37.67 nm radiation of 0.3 μJ was obtained from the pump laser energy of 12 mJ. We observed a strong 29.44 nm radiation, which is three times the intensity of neighbouring harmonics, as shown in Fig. 4 (d). For chromium and tellurium, the conversion efficiency of the 29th and 27th harmonics was estimated to be 1.2×10^{-5}, and 10^{-6}. The 21st harmonic at 37.67 nm for antimony, the 29th harmonic at 27.44 nm for chromium, and the 27th harmonic at 29.44 nm for tellurium was enhanced by the $4d^{10}5s^2 2p^3P_2 \rightarrow 4d^9 5s^2 5p^3(^2D)^3D_3$, the $3p \rightarrow 3d$, and the $4d^{10}5s^2 5p^3\ ^2D_{5/2} \rightarrow 4d^9 5s^2 5p^4(\ ^3P)^2F_{7/2}$ transition, respectively [13-15]. Thus we have successfully demonstrated the particular harmonic enhancement for short wavelength region by using the laser plasma appropriate solid target.

4 Cutoff energy extension

According to the three-step model [16] of HHs, the theoretically highest possible photon energy of HHG (cutoff) is predicted by the cutoff rule, $E_{cutoff} \sim I_p + 3.17U_p$. Here, E_{cutoff} is the photon energy of the maximum cutoff order, I_p is the ionization potential, and U_p is the ponderomotive energy. The ponderomotive energy is $U_p = 9.33\times10^{-14} I_L \lambda^2$, where I_L and λ are the intensity and wavelength of the pump laser, respectively. To obtain the highest possible cutoff energy, we need to either increase the ponderomotive energy and/or the ionization potential of the nonlinear medium. For pump laser with a specific wavelength, the ponderomotive energy depends strongly on the laser intensity, and therefore it is necessary to increase the laser intensity. However, if the gas medium is ionized before the peak of the laser intensity, the observable cutoff energy is limited to a value corresponding to the saturation intensity (I_S), if I_L is higher than I_S. Therefore, the cutoff energy in HHG can be increased either by using ultrashort laser pulse [2], or by using medium with high ionization potential, such as helium or neon. The highest harmonic observed to date, which exceeds photon energies of 3.5 keV, has been demonstrated by irradiating 12 fs pulses on to helium and neon gases [17].

An alternative method to extend the cutoff energy has been demonstrated, by using lowly charged ion from plasma. The major factor that favours such media is that their ionization potentials are higher than those of atoms, thereby also increasing the saturation intensity I_S for HHG. Therefore one can expect to generate HHGs with higher photon energies by using ions as nonlinear medium, pumped by ultrashort laser pulses. Figure 5 shows the typical harmonic spectra that are generated from laser-plasma of Ag and Mn [18, 19].

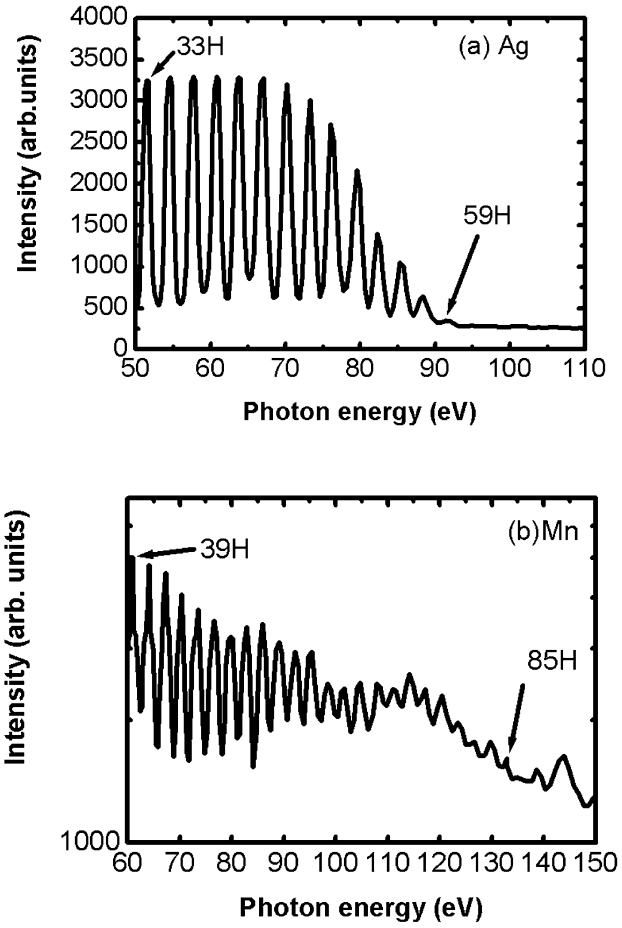

Fig. 5. The HHG spectra from the laser-ablation (a) Ag, and (b) Mn plumes. The ordinate of spectra was normalized in the each enhanced peak intensity.

The cutoff energies of harmonics from Ag and Mn targets were 93 and 135 eV, respectively. The second (third) ionization potential energy of Ag is 21.49 eV (34.83 eV), and for Mn is 15.64 eV (33.67 eV). Therefore, since the ionization potential of Ag is higher than Mn for both ionization states, the cutoff energy from Ag should be higher than that from Mn, if we assume that the harmonics near the cutoff were generated from the same ion state. However, our experimental results show the contrary, and the observed cutoff energy was higher for Mn than for Ag. Meanwhile the cutoff energy depends strongly on the effective laser intensity of I_L within the nonlinear medium. In particular, if the nonlinear medium is ionized before the peak intensity of the laser pulse, the cutoff energy will be limited to the barrier-suppression intensity I_{BSI}. Here, the theoretical I_{BSI} can be written as I_{BSI} [eV] =

$4.0\times10^{9}(I_p)^4/Z_i^2$ where I_p [Wcm^{-2}] and Z_i are the ionization potential and ionization level. This clearly shows that I_{BSI} depends clearly on I_p. Therefore, I_{BSI} for the singly and doubly charged ions of Ag should be higher than those of Mn. This again suggests that the cutoff for Ag is higher than that of Mn, which is contrary to our observation. This discrepancy between experiment and theory could only be alleviated if we attribute the 87th harmonic of Mn to originate from Mn^{2+}, while the 59th harmonic from Ag occurred from Ag^{+}. Simulations have shown that the electron density of Mn plasma differs considerably with other plasmas, and that defocusing of the pump laser could play a role in reducing the effective laser intensity I_L within the plasma [20].

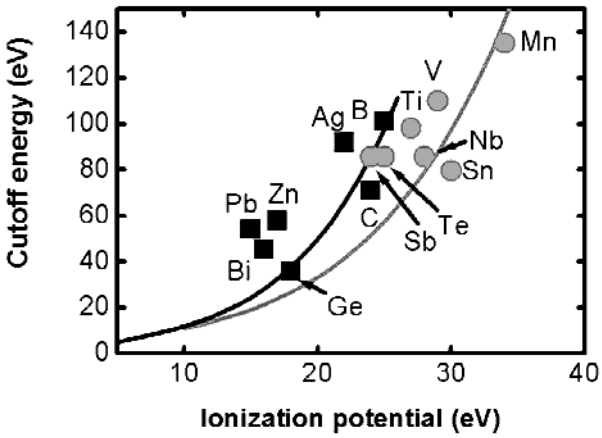

Fig. 6. The cut-off energy from experiments and calculations plotted as a function of the ionization potential for singly and doubly charged ions. The black and gray curves are the calculation results for singly and doubly charged ions, respectively. The black square and the gray circles are experimental data for singly and doubly charged ions, respectively.

To study the relation between the HHG cutoff energy and the ionization potential of the ions, we compared the experimentally observed cutoff energy with the theoretical cutoff energy E_{cutoff} [eV] ~ $I_p + 2.96 \times 10^{-13} \times I_{BSI} \times \lambda^2$. Figure 6 shows the experimentally observed cutoff energy (shown as data points) and the theoretical cutoff energy (shown as lines) calculated, for all targets as a function of the ionization potential energy. In Fig. 6, the gray and black curves are the theoretical cutoff energy for doubly charged and singly charged ions, respectively. The gray circles and black squares correspond to data points whose cutoff is determined by singly and doubly ionized ions, respectively. Figure 6 can be used to evaluate which ionization stage determines the harmonic cutoff. In the Fig. 6, we first plot a data point assuming singly charged ions (and the second ionization potential). If this data point falls far from the black theoretical curve, then the ionization stage

needs to be advanced to the doubly charged state. In this case, we need to replot the data point in the Fig. 6 using the third ionization potential. Once the data point falls on to or below the corresponding theoretical curve, then this shows that the cutoff is determined by that ionization stage.

5 Conclusion

In conclusion, we have demonstrated the HHG by using solid target laser plasmas. As quite interesting phenomena, single harmonic enhancement has been obtained, and furthermore generation of this intense single harmonic have been achieved for shorter wavelength region by selecting appropriate target material. For extending cutoff energy, we have demonstrated the HHG by using doubly charged ion in high density laser plasma plume. We expect that similar resonance enhancement at shorter wavelength region would be generated by doubly charged ions in laser plasma from appropriate target with ultrashort laser pulse irradiation.

Acknowledgement

This work was supported by Grant-in-Aid for Creative Scientific Research (14GS0206) of Japan Society for the Promotion of Science. The authors thank Dr. T. Ozaki for their helpful discussions.

References

1. Ganeev, R. A.,: ‘High-order harmonic generation in a laser plasma: a review of recent achievements’, *J. Phys. B: At Mol. Opt. Phys.* 40, R213-R253 2008
2. Ganeev, R. A., and Kuroda, H.:'Extremely broadened high-order harmonics generated by the femtosecond pulses propagating through the filaments in air', *Appl. Phys. Lett.* 95, 201117 2009
3. Ganeev, R. A., Singhal, H., Naik, P. A., Chakera, J. A., Tayyab, M., Baba, M., Kuroda, H., and Gupta, P. D.,:'Variation of harmonic spectra in laser-produced plasmas at variable phase of femtosecond laser pulses of different bandwidth', *J. Opt. Soc. Am. B*26, 2143 2009
4. Ganeev, R. A., Baba, M., Suzuki, M., and Kuroda, H: ‘High-order harmonic generation from silver plasma’, *Phys. Lett. A* 339, 103-109 2005
5. Ganeev, R. A., Suzuki, M., Baba, M., and Kuroda, H.:'Generation of strong coherent extreme ultraviolet radiation from the laser plasma produced on the surface of solid targets', *Appl. Phys. B* 81, 1081-1089 2005
6. Duffy G, Dunne P,:'The photoabsorption spectrum of an indium laser produced plasma', *J. Phys. B: At Mol. Opt. Phys.* 34, L173-L178 2001

7. Ganeev,R. A., Suzuki, M., Baba, M., Kuroda, H., and Ozaki, T.: 'Strong resonance enhancement of a single harmonic generated in the extreme ultraviolet range', Opt. Lett. 31, 1699-1701 2006
8. Suzuki, M., Baba, M., Ganeev, R. A., Kuroda, H., and Ozaki, T.: 'Anomalous enhancement of a single high-order harmonic by using a laser-ablation tin plume at 47 nm', *Opt. Lett.*31, 3306-3308 2006
9. Suzuki, M., Baba, M., Ganeev, R. A., Kuroda, H., and Ozaki, T.: 'Intense exact resonance enhancement of single-high-harmonic from an antimony ion by using Ti:Sapphire laser at 37 nm', *Opt. Express* 15, 1161-1166 2007
10. Ganeev, R. A., Naik, P. A., Singhal, H., Chakera, J. A., and Gupta, P. D.: 'Strong enhancement and extinction of single harmonic intensity in the mid- and end-plateau regions of the high harmonics generated in weakly excited laser plasmas', *Opt. Lett.* 32, 65-67 2007
11. Suzuki, M., Baba, M., Kuroda, H., Ganeev, R. A., and Ozaki, T.: 'Observation of single high-harmonic enhancement by quasi-resonance with a tellurium ion in a laser-ablation plume at 29.44 nm' *J. Opt. Soc. Am. B* 24 2686-2689 2007
12. Duffy, G., van Kampen, P., and Dunne, P.:'4d→5p transitions in the extreme ultraviolet photoabsorption spectra of Sn II and Sn III', *J. Phys. B: At Mol. Opt. Phys.* 34, 3171-3178 2001
13. D'Arcy, R., Costello, J. T., McGuinness, C., and O'Sullivan, G.:'Discrete structure in the 4d photoabsorption spectrum of antimony and its ions', *J. Phys. B: At Mol. Opt. Phys.* 32, 4859-4876 1999
14. McGuinness, C., Martins, M., Wernet Ph., Sonntag, B. F., van Kampen P., Mosnier, J. P., Kennedy, E. T., and Costello, J. T.,:' Metastable state contributions to the measured 3p photoabsorption spectrum of Cr+ ions in a laser-produced plasma', *J. Phys. B: At. Mol. Opt. Phys.* 32, L583 1999
15. Muephy, N., Costello, J. T., Kennedy, E. T., McGuinness, C., Mosnier, J. P., Weinmann, B., and O'Sullivan, G,:'Discrete structure in the 4d photoabsorption spectrum of tellurium and its ions' *J. Phys. B: At Mol. Opt. Phys.* 32, 3905-3922 1999
16. Corkum, P. B.: 'Plasma perspective on Strong-Field Multiphoton Ionization', *Phys. Rev. Lett.* 71, 1994-1997, 1993
17. Seres, E., Seres, J., and Spielmann, C.:'X-ray absorption spectroscopy in the keV range with laser generated high harmonic radiation', *Appl. Phys. Lett.* 89, 181919 2006
18. Suzuki, M., Elouga Bom, L. B., Ozaki, T., Ganeev, R. A., Baba, M., and Kuroda, H.: 'Seventy-first harmonic generation from doubly charged ions in preformed laser-ablation vanadium plume at 110 eV,' *Opt. Express* 15, 4112-4117 2007
19. Ganeev, R. A., Bom, L. B. E., Kieffer, J. C., Suzuki, M., Kuroda, H., Ozaki, T.: 'Demonstration of the 101st harmonic generated from a laser-produced manganese plasma', *Phys. Rev. A* 76 023831 2007
20. Elouga-Bom, L. B., Bouzid, F., Vidal, F., Kieffer, J. C., Ozaki, T.,:'Correlation of plasma ion densities and phase matching with the intensities of strong single high-order harmonics', *J. Phys. B: At Mol. Opt. Phys.*41, 215401 2008

High Harmonic Generation by using Laser-Ablation Two- Compounds Target Scheme

M. Suzuki[1,4], M. Baba[1, 2], R. A. Ganeev[1, 3], and H. Kuroda[1, 2]

[1] The Institute for Solid State Physics, The University of Tokyo
[2] Ophthalmology and Advanced Laser Medical Centre, Faculty of Medicine, Saitama Medical University
[3] Scientific Association Akadempribor, Academy of Sciences of Uzbekistan
[4] Present address: Photo-Medical Research Centre, Japan Atomic Energy Agency

Abstract. We have generated high harmonics by using the two-component laser-ablation plumes, which were irradiated by a femtosecond laser pulse. The harmonic spectra from double target schemes comprised those obtained from separate targets. For indium/chromium, the enhancement of two harmonics (13th and 29th harmonics) with conversion efficiencies of ~$10^{-5}$was obtained at wavelengths of 61.15 and 27.41 nm, respectively. We attribute the enhancement of the 13th and 29th harmonics to the multiphoton resonances with the strong radiative transitions of ions in indium and chromium plumes, respectively. This study shows that the control of cutoff energy and intensity of single high harmonics can be achieved by using the appropriate target combination.

1 Introduction

The interaction of strong laser field with atoms, molecules, and ions results in a high harmonic generation (HHG) in the extreme ultraviolet (XUV) region. Extensive studies in the past two decades have demonstrated many methods to control the HHG characteristics, such as the extension of cutoff energy, enhancement of conversion efficiency, and generation of ultrashort attosecond pulses. Recent advances research of this field allowed applying the HH for the photoelectron spectroscopy and holographic microscopy.

Various techniques for increasing the HH intensity have been demonstrated during last time, such as the chirp control of the laser pulse, improvement of the phase matching conditions, and application of the two-colour laser fields. Very recent results have also reported the enhancement of single harmonic originated from the multiphoton resonance with the ionic transitions possessing strong oscillator strengths. After the first demonstration of the the 13th harmonic enhancement at 61.15 nm in indium plasma [1], the intensity enhancement of single harmonics in Sn and Sb plasmas (17th harmonic at

J. Lee et al. (eds.), *X-Ray Lasers 2010,* Springer Proceedings in Physics 136,
DOI 10.1007/978-94-007-1186-0_25,

47.67 nm [2], and 21st harmonic at 37.67 nm [3]) by tuning the master oscillator wavelength of the driving laser has been reported.
All previous studies of the HHG from the laser-ablation plume were carried out using the *single-target* scheme. In this proceeding, we present the observation of the HHG from the laser-ablation plumes produced in *double-target* scheme. Among the advantages of the double-target scheme for the excitation of two-component plasma one can consider the search of resonance-enhanced harmonics in the XUV range [4]. In particular in the case of indium/chromium target, the simultaneous enhancement of two harmonics (the 13th and 29th) at wavelengths of 61.15 and 27.41 nm was obtained. These results showed that the HH are produced from two different types of ions. In particular, this demonstration of "two-colour" HH enhancement would open new fields in the laser-induced chemical dynamics by using a pump-probe XUV spectroscopy and a three-wave mixing in XUV nonlinear optics.

2 Experiments

The experimental setup is shown in Fig. 1. Niobium, indium, and chromium were used as the two targets placed close to each other as can be seen in Fig. 1. The targets were placed in the vacuum chamber. The pump source was a commercial CPA Ti:sapphire laser system (Spectra Physics: TAS-10F), whose output was further amplified using a homemade three-pass amplifier operating at a 10 Hz pulse repetition rate. A prepulse was split from the amplified laser beam by a beam splitter before a pulse compressor. The prepulse energy was 10 mJ with prepulse duration of 210 ps. A main pump pulse output at a centre wavelength of 793 nm had the maximum energy of 10 mJ with pulse duration of 120 fs. A cylindrical lens focused the prepulse on a solid target, which produced an ablation plume that contained the low-charged ions. The main pulse was focused onto the plume from the orthogonal direction by a 200 mm focal length spherical lens, 88 ns after the prepulse irradiation. The delay between two pulses was optimized. The cutoff energy at short delay (~24 ns) was lower than that at long delay (~88 ns). In a low-Z number target such as lithium and boron, the maximum cutoff energy has been obtained at a delay of 24 ns. In moderate- and high-Z number targets including indium silver, aluminium, manganese, tellurium, and chromium, the obtained maximum cutoff has been obtained at a delay of 88 ns. Adding the delay more, the cutoff energy by using moderate and high-Z number material has been decreased. The confocal parameter of the femtosecond laser pulse was defined to be 6 mm by measuring the focal spot size of the femtosecond laser pulse. The spectrum of generated HH was analyzed by a grazing incidence spectrometer with a gold-coated Hitachi 1200 grooves/mm flat-field

grating. The XUV spectrum was detected using a microchannel plate (MCP) with a phosphor screen read-out (Hamamatsu, model F2813-22P), and the optical output from the phosphor screen was recorded using a charge-coupled device (CCD) camera (Hamamatsu, model C4880). The details of the absolute calibration of the spectrometer were described in Ref. 5.

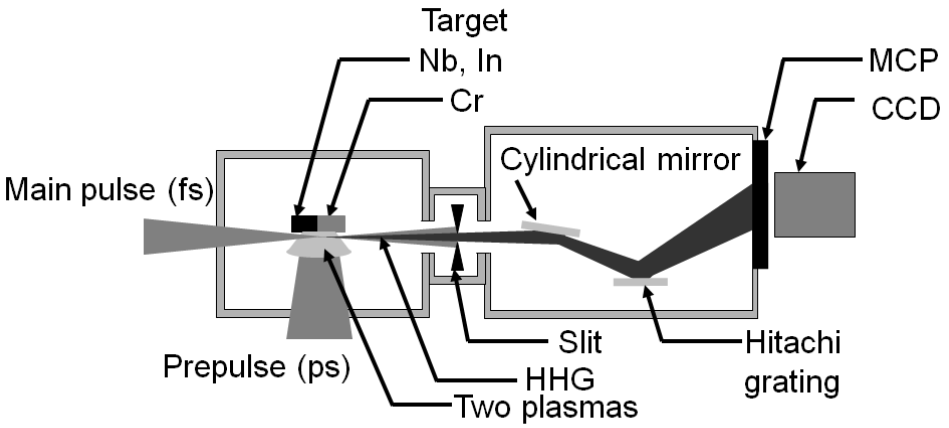

Fig. 1. Experimental setup. The prepulse was focused on the double-target surface and, after 88 ns, the femtosecond laser pulse was focused on the laser-ablated plume from the orthogonal direction. The generated harmonics were measured using the grazing incidence spectrometer with MCP and CCD camera.

3 Results and discussions

Figure 2 shows the HHG spectra from the (a) niobium/chromium, (b) niobium, and (c) chromium plumes. The change of pump laser polarization from the linear polarization to the circular one by using a quarter-wave plate led to the disappearance of harmonics. Therefore these radiations should be generated from HHG. By using the laser-ablation niobium plume, the HHs up to the 55th harmonic at a wavelength of 14.45 nm was observed. For chromium plume, the maximum harmonic cutoff was the 37th harmonic (λ= 21.49 nm). Strong enhanced radiation of the 29th harmonic at a wavelength of 27.41 nm was obtained, while the intensity of the 27th harmonic was considerably lower than that of neighbouring harmonics. The conversion efficiency of the 29th harmonic was estimated to be 1.2×10^{-5}. The increased yield of the 29th harmonic occurred from the laser-induced resonance enhancement caused by strong transitions associated with the singly charged chromium ions in the region of 27.3 nm [7].

For laser-ablation niobium/chromium plume, the HHs up to the 51st harmonic (λ= 15.59 nm) were observed (see Fig. 2a). At the same time, the intensity of

the 29th harmonic was considerably higher with regard to the neighbouring harmonics, as in the case of single chromium plume. Meantime, the 27th harmonic intensity (λ= 29.4 nm) was almost the same as those of the neighbouring harmonics excepting the 29th harmonic, contrary to the single chromium target. These results shows that the HHG by using laser-ablation niobium/chromium compound plume originated from the two compound ions (niobium and chromium), and the observed HHG cutoff from niobium/chromium plume was approximately the same as in the case of single niobium plume. On the other hand, there were no differences in these HHG spectra when we reverted to the target in the opposite way (chromium/niobium).

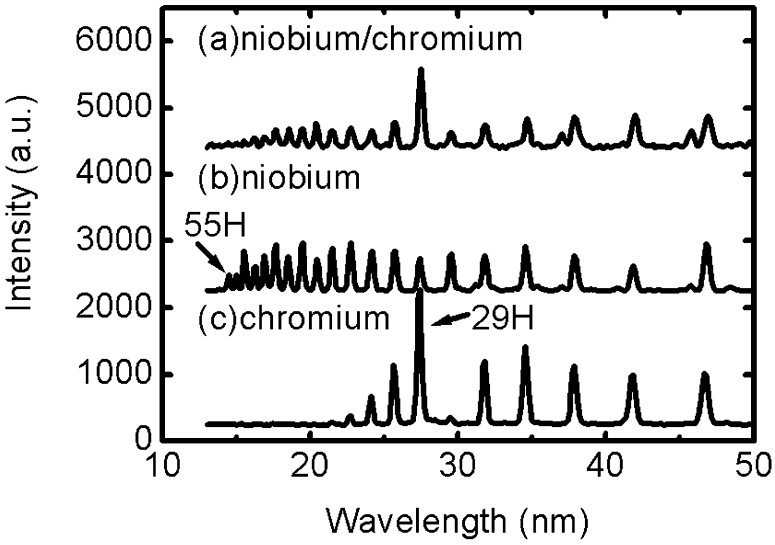

Fig. 2. The HHG spectra obtained from the laser-ablation (a) niobium/chromium, (b) niobium, and (c) chromium plumes

We also measured the harmonic spectrum generated from the indium/chromium plasma (Fig. 3). The HHs up to the 39th harmonic (λ= 20.38 nm) were observed by using this two-component plume. The 13th and 29th enhanced harmonics were clearly seen at wavelengths of 61.15 and 27.41 nm, respectively. The conversion efficiencies of these harmonics were estimated to be 10^{-5}. The same spectral pattern was observed when target was changed from indium/chromium to chromium/indium configuration. For indium, the enhancement of single harmonic was reported to be due to the strong resonance of the 13th harmonic and the ion transition possessing the strong oscillator strength [1]. In present work, we also observed the enhancement of the 13th harmonic. For the 13th harmonic, the $4d^{10}5s^2\ {}_1S^0 \rightarrow$

$4d^9 5s^2 5p\ (_2D)\ {}_1P^1$ transition of In II, which has the absorption oscillator strength (*gf*-value) of 1.11, can be driven into the resonance with the 13th harmonic by AC-Stark shift. For the 29th harmonic, the Cr II ions have been shown to possess the strong $3p \rightarrow 3d$ resonance transitions at the wavelengths of 27-28 nm [7].

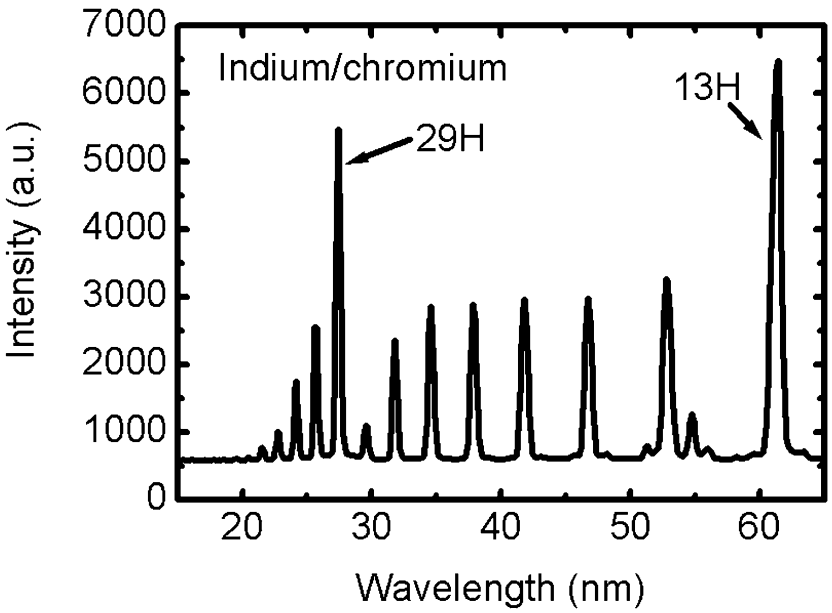

Fig. 3. The HHG spectrum from the laser-ablation indium/chromium plume. The strong 13th and 29th harmonics were obtained at the wavelengths of 61.15 and 27.41 nm, respectively.

The influence of the length of indium plume on the harmonic intensity was analyzed in Ref 6. The increase of the plasma length led to a considerable decrease of the 13th harmonic intensity with regard to the neighbouring harmonics. The ratio between the intensities of the 13th harmonic and neighbouring harmonics decreased from ~200 (for 0.6 mm long plasma) to ~30 (for 3 mm long plasma) and ~12 (for 6 mm long plasma). This decrease was attributed to the free electrons-induced dephasing of harmonics for large plasma lengths. Another reason of such a conversion efficiency decrease of resonance-enhanced harmonic could be the self-absorption in the vicinity of the transition possessing strong oscillator strength. This may restrict the possibility of using long indium plasma for further increase of the enhancement factor of the 13th harmonic radiation. In our present study, a considerable decrease of the 13th harmonic intensity compared to that of the neighbouring harmonics was observed when we used a 3 mm long plume.

4 Conclusion

In conclusion, we have demonstrated the generation of HHs by using the laser-ablation plume that contains two materials. We have shown that these harmonics occurred from two-compound ions in the laser-ablation plumes, which were produced from double-target configuration. The enhancement of these two harmonics originated from the laser-induced multiphoton resonance by using the strong radiative transition ions. This demonstration of two-colour enhancement in the short-wavelength range might be able to open new opportunities in their applications for XUV nonlinear optics and pump-probe XUV spectroscopy.

Acknowledgement

This work was supported by Grant-in-Aid for Creative Scientific Research (14GS0206) of Japan Society for the Promotion of Science. The authors thank Prof. T. Ozaki for their helpful discussions.

References

1. Ganeev, R. A., Suzuki, M., Baba, M., Kuroda, H., and Ozaki, T.: 'Strong resonance enhancement of a single harmonic generated in the extreme ultraviolet range', *Opt. Lett.* 31, 1699-1701 2006
2. Suzuki, M., Baba, M., Ganeev, R. A., Kuroda, H., and Ozaki, T.: 'Anomalous enhancement of a single high-order harmonic by using a laser-ablation tin plume at 47 nm', *Opt. Lett.*31, 3306-3308 2006
3. Suzuki, M., Baba, M., Ganeev, R. A., Kuroda, H., and Ozaki, T.: 'Intense exact resonance enhancement of single-high-harmonic from an antimony ion by using Ti:Sapphire laser at 37 nm', *Opt. Express* 15, 1161-1166 2007
4. Suzuki, M., Ganeev, R. A., Ozaki, T., Baba, M., and Kuroda, H.: 'Enhancement of two-color high harmonic by using two compound strong ionic transitions in double-target scheme' *Appl. Phys. Lett*. 90, 261104 2007
5. Ganeev, R. A., Baba, M., Suzuki, M., and Kuroda, H: 'High-order harmonic generation from silver plasma', *Phys. Lett. A* 339, 103-109 2005
6. Ganeev, R. A., Singhal, H., Naik, P. A., Arora, V., Chakravarty, U., Chakera, J. A., Khan, R. A., Kulagin, I. A., Redkin, P. V., Raghuramaiah, M., and Gupta, P. D.: 'Harmonic generation from indium-rich plasmas', *Phys. Rev. A* 74, 063824 2006
7. McGuinness, C., Martins, M., Wernet Ph., Sonntag, B. F., van Kampen P., Mosnier, J. P., Kennedy, E. T., and Costello, J. T.,:' Metastable state contributions to the measured 3p photoabsorption spectrum of Cr+ ions in a laser-produced plasma', *J. Phys. B: At. Mol. Opt. Phys.* 32, L583 1999

Part 6: Incoherent Short-Wavelength Sources

EUV-induced surface modification of polymers

A. Bartnik[1], H. Fiedorowicz[1], R. Jarocki[1], J. Kostecki[1], M. Szczurek[1], A. Biliński[2], O. Chernyayeva[2], J.W. Sobczak[2]

[1] Institute of Optoelectronics, Military University of Technology, 2 Kaliskiego Street,00-908 Warsaw, Poland
[2] Institute of Physical Chemistry Polish Academy of Sciences, 44-52 Kasprzaka Street, 01-224 Warsaw, Poland

Abstract. Radiation coming from a laser-plasma EUV source based on a gas puff target was used for surface modification of selected polymers. The source was equipped with a proper collector allowing for effective focusing of radiation of Kr plasmas within the wavelength range of 9 – 70 nm. Irradiation was performed with 10 Hz repetition rate and different time duration varying from 1s to 2 min. Different kinds of surface morphologies depending on a polymer and EUV intensity were obtained. Significant changes of the chemical structures after irradiation were revealed.

1 Introduction

Extreme ultraviolet (EUV) is part of the electromagnetic radiation with the wavelength range of approximately 5÷50 nm. Because of strong absorption in any material the EUV radiation propagates only in vacuum. Depending on material and the particular wavelength an absorption depth of the radiation in solids ranges from several to hundreds nanometers. The absorbed photons can excite or ionize any atom or molecule. In a case of polymers further radiationless relaxation leads to bond breaking or temperature increase. As a result polymer chains can be fragmented or some functional groups can be released. This way some volatile fractions can be removed from the near-surface layer changing its chemical structure and composition. The process is usually accompanied by significant changes in surface morphology in micro- or nanoscale. Such changes can influence hydrophobicity, wettability, adsorption, adhesive and optical properties of the polymer surface. Different methods are employed for such surface modification including chemical, plasma, or radiation treatment. In this work the radiation treatment was applied using a laser-plasma EUV source with a double stream Kr/He gas puff target. The morphology and chemical changes were investigated.

J. Lee et al. (eds.), *X-Ray Lasers 2010,* Springer Proceedings in Physics 136,
DOI 10.1007/978-94-007-1186-0_26,

2 Experiment

In the experiments, a 10 Hz laser plasma EUV source based on a double stream gas puff target was used. The target was irradiated with focused Nd:YAG laser pulses. Energy of the laser pulse was 0.8 J and its time duration 4 ns.J. The source was equipped with a gold plated grazing incidence EUV collector. The collector was an axisymmetrical part of the ellipsoidal surface with a collection angle 0.75 sr. The collector didn't reflect radiation with the wavelength below 8 nm. Also the spectrum of the reflected radiation was modified according to the direct plasma radiation. The low resolution spectrum consists of a narrow feature with maximum close to 10 nm and a long-wavelength tail up to 70 nm. Maximum fluence in the wavelength range 8÷17 nm was approximately 30 mJ/cm^2 while in the range 8÷70 nm exceeded 60 mJ/cm^2. More detailed information concerning the source and the EUV focusing optic can be found elsewhere [1].

Polymer samples employed in the experiments were irradiated over 1-120s at a 10-Hz repetition rate. No filters were applied. The surface morphology of the irradiated samples was investigated using a scanning electron microscope (SEM). The chemical changes were investigated by X-ray photoelectron spectroscopy. The measurements were performed using a VG Scientific spectrometer ESCALAB-210 using Al Ka radiation from an X-ray source operating at 15 kV and 20 mA. Survey spectra were recorded for all the samples in the energy range from 0 to 1350 eV with a 0.4 eV step. High resolution spectra were recorded with 0.1 eV step, 100 ms dwell time and 20 eV pass energy. The curve fitting was performed using the AVANTAGE software provided by Thermo Electron, which describes each component of the complex envelope as a Gaussian–Lorentzian sum function; a constant 0.3(±0.05) G/L ratio was used. The background was fitted using nonlinear Shirley model. Scofield sensivity factors and measured transmission function were used for quantification. Aromatic carbon C1s peak at 284.70 eV was used as reference of binding energy [2].

3 Results

Irradiation of polymers with the focused EUV pulses induces different kinds of changes in surface morphology. The changes depend mainly on the EUV fluence and chemical structure of the irradiated polymer. In a case of some polymers like for example PVDC (polyvinylidene chloride) or PEN (polyethylene naphthalate) even a single EUV pulse with the fluence close to the maximum value results in surface modification. The morphology changes in this case are very weak but can be revealed using SEM. Irradiation of these

polymers with 5 EUV pulses or more gives self-organized micro or sub-microstructures. An example of such a structure obtained on the PEN surface was shown in Fig. 1a. The structure is irregular without any orientation. Its characteristic dimension is approximately 700 nm. Irradiation with 25 EUV pulses gives a highly oriented quasi-periodic structure with the spatial period of approximately 2.3 μm. SEM image of the structure was shown in Fig. 1b. The period of the structure increases during consecutive pulses reaching 3.5 μm for 50 EUV pulses. It suggests that some pairs of the "walls" can join as a result of transient action of the ablation plume pressure and surface melting. Further irradiation leads to transverse fragmentation of the "walls". They become shorter and change their form. A SEM image of the structure obtained after irradiation with 100 EUV pulses was shown in Fig. 1c.

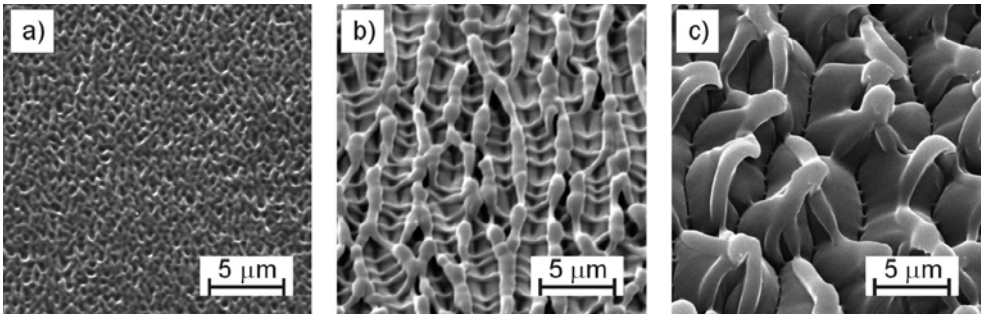

Fig. 1. SEM images of surface morphology of PEN after EUV irradiation: a) 5 pulses, b) 25 pulses, c) 100 pulses.

Irradiation of PET (polyethylene terephthalate) with a small number of pulses doesn't create any structure changing the surface morphology. Creation of a very weak rippled structure starts after irradiation with 10 EUV pulses. Further irradiation however gives similar structures to these created in PEN. SEM images of the structures obtained after 25 and 100 EUV pulses were presented in Fig. 2a,b. The significant difference appears in a case of irradiation with the fluence below 30 mJ/cm^2. In a case of PEN exposure with a large number of EUV pulses (over 300) results in strong erosion of the quasi-periodic microstructure in nanoscale but its form in microscale remains unchanged. In a case of PET the "walls" forming the quasi-periodic microstructure convert into the densely packed cones. Further irradiation doesn't influence much the structure. Fig. 2c shows the SEM image of such a structure obtained after irradiation with 900 EUV pulses. Totally different surface structures were obtained as a result of irradiation of PI (polyimide) Kapton HN foils. In this case material ablation is accompanied by formation of a pronounced rippled structure. Characteristic spatial dimension of the structure after irradiation with 100 EUV pulses is about 700 nm. Additionally the surface is covered with sparsely dispersed cones. Number of the cones and their size increases with consecutive pulses. The structures can be seen in Fig. 3a,b showing the surface morphology after irradiation with 100 and 300

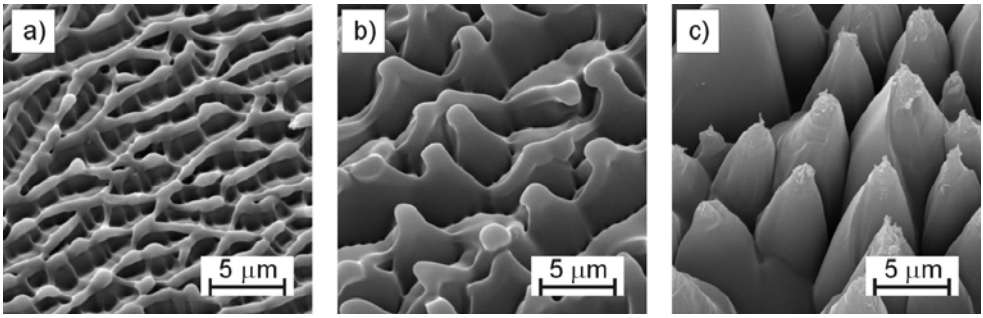

Fig. 2. SEM images of surface morphology of PET after EUV irradiation: a) 25 pulses , b) 100 pulses, c) 900 pulses (fluence below 30 mJ/cm^2).

EUV pulses with the fluence close to maximum. After 600 EUV pulses the central region of the focal spot is fully covered with the densely packed cones. There are two kinds of cones created on the Kapton surface. The cones created in the central zone of the focal spot are covered with peeling layers. Peeling doesn't appear at once but starts after about 300 EUV pulses. It suggests that the chemical structure of the layer covering the cones changes with the EUV exposure. As a result physical properties of the layer are modified causing tension leading to peeling of the layer. The zone is surrounded with different kind of cones shown in Fig. 3c. These cones are

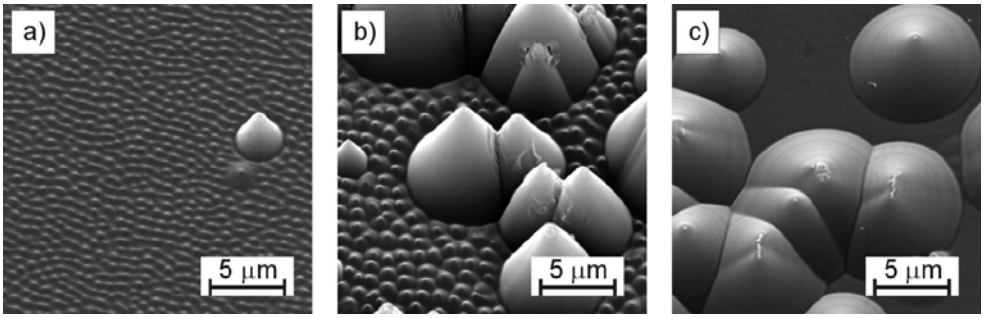

Fig. 3. SEM images of surface morphology of PI after EUV irradiation: a) 100 pulses, b) 300 pulses, c) 600 pulses (around the central zone).

very smooth and not covered with the peeling layers. There is a distinct border separating the zones with two kinds of cones. It suggests that there is some threshold effect. The EUV fluence in the central zone exceeds the threshold value while the fluence in the outer zone is below the threshold value.

The EUV induced bond breaking leads to shortening of the polymer chains or releasing of some functional groups. It results in changes of molecular structure and chemical composition of the polymer material in a near-surface layer with the thickness comparable with the EUV absorption depth. The chemical changes were investigated using XPS measurements. The XPS spectra obtained for the irradiated samples were compared to the spectra taken

for the pristine samples. Examples of the XPS spectra obtained for irradiated and non-treated PEN foils are presented in Fig. 4 and 5. The overall XPS

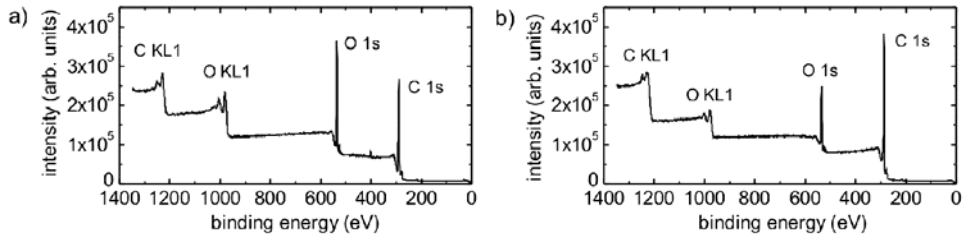

Fig. 4. Overall XPS spectra of PEN: a) non-treated, b) after EUV irradiation.

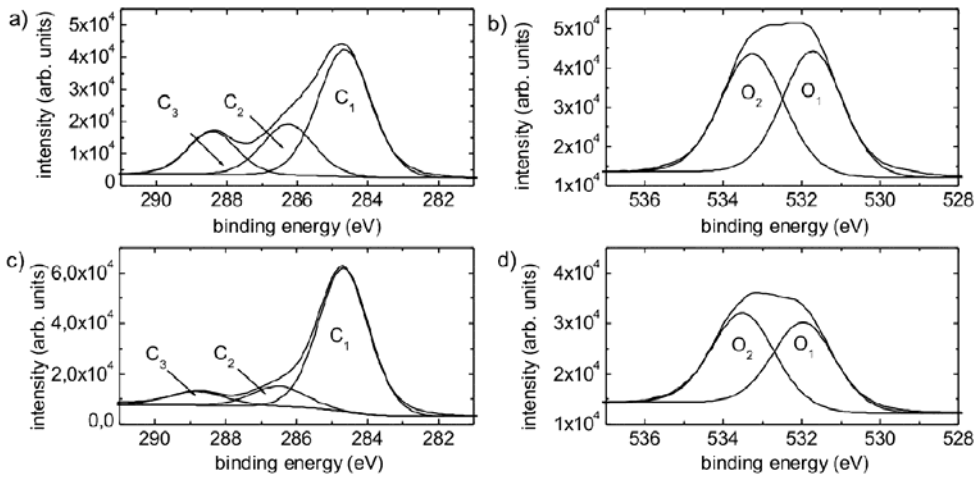

Fig. 5. High resolution XPS spectra of PEN: a) C1s PEN non-treated, b) O1s PEN non-treated, c) C1s PEN irradiated, d) O1s PEN irradiated.

spectra are shown in Fig. 4. As could be expected relative intensities of C and O signals changed after irradiation, indicating changes in chemical composition. Similar differences were revealed from XPS spectra for PET and PI. Details concerning relative concentrations of carbon and oxygen determined from the peaks areas, are reported in Table 1. In a case of Kapton additionally nitrogen concentration was calculated. In all cases relative concentration of carbon increases while the oxygen and nitrogen concentrations decrease. XPS measurements performed with 0.1 eV step gave information on concentrations of different chemical states of carbon C1s, oxygen O1s and nitrogen N1s. The corresponding XPS spectra for PEN are presented in Fig. 5. The C1s spectrum was fitted with three distinctly resolved peaks corresponding to carbon atoms located in benzene rings (C_1), singly bonded to oxygen (C_2), and ester atoms (C_3) respectively. The O1s spectrum was fitted with two contributions: carbonyl oxygen (O_1) and singly bonded oxygen (O_2). The C1s spectrum of the irradiated polymer revealed significant chemical changes created by the EUV irradiation.

Table 1. Relative concentrations of carbon, oxygen and nitrogen

polymer	PET		PEN		PI		
component	C1s	O1s	C1s	O1s	C1s	O1s	N1s
non-treated	72,07	27,94	70,67	26,92	75,9	17,51	6,58
irradiated	80,23	19,77	82,16	17,85	82,92	12,31	4,77

The peaks C_2 and C_3 remarkably decreased while O_1/O_2 ratio remained almost unchanged. It suggests that the benzene rings are more resistant against the EUV radiation in respect to the carbonyl and singly bonded oxygen. Almost unaffected O_1/O_2 ratio can suggest that oxygen is being removed as a whole O-C=O functional group. Similar results were obtained for PET [3]. In a case of Kapton the XPS spectra are more complicated because of additional presence of nitrogen atoms in the monomeric structure. Fitting of the spectra with peaks corresponding to different locations of atoms in the molecule gives different intensities and peak positions before and after irradiation. In the C1s spectrum a peak at 285,63 eV corresponding to the C-N bond vanishes and another one at 285,39 eV appears. The N1s peak decreases and is shifted from 400,60 eV to 399,76. Relative intensity of the O1s peak at 532,5eV corresponding to C=O bond decreases. These changes suggests that C-N and C=O bonds are being broken and =C-N bond appears.

4 Conclusions

In this paper results of surface modification of PEN, PET, PI samples by EUV irradiation using a laboratory radiation source based on a laser-irradiated gas-puff target were presented. Different kinds of microstructures were created in the near surface layers as a result of EUV irradiation of the polymer foils. XPS measurements of non-treated and irradiated polymers were performed. Significant chemical changes were created by the EUV irradiation. In particular, a decrease of oxygen and nitrogen concentrations were revealed.

References

1. A. Bartnik, H. Fiedorowicz, R. Jarocki, J. Kostecki, A. Szczurek, M. Szczurek, Appl Phys B 96, 727–730 (2009)
2. G. Beamson, D. Briggs, High Resolution XPS of Organic Polymers. The Scienta ESCA300 Database, John Wiley & sons, Chichester 1992
3. A. Bartnik, H. Fiedorowicz, R. Jarocki, J. Kostecki, M. Szczurek, A. Biliński, O. Chernyayeva, J.W. Sobczak, Appl Phys A, DOI 10.1007/s00339-010-5596-1, Published online 06 March 2010

Study on fundamental processes of laser welded metals observed with intense x-ray beams

T. Muramatsu[1], H. Daido[1,2], T. Shobu[2], K. Takase[3], K. Tsukimori[4], M. Kureta[3], M. Segawa[3], A. Nishimura[2,1], Y. Suzuki[1] and T. Kawachi[2]

[1]Applied Laser Technology Institute, Tsuruga Head Office,
Japan Atomic Energy Agency

[2]Quantum Beam Science Directorate, Japan Atomic Energy Agency

[3]Nuclear Science and Engineering Directorate,
Japan Atomic Energy Agency

[4]Advanced Nuclear System Research and Development Directorate,
Japan Atomic Energy Agency

Abstract. With use of photon techniques including visible light, soft and hard x-rays, precise fundamental laser welding processes in the repair and maintenance of nuclear plant engineering were reviewed mechanistically. We make discussions centered on the usefulness of an intense soft x-ray beams for evaluations of spatial residual strain distribution and welded metal convection behavior including the surface morphology. Numerical results obtained with a general purpose three-dimensional code SPLICE for the simulation of the welding and solidifying phenomena. Then it is concluded that the x-ray beam would be useful as one of the powerful tools for understanding the mechanisms of various complex phenomena with higher accuracy and higher resolution.

1 Introduction

In this paper, we will try to summarize the present activities on x-ray beam applications to the nuclear engineering field. Japan Atomic Energy Agency (JAEA) promotes a Japanese sodium-cooled Fast Breeder Reactor (FBR)

J. Lee et al. (eds.), *X-Ray Lasers 2010,* Springer Proceedings in Physics 136,
DOI 10.1007/978-94-007-1186-0_27,

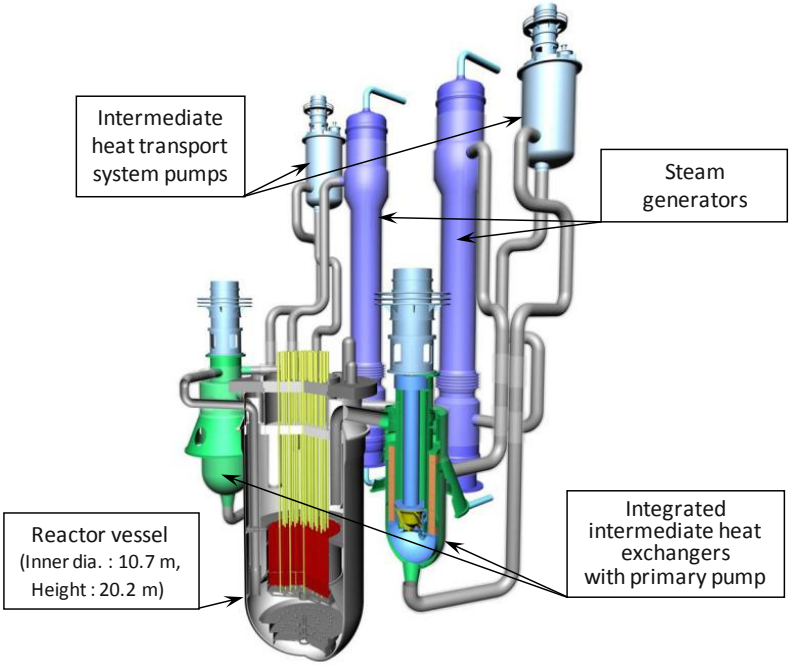

Fig. 1 A Japanese 1,500 MWe large-scaled FBR.

"Monju" as a main project. At the commercial use stage of the FBRs (Figure 1), a securing maintenance and repair more than those of present LWRs is required [Ref. 1]. Especially, the establishment of the repair technology that secures the plant integrity for long-term operation period becomes indispensable in the heat transport tubes of the steam generator that forms the boundary of liquid sodium and water as coolants. From this point of view, special attentions should be paid to the internal residual stress distribution arising in the repaired materials due to metal welding because it suffers the structural integrity resulting in a shorter plant life.

A laser can also contribute to the remote sensing in the nuclear power plants. On the basis of such practical applications, we also plan to perform a wide range of research on the laser interaction with matter to find out a guiding principle of our laser based research plans, which might also contribute to the industrial applications.

The organization of the paper is as follows. After this introduction, Chap.2 deals with the complex physics concerned about laser welding processes observed by a high speed visible camera and the result is compared with numerical simulations.

The remaining chapter describes spatial residual strain distribution and welded metal convection behavior including the surface morphology. For this purpose, we also describe the diagnostic techniques with x-ray beams for characterization of the welded materials.

2 Fundamental laser welding processes for repair and related numerical simulations

2.1 Sequence of the processes

Figure 2 shows fundamental phenomena in laser welding processes. The processes proceeded along the following sequence.

(1) *Irradiation of laser light on material surface*. Laser light irradiates a damaged area stuffed with a welding material. Consequently, heat generation is given to the material according to the Lambert-Beer law.

(2) *Heat conduction to base metal from the laser heated area.* Given heat is conducted into the base material based on the Fourier/Non-Fourier laws.

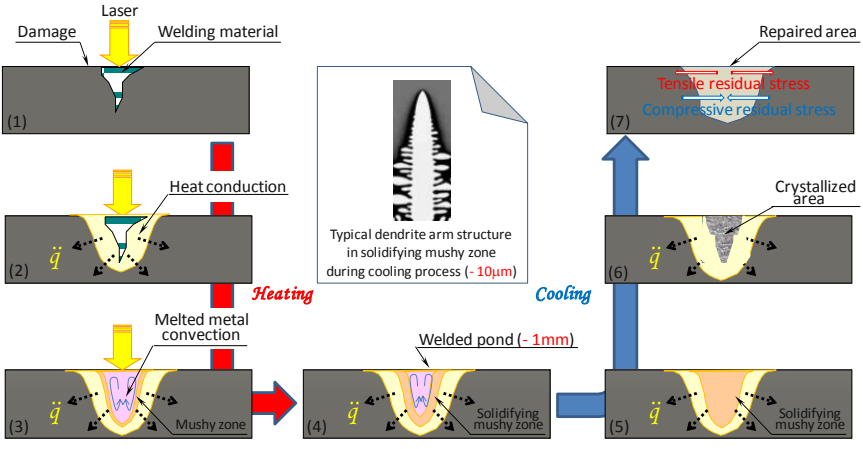

Fig. 2 Fundamental phenomena in a laser welding process.

(3) *Formation of welded pond containing liquid metal convection*. Liquid metal convection is produced by buoyancy effects due to spatial temperature distributions in the welded pond, and is affected due to the presence of a mushy zone formed at a solid and fluid boundary.

(4) *Growing thickness of the mushy zone.* A solidifying process begins from the outer region of the welded pond due to lack of the laser heating.

(5) *Disappearance of the liquid metal convection in the welded pond.* Dendrite arm structures grow into the thick mushy zone based on the nucleus formation theory.

(6) *Crystallization of the solidifying mushy zone.* The mushy zone crystallizes with a metallurgic-phase substance.

(7) *Generation of macroscopic residual stresses.* Tensile and compressive residual stresses form around the base metal surface.

As indicated above, the laser welding processes are characterized as complex phenomena containing phase change behavior. Therefore, physical understanding of the mechanisms with higher accuracy and higher resolution for the complex phenomena is extremely important towards the standardization of the laser welding technology.

2.2 Welded pond behaviour observed by a high speed visible camera

Preliminary visualization for the welded pond surface behaviour was carried out using a high speed camera during the laser irradiation to specimens. Figure 3 shows a schematic of the experimental set-up. The laser sweep speed were set to three conditions of 50 mm/s, 10 mm/s and 5 mm/s, and the camera scanning speed was 12500 frame/s with a field of view of 5 mm x 5 mm.

Figure 4 shows two types of a typical behavior of the welded pond surface. The first one is a steady-state type, which is characterized by a steady convection flow of the melted metal. The second behavior is an unsteady type with a violent blowing off of the welding materials due to a rapid gas expansion. Though both types of the typical behavior depend on the laser

sweep speed, it can be considered that the welded pond behavior is controlled by some physical properties of liquid metal: such as surface tension by the molecular cohesion forces, wettability determined by a force balance between adhesive and cohesive forces, buoyancy by axial temperature difference and thermal properties.

Therefore it is concluded that the welded pond behavior follows macroscopic continuous mechanics of flows.

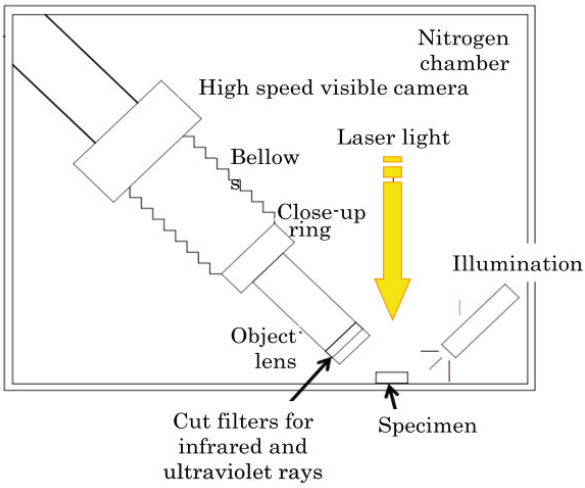

Fig. 3 Experimental apparatus of visualization for a welded pond behavior.

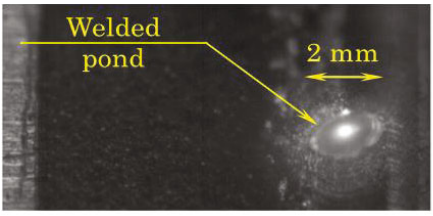

(a) Typical behavior of a steady welded pond observed in the condition of 0.1 mm depth simulating a crack and 10 mm/s of the laser sweep speed

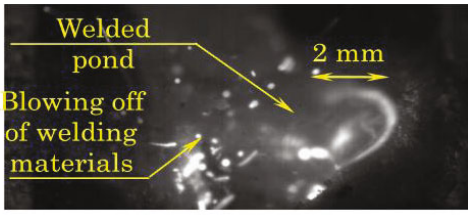

(b) Typical behavior of an unsteady welded pond observed in the condition of 1.0 mm depth simulating a crack and 10 mm/s of the laser sweep speed

Fig. 4 Photographs of the visualized welded pond behavior.

2.3 Numerical simulations for the welding and solidifying processes

A general purpose three-dimensional code SPLICE for the simulation of the welding and solidifying processes was developed at JAEA and deal with incompressible multi-phase flows in various welding applications. The code solves mass, momentum and energy conservation equations simultaneously in a finite volume form. The CIP (Cubic Interpolated Profiles) scheme [Ref. 2] is employed to approximate the convection terms in conservation equations.

The SPLICE code was applied to a butt welding problem of aluminum plates of 2 mm thickness to demonstrate the code performances. A computational domain (x-y-z : 5 mm x 5 mm x 5 mm) including gas region was divided into 100 meshes for each coordinate. Laser power (160 W), focused laser beam diameter (0.5 mm) and laser sweep speed (5 cm/s) were given as the welding conditions.

Figure 5 shows calculated distributions in a 50 ms interval for surface temperature on the welded plate. Qualitative agreement can be seen in those figures with respect to a welded pattern in the bead-on-plate problem.

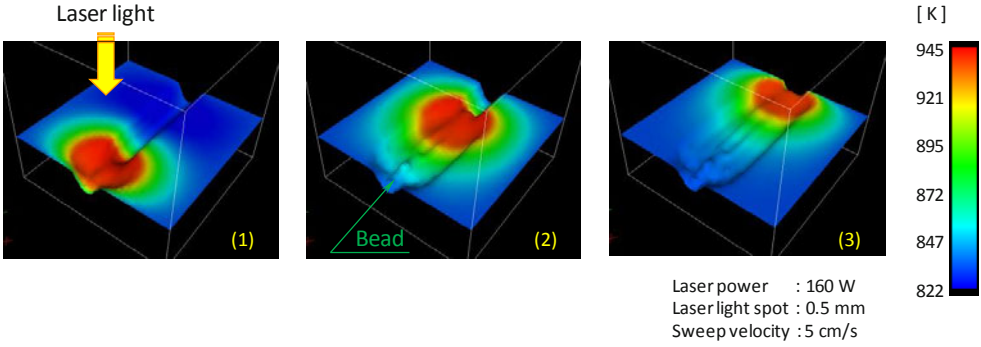

Fig. 5 Numerical results for a laser butt welding simulation.

3 High resolution experiments

3.1 Utilization of an intense synchrotron x-ray beam

3.1.1 Spatial residual strain measurements

Three-dimensional measurements of residual strain were performed using an intense synchrotron x-ray beam (BL22XU) from the SPring-8 facility [Ref. 3]. The photon energy of an intense synchrotron x-ray beam was 66.8 keV. The irradiated area made by the divergent slit was 0.5 mm x 0.1 mm and the CdTe diode detector was used so as not to measure the noise by x-ray fluorescence from the specimen. The strain scanning method using α-Fe 211 diffraction plane was utilized for the measurements of residual strain distributions generated by the laser welding repair processes (shown in Fig. 3).

Typical results of the residual strain distributions to the depth direction in S50C specimen are shown in Fig. 6. The relation between the lattice spacing, d and the strain normal to the diffraction plane, ε, is given by

$$\varepsilon = (d - d_0) / d_0, \quad (1)$$

where d_0 is the lattice spacing without a strain. The relation between the lattice spacing, d and the diffraction angle, 2θ is given by Bragg's law, which is shown in the following equation.

$$d = 12.398 / (2\,E \sin\theta), \quad (2)$$

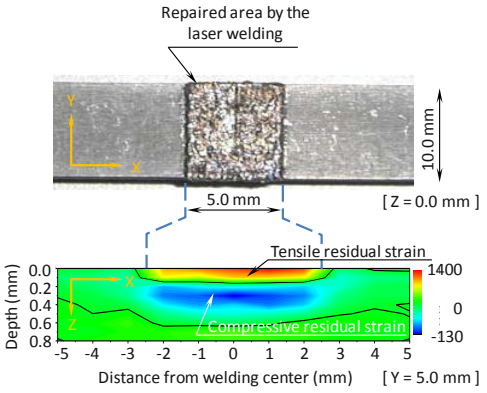

Fig. 6 Measured internal strain distribution for a S50C specimen repaired by the laser welding.

where E is the incident photon energy. Generally, a tensile residual strain area is created beneath the surface due to the solidifying from the periphery of the welded pond. On the other hand, a compressive residual strain area is formed in a deeper region of the repaired materials. Then, from the change of full width at half maximum in profile measured with above mentioned technique, we found that the organization beneath the surface is a state of tensile strain with plastic deformation and the internal organization is that of compression strain with elastic deformation generated in order to balance the tensile strain. Especially, it becomes clear that the absolute value of strain is increasing with the thermal input, and the area of strain distribution is changed by the laser sweep speed. As a conclusion, these are powerful data for the understanding of the phenomena to keep the structural integrity, and for the validation of the SPLICE code.

As indicated in section 2.1, accurate evaluations are required for liquid metal convections with the mushy zone having intermediate characteristics between liquid metal and solid. We are planning a new in-situ real time experiment such as PTV (Particle Tracking Velocimetry) measurements using an intense synchrotron x-ray beam from the SPring-8 facility.

3.2 Utilization of a soft x-ray laser beam

We describe briefly the application experiments using soft x-ray lasers for characterizing welding processes. The most significant feature of the soft x-ray laser in the saturated amplification regime is extremely high brightness which means that a well collimated (the beam divergence is less than a few mrad) x-ray beam with a narrow spectral band (the spectral width divided by the central wavelength is ~10^{-5}) and a short-pulse duration (a few ps to a few 100 ps) has been produced [Ref. 4]. A variety of parameters are now available for application experiments of the soft x-ray lasers [Ref. 5, Ref. 6]. The group of JAEA Kansai, ISSP (Institute of Solid State Physics) of Univ. Tokyo and

Univ. of Tokushima have made surface morphology experiment using a silver soft x-ray laser interferometer at 13.9 nm wavelength to see high resolution (1 nm resolution) profiles of the laser heated material with a few ps time resolution. Figure 7 shows the schematic view of the interferometer; (a) and typical interferograms of the platinum sample irradiated by a 100 fs-duration infrared laser pulse for various time delay of soft x-ray laser probe [Ref. 7]. Such an experiment will also contribute to the construction of useful simulation code for laser welding especially for the formation or early phase of the liquid metals such as viscosity, surface tension. The synchrotron machine provide us the powerful hard x-ray source to see internal phenomena of the laser welded materials such as convection and solidifying as well as crystallization. On the other hand the visible laser or visible imaging technique provides us the precise information of the surface phenomena. The soft x-ray laser provides us the intermediate regions between the regions being observed with visible and hard x-ray.

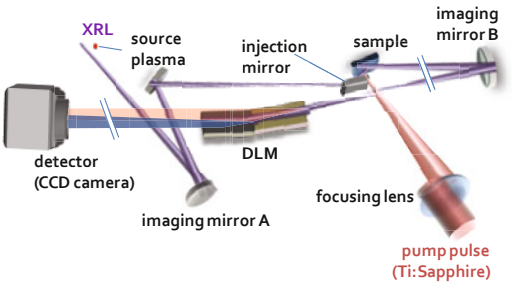

(a) Schematic of the soft x-ray laser interferometer

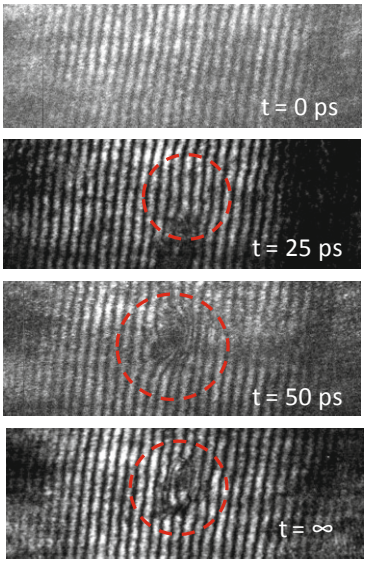

(b) Typical interferogram of the platinum surface pumped by a 100 fs-duration Ti:Sapphire laser pulse for various temporal delay, *t*, of soft x-ray laser probe

Fig.7 Ultra-fast morphology measurement of the welded pond surface dynamic behavior using a soft-x-ray laser beam (Planned).

4 Conclusions

The precise fundamental laser welding processes in the repair and maintenance of nuclear power plants were reviewed mechanistically with use of photon techniques including visible and soft and hard x-ray beams. In this review, discussions centered on the efficiency for intense and soft x-ray beams in evaluations of spatial residual strain distribution and welded metal convection behavior including the surface morphology. From the mechanistic review, the following results were obtained.

(1) The behavior of the welded pond around 2 mm diameter follows macroscopic continuous mechanics of flows in engineering situations from the observation using the high speed visible camera.

(2) The organization beneath the surface is a state of tensile strain with plastic deformation and the internal organization is that of compressive strain with elastic deformation generated in order to balance the tensile strain from the measurements using the intense synchrotron x-ray beam.

(3) The soft x-ray laser beam is applicable efficiently to the surface morphology evaluations for the formation or early phase of the welded pond generated by the laser heating.

The results obtained in this work are very encouraging: the x-ray beam would be useful as one of the powerful tools for understanding the mechanisms with higher accuracy and higher resolution of various complex phenomena such as the laser welding processes.

References

1. Nishimura, A., Shobu, T., Oka, K., Yamaguchi, T., Shimada, Y., et al., "Development of inspection and repair technology for heat exchanger tubes in fast breeder reactors", *The 5th International Congress on Laser Advanced Materials Processing (LAMP2009),* Vol. 9, pp. 146 (2009).

2. Yabe, T., Xiao, F., and Utsumi, T., "The constrained interpolation profile method

for multiphase analysis, *Journal of Computationa Physics*, Vol. 169, pp. 556 (2001).

3. Shobu, T., Okazawa K., Muramatsu T., Takase K., and Tsukimori K., "Stress/strain distributions in fiber laser welded materials using a mimute metal power", *MECA SENS V/QuBS2009 Laser welding and forming at Mito OS-59*(2009).
4. Daido, H., "Review of soft x-ray laser research and developments", Rep. Prog. Phys., Vol. 65, pp. 1513 (2002).
5. Rus, B., Mocek, T., Prag, A., Kozlova, M., Jamelot, G., Carillon, A., Ros, D., Joyeux, D. and Phalippou, D., *Phys. Rev*. A 66, 063806 (2002).
6. Kawachi, T., Kado, M., Tanaka, M., Sasaki, A., Hasegawa, N., Kilpio, A., Namba, S., Nagashima, Lu, K., P., Takahashi, K., Tang, H., Tai, R., Kishimoto, M., Koike, M., Daido, H. and Kato, Y., *Phys. Rev.* A 66, 033815 (2002).
7. Suemoto, T., Terakawa, K., Ochi, Y., Tomita, T., Yamamoto, M., Hasegawa, N., Deki, M., Minami, Y. and Kawachi, T., *Opt. Express* 18, 14114 (2010).

XUV Radiation Emitted by Capillary Pinching Discharge

M. Vrbova[1]*, A. Jancarek[2], P. Vrba[3], M. Nevrkla[2] and P. Kolar[1]

[1] CTU in Prague, Faculty of Biomedical Engineering, Czech Republic
[2] CTU in Prague, Faculty of Nuclear Sciences and Physical Engineering, Czech Republic
[3] Institute of Plasma Physics, Academy of Sciences, Czech Republic

Abstract. Fast capillary discharge in nitrogen is studied as a source of incoherent monochromatic radiation in "water window" wavelength range. Discharge system with current amplitude 13.5 kA and half period 140 ns was designed, realized and modeled. Strong spectral line at 2.88 nm corresponding to the quantum transition $1s2p \rightarrow 1s^2$ of helium -like nitrogen ions was detected. The initial pressure nitrogen in the alumina capillary was varied from 10 to 220 Pa. Peak value of the line intensity at about 50 Pa was found and proved by the computer modeling.

1 Introduction

Our aim is to develop a laboratory source of XUV radiation for microbeam and microscope experiments to be carried out in any typical biological research laboratory. Monochromatic radiation sources in the"water window" wavelength range are not readily available today outside synchrotron facilities.

We have decided to extend our previous research activities and to design a source based on the fast capillary discharge in nitrogen [1,2]. We have conducted simultaneously laboratory experiments and computer modeling which are reported here.

2 Experimental setup and results

Discharge plasma evolution and its emission has been studied in alumina capillary with inner radius $R_0 = 1.65$ mm, filled by nitrogen at pressures 10 – 220 Pa (Fig.1). The measured electric current peak value $I_{max} = 13.5$ kA, and quarter period $T_{1/4} = 75$ ns. (see Fig. 4). Time integrated spectra have been recorded by back illuminated CCD camera (M25 X-Vision Rigaku) placed in the diffracted field of free standing diffraction grating (with period 100 nm).

J. Lee et al. (eds.), *X-Ray Lasers 2010,* Springer Proceedings in Physics 136,
DOI 10.1007/978-94-007-1186-0_28, © Canopus Academic Publishing Limited 2011

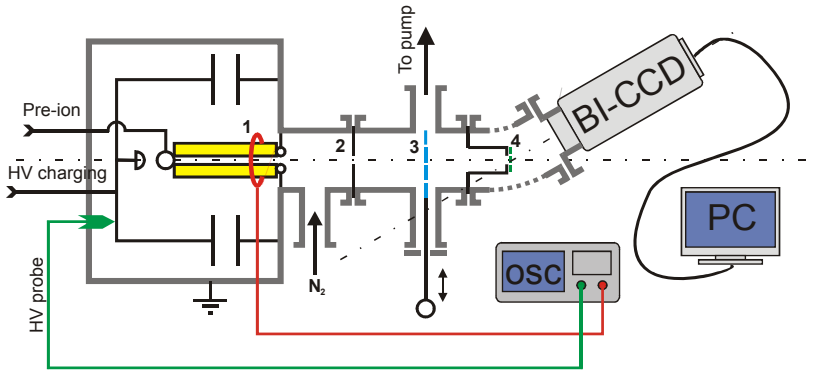

Fig. 1. Experimental setup; 1-Rogowski coil, 2-Aperture, 3-Filter set on mowing arm, 4-Diffractive grating

Various transmission filters between capillary output and the diffraction grating have been placed to identify the emitted spectral lines. The recorded spectra behind aperture 200 nm aperture without filters (n_p=100) and with the Titanium and Chromium filters (n_p=60) and 1.2 mm aperture are seen from Fig.2. Three registered diffraction orders are helpful for spectrometer calibration. The most intensive line with the wavelength 2.88 nm corresponds to the quantum transition 1s2p-1s^2 of the helium -like nitrogen ions.

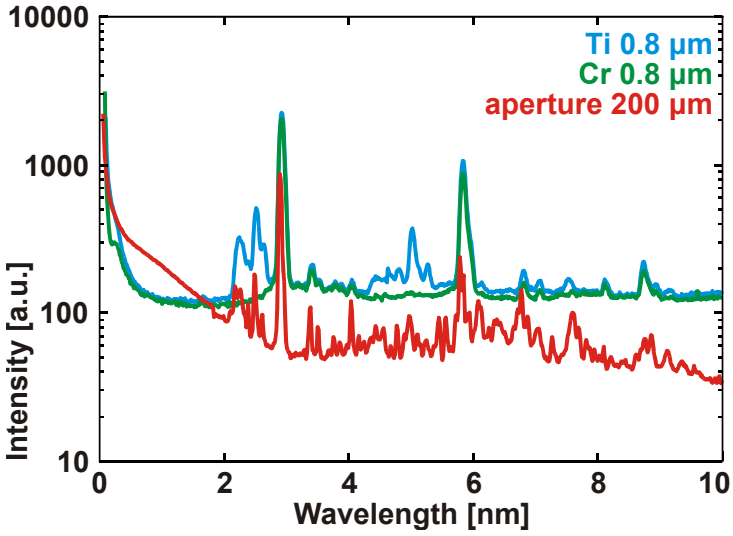

Fig. 2. Emission spectra recorded behind Titanium and Chromium filters (three diffraction orders identified)

The 2.88 nm spectral line was the most intensive for all pressures in the range 20 – 220 Pa. However, its intensity was highest for filling pressures around 50 Pa (see Fig.3).

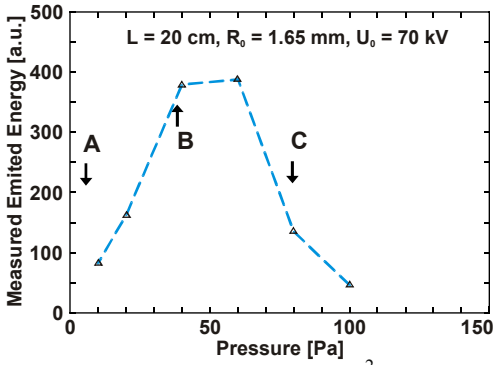

Fig. 3. Output energy at spectral line 2.88 nm ($1s2p\text{-}1s^2$) vs various nitrogen filling pressure

3 Computer modeling

The measured electric current is very near to damped sinus profile $I(t) = I_0.\sin(\pi t / 2t_0).\exp(-t/t_1)$, where the initial current $I_0 = 18$ kA, quarter period $t_0 = 72$ ns and damping time $t_1 = 235$ ns are guessed in our case (see Fig. 4).

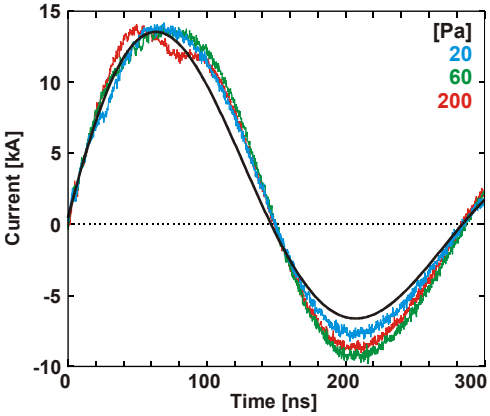

Fig. 4. Measured and fitted current pulse profiles

By introducing fitted current into MHD code NPINCH [3] and changing the initial pressure p_0 in the range from 10 Pa till 220 Pa (i.e. atom densities N_0 in the range 0.045×10^{17} cm^{-3} to 1.0×10^{17} cm^{-3}) we have evaluated radial-time dependencies of capillary plasma quantities such as: plasma density ρ, electron plasma temperatures T_e, current density etc. The selected results for the three pressures are shown in columns A, B and C of Fig. 5. The plasma volume movements are depicted at first row. There it is seen that the pinch time

increases with increasing initial pressure. The compression ratio $C=\rho/\rho_0$ (shown as the second row) decreases with increasing initial pressure. The last row illustrates that the capillary plasma around the axis is very heated at the lowest pressure. In the intermediate case (column B), the plasma temperature has values in the range of 20 eV till 40 eV in a large region around the axis. High density of He –like nitrogen ions is expected in this temperature range. For even higher pressures the electron temperature is rather low (less than 20 eV).

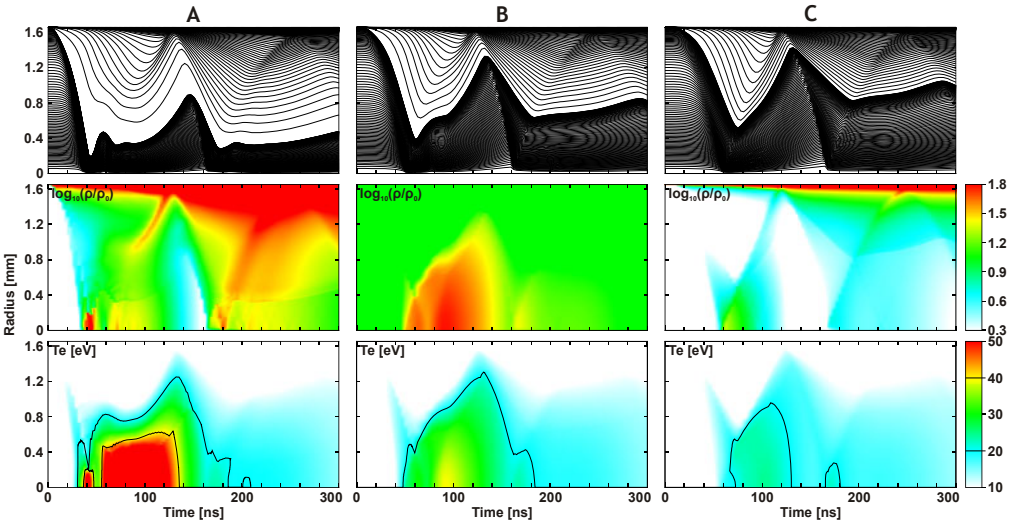

Fig. 5. Radial and time evolution of plasma trajectories, compression and electron temperature for various initial pressures (column A–10 Pa, B–44 Pa, C–88 Pa)

If the evolutions of plasma quantities are known, the abundance of nitrogen ions and densities of excited states of helium-like nitrogen ions may be evaluated by means of the kinetic code FLY [4]. The plasma ionization changes at the capillary axis for the initial atom density $N_0 = 0.4\ 10^{17}$ cm^{-3} (p_0 = 88 Pa) are seen from Fig.6. Substantial changes of ion abundances are found during the first pinch collapse ($t_p \sim 65$ ns). After the pinch the helium-like ions N^{5+} prevail the others for a long period. The time dependences of He -like and Li –like nitrogen ion densities for various initial gas pressures are seen from Fig. 7, 8. The maximum value of He –like N^{5+} in the first half period is achieved for initial pressure ions p_0 = 88 Pa (blue line) The maximum value of populations of Li –like N^{4+} nitrogen ion is one order less than He –like and it is found after the current peak pulse at ~100 ns at the pressure 220 Pa.

The intensities of spectral lines emitted from any plasma elements are given by the instantaneous nitrogen ion densities and by plasma electron temperature at the place.

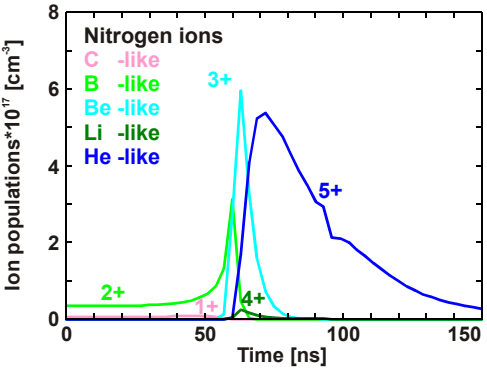

Fig. 6. Time dependence of nitrogen ion populations densities at the capillary axis for the initial pressure $p_0 = 88$ Pa

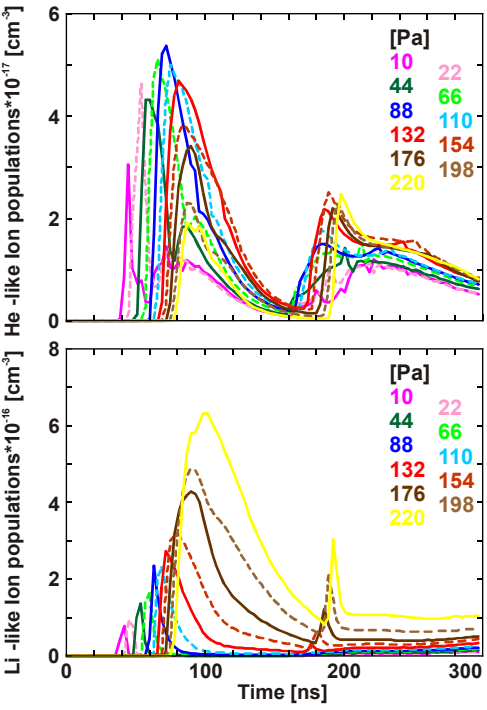

Fig. 7. Time dependences of He -like and Li -like nitrogen ion densities at the capillary axis for various initial gas pressures

4 Estimations of the emitted photon numbers

Energy emitted in the 2.88 nm spectral line corresponds to the spontaneously emitted photons at quantum transition 1s 2p – $1s^2$. The number of photons per second emitted from unit volume $\Phi = A_{21}.N_{2p}$, where the Einstein

coefficient $A_{21} = 1{,}79\ 10^{12} s^{-1}$ and population of the upper level $N_{2p} = N_{He} . \exp(-h\tilde{\nu}/k\ T_e)$, where N_{He} is the total number of He – like ions and quantum of excitation energy $h\nu = 430{,}683$ eV. Having in mind that the helium-like nitrogen ions dominate in the plasma, if the electron temperature $20 < T_e < 40$ eV, we use the approximation $N_{He} = N_{tot} = C\ N_0$ if $20 < T_e < 40$ and $N_{He} = 0$ outside this temperature range, C(r,t) is the mass compression ratio and N_0 is the filling nitrogen atom density. Radial and time distribution of the line emission intensity Φ is depicted as Fig. 9.

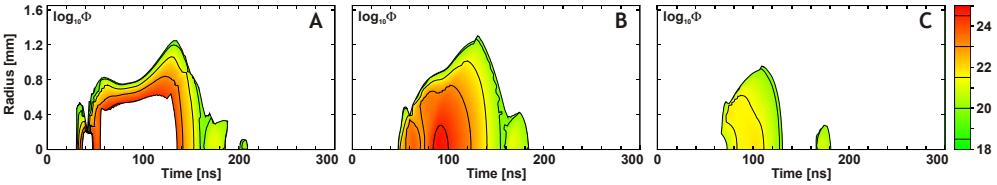

Fig. 9 Radial and time dependence of the logarithm of line emission intensity Φ at the wavelengths 2,88 nm ($1s^2$-1s.2p).

5 Conclusions

Following the experimental results and computer simulations we have estimated the maximum line emission equal to 10^{13} photons per steradian, if the initial gas pressure is optimized. Generally, to get an efficient source of radiation at this wavelength, the parameters of the device (electric current pulse, capillary geometry and initial gas pressure) should be chosen properly to get appropriately dense and hot plasma with predominating abundance of helium-like ions. Further optimization of this capillary source is in progress.

This research has been supported by grants of MEYS on the research project No. 6840770022 and in the frame of INGO Program on the project No. LA 080245.

References

1. Jancarek, A., Nevrkla, M., Vrba, P.,Vrbová, M., Tamas, M., and Pina, L.: Proceedings of 29th ICPIG, Cancun, Mexico (2009), http://www.icpig2009.unam.mx.
2. Vrba, P., Vrbova, M., Bobrova, N. A., and Sasorov, P. V.: Central European Journal of Physics **3**, (2005), pp 564-580.
3. Bobrova, N. A., Bulanov, S. V.,. Raznikova, T. L.,.: Plasma Phys. Rep. **22**, (1996), pp. 387-402.
4. Lee R. W. and. Larsen J. T. : J. Quant. Spectroscopy Radiat. Transf. **56**, (1996), pp. 535-556.

EUV radiation of pulse high-current proximity-wall-stabilized discharges

K. Kolacek[1], J. Straus[1], J. Schmidt[1], O. Frolov[1], V. Prukner[1], J. Sobota[2], T. Fort[2] and A. Shukurov[3]

[1] Institute of Plasma Physics AS CR, v.v.i., Za Slovankou 1782/3, 180 00 Prague 8, Czech Republic
[2] Institute of Scientific Instruments AS CR, v.v.i., Královopolská 147, 612 42 Brno, Czech Republic
[3] Faculty of Mathematics and Physics, Charles University in Prague, Ke Karlovu 3, 121 16 Prague 2, Czech Republic

Abstract. Proximity wall stabilized, fast (>4x10^{11} A/s), high current (>40 kA) discharges are capable to create long, dense, hot, "stable", non-equilibrium plasma column, suitable e.g. for amplification of EUV and soft X-ray radiation. Amplification on the wavelength of 46,9 nm of Ne-like Ar has been demonstrated by many laboratories; this paper shows its application to micro- and nano-structuring of solid surfaces. Simultaneously, an appraisal study is performed on possibilities to shorten the amplified wavelength: one way uses excited Ni-like Ag ions created at Ag wire explosion in water.

1 Introduction

From lasing point of view the best discharge-based radiation sources are capillary discharges [1], which can be very stable (due to proximity of wall), which have already proved strong amplification (up to saturation) – esp. on Ne-like Ar {λ = 46,9 nm}, but which failed, up to the present, in attempts to shorten their wavelength (not counting an amplification on hydrogen-like carbon {λ = 18,2 nm} supplied into the capillary by ablation of capillary walls, which is irreproducible).

Among already demonstrated applications of Ar^{8+} laser belong dense plasma diagnostics (plasma shadowgraphy, plasma interferometry with Lloyd´s mirror and with Mach-Zehnder type interferometer), other imaging, materials characterisation (determination of optical constants in XUV region), XUV optics characterisation, ablation of solid surfaces & micropatterning, and plasma generation. We wanted to test, how harmful for high-resolution imaging or for nanopatterning it could be a laser-induced periodic surface structure (LIPSS), natural side-effect appearing at some fluences on the substrate. While LIPSS of the first type (LIPSS-I, sometimes called

J. Lee et al. (eds.), *X-Ray Lasers 2010,* Springer Proceedings in Physics 136,
DOI 10.1007/978-94-007-1186-0_29,

"coherent" [2]), namely their space periodicity, depend on the wavelength, coherence, polarization and incidence-angle of the laser beam, LIPSS of the second type (LIPSS-II, "incoherent") are dependent mainly on fluency and interaction time of the laser beam.

Simultaneously, an appraisal study is performed on possibilities to shorten the amplified wavelength. The most perspective *excitation pumping scheme* requires for shorter wavelengths plasma of some metal (Pd, Ag, Cd, In, Sn) vapors with abundance of Ni-like ions. Despite there are some methods, how to feed metal vapors into the capillary (see also [3]), due to an unwanted metal deposit remaining on a solid capillary wall it is preferred to use a capillary with liquid – ever fresh – wall, which is formed during wire explosion in water [4]. Originally it was expected that a potential threat of channel fast expansion will be mitigated by a local compression of liquid (to the GPa pressure range) by linearly focused cylindrical shock wave. However, at present, such threat seems to be unsubstantiated. The *recombination pumping scheme* uses usually plasma of light elements (C, N, O, …) with abundance of elements nuclei [3]; at sufficiently fast cooling these nuclei recombine to H-like elements with population inversion on Balmer-alpha transition.

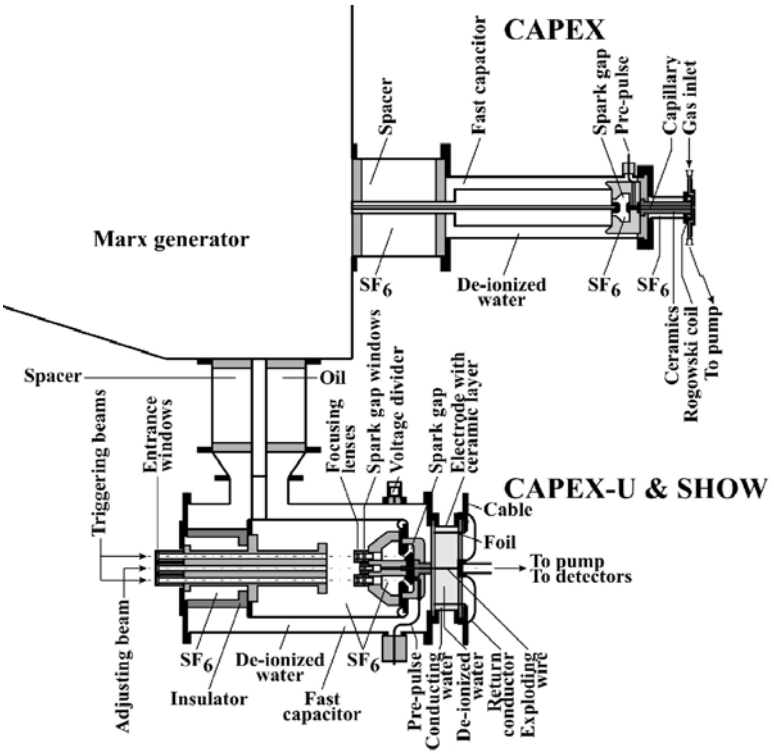

Fig. 1. Apparatus: CAPEX and CAPEX-U facilities

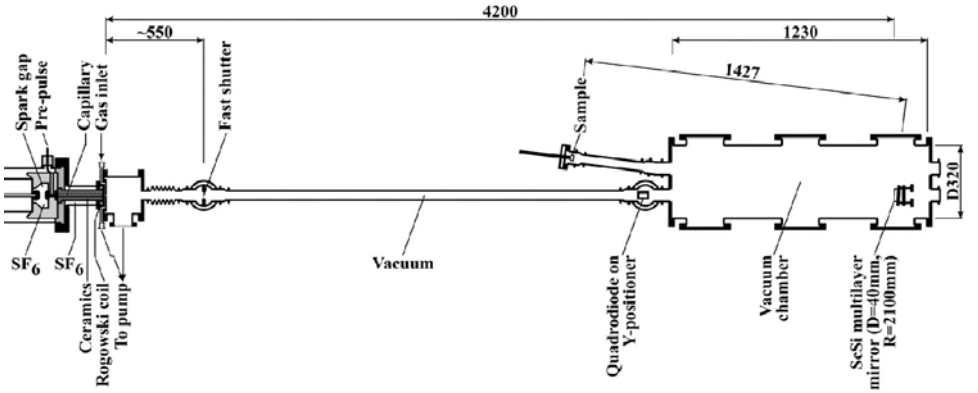

Fig. 2. Extension of CAPEX facility for ablation measurement

2 Apparatus

Our two experimental facilities (CAPEX, and CAPEX-U, see Fig. 1) are fed from one Marx generator with erected capacity 12,5 nF, which can be charged for CAPEX to 400 kV (stored energy 1 kJ), for CAPEX-U to 600 kV (stored energy 2,25 kJ). The CAPEX has fast capacitor 6 nF, characteristic impedance 3,37 Ω, self breakdown spark gap, and gas (Ar, N_2, …) filled capillary (∅3x200 mm). The CAPEX-U has fast capacitor 12,7 nF, characteristic impedance 1,7 Ω, laser triggered spark gap, and SHOW device (∅400x100 mm) enabling wire explosion in the focus of cylindrical shock wave in water.

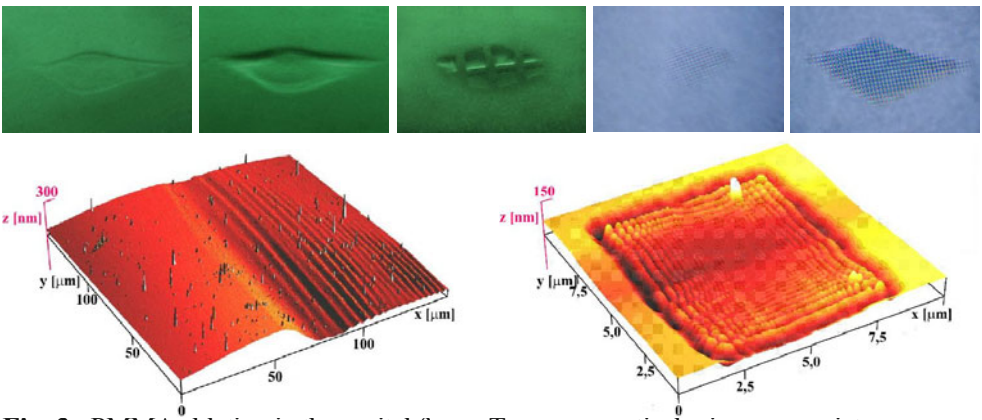

Fig. 3. PMMA ablation in the sagital focus. Top row – optical microscopy pictures – from left to right: 1 shot; 5 shots; 5 shots through Ni grid (step 100 μm, window 70 μm, traverse 30 μm); 1 and 5 shots through Au grid (step 12,5 μm, window 7,5 μm, traverse 5 μm). Bottom – AFM images – left: LIPSS generated by 5 shots (detail of top row, 2nd picture from the left); right: diffraction pattern written by 1 shot in one window of the Au 12,5 μm grid (detail of top row 2nd picture from the right).

3 Ablation experiments with 46,9 nm radiation

The CAPEX facility was extended by a new diagnostic part (see Fig. 2), consisting of electrically actuated mechanical shutter that allows to pass the discharge axial radiation, but stops the primary particles (due to their longer time-of-flight), of quadro-diode, which enables exact adjustment, of diagnostic chamber with multilayer Sc/Si mirror, and of the sample part with PMMA sample.

Unfortunately, the spherical multilayer mirror (∅40/R 2100 mm) changed with time its shape (~5 to 6 HeNe laser fringes across the mirror), therefore, besides astigmatism also a significant distortion of the focal spot shape was observed (see Fig. 3, top row). On the other hand it was encouraging that energy of our laser is sufficient for ablation of this larger (400x200 μm) laser spot. The EUV laser-beam footprint was analyzed by atomic force microscope (AFM). It turned out that practically the whole crater was covered by LIPSS-II (see Fig. 3, bottom left, where the right corner of the area ablated by 5 shots (detail of top row, 2nd picture from the left) is shown); the LIPSS period is ~2,8 μm, peak-to-peak depth is ~5-10 nm, maximum depth for 5 superimposed shots is ~200 nm.

Finally it was tested, if the LIPSS can influence the small scale imaging. Therefore, on the surface of PMMA the Au grid (step 12,5x12,5 μm, windows 7,5x7,5 μm, traverses 5 μm) was placed. Exposition of the surface through this grid resulted in well-developed 2D diffraction pattern in each grid window; period of this pattern changes from ~800 nm at the edge of this window down to ~125 nm in the middle of the window. The shallow ridge visible in the mid of the window could be attributed to the LIPSS.

4 Exploding Ag wire in water – a possible environment for amplification at shorter wavelengths

The Ag wire (∅0,2x20 mm) was placed on the SHOW (SHOck Wave) device axis and exploded by high electric current. It has been shown earlier [5] that

- axial radiation output (patent pending) was solved; it was proved that the detected radiation comes from the inner part of experimental chamber;
- around the wire a thin layer of water vapour is created; however, it is much later than it was originally expected: according to our model the wire surface heats to 100 ^{o}C in 17 ns, and to 200 ^{o}C in 24 ns, while H_{α} line appears in radial direction 120 ns or 170 ns after the current onset at the current amplitude 60 kA or 40 kA, respectively;
- broadening/shift of H_{α} line registered in radial direction (which reflects earlier stage of the discharge) is 19,09 nm/7,77 nm, which suggests Van

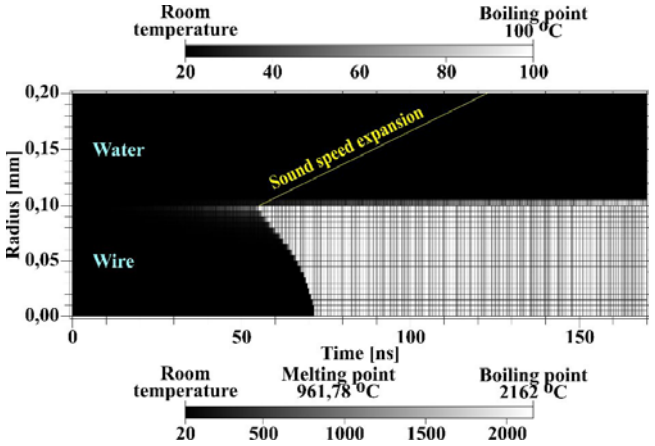

Fig. 4. Development of the temperature field; horizontal axis gives time since the current onset, lower gray scale gives the local temperature in the wire, upper gray scale, gives the local temperature in the water

der Waals main type interaction with particle density $n \sim 2.10^{21}$ cm^{-3} $\sim 2.10^{27}$ m^{-3}, which results in pressure $p \sim 6{,}4.10^{7}$ Pa $\sim$ 632 atm;

- broadening/shift of H_α line registered in axial direction (which reflects later stage of the discharge) is 19,30 nm/4,77 nm, which suggests Van der Waals interaction with Doppler broadening with particle density $n \sim 7{,}4.10^{19}$ cm^{-3} $\sim 7{,}4.10^{25}$ m^{-3}, and temperature 3,5 keV; this yields local pressure as high as $p \sim 4.10^{10}$ Pa $\sim 4.10^{5}$ atm; another composition of broadening mechanisms can give substantially different and probably more acceptable results.

The present, upgraded model of the wire explosion was extended to take into consideration an influence of the surrounding water (see Fig. 4). The model includes current density diffusion with space- and time-varying conductivity, and thermal balance with Joule heating, thermal diffusion, and phase transitions. It turns out that heat exchange between wire and water is relatively slow. Therefore, first melts and evaporates the surface of the wire; in the moment of its evaporation significantly increases the local pressure, heat exchange between wire and water is further reduced, and much later water vapour layer appears. This model supposes an “incompressible water”. A more realistic model requires determining the content of diluted gases and vapours in water and appropriate adjusting the Equation of state of water. This will yield the important information about plasma channel expansion, the rough estimate of which is also shown in the Fig. 4.

5 Conclusion

The focusing experiments with Ar^{8+} ion laser showed that practically the whole in-PMMA-ablated spot was covered by Laser Induced Periodic Surface Structure, currently called "incoherent" LIPSS-II, which is attributed either to solidified hydrodynamic distortions of melted surface (acoustic and capillary waves, or thermo-capillary and Kelvin-Helmholtz instabilities), or to relaxed inner tensions in the illuminated matter. However, it seems that the perfect ablated 2D diffraction pattern of sub-micrometer scale speaks against this interpretation.

The extended model of wire explosion in water included influence of water. It turned out that heat transfer through metal-water interface is very small. This explains the late appearance of H_α line in the spectrum. Therefore, the main pressure increase appears in the moment, when the wire starts to evaporate. Relevance for lasing can give later study of dense metal vapour plasma dynamics.

Acknowledgement

The experimental part of this work was performed under auspices and with the support of the Grant Agency of the Academy of Sciences CR (contracts KAN300100702 and KJB100430702), the theoretical part of this work was supported by the Ministry of Education, Youth, and Sports of the Czech Republic (contracts LA08024 and LC528).

References

1. Kolacek, K.: ´Principles and present state of capillary-discharge-pumped soft X-ray laserˇ, *Proc. SPIE,* 5228, 557-573, 2003
2. Bäuerle, D.: *Laser Processing and Chemistry*, 2nd ed., Springer-Verlag, Berlin-Heidelberg-New York, 1996
3. Kolacek, K., Schmidt, J., Prukner, V., Frolov, O., Straus, J.: ´Ways to discharge-based soft X-ray lasers with wavelength $\lambda < 15$ nm´, *Laser and Particle Beams*, 26, 167-178, 2008
4. Kolacek, K., Schmidt, J., Prukner, V., Sunka, P., Frolov, O., Straus, J., Martinkova, M.: ´Wire exploding in a focus of converging cylindrical shock wave in water – Introductory remarks´, *15th IEEE Int Pulsed Power Conf.*, Paper 2005_066, 280-283, 2005
5. Kolacek, K., Prukner, V., Schmidt, J., Frolov, O., Straus, J.: ´A potential environment for lasing below 15 nm initiated by exploding wire in water´, *Laser and Particle Beams*, 28, 61-67, 2010

Part 7: X-Ray Laser Applications

Probing high energy density plasmas with X-ray lasers

G J Tallents[1], L M R Gartside[1], A K Rossall[1], E Wagenaars[1], D S Whittaker[1], M Kozlova[2], J Nejdl[2], M Sawicka[2], J Polan[2], M Kalal[3] and B Rus[2]

[1] Department of Physics, University of York, York YO10 5DD, U.K.
[2] Department of X-ray lasers, PALS Research Centre, Institute of Physics, Academy of Sciences of the Czech Republic, 182 21 Prague 8, Czech Republic
[3] Department of Physical Electronics, Faculty of Nuclear Sciences and Physical Engineering, Czech Technical University in Prague, Brehova 7, 115 19 Prague 1, Czech Republic

Abstract. X-ray lasers can probe solid density plasmas as the critical density is well above the electron densities produced. We consider an experiment where interferometry has been utilized to provide phase information and transmission measurements for an extreme ultra-violet (EUV) laser beam at 21.2 nm probing longitudinally through a laser irradiated plastic (parylene-N) target. The transmission provides a good measure of ablation as hot plasma becomes transparent. We show that refractive indices significantly below the solid parylene-N and plasma refractive indices are produced in the warm dense plasma produced by laser irradiation.

1 Introduction

Soft x-ray lasers have been used to probe the properties of laser-plasmas since the mid-1990s [1, 2]. Interferometry using plasma-based x-ray lasers has elucidated the structure of expanding plasmas [3] and shown that anomalous refractive indices η (with $\eta > 1$) can exist in plasmas associated with strong absorption features [4]. Transmission measurements of plasma-based x-ray lasers have provided information on plasma opacity [5] and the rate of ablation of solid targets irradiated by optical lasers [6]. There are plans to use free-electron lasers (FELs) for plasma probing with the plasma being created by an optical laser [7] or a split FEL pulse [8].

Even with complete ionization, the critical density for an x-ray laser is well above the density of electrons in a solid material. Wavelengths λ in nm such that

J. Lee et al. (eds.), *X-Ray Lasers 2010,* Springer Proceedings in Physics 136,
DOI 10.1007/978-94-007-1186-0_30,

$$\lambda < \lambda_0 = 40\sqrt{\frac{M}{\rho Z^*}} \tag{1}$$

can be used to probe a plasma of density ρ (in gcm^{-3}) without collective absorption effects associated with electron densities close to the critical density affecting transmission measurements. Here M is the target atomic number, Z^* is the degree of ionisation and ρ is the density of the target. However, refraction effects on a probing beam can be significant. With an electron density n_e varying with scalelength Δx, probing radiation is refracted to an angle of refraction θ (in radians) given approximately by

$$\theta \approx \frac{L}{\Delta x}\frac{n_e}{2n_c} \tag{2}$$

where L is the length of probed plasma and n_c is the critical density. The refraction angle θ may cause apparent spatial movement of the probe beam resulting in distortion in interpreting probe beam spatial information or, in extreme cases, refraction can result in the probe beam deviating outside the solid angle of collection optics so that all probing information is lost. These issues have been extensively examined for optical interferometry of plasmas [9]. With x-ray lasers, for example at 21.2 nm, transverse probing of a plasma of width L = 100 μm and density scalelength Δx = 5 μm will cause a large amount of refraction with θ = 0.6 radian at electron density n_e = 0.01 n_c. EUV radiation of wavelength λ = 13.9 nm (corresponding to Ni-like Ag lasing) if we require θ < 0.6 radian can only probe to a density of $\rho \approx$ 0.1 gcm^{-3} (assuming full ionization with $M/Z^* \approx 2$). The difficulty of probing at high density with significant density gradients is illustrated in figure 1. Figure 1 also illustrates how density gradients transverse to the probe beam propagation direction are reduced by typically several orders-of-magnitude by probing longitudinally through the typical target used in laser-plasma experiments. Probing solid density material longitudinally ensures that the probed plasma conditions are limited only by the constraint of equation (1).

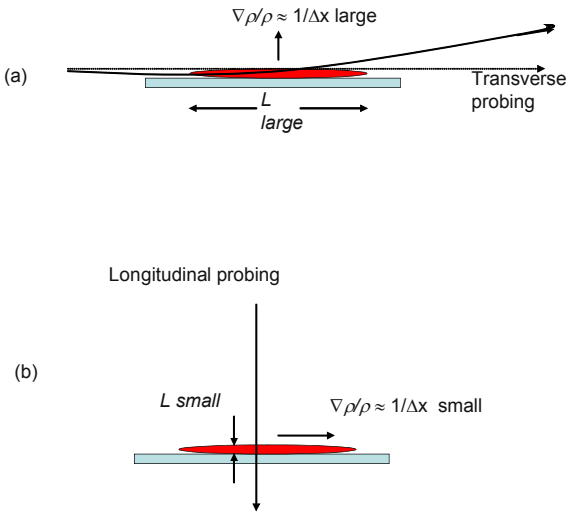

Fig. 1 Schematic geometries used in probing plasmas either (a) transversely or (b) longitudinally. Longitudinal probing minimises refraction effects.

We report an experiment where interferometry with a 21.2 nm wavelength x-ray laser is used to probe the effects of phase change and absorption through thin (350 nm) targets of parylene-N (C_8H_8). Interestingly, we show evidence for plasma refractive index *η lower* than that obtained using the standard expression

$$\eta = \left(1 - \frac{n_e}{n_c}\right)^{1/2} \approx 1 - \frac{n_e}{2n_c}. \qquad (3)$$

2 Experiment

The interferometer set-up and detailed analysis of this experiment is reported respectively by Kozlova et al [10] and Gartside et al [11]. Figure 2 illustrates the principle of the interferometer set-up on the PALS x-ray laser facility. Essentially, 350 nm thick parylene-N (C_8H_8) targets were interferometrically probed with 200 ps duration 21.2 nm wavelength x-ray laser pulses, while a second heating beam of 300 ps duration and wavelength 438 nm (3rd harmonic of the iodine laser wavelength) focused to 10^{12} Wcm^{-2} was used to ablate the target and produce a plasma. The interferometer records relative phase changes of a probing beam passing through unablated

solid C_8H_8, heated high density material and expanding carbon and hydrogen plasma compared to a reference beam passing through the unheated solid C_8H_8. By recording visibility changes to interference fringes, it is also possible to measure simultaneously the transmission of the ablating target to the probe beam [12]. Delaying the x-ray laser pulse relative to the optical heating pulse allows a measure of the transmission and phase change of the irradiated target as a function of time (figures 3 and 4).

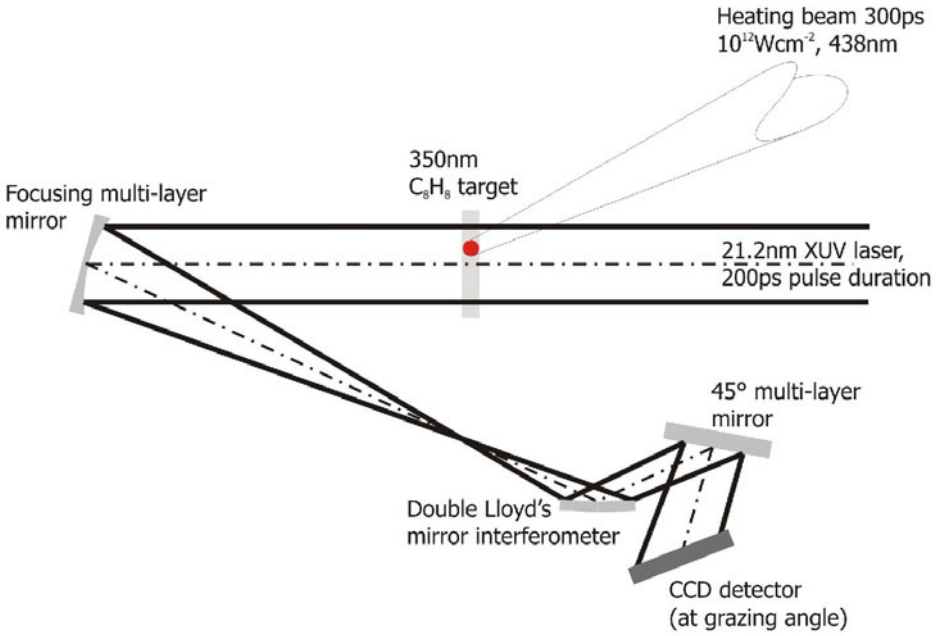

Fig. 2 Schematic experimental set-up used to undertake longitudinal interferometry at 21.2 nm on a solid parylene-N target irradiated by a heating beam.

3 Results

The transmission of the 21.2 nm probe beam through the irradiated target as a function of time is shown in figure 3. Simulations using a 2D code (h2d, see [13]) with plasma opacity values as calculated by the IMP code [14] predict transmissions in approximate agreement with the experimental results (the simulations are superimposed on figure 3). As found earlier with iron targets [6], ablated plastic material becomes transparent due to a rapid increase in temperature causing ionization to stages (C^{3+} and higher) where the photon energy (59 eV) is insufficient

to enable photoionisation from the ground state. Figure 3 shows that the transmission increases uniformly during the target irradiation as ablation reduces the thickness of the remaining solid unablated target.

In a one-dimensional expansion with refractive index given by equation (3), we might expect not to have any fringe shift with our interferometry measurements. The fringe shift is determined by the integration of 1 - η over distance x through the target and plasma compared to the integration of 1 - η_{solid} through the solid target (where η_{solid} = 0.946 is the refractive index of the solid parylene-N target). If we integrate 1-η over distance using equation (3), we effectively integrate $\int n_e dx$ which is constant in a one-dimensional expansion. Furthermore, assuming ionization to C^{5+} - C^{6+}, the refractive index for solid density plasma material calculated using equation (3) is 0.94 – 0.95 and so is close to the solid target value. However, the results of figure 4 clearly show negative phase changes in the probing beam relative to the reference beam passing through the solid material indicating that the refractive index η of some of the heated material has dropped below the plasma and the solid unheated target refractive index.

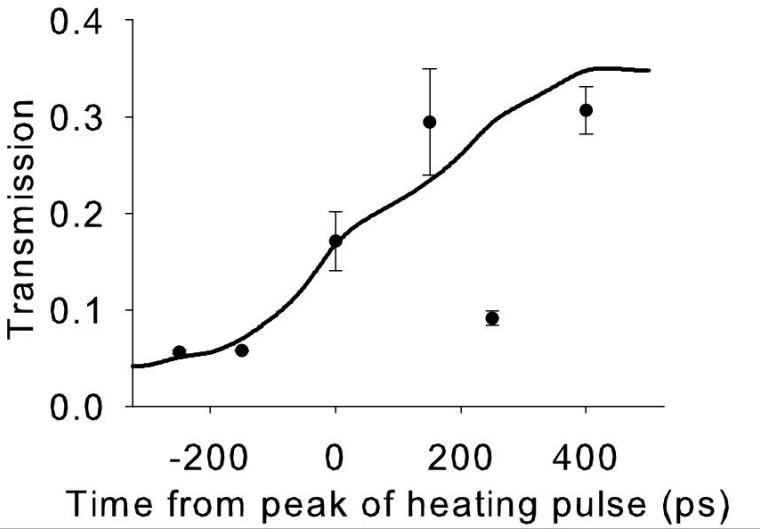

Fig. 3 The transmission of 21.2 nm XUV laser pulses through a 350 nm thick parylene-N target irradiated by a laser of peak irradiance 10^{12} Wcm^{-2} in a pulse of 300 ps duration. The solid curve is a simulation of the transmission using the h2d code with IMP opacities.

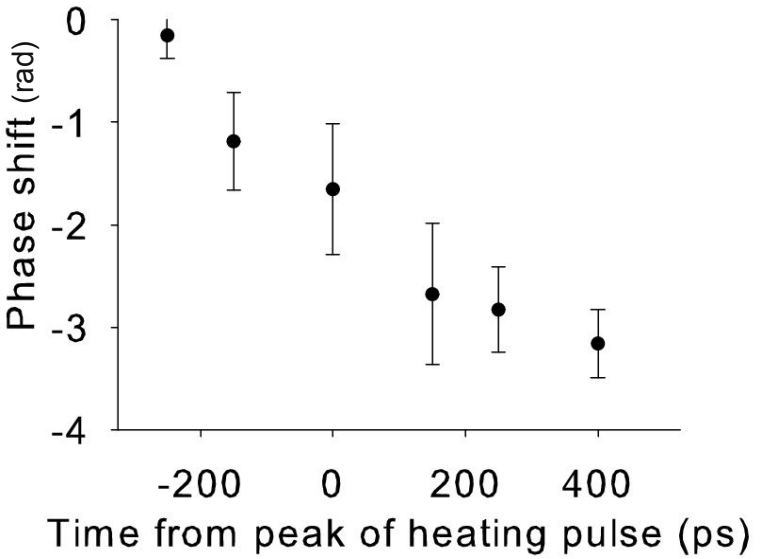

Fig. 4 The phase shift of the 21.2 nm XUV probe laser pulse through a 350 nm thick parylene-N target irradiated as for figure 3. Negative phase shift as shown implies refractive indices in the probed material less than $\eta_{solid} = 0.946$.

4 Analysis

The refractive indices of materials can be determined using the Kramers-Kronig (KK) relationship which shows that the real refractive index $\eta(\omega)$ at frequency ω is related to a weighted integration over the material absorption coefficient $\alpha(\omega)$ (see e.g. [4] for calculations relevant to plasmas). We can write that

$$\eta(\omega) = 1 + \frac{c}{\pi}\int_0^{\infty} \frac{\alpha(\omega^*)}{\omega^{*2} - \omega^2} d\omega^* . \quad (4)$$

Work by Filevich et al [15] has shown that there are no refractive index effects due to absorbing carbon lines in the region of the x-ray laser probing photon energy ($\hbar\omega$ = 59 eV). Consequently, we evaluate the refractive index of the heated target material by assuming that bound-free absorption dominates in the KK integration (equation 4). A bound-free absorption coefficient (in cm^{-1}) can be written

$$\alpha(\omega) = 2.44\times10^{-37}\,\frac{n_e^2 Z^*}{\sqrt{kT}\,(\eta\omega)^3}\left[1-\exp\left(-\frac{\eta\omega}{kT}\right)\right]\left[G\,\frac{\xi}{n^3}\,\frac{\eta\omega_o}{kT}\exp\left(\frac{\eta\omega_o}{kT}\right)\right] \tag{5}$$

where the electron temperature kT and photon energy $\hbar\omega$ are in eV and the electron densities are in cm^{-3}. Here Z^* is the degree of ionization, n is the principal quantum number of the ground state and ξ is the number of vacancies in the ground energy level of the relevant ion. The Gaunt factor G is taken to be zero for photon energy $\hbar\omega$ less than the ionization energy $\hbar\omega_o$ and unity otherwise. We approximate equation (5) by assuming that

$$\begin{aligned} \alpha(\omega) &= \alpha(\omega_o)\frac{\omega_o^3}{\omega^3} && (\omega > \omega_o) \\ 0 && (\omega < \omega_o) \end{aligned} \tag{6}$$

where ω_o is the appropriate photon frequency at an ionization edge. Using equation (6) in the KK relationship (equation 4), it is then possible to obtain an analytic solution for the refractive index. For $\omega > \omega_o$, we obtain

$$\eta(\omega) = 1 - \frac{c\alpha(\omega_o)}{2\pi\omega}\left[\frac{\omega_o}{\omega} + \frac{\omega_o^3}{\omega^3}\ln\left(\frac{\omega^2-\omega_o^2}{\omega_o^2}\right)\right] . \tag{7}$$

Evaluations of equation (7) illustrate that refractive index values less than the plasma refractive index (equation 3) and less than the solid parylene-N target refractive index ($\eta_{\text{solid}} = 0.946$) are found in the low temperature, high density plasmas formed by laser heating the target (see figure 5). The KK integral (equation 4) is dominated by the value of absorption coefficient $\alpha(\omega)$ near the frequency of interest so our approximation (equation 6) should be accurate. For the evaluation of figure 5, an LTE variation of the degree of ionization Z^* is assumed and we found that almost all the contribution to the refractive index defect (value below unity) arises from CIII (C^{2+}) bound-free absorption with ionization edge at $\hbar\omega_o = 47.887$ eV. Interestingly, figure 5 shows

that the KK evaluation of refractive index approaches the plasma refractive index value evaluated using equation (3) at temperatures greater than approximately 10 eV.

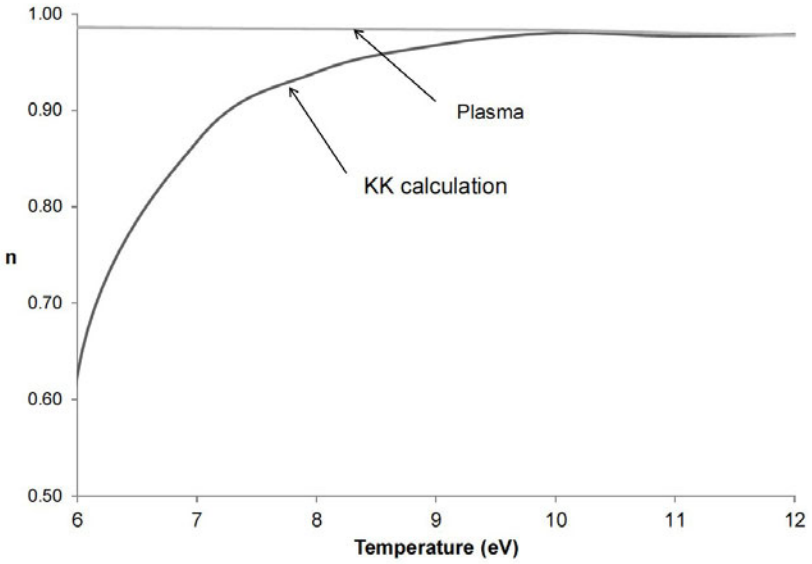

Fig. 5 Refractive index for a solid density parylene-N plasma calculated using the KK relationship assuming free-free and bound-free absorption for 21.2 nm (59 eV) radiation (thick black line) and assuming a plasma refractive index given by equation (3) (gray line).

5 Conclusion

We have shown that refractive indices significantly below the solid parylene-N and plasma refractive indices are produced in the warm dense plasma produced by laser irradiation of parylene-N targets at 10^{12} Wcm^{-2}. We have considered an experiment where interferometry has been utilized to provide phase information and transmission measurements for an extreme ultra-violet (EUV) laser beam at 21.2 nm probing longitudinally through a laser irradiated plastic (parylene-N) target. The transmission also provides a good measure of target ablation as hot plasma becomes transparent for ionization of C^{3+} and higher.

References

1. L B DaSilva, T W Barbee, R Cauble, P Celliers, D Ciarlo, S Libby, R A London, D Matthews, S Mrowka, JC Moreno, D Ress, J E Trebes, A S Wan and F Weber 1995 Phys. Rev. Lett. **74**, 3991.
2. E Wolfrum, J Wark, J Zhang, D Kalantar, M H Key, B A Remington, S V Weber, D Neely, S Rose, J Warwick, A MacPhee, C L S Lewis, A Demir, J Lin, R Smith and G J Tallents 1998 Phys. Plasmas **5**, 227-33.
3. R F Smith, J Dunn, J Nilson, V N Schlyaptsev, S Moon, J Filevich, J J Rocca, M C Marconi, J R Hunter and T W Barbee 2002 Phys. Rev. Lett. **89**, 065004.
4. J Filevich et al 2005 Phys. Rev. Lett. **94**, 035005.
5. M H Edwards, D Whittaker, P Mistry, N Booth, G J Pert, G J Tallents et al 2006 Phys. Rev. Lett. **97**, 03500
6. M H Edwards, D S Whittaker, G J Tallents, et al 2007 Phys. Rev. Lett. **99**, 195002
7. F B Rosmej, R W Lee and D H G Shneider High Energy Density Phys. **3**, 218.
8. D S Whittaker, E Wagenaars and G J Tallents 2010 *in preparation.*
9. G J Tallents 1984 J. Phys. D**17**, 721.
10. M Kozlova, J Polan, P Homer, B Rus et al 2010 *these proceedings.*
11. L M R Gartside et al 2010 *in preparation.*
12. M Kalal 1991 Czech J. Phys. **41**, 743.
13. Cascade Applied Sciences, Inc. Jon Larsen, creator. Larsen@casinc.com
14. S J Rose 1992 J. Phys. B: At. Mol. Opt. Phys. **25** 1667.
15. J Filevich et al 2007 Laser Particle beams **25**, 47.

Measuring the electron density gradients of dense plasmas by X-ray laser deflectometry

J. Nejdl[1,2], M. Kozlová[1], T. Mocek[1], and B. Rus[1]

[1] Institute of Physics Na Slovance 2, 18221 Prague, Czech Republic
[2] Czech. Tech. Univ. in Prague, FNSPE, Brehova 7, 115 19 Prague, Czech Republic

Abstract. A short abstract (summary) of your contribution may be inserted here. Use short, direct sentences. It should be as concise as possible. It should be complete, self-explanatory and should not require reference to the paper itself. The abstract should be informative, giving the scope and emphasizing the main conclusions, results, or significance of the work described.

1 Introduction

As the interest of dense laser plasma has been increasing since last few decades stimulated by rapid development of laser technology as well as by the search for the optimal mechanism for inertial confined fusion [1], many various experimental techniques for characterization of such plasma have been developed.

Because of natural constraint for electromagnetic radiation that propagates through the plasma only if the electron density does not reach the critical density that scales as λ^{-2}, one is obliged to use the short-wavelength probe in order to investigate the region close to the critical density for VIS or UV laser light, where a lot of interesting phenomena occur. Besides the wavelength criterion, the probe beam must be bright enough to overcome the thermal radiation of the investigated plasma. Therefore the most suitable plasmatic sources for dense plasma probing are X-ray K-alpha radiation sources, or X-ray lasers [2] emitting in soft X-ray or extreme ultra-violet range.

The techniques used for such characterization evolved mostly from the ones developed for the visible radiation using suitable optical elements. The simplest one is shadowgraph or back-lighting [3-8] that, however, usually does not allow reveal more than the qualitative information about the plasma density profile.

In order to resolve the electron density quantitatively, the more complex techniques such as interferometry must be employed. This technique in the form of wave-front division interferomery [9] poses significant restriction on

J. Lee et al. (eds.), *X-Ray Lasers 2010,* Springer Proceedings in Physics 136,
DOI 10.1007/978-94-007-1186-0_31,

the spatial coherence of the probing source or demands very complex instrumentation in the amplitude-division form [10]. In the XRL case the spatial coherence can be additionally improved by seeding the high-order harmonic beam in the gain medium [11]. Nevertheless, experimental setup for such experiments gets rather complex. Moreover, the K-alpha radiating plasmas can be always considered as delta-correlated sources.

Another technique that can be used to obtain the density profile in a quantitative way via deflections of the probe that are given by the density gradients is referred to as Moiré deflectometry [12-15]. This technique employs one grating placed in the probing beam behind the plasma and second slightly rotated grating placed after the first one. The ray deflections, i.e. density gradients, can be evaluated in one direction only.

In this paper we introduce a new simple deflectometric technique that enables to resolve the gradients in both directions of the projection plane using the deformation of the Talbot pattern of a single 2D grating. The simplicity and low demands on spatial coherence of the probing beam enables the use of our method in complex experiments, where the previous techniques would not be acceptable. After introducing basic principles, we will focus mainly on evaluating the dependences of all free parameters of the experimental setup that affect the spatial resolution and sensitivity of our technique.

2 Two-dimensional grating as a wave-front sensor

The probing technique presented in this paper is based on a modification of the Talbot reconstruction of the 2D grating, caused by density gradients in probed plasma. In general it is applicable to any radiation wavelength and object with a gradient of index of refraction, but here we will focus mainly on its employment in the probing of dense plasmas by radiation of currently available XRLs.

2.1 Talbot effect

When the electromagnetic plane wave of wavelength λ diffracts on a grating, the image of this grating is repeated in discrete distances behind it. This near-field diffraction effect is called Talbot effect [16]. The position of Talbot image z_T reads [17]

$$z_T = q\frac{p^2}{\lambda} \qquad (1)$$

where p is the period of the grating and q is a rational number. We can always find a pair of integers m,n so that $q=n^2/m$, then pn/m is the period of the

pattern. For odd *m,* the pattern is shifted by half of its period (Talbot sub-plane) and for even *m* the pattern has the same phase as the grating. For example the distance of the plane, where the grating is reconstructed with the same period but shifted in phase (spaces in the place of bars) is $z_T = p^2/\lambda$, ($q = m = n = 1$). This plane is called the first Talbot sub-plane. The first Talbot plane (reconstruction with the same period and phase) is placed at $z_T = 2p^2/\lambda$, ($q = m = n = 2$).

More generally, describing this effect in a configuration with an incident spherical wave with radius of curvature R ($R > 0$ for a diverging wave; $R < 0$ for a converging wave), which is the case when imaging is employed, the Talbot patterns will be formed in the distance z that relates to z_T from (1) by

$$\frac{1}{z} = \frac{1}{z_T} - \frac{1}{R}. \qquad (2)$$

Also the grating period is not the same as for the incident plane wave. It will be magnified or demagnified by factor $z/z_T = R/(R-z_T)$.

2.2. Designed experimental setup

The suggested experimental setup is a simple modification of the setup used for X-ray laser backlighting [8]. First, the plasma is imaged on a charge coupled device (CCD) camera with sufficiently high magnification, so that good spatial resolution is achieved. Then the pinhole is placed in the position of the probing source image in order to eliminate most of the plasma self-emission and enhance the signal-to-noise ratio. The size of the pinhole must be set as a compromise between this ratio and maximum detectable wave-front tilt (maximum detectable density gradient). Then a 2D-grating is placed between the pinhole and CCD so it has its first Talbot sub-plane (or plane) on the CCD. The schematic of the experimental setup is shown in **Fig. 1**.

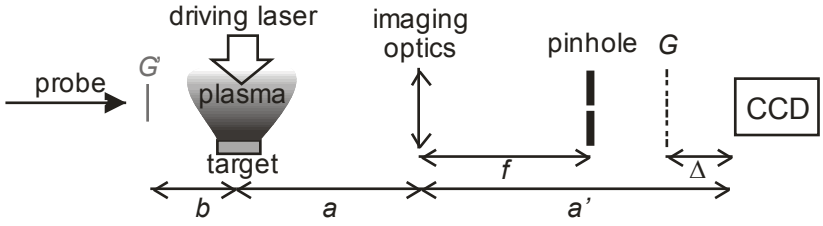

Fig.1. Experimental setup of the density gradient measurement. *a* is a object distance, *a'* is the image distance, *f* denotes focal length of the imaging element, *Δ* is the distance between 2D grating and CCD. G' denotes the virtual image of grating G that is placed at a distance *b* in front of the probed plasma.

To derive the distance between the grating and the CCD denoted as Δ let's first consider that the source of the probing beam is placed far enough from the plasma, so that the radius of curvature $R_S \to +\infty$. The curvature of the wave-front on the grating caused by imaging is then $R=a' - \Delta - f$, where a' is the distance of the plasma image and f is the focal length of the imaging element. Substituting this to Eq. 2 yields a quadratic equation for Δ

$$\Delta^2 - (a'-f)\Delta + z_T(a'-f) = 0 \tag{3}$$

with solutions

$$\Delta_{1,2} = \frac{a'-f}{2}\left(1 \pm \sqrt{1 - \frac{4z_T}{a'-f}}\right) \tag{4}$$

If we consider the finite wave-front curvature of the probing beam ($R_S < \infty$) we can keep results (3) and (4) and replace f by f' such that

$$\frac{1}{f'} = \frac{1}{f} - \frac{1}{R_S} \tag{5}$$

with R_S denoting the wave-front curvature at the position of imaging element.

Note that the proposed setup greatly benefits from placing the real grating to the image space, i.e. behind the imaging optics that becomes the closest element to the plasma. This fact also allows for improvement of the spatial resolution by demagnification of the virtual grating G' (see **Fig. 1**).

2.3 Sensitivity and spatial resolution

Sensitivity of the measurement could be defined as minimal detectable ray deviation (wave-front tilt) $\phi_{\min}$, meaning the deviation that moves the intensity pattern on CCD by a pixel size s, i.e.

$$\phi_{\min} = \frac{s}{Mb} \tag{6}$$

with M denoting the magnification of the optical system and b the distance between the plasma and virtual grating image G'. The spatial resolution is then estimated from the period of the Talbot image of the virtual grating in the plane of the plasma (object plane). In order to derive the resolution we use the period of the Talbot pattern on CCD divided by magnification of the imaging system. Then we can write the spatial resolution as

$$\text{res.} = (q+1)\frac{\Delta}{z_T}\frac{p}{M} \tag{7}$$

with q=1 for the first Talbot sub-plane and q=2 for the first Talbot plane. The factor (q+1) reflects the fact that the Talbot image is a diffraction pattern, i.e.

it is created by contributions from different slits (windows). If we assume a grating with the bar/space ratio 1/1 we can consider only diffraction to the zero-th and first orders, because of lower diffraction efficiency of higher orders and also frequently lower degree of spatial coherence, which is advantageous in this case, because it reduces the contribution from farther slits. However, the size of the coherence area of the probe beam at the object plane must be at least similar to the resolution given in Eq. 7, in order to ensure the Talbot pattern formation. If we would consider a quasi-monochromatic delta-correlated source emitting at central wavelength λ from the area of diameter S, the size of the coherence area in distance L would be given by the van Cittert-Zernike theorem [18] as $x_{coh} \cong 0.35\lambda L/S$.

In order to find the optimal parameters of the imaging system (magnification M and focal length f), let's consider the situation, when Eq. 3 has only one real solution, i.e. we will use the grating with maximum possible period for given imaging setup $p_{\max} = \frac{1}{2}\sqrt{\frac{\lambda f}{q}\left(M - \frac{f}{R_S - f}\right)}$ and $\Delta(p = p_{\max}) = \frac{a' - f'}{2} = \frac{f}{2}\left(M - \frac{f}{R_S - f}\right)$. This configuration yields minimal detectable wave-front tilt

$$\phi_{\min}(p = p_{\max}) = \frac{s}{f}\left[1 - \frac{2f}{M(R_S - f) + f}\right]^{-1} \qquad (8)$$

and the spatial resolution

$$\text{res.}(p = p_{\max}) = (q+1)\sqrt{\frac{\lambda}{q}}\sqrt{\frac{f}{M}}\sqrt{1 - \frac{f}{M(R_S - f)}} \qquad (9)$$

If the distance from the probing source is sufficiently long ($M(R_S - f) >> f$) we get $\phi_{\min}(p = p_{\max}) \approx s/f$ and $\text{res.}(p = p_{\max}) \approx (q+1)\sqrt{\lambda/q}\sqrt{f/M}$. From (9) it is obvious that the best spatial resolution is obtained for first Talbot sub-plane (q=1). The dependencies of maximum grating period $p_{\max}$, sensitivity $\phi_{\min}$, and spatial resolution on parameters of the imaging system (magnification M and focal length of the imaging element f) for the configuration with the first Talbot sub-plane (q=1) and probe source of wavelength 21.2 nm in a distance 2.8m are shown in **Fig. 2**.

Using the grating with period smaller then $p_{\max}$ ensures that there are two possible positions Δ (two real solutions of Eq. 3). These are shown in **Fig. 3**. Note that the position closer to the detector (smaller Δ), corresponds to lower

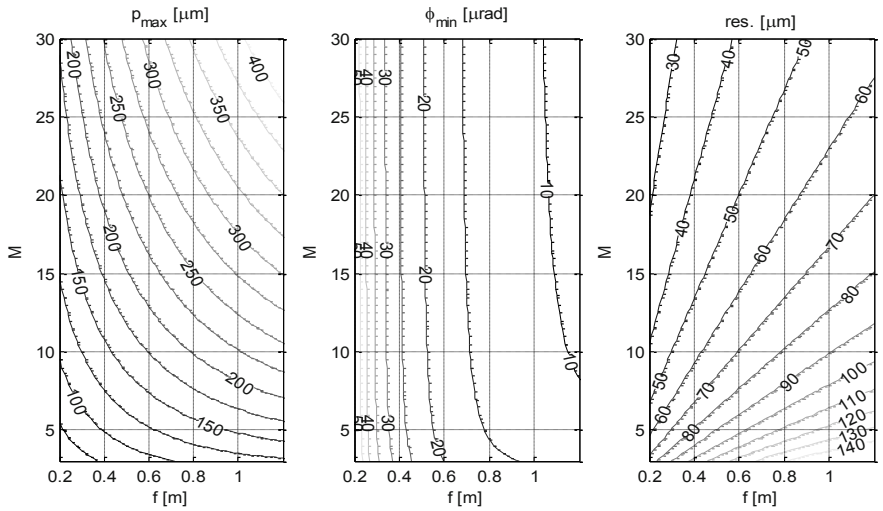

Fig. 2. Maximum grating period (left), sensitivity of the setup using $p=p_{\max}$ in terms of minimal detectable wave-front tilt (center), and spatial resolution of this setup (right) as functions of parameters of the imaging system: magnification M and focal length f. The assumed pixel size is s=10 μm, wavelength of the probe λ=21.2nm and distance between probe source and imaging element R_S= 2.8m. The configuration with first Talbot sub-plane (q=1) is considered.

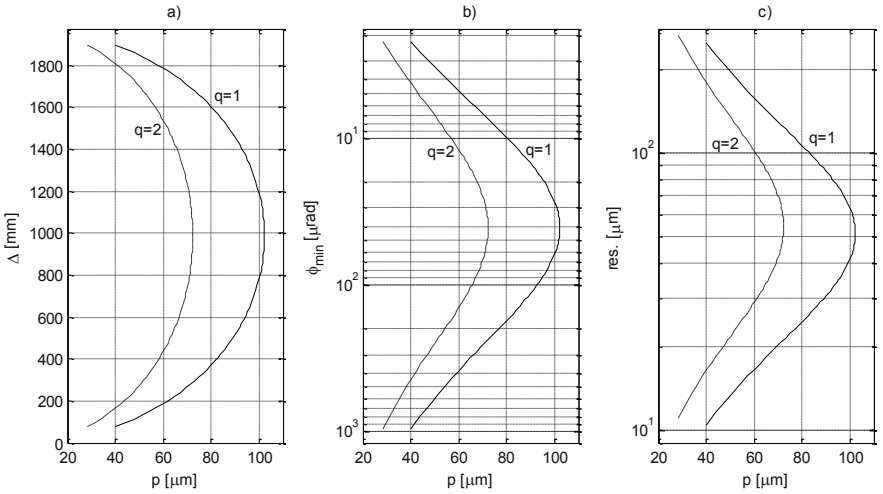

Fig. 3. Dependencies of the distance grating - CCDΔ (a), sensitivity (minimal detectable wave-front tilt) (b), and spatial resolution of the setup (c) on the grating period. Experimental setup with f = 250mm, Magnification M = 8, λ = 21.2nm, and distance XRL-imaging mirror R_S = 2.8m was considered. Curves for configuration using first Talbot sub-plane (q=1, solid line) with maximum grating period $p_{\max}$=102.3μm and first Talbot plane (q=2, dashed line) with $p_{\max}$=72.4μm.

sensitivity and better spatial resolution, i.e. lower branch of **Fig.3a** corresponds to lower branch of **Fig.3b** (with reversed $\phi_{\min}$ axis) and **Fig.3c**, and vice versa.

The main limitation of the presented technique could be the second order derivatives of the electron density of the probed plasma $\partial^2 n_e/\partial x^2$, $\partial^2 n_e/\partial y^2$, $\partial^2 n_e/\partial x \partial y$ (probing beam is propagating in z direction) due to the fact that the image of a grating's window is formed by constructive superposition of the fields from the windows in its vicinity. If the change of wave-front tilt within one grating's period is so high that the contribution from the adjacent window will be shifted by one half of image period then the Talbot reconstruction will be completely destroyed. In that case a setup with better spatial resolution (lower sensitivity) must be used.

2.4 Evaluation of the density gradients from the disturbed Talbot pattern

We can easily estimate the integral value of the electron density gradient from the wave-front tilt (ray deviation), measured as $\phi(x,y) = \Delta\mathbf{r}(x,y)/b$, where $\Delta\mathbf{r}$ is the pattern shift with respect to the undistorted image in the object plane and b is the distance between the virtual image of the grating (G') and the object plane. Employing the ray equation in the limit of the paraxial approximation one gets

$$\int_0^L \nabla n(x,y,z)\mathrm{d}z = \phi(x,y) \tag{10}$$

with L denoting the length of the plasma and index of refraction n equal to (only free electron contribution is assumed)

$$n(x,y,z,\lambda) = \sqrt{1-\frac{n_e(x,y,z)}{n_c(\lambda)}}\,,\quad \nabla n = -\frac{\nabla n_e}{2n_c\sqrt{1-n_e/n_c}} \approx -\frac{\nabla n_e}{2n_c} \tag{11}$$

where n_e is the electron density and n_c the critical electron density for a given wavelength. In (10) we also assume $n\big|_{z\notin\langle 0,L\rangle} \equiv 1$.

Assuming $n_e << n_c$ we could estimate the sensitivity in terms of integral value of electron density gradient in SI units as

$$\min\left\{\int_0^L \nabla n_e(x,y,z)\mathrm{d}z\right\} \approx 2n_c\phi_{\min}(x,y) \approx \frac{2.2\times 10^{15}}{\lambda^2}\frac{s}{Mb}\,, \tag{12}$$

3 Experimental verification

The technique proposed above was employed within studies of fusion-relevant plasmas at PALS centre [19]. Plasmas created by focusing the laser beam into the spot or line foci were probed by an X-ray laser beam.

3.1 Experimental setup

The simplified scheme of the experimental setup is shown in **Fig. 2**. The beam of the Ne-like zinc X-ray laser emitting at 21.2nm [20] was used as a probe beam. This source delivers up to 10mJ in 200-ps pulses in the mode employing the half-cavity, however, for these measurements it was operated in the single pass regime, i.e. with the 150-ps (FWHM) pulses of 200μJ estimated energy in a pulse. The Mo-Si multilayered spherical mirror with f=250mm was used to image the plasma on back-illuminated X-ray CCD with magnification factor M=8.2. The pinhole of diameter 0.5mm was put to the image of the XRL source in order to reduce the signal of plasma self-emission [8]. The XRL source was 2800mm from the imaging mirror. Then the 100μm-period laser-drilled 2D grating made of 5-μm thick steel sheet was placed to the distance Δ=1275mm from the CCD, i.e. the higher sensitivity and worse spatial resolution configuration for the first Talbot sub-plane (q=1) was used.

3.2 Linear plasma

The plasma was created by focusing the 40-J 250-ps pulse of 1.3-μm laser by pair of cylindrical and spherical lenses with focal lengths of 6m and 1.2m, respectively, into the 150-μm-wide and 1.5-mm-long line, overfilling the 1-mm-wide slab in order to produce uniform irradiation on the target with intensity of 1.3×10^{14}Wcm^{-2}. The plasmas created by irradiation of Al, Fe, and Ag slabs as well as polypropylene foil were investigated.

When analyzing the results, the plasma was regarded as uniform in probing beam direction, thus Eq. 10 could be simplified to $L\nabla n(x,y)=\phi(x,y)$, and supposing $n_e<<n_c$ the relation $\nabla n_e(x,y)=-2n_c\phi(x,y)/L$ could be employed. The example of recorded patterns and evaluated electron density gradients are shown **in Fig.4** and **Fig.5**, respectively.

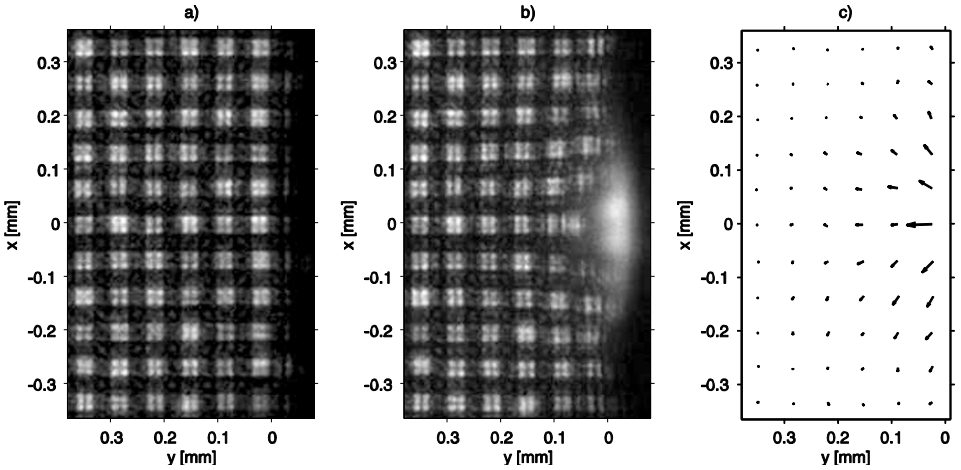

Fig. 4. Deflectometry images from 21.2nm XRL probing of Al plasma created by line focus with irradiation 1.3×10^{14}Wcm^{-2} 0.3ns after the driving pulse arrival. Reference shot (a), intensity pattern when probing the plasma (b), pattern deformation field (c).

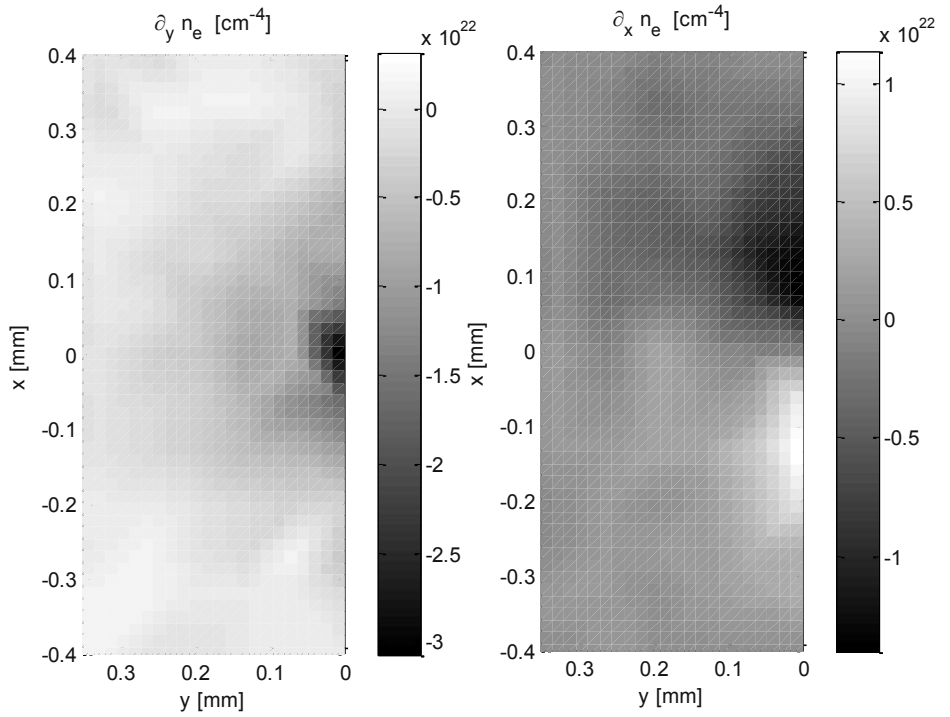

Fig. 5. Gradients of electron density of Al plasma created by line focus 0.3ns after driving pulse arrival. Gradients are resolved from measurement shown in **Fig.4**. The cubic spline interpolation was used.

3.3 Cylindrically symmetric plasma

The proposed technique was also employed for probing the plasmas created by circular laser spot interacting with CH foil. The plasma was produced by 250ps-long 1.3μm laser pulse of energy 40J focused by aspheric lens of f=1200mm into 900μm size circular spot implying the irradiation 2.5×10^{13}Wcm^{-2} on 50μm-thick chlorinated CH foil. This plasma was probed by X-ray laser beam in different times after its creation.

When probing cylindrically symmetric objects, the index of refraction can be directly calculated from deflections of the rays (local wave-front tilts) in direction perpendicular to the axis of symmetry using inverse Abel transform expressed by formula [21]

$$n(r,y) = 1 - \frac{1}{\pi}\int_{r}^{r_m} \frac{\phi_x(x,y)}{\sqrt{x^2 - r^2}}\,dx\,, \tag{13}$$

where the axis of symmetry is parallel to y axis, r is the distance from this axis, ϕ_x is the deflection in x-direction, r_m is the radius of the plasma boundary (we took the value of maximum distance from the axis of symmetry with detectable deflections). The index of refraction of surrounding medium is equal to one in our case.

Employing the inverse Abel transform for the deflections in y-direction ϕ_y, i.e. along the axis of symmetry, one can resolve $\partial_y n(r,y)$, which, together with electron density $n_e(r,y)$ obtained from (13) and (11), enables to calculate $\partial_y n_e(r,y)$, that could be further used for cubic spline interpolation of the

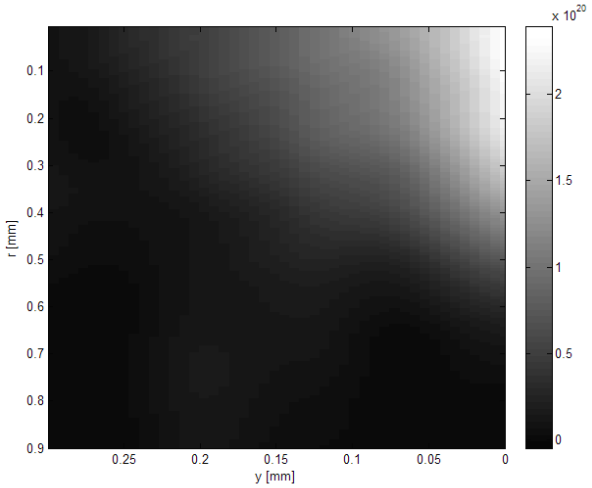

Fig. 6. Electron density profile in cm^{-3} of the cylindrically symmetric CH plasma 0.3ns after the plasma creating pulse arrival. The cubic spline interpolation was used to increase the sampling rate.

electron density profile. However, this interpolation has no other reason but a check of the consistency of electron density profiles calculated in two orthogonal directions *r,y*, because the technique does not enable to have better spatial resolution than the one evaluated by Eq. 7. The reconstructed profile of the electron density 0.3ns after the interaction of plasma creating pulse with CH target is shown in **Fig. 6**.

4 Conclusion

We present a novel and experimentally simple technique for measurements of electron density gradients in dense plasmas based on deformation of the Talbot pattern of 2D transmission grating. The spatial resolution of the measurement can be significantly lower than the period of the grating, due to the imaging that, in this sense, not only reduces the demands on grating fabrication, but also eliminates the risk of damaging the grating by plasma debris. The method was experimentally verified using probe beam of Ne-like zinc XRL, but in general, is applicable for any wavelength of the probe, so e.g. K-alpha source of X-ray radiation in combination with spherically bent crystal acting as imaging element could be used in order to investigate the plasmas of even higher densities. Moreover, the low demands on spatial coherence of the probe beam are particularly advantageous as the probing wavelength decreases.

Acknowledgement

This work was partially supported by the Academy of Sciences of the Czech Republic (project M100100911), by the Czech Ministry of Education, Youth and Sports (projects 7E08099 and 7E09092), and by the Czech Science Foundation (grant 202/08/1734).

References

1. J. Lindl, *Phys. Plasmas* 2, 3933, doi:10.1063/1.871025 (1995)
2. G.J. Tallents et al.: *Laser and Particle Beams* 20, 201-209 (2002)
3. A.L. Kritcher et al., *High Energy Density Physics* 3, 156-162, (2006)
4. K. B. Fournier et al., *Phys. Plasmas* 17, 082701 (2010).
5. M. H. Key et al., *Phys. Rev. Lett.* 41, 1467–1470 (1978).
6. J. A. King et al., *Appl. Phys. Lett*. 86, 191501, (2005).
7. A. Ravasio et al., *Phys. Plasmas* 15, 060701, (2008).
8. M. Kozlová et al., *Springer Proceedings In Physics* 130, 417, (2009).

9. M. Kozlová et al., *SPIE Proceedings*, 5919, (2005)
10. J. Filevich et al., *Opt. Lett.* 25, 356-358 (2000).
11. Y. Wang et al., *Phys. Rev. Lett.* 97, 123901 (2006).
12. O. Kafri, *Opt. Lett.* 5, 12, 555 (1980).
13. B. Moosmanet al., *Rev. Sci. Instrum*. 67, 170 (1996).
14. J. Ruiz-Camacho et al., *J. Phys. D: Appl. Phys*. 40, 2026 (2007).
15. D. Ress et al., Science 265, 514 (1994).
16. F. Talbot, *Phil. Mag.* 9, 401, (1836).
17. P. Latimer, *Appl. Opt.* 32, 1078 (1993).
18. L. Mandel and E. Wolf, *Optical Coherence and Quantum Optics*, Cambridge University Press, 1995.
19. K. Jungwirth et al., *Phys. Plasmas* 8, 2495, (2001).
20. B. Rus et al., *Phys. Rev. A* 66, 063806, (2002).
21. R. Rubinstein et al., *Appl. Opt*. 33, 1141, (1994).

Laser-matter interaction studies using X-ray laser and double Lloyd's mirror interferometer

M. Kozlová[1], J. Nejdl[1], B. Rus[1], M. Sawicka[1], J. Polan[1], L. Gartside[2], A. Rossall[2], G. Tallents[2]

[1]*Institute of Physics/ PALS Centre, Na Slovance 2, 18221 Prague, Czech Republic*

[2]*University of York, Heslington, York, YO10 5DD, UK*

Abstract. Inertial confinement fusion (ICF) is one of the promising approaches how to get a new resource of energy. In order to model ICF implosions reliably, the measurements of the mass ablation rates are needed. Such a measurement was performed at PALS; using the Ne-like Zn X-ray laser (XRL) as a probe beam and the Double Lloyd's mirror interferometer as the main diagnostic. The Parylene N foil (200nm and 350nm) was heated by 250-ps pulse of 3ω iodine laser with nominal energy of 1J. The size of the focal spot was ~300μm then the maximum resulting intensity was ~10^{12}W/cm^2. The plasma probed by XRL was imaged by Mo:Si spherical mirror to CCD detector with magnification 8. The expected phase shift for the chosen thicknesses, which corresponds to reasonable fringe visibility, was from π to 2π. The recorded interferograms were taken for different time delays between the heating pulse and the probe.

Introduction

Accurate knowledge of the mass ablation rate and its dependence on the heating laser conditions is an essential condition for reliable modelling of inertial confinement fusion based on direct-drive implosions. In this experiment the direct measurement of ablation rates of plastic foils was performed by sensing the phase change of a soft X-ray laser radiation illuminating the area heated by the ablating beam. This technique is expected to provide more accurate data than e.g. x-ray burnthrough spectroscopy measurements using buried tracer layers. It has long been a goal of laser-produced plasma research to develop diagnostic techniques for determining plasma properties between the laser critical surface and the ablation surface. It is not possible to undertake interferometry here using infra-red and visible light as the plasma frequency exceeds the probing light frequency. The x-ray laser beam will be unaffected by plasma collective processes as the plasma frequency of ionized plastic at solid density (≈ 10^{23} cm^{-3}) is much less than the x-ray laser frequency (critical density 2.5 × 10^{24} cm^{-3}). The measurement is conceptually simple and consists of measurements of the phase shift of the x-ray laser after passing through the ablated foil. The matter ablated away from the target will cause a readily measurable phase shift due to the reduction in thickness of the solid material, while the phase shift caused by the heated plasma is negligible.

J. Lee et al. (eds.), *X-Ray Lasers 2010,* Springer Proceedings in Physics 136,
DOI 10.1007/978-94-007-1186-0_32,

Experimental setup and requirements

The experimental setup was designed to measure the change of the XRL phase and intensity due to ablation of the foil target. The auxiliary ASTERIX beam, converted to 3rd harmonics (438nm @ 250ps), ablate the Parylene N (C_8H_8) foil target, while it was probed by XRL. Part of XRL beam path through the ablated foil and the rest of the beam were used as a reference beam, passing through unaffected foil. Therefore, the target thicknesses were chosen from the domain, where the transmission >1% and with phase shift of the order of (π -2π) (see Graph 1). Hence the resulting thicknesses of the Parylene N were 200nm and 350nm, corresponding to transmission 0.2 resp. 0.07 and phase shift about π resp. 2π.

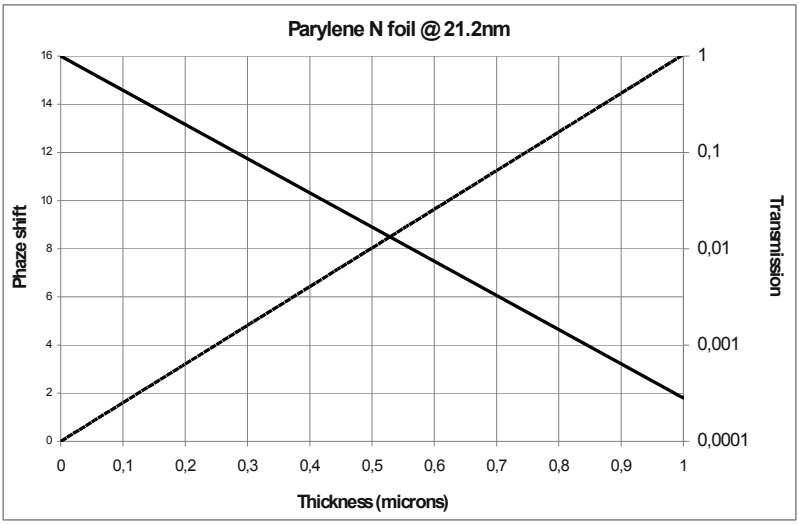

Graph 1: The solid line represent the transmission of Zn XRL @ 21nm through the not heated Parylene N foil in logarithmic scale, and the dashed line represent corresponding phase shift.

To estimate the contrast of the fringes, for chosen foils, firstly we calculate the "ideal" visibility, which is the case of fully coherent XRL beam, when the foil is burned through completely, hence:

$$V_{ideal} = \frac{2\sqrt{T}}{T+1} \tag{1}$$

where the T is transmission. If T is replaced with real values, then the "ideal" visibility for 200nm is equal to 0.75 and the value 0.46 corresponds to 350 nm. Using the Van Citter-Zernike theorem [1] we can estimate the minimum size of the coherence area of XRL beam at the target as $\Delta x \geq 190$ μm (L=2.5m, S=100μm, λ=21.2nm).

Implementation of the experiment setup is shown in Figure 1. The experiment was held at PALS facility where the Ne-like Zn X-ray laser operates as a standard beamline [2].

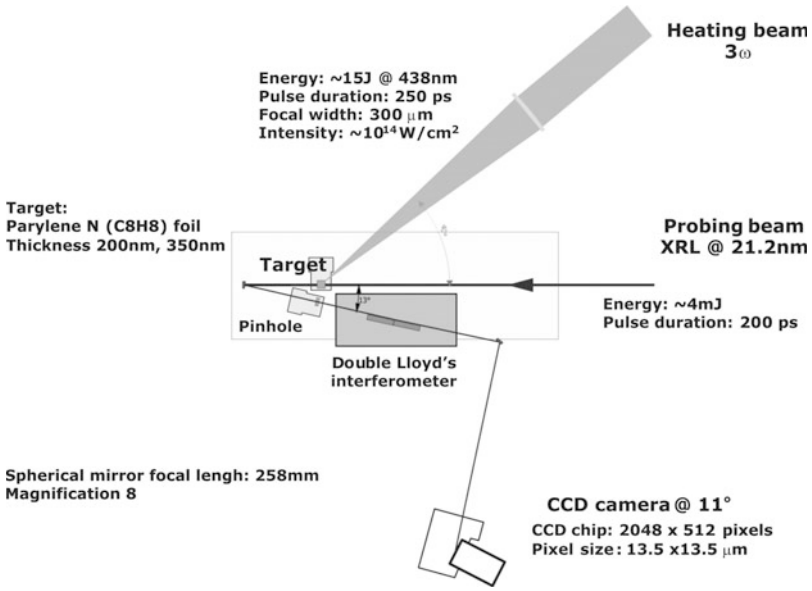

Figure 1: The layout of the experimental setup. While the third harmonic of auxiliary beam is focused at the target, X-ray laser probe beam passes through both unheated and ablated part of the foil. In the recorded interferometric pattern there is encoded the information about the relative phase shift and the transmission. To have better resolution the output plane of the target was imaged by the spherical mirror to CCD camera with magnification 8.

As a probing beam the Zn XRL was used in double pass regime with output energy 4mJ in 150-ps pulses, emitting at 21.2 nm. The XRL source was placed 2.5 m away from the target; the size of the emitting area is roughly 100μm and divergence 3.5x5.5 mrad. The C_8H_8 foil target was probed, while it was heated by 3rd harmonic (438m) of auxiliary ASTERIX beam focused to 300μm spot. The maximum energy in the heating pulse was 15J @ 250ps, to ablate the target within the same conditions as that for ICF we attenuated the beam to less than 1J, therefore the intensity on target was about 10^{12}W/cm^2. The output plane of the target was imaged by the spherical mirror (f=258mm) to CCD camera with magnification 8, which worked at grazing incidence angle (11°). The camera was protected by 400nm Al foil to cut off the visible light. In order to suppress the XUV radiation from the plasma self-emission the pinhole was placed to the position of the image of the XRL source [3].

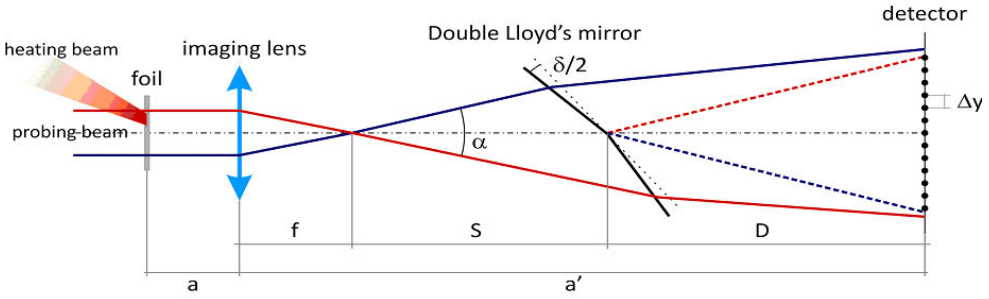

Figure 2: Principle of the interferometric probing of the thin foil heated by ASTERIX auxiliary beam, drawn in unfolded geometry. In reality, the X-ray laser beam is coming through the ablated foil, and then is reflected by the imaging element (concave mirror) and as well as from the Double Lloyd's mirror.

Figure 2 depicts the basic optical geometry of the experimental arrangement. The fringe spacing (Δy) is depending on the probe wavelength λ, divergence of the beam α and angle between the Lloyd's mirrors δ [4]:

$$\Delta y = \frac{\lambda}{2\delta - \alpha} \tag{2}$$

The distance between the vertex of the Double Lloyd's mirror and the detector *D* is given by:

$$D = \frac{S\alpha}{2\delta - \alpha}, \tag{3}$$

where *S* is the distance between the source and vertex of the Double Lloyd's mirror. By substituting the Eq. (3) into Eq. (2) we can get the fringe spacing as:

$$\Delta y = \frac{D\lambda}{S\alpha} \tag{4}$$

Since the *S* (0.5m), *D* (1.5m), α(2mrad) and λ(21nm) are given by the experimental setup the fringe space is 40μm. To be able resolve a fringe shift across sufficient number of pixels, the pixel size is 13.5μm, the interference pattern was recorded onto CCD camera under a grazing angle 11° (hence the Δy=40μm/sin(11°)=210μm and it's equal to 15 pixels).

Results

The experiment was dedicated to measure interferometrically the phase shift and transmission of Zn X-ray beam through the plastic target (Parylene N) irradiated by

3ω laser beam. Furthermore, delaying the X-ray laser pulse relative to the optical heating pulse allows a measurement of the transmission and phase change of the irradiated target as a function of time [5]. To collect data, for each target, the set of two interferograms was recorded. First interferometric pattern show intact target (reference shot) and second pattern corresponds to the target perturbed by heating laser. The example of reference shot is shown in Figure 3.

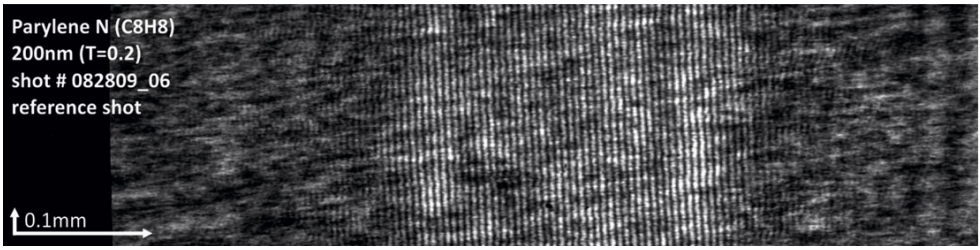

Figure 3: Raw data of the reference shot of 200nm Parylene N foil. The different scaling in *x* and *y* is given by the tilt of CCD camera (11°). The fringe spacing corresponds to 40μm and the visibility of the fringes corresponds to 0.6.

Measurements were made for different time delays; -250ps, -150ps, 0ps, 150ps, 250ps, 400ps, and the thickness of both 200nm and 350nm. The probing pulse was shifted in time with respect to the heating pulse (see Figure 4). Therefore we can observe a phase changes in early times of heating process and also after all energy is deposited on the target.

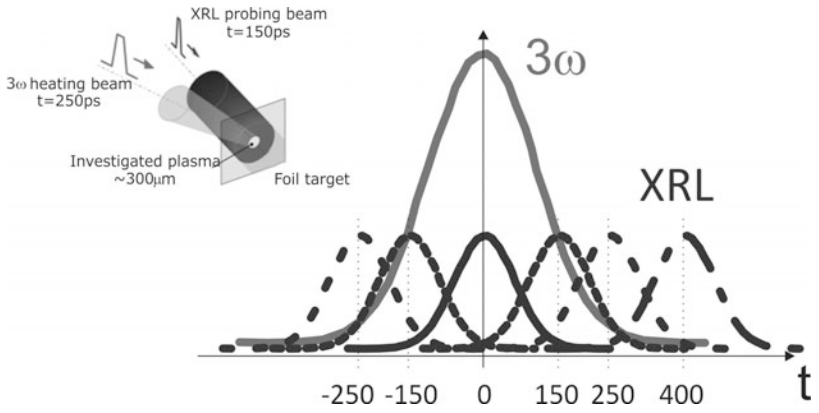

Figure 4: Illustration of delay times and schematic view of pump and probe beam.

In early times the fringe shift is minimal, but when the probing beam is peak-to-peak with the heating beam, interferometric pattern (see in Figure 5) shows clear fringe shift and transmission enhancement.

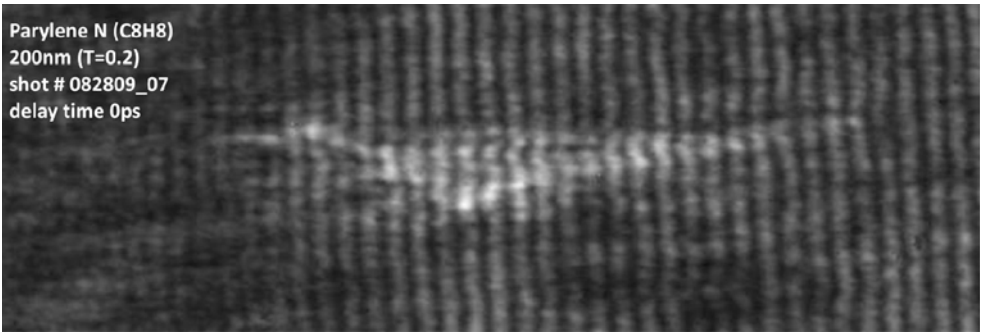

Figure 5: The zoom of the recorded interferometric pattern (size 1x0.35mm) for Parylene N 200nm target foil, the probing beam is peak-to-peak with the heating pulse. The significant enhancement of transmission in the zone of the heating beam impact is visible.

In Figure 6 is shown interferometric pattern of 200nm Parylene N foil, where the probing pulse is 400ps after the heating pulse. The enlargement of the plasma can be clearly observed via increased transmission of XRL probe.

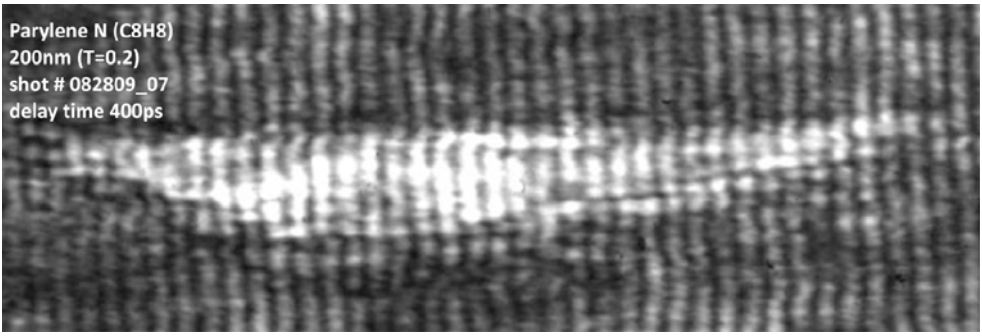

Figure 6: The zoom of the recorded interferometric pattern (size 1x0.35mm) for Parylene N 200nm target foil, the probing pulse is 400ps after the heating pulse (all the energy of heating pulse is deposited on the target). The significant enhancement of transmission in the zone of heating beam impact is visible.

In one of the reference shot we found an artefact (see white circle in Figure 7), which was taken as a marker for data analysis. In evaluation the negative phase shift was found implying that refractive indices in the probed material are less than n_{solid} = 0.946 [6].

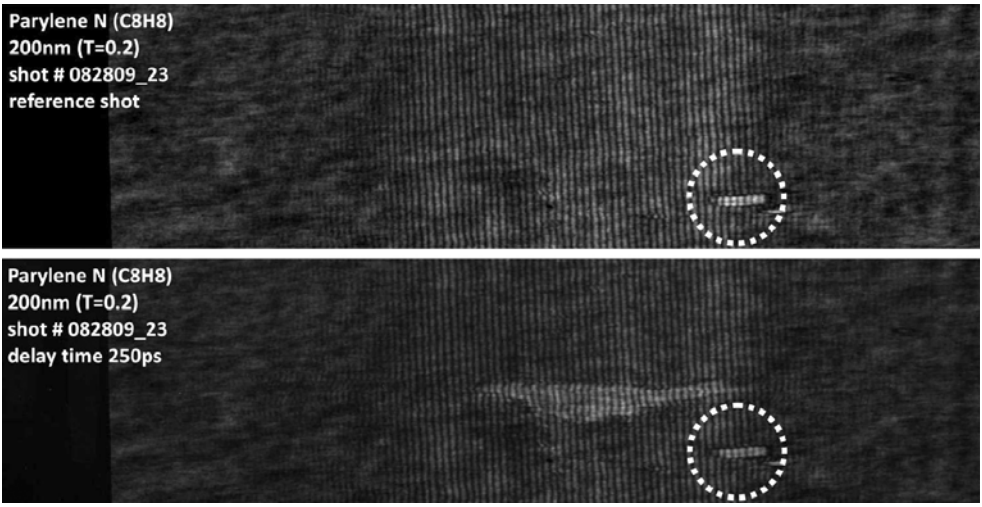

Figure 7: The sequence of shots, where the artifact indicates the fringe shift in the ablated area.

Conclusion

In this experiment we have demonstrated that wave-front division soft X-ray interferometry can be used for simultaneous measurement of phase shift and transmission allowing to determine both the ablation rate and change of density of the foil due to ablation process. The set of interferograms from different times was recorded; hence the transmission as a function of time can be evaluated. The advantage of the use of XRL for the measurement is that even with complete ionization, the critical density for the X-ray laser is above the electron density in a solid material. The soft X-ray interferometry can be used for warm dense matter or hot dense plasma measurements, e.g. the ones relevant to ICF.

ACKNOWLEDGEMENT

This work was partially supported by the Czech Ministry of Education, Youth and Sports (projects 7E08099 and 7E09092), and by the Czech Science Foundation (grant 202/08/1734).

References

[1] E. Hecht, Optics, 4th edition, 2002

[2] B. Rus et al., "Multimillijoule, highly coherent x-ray laser at 21 nm operating in deep saturation through double-pass amplification" PRA 66, 2002

[3] M. Kozlova et al., "High resolution X-ray laser backlighting of plasmas using spatial filtering technique", ICXRL, Belfast, 2008

[4] M. Kozlova, "Advanced soft x-ray interferometer for diagnostics of dense plasmas and surface holography", PhD thesis, 2010

[5] G. Tallents et al., "Probing high energy density plasmas with X-ray lasers", these proceedings

[6] L. Gartside et al., "Extreme ultra-violet interferometry of warm dense matter in laser-plasmas", Optics Letter, submitted

Application of Laser Plasma X-ray Beam in Radiation Biology

Masaharu Nishikino[1], Katsutoshi Sato[1,2] , Noboru Hasegawa[1], Masahiko Ishino[1], Tetsuya Kawachi[1], Takashi Imazono[1], Hodaka Numasaki[2], Teruki Teshima[2], and Hiroaki Nishimura[3]

[1]Quanum Beam Science Directorate, Japan Atomic Energy Agency, 8-1-7 Umemidai, Kizugawa, Kyoto 619-0215, Japan.
[2] Department of Medical Physics and Engineering, Graduated School of Medicine, Osaka University, 1-7 Yamadaoka, Suita, Osaka 565-0871, Japan.
[3] Institute of Laser Engineering, Osaka University, 2-6 Yamadaoka, Suita, Osaka 565-0871, Japan

Abstract. The short duration of laser produced plasma source could be used as a new source in contrast to conventional x-ray sources in investigating the mechanism of the affect of radiation on biological cells. We have started to develop a focused x-ray beam irradiation system for use in studying radiobiological effects on cells, and demonstrated a preliminary study of radiation effect on culture cells irradiated with the x-ray laser and laser produced plasma Kα x-rays.

1 Introduction

Recently high energy monochromatic x-rays emanating from a Laser-Produced Plasma (LPP) have been attracting a lot of attention as a new indispensable radiation source in high energy density physics, bioscience, and material sciences. Techniques for generating high energy bright short-pulse x-rays, such as a soft x-ray laser and Kα line emitted from LPP have been rapidly developed in recent progress made in utilizing intense ultrashort laser pulses.[1,2] Monochromaticity is important when x-rays are handled with narrow-band optics or used to selectively excite a specific material involved in matter. In addition, the time duration of the XRL and the Kα x-ray source is typically in the order of pico-seconds.[3-5] Temporal sequences of physical (10^{-18}~10^{-11} sec.) and physicochemical (10^{-14}~10^{-6} sec.) stages of actions in biological systems irradiated with energetic radiation take place within the order of picoseconds.[6] The short duration LPP source could be used as a new source in contrast to conventional x-ray sources in investigating the mechanism of the affect of radiation on biological cells. Then, we propose to develop an ultrashort, intense x-ray microbeam system to study the radiobiological effect and the bystander effect[7,8]. Here, We describe the

J. Lee et al. (eds.), *X-Ray Lasers 2010,* Springer Proceedings in Physics 136,
DOI 10.1007/978-94-007-1186-0_33,

development of a focused x-ray beam irradiation system for use in studying radiobiological effects on cells, and the affect of radiation on culture cells irradiated with the XRL and the LPP Kα x-ray demonstrated.

2 Experiment

2.1 Generation of LPP x-ray microbeam

We have started to develop a focused x-ray beam irradiation system for use in studying radiobiological effects on cells. Two types of LPP x-ray source have been developed as for the x-ray microbeam system. One is a highly coherent XRL extracted from LPP. The soft XRL (90 eV) is generated by amplification of spontaneous emission (ASE) in plasmas with the population inversion. The output energy is about 1 μJ, corresponding to a flux of about 10^{11} photns/pulse[9]. The pulse width of the x-ray laser is about 7 ps[3]. The other source is Kα x rays generated with an ultrashort high intensity laser pulse at intensities of 10^{17}-10^{18} W/cm^2 and duration of 50-100 fs. Energetic electrons generated via laser-plasma interaction propagate deeply into a solid material. As a result, bremsstrahlung and characteristic x-ray radiation are produced. A tabletop Ti:sapphire laser system, that produces 70 fs, 150 mJ pulses at 10 Hz repetition rate was used to generate Kα x-ray pulse from a copper (Cu) target. The conversion efficiency is about 10^{-5} of incidence, corresponding to the number of Cu- Kα photons (8 keV) of about 3 x 10^{10} photons/4πsr/pulse. The pulse width of Kα emission, that is comparable to the life-time of hot electrons in the plasma, is estimated to be about 1 ps.

An x-ray micro-beam, focused down to a micrometer scale is expected to be a new tool for the study of radiobiological effects by irradiating a single biological cell. Many types of x-ray focusing device have been developed to generate the x-ray microbeams. The sub-micron spot size has already been achieved in the hard x-ray region with a synchrotron x-ray source and soft x-ray region with LPP x-ray source.[10-12] In these cases, Fresnel zone plates (FZPs) are mostly used but monochromatic radiation source is primally needed. In the case of the SXRL, the beam is focused to about 10-20 μm with a spherical multilayer mirror. Figure 1(a) shows a focused XRL image of the focal spot recorded with the x-ray CCD camera. In the case of LPP Kα x rays, we adopt a polycapillary x-ray lens[13] in order to collect diverging x rays from LPP to a spot of about 300 μm in diameter, and simultaneously a pinhole of 50-100 μm diam. to limit irradiation area. Figure 1(b) shows a focused Kα x-ray image of the focal spot recorded with the Gafchromic EBT film. Figure 1(c) shows the photograph of the XRL microbeam system. The microbeam system[14] is consisting of automatic micro-stages and an optical microscope and these x-ray beams.

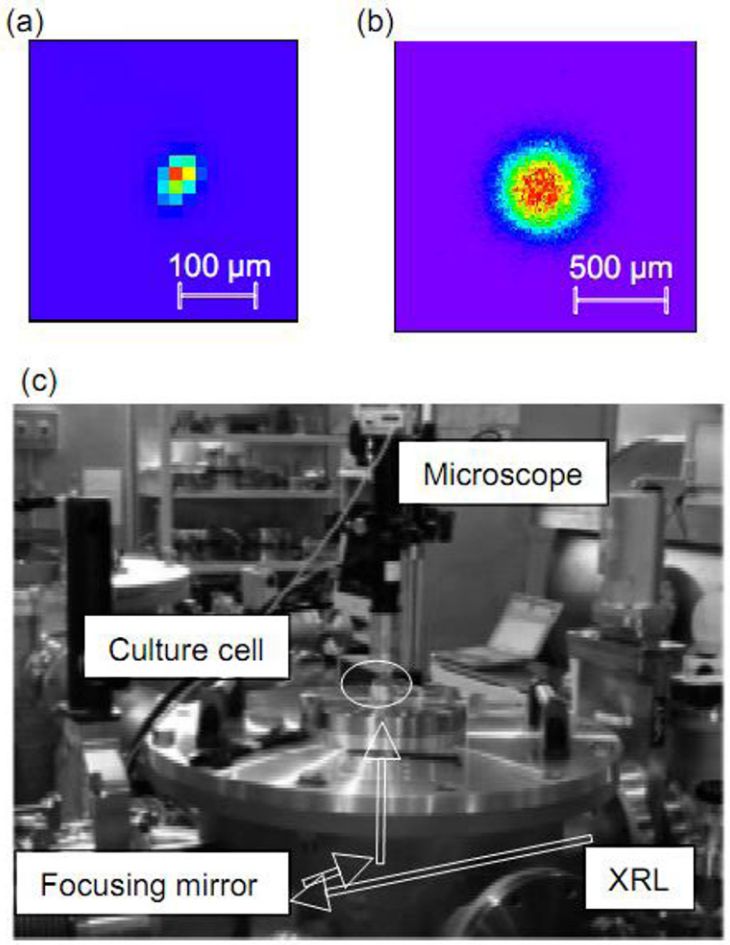

Fig. 1. X-ray image of x-ray microbeam beam with (a) the x-ray laser and (b) the Kα x-ray microbeam. (c) Photograph of the x-ray microbeam irradiation system.

2.3 DNA double strand break induced by LPP x-rays

We have started preliminary experiments of the DNA double-strand breaks (DSBs) formation in the culture cells with the XRL and the Kα x-rays. The DNA DSBs were investigated using phosporylated Ataxia Telangiectasia Mutated (ATM)[15] immunostaining and phosporylated histone H2AX (generally known as γ-H2AX)[16]. The immunostaining was an antibody-based method used to detect specific proteins in a cell, with the detected foci of the γ-H2AX and ATM being useable as the criterion for the DSBs of the DNA.[14-17] Biological specimens are irradiated through the bottom of culture dishes so that the specimen does not necessarily need to be extracted from the dish throughout the exposure experiment. A custom-made culture dish was therefore designed for the irradiation of culture cells in a nominal atmosphere.

In order to reduce absorption of the x-rays a Silicon Nitride (SiN) membrane 0.1-1 μm thick coated with collagen was used as the cell adhesion substrate.[14] The A549 cell line (human lung adenocarcinoma cell line) was used. A day before the x-ray irradiation the membrane was seeded with a sufficiently large number of cells. Cells cultured on the SiN membrane were then attached to the culture dishes with 2 mm diameter holes before being irradiated.

The distribution of nuclei with ATM foci depended on the irradiated beam size of the XRL of 10 shots, as revealed in Figure 2(a). The size of ATM foci region was about 100 μm in the horizontal and vertical directions, which is consistent with the XRL spot size of 90 μm. The distribution of nuclei with γ-H2AX foci clearly depended on the irradiated beam size of the Kα x-ray of about 2 Gy, as revealed in Figure 2(b). The size of γ-H2AX foci region was about 800 μm in the horizontal and vertical directions, which is consistent with the x-ray spot size of 700 μm. Figures 2(c) and (d) reveal the γ-H2AX and ATM foci in the nucleus irradiated with an irradiation dose of about 2 Gy.

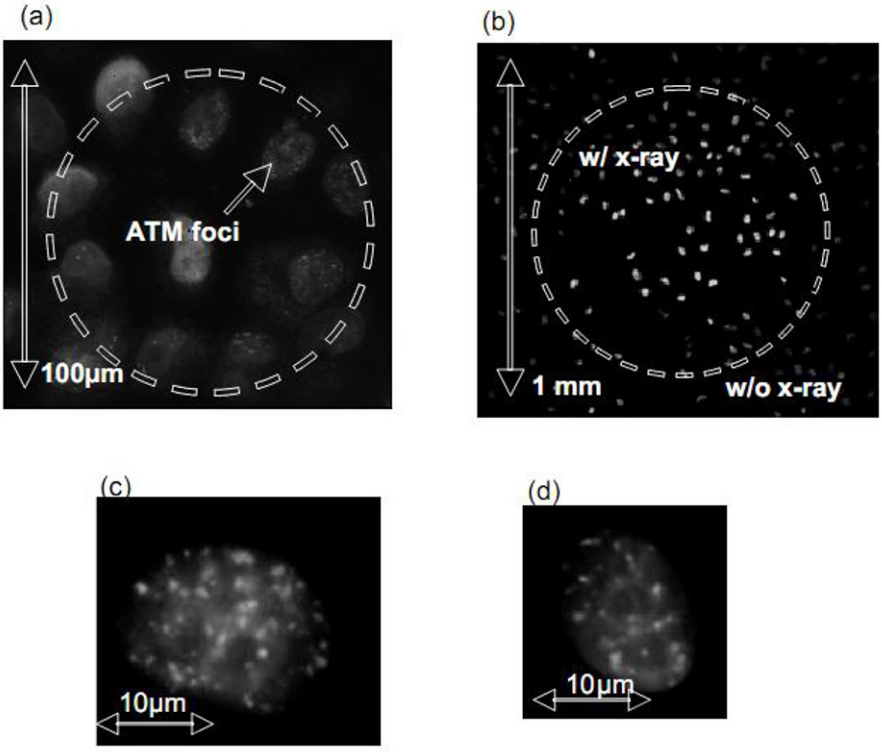

Fig. 2. (a) ATM focus formation (bright spots) and in nucleus induced by 10 shots of the XRL (b) γ-H2AX focus formation (bright region) induced by a Kα x-ray microbeam at 2 Gy dose. γ-H2AX and nucleus are stained with anti-γ-H2AX antibody and DAPI. (c) γ-H2AX (bright spots) and (d) ATM (bright spots) focus formation and in nucleus at 2 Gy.

3 Summary

We have developed a LPP x-ray microbeam system for use in radiobiological applications and demonstrated its applicability in radiation effects on culture cells such as the bystander effect through use of LPP x-rays. Practical application of the system in studying the radiobiological effect on specific regions of cells is currently underway.

Acknowledgement

This work was in part supported by the "Mono-energetic quantum beam science with petawatt lasers" of MEXT and a grant-in-aid for young scientists (B) 20710046 and scientific research (B) 08041858 from the Japan Society for the Promotion of Science. The results were achieved at the Facilities Utilization system of the Japan Atomic Energy Agency. The authors are grateful to Prof. N. Matsuura of Osaka University, Prof. K. Shinohara of Waseda University, Dr. Y. Kobayashi and Dr. T. Funayama of JAEA for their fruitful comments and technical support.

References

1. T. Guo, Ch. Spielmann, B. C. Walker, C. P. J. Barty, Rev. Scie. Inst. **72**, 41 (2001).
2. W. Liu, M. Nicoul, U. Shymanovich, A. arasevitch, P. Zhou, K. Sokolowski-Tinten, D. von der Linde, M. Masek, P. Gibbon, and U. Teubner, Phys. Rev. E **80**, 026404 (2009).
3. Y. Ochi, T. Kawachi, N. Hasegawa, A. Sasaki, K. Nagashima, K. Sukegawa, M. Kishimoto, M. Tanaka, M. Nishikino, M. Kado, R. Tai, and H. Daido, Appl. Phys. B 71, 961(2004).
4. Ch. Reich, P. Gibbon, I. Usxhmann, and E. Förster, Phys. Rev. Lett. 84, 4846 (2000).
5. T. Feurer, A. Morak, I. Ushmann, Ch. Ziener, H. Schoerer, E. Förster R. Sauerbrey, K. Ortner and C. R. Becker, Phys. Rev. E **65**, 016412 (2001).
6. A. Mozumder and Y. Hatano, *Charged Particle and Photon Interactions with Matter*, (Marcel Dekker, Inc., New York, 2004).
7. Kevin M. Prise and Joe M. O'Sullivan, Nature Reviews Cancer **9**, 351(2009).
8. Tomoo Funayama, Seiich Wada, Yuichiro Yokota, Kana Fukamoto, Tetsuya Sakashita, Mitsumasa Taguchi, Takehiko Kakizaki, Nobuyuki Hamada, Michiyo Suzuki, Yoshiya Furusawa, Hiroshi Watanabe, Kenji Kiguchi, and Yasuhiko Kobayashi, J. Radiat. Res., **49**, 71 (2008).
9. M. Nishikino, N. Hasegawa, T. Kawachi, H. Yamatani, K. Sukegawa, and K. Nagashima, Appl. Opt. 47, 1129 (2008).

10. Y. Suzuki, M. Awaji, Y. Kohmura, A. Takeuchi, H. Takano, N. Kamijo, S. Tamura, M. Yasumoto, and K. Hamada, Nucl. Instrum. Methods Phys. Res., sect. A **467-468**, 951 (2001).
11. Y. Iketaki, Y. Horikawa, S. Mochimaru, K. Nagai, M. Atsumi, H. Kamijou, and M. Shibuya: Opt. Lett. **19**, 1804 (1994).
12. G. Vaschenko, A. Garcia Etxarri, C. S. Menoni, J. J. Rocca, O. Hemberg, S. Bloom, W. Chao, E. H. Anderson, D. T. Attwood, Y. Lu, and B. Parkinson, Opt. Lett. **31**, 3615 (2006).
13. IfG- Institute for Scientific Instruments GmbH, http://www. Ifg-adlershof.de
14. M. Nishikino, K. Sato, N. Hasegawa, M. Ishino, S. Ohshima, Y. Okano, T. Kawachi, H. Numasaki, T. Teshima, and H. Nishimura, Rev. Sci. Instrum. 81, 20266217 (2010).
15. Christopher J. Bakkenist and Michael B. Kastan, Nature **421**, 499 (2003).
16. A. J. Downs, C. M. Nussenzweig, and A. Nussenzweig, Nature (London) **447**, 951 (2007).
17. A. Yogo, K. Sato, M. Nishikino, M. Mori, T. Teshima, H. Numasaki, M. Murakami, Y. Demizu, S. Akagi, S. Nagayama, K. Ogura, A. Sagisaka, S. Orimo, M. Nishiuchi, A. S. Pirozhkov, M. Ikegami, M. Tampo, H. Sakaki, M. Suzui, I. Daito, Y. Oishi, H. Sugiyama, H. Kiriyama, H. Okada, S. Kanazawa, S. Kondo, T. Shimomura, Y. Nakai, M. Tanoue, H. Sasao, D. Wakai, P. R. Bolton, and H. Daido, Appl. Phys. Lett. **94**, 181502 (2009).

Energy Spectra of Photo- and Auger Electrons Generated by a Soft X-Ray Laser and Xe Cluster Interaction

S. Namba[1], N. Hasegawa[2], M. Kishimoto[2], M. Nishikino[2], T. Kawachi[2]

[1]Graduate school of Engineering, Hiroshima University, Kagamiyama 1-4-1, Higashi-Hiroshima, Hiroshima, 739-8527, JAPAN
[2] Quantum Beam Science Directorate, Japan Atomic Energy Agency, Umemidai 8-1, Kizugawa, Kyoto,619-0215, JAPAN

Abstract. In order to clarify an interaction between xenon (Xe) clusters and a soft x-ray laser (wavelength: 13.9 nm, pulse width: ~7 ps, intensity: 2×10^{10} W/cm^2), we measured the energy distribution of photo- and Auger electrons as well as the ion mass spectrum. Since the photon energy of the soft x-ray laser (89.2 eV) is sufficiently high to photoionize Xe 4*d* inner electrons, inner-shell ionization rather than valence-shell ionization is the dominant ionization process, resulting in the Auger decay. It was found that prominent photo- and Auger electron peaks were not observed, while the continuum energy spectra dominated line peaks. Moreover, the energy distribution obtained implies the production of low temperature plasma.

1 Introduction

The hot dense plasmas created by intense laser pulses have been extensively studied for various applications, such as the development of bright x-ray light sources and the generation of high energy charged particles. On the other hand, the strongly coupled plasma with a low temperature and high density, which can also be produced by the photoionization processes, has been attracted for fundamental atomic physics. In fact, Jungreuthmayer *et al* pointed out that the extremely strongly coupled plasma could be generated by intense vacuum ultraviolet free electron laser (VUV-FEL) pulse, where it is expected that the new process, many body recombination, could occur frequently [1].

Generally, the photoionization process involving the inner shell electron has been investigated by using the synchrotron radiation [2]. Although this x-ray light source has provided the powerful experimental tools for medical, chemical and engineering fields, the intensity was not sufficient to produce the photo-ionized plasma.

In order to understand the photoionization dynamics in the matters subjected to the intense x-ray light, we have tried to examine the characteristics of xenon (Xe) clusters irradiated with a plasma excited x-ray

J. Lee et al. (eds.), *X-Ray Lasers 2010,* Springer Proceedings in Physics 136,
DOI 10.1007/978-94-007-1186-0_34,

laser pulse (λ=13.9 nm). The photon energy of the x-ray laser ($h\nu$=89.2 eV) is sufficiently high to photoionize Xe 4*d* inner-shell electrons (threshold energies: 67.55 eV for $4d_{5/2}$ and 69.54 eV for $4d_{3/2}$) and its cross section is by ten times larger than that of the valence electron. Subsequently, the valence electron will fill the inner vacancy, resulting in the productions of an Auger electron and a Xe^{2+} ion (normal Auger decay as shown in Fig.1), which has been investigated extensively by synchrotron radiation experiments involving free Xe atoms [3]. On the other hand, Xe^{3+} ions can also be generated by double Auger (DA) decay of a 4*d* vacancy, although the transition probability for this process is small.

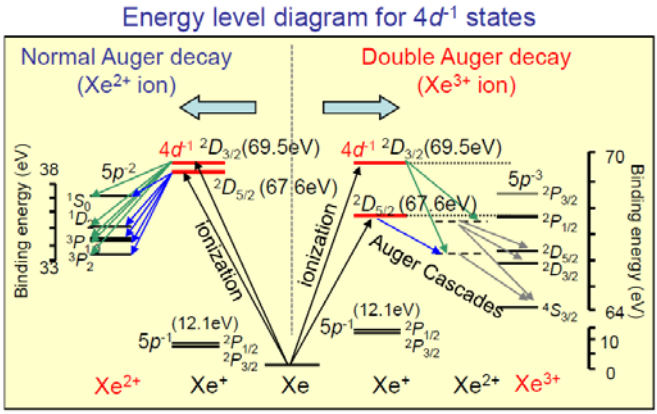

Fig. 1. Partial energy level diagram of Xe $4d^{-1}$ hole states. The normal Auger decay is shown on the left, whereas the double Auger cascade decay is displayed on the right.

In this study, the electron energy spectrum as well as the ion charge state was examined using time-of-flight (TOF) spectrometers. It was found that Xe^{3+} ions arising from double Auger transition became the dominant final ionic product with increasing cluster size and laser intensity, which was in contrast to the results of synchrotron radiation experiments [4]. The results obtained in the present study suggest that the strongly coupled cluster plasmas with a temperature of a few eV could be generated by x-ray irradiations, whereby the ionization potential lowering occurs due to plasma screening.

2 Experimental Setup

The plasma excited soft x-ray laser pulse having a wavelength of 13.9 nm, a pulse duration ~7 ps and a resolution of $\lambda/\Delta\lambda < 1 \times 10^{-4}$ was generated by transient collisional excitation (TCE) scheme for nickel-like silver [5]. The highest laser intensity focused using a Mo/Si multilayer spherical mirror (R=2

m) was around 2×10^{10} W/cm^2 on target. To measure the incoming laser intensity, a soft x-ray CCD camera was installed 50 cm from the intersection of the laser and cluster beams.

On the other hand, the Xe clusters were generated by an adiabatic free expansion of the high pressure gas into a vacuum using a conical shaped nozzle with a throat diameter of 200 μm [6]. The average cluster size was estimated by Hagena scaling law and its range was estimated to be 3×10^2 to 4×10^5 atoms/cluster [7, 8].

The Xe^{q+} ion stages and their energies were measured using a TOF mass spectrometer, while the electron was also detected using the other TOF device, by which the energy spectrum was determined. Both observations were carried out in the direction parallel to the laser polarization axis.

3 Results and Discussion

Typical ion TOF spectra are shown in Fig. 2 for various cluster sizes. As seen below, the highly-charged ion mass spectra up to Xe^{3+} were observed. Moreover, with increasing cluster size, the 3+ ion became the dominant final ionic species [9]. According to the similar experiment using synchrotron radiations, the dominant decay process following the inner vacancy is the normal Auger process generating 2+ ion, and the ratio of Xe^{2+} to Xe^{3+} ion yield was estimated to be ~4 [4]. The results obtained in this study, therefore, implies that the double Auger decay should be preferable for larger Xe clusters exposed to brighter x-ray laser pulse.

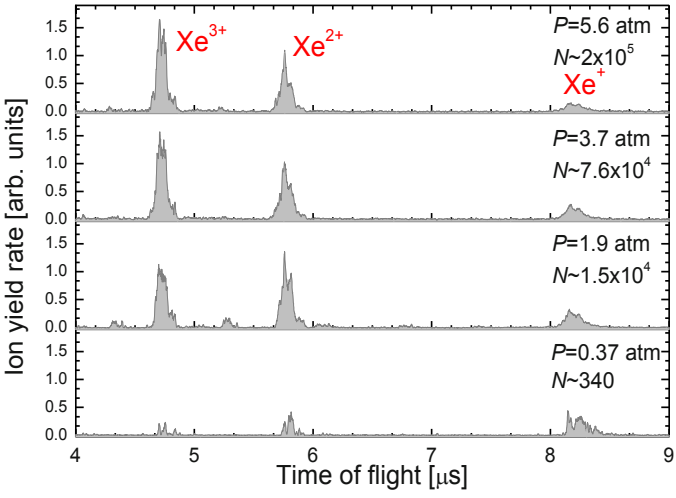

Fig. 2. Typical ion TOF mass spectra for various cluster sizes. With increasing cluster size, the Xe^{3+} ion became the dominant final ionic species.

The question we have to ask here is how much the collisional ionization process influences the charge state distribution. In order to estimate the ionization events, a set of coupled rate equations involving Xe atom and Xe^{q+} ions were solved. As a result, it was found that the collisional ionization with *atoms,* $Xe + e \rightarrow Xe^{+} + 2e$, plays an important role in further ionization. However, neither simple photoionization nor collisional ionization provides a reasonable explanation for the enhancement of the Xe^{3+} ion yield [10]. Therefore, the electron energy spectrum was determined by the TOF measurement.

Figure 3 shows the experimental results of the electron energy distribution for various cluster sizes. The calculated energy curve is also depicted on the top figure, which was determined by the photo- and Auger line positions, their intensities [11] and the resolution of the spectrometer used. As seen below, prominent photo- and Auger peaks were not observed due to the interaction with phonons and charged particles (density inside the cluster: $\sim 1 \times 10^{22}$ cm^{-3}). Instead, the distribution indicates that the low temperature cluster plasma with a few eV could be produced.

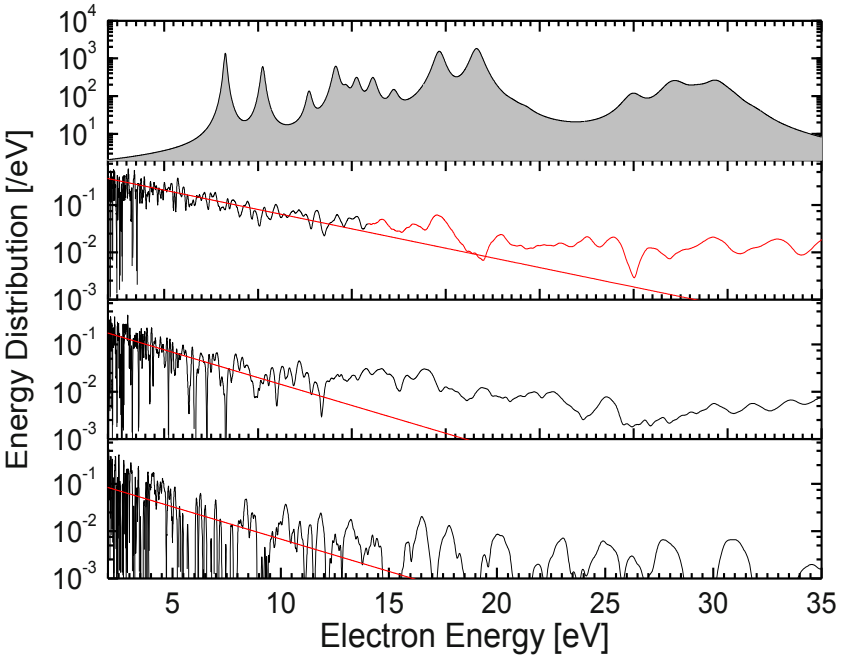

Fig.3. Electron energy spectra for various sizes of Xe clusters. The calculated curve which is determined by the photo and Auger lines is also shown on the top.

The result obtained by Get *et al* could provide a clue to understand the phenomenon that occurred in the cluster subjected to x-ray laser pulses [12].

According to their calculation using Debye shielding model, the ionization potential of Xe^{3+} ion decreases from 40 eV to 8 eV in 30-eV cluster plasma. If the energies of the Xe^{3+} state are reduced inside the cluster, the number of possible final Xe^{3+} states increases. As a result, we expect that the probability of $4d^{-1}$ decaying to the Xe^{3+} states via the double Auger decay also increases. In fact, the SR experiment shows that the number of the final Xe^{3+} states drastically changes the transition probability of the double Auger decay [4]. Therefore, we conclude that the enhancement of Xe^{3+} ion yield observed arises from the increase of the double Auger decay channel due to depression of Xe^{3+} state energies in the cluster plasmas.

4 Summary

The interaction of Xe clusters with an x-ray laser pulse (λ=13.9 nm, I~10^{10} W/cm^2) has been investigated, in which photoionization of 4*d* inner electrons dominates other ionization processes. In contrast to the results obtained in SR experiments involving free Xe atoms, an anomalous enhancement of Xe^{3+} yield has been observed with increasing cluster size and laser intensity. The electron energy distribution, indicating the production of low temperature cluster plasma, has also been obtained. Thus, the lowering of ionization potential could occur in the cluster. Therefore, the number of Xe^{3+} states accessible from 4*d* vacancy increases. This is the main reason why the probability of the double Auger decaying into Xe^{3+} ion also increases.

References

1. Jungreuthmayer, C. *et al* : *J. Phys. B: At. Mol. Opt. Phys*. **38**, 3029, 2005
2. Schmidt, V. : *Electron Spectroscopy of Atoms using Synchrotron Radiation, Cambridge Press*, 1997
3. Becker, U. *et al* : *Phys. Rev. A* **39**, 3902, 1989
4. Luhmann, T *et al* : *Phys. Rev. A* **57**, 282, 1998
5. Kawachi, T. *et al : Phys. Rev. A* **66**, 033815, 2002
6. Namba, S. *et al* : Phys. Rev. A, **73**, 013205, 2006
7. Hagena, O. F. and Obert, W. : *J. Chem. Phys.* **56**, 1739, 1972
8. Holland, D. M. *et al* : *J. Phys. B: Atom. Molec. Phys*. **12**, 2465, 1979
9. Namba, S. *et al* : Phys. Rev. Lett. **99**, 043004 ,2007
10. Namba, S. *et al* : J. Phys. Conf. Series, **112**, 042057, 2008
11. Kivimäki, A. : J. Electron. Spectrosc. Relat. Phenom. **101-103**, 43, 1999
12. Gets, A. V. and Krainov, V. P. : *J. Phys. B: At. Mol. Opt. Phys*. **39**, 1787, 2006

Observation of Phase Transition Dynamics in $BaTiO_3$ by X-ray Laser Speckle Technique

K. Namikawa[1, 2, 6], M. Kishimoto[2, 6], R. Z. Tai [3, 6], K. Nasu[4, 6], E. Matsushita[5, 6]

[1]Reserch Institute for Science and Technology, Tokyo University of Science, Noda, Chiba 278-8510, Japan
[2]Quantum Beam Science Directorate, Japan Atomic Energy Agency, Kizugawa, Kyoto 619-0215, Japan
[3]Shanghai Synchrotron Radiation Facilities, Shanghai Institute of Applied Physics, Chinese Academy of Science, Shanghai 201204, China
[4]Institute for Material Structural Science, KEK Tsukuba, Ibaraki 305, Japan
[5]Faculty of Engineering, Gifu University, Gifu, Gifu 501-1193, Japan
[6]CREST, Japan Science and Technology Agency, Chiyoda, Tokyo 102-0075, Japan

Abstract. A single shot soft x-ray laser speckle observation technique has been developed and applied to the ferroelectric phase transition of $BaTiO_3$. Domain evolutions near the phase transition are investigated. A critical region continues to exist down to 6*K* below the Currier temperature (T_C). A snap shot x-ray speckle in the parraelectric critical region revealed an existence of the polarization clusters in $BaTiO_3$. The cluster size, the cluster distance, and the polarization of the clusters are evaluated from the spatial correlation functions of the speckle intensity. A new time correlation method based on the delayed double pulses scattering revealed the temperature dependence of the critical relaxation time of the dipole moment in polarization clusters. A maximum relaxation time appears at 4.5 K above the T_C exhibiting a critical slowing down take place at this temperature within the polarization clusters. A new scenario of the phase transition of $BaTiO_3$ was proposed.

1 Introduction

Ferroelectric phase transition in prototype ferroelectrics $BaTiO_3$ has long been a debating subject. Soft phonon mode displacive-type mechanism has proposed [1, 2], however, anomalies were also known near the phase transition temperature which was unable to be interpreted simply by a displacive model. Hyper Raman spectroscopy [3, 4] revealed a relaxation dynamics appearing in paraelectric phase of $BaTiO_3$ near the T_C. NMR experiments [5] have shown that Ti ion in the paraelectric phase of $BaTiO_3$ flutters among off-centre sites, claiming the coexistence of order-disorder and displacive characters. It is still not clear how the dipole fluctuations correlate

J. Lee et al. (eds.), *X-Ray Lasers 2010,* Springer Proceedings in Physics 136,
DOI 10.1007/978-94-007-1186-0_35,

spatially each other and evolve into ferroelectric domains. Molecular dynamics simulation [6] and theory [7], concerning to the phase transition mechanism, have shown existence of polarization clusters in paraelectric $BaTiO_3$ near the T_C. Such experiments as neutron scattering [8], x-ray diffuse scattering [9], and optical birefringence [10, 11] showed strongly fluctuating polarization clusters existing in paraelectric phase of $BaTiO_3$. Nanometre scale dipole moments in the polarization clusters in $BaTiO_3$ are supposed to be thermally excited and thermally relaxed within a picoseconds time scale.

X-ray speckle techniques have progressed greatly since the advent of the high brilliant synchrotron radiation sources. Observation of the fluctuation in the nanometer region has been investigated by mean of speckle intensity correlation measurement. However, these measurements so far performed are restricted to the slow phenomena from several sec to several microseconds because of comparatively low coherence of the synchrotron radiations; the coherent flux at most is only an order of 0.1 % of the total flux. Even with its low repetition rate, 0.1 Hz, transient excitation scheme Ni-like-Ag-plasma based soft x-ray pulse laser (SXRL) is a suitable source to perform stroboscopic single shot experiments. Within its comparatively short pulse width, 7psec, more than 10^{11} photons are contained. The band width, $\Delta\lambda/\lambda$ at 13.9nm is typically an order of 10^{-4}. Moreover, the coherent flux of the SXRL with a double target configuration is over the 90% [12]. This peculiar space-time characteristic of SXRL credits us to full application of speckle measurement techniques to the dynamical study of nanostructures.

This is a cumulative report of our series of investigations of the phase transition of prototype ferroelectrics $BaTiO_3$ by use of SXRL speckle techniques. Here we show a stroboscopic observation of ferroelectric domain evolution [13], a snapshot observation of polarization clusters above the T_C [14], and direct observation of the decay dynamics in polarization clusters [15]. A new scenario of the phase transition of $BaTiO_3$ was discussed.

2 Experimental

The experimental configuration for the observation of ferroelectric domain is shown in Fig.1. A Mo/Si multilayer mirror was used to prepare a vertically polarized soft x-ray beam. An $80\mu m$ (horizontal) × $200\mu m$ (vertical) slit located at $1.9m$ from Ag slab target was used to produce fully spatially coherent soft x-ray beam. The sample used in experiment was a flux-grown ferroelectric $BaTiO_3$ single crystal with alternative a/c domain aligned in parallel. The sample was set close to the slit with its domain boundaries lie in the vertical direction. The T_C of the sample was $395K$. The temperature of the sample was controlled from room temperature up to $403K$ with a precision of

0.5*K*. Speckle patterns were recorded on a soft x-ray CCD camera located at 0.5*m* far from the slit. Observation of the polarization clusters was conducted with almost the same setup as described above; 0.2*m* sample to CCD camera distance, 80μm (horizontal) ×50μm (vertical) slit width. The temperature was controlled by 0.1*K*. A uniform high DC electric field, 2*KV*/*cm* normal to the sample, can be applied with a slab electrode set at 2.5*mm* front of the sample. Estimated electric field within the sample, 0.4*V*/*cm*, was sufficiently large to reverse the polarization of the clusters.

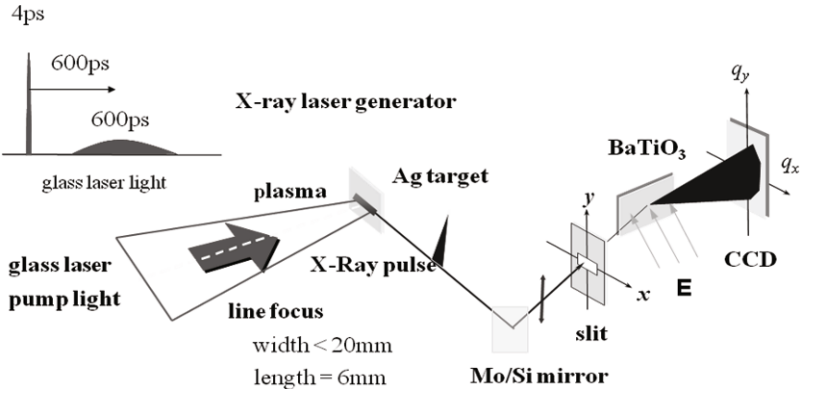

Fig.1. Experimental setup for observation of x-ray speckle by $BaTiO_3$ nanostructures.

The soft x-ray speckle intensity correlation measurement system [16] is shown in Fig.2. In this experiment, a double target SXRL configuration was employed. Divergence of the SXRL beam and the shot-by-shot fluctuation of its pointing was an order of 0.5*mrad*. The SM transfers the x-ray source image,

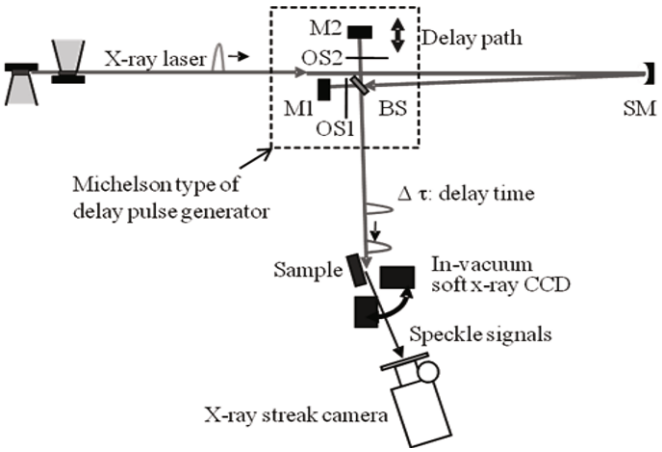

Fig.2. A double pulse x-ray speckle intensity correlation measurements system.

approximately 60μm (FWHM) in diameter, onto the sample by 1-to-1. Double pulses of coherent SXRL were generated by use of a Michelson type delay pulse generator, which consists of a beam splitter BS and two normal incident Mo/Si multilayer mirrors M1, M2. Optical shutters OS1 and OS2 were placed in front of the M1 and the M2, respectively. The delay time between the first x-ray pulse and the second x-ray pulse was adjusted by turning the distance between the BS and the M1. The sample temperature was controlled from the room temperature up to 500K with an accuracy of ±0.1K. Observation of the speckle pattern was conducted with an in-vacuum removable soft x-ray CCD camera. Time resolved recording of the doubled x-ray speckles was performed by soft x-ray streak camera in the range of picoseconds.

3 Results

3.1 Single shot observation of the ferroelectric domain

Free propagation x-ray beam pattern through the slit, nothing but a Fresnel diffraction pattern of the slit, is shown in Fig. 3(a). Fig. 3(b)-3(h) show a series of the speckles from the region of multiple a/c domains when heating the sample from 397K to 403K. Fig. 3(b) is a typical pattern observed at room temperature 397K, where the pattern is clearly divided into two groups. As temperature increased toward the T_C, the speckle patterns apparently evolved into one group, as shown in Fig. 3(c)-3(g). Above the T_C, the structures in the speckle pattern disappeared and turned into one spot, as shown in Fig. 3(h). As shown in Fig. 3(b) and (c), the feature of the two

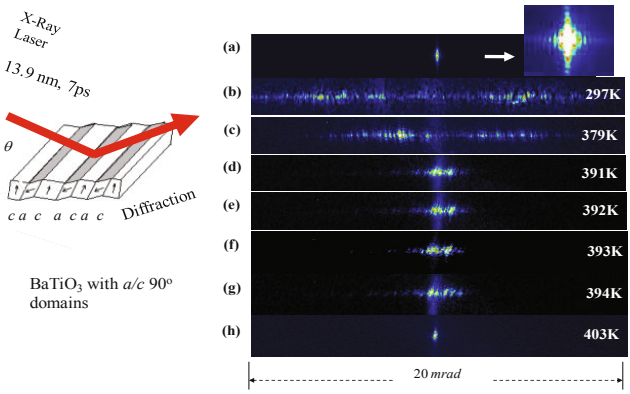

Fig.3. SXRL speckle pattern observed for $BaTiO_3$ ferroelectric domain distribution.

obvious groups in each pattern for a relatively low temperature indicate a stable twin angle distribution along the *a*/*c* domain region.

3.2 Snapshot observation of the polarization clusters above Tc

We can recognize diffuse like structure around the specular reflection above the *T*c in enlarged scale as shown in Fig. 4(a) and 4(b). Fig. 4(a) was obtained at 403.0*K*, while Fig. 4(b) was obtained at 413.0*K*. The strong diffuse pattern in Fig. 4(a) especially indicates the existence of some microscopic-scale structures in the paraelectric phase. Fig. 4(c) shows the quantitative vertical intensity distributions of the speckles, which are cross-sectional intensities along q_y direction (q_x averaged) on CCD. The normalization was made with the total photons of each shot. Here the data with figure (E) mean which were obtained under the application of electric field. The sensitivity of diffuse pattern to an electric field shown in Fig. 4(c) suggests these microscopic-scale structure is a dipole original type structure, as so-called polarization clusters. Polarization clusters acts as phase material via birefringence and results in the speckles. Application of the electric field perpendicular to the sample surface turns the polarization direction to parallel to the scattering plane resulting in no contribution of birefringence to the speckles. The tail for 396.5*K* (E) still remained is due to the incomplete reversing of the relevant polarization because of weakness of the local field at 396.5*K*. Similar behaviour of both profiles observed at 413.0*K* and 408.0*K* (E) indicates here the speckles are free from influence of microscopic-scale polarization clusters.

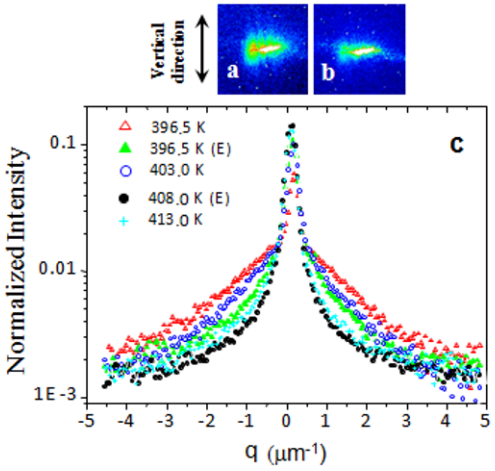

Fig.4. SXRL speckle pattern observed for $BaTiO_3$ paraelectric polarization clusters.

By using the Fourier analysis, we obtained the spatial correlation function from the intensity profiles in Fig. 4(c). The cluster size, the cluster

distance, and the polarization of the clusters were evaluated from the spatial correlation functions. Fig. 5(a) shows the evolution of the mean size σ_s and the mean distance d of those y-polarized clusters with respect to the temperature ΔT ($=T-T_C$). There seems no significant change of the mean cluster size. However, the mean distance increases with temperature approximately linearly. By extrapolating the two dashed line (linear fitting) in Fig. 5(a), one may find a crossover at $6K$ lower temperature below the T_C. This temperature might be understood as the temperature where polarization clusters condensate into ferroelectric domain completely. Fig. 5(b) shows mean magnitude of the polarizations within clusters $|P|^2$, where a peak was observed at temperature around $5K$ above T_C.

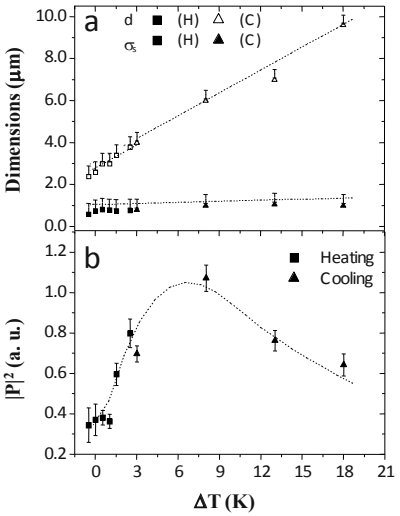

Fig.5. Evolution of (a) the size and the distance, (b) $|P|^2$ of polarization clusters.

3.3 Direct observation of critical relaxation in polarization clusters

We developed a new type intensity correlation method based on the delayed double pulses scattering. The first pulse creates an excess polarization in polarization cluster and storks type Raman scattering takes place, then the second pulse annihilates the residual polarization and anti-storks type Raman scattering takes place. Under the assumption that an excitation of the polarization is subject to chaotic distribution, intensity correlation $g^{(2)}$ between these two speckles can be expressed by an exponential decay curve as follows,

$$g^{(2)} = 1 + \beta \exp(-\frac{2\tau}{\tau_0}),$$

where β is given by a square of the visibility; an indication of the coherence of the incident SXRL, τ is the delay time between the double x-ray pulses, and τ_0 is relaxation time of the excess polarization.

An example of an X-Ray streak image of the speckle to the first and to the second SXRL pulse is shown in Fig.6 (a), and the intensity profile of these streak images in the horizontal direction are shown in Fig. 6(b). We have

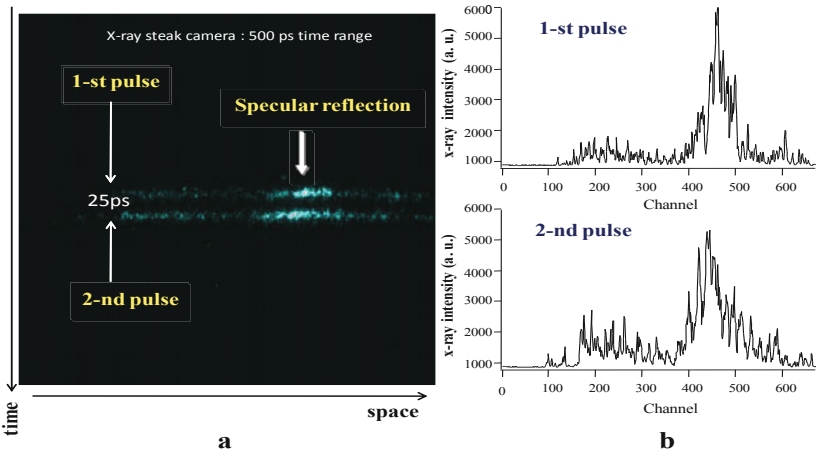

Fig.6. A streak camera image and intensity profiles of the relevant speckle intensities.

measured several pairs of X-Ray speckle intensities with several delay times for each temperature, and then we calculated the intensity correlation. The results of the fitting to $g^{(2)}$ are shown in Fig. 7(a) and 7(b). Fig. 7(a) shows the relaxation behaviour of the intensity correlation from 393K to 405K by 2K, while the Fig. 7(b) shows the relaxation behaviour from 401K to 405K by 0.5K. Relaxation time τ_0 for each temperature is obtained from the curve

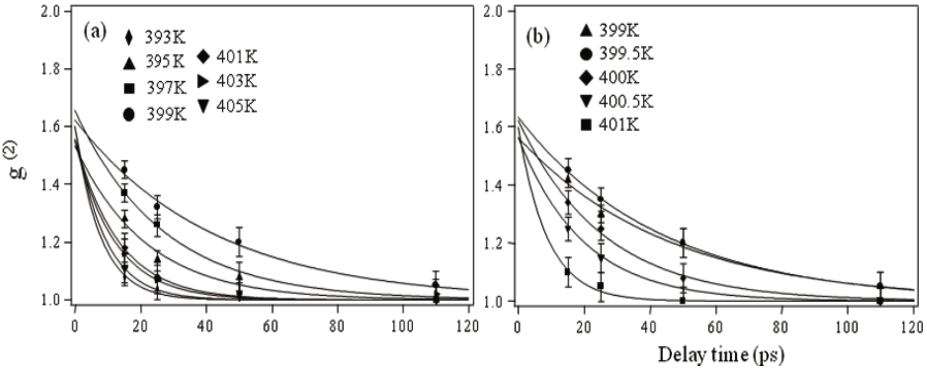

Fig.7. Decay curves of $g^{(2)}$ as a function of delay time at several sample temperature.

fitting. The intercept at τ=0, namely β, was found to be about 0.6 for almost all temperature. The fact that the value of β is 0.6 means that the visibility of the x-ray is 0.8, which is consistent with the experimental estimation.

Behaviour of the relaxation time with the temperature ΔT is shown by solid marks in Fig. 8. Open square marks in Fig. 8 show the temperature dependence of the cluster polarization $|P|$, reproduced from Fig. 5(b). As the temperature decreases, the relaxation suddenly become slower at 4.5K above the T_C, and then become faster again across the T_C, while $|P|$ increases monotonically with decreasing the temperature and takes maximum value at around 5K above T_C, and then it decreases similarly as the relaxation time.

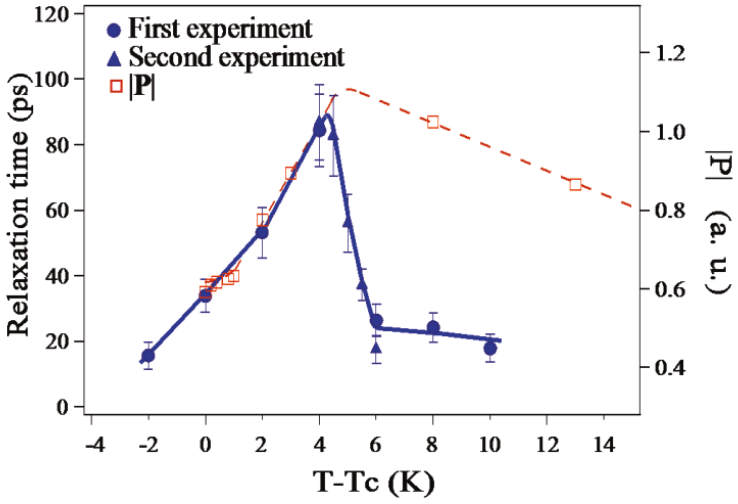

Fig. 8. Temperature dependence of the relaxation time τ_0 and the polarization $|P|$.

4 Discussion

The key factor of phase transition of $BaTiO_3$ between paraelectric phase and ferroelectric phase is the polarization clusters. Appearance of the polarization clusters and its behaviours in precursor region of phase transition are the matters of vital importance. These polarization clusters are believed to be dynamical existence of nanosecond time scale. Moreover, the time scale of the fluctuation of individual dipole moment within the polarization clusters is believed to be picoseconds order. From our picoseconds experimental results described in section 3, we propose a scenario of the ferroelectric phase transition of $BaTiO_3$ as follows.

Polarization clusters begin to appear from more than 200K above the T_C as first mentioned by Barns [10]. The number of the polarization clusters increase gradually, then as approaching to the critical region the volume

density of clusters increases by cubic inverse of ΔT; a consequence of the results shown in Fig. 5(a). While the polarizations of the clusters increase monotonically as ΔT decreases at relatively higher temperature region as shown in Fig. 5(b); it takes maximum value at about $5K$ above the T_C and then it decreases again when the temperature approaching the T_C. This behaviour of polarization means as well dynamical displacement of the Ti ion relative to the O ion in unit cell. Relaxation behaviour of the polarization in polarization clusters shown in Fig.8 indicate that the relaxation time is an order of $20ps$ at relatively higher temperature, it increases suddenly from $5.5K$ above the T_C, and it takes a maximum value about $90ps$ at $4.5K$ above the T_c, and then decreases to an order of $20ps$ again. This behaviour means a kind of critical slowing down takes place at $4.5K$ above T_C. Zalar et al. suggested from NMR experiments a possibility of coexistence of the displacive type and the order-disorder type at the vicinity of the phase transition. Decrease in relaxation time means that the polarization becomes hard to change. Molecular dynamics simulations have shown that the polarization clusters become solid and are subject to the order-disorder type phase transition. From these results we speculate crossover from displacive type to order-disorder type phase transition takes place around 4.5K above T_C. Our proposed scenario is shown

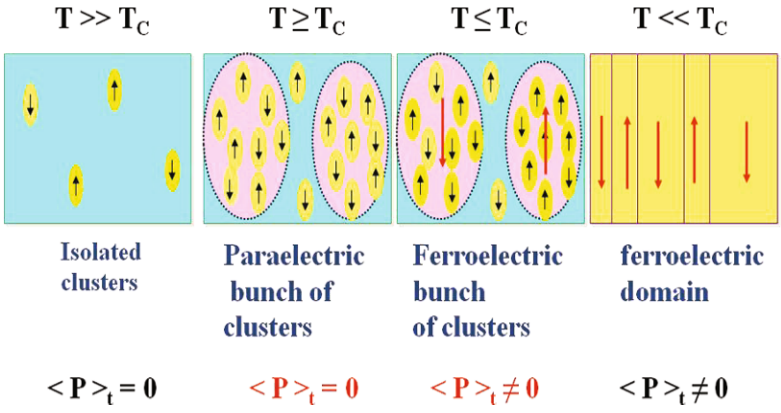

Fig.9. Speculated scenario of ferroelectric phase transition of $BaTiO_3$.

pictorially in Fig.9. Solid polarizations of clusters appear at $4.5K$ above the T_C. Macroscopic polarization appears at T_C. Each ferroelectric domain is condensed from relevant group of polarization clusters at $6K$ below the T_C.

Here we successfully applied plasma X-Ray laser to one of the debating subject of solid state physics: ferroelectric phase transition of $BaTiO_3$. This kind of experiment can be widely applicable not only to other ferroelectrics such as relaxers, but also to other solid sate systems such as charge density wave in $Pr_{0.7}Ca_{0.3}MnO_3$, spin density wave in Cr, and dynamical stripes in cuprate high T_C. For the application to the ferroelectrics, less than $1ps$ pulse

width is preferable, while for the application to other solid state system, order of 10*fs* pulse width is requested. Such short pulse width will be realized by XFEL or HHG soft X-Ray sources.

References

1. Cochran W., 'Crystal stability and the theory of ferroelectricity', *Adv. Phys*. **9**, 387-423, 1960.
2. Cochran W., 'Crystal stability and the theory of ferroelectricity: Part II. Piezoelectric crystals', *Adv. Phys*. **10**, 401-420, 1961.
3. Vogt, H., Sanjurjo J. A., and Rossbroich G., 'Soft-Mode Spectroscopy in Cubic $BaTiO_3$ by Hyper-Raman Scattering', *Phys. Rev. B* **26**, 5904-5910, 1982.
4. Inoue K.., 'STUDY OF STRUCTURAL PHASE TRANSITIONS BY THE HYPER-RAMAN SCATTERING', *Ferroelectrics*, **52**, 253-262, 1983.
5. Zalar B., Laguta V. V., and Blinc R., 'NMR Evidence for the Coexistence of Order-Disorder and Displacive Components in Barium Titanate' *Phys. Rev. Lett*., **90**, 037601, 2003.
6. Stachiotti M., Dorby A., Migoni R. and Bussmann-Holder A., 'Crossover from a Displacive to an Order-Disorder Transition in the Nonlinear-Polarizability Model' *Phys. Rev. B* **47**, 2473-2479, 1993.
7. Takahashi H., 'A Note on the Theory of Barium Titanate', *J. Phys. Soc. Jpn*., **16**, 1685-1689, 1961.
8. Yamada Y., Shirane G. and Linz A., 'Study of Critical Fluctuations in $BaTiO_3$ by Neutron Scattering', *Phys. Rev*., **177**, 848-857, 1969.
9. Comes R., Lambert M., and Guinier A., 'The chain structure of $BaTiO_3$ and $KNbO_3$', *Solid State Commun*., **6**, 715-719, 1968
10. Burns G., and Dacol F. H., 'Polarization in the cubic phase of $BaTIO_3$', *Solid State Commun*., **42**, 9-12, 1982
11. Takagi M., and Ishidate T., 'Anomalous birefringence of cubic $BaTiO_3$', ,*Solid State Commun.*, **113**, 423-426, 2000.
12. Nishikino M., Tanaka M., Nagashima K., et al., 'Demonstration of a Soft-X-Ray Laser at 13.9 nm with Full Spatial Coherence', *Phys. Rev. A* **68**, 061802(R), 2003.
13. Tai, R. Z., Namikawa, K., Sawada, A., et al., 'Picosecond Snap Shot of the Speckle from Ferroelectric $BaTiO_3$', *Phys. Rev. Lett.*, **89**, 257601, 2002.
14. Tai, R. Z., Namikawa, K., Kishimoto, M., et al., 'Picosecond View of the Microscopic-Scale Polarization Clusters Paraelectric $BaTiO_3$', *Phys. Rev. Lett.*, **93**, 087601, 2004.
15. Namikawa, K., Kishimoto, M., Nasu, K.., et al. 'Direct Observation of the Critical Relaxation of Polarization Clusters in $BaTiO_3$ Using a Pulsed X-ray Laser Technique', *Phys. Rev. Lett.*, **103**, 197401, 2009.
16. M. Kishimoto, K. Namikawa, Sukegawa K. et al. 'Intensity Correlation Measurement System by Picosecond Single Shot Soft X-ray Laser', *Rev Sci. Instrum*., **81**, 013905, 2010.

Single-Shot Nanometer-Scale Fourier Transform Hologram Using Ni-like Ag X-Ray Laser

H. T. Kim[1], I J. Kim[1], C. M. Kim[1], T. J. Yu[1], S. K. Lee[1], J. H. Sung[1], J. W. Yoon[1], H. Yun[2], T. M. Jeong[1], I. W. Choi[1], and J. Lee[1]

[1] Advanced Photonics Research Institute, GIST, Oryongdong 1, Bukgu, GwangJu, Korea.
[2] Department of Physics, KAIST, Yuseong-gu, Daejeon 305-701, Korea.

Abstract. Nanometer-scale imaging techniques using only a single shot of ultrafast x-ray pulse are becoming increasingly important because of their potential application in the real-time investigations of nanomaterials. X-ray lasers have a great potential to achieve single-shot nano-imaging due to their coherence and high flux. Here, we will report on single-shot Fourier Transform hologram using Ni-like Ag x-ray laser driven by a single-profiled pumping pulse. We achieved lensless Fourier transform holograms with a single pulse of x-ray laser and the reconstructed image has a minimum resolution of 87 nm.

1 Introduction

Single-shot nano-imaging technique is one of the important issues due to its potential to reveal structural dynamics of nano-materials. One of reason for the massive construction of X-ray free electron lasers (XFELs) is the time-resolved x-ray imaging for various materials with femtosecond temporal resolution and nanometer spatial resolution [1], even though XFELs are very huge and expensive facilities. Recently, table-top x-ray lasers using ultrashort intense lasers have been achieved high photon flux and quality [2-4] that is enough for nano-imaging techniques [5, 6]. In this proceeding, we report on single shot x-ray hologram with nanometer scale resolution using Ni-like Ag x-ray laser. We successfully obtained Fourier Transform (FT) holograms [7, 8] with a single shot of x-ray laser pulse and the reconstructed image has a minimum resolution of 87 nm [9].

The paper is organized as follows. In section 2, we explain the experimental arrangement and sample preparation for the holography. The results of holographic imaging using Ni-like Ag x-ray laser and summary of the results are given in section 3 and section 4, respectively.

J. Lee et al. (eds.), *X-Ray Lasers 2010,* Springer Proceedings in Physics 136,
DOI 10.1007/978-94-007-1186-0_36,

2. Experimental setup and sample fabrication for Fourier transform holography

FT hologram technique is well known imaging method for high-resolution microscopy. The FT holograms are formed by the interference between diffracted waves from unknown sample and known reference holes. For observing the FT hologram, we used an Ni-like Ag x-ray laser pumped by table-top-scale Ti:Sapphire laser system at Advanced Photonics Research Institute. We use our recently developed variant of the GRIP x-ray laser by using a temporally profiled pulse from a single beam line [10]. This new GRIP method has advantages of very simple optical arrangement and stable operation. Figure 1 shows the experimental scheme of the FT hologram obtained using the x-ray laser pulse. 2-J, 8-ps pumping laser pulse was focused on a 9-mm long Ag medium in order to generate the x-ray laser. A Mo:Si mirror was used to collect and focus x-ray laser beam on the sample plate. A 200-nm thick Zr filter was positioned before the sample plate in order to block scattered lights, and the sample plate was installed 48 mm before the soft x-ray CCD.

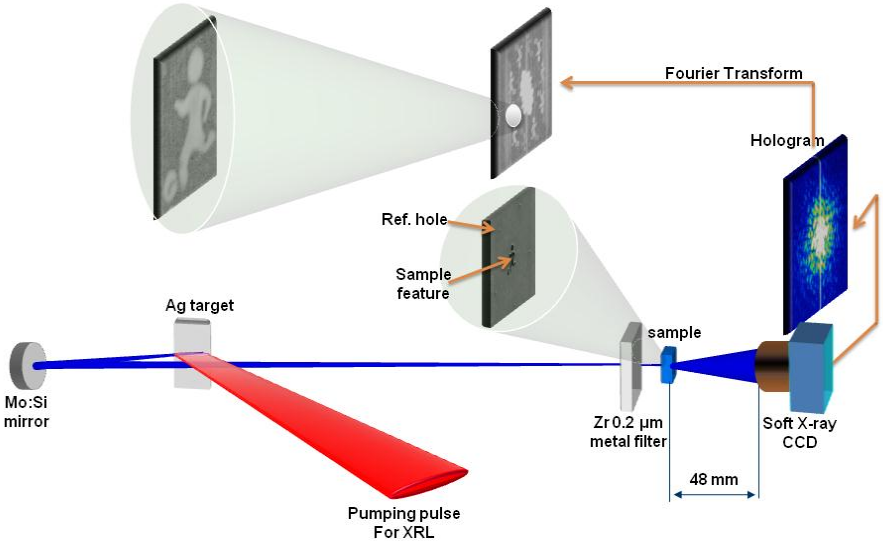

Figure 1. Experimental scheme for the FT hologram using x-ray laser pulse

As shown in Fig. 1, a sample feature and reference holes are illuminated by the Ni-like Ag x-ray laser at the wavelength of 13.9 nm. The beam diffracted from the reference holes and sample figure then interferes on the CCD and forms an FT hologram. The Fourier transformation of the FT hologram provides the spatial autocorrelation of the whole sample plate. In the

experiment, we used 5 reference holes surrounding the central sample figure in order to increase the signal to noise ratio and improve the quality of reconstructed image. For each reference hole, a real subimage and its complex conjugate are produced from a cross-correlation of the sample feature and reference hole. Therefore, Fourier transform of the holograms with 5 reference holes provide 10 sub-images of 5 real and 5 virtual images.

Figure 2 shows the structure of sample plate for the FT holography. The sample plate was fabricated by focusing an ion beam on the 300-nm or 500-nm thick gold film that was previously deposited on a 100-nm thick Si3N4 membrane. Using the focused ion beam (FIB), the central figure was carved on the gold surface down to the Si3N4 membrane, while the circular reference holes were drilled through the entire sample plate. Figure 2 b shows a scanning electron microscope image of a test sample that is fabricated on thick Si substrate to survey FIB condition and confirm the sectional view of the sample. As shown in sectional view of test sample in Fig. 2 c, the edge of carved pattern is declined due to the focusing geometry of the ion beam and redeposition problem. This side effect of FIB milling causes the reference holes to be different sizes when viewed from the front and back sides. In the experiment, even the size of the reference holes in front side is around 200 nm, the back side can be about 100 nm. Therefore effective size of reference holes, which determines the resolution of reconstructed image, can be smaller than the size captured by scanning electron microscopy at the front size.

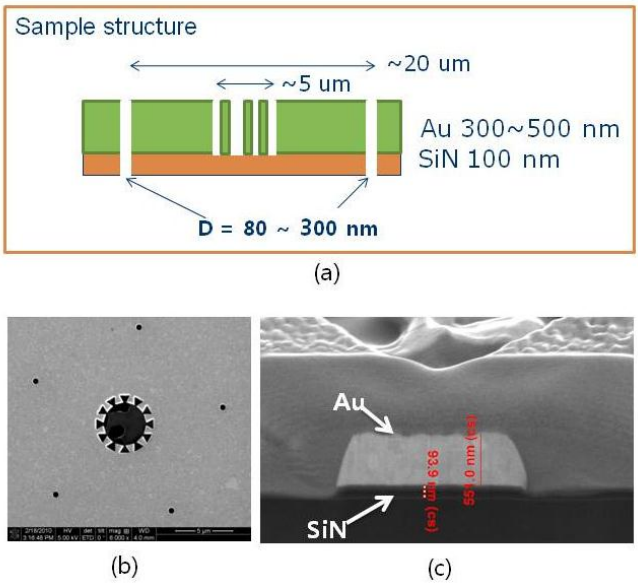

Figure 2. (a) Sample structure, (b) SEM image and (c) sectional view of test sample.

3. Single-shot nano-meter-scale holographic imaging

We attempted the imaging of various samples in order to examine the capabilities of imaging complex features via FT holography (Fig. 3). The first sample shows the shape of sunflower. Figure 3a-i shows the SEM image of the sample feature. In this case, the size of the reference holes was around 500 nm and the thickness of Au film was 500 nm. Figure 3a-ii and 3a-iii shows the measured hologram by soft x-ray CCD and reconstructed image for the sample with shape of sunflower, respectively. The best resolution of the reconstructed image was about 300 nm. The second sample is "Taegeuk", the central mark of the national flag of Korea. The reference-hole at the front side of the sample is about 300 μm, and the thickness of sample Au film was 300 nm. The reconstructed image (Fig. 3b-iii) has a resolution about 200 nm. The third image (Fig. 3c) shows a soccer player, which was a much more complex sample than the others. Again, the figure shows that the reference hole was about 200 nm at the front side and the thickness of the Au film was 300 nm. The diffracted signal (Fig. 3c-ii) and reconstructed image (Fig. 3c-iii) were well obtained for this complex figure, with a resolution around 100 nm. Consequently, we succeeded in obtaining images via FT holography from samples of various shapes, even those with complex structures.

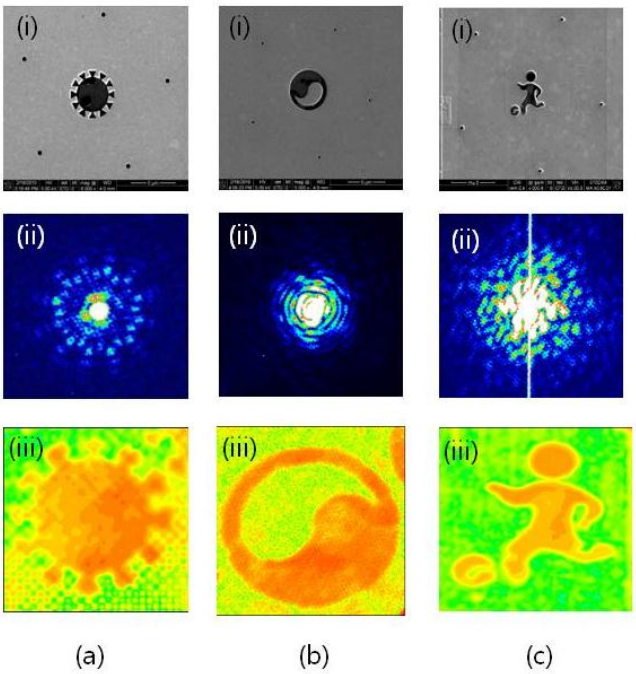

Figure 3. Holographic imaging with various samples (i) SEM image of sample fearue (ii) measured hologram on soft x-ray CCD and (iii) reconstructed images.

Next, we tested the FT hologram using a simple bar-shaped sample figure (Fig. 4a). In this case, the Au film has thickness of 300 nm and the reference hole size at the front side was around 200 nm. Figure 2b shows reconstructed image that is accumulated the individual sub-images from the 5 reference holes. Fig. 2c shows the line cut of the reconstructed image. From the line profile of the image, the minimum resolution of this holographic imaging was 87 nm, in which the intensity contrast varied from 10 % to 90 %. Consequently, we succeeded in the single-shot measurement of images with sub 100-nm resolution via FT holography using a table-top x-ray laser source.

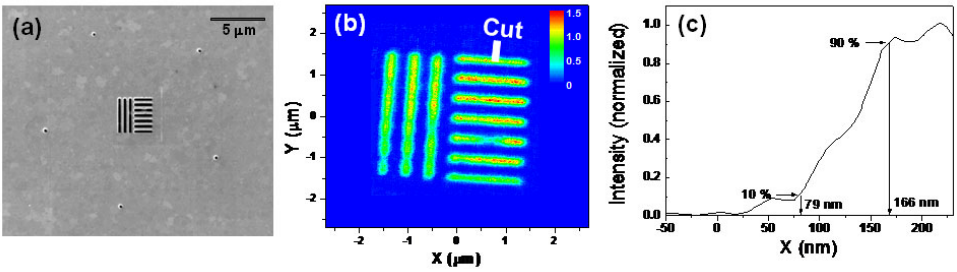

Figure 4. (a) SEM image of bar-shaped sample (b) reconstructed image and (c) line cut of the reconstructed image.

4. Summary

We successfully demonstrated a single-shot nano-imaging technique with sub 100-nm spatial resolution, 87-nm minimum resolution in line cut graph, by the FT holography with a table-top laser-based x-ray laser source. Various samples were tested with the FT hologram technique and it is confirmed that this technique can be applied even to samples with complex structures. This result will provide a useful measurement technique to nanotechnologies and material sciences due to its possibility of temporally resolved nanometer-scale imaging. This single-shot nanometer-scale imaging technique by a table-top x-ray laser can provide easily accessible high-resolution nanoscopy because x-ray lasers pumped by high power lasers can be generated by using commercial Ti:Sapphire laser systems or comparable table-top laser systems,

Acknowledgement

This work was supported by the Ministry of Knowledge and Economy of Korea through the Ultrashort Quantum Beam Facility Program.

References

1. Chapman, H. N. et al.: 'Femtosecond diffractive imaging with a soft-X-ray free-electron laser', *Nat. Phys.* 2, 839 (2006).
2. Keenan, R. et al.: 'High-Repetition-Rate Grazing-Incidence Pumped X-Ray Laser Operating at 18.9 nm', *Phys. Rev. Lett.*, 94, 103901, 2005
3. Wang Y. et al.: 'Demonstration of high-repetition-rate tabletop soft-x-ray lasers with saturated output at wavelengths down to 13.9 nm and gain down to 10.9 nm', *Phys. Rev. A* 72, 053807 (2005).
4. Tümmler, J. et al.: '10-Hz grazing-incidence pumped Ni-like Mo x-ray laser', *Phys. Rev. E* 72, 037401 (2005)
5. Brewer, C. et al.: 'single-shot extreme ultraviolet laser imaging of nanostructures with wavelength resolution', *Opt. Lett.* 33, 518, 2008.
6. Sandberg, R. L. et al.: 'High numerical aperture tabletop soft x-ray diffraction microscopy with 70-nm resolution' , *Proc. Natl. Acad. Sci. U.S.A.* 105, 24 (2008).
7. Stroke, G. W., 'Lensless Fourier-transform method for optical holography', *Appl. Phys. Lett.* 6, 201 (1965).
8. McNulty, I. et al.: 'High-Resolution Imaging by Fourier Transform X-ray Holography', *Science* 256, 1009-1012 (1992).
9. Kim, H. T. et al.: 'Single-shot nanometer-scale holographic imaging with laser-driven X-ray laser', submitted to *Appl. Phys. Lett.*
10. Kim, H. T. et al.: "Demonstration of a saturated Ni-like Ag x-ray laser pumped by a single profiled laser pulse from a 10-Hz Ti:sapphire laser system," *Phys. Rev. A* 77, 023807 (2008).

Theory and computation towards coherent reflection imaging of tilted objects

I. A. Artyukov, A. N. Mitrofanov, A.V. Popov, N. L. Popov and A.V.Vinogradov

Lebedev Physical Institute, Leninsky Prospekt 53, 119991 Moscow, Russia

Abstract. The goal of this study is to develop a theoretical basis for lensless coherent imaging in the reflection mode. To describe the wave field produced by a reflective obliquely illuminated object we introduce the tilted object integral (TOI) which is the extension of Fresnel propagation integral (FI) used in the theory of coherent transmission mode imaging. The properties of TOI are studied analytically and numerically in 2D and 3D geometries for various field distributions at the surface of a tilted object. The considerable difference between TOI and FI is observed and explained at small grazing angles of object illumination.

1 Introduction

Since early times of X-ray lasers they are used for X-ray imaging in reflection and transmission modes [1-3]. Then due to the improved beam coherence high harmonic generators and soft X-ray lasers allowed quantitative microscopy based on lensless coherent imaging [4-6][1]– the technique well developed in hard X-rays [7]. The latter is known for the transmission mode that for soft X-rays means submicron and even ~100nm thick samples. Coherent reflection imaging will not have this limitation. Another quest comes from hard X-ray SR beamlines where reflection imaging provides information about the structure of interfaces in complex environment [9,10]. In this paper we continue the analysis of coherent reflection imaging using the method of parabolic wave equation (PWE) [11], while the authors of [12] are basing on the Huygens-Fresnel principal.

2 Field propagation from a tilted object

In the standard formulation of coherent transmission imaging the image transfer from the object to detector by laser beam is governed by PWE, the solution to which is the Fresnel integral (FI) [7]. In case of laser illumination

[1] Soft X-ray coherent imaging is also used at SR facilities in sub-keV range [8].

J. Lee et al. (eds.), *X-Ray Lasers 2010,* Springer Proceedings in Physics 136,
DOI 10.1007/978-94-007-1186-0_37,

of a tilted object we assume that laser beam after reflection is modified but still remains collimated in specular direction (Fig.1) and therefore can be described by PWE:

$$2ik\frac{\partial u(x,z)}{\partial z}+\frac{\partial^2 u(x,z)}{\partial x^2}=0. \tag{1}$$

Initial (boundary) condition is posed on the plane of an object tilted to an angle θ:

$$u(x,z)\Big|_{x=-ztg\theta}=u_0(z). \tag{2}$$

Introduce a new coordinate ξ and a wavefunction $w(\xi,z)$:

$$\xi=x+ztg\,\theta,\quad w(\xi,z)=\exp(ikxtg\theta+ikz\frac{tg^2\theta}{2})u(x,z). \tag{3}$$

Substitution of (3) into (1) and (2) again gives PWE:

$$2ik\frac{\partial w(\xi,z)}{\partial z}+\frac{\partial^2 w(\xi,z)}{\partial \xi^2}=0, \tag{4}$$

but with boundary condition posed on a plane $\xi = 0$ parallel to the wave vector:

$$w(\xi,z)\Big|_{\xi=0}=w_0(z)=e^{-ikztg^2\theta/2}u_0(z). \tag{5}$$

Equations (4) and (5) show that the new wave function $w(\xi,z)$ satisfies the

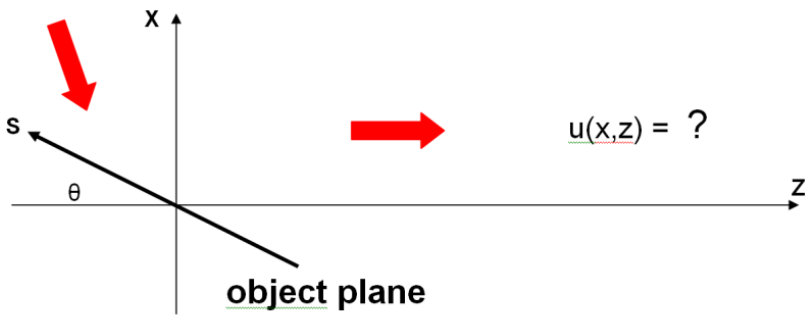

Fig.1 Lensless imaging in the reflection mode. An obliquely illuminated object is located in the plane *S*. The reflected beam is collimated around the *Z*-axis allowing application of PWE.

same PWE but with the "side" boundary condition. The solution to this new problem is:

$$w(\xi,z)=\sqrt{\frac{k}{2\pi i}}\xi\int_{-\infty}^{z}\frac{w_0(z')dz'}{(z-z')^{3/2}}\exp\left[i\frac{k\xi^2}{2(z-z')}\right]. \tag{6}$$

The final result is obtained from (6) by coming back to *u(x,z)* with the help of (3) (see also [11]):

$$u(x,z)=\sqrt{\frac{k}{2\pi i}}(x+ztg\theta)\int_{-\infty}^{z}\frac{u_0(z')dz'}{(z-z')^{3/2}}\exp\left[i\frac{k(x+z'tg\theta)^2}{2(z-z')}\right]. \tag{7}$$

Substituting $z' = -s\cos\theta$ the wave field (7) can be written in the form of the integral over the object plane:

$$u(x,z)=\sqrt{\frac{k}{2\pi i}}(x\cos\theta+z\sin\theta)\int_{-z/\cos\theta}^{\infty}\frac{u_0(s)ds}{(z+s\cos\theta)^{3/2}}\exp\left[i\frac{k(x-s\sin\theta)^2}{2(z+s\cos\theta)}\right]. \tag{8}$$

Tilted object integral (TOI) given by (7) and (8) exhibits the space field distribution produced by a wave propagating from a tilted object. TOI as is seen from (8) (and (7)) for $\theta = \pi/2$ is reduced to ordinary FI:

$$u(x,z)=\sqrt{\frac{k}{2\pi iz}}\int_{-\infty}^{\infty}u_0(s)ds\exp\left[i\frac{k(x-s)^2}{2z}\right]. \tag{9}$$

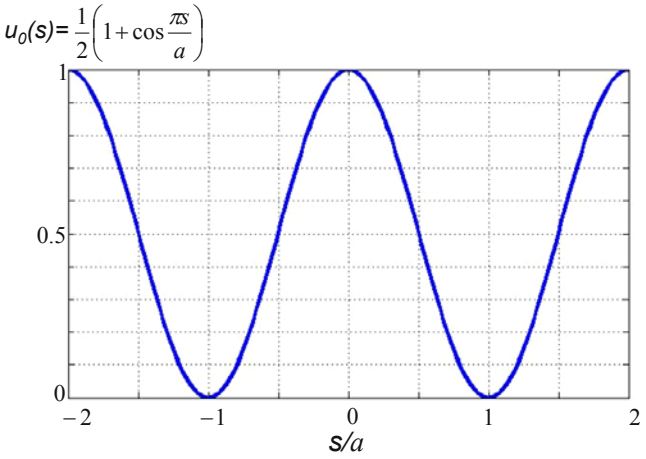

Fig. 2. The wave profile at the surface of a tilted object used in Figs. 3 – 6 for 2D simulation of lensless reflection imaging at oblique illumination.

3 Discussion. Propagation of spatial harmonics

A simple consideration illustrates the reason to extend the Fresnel integral formalism to tilted objects. Really the information about the object is transferred by the reflected beam inside the diffraction angle $\delta\theta \approx \lambda/(a\theta)$, where a is the feature size at the surface of the object. Until $\delta\theta << \theta$ the beam formed after reflection does not "feel" the surface of the object and the space field distribution well corresponds to the Fresnel propagation theory. However if the grazing angle θ decreases δθ increases. Finally the beam cone defined by Fresnel diffraction theory touches and then intercepts the surface of the object. This evidently happens when $\delta\theta \approx \theta$ or

$$\theta \approx \sqrt{\frac{\lambda}{a}}. \tag{10}$$

So if the grazing (tilt) angle is of the order or smaller than (10) the space field distribution is expected to rearrange and to differ from that given by FI. Instead the TOI (8) has to be used to calculate the spatial field distribution produced by obliquely illuminated object. To investigate the problem in more details assume that the field at the surface of the object has the form of a spatial harmonic:

$$u_\mu(x,z)\Big|_{x=-ztg\theta} = u_0(z) = u_0(s) = e^{i\mu s},\ z = -s\cos\theta. \tag{11}$$

The solution to PWE (1) with boundary condition (11) is:

$$\begin{gathered} u(x,z) = \exp(i\sqrt{2k\kappa}x - i\kappa z),\ \kappa = \frac{ktg^2\theta}{2}\left(\sqrt{1+\Phi}-1\right)^2, \\ \Phi = \frac{2\mu\cos\theta}{k\sin^2\theta} = \frac{2\lambda\cos\theta}{a\sin^2\theta}, \end{gathered} \tag{12}$$

where $a = 2\pi/\mu$ – spatial period at the object surface. The wave field (12) looks very simple if the detector plane is parallel to the surface of the object:

$$u_\mu(s,l) = e^{i\mu s - i\kappa l}, \tag{13}$$

where l – the object to detector distance. Formula (13) shows that initial spatial harmonic does not change except of acquiring the phase factor.

According to (13) the Talbot effect takes place if the distance L exists for which the value $\kappa(n\mu)L/2\pi$ is integer for any integer n. On the other hand $\kappa(\mu)$ is a complex function of μ (see (12)). Hence strictly speaking the Talbot effect is not valid for tilted objects. However the solution (12) says that depending on the value of the parameter Φ the Talbot effect can be valid approximately and at the restricted distances. If Φ << 1 - short wavelengths,

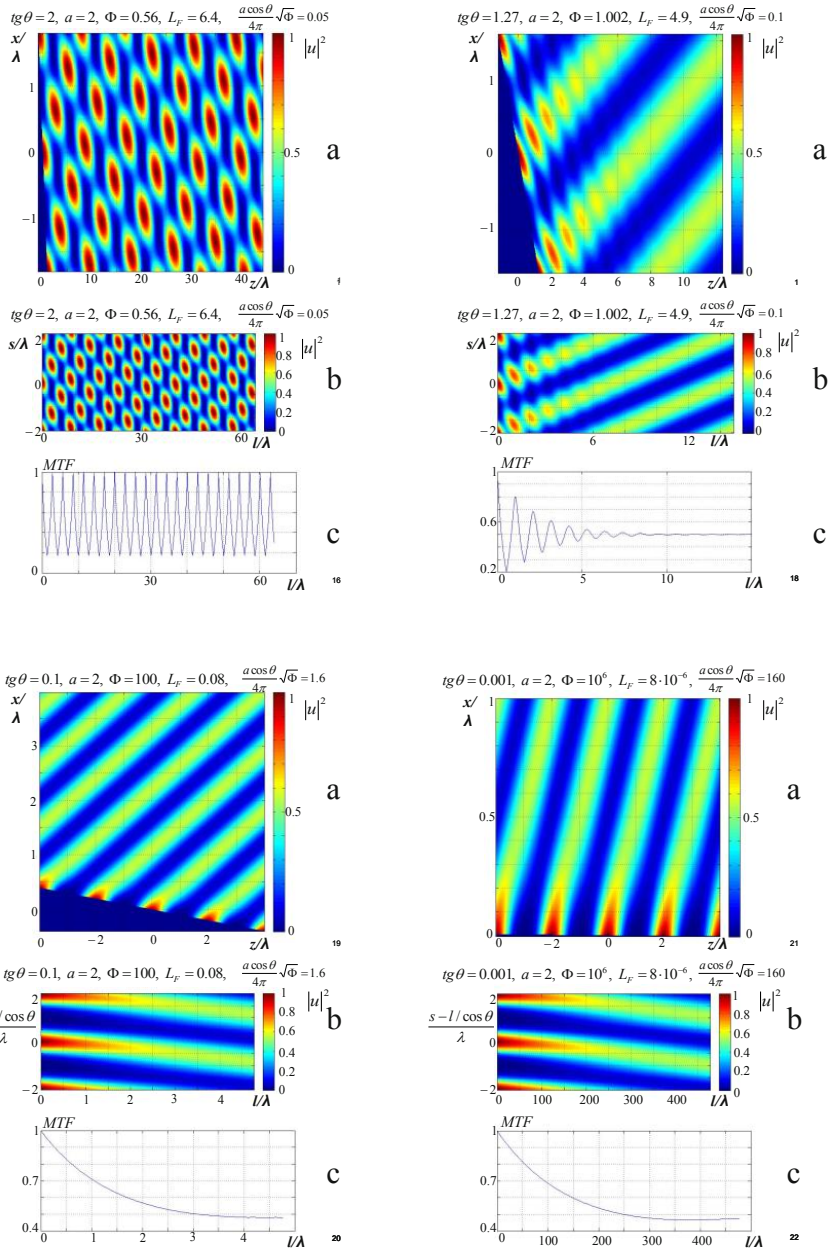

Figs. 3 – 6. Global field distribution for various tilt angles θ and object to detector distances l (or z). At each figure (a) shows the results for detector in the vertical position (perpendicular to the wave vector of the reflected beam, (b) – detector is parallel to the object plane, (c) – shows space evolution of the modulation transfer function for detector parallel to the object plane. In Figs. 5(b) and 6(b) the vertical coordinate is shifted to illustrate the effect of large Φ discussed in Sec. 3.

large feature size a or large θ (near normal incidence illumination) - the field (13) is reduced to

$$u_\mu(s,l) = \exp\left(i\mu s - i\frac{\mu^2}{2k\sin^2\theta} l \right), \tag{14}$$

that exactly corresponds to Talbot effect. The corresponding integral form can be derived from (8):

$$u(s,l) = \sqrt{\frac{k\sin^2\theta}{2\pi i l}} \int_{-\infty}^{\infty} u_0(s')ds' \exp\left[i\frac{k\sin^2\theta}{2l}(s-s') \right]. \tag{15}$$

As follows from (12), (13) formulas (14) and (15) are true for:

$$\Phi << 1 \quad \text{and} \quad l << L_F/\Phi, \tag{16}$$

where $L_F = \frac{2a^2}{\lambda}\sin^2\theta$ - Fresnel (Talbot) length.

Formula (15) evidently exhibits the scaling of the FI (9) to tilted objects that is valid for $\Phi << 1$. As was shown above for $\Phi \geq 1$ the field propagating from a tilted object rearranges and is expected to change drastically, that is described by TOI (8). For $\Phi >> 1$ - long wavelengths, small feature sizes and grazing angles θ formula (13) reduces to:

$$u_\mu(s,l) = \exp\left(i\mu s - i\frac{\mu}{\cos\theta} l \right), \quad \Phi << 1, \quad l << \frac{a\cos\theta}{4\pi}\sqrt{\Phi}\,. \tag{17}$$

Therefore for arbitrary field distribution at the object $u_0(s)$ one has:

Fig. 7. Two reflective objects used for 3D simulation of diffraction patterns produced by oblique illumination at wavelength λ = 10 nm.

$$u(l,s)=u_0(s-\frac{l}{\cos\theta}),\quad \Phi<<1,\quad l<<\frac{a\cos\theta}{4\pi}\sqrt{\Phi}. \tag{18}$$

The last formula indicates the range of the "shadow" zone at grazing incidence illumination of the object and the up-shift of the image in this zone.

The conclusion to the analysis of this section is: the spatial picture of the wave field propagating from a tilted object crucially depends on the parameter Φ (see (12)) that includes main physical parameters of the problem: wavelength λ, feature size a and tilt angle θ.

4 Simulation results

The Talbot effect offers a good opportunity to demonstrate the difference between FI (see (9)) and TOI (see (8)) describing horizontal wave propagation from vertical ($\theta=\pi/2$) and tilted ($\theta\neq\pi/2$) objects. In general a periodical object is characterized by a sum of harmonics (11):

$$u_0(s)=\sum_n C_n e^{in\mu s}. \tag{19}$$

Correspondingly instead of (13) we have:

$$u(s,l)=\sum_n C_n \exp\left(in\mu s+i\kappa_n l\right),\quad \kappa_n=k\frac{tg^2\theta}{2}\left(\sqrt{1+n\Phi}-1\right)^2, \tag{20}$$

where Φ is given by (12). As is seen from (20) the field $u(s,l)$ remains to be

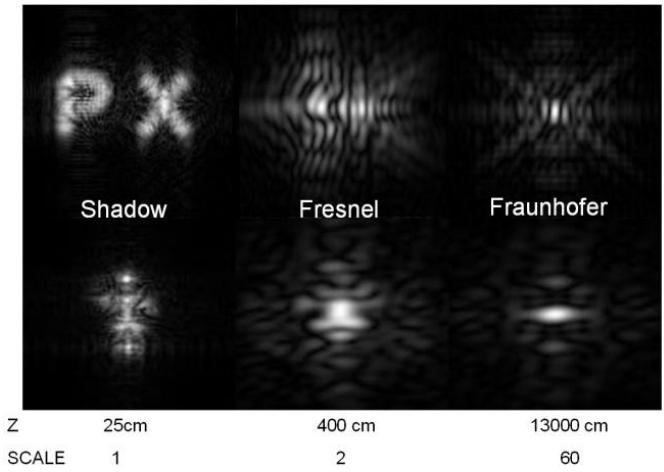

Fig. 8. Fresnel propagated diffraction patterns of objects shown in Fig. 7 at different object to detector distances. The objects are in vertical position ($\theta = \pi/2$).

periodical on s in any plane parallel to the object. At the same time due to complexity of κ_n at least for large negative n in general case there is no periodicity on the object to detector distance l, i.e. no Talbot effect for tilted objects as was mentioned in the previous section. Note that in case of periodical objects FI is obtained from (20) at $\theta = \pi/2$ (small Φ) :

$$\kappa_n \approx k\frac{tg^2\theta}{8}n^2\Phi^2 = \frac{\mu^2 n^2}{2k}, \tag{21}$$

$$u(s,l) = \sum_n C_n \exp\left(in\mu s + i\frac{\mu^2 n^2}{2k}l\right). \tag{22}$$

Expression (22) is a usual formal explanation of the Talbot effect. Formulas (20) and (22) represent TOI and FI for periodical objects (periodical $u_0(s)$). Comparing them we see that for TOI the spatial harmonics for which $1+n\Phi > 0$ (or $n > -1/\Phi$) propagate, whereas those for which $1+n\Phi < 0$ damp with l when going far away from the object surface. This circumstance is responsible for evolution of MTF calculated for the initial distribution shown in Fig. 2. Calculations reveal that at large angles close to normal incidence (Fig. 3) the global wave field keeps the Talbot behavior. Besides large angles θ this is due to the fact that $u_0(s)$ contains only 3 harmonics: $n = 0$ and $n = \pm 1$. At smaller angles the wave vector κ_n of $n = -1$ harmonic acquires imaginary part and the contribution of this harmonic into $u(s,l)$ falls to zero at large distances l. So only $n = 0$ and $n = 1$ harmonics survive that results in damping of oscillations in MTF (see. Fig 4 and Fig 5). At the same time at $l \to \infty$ the shape of $|u(s,l)|$ as a function of s does not change acquiring only a shift depending on l. This behavior is illustrated in Figs 4-6 that demonstrate the structure of the global field produced by a periodical object at various tilt angles.

The conclusion of this consideration is that if a periodical field at the surface of a tilted object contains a finite number of spatial harmonics the Talbot effect keeps inside some angular interval around normal incidence. At smaller tilt angles it is true only approximately. The smaller is the tilt angle θ the shorter is the maximum distance l until the Talbot effect appears.

5 3D simulations

The 2D theory given in Sec. 2 can be extended to 3D case. Similar to Sec.II consider an object tilted in the plane XZ with Y-axis fixed in the plane of the

object surface. Then the 3D wave field produced by an initial field distribution $u_0(s,y)$ in the object plane has the form:

$$u(x,y,z)=\frac{k(x\cos\theta+z\sin\theta)}{2\pi i}\int_{-\infty}^{\infty}\int_{\frac{z}{\cos\theta}}^{\infty}\frac{u_0(y',s)dy'ds}{(z+s\cos\theta)^2}\exp\left\{ik\frac{(y-y')^2+(x-s\sin\theta)^2}{2(z+s\cos\theta)}\right\}. \quad (23)$$

Formula (23) implies that YOS is the plane of the tilted object. For $\theta=\pi/2$ the TOI (23) is reduced to the 3D form of FI:

$$u(x,y,z)=\frac{k}{2\pi iz}\int_{-\infty}^{\infty}\int_{-\infty}^{\infty}dsdy'u_0(y',s)\exp\left\{ik\frac{(y-y')^2+(x-s)^2}{2z}\right\}. \quad (24)$$

Figs 9-10 compare at different tilt angles θ the free space propagation images of the tilted objects shown in Fig. 7 with the free space propagation images of the same objects in vertical position (Fig. 8). The latter are calculated with the standard FI (24). A strong asymmetry in horizontal and vertical directions is evident for tilted objects that correlates with the results of the previous section.

6 Inverse problem and concluding remarks

Coherent imaging is now one of the leading methods for quantitative microscopy i.e. for quantitative object characterization. Whether the phase of the wave field at the detector is measured or not the full image reconstruction requires the solution of the inverse problem [7,13]. In other words for full image reconstruction both the direct and inverse formulas relating the fields in the object and detector planes (see Fig 11) have to be found. In 2D case this can be done with the help of (7). The first step is to rewrite it in the form of the integral over x instead of z in order to make use of the physical symmetry

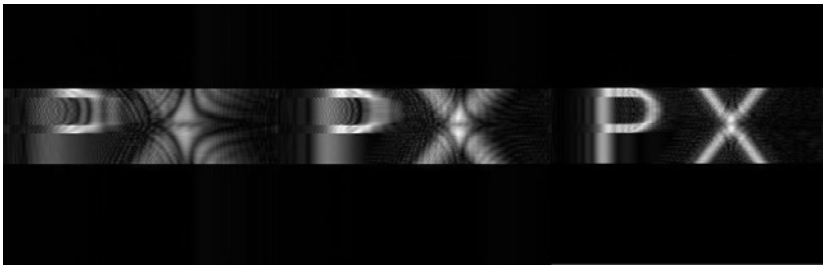

Fig. 9. Diffraction patterns of letters produced at oblique illumination for θ = 1, 2 and 3 degrees. Object to detector distance is 0.5 mm. Detector is parallel to the object plane.

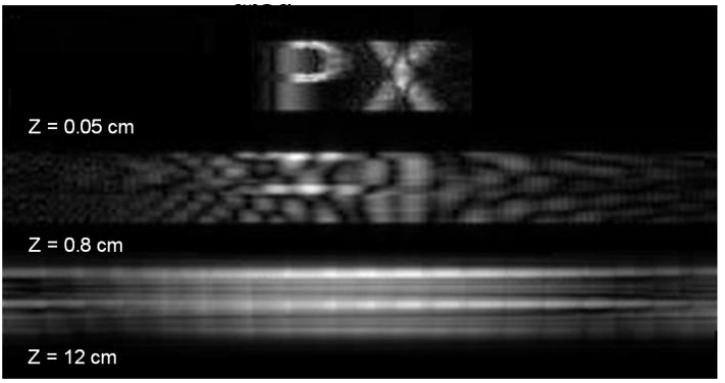

Fig. 10. Diffraction patterns of letters produced at oblique illumination for θ = 2 degrees and various object to detector distances. Detector is parallel to the object plane.

between the object and image:

$$u(x') = \sqrt{\frac{k}{2\pi i}\left[(p+p')x'+l\right]} \int\limits_{-\frac{l+px'}{p'}}^{\infty} \frac{u_0(x)}{\left(l+px+p'x'\right)^{3/2}} \times \\ \times \exp\left[\frac{ik}{2}\frac{(x'-x)^2}{l+px+p'x'}\right]dx. \tag{25}$$

Omitting the details for the sake of brevity we give here the final result:

$$u_0(x) = \sqrt{\frac{ik}{2\pi}\left[(p+p')x+l\right]} \int\limits_{-\frac{l+px}{p'}}^{\infty} \frac{u(x')}{\left(l+px+p'x'\right)^{3/2}} \times \\ \times \exp\left[-\frac{ik}{2}\frac{(x'-x)^2}{l+px+p'x'}\right]dx'. \tag{26}$$

Similar relations should be found for the 3D geometry.

In various experimental schemes with horizontal X-ray beam and vertical object the latter is located in Fraunhofer zone of FI (9). Then the relations (25), (26) between field distributions in the image and object planes are reduced to Fourier transform [7]. It can be shown that for large distances *l* from a tilted object the analog of the Fraunhofer zone exists. The corresponding formula for the wave field can be found from TOI (8):

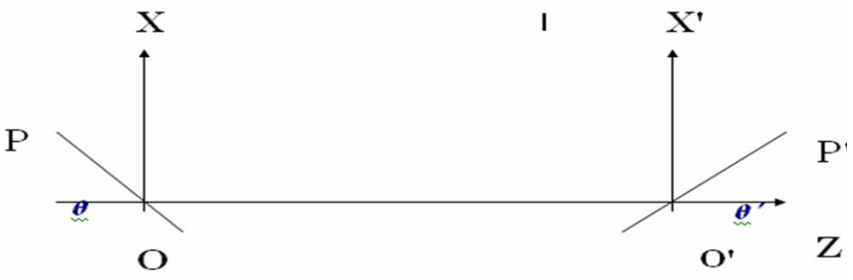

Fig. 11. Coordinate system used for direct and inverse transforms (25) and (26).

$$u(x,z) \approx \sqrt{\frac{k}{2\pi i z}}\left(\frac{x}{z}\cos\theta + \sin\theta\right) e^{i\frac{kx^2}{2z}} \int u_0(s) e^{-i\frac{kx}{z}\left(\frac{x}{z}\cos\theta+\sin\theta\right)s}\, ds. \qquad (27)$$

We see that Fourier conjugated variables here are $s \leftrightarrow k\left(\frac{x}{z}\cos\theta + \sin\theta\right)$ in contrast to $s \leftrightarrow k\frac{x}{z}$ for standard FI. Of course for $\theta = \pi/2$ formula (27) is reduced to the usual Fraunhofer integral [7].

7 Summary

The theory towards lensless coherent imaging of reflective objects is developed basing on parabolic wave equation. The solution is given in the form of tilted object integral (TOI) over the surface of obliquely illuminated object. The relation between TOI and standard Fresnel propagation integral (FI) is investigated. It depends on the dimensionless parameter $\Phi = \frac{2\lambda\cos\theta}{a\sin^2\theta}$ that includes wavelength λ, feature size a and tilt angle θ. At small Φ ($\theta \approx \pi/2$) TOI is reduced to FI. At large Φ (grazing angle $\theta \to 0$) the difference between TOI and FI is dramatic that is connected with the influence of the object surface on the diffracted field. Simulations in 2D and 3D cases confirmed strong asymmetry of the reflected image produced by a tilted object. The analogue of the Fraunhofer zone in 2D geometry is found as well as the inversion of TOI expressing the field at the tilted object in terms of the field at the detector plane. The theory of coherent reflection imaging at oblique angles may be important for ~few tens – hundred eV photon energy range where laboratory X-ray lasers and high harmonic generators presently operate.

References

1. DiCicco, D.S.; Kim, D.; Rosser, R.; Suckewer, S.: 'First stage in the development of a soft-x-ray reflection imaging microscope in the Schwarzschild configuration using a soft-x-ray laser at 18.2 nm', *Optics Letters*, **17**, 157-159, 1992
2. Da Silva, L. B., Trebes, J. E.; Mrowka, S., Barbee Jr, T. W.; Brase, J., Koch, J. A., London, R. A., MacGowan, B. J., Matthews, D. L., Minyard, D.; Stone, G., Yorkey, T., Anderson, E., Attwood, D. T., Kern, D.: 'Demonstration of x-ray microscopy with an x-ray laser operating near the carbon K edge', *Optics Letters*, **17**, 754-756, 1992
3. Menoni, C.S.; Brizuela, F., Wang, Y, Brewer, C. A.; Luther, B. M., Pedaci, F, Wachulak, P. W., Marconi, M, C., Rocca, J. J., Chao, W, Anderson, E, H., Liu,Y., Goldberg, K. A., Attwood, D. T., Vinogradov, A. V., Artyukov, I. A., Pershyn, Y. P., Kondratenko, V.: 'Advances in full field microscopy with table-top soft x-ray lasers', *Proc. SPIE*, **7451**, 74510I-74510I-8, 2009
4. Sandberg, R.L., Paul, A., Raymondson D.; Hädrich, S., Gaudiosi, D., Holtsnider, J., Tobey, R., Cohen, O., Murnane, M. M., Kapteyn, H. C., Song, C., Miao, J., Liu, Y., Salmassi, F.: 'Lensless diffractive imaging using tabletop, coherent, high harmonic soft x-ray beams', *Phys. Rev. Lett.,* **99**, 098103, 2007
5. Wachulak, P. W.; Marconi, M. C.; Bartels, R. A.; Menoni, C. S., Rocca, J. J.: 'Soft x-ray laser holography with wavelength resolution', *JOSA B*, **25**, 1811-1814, 2008
6. Sandberg, R., L., Song C., Wachulak P., Raymondson, D.A., Paul, A., Amirbekian, B., Lee, E., Sakdinawat, A. E., La-O-Vorakiat, C., Marconi, M. C., Menoni, C. S., Murnane, M. M., Rocca, J. J., Kapteyn, H. C., Miao, J.: 'High numerical aperture tabletop soft x-ray diffraction microscopy with 70-nm resolution', *Proc Natl. Acad. Sci.,***105**, 24–27, 2008
7. Paganin, D. M.: *Coherent X-ray Optics*, Clarendon Press, Oxford, 2005
8. http://www.esrf.eu/news/spotlight/spotlight102, 09-03-2010; Tieg C., et al., *J. Phys.: Conf. Ser.*, **211**, 012024, 2010
9. Fenter, F., Park, C., Kohli, V., Zhang, Z.: 'Image contrast in X-ray reflection interface microscopy: comparison of data with model calculations and simulations'*, J. Synchrotron Rad.,* **15**, 558-571, 2008
10. Fenter, P., Lee, S. S.; Park, C., Catalano, J.G., Zhang, Z., Sturchio N.C.: 'Probing interfacial reactions with X-ray reflectivity and X-ray reflection interface microscopy: Influence of NaCl on the dissolution of orthoclase at pOH 2 and 85 C', *Geochimica et Cosmochimica Acta*, **74**, 3396-3411, 2010
11. Artyukov I. A.; Popov A.V.;Vinogradov A.V.: 'Wave field transformation at coherent imaging of a flat reflection mask', *Proc. SPIE*, **7451**, 745114-1 - 745114-3, 2009
12. Marathe, S.,Kim, S.S. Kim,S. N., Kim,C., .Kang, H.C., Nickles, P.V., Noh, D.Y.: 'Coherent diffraction surface imaging in reflection geometry', *Optics Express*, **18**, 7253-7262, 2010
13. Nugent, K. A.:'Coherent methods in the X-ray sciences', 21 Aug 2009, http://arxiv.org/ftp/arxiv/ papers/0908/0908.3064.pdf

Highly efficient soft X-ray microscope using a PMMA phase-reversal zone plate

Kyoung Hwan Lee[1], Seung Beom Park[1], Jong Ju Park[1], Deuk Su Kim[1], Ju Yun Park[1], Jae Hwan Lee[1] and Chang Hee Nam[1]

[1]Department of physics and Coherent X-ray Research Center (CXRC), KAIST, Daejeon 305-701, Korea

Abstract. Compact soft X-ray microscopes, using high harmonics as a light source, were constructed. A phase-reversal zone plate fabricated with polymethyl methacrylate was adopted to improve the focusing efficiency. Microscope images at 13 nm were acquired with sub-100 nm resolution, and the exposure time was reduced by a half, compared to that of the one using a gold Fresnel zone plate. A single-shot microscope image could be obtained using a strong harmonic at 22 nm generated in the two-color laser field consisting of the fundamental and the second harmonic of a femtosecond laser.

Introduction

Soft x-ray microscopy has been enthusiastically investigated in recent years with the development of various soft x-ray sources. Soft x-ray microscopes based on synchrotron have produced good imaging results due to its high reliability and intense x-ray photon flux. The limited accessibility and high machine cost of synchrotron has driven the development of table-top x-ray sources, such as laser-produced plasmas, x-ray lasers, and high harmonics. The high harmonic x-ray source has several advantages over the other compact x-ray sources because of short pulse duration, broad spectral range, and high coherency [1]. In order to construct the soft x-ray microscope using high harmonics, however, the relatively weak source strength, compared to other x-ray sources, should be overcome.

One of difficulties in constructing soft x-ray microscopes is the limited availability of efficient optics. As a large portion of photons is lost in the focusing process of an x-ray microscope, efficient imaging optics should be used. As an attempt to avoid this difficulty, lens-free imaging methods can be used, such as Fourier transform holography [2] and coherent diffractive imaging [3]. Though lens-free imaging methods have merits of preventing the loss of x-ray photons and eliminating aberration and distortion from imaging optics, their imaging efficiency may not be much better than other methods

J. Lee et al. (eds.), *X-Ray Lasers 2010,* Springer Proceedings in Physics 136,
DOI 10.1007/978-94-007-1186-0_38,

using imaging optics. In addition it usually requires heavy data processing to retrieve images from measured results.

Diffractive optics is frequently used in order to avoid strong absorption loss in most materials in the soft x–ray region. Using a Fresnel zone plate (FZP) as an objective optics, microscope images can be directly recorded. Since its low focusing efficiency demands long exposure time, efficiency enhancement of FZP is essential for fast image acquisition. A phase-reversal zone plate (PRZP) can be a good solution for this matter because it can provide higher efficiency, with a factor of up to four, without sacrificing spatial resolution [4]. We fabricated PRZP's with polymethyl methacrylate (PMMA), widely used in E-beam lithography as a photo resist material, with much simpler manufacturing procedure than that containing a metal layer [5].

In addition, single-shot imaging has been performed by using strong harmonics along with an efficiency-enhanced PRZP objective. Strong high harmonics were generated by applying a two-color laser. Since the pulse duration of harmonics is much shorter than the duration of a driving laser, femtosecond temporal resolution and nanometer spatial resolution can be achieved. Since the temporal resolution in this case is much improved over those of other x-ray microscopes using different x-ray sources, the high-harmonic x-ray microscope can provide the dynamic imaging of ultrafast phenomena with very high resolution.

PMMA phase-reversal zone plate

FZP consists of concentric circles with consecutive opaque zones and transparent zones. The light that has passed through the transparent zones of FZP is focused at the focal point by constructive interference. The focusing efficiency in this case is, however, only about 10%. The low efficiency of FZP can be improved by replacing the opaque zones with phase-shifted zones of PRZP. The efficiency of the PRZP can be expressed as

$$I_1 = \frac{I_{inc}}{\pi^2}\left(1 + e^{-2\eta\varphi} - e^{-\eta\varphi}\cos\varphi\right), \tag{1}$$

where η is the ratio of δ to β, the real and imaginary parts of the refractive index, $n = 1 - \delta - i\beta$. A material with low η is a good candidate for PRZP.

The other consideration in choosing a material of PRZP is the fabrication procedure. The PRZP, made of molybdenum or niobium, can have a focusing efficiency at 13.3 nm as high as 30%, but the difficulty of fabrication is an obstacle using it. PMMA, a popular material for the resist of E-beam lithography, also has a quite low η value of 0.228, so the focusing efficiency

can be comparable. The PRZP with 250 nm thick PMMA can provide the focusing efficiency of 23% and the optimum phase shift of 0.89π.

The biggest advantage of the PMMA PRZP is in the simple manufacturing procedure. First, a silicon wafer with silicon nitride window is prepared. The zone plate pattern is then drawn with an E-beam lithography device after PMMA coating. Lastly, the development of the zone plate in a mixed solution of methyl isobutyl ketone(MIBK) and isopropyl alcohol(IPA) finishes the fabrication procedure. The PMMA PRZP used here has 200 zones with an outermost zone width of 80 nm and a focal length of 385 μm .

Soft X-ray microscope using PMMA PRZP

A soft X-ray microscope, constructed with PMMA PRZP as an objective optics and high harmonics as a light source, is shown in Fig. 1. A 1-kHz femtosecond Ti:Sapphire laser at 820 nm was used to generate high harmonics. The laser light with 0.6-mJ energy was focused into a 3-mm neon gas cell by a concave mirror, and the 61st harmonic at 13 nm was generated with the spectral resolution $\left(\lambda/\Delta\lambda\right)$ of 280. A zirconium foil of 200-nm thickness blocked the co-propagating laser light, and two molybdenum-silicon multi-layer mirrors selected the 61st harmonic. Especially the second mirror, a concave mirror with 30-cm focal length, focuses the 61st harmonic into a target. Samples with a variety of patterns, including siemens star, elbow grating, and bar patterns in several different sizes, were used. The sample was fabricated on a 150-nm thick Hydrogen-silsesquioxane(HSQ)-coated silicon nitride window using a E-beam lithography machine. An additional zirconium filter is placed in front of the x-ray CCD to block the influx of leakage beam by any chance and to prevent damage of the CCD. The x-ray CCD employed for imaging has 2048×2048 pixels with a pixel size of $13.5\mu m\times13.5\mu m$. In order to reduce the exposure time 2×2 binning was used, which corresponds to a pixel size of 42 nm at the sample plane, setting the maximum resolution limit. The magnification of the microscope was 650.

The soft x-ray microscopic image of 150-nm half-period elbow grating, acquired with 10-second acquisition time, is shown in Fig. 2 (a). The PMMA PRZP reduced the exposure time by 2 times due to a higher efficiency than that obtained normally with FZP. From the intensity profile in Fig. 2 (b) the resolution of the microscope was measured to be 84 nm, which corresponds to the resolution limit set by the outermost zone width, 80 nm, of the PMMA PRZP.

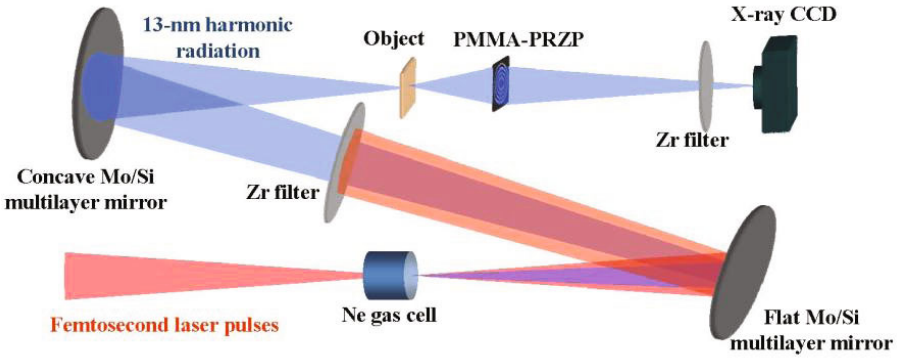

Fig.1. Experimental setup of a soft x-ray microscope employing a PRZP imaging optics.

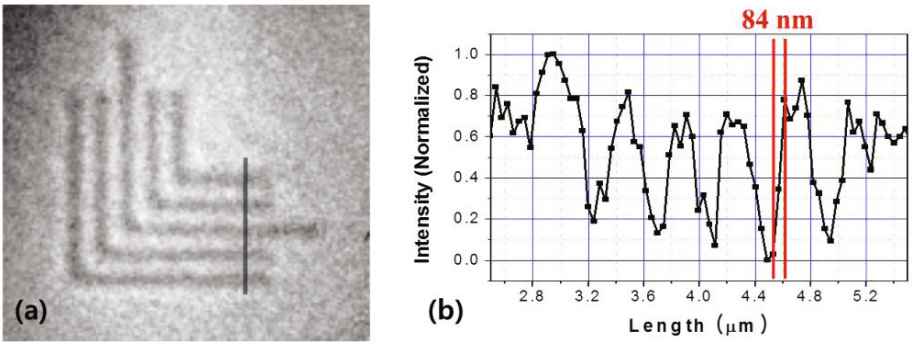

Fig. 2. (a) Soft x-ray microscopic image of an elbow grating with 150-nm half-period, and (b) intensity profile along the grey line in (a).

Single-shot X-ray microscope with femtosecond temporal resolution

For the realization of single-shot imaging the strong harmonic x-ray source at 22 nm, generated in a two-color laser field, was used. By exposing atoms to a two-color laser field consisting of the fundamental and second harmonic of the femtosecond laser, efficient high-harmonic generation was demonstrated at CXRC [6]. The schematic of high-harmonic generation using the 2-color laser field is shown in Fig. 3. The femtosecond laser with pulse duration of 26 fs and energy of 2 mJ was focused into a 6-mm gas nozzle. The BBO crystal was placed 40 cm away from the concave mirror, and the conversion efficiency was about 20 %. The strong 38^{th} harmonic at 21.6 nm was generated to from the harmonic generation medium of helium [7].

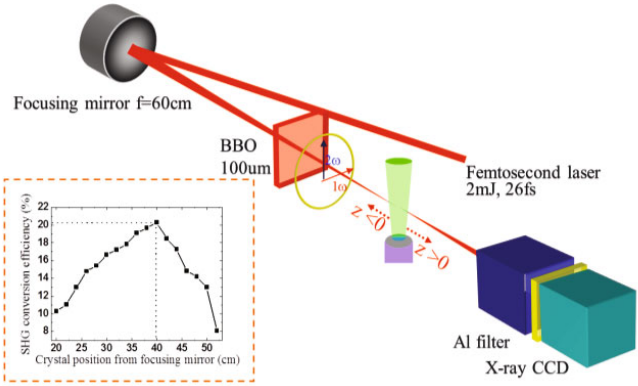

Fig. 3. Experimental setup of high harmonic generation in a 2 color laser field.

The soft x-ray microscope with a magnification of 260 was constructed to acquire single-shot microscopic images. The setup was the same as the one in Fig. 1, except the light source and the optics were changed for efficiency at 21.6 nm. A 200-nm aluminium foil was used, instead of zirconium, to block the laser light. A PMMA PRZP was fabricated to take into account the η value at 21.6 nm. It had 400 zones with 100-nm outermost zone width and 750-nm focal length. A sample, fabricated by focused ion beam (FIB), had several different sizes of square-shaped grating patterns.

In Fig. 4 the SEM image (a) and soft x-ray microscopic images of 4 μm (b) and 3 μm(c) half-period grating hole are shown. Figure 4 (b) was acquired with 5 laser shots with 2×2 binning, and Fig. 4 (c) with a single shot and 4×4 binning. Although this image is a little bit blurry due to low photon flux, the bar patterns are clearly resolved. The intensity profile in Fig. 4 (d), taken from the image of Fig. 4 (c), shows that the edge of the grating hole can be resolved within 2 pixels, which corresponds to 400 nm. One reason for this resolution degrade comes from the chromatic aberration due to the larger number of zones in the PRZP than the resolving power of the harmonic. To reduce this effect, the present number of zones (400) should be smaller than the spectral resolution $\left(\lambda/\Delta\lambda = 160\right)$.

Conclusion

We constructed table-top soft x-ray microscopes using PMMA PRZP and high harmonics at 13 nm. A microscopic image with sub-hundred nanometer resolution was obtained with an acquisition time reduced by a factor of 2, compared to the one with a FZP-adopted microscope. In addition, a single-

shot image was acquired with fs-temporal resolution and 400 nm spatial resolution using the sub-μJ high harmonic at 22 nm. For further improvement in spatial resolution, the parameters of PRZP will be further optimized.

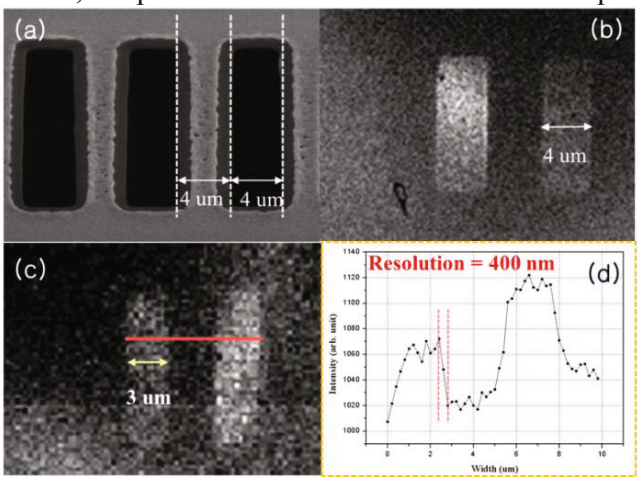

Fig. 4. (a) SEM image of 4-μm half-period square hole, and soft x-ray microscope images acquired with (b) 5 shots and (c) single-shot(3-μm half period). (d) Intensity profile of (c)

Reference

1. Paul, P. M., Toma, E. S., Breger, P., Mullot, G., Augé, F., Balcou, Ph., Muller, H. G., and Agostini, P. : 'Observation of a train of attosecond pulses from high harmonic Generation' Science292, 1689, 2001
2. Gauthier, D., Guizar-Sicairos, M, Ge, X., Boutu, W., Carré, B., Fienup, J. R., and Merdji, H. : 'Single-shot femtosecond x-ray holography using extended reference', Phys. Rev. Lett. 105, 093901, 2010
3. Miao, J., Tetsuya, I., Anderson, E. H., Hodgson, K. O. : 'Phase retrieval of diffraction patterns from noncrystalline samples using the oversampling method', Phys. Rev. B 67, 174104, 2003
4. Kirz, J.: 'Phase zone plates for x rays and the extreme uv', J. Opt. Soc.Am. 64, 301, 1974
5. Park, J. J., Kim, D. S., Jeon, S. C., Park, J., Lee, K. H., Lee, J.-H., Kim, K. N., Yoo, J. J., and Nam, C. H.: 'Soft x-ray microscope constructed with a PMMA phase-reversal zone plate', Opt. Lett. 34, 235, 2009
6. Kim, I J., Kim, C. M., Kim, H. T., Lee, G. H., Lee, Y. S., Park. J. Y., Cho, D. J., and Nam, C. H.: 'Highly Efficient High-Harmonic Generation in an Orthogonally Polarized Two-Color Laser Field', Phys. Rev. Lett. 94, 243901, 2005
7. Kim, I J., Lee, G. H., Park, S. B., Lee, Y. S., Kim, T. K., and Nam, C. H., Mocek, T. and Jakubczak, K. : 'Generation of submicrojoule high harmonics using a long gas jet in a two-color laser field', Appl. Phys. Lett. 92, 021125, 2008

Single-Photon Ionization Soft-X-Ray Laser Mass Spectrometry of Potential Hydrogen Storage Materials

F. Dong[1,3] , E.R. Bernstein[1,3] and J.J. Rocca[1,2,4]

[1] NSF ERC for Extreme Ultraviolet Science and Technology, Colorado State University, USA
[2] Department of Electrical and Computer Engineering, Colorado State University,
[3] Department of Chemistry, Colorado State University
[4] Department of Physics, Colorado State University

Abstract. A desk-top size capillary discharge 46.9 nm lasear is applied in the gas phase study of nanoclusters. The high photon energy allows for single-photon ionization mass spectrometry with reduced cluster fragmentation. In the present studies, neutral Al_mC_n and $Al_mC_nH_x$ cluster are investigation for the first time. Single photon ionization through 46.9 nm, 118 nm, 193 nm lasers is used to detect neutral cluster distributions through time of flight mass spectrometry. Al_mC_n clusters are generated through laser ablation of a mixture of Al and C powders pressed into a disk. An oscillation of the vertical ionization energies (VIEs) of Al_mC_n clusters is observed in the experiments. The VIEs of Al_mC_n clusters changes as a function of the numbers of Al and C atoms in the clusters. $Al_mC_nH_x$ clusters are generated through an Al ablation plasma-hydrocarbon reaction, an Al-C ablation plasma reacting with H_2 gas, or through cold Al_mC_n clusters reacting with H_2 gas in a fast flow reactor. DFT and *ab inito* calculations are carried out to explore the structures, IEs, and electronic structures of $Al_mC_nH_x$ clusters. C=C bonds are favored for the lowest energy structures for Al_mC_n clusters. $Be_mC_nH_x$ are generated through a beryllium ablation plasma-hydrocarbon reaction and detected by single photon ionization of 193 nm laser. Both $Al_mC_nH_x$ and $Be_mC_nH_x$ are considered as potential hydrogen storage materials.

1 Introduction

Aluminium carbide clusters, considered as non-classical and non-stoichiometric structures[1-6] are different from most metal carbide clusters with cubic frameworks and layered structures.[7] To date, no report is found for the experimental study of neutral aluminium carbide clusters. The distribution, definitive structures, and formation mechanisms for neutral Al_mC_n clusters are still not well known. $Al_mC_nH_x$ clusters can be a potential material for hydrogen storage as complex aluminium hydrides; however, no experimental or theoretical study has been carried out on $Al_mC_nH_x$ clusters.

J. Lee et al. (eds.), *X-Ray Lasers 2010,* Springer Proceedings in Physics 136,
DOI 10.1007/978-94-007-1186-0_39,

In the present work, neutral aluminium carbide clusters (Al_mC_n) and aluminium carbon hydride clusters ($Al_mC_nH_x$) are studied by time of flight mass spectrometry coupled with single photon ionization (SPI) by 193 (6.4 eV, UV), 118 (10.5 eV, VUV), and 49.6 (26.5 eV soft X-ray) nm lasers. Neutral Al_mC_n clusters are generated by laser ablation of mixed aluminium/carbon targets into a carrier gas of pure helium. Only some Al_mC_n clusters can be detected by SPI with 193 nm photons; however, all Al_mC_n clusters can be detected by 26.5 eV, soft X-ray laser ionization. A significant alternating behaviour is found for the ionization energies of neutral Al_mC_n clusters. Neutral $Al_mC_nH_x$ clusters are generated by hydrocarbon plasma reaction method. A series of $Al_mC_nH_x$ clusters are thereby observed by mass spectrometry, implying that a different mechanism is operative for $Al_mC_nH_x$ cluster formation than for early transition metal carbides. Ionization energies of $Al_mC_nH_x$ clusters change systematically with the numbers of H atoms in the clusters. Theoretical calculations are carried out to investigate the structures, molecular orbitals, and vertical ionization energies of neutral Al_mC_n and $Al_mC_nH_x$ clusters. Additionally, $Be_mC_nH_x$ clusters are studied for the first time in the present work. $Be_mC_nH_x$ are generated through a beryllium ablation plasma-hydrocarbon reaction and detected by single photon ionization of 193 nm laser.

2 Experimental Procedures and theoretical methods

The experimental studies of neutral Al_mC_n and $Al_mC_nH_x$ clusters involve a time of flight mass spectrometer (TOFMS) coupled with SPI at 193 nm, 118 nm, and 46.9 nm. The experimental apparatus and laser sources have been described in previous publications from this laboratory,[8] and therefore only a general outline of the experimental scheme will be presented in this report. Briefly, the neutral aluminium carbide clusters are generated in a conventional laser ablation/expansion source through laser ablation (focused 532 nm laser, 10-20 mJ/pulse) of an mixed Al/C target into a carrier gas of pure helium gas at 80 psi. The target is made by pressing a mixture of carbon and aluminium powders. To generate aluminium carbon hydride clusters, a pure aluminium foil target is used for laser ablation and a mixture of 5% hydrocarbon (CH_4, C_2H_4, or C_2H_6) and helium is used for the expansion gas.

The soft X-ray laser (26.5 eV photon energy)[9] emits pulses of about 1 ns duration with an energy/pulse of 10 μJ that is reduced to 3 ~ 5 μJ after the light transverses a z-fold mirror system.

All the calculations reported in the present work are performed with the Gaussian03 program package.[10] The structures of neutral Al_mC_n and $Al_mC_nH_x$ clusters are initially optimized using a hybrid method including a mixture of Hartree–Fock exchange with density functional exchange-correlation (B3LYP)[11] and a polarized split-valence basis set (6-311+G*)[12]. The structures

and ionization energies of the lowest energy structures for some Al_mC_n and $Al_mC_nH_x$ clusters are refined using the second order Moller-Plesset perturbation theory (MP2)[13] with the same basis set.

3 Results

Al_mC_n Clusters

Neutral Al_mC_n clusters are generated in the ablation/expansion source in our experiments through laser ablation of an Al/C target into pure helium expansion gas. Fig.1a displays the distribution of neutral Al_mC_n clusters ionized by SPI employing 193 nm light. Several series of the Al_mC_n clusters are identified in the mass spectrum; for example, Al_3C_2, Al_3C_4, Al_3C_6, Al_3C_8, and Al_3C_{10}, Al_5C, Al_5C_3, and Al_5C_5, and Al_7C_2 and Al_7C_4. Under the same experimental conditions, using the 26.5 eV soft X-ray laser for ionization, many more aluminium carbide clusters, including $Al_2C_{2\text{-}4}$, $Al_3C_{2\text{-}5}$, $Al_4C_{2\text{-}6}$, and $Al_5C_{2\text{-}5}$, are detected as shown in Fig.1b.

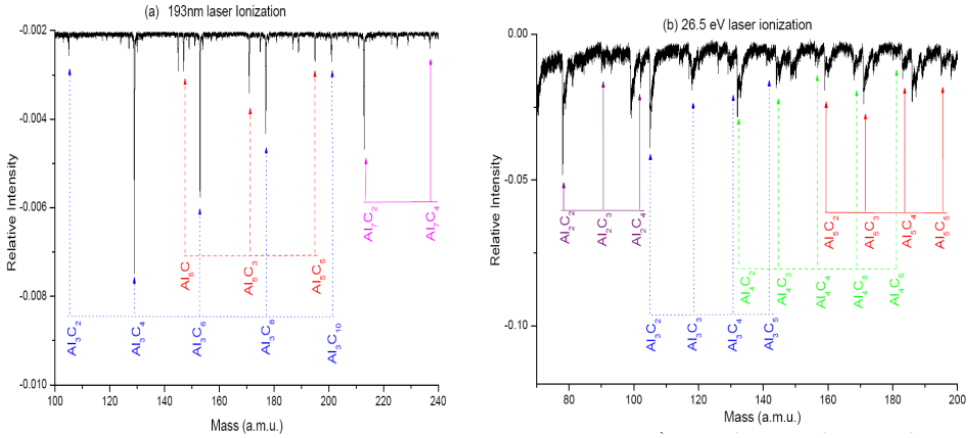

Fig. 1 Mass spectra of Al_mC_n clusters ionized by (a) a 193 nm (6.4 eV) UV laser and (b) a 46.9 nm (26.5 eV) soft X-ray laser. Clusters are generated by laser ablation of a mixed Al-C target into a pure He expansion gas at 80 psi backing pressure.

Al_5C_2, Al_6C_2, Al_2C_4 and Al_3C_3) clusters are calculated. A significant even-odd alternation is found for VIEs of neutral Al_mC_n clusters as plotted in Fig.2. The calculational results are in very good agreement with experimental observation. The same trend of VIEs for Al_mC_n clusters found through theoretical calculations is observed in the experiment; this indicates that the predicted structures of the calculated clusters can be believable and further, that their calculated formation mechanisms and chemical reactivity can be realistically explored through a similar level of theory. Thus, the experimental

data yield not only which clusters are observed, but also present an observed parameter (VIE) to be compared to theory for its validation.

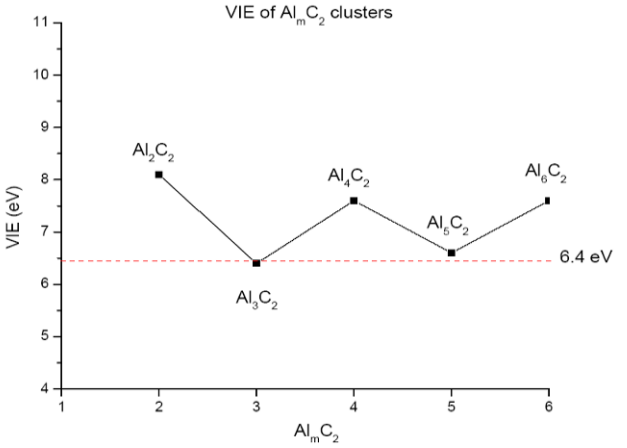

Fig.2 The VIEs of Al_mC_2 clusters plotted against the number of Al atoms m in the clusters.

$Al_mC_nH_x$ Clusters

The $Al_mC_nH_x$ clusters are generated in the experiments: pure aluminium foil is used as the ablation target, and mixtures of a hydrocarbon (CH_4, C_2H_4 or C_2H_6) and He are used as the expansion gas, an Al-C ablation plasma reacting with H_2 gas, or through cold Al_mC_n clusters reacting with H_2 gas in a fast flow reactor. An abundance of aluminium carbon hydride clusters is observed in the mass spectrum by using a 193 nm laser for SPI. $Al_mC_nH_x$ clusters with odd mass number are identified. $Al_mC_nH_x$ clusters are also detected by 118 nm laser SPI. As shown in Fig.3, many signals are identified as $Al_mC_nH_x$ clusters with both odd and even mass numbers, for example, $Al_2C_2H_{1\text{-}12}$, $Al_2C_3H_{1\text{-}12}$, $Al_3C_2H_{1\text{-}12}$, $Al_3C_3H_{1\text{-}12}$, and etc. This experimental observation must involve the ionization energies of the $Al_mC_nH_x$ clusters.

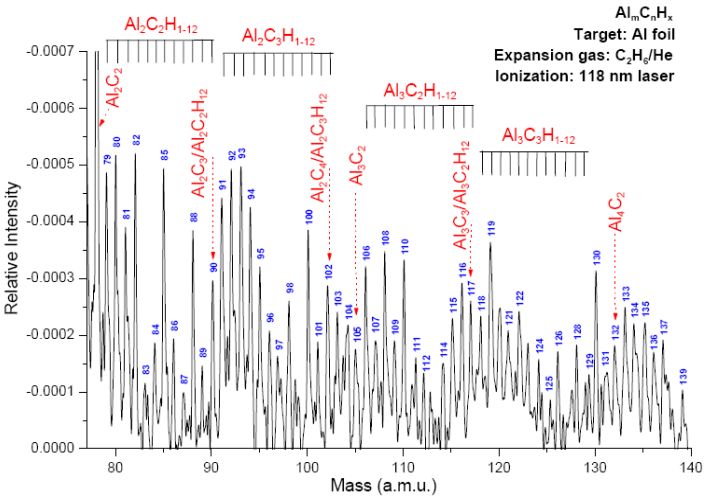

Fig.3 Mass spectrum of $Al_mC_nH_x$ clusters ionized by a 118 nm laser. Clusters are generated by laser ablation of Al foil into a mixture of 5% C_2H_6/He expansion gas at 80 psi backing pressure.

Stable structures and VIEs for $Al_2C_2H_x$ clusters are calculated. The VIEs of $Al_2C_2H_x$ clusters change with the number of H atoms as shown in Fig. 4. The Al_2C_2H (VIE = 6.3 eV) and $Al_2C_2H_3$ (VIE = 7.0 eV) clusters, detected in the 193 nm ionization experiment, have low ionization energies (ca. 6.4 eV, while the clusters Al_2C_2 (VIE = 8.1 eV), $Al_2C_2H_2$ (VIE = 8.7 eV), and $Al_2C_2H_4$ (VIE = 10.3 eV) have obviously higher ionization energies than 6.4 eV. The alternation trends of calculated VIEs of the Al_mC_n and $Al_mC_nH_x$ clusters are in good agreement with our experimental observations that some members of the Al_mC_n and $Al_mC_nH_x$ cluster distributions have low VIEs and some have high VIEs. This observed VIE alternation depends on the numbers of Al, C, and H atoms in the clusters and the calculations completely explain the experimental observations.

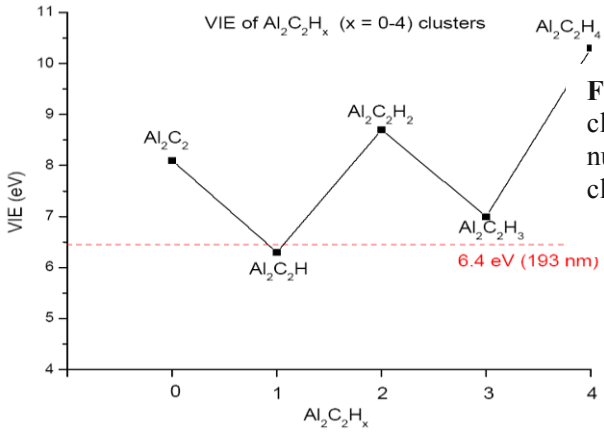

Fig.4 VIEs of $Al_2C_2H_x$ clusters plotted against the number of H atoms x in the clusters.

Experiments show that clusters containing more than 8 hydrogen atoms, such as $Al_2C_2H_{9,11}$ (193 nm ionization experiment, Fig.1) and $Al_2C_2H_{9\text{-}12}$ (118 nm ionization experiment, Fig.3) are readily identified in the mass spectra, indicating that hydrogen containing clusters $Al_2C_2H_{9\text{-}12}$ are generated under the present experimental condition. This observation suggests that H_2 molecules can possibly be adsorbed on $Al_mC_n/Al_mC_nH_x$ clusters through chemisorptions, causing more hydrogen to be associated with the clusters than can be accounted for by a saturated classical chemical bond structure. Recently, Durgun et al.[14] calculated H_2 adsorption on a transition metal-ethylene $C_2H_4M_2$ (TM-ethylene) complex, in which two metal atoms are bonded to a C=C through a bridge structure. They found that, based on calculation, up to 12 H_2 molecules can be adsorbed around the $C_2H_4Ti_2$ complex: up to ~ 14 wt.% hydrogen storage for this complex. We can not identify $Al_mC_nH_x$ clusters containing more than 12 H atoms in the mass spectra, since the mass number of carbon is 12.

$Be_mC_nH_x$ clusters are generated through ablation of beryllium foil into a mixture of hydrocarbon/He carrier gas. Many $Be_mC_nH_x$ clusters are detected by single photon ionization of 193 nm laser. Calculations of the stable

structures and VIEs are performing in order to explain the experimental observations.

Conclusions

1. Neutral $Al_mC_nH_x$ and $Be_mC_nH_x$ clusters are observed and systematically studied for the first time by experimental and theoretical methods.
2. $Al_mC_nH_x$ and $Be_mC_nH_x$ clusters have unique properties that make them a potential hydrogen storage material; for example, up to 13% hydrogen storage by weight for $Al_2C_2H_{12}$.
3. Neutral $M_mC_nH_x$ clusters are generated through a hydrocarbon plasma reaction. Formation mechanism: $M_mC_n + xH/H_2 \rightarrow M_mC_nH_x$
4. VIEs of Al_mC_n and $Al_mC_nH_x$ clusters oscillate with the numbers of Al, C, and H atoms.

Acknowledgments

This work is supported by the NSF ERC for Extreme Ultraviolet Science and Technology under NSF Award No. 0310717, Philip Morris, U.S.A., and the U.S. DOE BES program.

References

1. A. I. Boldyrev et al., J. *Am. Chem. Soc.* 121, 10193, 1999
2. X. Li, et al., *J. Am. Chem. Soc.* 121, 6033, 1999
3. (a) N. Cannon, et al., *J. Chem. Phys.* 113, 2671, 2000; (b) X. Li et al., *J. Chem. Phys.* 116, 1330, 2002
4. X. Li et al., *Angew. Chem. Int. Ed.* 39, 3630, 2000
5. (a) A. I. Boldyrev et al., *J. Chem. Phys.* 111, 4993, 1999; (b) A. I. Boldyrev et al., *J. Chem. Phys.* 110, 8980, 1999
6. F. Y. Naumkin, *J. Phys. Chem. A* 112, 4660, 2008
7. (a) K. L. Knappenberger et al., *J. Phys. Chem. A 110*, 12814, 2006; (b) M. W. Heaven et al., *J. Phys. Chem. A* 104, 3308, 2000
8. (a) F. Dong, et al., *J. Am. Chem. Soc.* 131, 1507, 2009; (b) F. Dong et al., *J. Am. Chem. Soc.* 130, 1932, 2008; (c) F. Dong et al., *J. Chem. Phys.* 125, 164318, 2006; (d) F. Dong et al., *J. Chem. Phys.*, 124, 224319, 2006; (e) F. Dong et al., *J. Chem. Phys*, 125, 154317, 2006
9. (a) S. Heinbuch et al., *J. Opt. Express*, 13, 4050, 2005; (b) J. J. Rocca et al., *Phys. Rev. Lett.* 73, 2192, 1994; (c) J. J. Rocca, *Rev. Sci. Instrum.* 70, 3799, 1999
10. M. J. Frisch, et al. *Gaussian 03, Gaussian*, Inc, Wallingford CT, 2004.
11. (a) A. D. Becke, *Phys. Rev. A* 38, 3098, 1988; (b) A. D. Becke, *J. Chem. Phys.*, 98, 5648, 1993; (c) C. T. Lee et al., *Phys. Rev. B* 37, 785, 1988
12. (a) A. D. McLean and G. S. Chandler, *J. Chem. Phys*. 72, 5639, 1980; (b) T. Clark et al., *J. Comput. Chem*. 4, 294, 1983
13. R. Krishnan et al., *J. Chem. Phys*. 72, 650, 1980
14. (a) E. Durgun et al., *Phys. Rev. Lett.* 97, 226102, 2006; (b) W. Zhou et al., *Phys. Rev. B* 76, 085434, 2007; (c) N. Akman et al., *J. Phys: Condens. Matter*, 18, 9509, 2006

Development of the x-ray interferometer and the method of spatial and temporal synchronization of XRL and optical pulse

N. Hasegawa[1], Y. Ochi[1], T. Kawachi[1], K. Terakawa[2], T. Tomita[3], M. Yamamoto[3], M. Nishikino[1], T. Ohba[1], T. Kaihori[1], T. Imazono[1], A. Sasaki[1], M. Kishimoto[1], M. Ishino[1], M. Kado[1], M. Tanaka[1], T. Nakazato[4], N. Sarukura[4] and T. Suemoto[2]

[1] Quantum Beam Science Directorate, Japan Atomic Energy Agency
[2] Institute of Solid State Physics, University of Tokyo
[3] Faculty of Engineering, University of Tokushima
[4] Institute of Laser Engineering, Osaka University

Abstract. We have developed a pump-probe soft x-ray laser (SXRL) interferometer and its instrumentation for spatial and temporal synchronization of optical pump and SXRL probe to observe nano-meter structure dynamics. The depth and lateral resolution of the interferometer was 1 nm and 1.8 μm, respectively. By using this interferometer, the initial state dynamics of the Pt surface irradiated by the 70 fs laser pulse was firstly observed.

1 Introduction

In recent years, the interest for the laser ablation of solid target irradiated by a ultra-short laser pulse (Ti:sapphire laser) grows up. In particular, the understanding of the dynamics of the initial process is important for the micro processing and welding by the ultra-short laser pulse. There are some reports that the sub-micron scale structures (ripple formation and bubble structures) are formed by the irradiation of the femto-second lasers [1]. However the details of the process have not been understood because of the following characteristics of laser ablation; it is non-repetitive, unrepeatable, very rapid (pico-second) and very small (micron) phenomenon.

In this study, we developed the soft x-ray laser (SXRL) interferometer toward the single-shot imaging of the nano-meter structure dynamics. The SXRL is suitable for probing this initial process because it has short wavelength (Ni-like Ag, 13.9 nm), short duration (< 10 ps) and spatial coherence [2]. This interferometer was applied to observe the nano-meter-scale dynamics of initial stage of laser ablation (section 2) [3]. In order to further extension of this measurement, more precise spatial and temporal

J. Lee et al. (eds.), *X-Ray Lasers 2010,* Springer Proceedings in Physics 136,
DOI 10.1007/978-94-007-1186-0_40,

synchronization between the optical pump and SXRL-probe on the sample surface is very important. Thus we investigated the use of ZnO scintillation plate (section 3) [4] and the plasma gate technique (section 4).

2 Single shot soft x-ray laser interferometer for the research of the nano-meter scale dynamics

The SXRL interferometer has been developed for the purpose of observing the nano-meter scale structure and understanding its dynamics. The fully spatial coherent nickel-like silver XRL (λ = 13.9 nm) was used as the probe beam of the interferometer. The output energy and the duration were 0.5 μJ and 7 ps, respectively. The SXRL is suitable for the measurement of the solid surface that is irradiated by the ultra-short pulse laser as follows;

i) In comparison with the visible light, the transmittance of the SXRL for the plasmas at the surface is high. The critical electron density at the wavelength of 13.9 nm is ~ 10^{24}cm^{-3} and the cross section of the interaction with free electrons is smaller by more than three orders of magnitude.

ii) The SXRL penetration depth for Pt, ~ less than 10 nm, is smaller than that of hard x-ray. Therefore we can obtain the surface information.

iii) The pico-second duration and large photon number per pulse of the SXRL are suitable for the single shot measurement.

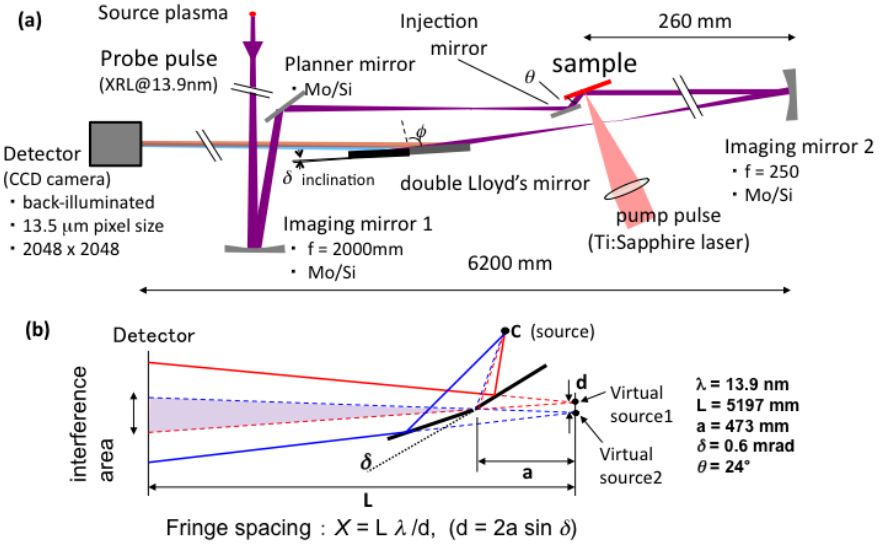

Fig. 1. (a) SXRL interferometer. (b) Schematic image of the double Lloyd's mirrors**.**

The set up of single shot SXRL interferometer is shown in Fig.1(a). The interferometer consists of the reflection optics (Mo/Si multi-layer mirrors or

Pt mirror) all that were made in JAEA. The SXRL was focused 460 mm before the Pt sample by the imaging mirror 1. The incident angle (θ) to the sample surface was set to 24 degrees by the injection mirror. The image on the sample was transferred onto the back-illuminated CCD camera by a second concave imaging mirror 2 with a magnification factor of 21. The interference fringes were produced on the CCD surface by the two mirrors having a relative incline angle of $\delta = 0.03$ degrees, that are called the double Lloyd's mirrors. Schematic image of the double Lloyd's mirrors is shown in Fig.1(b). The double Lloyd's mirrors bring two virtual sources. The interference fringes appear on the detector plane at the area that objective and reference beams overlap. The fringe spacing X is described to be $X = L\lambda / (2a \sin\delta)$, where L and a are defined in Fig.1(b). The fringe shift of one period shows the difference of the depth of $D_1 = \lambda / (2\sin\theta)$. In the present case, $X \sim 130$ μm, $D_1 = 17$ nm, these lead to the result that the depth resolution is estimated ~ 2 nm and fringe area is about 500 μm on the sample surface.

In the present set up, Ti:sapphire laser with the duration of 70 fs was focused on the sample surface. Ti:sapphire laser was synchronized to the pumping glass laser of the SXRL (CPA glass laser). The timing jitter between the Ti:sapphire laser and the glass laser was measured to be ±3 ps, it was smaller than the duration of the SXRL.

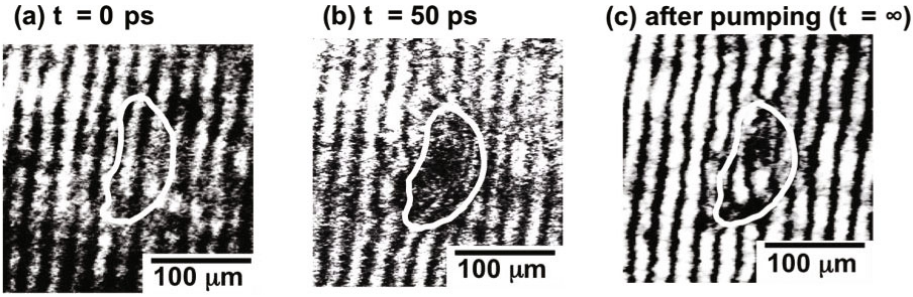

Fig. 2. Interferogram of the Pt surface irradiated by Ti;sapphire laser. (a) t = 0 ps, (b) t = 50 ps, (c) After laser irradiation.

We measured the ablation dynamics of Pt (100 nm thickness) surface by using this system. The pump beam diameter and intensity on the sample surface were around 100 μm and 10^{13} W/cm^2, respectively. Figure 2 shows the temporal evolution of the interferogram. The solid loop indicates the irradiated area by the laser. Figure 2(b) shows that at the time of $t = 50$ ps. The apparent fringe shift can be seen. The right-side fringe shift corresponds to the positive deviations, and the height of the center of the ablation area was estimated to be 30 nm. In Fig.2(c), a crater was generated after the laser irradiation ($t = \infty$). This is the first observation of the nano-meter scale surface dynamics of the initial stage of laser ablation.

3 Spatial resolution measurement of the scintillation plate toward using for the spatial alignment

In the present experiment, the SXRL and Ti:sapphire laser were aligned indirectly. We carved a cross marker at the irradiated position of the Ti:sapphire laser on the sample. A laser diode (LD) beam is set to the SXRL axis and is steered to the cross marker by adjusting one of the Mo/Si planer mirror. The spatial synchronization was assured by observing a scattered light from the cross marker. The precision of this method was limited by the accuracy of the optical axis between the LD and SXRL, and the expected value was only a few tens micron on the sample. In order to establish further precise alignment method, we performed preliminary experiment.

For the spatial synchronization, we used ZnO scintillation plate. ZnO plate, supplied from ILE, Osaka University, is transparent for the visible light and strongly absorb the SXRL light by accompanying UV fluorescence. The SXRL was focused on the ZnO surface by a Fresnel zone plate, and the fluorescence was measured from the backside by use of an optical microscope. Figure 3(a) shows the image of the fluorescence. Figure 3(b) shows the spot size of the fluorescence as the function of distance between the Fresnel zone plate and ZnO. The minimum spot size was measured to be 2 μm, so the spatial resolution of the ZnO as a scintillation plate was 2 μm. It was enough to use the spatial alignment between the SXRL and optical pulse.

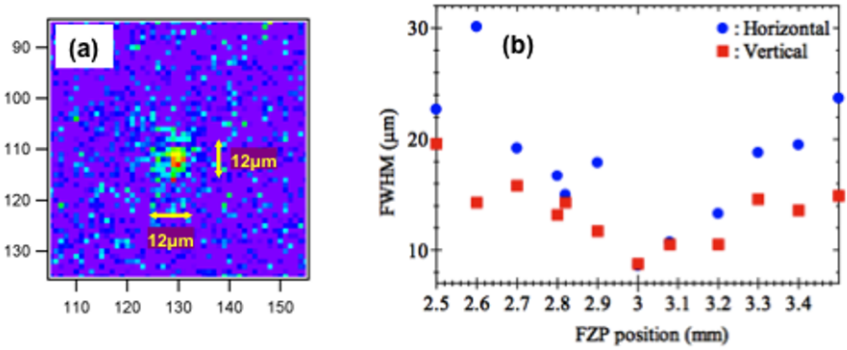

Fig. 3. (a) Image of florescence from ZnO irradiated by SXRL. (b) Spot size of florescence as a function of the distance between zone plate and ZnO.

4 Plasma gate technique toward the temporal synchronization

In the present experiment, temporal synchronization was obtained between the glass laser and Ti:sapphire laser by using the visible streak camera, in which we derived the temporal synchronization of the SXRL pulse to the Ti:sapphire pulse by taking into account the rise time (~ 30 ps) of the SXRL pulse [5; hasegawa]. Since other reports implied that the rise time of the SXRL pulse depends on the irradiation condition [6,7], more sophisticated method for the temporal synchronization is desired. One of the possibilities is plasma gate technique. Schematic image is shown in Fig. 4(a). A gold foil is irradiated by an ultra-short pulse. After certain time delay, the SXRL pulse illuminate the pumping position. The ionization potential of Au from 7+ to 8+ (= 96eV) is larger than Ni-like Ag XRL photon energy (= 89 eV). If the ionization reaches to the backside of the foil, SXRL can through the foil. The rise time of transmittance of SXRL depends on the ionization speed, and ps rise time may be possible in the cases that the pump laser energy is high enough and the foil thickness is thin enough [8].

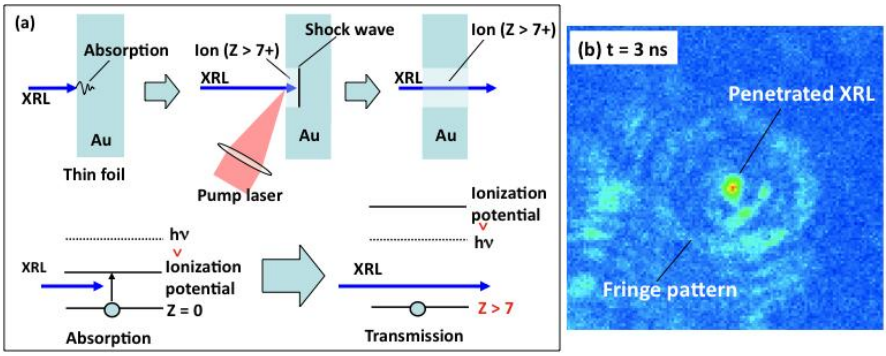

Fig. 4. (a) Schematic image of the plasma gate technique. (b) Image of SXRL penetrated the Au foil at the time of 3ns after laser irradiation.

Figure 4(b) shows the preliminary result of this experiment. The pump laser condition was the energy of 0.3 mJ, duration of 70 fs, spot size of 55 μm (FWHM) and intensity of 10^{14} W/cm^2. The SXRL was measured by back-illuminated CCD camera from backside of Au foil (100 nm thickness). At the time of 3 ns after pump laser irradiation, SXRL penetrated the Au foil, and the transmittance was measured to be 2 %. Pin-hole size at that time was estimated from fringe pattern, it was 60 μm. It was almost consistent with the spot size of pump laser. However the raise time of transmittance was very slow. The cause of this result may be pumping energy was insufficient. In the next experiment, we will try to use over 30 mJ laser and decrease the foil thickness.

5 summary

We have developed a pump-probe soft x-ray laser (SXRL) interferometer and its instrumentation for spatial and temporal synchronization of optical pump and SRL probe to observe nano-meter structure dynamics. Preliminary investigation for the spatial and temporal synchronization of the optical pump and SXRL probe are also performed. This will make it possible for us to conduct more precise experiment and bring us deeper understanding of the fundamental processes in the laser-matter interaction, laser processing and laser welding.

References

1. Tomita T., *et al.,* "Distinct Fine and Coarse Ripples on 4H-SiC Single Crystal Induced by Femtosecond Laser Irradiation", *Jpn. J. Appl. Phys.*, **45**, pp. L444-L446, 2006.
2. Tanaka M., *et al.,* "X-ray laser beam with diffraction-limited divergence generated with two gain media", *Opt. Lett.* **28**, 1680-1682, 2003.
3. Suemoto T. *et al.*, "Single-shot picosecond interferometry with one-nanometer resolution for dynamical surface morphlogy using a soft x-ray laser", *Opt. Exp*. **18**, 14114, 2010.
4. Tanaka M., *et al.*, "Evaluation of fast EUV scintillator using 13.9 nm x-ray laser", *Proceedings of IFSA 2007*, IOP conf. series **112** 042058, 2008.
5. Hasegawa N., *et al.*, "Direct measurement of the temporal profile of the amplification gain of the transient collisional excitation neonlike manganese x-ray laser medium", *Phys. Rev. A* **76**, 043805, 2007.
6. Wang Y., *et al.*, "High-Brightness Injection-Seeded Soft-X-Ray-Laser Amplifier Using a Solid Target", *Phys. Rev. Lett.* **97** 123901, 2006.
7. Zeitoun Ph., *et al.*, "A high-intensity highly coherent soft X-ray femtosecond laser seeded by a high harmonic beam"**,** *Nature* **431**, 426, 2004.
8. Edwards M. H., *et al.*, "Opacity Measurements of a Hot Iron Plasma Using an X-ray Laser", *Phys. Rev. Lett.* **21**, 035001, 2006.

Reflection microscope for actinic mask inspection and other progress in soft x-ray laser nano-imaging

C. S. Menoni[1], F. Brizuela[1], S. Carbajo[1], Y. Wang[1], D. Alessi[1], D. H. Martz[1], B. Luther[1], M. C. Marconi[1], J. J. Rocca[1], A. Sakdinawat[2], W. Chao[3], Y. W. Liu[2], E. H. Anderson[3], K. A. Goldberg[3], D. T. Attwood[2], A. V. Vinogradov[4], I. A. Artioukov[4], B. LaFontaine[5]

[1] NSF ERC for Extreme Ultraviolet Science and Technology, and ECE Department, Colorado State University, Fort Collins, USA
[2] NSF ERC for Extreme Ultraviolet Science and Technology, and ECE Department, University of California, Berkeley
[3] NSF ERC for Extreme Ultraviolet Science and Technology, and Center for X-Ray Optics, LBNL, Berkeley, USA
[4] P. N. Lebedev Physical Institute, Moscow, Russia
[5] GLOBALFOUNDRIES, 1050 E. Arques Avenue, Sunnyvale, CA, USA

Abstract. We describe the implementation of a zone plate microscope for at-wavelength characterization of extreme ultraviolet masks. The microscope uses as illumination the 13.2 nm wavelength output from a table-top Ni-like Cd laser. The microscopy allows inspection of EUVL masks under illumination conditions similar to those used in a 4×-demagnification lithographic stepper. High quality EUV images of absorption patterns in EUVL masks have been obtained. Analysis of these images allows characterizing the printability of patterns and defects on the wafer prior to utilization of the mask for production.

1 Introduction

Advances in the development of small laboratory scale soft x-ray (SXR) and extreme ultraviolet (EUV) lasers are driving the implementation of applications, including microscopy, holography, patterning and spectrometry. These techniques exploit the high energy per pulse, short wavelength (high photon energy), to achieve tens of nanometers spatial resolution as is the case of imaging and patterning, and to analyse the chemical composition and reactions of nanoclusters with unprecedented resolution. [1-4]

Several aspects of SXR lasers make them attractive as illumination sources for full field microscopy. The low beam divergence allows for complete

J. Lee et al. (eds.), *X-Ray Lasers 2010,* Springer Proceedings in Physics 136,
DOI 10.1007/978-94-007-1186-0_41,

collection of the SXR light using typical EUV/SXR optics resulting in high throughput efficiency. The narrow spectral bandwidth of the laser output when combined with diffractive optics eliminates chromatic aberrations in the imaging systems. The tuneable degree of coherence allows for a variety of imaging configurations from coherent imaging to imaging under partially coherent light. Furthermore the large number of photons per pulse allows to capture images with a single laser shot thus enabling stop-motion imaging of fast processes due to their short pulse duration of the laser output.

At Colorado State University we have developed full field microscopes that use as illumination the output from SXR lasers based on discharge and laser produced plasma excitation. [1, 5-8]These wavelength-scalable microscopes operate in transmission and reflection configurations to image nanostructures and surfaces with tens of nanometer. Using a very compact microscope illuminated by a SXR laser emitting at 46.9 nm wavelength, we have demonstrated imaging with a near-wavelength spatial resolution of 50 nm, and temporal resolution of 1.2 ns obtained with single laser shot exposure in transmission mode [1]. The same system has been demonstrated in reflection mode with measured spatial resolution better than 200 nm [6]. We have also demonstrated a full-field transmission mode microscope using a SXR laser emitting at either 13.2 nm or 13.9 nm [8]. Using this system, the highest spatial resolution achieved using a SXR/EUV laser based microscope, 38 nm, was obtained with exposure times of 20 seconds and the laser operating at 5 Hz. [8]

In this paper we describe the demonstration of the first compact SXR/EUV laser-based actinic microscope developed specifically to address the evaluation of printability of patterns and defects on extreme ultraviolet lithography (EUVL) masks.

2. Actinic microscopy for Extreme Ultraviolet Mask characterization

The implementation of a reflection microscope at λ=13.2 nm was motivated by the critical needs of EUV lithography (EUVL) to have alternative methods to evaluate the masks used in EUVL steppers. The resonant-reflective nature of these multilayer-coated masks requires that these aerial imaging systems operate at SXR/EUV wavelengths near 13.4 nm.

Actinic (at-wavelength) aerial imaging systems are full-field microscopes that can render information on the printability of patterns and defects prior to wafer printing and are greatly needed for the implementation of EUVL at high-volume manufacturing [9]. Actinic full-field microscopes have been demonstrated using synchrotron illumination and though they have greatly

impacted the development of EUVL masks, they are not practical for manufacturing settings. [10-12]

The table-top aerial EUVL mask characterization microscope described herein combines the output of a table-top 13.2 nm wavelength laser with state-of-the-art diffractive optics to render high quality images of periodic patterns on EUVL masks with acquisition times of less than 90 seconds. From these high quality images we have obtained the line-edge roughness and normalized intensity line slope of EUVL mask. This is significant because, using this table-top microscope, that emulates the imaging conditions of a 4×-demagnification stepper, it is possible to assess the mask quality and printability without the need to test it using an EUVL stepper.

2 Microscope setup

The compact full-field actinic microscope is schematically shown in Fig. 1. The illumination is provided by a table-top, optically pumped, collisional EUV laser that produces a pencil-like output consisting of pulses with a time duration of ~5 ps at a wavelength of 13.2 nm[13]. This laser has been recently operated at repetition rates of up to 2.5 Hz producing an average power of approximately 20 μW at 13.9 nm wavelength using a silver target [14]. To obtain the results reported here, the laser was operated at 1 Hz repetition rate to produce an average power of a several μW in the 13.2 nm line of nickel-like cadmium. The laser produces highly monochromatic ($\Delta\lambda/\lambda<1x10^{-4}$) light pulses with a divergence of 9±0.5 mrad FWHM parallel to the slab target and 10±0.5 mrad in the perpendicular direction. Figure 1 shows schematically the microscope geometry. The laser output is guided to a zone plate condenser that focuses the light onto the EUVL mask. A bright field image of the illuminated region is formed onto a EUV/SXR-sensitive array detector by an off-axis zone plate.

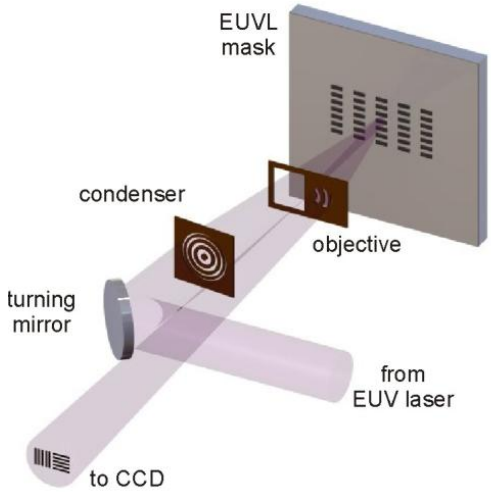

Fig. 1. Schematic of the aerial actinic mask inspection full-field microscope. The system is designed to image the mask with illumination conditions that are similar those of a 0.25 NA, 4×-demagnification EUVL stepper.

The microscope is designed to illuminate the mask as it is done using a 0.25 NA, 4×-demagnification EUVL stepper to correctly evaluate the printability of patterns and defects. This configuration is achieved by selecting the angle of incidence of the illumination onto the mask to be 6 degrees and by tailoring the numerical apertures of the condenser and objective lenses. The condenser zone plate is shown in Fig. 2. The zone plate has a 5 mm diameter, 12000 zones and an outer zone-width of 100 nm, resulting in a numerical aperture (NA) of 0.066 and a focal distance of 38 mm. The diameter of the condenser ensures complete collection of the laser beam.

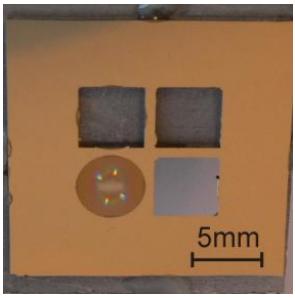

Fig. 2. Photograph of the condenser zone plate. The open window next to the zone plate allows the image formed by the objective to reach the CCD detector.

A scanning electron microscope (SEM) image of the objective zone plate is shown in Fig. 3. The off-axis zone plate was designed from a regular 'parent'

zone plate (dashed line in the figure) with a diameter of 0.33 mm and an outer zone width of 40 nm onto which a smaller pupil is overlapped. The pupil, ~0.12 mm in diameter, is placed ~0.10 mm from the axis of the parent zone plate, tangent to its edge. This pupil defines the numerical aperture of the objective, 0.0625NA, while the focal distance, 1 mm is defined by the outer zone width of the parent zone plate. A rectangular window next to the off-axis objective zone plate is left uncoated. This window allows transmission of the condenser illumination to the mask at an angle of incidence of 6 degrees. The reflected light from the mask efficiently fills the pupil of the off-axis zone. The off-axis zone plate produces a near-normal image of the mask onto the EUV/SXR sensitive array detector.

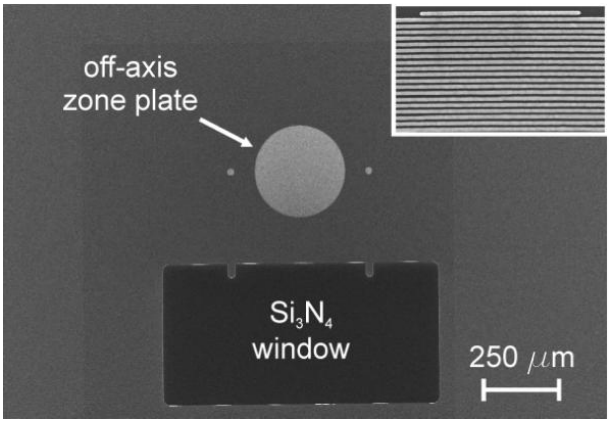

Fig. 3. SEM image of the off-axis zone plate. The Si_3N_4 window provides a path for the illumination from the condenser to reach the EUVL mask. The off axis zone plate produces a near-normal image of the mask onto an EUV sensitive CCD. The insert shows the 40 nm outer zones of the zone plate.

Both zone plates were produced by e-beam lithography on 100 nm thick Si_3N_4 membranes. To increase the efficiency of the microscope the membrane of the objective was further thinned down to 40 nm.

Two samples were available for imaging. One sample consisted of a Mo/Si multilayer coated 500 μm thick Si wafer onto which an absorption test pattern was written. The Mo/Si multilayer was centred at 13.5 nm wavelength to properly simulate an EUVL mask. The sample contained periodic features of different size, from 300 nm half-pitch down to 80 nm half-pitch. Vertical and horizontal 1:1 and 2:1 lines and elbow absorption patterns were available at each half-pitch. The latter are especially useful in characterizing the degree of aberration present in the EUV images since they provide information in two orthogonal directions within the same field-of-view.

The second sample was an EUVL mask from GLOBALFOUNDRIES, Inc. It consisted of a Mo/Si coated, 6×6 in^2, low thermal expansion glass that

contained a series of dark-field and bright-field regions with a variety of test features and extended line patterns. The smallest grating available had a half-pitch of 125 nm.

3 Results

The resolving power of the microscope was evaluated by analyzing the modulation in intensity of EUV images of grating patterns of decreasing half-pitch. Figure 4 shows EUV images of the 140 nm, 120 nm, 100 nm, and 80 nm half-pitch elbow structures along with their respective intensity cross-sections (lineouts). These images were obtained using exposure times of 20 seconds with the laser operating at a repetition rate of 5 Hz. The images have a field of view of ~5×5 μm^2, limited by the size of the illumination beam. They were taken with a magnification of ~610× at which each pixel on the CCD corresponds to 22 nm in the sample plane. This magnification was selected to allow approximately 8 pixels per period in the smallest structures available. The intensity cross-sections, obtained by averaging the intensity of 5 consecutive rows of pixels, were measured for the horizontal and vertical lines. The high modulation obtained for the 80 nm half-pitch structure indicates that the spatial resolution of the system is better than 80 nm.

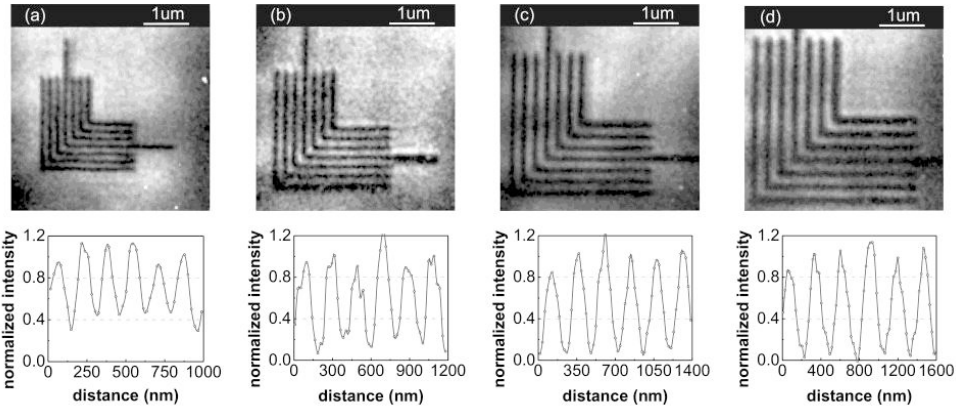

Fig. 4. EUV images and corresponding intensity cross-sections of elbow patterns of 80 nm, 100 nm, 120 nm, and 140 nm half pitch. The high modulation in the intensity cross section of the 880 nm half-pitch elbow indicates that the features are fully resolved.

The Rayleigh resolution of the microscope was independently assessed by analysing the EUV images of Fig. 4 with a correlation method that performs a global assessment of an image and returns a value for the image resolution [15]. The image resolution is obtained from the correlation between a raw SXR image and a series of computer generated templates with decreasing resolution. The templates are constructed by applying different Gaussian filters to a master binary template constructed from the original image. The only required input parameter for the analysis is the microscope's magnification which determines the size of the pixel in the image. To relate the image resolution to the Rayleigh resolution, the method uses a computer generated image of two circular objects separated a distance corresponding to the first minimum of the Airy function as used in the Rayleigh resolution. A value of half-pitch Rayleigh resolution of 53±10 nm was obtained. It is important to point out that this result further assumes incoherent illumination. As it will be shown below, the illumination of the microscope has some degree of coherence.

The Modulation Transfer Function (MTF) of the microscope, which gives a measure of the ability of the microscope for transferring different spatial frequencies, was constructed using the intensity modulation data obtained from the images of Fig. 4 along with the results correlation test. As shown in Fig. 5, the modulation starts to roll off for structures smaller than 120 nm, in agreement with simulations for a 0.0625 NA objective under partially coherent illumination. The dashed line was added to guide the eye.

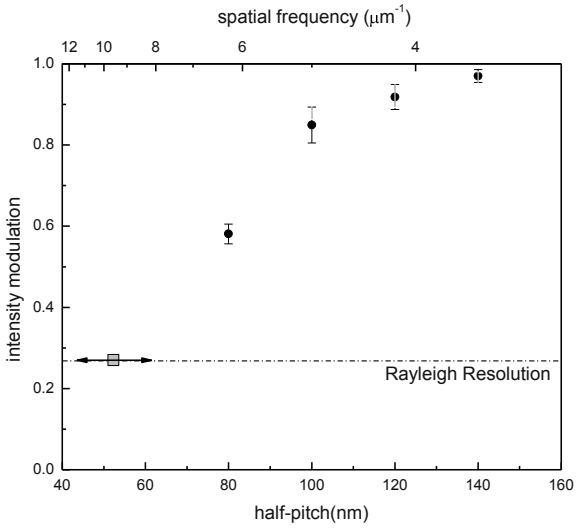

Fig. 5. Modulation Transfer Function for the 13.2 nm wavelength reflection microscope. The MTF was constructed using the line-outs from the images of Fig. 4 (full circles). The results of the correlation method are shown by the square.

The spatial coherence of the microscope was evaluated using a through-focus analysis. For a partially coherent system intensity maxima appear at defocus distances corresponding to the Talbot distances, given by $n \times a^2/\lambda$, where a is the period of the grating; λ, the wavelength of illumination; and n, an integer. Figure 6 shows the intensity modulation for EUV images of a 200 nm half-pitch grating at different defocus distances. The occurrence of secondary maxima indicates that the microscope operates in the partially coherent regime. Comparisons with simulated data using SPLAT [16] indicate that the coherence value, m, of the microscope is approximately 0.25. The coherence parameter can easily be increased to ~0.5, the typical value in an EUVL stepper, by moving the turning mirror (Fig. 1) from shot to shot during image acquisition.

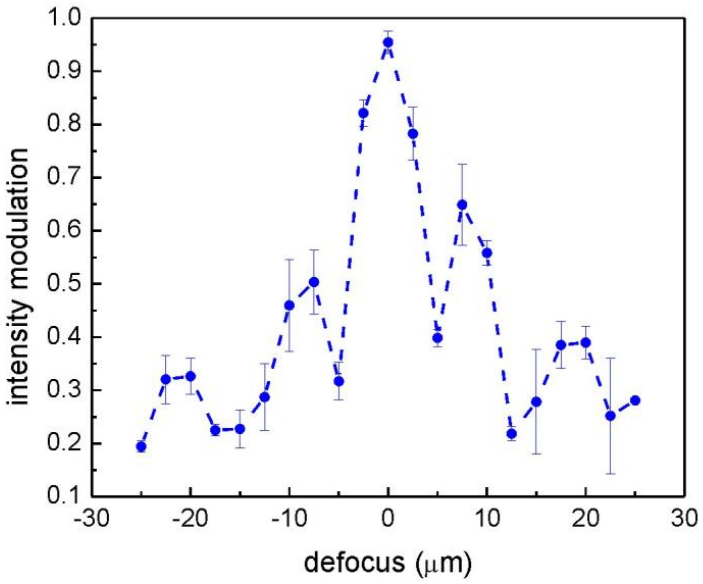

Fig. 6. Intensity modulation versus defocusing distance. The through-focus data indicates that the microscope has a partial coherence parameter, m, of 0.25.

Analysis of the masks print quality requires images, such as those shown in Fig. 7. The images were obtained with an exposure time of 90 seconds with the laser operating at 1 Hz. The condenser was slightly moved from shot to shot during acquisition to increase the illumination uniformity. The images show high illumination uniformity with no discernable aberrations.

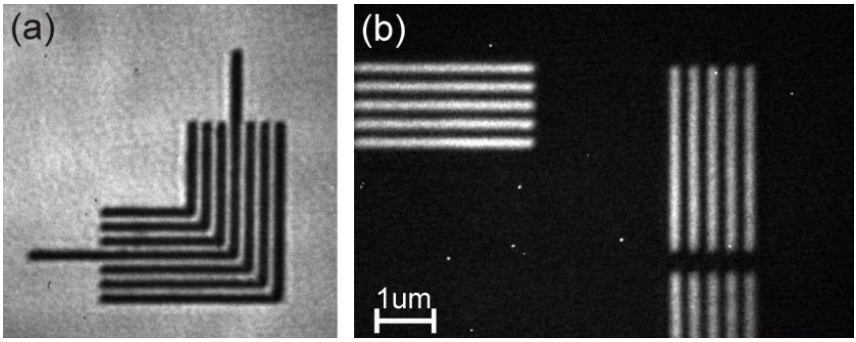

Fig. 7. EUV image of a) a 180 nm half-pitch elbow structure, b) 200 nm half-pitch lines on a GLOBALFOUDRIES mask.

The microscope was used to evaluate the quality of the absorber patterns on the GLOBALFOUNDRIES mask through measurements of line-edge roughness (LER) and normalized image log-slope (NILS). Normalized image log-slope (NILS), measured as the derivative of the logarithm of the image's intensity, assesses the steepness of the intensity slope along the imaged features. Line edge roughness (LER) is a statistical measure of the variation of a feature's edge along the feature's extent and is typically expressed as three times the standard deviation, $3\sigma_{dev}$. Values of LER below 10% of the critical dimension (CD) of the features are considered acceptable. Figure 8 shows the analysis of NILS and LER for a 175 nm half-pitch grating. To obtain these parameters, the image (Fig. 8.a) was normalized in intensity and a threshold value corresponding to the normalized intensity value for which the lines and spaces have a 1:1 ratio was obtained (Fig. 8.b). In this case, the threshold value was ~0.4. A NILS value of 3.58 was obtained by averaging the NILS measured at the intensity threshold for each slope of the average intensity cross-section. LER for each line was measured by evaluating the magnification-corrected location of the occurrence of the intensity threshold for each pixel row of the images (Fig. 8.c). The standard deviation of these values was subsequently calculated for each edge. The measurements were performed across the central 1 μm region of the grating. For the 175 nm half-pitch grating the LER value, 13.55, is below 10% of CD (LER/CD < 0.1).[5]

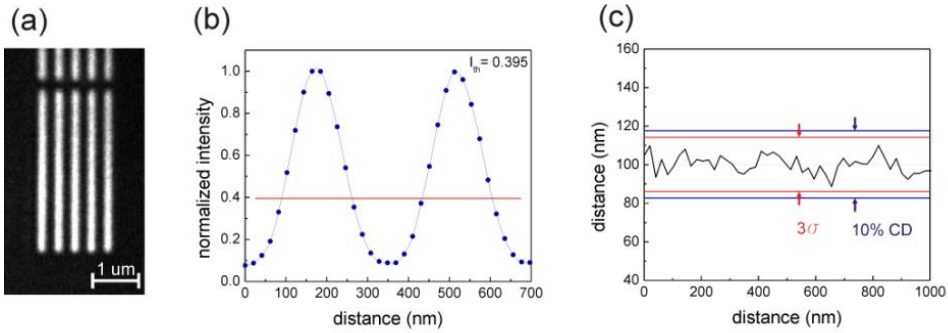

Fig. 8. LER and NILS measurements on 175 nm half-pitch lines

4 Summary

We have demonstrated a compact, actinic aerial image microscope based on EUV/SXR laser illumination capable of obtaining high quality images for the evaluation of EUVL masks. The microscope uses a 13.2 nm wavelength, table-top EUV laser and diffractive optics in a configuration designed to operate under the same illumination condition of a 0.025 NA, 4×-demagnification, EUVL stepper ensuring accurate evaluation of the printability of patterns and defects. The system, can obtain images with a spatial resolution of approximately 55 nm using exposure times of 5 to 90 seconds. Due to the high uniformity and intensity of the illumination, information on key parameters of mask pattern printability such as NILS and LER can readily be obtained from the images. The performance of the microscope, combined with its small footprint make it ideal for mask characterization in industrial settings. Also, the flexible optical design will allow extension to higher numerical apertures as steppers with increasing NA become available. The results presented, and the flexibility of the microscope to extend to smaller technological nodes, opens the path to the realization of practical standalone EUVL metrology tools for HVM.

This work was supported by the Engineering Research Center Program of the National Science Foundation under NSF Award Number EEC-0310717.

5 References

1. C.A. Brewer, F. Brizuela, P. Wachulak, D.H. Martz, W. Chao, E.H. Anderson, D.T. Attwood, A.V. Vinogradov, I.A. Artyukov, A.G.

Ponomareko, V.V. Kondratenko, M.C. Marconi, J.J. Rocca, and C.S. Menonil, *Single-shot extreme ultraviolet laser imaging of nanostructures with wavelength resolution.* Optics Letters, 2008. **33**(5): p. 518-520.

2. P.W. Wachulak, R.A. Bartels, M.C. Marconi, C.S. Menoni, J.J. Rocca, Y. Lu, and B. Parkinson, *Sub 400 nm spatial resolution extreme ultraviolet holography with a table top laser.* Optics Express, 2006. **14**(21): p. 9636-9642.
3. P.W. Wachulak, M.G. Capeluto, M.C. Marconi, C.S. Menoni, and J.J. Rocca, *Patterning of nano-scale arrays by table-top extreme ultraviolet laser interferometric lithography.* Optics Express, 2007. **15**(6): p. 3465-3469.
4. S. Heinbuch, F. Dong, J.J. Rocca, and E.R. Bernstein, *Single photon ionization of hydrogen bonded clusters with a soft x-ray laser: (HCOOH)(x) and (HCOOH)(y)(H2O)(z).* Journal of Chemical Physics, 2007. **126**(24).
5. F. Brizuela, S. Carbajo, A. Sakdinawat, D. Alessi, D.H. Martz, Y. Wang, B. Luther, K.A. Goldberg, I. Mochi, D.T. Attwood, B. La Fontaine, J.J. Rocca, and C.S. Menoni, *Extreme ultraviolet laser-based table-top aerial image metrology of lithographic masks.* Optics Express, 2010. **18**(14): p. 14467-14473.
6. F. Brizuela, G. Vaschenko, C. Brewer, M. Grisham, C.S. Menoni, M.C. Marconi, J.J. Rocca, W. Chao, J.A. Liddle, E.H. Anderson, D.T. Attwood, A.V. Vinogradov, I.A. Artioukov, Y.P. Pershyn, and V.V. Kondratenko, *Reflection mode imaging with nanoscale resolution using a compact extreme ultraviolet laser.* Optics Express, 2005. **13**(11): p. 3983-3988.
7. F. Brizuela, Y. Wang, C.A. Brewer, F. Pedaci, W. Chao, E.H. Anderson, Y. Liu, K.A. Goldberg, P. Naulleau, P. Wachulak, M.C. Marconi, D.T. Attwood, J.J. Rocca, and C.S. Menoni, *Microscopy of extreme ultraviolet lithography masks with 13.2 nm tabletop laser illumination.* Optics Letters, 2009. **34**(3): p. 271-273.
8. G. Vaschenko, C. Brewer, F. Brizuela, Y. Wang, M.A. Larotonda, B.M. Luther, M.C. Marconi, J.J. Rocca, and C.S. Menoni, *Sub-38 nm resolution tabletop microscopy with 13 nm wavelength laser light.* Optics Letters, 2006. **31**(9): p. 1214-1216.
9. A. Barty, Y.W. Liu, E. Gullikson, J.S. Taylor, and O. Wood, *Actinic inspection of multilayer defects on EUV masks*, in *Emerging Lithographic Technologies IX, Pts 1 and 2*, R.S. Mackay, Editor. 2005. p. 651-659.
10. K.A. Goldberg, A. Barty, Y.W. Liu, P. Kearney, Y. Tezuka, T. Terasawa, J.S. Taylor, H.S. Han, and O.R. Wood, *Actinic inspection of extreme ultraviolet programed multilayer defects and cross-*

comparison measurements. Journal of Vacuum Science & Technology B, 2006. **24** (6): p. 2824-2828.

11. K.A. Goldberg, P.P. Naulleau, A. Barty, S.B. Rekawa, C.D. Kemp, R.F. Gunion, F. Salmassi, E.M. Gullikson, E.H. Anderson, and H.S. Han, *Performance of actinic EUVL mask imaging using a zoneplate microscope - art. no. 67305E*, in *Photomask Technology 2007, Pts 1-3*, R.J. Naber, Editor. 2007. p. E7305-E7305.
12. K.A. Goldberg, P. Naulleau, I. Mochi, E.H. Anderson, S.B. Rekawa, C.D. Kemp, R.F. Gunion, H.S. Han, and S. Huh. *Actinic extreme ultraviolet mask inspection beyond 0.25 numerical aperture*. 20082220-2224.
13. J.J. Rocca, Y. Wang, M.A. Larotonda, B.M. Luther, M. Berrill, and D. Alessi, *Saturated 13.2 nm high-repetition-rate laser in nickellike cadmium.* Optics Letters, 2005. **30**(19): p. 2581-2583.
14. D.H. Martz, D. Alessi, B.M. Luther, Y. Wang, D. Kemp, M. Berrill, and J.J. Rocca, *High-energy 13.9 nm table-top soft-x-ray laser at 2.5 Hz repetition rate excited by a slab-pumped Ti:sapphire laser.* Optics Letters. **35**(10): p. 1632-1634.
15. P.W. Wachulak, C.A. Brewer, F. Brizuela, C.S. Menoni, W. Chao, E.H. Anderson, R.A. Bartels, J.J. Rocca, and M.C. Marconi. *Analysis of extreme ultraviolet microscopy images of patterned nanostructures based on a correlation method*. 2008B20-B26.
16. *SPLAT*. -Available from: http://cuervo2.eecs.berkeley.edu/.